



UNIVERSITEIT VAN PRETORIA
UNIVERSITY OF PRETORIA
YUNIBESITHI YA PRETORIA

Thermal Performance of an Air Channel with Cylindrical Cross-bars

by

Frans Jozef Jacobus Coetzee

Submitted in partial fulfillment of the requirements of the degree

Master of Engineering

In the Faculty of Mechanical and Aeronautical Engineering

University of Pretoria

Supervised by Dr. G.I. Mahmood

July 2021

Abstract

Title: Thermal Performance of an Air Channel with Cylindrical Cross-bars

Supervisor: Dr. G.I. Mahmood

Department: Mechanical and Aeronautical Engineering

Degree: Master of Engineering (Mechanical Engineering)

Heat exchangers are used in a wide variety of industrial applications. Augmentation of heat transfer can realize a reduction in heat transfer size and increase the effectiveness and efficiency of heat exchangers. Heat transfer can be enhanced with various methods where the turbulence of the fluid flow is enhanced: by adding ribs, grooves or steps to the channel wall, using helical inserts, or by adding bluff bodies in the channel flow. By using these methods, there is also an increase in pressure drop penalty and larger pumping power is required to achieve the same flow rate. Circular cylindrical bluff bodies have been found to have smaller drag coefficients than square, rectangular or triangular cylindrical bluff bodies in the channel flow.

Heat transfer and pressure drop experimental tests were done for eight different circular cylindrical cross-bar arrays at 15 different Reynolds numbers, in the range of 640 to 12 500. Eight different cross-bar configurations were tested: the cylinder diameter to pitch ratios were, $d/p = 0.025$, $d/p = 0.05$, $d/p = 0.1$ and $d/p = 0.2$, and the angle to the flow direction, was $\theta = 90^\circ$ and $\theta = 45^\circ$ for each of the four different diameter-to-pitch ratios.

Transient CFD simulations were done using Ansys fluent for $d/p = 0.05$ and $d/p = 0.2$, for $\theta = 90^\circ$, at Reynolds numbers 920 and 9 700, to analyze the secondary flow structures in the wake of the cylinders, partly responsible for the heat transfer and pressure drop increase in the channel flow in comparison to the smooth channel. The k- Ω shear stress transport (SST) model was used for the simulations. A mesh dependence study was done for spatial discretization, temporal discretization and validated against the experimental setup.

The pressure drop gradient was found from the test data for the hydraulically developed part of the test section to calculate the friction factors. With an increase in Reynolds number, the friction factors decreased until reaching an asymptotic value for all the cross-bar configurations. For $\theta = 90^\circ$ the friction factors were larger than for $\theta = 45^\circ$ for the same d/p ratio and Reynolds number. With an increase in d/p , the friction factors increased. The largest measured friction factor was $f = 0.3$, for configuration $d/p = 0.2$, $\theta = 90^\circ$, at $Re = 640$ and the smallest measured friction factor $f = 0.02$, for $d/p = 0.025$, $\theta = 45^\circ$, at $Re = 12\ 500$. The friction factor ratio was then used to quantify the pressure penalty for using cylindrical cross-bars in the channel flow to enhance heat transfer. The maximum friction factor ratio, $f/f_0 = 16.7$ occurred at $Re = 9\ 700$, for $d/p = 0.2$, $\theta = 90^\circ$ and the minimum friction factor ratio, $f/f_0 = 2.1$, at $Re = 640$, for $d/p = 0.025$, $\theta = 45^\circ$.

The average Nusselt numbers were then calculated using the spatial integral average of the local Nusselt numbers. With an increase in Reynolds number, there was an increase in the average Nusselt number for all the cylindrical cross-bar configurations. For larger d/p ratios and $\theta = 90^\circ$ cases, the average Nusselt numbers were larger than for smaller d/p ratios and $\theta = 45^\circ$. The largest average Nusselt number was $Nu_{avg} = 66.3$, at $Re = 9\ 700$ for $d/p = 0.2$, $\theta = 90^\circ$ and the smallest average Nusselt number, $Nu_{avg} = 8.7$, at $Re = 640$ for $d/p = 0.025$, $\theta = 45^\circ$. The Nusselt number ratio could then be used

to quantify the heat transfer enhancement of the cylindrical cross-bar channel to that of the smooth channel, where the largest Nusselt number ratio was, $Nu_{avg}/Nu_{0,avg} = 3.3$, for $d/p = 0.2$, $\theta = 90^\circ$, at $Re = 3\ 000$ and the smallest $Nu_{avg}/Nu_{0,avg} = 1.1$, for $d/p = 0.025$, $\theta = 45^\circ$, at $Re = 640$.

The CFD results concluded that the pressure drop increase and heat transfer enhancement were caused by the flow acceleration, flow separation, eddy formation, vorticity increase, and boundary layer deformation next to and behind the cylinders. The Strouhal number for the larger d/p ratios suggested that the unsteadiness in the flow is higher for the cylinder arrays with a larger diameter, increasing both the heat transfer enhancement and friction factor in comparison with the smaller diameter cylinder arrays.

Finally, the thermal performance coefficients could be calculated by using the friction factor ratios and Nusselt number ratios. The thermal performance coefficient combines the effects of the heat transfer and pressure penalty increase. The thermal performance coefficients increased from $Re = 640$ until $Re = 3\ 000$ after which it decreased with an increase in Reynolds number. This is because the pressure penalty starts to outweigh the heat transfer increase caused by the turbulators. The largest thermal performance coefficient was $\eta = 1.6$, for $d/p = 0.025$, $\theta = 45^\circ$, at $Re = 3\ 000$, and the lowest, $\eta = 0.79$, for $d/p = 0.05$, $\theta = 90^\circ$, at $Re = 640$.

Acknowledgements

I would like to express my gratitude to the following people for their help and support:

- Dr. Gazi Mahmood, my supervisor, for his guidance during this project
- Chris Govender and Donald Keetse in the wind tunnel labs
- The University of Pretoria for the infrastructure to conduct research
- And to my parents and friends for their support

Table of Contents

Abstract.....	i
Acknowledgements.....	iii
Table of Figures.....	viii
List of Tables	xix
Nomenclature	xx
1. Introduction	1
1.1. Background	1
1.2. Problem statement	2
1.3. Aim	2
1.4. Objectives.....	2
1.5. Scope.....	3
1.6. Overview of dissertation structure	3
2. Literature Review	5
2.1. Introduction	5
2.2. Dimensionless parameters.....	5
2.2.1. Reynolds number	5
2.2.2. Friction factor.....	5
2.2.3. Nusselt number	5
2.2.4. Thermal performance coefficient	6
2.3. Nusselt number and friction factor correlations for smooth channel.....	6
2.4. Previously done research.....	9
2.5. CFD modelling	11
2.6. Summary	12
3. Experimental Set-up and Data Reduction.....	13
3.1. Introduction	13
3.2. Experimental test-setup.....	13
3.3. Cylindrical cross-bar configurations.....	14
3.4. Test section	16
3.4.1. Heat transfer tests	16
3.4.2. Pressure drop tests	17
3.5. Instrumentation	18
3.5.1. Pressure transducers.....	18
3.5.2. Orifice plates	18
3.5.3. Control and data logging.....	19

3.6.	Data reduction	19
3.7.	Experimental procedure	20
3.8.	Experimental test matrix.....	21
3.9.	Uncertainty analysis.....	22
3.10.	Repeatability	27
3.11.	Summary	30
4.	Baseline Measurements without Inserts	31
4.1.	Introduction	31
4.2.	Local Nusselt numbers.....	31
4.3.	Average Nusselt numbers	33
4.4.	Friction Factors	35
4.5.	Summary and conclusions	38
5.	Numerical Study.....	39
5.1.	Introduction	39
5.2.	Domain and mesh structure	39
5.3.	Mathematical model.....	40
5.4.	Boundary conditions	41
5.5.	Mesh validation.....	42
5.6.	CFD to experimental validation	43
5.6.1.	Pressure profile on rods.....	43
5.6.2.	High-resolution wall pressure	46
5.7.	CFD results	47
5.8.	Summary and conclusions	54
6.	Experimental Results	55
6.1.	Introduction	55
6.2.	Local Nusselt number.....	55
6.3.	Average Nusselt number.....	60
6.4.	Nusselt number ratio	64
6.5.	Friction factor.....	66
6.6.	Friction factor ratio	69
6.7.	Thermal performance	71
6.8.	Summary and conclusions	74
7.	Summary, Conclusion and Recommendations	75
7.1.	Summary	75
7.2.	Conclusion.....	76
7.3.	Recommendations	77

Appendix A : Finding the Reynolds Number	83
Appendix B : Calibration of Thermocouples	85
B.1. Introduction	85
B.2. Calibration process.....	85
Appendix C : Calibration of Pressure Transducers.....	86
C.1. Introduction	86
C.2. Calibration procedure	86
C.3. Calibration figures of pressure transducers.....	86
Appendix D : Uncertainty Analysis.....	88
D.1. Introduction	88
D.2. Formulation.....	88
D.3. Sensor calibration uncertainty.....	88
D.4. Fluid properties uncertainty	89
D.5. Test section geometry uncertainty	90
D.6. Reynolds number uncertainty	90
D.7. Nusselt number uncertainty	91
D.8. Friction factor uncertainty	93
D.9. Thermal performance coefficient uncertainty.....	93
D.10. Sample uncertainty calculation.....	94
D.10.1 Thermocouples	94
D.10.2 Pressure transducers.....	95
D.10.3 Fluid density	96
D.10.4 Hydraulic diameter.....	96
D.10.5 Cross-sectional channel area	96
D.10.6 Mass flow rate.....	97
D.10.7 Flow mean velocity	97
D.10.8 Reynolds number	97
D.10.9 Wall heat input.....	98
D.10.10 Heat flux.....	98
D.10.11 Local mean temperature.....	98
D.10.12 Nusselt number.....	99
D.10.13 Friction factor.....	99
D.10.14 Thermal performance coefficient	100
Appendix E : Local Nusselt Numbers	101
Appendix F : Temperature Data.....	106
F.1. Temperature data: smooth channel	106

F.2.	Temperature data: $d/p = 0.05$, 90° orientation to the flow direction	111
F.3.	Temperature data: $d/p = 0.05$, 45° orientation to the flow direction	116
F.4.	Temperature data: $d/p = 0.025$, 90° orientation to the flow direction	121
F.5.	Temperature data: $d/p = 0.025$, 45° orientation to the flow direction	126
F.6.	Temperature data: $d/p = 0.2$, 90° orientation to the flow direction	131
F.7.	Temperature data: $d/p = 0.2$, 45° orientation to the flow direction	135
F.8.	Temperature data: $d/p = 0.1$, 90° orientation to the flow direction	139
F.9.	Temperature data: $d/p = 0.1$, 45° orientation to the flow direction	144
Appendix G : Pressure Data		150
G.1.	Pressure data for smooth channel.....	150
G.2.	Pressure data: $d/p = 0.05$, 90° orientation to the flow direction	155
G.3.	Pressure data: $d/p = 0.05$, 45° orientation to the flow direction	160
G.4.	Pressure data: $d/p = 0.025$, 90° orientation to the flow direction	165
G.5.	Pressure data: $d/p = 0.025$, 45° orientation to the flow direction	170
G.6.	Pressure data: $d/p = 0.2$, 90° orientation to the flow direction	175
G.7.	Pressure data: $d/p = 0.2$, 45° orientation to the flow direction	179
G.8.	Pressure data: $d/p = 0.1$, 90° orientation to the flow direction	184
G.9.	Pressure data: $d/p = 0.1$, 45° orientation to the flow direction	189

Table of Figures

Figure 1.1: Examples of turbulators: (a) Bluff bodies. (b) Ribs. (c) Grooves. (d) Pin fins. (e) Twisted helical tape.....	1
Figure 2.1: Thermal performance coefficient, Li et al. [26].....	9
Figure 2.2: Thermal performance coefficient, Skullong et al. [29].....	10
Figure 3.1: Schematic diagram of the experimental test set-up.	13
Figure 3.2: Picture of the experimental test setup.....	14
Figure 3.3: (a) Partial picture of cylindrical cross-bar array $d/p = 0.2$, $\theta = 45^\circ$. (b) Cylinder schematic.	14
Figure 3.4: Cylindrical geometries of (a) $d = 1$ mm, staggered rods. (i) $\theta = 45^\circ$, $d/p = 0.025$. (ii) $\theta = 90^\circ$, $d/p = 0.025$. (iii) $\theta = 45^\circ$, $d/p = 0.05$. (d) $\theta = 90^\circ$, $d/p = 0.05$. (b) $d = 2$ mm, in-line rods. (i) $\theta = 45^\circ$, $d/p = 0.1$. (ii) $\theta = 90^\circ$, $d/p = 0.1$. (iii) $\theta = 45^\circ$, $d/p = 0.2$. (d) $\theta = 90^\circ$, $d/p = 0.2$	15
Figure 3.5: Heat transfer test setup.....	16
Figure 3.6: Thermocouples. (a) Wall temperature thermocouple locations. (b) Heat loss thermocouple locations. (c) Detail of thermocouple installation.	17
Figure 3.7: Section view of pressure tap wall with the location of pressure taps on the test section wall.....	18
Figure 3.8: Orifice plate geometry.....	18
Figure 3.9: Temperature change with time at $x/H = 50$ and $Re = 920$	21
Figure 3.10: Flow rate uncertainty.	23
Figure 3.11: Nusselt number uncertainty, $\theta = 90^\circ$	24
Figure 3.12: Nusselt number uncertainty, $\theta = 45^\circ$	24
Figure 3.13: Friction factor uncertainty, $\theta = 90^\circ$	25
Figure 3.14: Friction factor uncertainty, $\theta = 45^\circ$	25
Figure 3.15: Thermal performance coefficient uncertainty, $\theta = 90^\circ$	26
Figure 3.16: Thermal performance coefficient uncertainty, $\theta = 90^\circ$	26
Figure 3.17: Wall and mean local air temperature data of $d/p = 0.025$, $\theta = 90^\circ$ at $Re = 9\ 700$ plotted with repeated test data.	28
Figure 3.18: Local Nusselt number data of $d/p = 0.025$, $\theta = 90^\circ$ at $Re = 9\ 700$ plotted with repeated test data.	28
Figure 3.19: Pressure data of $d/p = 0.025$, $\theta = 90^\circ$ at $Re = 9\ 700$ plotted with repeated test data.	30
Figure 4.1: Local Nusselt number plotted against x/H at $Re = 920$ for the smooth channel.	31
Figure 4.2: Local Nusselt number plotted against x/H at $Re = 4\ 000$ for the smooth channel.	32
Figure 4.3: Local Nusselt number plotted against x/H at $Re = 10\ 500$ for the smooth channel.	32
Figure 4.4: Average Nusselt numbers for the smooth channel with laminar flow.....	33
Figure 4.5: Average Nusselt numbers for the smooth channel with transitional flow.	33
Figure 4.6: Average Nusselt numbers for the smooth channel with turbulent flow.....	34
Figure 4.7: Laminar friction factor for the smooth channel plotted with correlations.	35
Figure 4.8: Transitional friction factor for smooth channel plotted with correlations.	36
Figure 4.9: Turbulent friction factor for smooth channel plotted with correlations.	37
Figure 5.1: Geometry and mesh detail of (a) $d/p = 0.05$, $\theta = 90^\circ$. (b) $d/p = 0.2$, $\theta = 90^\circ$	40
Figure 5.2: Parameter used to estimate grid convergence.	42
Figure 5.3: Grid convergence of $d/p = 0.05$, $\theta = 90^\circ$	42
Figure 5.4: Grid convergence of $d/p = 0.2$, $\theta = 90^\circ$	43
Figure 5.5: Schematic diagram of the pressure profile test setup.	43

Figure 5.6: Stagnation point, Cengel and Ghajar [22].....	44
Figure 5.7: Flow separation points, $d/p = 0.05$, $\theta = 90^\circ$	44
Figure 5.8: ΔP_α , $\theta = 90^\circ$, $d/p = 0.05$, $Re = 9\ 700$	45
Figure 5.9: ΔP_α , $\theta = 90^\circ$, $d/p = 0.2$, $Re = 9\ 700$	45
Figure 5.10: Fine spacing between pressure taps in the channel wall for measurements to validate CFD results.....	46
Figure 5.11: ΔP for $d/p = 0.05$, $\theta = 90^\circ$ at $Re = 9\ 700$	47
Figure 5.12: ΔP for $d/p = 0.2$, $\theta = 90^\circ$, at $Re = 9\ 700$	47
Figure 5.13: ω^* and streamlines for $Re = 920$, $\theta = 90^\circ$. (a) $d/p = 0.05$. (b) $d/p = 0.2$. (i) $t^* = 0.16$. (ii) $t^* = 0.32$. (iii) $t^* = 0.48$. (iv) $t^* = 0.64$. (v) $t^* = 0.8$. (vi) $t^* = 0.94$	50
Figure 5.14: v_x^* for $Re = 920$, $\theta = 90^\circ$. (a) $d/p = 0.05$. (b) $d/p = 0.2$. (i) $t^* = 0.16$. (ii) $t^* = 0.32$. (iii) $t^* = 0.48$. (iv) $t^* = 0.64$. (v) $t^* = 0.8$. (vi) $t^* = 0.94$	51
Figure 5.15: ω^* and streamlines for $Re = 9\ 700$, $\theta = 90^\circ$. (a) $d/p = 0.05$. (b) $d/p = 0.2$. (i) $t^* = 0.16$. (ii) $t^* = 0.32$. (iii) $t^* = 0.48$. (iv) $t^* = 0.64$. (v) $t^* = 0.8$. (vi) $t^* = 0.94$	52
Figure 5.16: v_x^* for $Re = 9\ 700$, $\theta = 90^\circ$. (a) $d/p = 0.05$. (b) $d/p = 0.2$. (i) $t^* = 0.16$. (ii) $t^* = 0.32$. (iii) $t^* = 0.48$. (iv) $t^* = 0.64$. (v) $t^* = 0.8$. (vi) $t^* = 0.94$	53
Figure 6.1: Temperature plotted against x/H at $Re = 9\ 700$ for setup: $d/p = 0.025$, $\theta = 90^\circ$. Cylinders are arranged in staggered array.....	55
Figure 6.2: Local Nusselt number plotted against x/H coordinate for array: $d/p = 0.025$, $\theta = 90^\circ$ at $Re = 920$, $Re = 4\ 000$ and $Re = 91700$. Cylinders are arranged in staggered array.	56
Figure 6.3: Local Nusselt number plotted against x/H coordinate for array: $d/p = 0.025$, $\theta = 45^\circ$ at $Re = 920$, $Re = 4\ 000$ and $Re = 91700$. Cylinders are arranged in staggered array.	57
Figure 6.4: Local Nusselt number plotted against x/H coordinate for array: $d/p = 0.05$, $\theta = 90^\circ$ at $Re = 920$, $Re = 4\ 000$ and $Re = 91700$. Cylinders are arranged in staggered array.	57
Figure 6.5: Local Nusselt number plotted against x/H coordinate for array: $d/p = 0.05$, $\theta = 45^\circ$ at $Re = 920$, $Re = 4\ 000$ and $Re = 91700$. Cylinders are arranged in staggered array.	58
Figure 6.6: Local Nusselt number plotted against x/H coordinate for array: $d/p = 0.1$, $\theta = 90^\circ$ at $Re = 920$, $Re = 4\ 000$ and $Re = 91700$. Cylinders are arranged in in-line array.	59
Figure 6.7: Local Nusselt number plotted against x/H coordinate for array: $d/p = 0.1$, $\theta = 45^\circ$ at $Re = 920$, $Re = 4\ 000$ and $Re = 91700$. Cylinders are arranged in in-line array.	59
Figure 6.8: Local Nusselt number plotted against x/H coordinate for array: $d/p = 0.2$, $\theta = 90^\circ$ at $Re = 920$, $Re = 4\ 000$ and $Re = 91700$. Cylinders are arranged in in-line array.	60
Figure 6.9: Local Nusselt number plotted against x/H coordinate for array: $d/p = 0.2$, $\theta = 45^\circ$ at $Re = 920$, $Re = 4\ 000$ and $Re = 91700$. Cylinders are arranged in in-line array.	60
Figure 6.10: Average Nusselt number plotted against Reynolds number for cylindrical arrays with $\theta = 90^\circ$ and the Eiamsa-ard and Promvonge [52] data for TR and TG, $PR = 6.6$	61
Figure 6.11: Average Nusselt number plotted against Reynolds number for cylindrical arrays with $\theta = 45^\circ$	62
Figure 6.12: Comparison between Nusselt number average and correlations, including all the correlations from Equation (6.1) to (6.8).....	63
Figure 6.13: Nusselt number ratio plotted against Reynolds number for with cylindrical arrays with $\theta = 90^\circ$	64
Figure 6.14: Nusselt number ratio plotted against Reynolds number for with cylindrical arrays with $\theta = 45^\circ$	64
Figure 6.15: Comparison between Nusselt number ratio and correlations, including all the correlations from Equation (6.9) to (6.16).	65
Figure 6.16: Static pressure plotted against the x coordinate at $Re = 9\ 700$ for setup: $d/p = 0.025$, 90° and $d/p = 0.025$, 45°	66

Figure 6.17 Friction factor plotted against Reynolds number for cylindrical arrays with $\theta = 90^\circ$ and the Eiamsa-ard and Promvonge [52] data for TR and TG, PR = 6.6.	67
Figure 6.18. Friction factor plotted against Reynolds number for cylindrical arrays with $\theta = 45^\circ$	68
Figure 6.19: Comparison between friction factor and correlations, including all the correlations from Equation (6.17) to (6.24).....	69
Figure 6.20: Friction factor ratio plotted against Reynolds number for with cylindrical arrays with $\theta = 90^\circ$	69
Figure 6.21: Friction factor ratio plotted against Reynolds number for with cylindrical arrays with $\theta = 45^\circ$	70
Figure 6.22: Comparison between friction factor ratio and correlations, including all the correlations from Equation (6.25) to (6.32).....	71
Figure 6.23: Thermal performance plotted against Reynolds number for with cylindrical arrays with $\theta = 90^\circ$ and the Eiamsa-ard and Promvonge [52] data for TR and TG, PR = 6.6.....	72
Figure 6.24: Thermal performance plotted against Reynolds number for with cylindrical arrays with $\theta = 45^\circ$	72
Figure 6.25: Comparison between friction factor ratio and correlations, including all the correlations from Equation (6.33) to (6.40).....	73
Figure B.1: Thermocouple calibration curve.	85
Figure C.1: Orifice pressure transducer calibration curves. (a) $3\,000 \leq Re \leq 7\,000$. (b) $7\,000 < Re \leq 10\,500$. (c) $12\,500 \geq Re$. (d) $Re < 2\,000$	86
Figure C.2: Channel pressure transducer calibration curves. (a) $0 \leq P \leq 125$. (b) $250 < P \leq 450$. (c) $450 < P < 1\,875$. (d) $1\,875 \leq P \leq 3\,750$. (e) $3\,750 \leq P \leq 7\,500$	87
Figure E.1: Local Nusselt numbers, Nu_x , for $d/p = 0.025$, $\theta = 45^\circ$	101
Figure E.2: Local Nusselt numbers, Nu_x , for $d/p = 0.025$, $\theta = 90^\circ$	102
Figure E.3: Local Nusselt numbers, Nu_x , for $d/p = 0.05$, $\theta = 45^\circ$	102
Figure E.4: Local Nusselt numbers, Nu_x , for $d/p = 0.05$, $\theta = 90^\circ$	103
Figure E.5: Local Nusselt numbers, Nu_x , for $d/p = 0.1$, $\theta = 45^\circ$	103
Figure E.6: Local Nusselt numbers, Nu_x , for $d/p = 0.1$, $\theta = 90^\circ$	104
Figure E.7: Local Nusselt numbers, Nu_x , for $d/p = 0.2$, $\theta = 45^\circ$	104
Figure E.8: Local Nusselt numbers, Nu_x , for $d/p = 0.2$, $\theta = 90^\circ$	105
Figure F.1. Temperature plotted against x/H at $Re = 640$ for smooth channel.....	106
Figure F.2. Temperature plotted against x/H at $Re = 920$ for smooth channel.....	106
Figure F.3. Temperature plotted against x/H at $Re = 1\,400$ for smooth channel.....	107
Figure F.4. Temperature plotted against x/H at $Re = 1\,800$ for smooth channel.....	107
Figure F.5. Temperature plotted against x/H at $Re = 3\,000$ for smooth channel.....	107
Figure F.6. Temperature plotted against x/H at $Re = 4\,000$ for smooth channel.....	108
Figure F.7. Temperature plotted against x/H at $Re = 5\,000$ for smooth channel.....	108
Figure F.8. Temperature plotted against x/H at $Re = 6\,000$ for smooth channel.....	108
Figure F.9. Temperature plotted against x/H at $Re = 7\,000$ for smooth channel.....	109
Figure F.10. Temperature plotted against x/H at $Re = 8\,000$ for smooth channel.....	109
Figure F.11. Temperature plotted against x/H at $Re = 9\,000$ for smooth channel.....	109
Figure F.12. Temperature plotted against x/H at $Re = 9\,700$ for smooth channel.....	110
Figure F.13. Temperature plotted against x/H at $Re = 10\,500$ for smooth channel.....	110
Figure F.14. Temperature plotted against x/H at $Re = 11\,500$ for smooth channel.....	110
Figure F.15. Temperature plotted against x/H at $Re = 12\,500$ for smooth channel.....	111
Figure F.16. Temperature plotted against x/H at $Re = 640$ for setup: $d/p = 0.05$, $\theta = 90^\circ$	111
Figure F.17. Temperature plotted against x/H at $Re = 920$ for setup: $d/p = 0.05$, $\theta = 90^\circ$	111
Figure F.18. Temperature plotted against x/H at $Re = 1\,400$ for setup: $d/p = 0.05$, $\theta = 90^\circ$	112

Figure F.115. Temperature plotted against x/H at $Re = 12\,500$ for setup: $d/p = 0.1$, $\theta = 90^\circ$	144
Figure F.116: Temperature plotted against x/H at $Re = 640$ for setup: $d/p = 0.1$, $\theta = 45^\circ$	144
Figure F.117: Temperature plotted against x/H at $Re = 920$ for setup: $d/p = 0.1$, $\theta = 45^\circ$	145
Figure F.118: Temperature plotted against x/H at $Re = 1\,400$ for setup: $d/p = 0.1$, $\theta = 45^\circ$	145
Figure F.119: Temperature plotted against x/H at $Re = 1\,800$ for setup: $d/p = 0.1$, $\theta = 45^\circ$	145
Figure F.120: Temperature plotted against x/H at $Re = 3\,000$ for setup: $d/p = 0.1$, $\theta = 45^\circ$	146
Figure F.121: Temperature plotted against x/H at $Re = 4\,000$ for setup: $d/p = 0.1$, $\theta = 45^\circ$	146
Figure F.122: Temperature plotted against x/H at $Re = 5\,000$ for setup: $d/p = 0.1$, $\theta = 45^\circ$	146
Figure F.123: Temperature plotted against x/H at $Re = 6\,000$ for setup: $d/p = 0.1$, $\theta = 45^\circ$	147
Figure F.124: Temperature plotted against x/H at $Re = 7\,000$ for setup: $d/p = 0.1$, $\theta = 45^\circ$	147
Figure F.125: Temperature plotted against x/H at $Re = 8\,000$ for setup: $d/p = 0.1$, $\theta = 45^\circ$	147
Figure F.126: Temperature plotted against x/H at $Re = 9\,000$ for setup: $d/p = 0.1$, $\theta = 45^\circ$	148
Figure F.127: Temperature plotted against x/H at $Re = 9\,700$ for setup: $d/p = 0.1$, $\theta = 45^\circ$	148
Figure F.128: Temperature plotted against x/H at $Re = 10\,500$ for setup: $d/p = 0.1$, $\theta = 45^\circ$	148
Figure F.129: Temperature plotted against x/H at $Re = 11\,500$ for setup: $d/p = 0.1$, $\theta = 45^\circ$	149
Figure G.1: Static pressure plotted against the x coordinate at $Re = 640$ for smooth channel.	150
Figure G.2: Static pressure plotted against the x coordinate at $Re = 920$ for smooth channel.	150
Figure G.3: Static pressure plotted against the x coordinate at $Re = 1\,400$ for smooth channel.	151
Figure G.4: Static pressure plotted against the x coordinate at $Re = 1\,800$ for smooth channel.	151
Figure G.5: Static pressure plotted against the x coordinate at $Re = 3\,000$ for smooth channel.	151
Figure G.6: Static pressure plotted against the x coordinate at $Re = 4\,000$ for smooth channel.	152
Figure G.7: Static pressure plotted against the x coordinate at $Re = 5\,000$ for smooth channel.	152
Figure G.8: Static pressure plotted against the x coordinate at $Re = 6\,000$ for smooth channel.	152
Figure G.9: Static pressure plotted against the x coordinate at $Re = 7\,000$ for smooth channel.	153
Figure G.10. Static pressure plotted against the x coordinate at $Re = 8\,000$ for smooth channel. ...	153
Figure G.11: Static pressure plotted against the x coordinate at $Re = 9\,000$ for smooth channel. ...	153
Figure G.12: Static pressure plotted against the x coordinate at $Re = 9\,700$ for smooth channel. ...	154
Figure G.13: Static pressure plotted against the x coordinate at $Re = 10\,500$ for smooth channel. .	154
Figure G.14: Static pressure plotted against the x coordinate at $Re = 11\,500$ for smooth channel. .	154
Figure G.15: Static pressure plotted against the x coordinate at $Re = 12\,500$ for smooth channel. .	155
Figure G.16: Static pressure plotted against the x coordinate at $Re = 640$ for setup: $d/p = 0.05$, 90° to the flow direction.....	155
Figure G.17: Static pressure plotted against the x coordinate at $Re = 920$ for setup: $d/p = 0.05$, 90° to the flow direction.....	155
Figure G.18: Static pressure plotted against the x coordinate at $Re = 1\,400$ for setup: $d/p = 0.05$, 90° to the flow direction.	156
Figure G.19: Static pressure plotted against the x coordinate at $Re = 1\,800$ for setup: $d/p = 0.05$, 90° to the flow direction.	156
Figure G.20: Static pressure plotted against the x coordinate at $Re = 3\,000$ for setup: $d/p = 0.05$, 90° to the flow direction.	156
Figure G.21: Static pressure plotted against the x coordinate at $Re = 4\,000$ for setup: $d/p = 0.05$, 90° to the flow direction.	157
Figure G.22: Static pressure plotted against the x coordinate at $Re = 5\,000$ for setup: $d/p = 0.05$, 90° to the flow direction.	157
Figure G.23: Static pressure plotted against the x coordinate at $Re = 6\,000$ for setup: $d/p = 0.05$, 90° to the flow direction.	157
Figure G.24: Static pressure plotted against the x coordinate at $Re = 7\,000$ for setup: $d/p = 0.05$, 90° to the flow direction.	158

Figure G.25: Static pressure plotted against the x coordinate at Re = 8 000 for setup: d/p = 0.05, 90° to the flow direction.	158
Figure G.26: Static pressure plotted against the x coordinate at Re = 9 000 for setup: d/p = 0.05, 90° to the flow direction.	158
Figure G.27: Static pressure plotted against the x coordinate at Re = 9 700 for setup: d/p = 0.05, 90° to the flow direction.	159
Figure G.28: Static pressure plotted against the x coordinate at Re = 10 500 for setup: d/p = 0.05, 90° to the flow direction.	159
Figure G.29: Static pressure plotted against the x coordinate at Re = 11 500 for setup: d/p = 0.05, 90° to the flow direction.	159
Figure G.30: Static pressure plotted against the x coordinate at Re = 12 500 for setup: d/p = 0.05, 90° to the flow direction.	160
Figure G.31: Static pressure plotted against the x coordinate at Re = 640 for setup: d/p = 0.05, 45° to the flow direction.....	160
Figure G.32: Static pressure plotted against the x coordinate at Re = 920 for setup: d/p = 0.05, 45° to the flow direction.....	160
Figure G.33: Static pressure plotted against the x coordinate at Re = 1 400 for setup: d/p = 0.05, 45° to the flow direction.	161
Figure G.34: Static pressure plotted against the x coordinate at Re = 1 800 for setup: d/p = 0.05, 45° to the flow direction.	161
Figure G.35: Static pressure plotted against the x coordinate at Re = 3 000 for setup: d/p = 0.05, 45° to the flow direction.	161
Figure G.36: Static pressure plotted against the x coordinate at Re = 4 000 for setup: d/p = 0.05, 45° to the flow direction.	162
Figure G.37: Static pressure plotted against the x coordinate at Re = 5 000 for setup: d/p = 0.05, 45° to the flow direction.	162
Figure G.38: Static pressure plotted against the x coordinate at Re = 6 000 for setup: d/p = 0.05, 45° to the flow direction.	162
Figure G.39: Static pressure plotted against the x coordinate at Re = 7 000 for setup: d/p = 0.05, 45° to the flow direction.	163
Figure G.40: Static pressure plotted against the x coordinate at Re = 8 000 for setup: d/p = 0.05, 45° to the flow direction.	163
Figure G.41: Static pressure plotted against the x coordinate at Re = 9 000 for setup: d/p = 0.05, 45° to the flow direction.	163
Figure G.42: Static pressure plotted against the x coordinate at Re = 9 700 for setup: d/p = 0.05, 45° to the flow direction.	164
Figure G.43: Static pressure plotted against the x coordinate at Re = 10 500 for setup: d/p = 0.05, 45° to the flow direction.	164
Figure G.44: Static pressure plotted against the x coordinate at Re = 11 500 for setup: d/p = 0.05, 45° to the flow direction.	164
Figure G.45: Static pressure plotted against the x coordinate at Re = 12 500 for setup: d/p = 0.05, 45° to the flow direction.	165
Figure G.46: Static pressure plotted against the x coordinate at Re = 640 for setup: d/p = 0.025, 90° to the flow direction.....	165
Figure G.47: Static pressure plotted against the x coordinate at Re = 920 for setup: d/p = 0.025, 90° to the flow direction.....	165
Figure G.48: Static pressure plotted against the x coordinate at Re = 1 400 for setup: d/p = 0.025, 90° to the flow direction.	166

Figure G.49: Static pressure plotted against the x coordinate at Re = 1 800 for setup: d/p = 0.025, 90° to the flow direction.	166
Figure G.50: Static pressure plotted against the x coordinate at Re = 3 000 for setup: d/p = 0.025, 90° to the flow direction.	166
Figure G.51: Static pressure plotted against the x coordinate at Re = 4 000 for setup: d/p = 0.025, 90° to the flow direction.	167
Figure G.52: Static pressure plotted against the x coordinate at Re = 5 000 for setup: d/p = 0.025, 90° to the flow direction.	167
Figure G.53: Static pressure plotted against the x coordinate at Re = 6 000 for setup: d/p = 0.025, 90° to the flow direction.	167
Figure G.54: Static pressure plotted against the x coordinate at Re = 7 000 for setup: d/p = 0.025, 90° to the flow direction.	168
Figure G.55: Static pressure plotted against the x coordinate at Re = 8 000 for setup: d/p = 0.025, 90° to the flow direction.	168
Figure G.56: Static pressure plotted against the x coordinate at Re = 9 000 for setup: d/p = 0.025, 90° to the flow direction.	168
Figure G.57: Static pressure plotted against the x coordinate at Re = 9 700 for setup: d/p = 0.025, 90° to the flow direction.	169
Figure G.58: Static pressure plotted against the x coordinate at Re = 10 500 for setup: d/p = 0.025, 90° to the flow direction.	169
Figure G.59: Static pressure plotted against the x coordinate at Re = 11 500 for setup: d/p = 0.025, 90° to the flow direction.	169
Figure G.60: Static pressure plotted against the x coordinate at Re = 12 500 for setup: d/p = 0.025, 90° to the flow direction.	170
Figure G.61: Static pressure plotted against the x coordinate at Re = 640 for setup: d/p = 0.025, 45° to the flow direction.....	170
Figure G.62: Static pressure plotted against the x coordinate at Re = 920 for setup: d/p = 0.025, 45° to the flow direction.....	170
Figure G.63: Static pressure plotted against the x coordinate at Re = 1 400 for setup: d/p = 0.025, 45° to the flow direction.	171
Figure G.64: Static pressure plotted against the x coordinate at Re = 1 800 for setup: d/p = 0.025, 45° to the flow direction.	171
Figure G.65: Static pressure plotted against the x coordinate at Re = 3 000 for setup: d/p = 0.025, 45° to the flow direction.	171
Figure G.66: Static pressure plotted against the x coordinate at Re = 4 000 for setup: d/p = 0.025, 45° to the flow direction.	172
Figure G.67: Static pressure plotted against the x coordinate at Re = 5 000 for setup: d/p = 0.025, 45° to the flow direction.	172
Figure G.68: Static pressure plotted against the x coordinate at Re = 6 000 for setup: d/p = 0.025, 45° to the flow direction.	172
Figure G.69: Static pressure plotted against the x coordinate at Re = 7 000 for setup: d/p = 0.025, 45° to the flow direction.	173
Figure G.70: Static pressure plotted against the x coordinate at Re = 8 000 for setup: d/p = 0.025, 45° to the flow direction.	173
Figure G.71: Static pressure plotted against the x coordinate at Re = 9 000 for setup: d/p = 0.025, 45° to the flow direction.	173
Figure G.72: Static pressure plotted against the x coordinate at Re = 9 700 for setup: d/p = 0.025, 45° to the flow direction.	174

Figure G.73: Static pressure plotted against the x coordinate at Re = 10 500 for setup: d/p = 0.025, 45° to the flow direction.	174
Figure G.74: Static pressure plotted against the x coordinate at Re = 11 500 for setup: d/p = 0.025, 45° to the flow direction.	174
Figure G.75: Static pressure plotted against the x coordinate at Re = 12 500 for setup: d/p = 0.025, 45° to the flow direction.	175
Figure G.76: Static pressure plotted against the x coordinate at Re = 640 for setup: d/p = 0.2, 90° to the flow direction.....	175
Figure G.77: Static pressure plotted against the x coordinate at Re = 920 for setup: d/p = 0.2, 90° to the flow direction.....	175
Figure G.78: Static pressure plotted against the x coordinate at Re = 1 400 for setup: d/p = 0.2, 90° to the flow direction.....	176
Figure G.79: Static pressure plotted against the x coordinate at Re = 1 800 for setup: d/p = 0.2, 90° to the flow direction.....	176
Figure G.80: Static pressure plotted against the x coordinate at Re = 3 000 for setup: d/p = 0.2, 90° to the flow direction.....	176
Figure G.81: Static pressure plotted against the x coordinate at Re = 4 000 for setup: d/p = 0.2, 90° to the flow direction.....	177
Figure G.82: Static pressure plotted against the x coordinate at Re = 5 000 for setup: d/p = 0.2, 90° to the flow direction.....	177
Figure G.83: Static pressure plotted against the x coordinate at Re = 6 000 for setup: d/p = 0.2, 90° to the flow direction.....	177
Figure G.84: Static pressure plotted against the x coordinate at Re = 7 000 for setup: d/p = 0.2, 90° to the flow direction.....	178
Figure G.85: Static pressure plotted against the x coordinate at Re = 8 000 for setup: d/p = 0.2, 90° to the flow direction.....	178
Figure G.86: Static pressure plotted against the x coordinate at Re = 9 000 for setup: d/p = 0.2, 90° to the flow direction.....	178
Figure G.87: Static pressure plotted against the x coordinate at Re = 9 700 for setup: d/p = 0.2, 90° to the flow direction.....	179
Figure G.88: Static pressure plotted against the x coordinate at Re = 640 for setup: d/p = 0.2, 45° to the flow direction.....	179
Figure G.89: Static pressure plotted against the x coordinate at Re = 920 for setup: d/p = 0.2, 45° to the flow direction.....	179
Figure G.90: Static pressure plotted against the x coordinate at Re = 1 400 for setup: d/p = 0.2, 45° to the flow direction.....	180
Figure G.91: Static pressure plotted against the x coordinate at Re = 1 800 for setup: d/p = 0.2, 45° to the flow direction.....	180
Figure G.92: Static pressure plotted against the x coordinate at Re = 3 000 for setup: d/p = 0.2, 45° to the flow direction.....	180
Figure G.93: Static pressure plotted against the x coordinate at Re = 4 000 for setup: d/p = 0.2, 45° to the flow direction.....	181
Figure G.94: Static pressure plotted against the x coordinate at Re = 5 000 for setup: d/p = 0.2, 45° to the flow direction.....	181
Figure G.95: Static pressure plotted against the x coordinate at Re = 6 000 for setup: d/p = 0.2, 45° to the flow direction.....	181
Figure G.96: Static pressure plotted against the x coordinate at Re = 7 000 for setup: d/p = 0.2, 45° to the flow direction.....	182

Figure G.97: Static pressure plotted against the x coordinate at $Re = 8\ 000$ for setup: $d/p = 0.2$, 45° to the flow direction.....	182
Figure G.98: Static pressure plotted against the x coordinate at $Re = 9\ 000$ for setup: $d/p = 0.2$, 45° to the flow direction.....	182
Figure G.99: Static pressure plotted against the x coordinate at $Re = 9\ 700$ for setup: $d/p = 0.2$, 45° to the flow direction.....	183
Figure G.100: Static pressure plotted against the x coordinate at $Re = 10\ 500$ for setup: $d/p = 0.2$, 45° to the flow direction.	183
Figure G.101: Static pressure plotted against the x coordinate at $Re = 11\ 500$ for setup: $d/p = 0.2$, 45° to the flow direction.	183
Figure G.102: Static pressure plotted against the x coordinate at $Re = 12\ 500$ for setup: $d/p = 0.2$, 45° to the flow direction.	184
Figure G.103: Static pressure plotted against the x coordinate at $Re = 640$ for setup: $d/p = 0.1$, 90° to the flow direction.....	184
Figure G.104: Static pressure plotted against the x coordinate at $Re = 920$ for setup: $d/p = 0.1$, 90° to the flow direction.....	184
Figure G.105: Static pressure plotted against the x coordinate at $Re = 1\ 400$ for setup: $d/p = 0.1$, 90° to the flow direction.	185
Figure G.106: Static pressure plotted against the x coordinate at $Re = 1\ 800$ for setup: $d/p = 0.1$, 90° to the flow direction.	185
Figure G.107: Static pressure plotted against the x coordinate at $Re = 3\ 000$ for setup: $d/p = 0.1$, 90° to the flow direction.	185
Figure G.108: Static pressure plotted against the x coordinate at $Re = 4\ 000$ for setup: $d/p = 0.1$, 90° to the flow direction.	186
Figure G.109: Static pressure plotted against the x coordinate at $Re = 5\ 000$ for setup: $d/p = 0.1$, 90° to the flow direction.	186
Figure G.110: Static pressure plotted against the x coordinate at $Re = 6\ 000$ for setup: $d/p = 0.1$, 90° to the flow direction.	186
Figure G.111: Static pressure plotted against the x coordinate at $Re = 7\ 000$ for setup: $d/p = 0.1$, 90° to the flow direction.	187
Figure G.112: Static pressure plotted against the x coordinate at $Re = 8\ 000$ for setup: $d/p = 0.1$, 90° to the flow direction.	187
Figure G.113: Static pressure plotted against the x coordinate at $Re = 9\ 000$ for setup: $d/p = 0.1$, 90° to the flow direction.	187
Figure G.114: Static pressure plotted against the x coordinate at $Re = 9\ 700$ for setup: $d/p = 0.1$, 90° to the flow direction.	188
Figure G.115: Static pressure plotted against the x coordinate at $Re = 10\ 500$ for setup: $d/p = 0.1$, 90° to the flow direction.	188
Figure G.116: Static pressure plotted against the x coordinate at $Re = 11\ 500$ for setup: $d/p = 0.1$, 90° to the flow direction.	188
Figure G.117: Static pressure plotted against the x coordinate at $Re = 12\ 500$ for setup: $d/p = 0.1$, 90° to the flow direction.	189
Figure G.118: Static pressure plotted against the x coordinate at $Re = 640$ for setup: $d/p = 0.1$, 45° to the flow direction.....	189
Figure G.119: Static pressure plotted against the x coordinate at $Re = 920$ for setup: $d/p = 0.1$, 45° to the flow direction.....	189
Figure G.120: Static pressure plotted against the x coordinate at $Re = 1\ 400$ for setup: $d/p = 0.1$, 45° to the flow direction.	190

Figure G.121: Static pressure plotted against the x coordinate at Re = 1 800 for setup: d/p = 0.1, 45° to the flow direction.	190
Figure G.122: Static pressure plotted against the x coordinate at Re = 3 000 for setup: d/p = 0.1, 45° to the flow direction.	190
Figure G.123: Static pressure plotted against the x coordinate at Re = 4 000 for setup: d/p = 0.1, 45° to the flow direction.	191
Figure G.124: Static pressure plotted against the x coordinate at Re = 5 000 for setup: d/p = 0.1, 45° to the flow direction.	191
Figure G.125: Static pressure plotted against the x coordinate at Re = 6 000 for setup: d/p = 0.1, 45° to the flow direction.	191
Figure G.126: Static pressure plotted against the x coordinate at Re = 7 000 for setup: d/p = 0.1, 45° to the flow direction.	192
Figure G.127: Static pressure plotted against the x coordinate at Re = 8 000 for setup: d/p = 0.1, 45° to the flow direction.	192
Figure G.128: Static pressure plotted against the x coordinate at Re = 9 000 for setup: d/p = 0.1, 45° to the flow direction.	192
Figure G.129: Static pressure plotted against the x coordinate at Re = 9 700 for setup: d/p = 0.1, 45° to the flow direction.	193
Figure G.130: Static pressure plotted against the x coordinate at Re = 10 500 for setup: d/p = 0.1, 45° to the flow direction.	193
Figure G.131: Static pressure plotted against the x coordinate at Re = 11 500 for setup: d/p = 0.1, 45° to the flow direction.	193
Figure G.132: Static pressure plotted against the x coordinate at Re = 12 500 for setup: d/p = 0.1, 45° to the flow direction.	194

List of Tables

Table 2.1: Laminar local Nusselt number.	6
Table 2.2: Laminar fully developed Nusselt numbers.	7
Table 2.3: Laminar friction factors.....	7
Table 2.4: Transition to turbulent local Nusselt number.	7
Table 2.5: Transition to turbulent fully developed Nusselt number.	8
Table 2.6: Transition to turbulent friction factor.	8
Table 2.7: Turbulent fully developed Nusselt numbers.	8
Table 2.8: Turbulent friction factors.....	9
Table 3.1: Summary of cylindrical inserts.....	16
Table 3.2: Orifice plate dimensions.....	19
Table 3.3: Experimental test matrix	22
Table 3.4: Instrumentation.....	23
Table 3.5: Nusselt number average repeatability.	27
Table 3.6: Friction factor repeatability.	29
Table 4.1: Comparison of experimental laminar local Nusselt number to correlations at Re 920.	31
Table 4.2: Qualification of experimental transitional average Nusselt number to correlations.....	34
Table 4.3: Qualification of experimental turbulent average Nusselt number to correlations.....	34
Table 4.4: Difference between laminar experimental friction factor and correlations for smooth channel.....	35
Table 4.5: Difference between transitional experimental friction factor and correlations for the smooth channel.	36
Table 4.6: Difference between turbulent experimental friction factor and correlations for the smooth channel.....	37
Table 6.1: Correlation power function for average Nusselt numbers, Nu_{avg}	63
Table 6.2: Correlation power functions for Nusselt number ratios $Nu_{avg}/Nu_{0,avg}$	65
Table 6.3: Correlation functions for friction factors, f	68
Table 6.4: Correlation functions for the friction factor ratios, f/f_0	70
Table 6.5: Correlation power functions for thermal performance coefficients, η	73
Table A.1: Properties of Orifice Plates.....	83
Table D.1: Fluid properties' uncertainty.....	89

Nomenclature

A	Area	m^2
A_c	Cross-sectional area of test section	m^2
a^*	Aspect ratio	
b	Bias error	
C	Coefficient of discharge	
d	Cylinder diameter	m
D	Diameter	m
f	Friction factor	
F	Frequency	$1/s$
e	Perimeter	m
G	Offset between cylinders	m
h	Heat transfer coefficient	W/m^2K
H	Channel height	m
k	Thermal conductivity	W/mK
l	Length	m
L	Test section length	m
\dot{m}	Air mass flow rate	kg/s
n	Number of readings	
Nu	Nusselt number	
p	Pitch of the cylinders	m
P	Pressure	Pa
Pr	Prandtl number	
Pu	Pumping power	W
\dot{q}	Heat flux	W/m^2
\dot{Q}	Heat transfer rate	W
R	Ideal gas constant	$J/kg.K$
Re	Reynolds number	
St	Strouhal number	
s	Length from channel wall to cylinder	m
T	Temperature	$^{\circ}C$
t	Time	s
v	Velocity	m/s
V	Voltage	V
W	Test section width	m

Greek symbols

α	Angle around rod	$^{\circ}$
β	Orifice plate diameter ratio	
δ	Uncertainty	
Δ	Difference	
ϵ	Expansion factor	
η	Thermal performance	
θ	Angle to flow direction	$^{\circ}$
μ	Viscosity	$Pa.s$

ρ	Density	kg/m ³
ω	Vorticity	1/s

Subscripts

*	Non-dimensional
0	Smooth channel
<i>a</i>	Air
<i>amb</i>	Ambient
<i>avg</i>	Average
<i>b</i>	Bulk
<i>cal</i>	Calibration
<i>con</i>	Convection
<i>cyl</i>	Cylinders
<i>h</i>	Hydraulic
<i>heater</i>	Heater
<i>ins</i>	Insulation
<i>loc</i>	Local
<i>m</i>	Mean
<i>t</i>	Tube
<i>stag</i>	Stagnation
<i>th</i>	Theoretical
<i>wall</i>	Wall
<i>x</i>	x-Direction
<i>y</i>	y-Direction
<i>z</i>	z-Direction

1. Introduction

1.1. Background

Heat exchangers serve crucial roles in a wide spectrum of different engineering applications where energy is being generated or consumed. The industrial applications of heat exchangers include but are not limited to air-conditioning (HVAC), refrigeration, steam power cycles, condensation, energy recovery, fuel cell cooling, and engine cooling jacket.

Enhancing the performance of heat exchangers is important to optimize the energy efficiency which depends on the effectiveness of the heat exchangers. There are different methods of augmenting heat transfer in heat exchangers for example enlarging the heat transfer area, increasing the Reynolds number, and using turbulators as an insert or on the surface. Bluff bodies, grooves, ribs, pin fins, and twisted helical tape inserts are examples of turbulators used for heat transfer enhancement. By using turbulators, turbulent flow is promoted at lower Reynolds numbers which increases heat transfer but also increases the pressure drop penalty and therefore pumping power. Figure 1.1 shows examples of different turbulators used in channel flow.

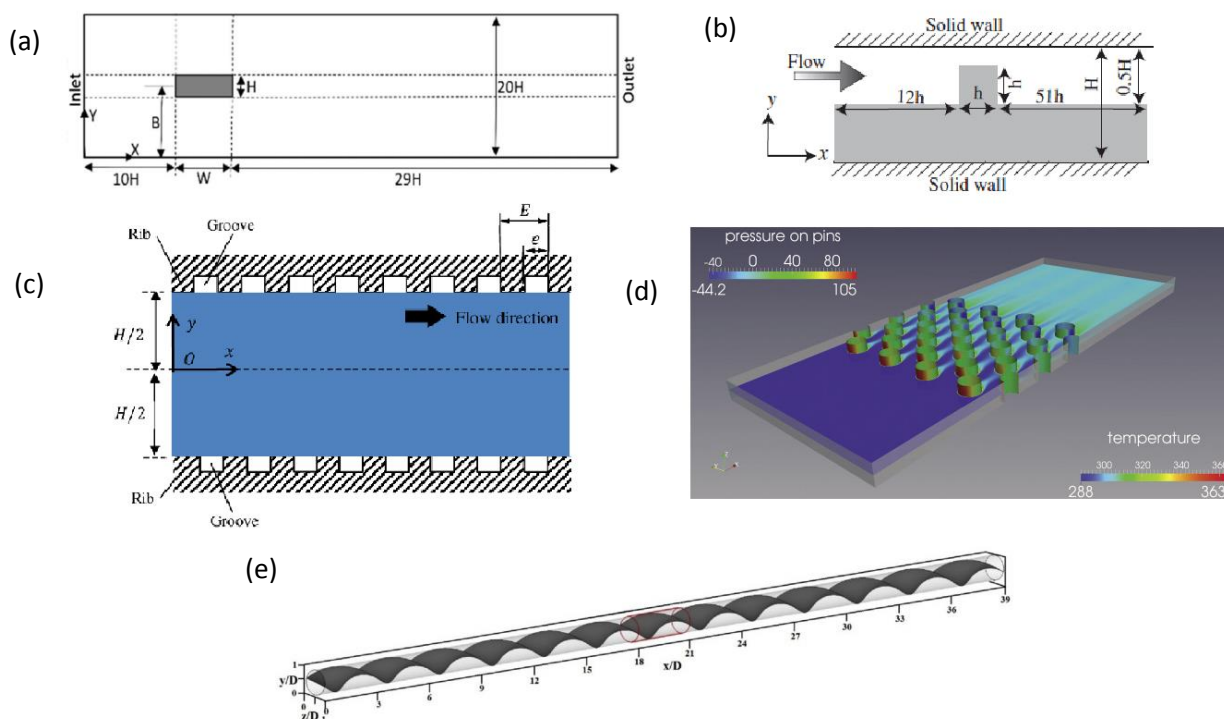


Figure 1.1: Examples of turbulators: (a) Bluff bodies. (b) Ribs. (c) Grooves. (d) Pin fins. (e) Twisted helical tape.

The thermal performance coefficient compares the increase in heat transfer to the increase in pumping power and is valid in cases with either constant wall temperature or constant heat flux. The ratio of the Nusselt number of the adapted channel to that of the smooth channel is the method used in literature to find the heat transfer increase. This ratio is then divided by the friction factor ratio to the cube root to find the thermal performance coefficient. If this ratio is larger than one, the thermal performance of the adapted channel is larger than the smooth channel. The thermal performance coefficient is defined as:

$$\eta = \frac{Nu}{\overline{Nu}_0} \left(\frac{f}{f_0} \right)^{1/3} \quad (1.1)$$

The derivation of the thermal performance coefficient follows from Webb and Eckert [1].

Heat transfer enhancement, employing turbulators, often uses the thermal performance coefficient to quantify the magnitude of the thermal performance increase of the adapted channel. A lot of research has been done in cases where grooves, ribs, helical inserts, and a single rod at the test section inlet are being used, but not in the case for circular cylindrical cross-bars. Arrays of cylindrical cross-bars were investigated in this study between a Reynolds number of 640 and 12 500. Heat transfer and pressure drop tests were done to see the effects of changing the diameter to pitch ratio and the angle to the flow direction. A CFD study was done to investigate the secondary flow fields caused by the cylinders.

1.2. Problem statement

Circular cylindrical bluff bodies have been found to have smaller drag coefficients than shapes of other cross-sections and therefore suffer a smaller pressure penalty. Investigations on the effects of rod-like turbulators on heat transfer and pressure drop characteristics in channel flow have previously been done mostly with the insert of a single rod or arrays of cross-bars with different cross-sectional shapes. The drawback of using only a single rod for heat transfer augmentation is that it is not viable for applications in heat exchangers because only the local Nusselt number increases and for heat exchangers increasing the average Nusselt number throughout the channel is favourable. The thermal augmentation and pressure drop of circular rod-like turbulators in array geometries have not received enough attention. In-line bluff bodies in the centre of channels do not cause as much near-wall fluid acceleration and turbulence on both heated walls as staggered bluff bodies. Bluff bodies with an angled arrangement to the flow direction have smaller pressure drops but cover more projected areas on the surface.

1.3. Aim

This study aims to find the heat transfer and pressure drop characteristics in channel flow by using arrays of cylindrical cross-bars with different diameters, pitches, and orientations to the flow.

1.4. Objectives

The objectives of this study were as follows:

- Increase the average Nusselt numbers relative to the smooth channel by employing the arrays of cylindrical inserts in the channel
- Study the pressure drop penalty in the channel with the inserts to find the thermal performance coefficients
- Investigate the physical mechanisms in the local flow structures responsible for the augmentation of local heat transfer on the wall and pressure in the channel

The following was done to fulfil the objectives:

- Obtain the local and developed mean Nusselt numbers in the centre line of the rectangular channel wall for the plane channel as well as the cylindrical cross-bar geometries. The Nusselt numbers are calculated at Reynolds numbers ranging from laminar to turbulent flow
- Measure the pressure drops along the channel with and without inserts

- Find the friction factor using the slope of the pressure drop from laminar to turbulent Reynolds number range
- Use the plane channel Nusselt numbers and friction factors to qualify the experimental method
- Numerically model the flow inside the channel with the inserts by a commercial CFD solver and validate the model by experimental studies in a scaled-up channel with the inserts
- Use the results from the CFD solver to explain the increase in heat transfer coefficients and friction factors
- Estimate the augmentation of average heat transfer coefficients and friction factors as well as the thermal performance in the channel with the inserts from the measured data

1.5. Scope

The current study aims to find the heat transfer and pressure drop characteristics of a rectangular channel with arrays of circular cylindrical cross-bars in the flow to enhance the heat transfer with minimal pressure penalty and air as the working fluid. Experimental investigations were done with eight different turbulence promoting geometries at Reynolds numbers ranging from 640 to 12 500. The Nusselt number, friction factor, and thermohydraulic performance were found experimentally. The investigated parameters were the cylinder diameter to pitch ratio (d/p) from 0.025 to 0.2 and the orientation of the cylinders, 90° or 45°, to the flow direction. The orientation of 45° to the flow direction was selected instead of 30° or 60° because it has shown the best results in previous studies [2].

A constant channel aspect ratio of $H/W = 0.025$ and a test section length of $L = 0.5\text{m}$ were used. The cylindrical cross-bars with smaller diameters were staggered and larger diameters inline to keep the blockage ratio constant at 0.4. Numerical studies were done to find the flow structure for the explanation of the increase in the heat transfer rate of a channel with cylindrical cross-bars to that of a smooth channel. The k- Ω SST model was used with velocity profiles at the inlet of the channel. Two-dimensional transient simulations were done for the cases where the cylinders are 90° to the flow direction and three-dimensional simulations for 45° to the flow direction.

1.6. Overview of dissertation structure

The literature study is shown in Chapter 2, where previous studies of similar nature are analysed and empirical formulations for the plane channel are introduced that were later used for the qualification of the experimental method. Numerical formulations were also analysed in Chapter 2 so that the most valid numerical model could be used for the CFD simulations for the current study, considering the geometry and estimated turbulent conditions.

Chapter 3 explains the experimental setup, with the cylindrical cross-bar array configurations and the method of data reduction used to convert the raw data into the required variables. Included in Chapter 3 are the instrumentation used for the experimental tests and an explanation of the experimental procedure used to conduct the research. An uncertainty analysis and repeatability study were also done in Chapter 3 to investigate if the experimental tests are repeatable.

In Chapter 4 the qualification of the experimental method was done to clarify that the results of previously done experiments correlate with the current study and was done before adding the cylindrical cross-bars to the test section. Smooth/plane channel tests were done during this phase of the experimental testing.

To explain the secondary flow patterns responsible for the heat transfer and pressure drop augmentation, a numerical study was done and is shown in Chapter 5. The domain, boundary

conditions, mathematical model, mesh validation, and validation for the CFD results against experimental results are the first steps that were required. Transient simulations were done to show each time step so that the vortex shedding behind the cylinders could be investigated and was the main objective of this chapter.

The experimental results are analysed in Chapter 6, including the local Nusselt numbers, average Nusselt numbers, and friction factors of all the tested geometrical configurations as well as the ratios of the turbulated channels to that of the smooth channel so that the thermal performance could be found, which is the ultimate variable that this study is aiming to analyse.

The conclusion of the study is presented in Chapter 7 with a compilation of the Reynolds number calculation, calibration of the thermocouples, pressure transducers, uncertainty analysis, local Nusselt numbers, wall temperature data, and pressure data in Appendix A to Appendix G respectively.

2. Literature Review

2.1. Introduction

The literature review covers work by previously done research studies. It includes explanations of flow regimes, the definition of Reynolds numbers, friction factors, Nusselt numbers, and thermal performance coefficients in Section 2.2. Empirical Nusselt number and friction factor correlations for smooth rectangular channel flow, that was used to qualify the experimental method is shown in Section 2.3. Previously researched heat transfer augmentation is analysed in Section 2.4, where the thermal performance coefficients are shown for different heat transfer enhancement techniques as well as for studies where the addition of bluff bodies to the channel flow was used. Literature on CFD modelling for channel flow is reviewed in Section 2.5.

2.2. Dimensionless parameters

Dimensionless numbers are used to represent experimental results in a simplified form, i.e. to reduce the number of variables needed to show in tables and graphs which makes it easier for the reader to digest, White [3].

2.2.1. Reynolds number

The Reynolds number of the flow inside the channel with and without the inserts is defined by the following equation:

$$Re = \frac{\rho v D_h}{\mu} \quad (2.1)$$

There are three levels describing the turbulence of channel flows: linear flow, transitional flow and turbulent flow. In plane/smooth rectangular channel flow, linear flow is expected for Reynolds numbers below 2 300, with transitional flow up to a Reynolds number of 6 000 after which fully turbulent flow dominates, in a parallel plate duct with uniform wall temperatures at both walls, Rohsenow *et al.* [4]. Flow in rectangular ducts become fully turbulent at a Reynolds number of 5 772, Steven A. Orszag [5].

2.2.2. Friction factor

The friction factor of the flow inside the channel with and without the inserts is defined by the following equation:

$$f = \frac{\frac{\Delta P D_h}{\Delta x} \cdot 4}{\frac{1}{2} \rho v^2} \quad (2.2)$$

2.2.3. Nusselt number

The Nusselt number of the flow inside the channel with and without the insert is defined by the following equation:

$$Nu = \frac{h D_h}{k} \quad (2.3)$$

With D_h the hydraulic diameter of the unobstructed and turbulated channel defined as:

$$D_h = \frac{2WH}{W + H} \quad (2.4)$$

and k the thermal conduction coefficient. The heat transfer coefficient, h , is defined as:

$$h = \frac{Q}{A_s(T_{wall} - T_{mx})} \quad (2.5)$$

2.2.4. Thermal performance coefficient

The thermal performance coefficient from Webb and Eckert [1] defines the performance of the turbulated channel in comparison with the smooth channel, in terms of heat transfer increase relative to the increase in pressure drop, and is defined as:

$$\eta = \frac{\frac{Nu}{Nu_0}}{\left(\frac{f}{f_0}\right)^{\frac{1}{3}}} \quad (2.6)$$

2.3. Nusselt number and friction factor correlations for smooth channel

This Section shows tables with equations from previously done studies in smooth channels that will later be used to qualify the experimental setup in Chapter 4. The equations for local Nusselt numbers, average Nusselt numbers, where the flow is fully thermally developed, and friction factors for hydraulically developed flow in laminar, transition, and turbulent flow will be shown.

The local Nusselt numbers between parallel plates for laminar flow are shown in Table 2.1. The aspect ratio of the channel is very small, $a^* = H/W = 0.025 \approx 0$, so parallel plate correlations are valid because the channel width is very large in comparison with the channel height that it almost mimics flow between parallel plates. The local Nusselt number as a function of x is shown for the correlations of Worsøe-Schmidt [6], Equation (2.7), and Shah [7] Equations (2.9) to (2.14).

Table 2.1: Laminar local Nusselt number.

Worsøe-Schmidt [6]			
$\frac{1}{Nu_{x,0}}$	$= 0.67096078x^{*1/3} + 0.159064137x^{*2/3} + 0.12012x^* + 0.12495x^{*4/3}$	$+ 0.15602x^{*5/3} + 0.22176x^{*2} + 0.34932x^{*7/3} - 4x^*$	(2.7)
	$x^* = x/D_h RePr$		(2.8)
	$10^{-6} \leq x^* \leq 10^{-2}$		
	Parallel plates		
Shah [7]a			
$Nu_{x,0}$	$= \begin{cases} 1.490x^{*-1/3} & \text{for } x^* \leq 0.0002 \end{cases}$		(2.9)
	$\begin{cases} 1.490x^{*-1/3} - 0.4 & \text{for } 0.0002 < x^* \leq 0.001 \end{cases}$		(2.10)
	$\begin{cases} 8.235 + 8.68(10^3 x^{*-0.506} e^{-164x^*}) & \text{for } x^* > 0.001 \end{cases}$		(2.11)
	Parallel plates		
	Percentage deviation: $\pm 0.6\%$		
Shah [7]b			
$Nu_{x,0}$	$= \begin{cases} 2.236x^{*-1/3} & \text{for } x^* \leq 0.001 \end{cases}$		(2.12)
	$\begin{cases} 2.236x^{*-1/3} + 0.9 & \text{for } 0.0002 < x^* \leq 0.001 \end{cases}$		(2.13)
	$\begin{cases} 8.235 + \frac{0.0364}{x^*} & \text{for } x^* > 0.001 \end{cases}$		(2.14)

Parallel plates

Percentage deviation: +2.7%

The Nusselt numbers for thermally fully developed laminar flow are shown in Table 2.2. The correlations of Schmidt [8] is shown in Equation (2.15) and Marco and Han [9] is shown in Equation (2.16).

Table 2.2: Laminar fully developed Nusselt numbers.

Schmidt [8]	$Nu_0 = 8.235$	(2.15)
	Rectangular channels	
Marco and Han [9]	$Nu_0 = 8.235(1 - 2.0421a^* + 3.0853a^{*2} - 2.4765a^{*3} + 1.0578a^{*4} - 0.1861a^{*5})$	(2.16)
	$a^* = H/W$	(2.17)
	Rectangular channels	
	Percentage deviation: $\pm 0.03\%$	

Laminar friction factor correlations are shown in Table 2.3. The correlations of Rohsenow and Choi [10] and McCuen *et al.* [11] is shown in Equation (2.18), Shah and London [12] in Equation (2.19), Tirunarayanan and Ramachandran [13] in Equation (2.20), and Rothfus *et al.* [14] in Equation (2.22).

Table 2.3: Laminar friction factors.

Rohsenow and Choi [10] and McCuen <i>et al.</i> [11]	$f_0 = \frac{24}{Re}$	(2.18)
	Parallel plates	
Shah and London [12]	$f_0 = \frac{24(1 - 1.3553a^* + 1.9467a^{*2} - 1.7012a^{*3} + 0.9564a^{*4} - 0.2537a^{*5})}{Re}$	(2.19)
	Rectangular channels	
Tirunarayanan and Ramachandran [13]	$f_0 = \frac{14.227 + 1402.5 \left(\frac{\bar{B}}{\bar{P}} - \frac{\sqrt{2}}{8} \right)^{1.90}}{Re}$	(2.20)
	$\frac{\bar{B}}{\bar{P}} = \frac{W + H(\sqrt{2} - 1)}{4(W + H)}$	(2.21)
	Rectangular channels	
Rothfus <i>et al.</i> [14]	$f_0 = \frac{8.968 \left(\frac{1 + a^*}{\sqrt{a^*}} \right)^{0.75}}{Re}$	(2.22)
	Rectangular channels, $a^* \geq 0.125$	

The local Nusselt number for transitional to turbulent flow from Gnielinski [15] is shown in Table 2.4, Equation (2.23).

The fully thermally developed Nusselt number for transitional to turbulent flow from Gnielinski [15] is shown in Table 2.5, Equation (2.24).

Table 2.4: Transition to turbulent local Nusselt number.

Gnielinski [15]a

$$Nu_{x,0} = 0.0214(Re^{0.8} - 100)(1 + (D_h/L)^{0.66})(T_{mx}/T_{wall})^{0.45} Pr^{0.4} \quad (2.23)$$

$2300 \leq Re \leq 10^6$
Rectangular channels

Table 2.5: Transition to turbulent fully developed Nusselt number.

Gnielinski [15]b

$$Nu_0 = \frac{(f/2)(Re - 1000)Pr}{1 + 12.7(f/2)^{0.5}(Pr^{2/3} - 1)} \quad (2.24)$$

$3 \times 10^3 < Re < 5 \times 10^6$
 $0.5 \leq Pr \leq 2000$

The friction factor for transitional to turbulent flow in a smooth channel is shown in Table 2.6. The Blasius [16] correlation is shown in Equation (2.25), Modified Blasius [17] in Equation (2.26), and Taitel and Dukler [18] in Equation (2.27).

Table 2.6: Transition to turbulent friction factor.

Blasius [16]

$$f_0 = \frac{0.079}{Re^{0.25}} \quad (2.25)$$

$3000 \leq Re \leq 10^5$

Modified Blasius [17]

$$f_0 = \frac{0.085}{Re^{0.25}} \quad (2.26)$$

$3000 \leq Re \leq 10^5$

Taitel and Dukler [18]

$$f_0 = \frac{0.046}{Re^{0.2}} \quad (2.27)$$

$3000 \leq Re \leq 10^5$

The thermally fully developed Nusselt numbers are shown in Table 2.7. The Chilton and Colburn [19] correlation is shown in Equation (2.28), Colburn [20] in Equation (2.29), Dittus-Boelter [21] in Equation (2.30) and Second Petukhov [22] in Equation (2.31).

Table 2.7: Turbulent fully developed Nusselt numbers.

Chilton and Colburn [19]

$$Nu_0 = 0.125fRePr^{1/3} \quad (2.28)$$

Colburn [20]

$$Nu_0 = 0.023Re^{0.8}Pr^{1/3} \quad (2.29)$$

$Re > 10^4$
 $0.7 \leq Pr \leq 160$

Dittus-Boelter [21]

$$Nu_0 = 0.023Re^{0.8}Pr^n \quad (2.30)$$

$n = 0.3$ for cooling and $n = 0.4$ for heating
 $Re > 10^4$
 $0.7 \leq Pr \leq 160$

Second Petukhov [22]

$$Nu_0 = \frac{(f/2)RePr}{1.07 + 12.7(f/2)^{0.5}(Pr^{2/3} - 1)} \quad (2.31)$$

$10^4 < Re < 5 \times 10^6$
 $0.5 \leq Pr \leq 2000$

Table 2.8 shows the turbulent friction factors for the implicit correlation of Kármán-Nikuradse [23] in Equation (2.32), which is solved iteratively, and the explicit correlation of Petukhov [24] in Equation (2.33).

Table 2.8: Turbulent friction factors.

Kármán-Nikuradse [23]	$\frac{1}{\sqrt{f_0/2}} = 2.46 \ln(Re\sqrt{f_0/2}) + 0.3$ $10^4 \leq Re \leq 10^6$ Circular tubes	(2.32)
Petukhov [24]	$f_0 = 2(2.236 \ln(Re) - 4.639)^{-2}$ $10^4 \leq Re \leq 10^6$ Circular tubes	(2.33)

Equation (2.32) and (2.33) holds well for noncircular cylindrical channels if D_h is used instead of D for the calculation of Re , Kays and Crawford [25].

2.4. Previously done research

By adding arrays of rib extrusions in the channel flow, on the channel wall, the heat transfer can be enhanced. Li *et al.* [26] noted in a numerical study, with a Reynolds number range of between 20 000 and 80 000, and rib pitch to height ratio ranging between 5 and 20, that the thermal performance coefficient of all of their tested configurations, were less than one, throughout the Reynolds number range. This implies that the pressure penalty was too large for the tested geometries to be a viable method of heat transfer augmentation in the Reynolds number range that they conducted their study, for the selected configurations. Figure 2.1 shows the thermal performance coefficients of their study. A similar notion was observed by Zheng *et al.* [27], with a numerical study in a Reynolds number range of 10 000 to 25 000, where the thermal performance coefficient reduced as the Reynolds number increased for all their tested rib configurations. In another numerical study of airflow in a rectangular duct, done by Sahu *et al.* [28], the same trend was observed. The study was done for a Reynolds number range of 12 640 to 52 410, where the thermal performance coefficient decreased with an increase in Reynolds number, for all the tested rib configurations.

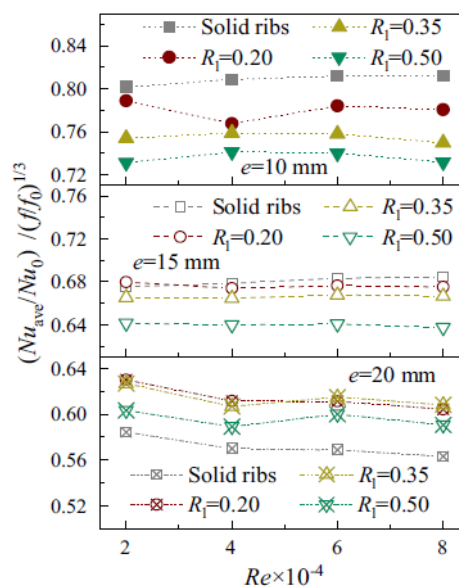


Figure 2.1: Thermal performance coefficient, Li *et al.* [26].

Groove extruded cuts in the channel wall is another method of heat transfer augmentation in channel flow. In a study conducted by Skullong *et al.* [29], with a Reynolds number range of 4 500 to 22 000, using w-shaped rib-and-groove configurations, found that the thermal performance coefficient declined with an increase in Reynolds number. The rib and groove combination outperformed the use of either ribs or grooves alone. At $Re = 4\,500$, the thermal performance coefficient was 2.15 and reduced to 1.9 as the Reynolds number increased to 22 000 and is shown in Figure 2.2. Brodniaska [30] did an experimental investigation of triangular grooves in a rectangular channel. She investigated the thermal performance in a Reynolds number range of 732 to 3 020. The configuration with the largest thermal performance coefficient, 0.819, was with a height of the gap between heated surfaces of 0.05 m. By using an offset between the grooves on the upper and lower wall for flow in a rectangular channel, the pressure penalty reduces without much reduction on the effect of heat transfer increase, Chen *et al.* [31].

The use of pin fins is a relatively common way to augment heat transfer in rectangular channel flow. An experimental investigation was done by Eren and Caliskan [32], with cylindrical and triangular grooved pin fins in a Reynolds number range of 3 188 to 15 146, where the effect of grooved distanced rates was varied between 1 and 3.446. The triangular grooved pin fins outperformed the cylindrical grooved pin fins with a relatively constant thermal performance coefficient of 2.7 for the entire tested Reynolds number range. Hsieh *et al.* [33] investigated pin fins with different cross-sectional shapes of pin fins in a low Reynolds number range of 3 to 25. The pin fin geometry with the largest Nusselt number ratio was for the square-shaped pin fins. A numerical and experimental analysis was done on diamond-shaped pin fins by Xie *et al.* [34], in the laminar Reynolds number range of 50 to 600. They concluded that the pressure drop magnitude increases drastically above the Reynolds number of 300 because vortex shedding started being present. It was also noted that for a fluctuating velocity, there is a rapid increase in turbulent kinetic energy without having much of an increase in Nusselt number.

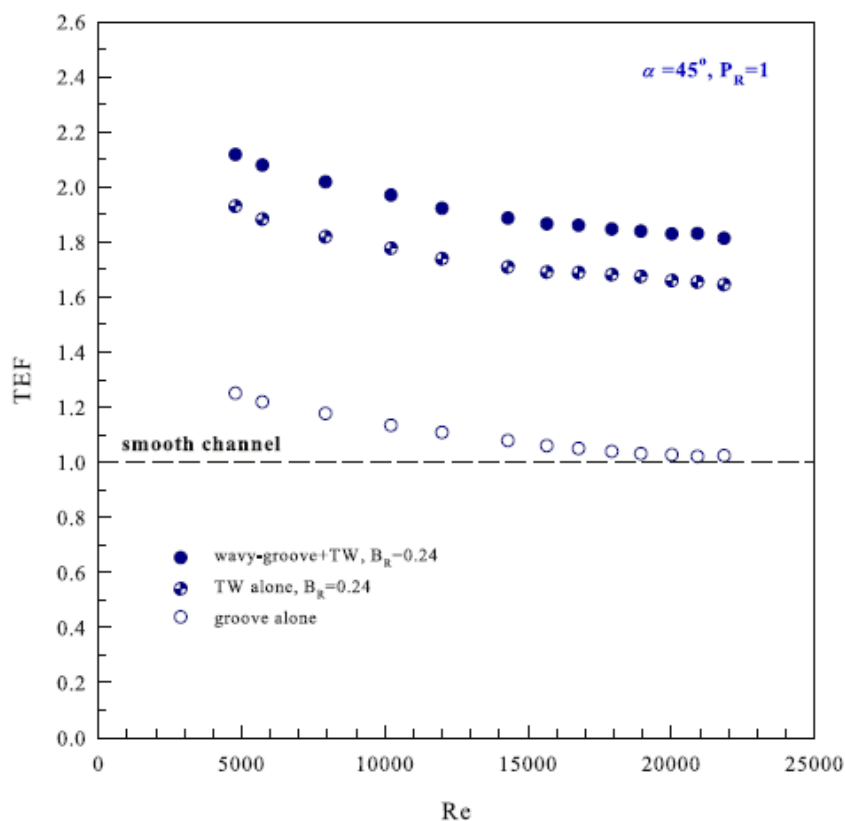


Figure 2.2: Thermal performance coefficient, Skullong *et al.* [29].

Implementing helical inserts in either circular or rectangular channel flow can increase the thermal performance of the channel. Nanan *et al.* [35] tested transverse twisted baffles experimentally and numerically in a comparison with flat transverse baffles, for flow in a circular duct. The tests were done in a Reynolds number range of 6 000 to 20 000. They found that the thermal performance coefficients for the twisted baffles were much larger than for the flat baffles. The twisted baffles gave thermal performance coefficients in the range of 1.46 – 1.69, decreasing with an increase in Reynolds number as observed in the other studies shown in the literature review of this dissertation. In an experimental study by Eiamsa-Ard *et al.* [36], the thermal performance of dual-and-triple twisted helical tapes was compared to that of single twisted helical tapes, for flow in a circular tube. The tests were done in a Reynolds number range of 5 000 to 20 000, with the thermal performance coefficient decreasing with an increase in Reynolds number for all the tested configurations. The single-helical twisted tape configuration's performance was the lowest, with the double and triple-helical twisted tape geometries being approximately equal in a range of 1.1 to 1.31. Jehad *et al.* [37] tested the thermal performance of straight and helical baffles in a circular duct numerically in a Reynolds number range of 100 to 2 000. The double-helical fin geometry had the best performance, with a thermal performance ranging from 1.1 to 1.7, where the lowest measurement was at $Re = 100$, after which the thermal performance coefficient increased to 1.7 at $Re = 500$, after which it remained relatively constant with an increase in Reynolds number to $Re = 2 000$. An experimental and numerical study of heat transfer enhancement with twisted helical inserts in a circular channel was done by Suri *et al.* [38] in a Reynolds number range of 5 000 to 27 000. The thermal performance coefficient increased with an increase in Reynolds number in the range of 2.45 to 3.91 for the geometry tested with the best performance. This seems unlikely as it contradicts the other studies done on heat transfer augmentation, where the thermal performance coefficient decreases with an increase in Reynolds number and did not have such large values. Twisted helical inserts were used in rectangular duct flow by Kumar and Layek [39] by using liquid crystal thermography as the measuring technique for finding the wall temperature. They tested the helical coil parameters' effect on heat transfer enhancement and pressure drop in a Reynolds number range between 11 000 and 23 000. It was found that the optimal relative pitch ratio was 8 because the largest percentage of flow reattachment per unit length occurred at this ratio without having a large effect on the pressure penalty. The effect of different combinations of ribs, grooves, and twisted helical inserts with teeth on heat transfer and pressure drop was studied by Ranjan *et al.* [40], in the laminar Reynolds number range of 60 to 800. They found that the performance of the combinations of turbulators was better than using individual methods for all the configurations of their tests.

By making use of circular cross-section cylindrical cross-bar arrays, heat transfer can be enhanced. Leonardi *et al.* [41] compared the thermal performance of circular and square bars and found that the maximum heat transfer difference between the two shapes is less than 5%, but that the pressure penalty for the circular bars was 12% less than for the square bars. An experimental study was done by Vujisic [42], on the turbulence/eddy promotion in rectangular channel flow, where he made use of cylindrical cross-bars. It was found that the transition to turbulent flow was found at a lower Reynolds number in comparison to plane channel flow. At larger Reynolds numbers, the heat transfer augmentation from the turbulated channel asymptotically correlated to that of the plane channel with an increase in Reynolds number due to the shear effects and vorticity production of the channel wall.

2.5. CFD modelling

The $k-\Omega$ SST turbulence model was developed by Menter [43] to change between $k-\varepsilon$ and $k-\Omega$ modelling at different cells in the mesh domain. The $k-\varepsilon$ model predicts accurate shear stress behaviour in the free stream flow, but over predicts the shear stress in near-wall flow. Two continuous

blending functions are used in the SST model to better predict flow separation and adverse pressure gradients. These functions are dependent on the distance of the cell centre to the geometry wall. The first blending function transforms the transport function from the $k-\epsilon$ to the $k-\Omega$ model for near-wall flow. The second blending function further relaxes the shear stress at flow near the wall to compare better with experimental results, Apsley and Leschziner [44]. The $k-\Omega$ SST turbulence model has been adapted into many different versions since it was first developed, Rumsey [45].

Based on previous numerical studies done on heat transfer enhancement in channel flow, where the $k-\Omega$ SST turbulence model has been used [46] [47] and [48], it has been decided that it is a good model to use for the requirements of this study. Note that a CFD analysis was done to show the flow field in the wake of the cylindrical cross-bars, to better describe the secondary flow patterns responsible for the heat transfer augmentation.

2.6. Summary

Dimensionless parameters are used to convey research data more compactly. The Reynolds number is used to quantify channel flow rate, the Nusselt number to non-dimensionalize the heat transfer coefficient, friction factor to the pressure drop, and the thermal performance coefficient to quantify the comparison of a modified channel, to that of the smooth channel flow at the same Reynolds number. Empirical formulas that were used for the qualification of the experimental method for the heat transfer and pressure drop tests are shown in Section 2.3.

Heat transfer augmentation in channel flow can be done by a variety of different techniques: rib extrusions, grooves in the channel walls, pin fins in the channel flow, helical inserts, and cylindrical cross-bars included in the channel flow. They all increase the Nusselt number but have a pressure drop penalty. By finding the thermal performance coefficient, it is possible to quantify the change in efficiency in comparison to plane channel flow. There seem to be larger advantages in using these methods of heat transfer enhancement at lower Reynolds numbers, after which the thermal performance coefficient seems to decrease until it reaches an asymptotic value. The difference between the research done from the references and this study is that there has not been a focus on arrays of round cylindrical cross-bars which might suffer a smaller pressure penalty because of the lower drag coefficients for a comparable heat transfer increase.

The $k-\Omega$ SST mathematical model is used as a combination of the $k-\Omega$ and $k-\epsilon$ models, to find better approximations for flow near the wall and in free channel flows respectively. Because it is a well-adapted and frequently used model in heat transfer enhancement studies with channel flow, it will be used in this study to find the secondary flow fields near the cylinder walls, responsible for the heat transfer enhancement and increase in pressure drop for flow at the same Reynolds numbers to that in smooth channel flows.

3. Experimental Set-up and Data Reduction

3.1. Introduction

The purpose of this chapter is to describe the experimental test set-up and all its components and instrumentation that were used to find the pressure drop and heat transfer data during the experiments. The experimental test setup is shown in Section 3.2 with a schematic diagram and a picture. The different cylindrical cross-bar arrays of inserts are shown in Section 3.3, with a description of the different parameters including diagrams and a picture. The detailed test section is shown that was used in the heat transfer and pressure drop tests and how the equipment was calibrated, in Section 3.4. The geometry of the orifice plates used for finding the mass flow rate in the test section is shown in Section 3.5. The method and equations used during the process of data reduction are given in Section 3.6 as well as a description of the experimental procedures in Section 3.7. For purposes of clarification and to summarise all the experimental tests done in this study, an experimental test matrix is included in Section 3.8. An uncertainty analysis and repeatability study were done in Section 3.9 and Section 3.10 respectively where the equipment uncertainties are mentioned with sample calculations in Appendix D.

3.2. Experimental test-setup

Figure 3.1 shows a schematic diagram of the experimental set-up used to find the Reynolds number, wall temperature, and pressure drop during the experimental tests. The contraction funnel at the inlet allows the air to enter the test section with a laminar flow field. The flow is then developed in the 2m section that leads towards the test section where the 500mm in length cylindrical cross-bar arrays are placed. There were eight different cylinder configurations tested and is explained in Section 3.3. The two pipes after the exit plenum space are used independently by using the valves. For laminar flow, the 51mm diameter pipe was used and for flow larger than a Reynolds number of 2 000, the 101mm diameter pipe was used. The pressure drops over the orifice plates were used to find the mass flow rate in the pipes and is explained in Section 3.5.2. A blower was used to create a pressure drop over the test section for the airflow and a variable-frequency drive was used to control the flow rate.

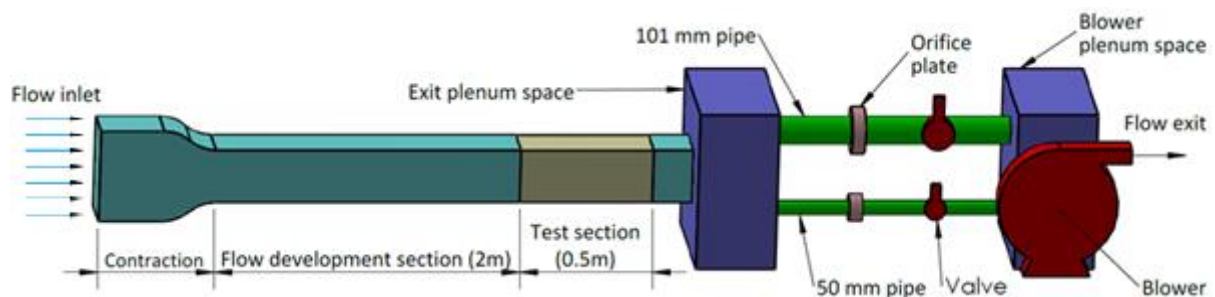


Figure 3.1: Schematic diagram of the experimental test set-up.

A picture of the experimental test setup is included in Figure 3.2. From the left to the right of the picture it shows: the inlet, contraction section, flow development section, test section, exit plenum space, 101 mm and 50 mm pipes, power supplies, orifice plates, valves, blower plenum space, blower

and flow exit. The 50 mm pipe was used for tests done at $Re \leq 1\,800$ and the 101 mm pipe was used for tests done at $Re > 1800$.



Figure 3.2: Picture of the experimental test setup.

3.3. Cylindrical cross-bar configurations

Eight different cylindrical arrays were experimentally tested. The length, $L = 500$ mm, height, $H = 5$ mm, width, $W = 203$ mm, and aspect ratio, $W/H = 40.6$ of the test section were kept constant. The pitch between the cylinders, p , diameter of cylinders, d , and angle to the direction of the flow field, θ , is varied. The 1 mm diameter cylinders are staggered, and the 2 mm diameter cylinders are in-line to keep the blockage ratio, A_{cyl}/A_c , constant at 0.4.

The cylindrical rods were fastened to six evenly spaced strips of 3D printed PLA plastic with a thickness of 1 mm which keeps the cylinders in the desired position inside of the array. These assemblies fit snugly into the test section. A picture of the $d/p = 0.2$, $\theta = 45^\circ$ is shown in Figure 3.3.

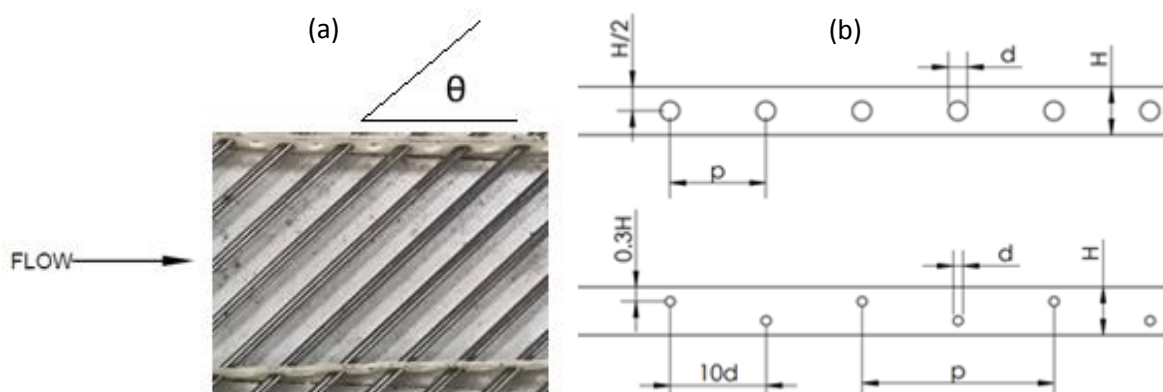


Figure 3.3: (a) Partial picture of cylindrical cross-bar array $d/p = 0.2$, $\theta = 45^\circ$. (b) Cylinder schematic.

The test section with the cylindrical cross-bar arrays is shown in Figure 3.4 indicating how the pitch-diameter ratio, and the angle to the flow direction, θ , are defined. The normalized length, width, and height of the channel are also shown. The x-direction of the coordinate system is orientated in the flow direction, with the y-direction orientated parallel to the height of the channel, and the z-direction to the width of the channel.

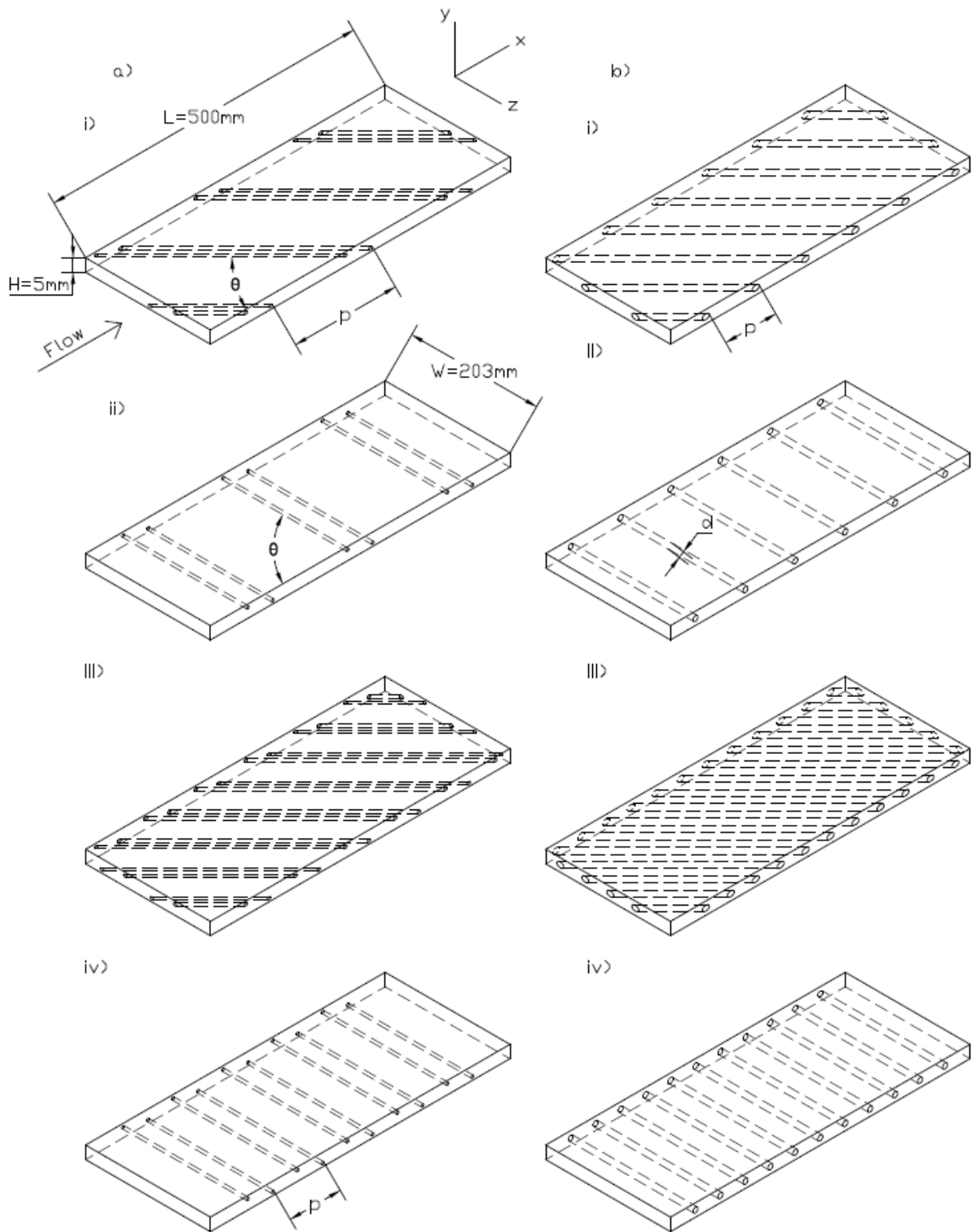


Figure 3.4: Cylindrical geometries of (a) $d = 1$ mm, staggered rods. (i) $\theta = 45^\circ$, $d/p = 0.025$. (ii) $\theta = 90^\circ$, $d/p = 0.025$. (iii) $\theta = 45^\circ$, $d/p = 0.05$. (d) $\theta = 90^\circ$, $d/p = 0.05$. (b) $d = 2$ mm, in-line rods. (i) $\theta = 45^\circ$, $d/p = 0.1$. (ii) $\theta = 90^\circ$, $d/p = 0.1$. (iii) $\theta = 45^\circ$, $d/p = 0.2$. (d) $\theta = 90^\circ$, $d/p = 0.2$.

The different cylindrical cross-bar arrays are summarized in Table 3.1, sorted from the lowest to the highest d/p . Note that the 1mm diameter cylindrical rods are staggered and the 2mm diameter rods

are in-line with the flow direction to keep the blockage ratio constant. All the different diameter to pitch ratio geometries were tested in a perpendicular orientation and 45° to the flow direction.

For the rest of the text, the cylindrical arrays will be referred to by the pitch to diameter ratio, d/p , the angle to the flow direction, θ , and whether the cylinders are staggered or in line with the flow, and the test section geometry with to the normalized dimension to the channel height.

Table 3.1: Summary of cylindrical inserts.

d	p	θ	d/p	Staggered/In-line
1 mm	40 mm	90°	0.025	Staggered
1 mm	40 mm	45°	0.025	Staggered
1 mm	20 mm	90°	0.05	Staggered
1 mm	20 mm	45°	0.05	Staggered
2 mm	20 mm	90°	0.1	In-line
2 mm	20 mm	45°	0.1	In-line
2 mm	10 mm	90°	0.2	In-line
2 mm	10 mm	45°	0.2	In-line

3.4. Test section

3.4.1. Heat transfer tests

Both walls are being heated with the same heat flux during all the heat transfer tests. A constant heat flux, \dot{q} , was imposed on the walls of the test section. The test section was insulated by polystyrene plates to limit the convection heat loss to the surroundings. The length of the insulation was 700mm, with a width of 203mm, and a height of 40 mm. The thermal conduction of the polystyrene insulation is 0.041 W/mK. A wall thickness of 6 mm was used instead of 12 mm to further limit the conduction losses in the x-direction.

The heaters were connected in parallel to a 60 V, 10 A dual power supply. The selected silicone encapsulated etched foil heaters are 610x203x1 mm in dimension, with a maximum power density of 7.75 kW/m². The power supply was adequate to increase the mean air temperature by 10°C relative to the local wall temperature at higher Reynolds numbers and more at smaller Reynolds numbers. The selected heater size ensures that the entire test section area is being heated by a constant heat flux. Figure 3.5 shows the test section setup used for heat transfer tests.

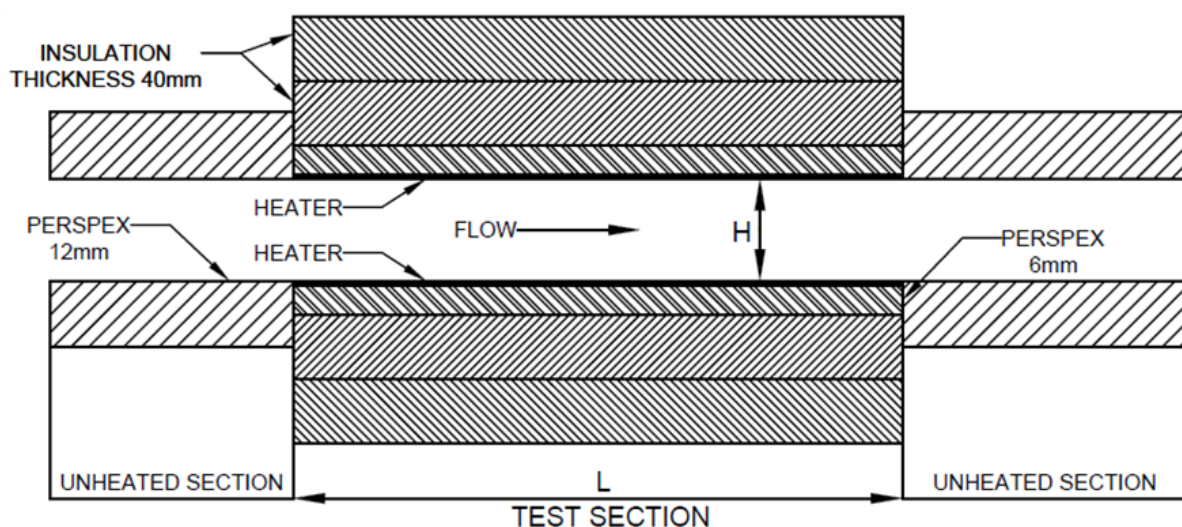


Figure 3.5: Heat transfer test setup.

Type-T thermocouples with a 32-gauge diameter were used. The thermocouples were calibrated using a thermal bath. Thermocouples were spaced more densely at the inlet and outlet of the test section with a pitch of 5 mm in the first and last third of the test section and 10 mm in the middle third. For measuring heat loss, thermocouples were placed between the insulation and the Perspex wall and between the two layers of insulation. The thermocouples for measuring wall temperature were fixed inside holes on the centre line of the top wall with thermal paste to the back of the heater. The heater thickness was 1mm and assumed to be small enough for the temperatures measured by the thermocouples to be equal to the wall temperatures on the fluid side of the heater.

The locations of the wall temperature thermocouples are shown in Figure 3.6 (a) with the heat loss thermocouple positions shown in (b). The heat loss thermocouples have the same layout in between the Perspex plate and the first layer of insulation, as in between the two layers of insulation. The thermocouples measuring the heat loss is placed in between the two layers of insulation and not on the outside of the insulation to ensure that the thermocouple temperature is not affected by the ambient air temperature on the outside of the test section. A detailed view of the thermocouple installation is shown in Figure 3.6 (c).

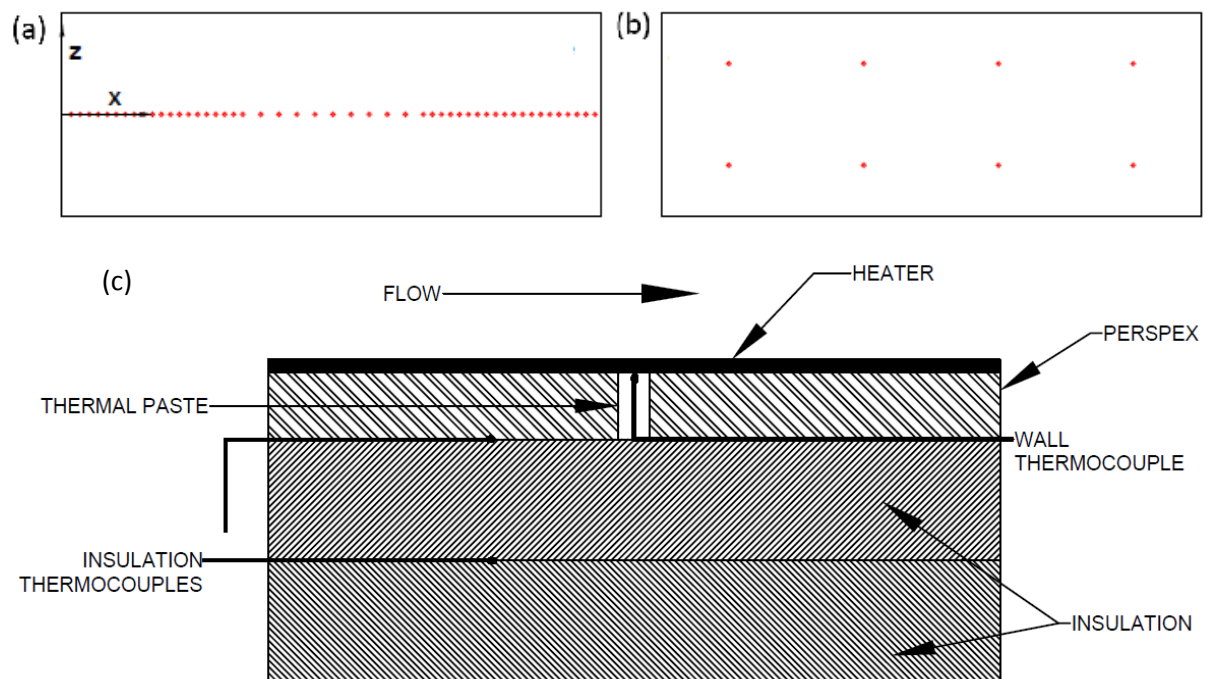


Figure 3.6: Thermocouples. (a) Wall temperature thermocouple locations. (b) Heat loss thermocouple locations. (c) Detail of thermocouple installation.

3.4.2. Pressure drop tests

The holes in the 12 mm thick pressure wall have 0.3 mm diameter holes on the flow side to have a minimum disturbance on the flow field. Copper tubes are inserted into the larger concentric holes on the outside of the wall and connected to the pressure scanning valve with silicone tubes. The wall pressure was measured in the centre of the wall in steps of 15 mm. A section-view of the pressure tap wall is shown in Figure 3.7.

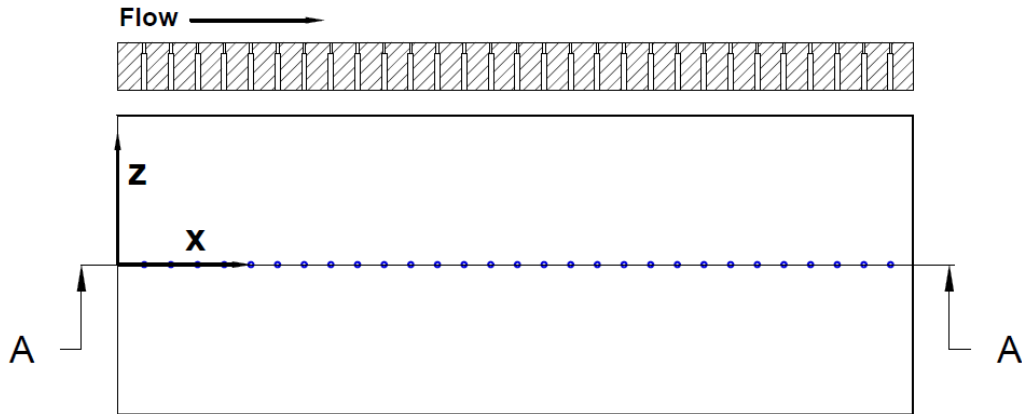


Figure 3.7: Section view of pressure tap wall with the location of pressure taps on the test section wall.

3.5. Instrumentation

3.5.1. Pressure transducers

Electronic differential pressure transducers were used during the pressure drop tests and for finding the mass flow rate with the orifice plates. Five different pressure transducers were used during the pressure drop tests. More sensitive pressure transducers were used at low flow rates where the pressure drop is smaller, to keep the uncertainty at a minimum. The transducer with the smallest full-scale capabilities used is 125 Pa and the largest 7 500 Pa.

Different sized pressure transducers were used at the orifice plates. A transducer with a full-scale of 500 Pa was used for Reynolds numbers smaller than 2 000 and three different pressure transducers were used at Reynolds numbers higher than 2 000 with the smallest full scale was 65 Pa and the largest 250 Pa.

The transducers were calibrated using a low-pressure calibrator. During the calibration process of the pressure transducers, voltage readings were taken with an inclination and declination of pressure to ensure that the hysteresis is small enough not to have a remarkable effect on the data.

3.5.2. Orifice plates

The pressure drops over the orifice plates were used to find the mass flow rate in the test section by assuming continuity and is described in Appendix A. The orifice plate geometry is shown in Figure 3.8.

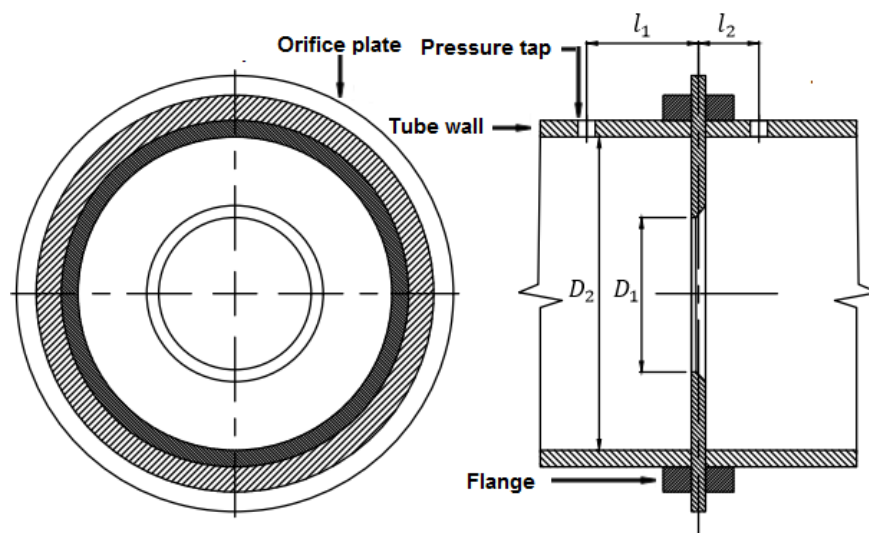


Figure 3.8: Orifice plate geometry

The dimensions of the orifice plates used in the 2" and 4" pipes are shown in Table 3.2. Larger pressure drops occur over the orifice plate in the 2" pipe and therefore a larger pressure transducer was used. For laminar flow, the 2" diameter pipe was used and for flow larger than 2 000 Reynolds number, the 4" diameter pipe was used.

Table 3.2: Orifice plate dimensions.

Pipe diameter	l_1	l_2	D_1	D_2
2"	50 mm	25 mm	15.4 mm	50.8 mm
4"	120 mm	60 mm	50.8 mm	101.6 mm

3.5.3. Control and data logging

The flow rate was controlled by a variable speed drive on the blower. A data acquisition system connected to a personal computer was used to measure the output from the pressure transducers and the thermocouples. The data was logged by National Instruments LabVIEW software. The post-processing was done by making use of MATLAB software where the text file output was loaded, and the output calculation saved in Excel books.

3.6. Data reduction

The Reynolds number in the test section was calculated as:

$$Re = \frac{\rho v_{ave} D_h}{\mu} \quad (3.1)$$

Where ρ was the density of the air at the channel inlet (the flow was assumed to be incompressible, see Appendix A), v_{ave} was the mean velocity of the flow, D_h the hydraulic diameter, and μ the dynamic viscosity. The density of the air, ρ , was found using the ideal gas law:

$$\rho = \frac{P_{amb}}{RT_{amb}} \quad (3.2)$$

With P_{amb} and T_{amb} the ambient pressure and temperature measured with the weather meter and R the ideal gas constant of air. The mean flow velocity in the channel, v_{ave} , was found using the mass flow rate, \dot{m} , through the orifice plate:

$$v_{ave} = \frac{\dot{m}}{\rho A_c} \quad (3.3)$$

Where A_c is the cross-sectional area of the channel:

$$A_c = WH \quad (3.4)$$

With D_t the tube diameter. And D_h , the hydraulic diameter of the test section with W the channel width and H the channel height:

$$D_h = \frac{2WH}{W + H} \quad (3.5)$$

The local Nusselt number was calculated using Equation (3.6):

$$Nu_x = \frac{\dot{q}_{con} D_h}{k_{air} (T_{wall} - T_{mx})} \quad (3.6)$$

Where \dot{q}_{con} is the convective heat flux after the heat loss have been subtracted from the flux of the heater power, \dot{q}_{heater} . The thermal conductivity of air, k_{air} , was found by using the CoolProp add-in with Python, at the bulk fluid temperature, and T_{wall} and T_{mx} the local wall and mean air temperature respectively.

$$\dot{q}_{con} = \dot{q}_{heater} - \dot{q}_{loss} \quad (3.7)$$

The local mean air temperature was found using the law of conservation of energy as there were only wall thermocouples:

$$T_{mx} = T_{amb} + \frac{\dot{q}_{con}A(x)}{\dot{m}C_p} \quad (3.8)$$

Note that the area in Equation (3.8), $A(x)$, refers to the total area where heat is gained to the fluid from the inlet of the test section up to the local wall thermocouple. The inlet air temperature was equal to the ambient temperature. The heat flux imposed on the test section from the heaters was:

$$\dot{q}_{heater} = \frac{VI}{A_{heater}} \quad (3.9)$$

And the total heat loss was found by numerically integrating the local heat loss with the trapezoidal rule:

$$\dot{q}_{loss} = \frac{1}{L} \int_0^L \dot{q}_{loss}(x) dx \quad (3.10)$$

Where the local heat loss was conduction losses over the insulation plates:

$$\dot{q}_{loss}(x) = k_{ins} \frac{T_2 - T_1}{\Delta x_{ins}} \quad (3.11)$$

The average Nusselt number was then found by the numerical integral average after the thermal entrance length of the test section, x , by using the trapezoidal rule:

$$Nu = \frac{1}{L - x} \int_x^L Nu_x dx \quad (3.12)$$

The pressure data is non-dimensionalized by making use of the friction factor. To find the friction factor, f , it is necessary to find the slope of the pressure drop in the test section, $\Delta P/\Delta x$. This was done by using the slope of a linear least-squares regression line after the flow has been estimated to be fully hydraulically developed in the test section.

$$f = \frac{(\Delta P/\Delta x)(D_h)}{2\rho v^2} \quad (3.13)$$

The thermohydraulic performance can then finally be calculated by using Equation (3.14):

$$\eta = \frac{\frac{Nu}{Nu_0}}{\left(\frac{f}{f_0}\right)^{\frac{1}{3}}} \quad (3.14)$$

Where the performance of the channel with cylindrical arrays is compared to the smooth channel at each Reynolds number.

3.7. Experimental procedure

All measurements were taken during steady-state when there was no significant change in measurements with time. The time to reach a quasi-steady-state during the heat transfer tests

reduced as the Reynolds number increased. The heat transfer tests reached a steady state after logging data for approximately one hour in the laminar flow regime, half an hour in the transitional regime, and ten minutes in the turbulent regime. Three thermocouples were used to monitor steady-state convergence, see Figure 3.9 for the convergence of one thermocouple. See Appendix B for the calibration of the thermocouples.

The thermocouple data was logged at a frequency of 1 Hz and 500 readings were averaged, once steady-state had been achieved, to find a single data point for each thermocouple, shown in Appendix F, for the calculation of the local surface Nusselt numbers. The temperature measurements of the thermocouple are dependant only on the resistance of the wire and therefore no hysteresis was expected during the heat transfer tests [49].

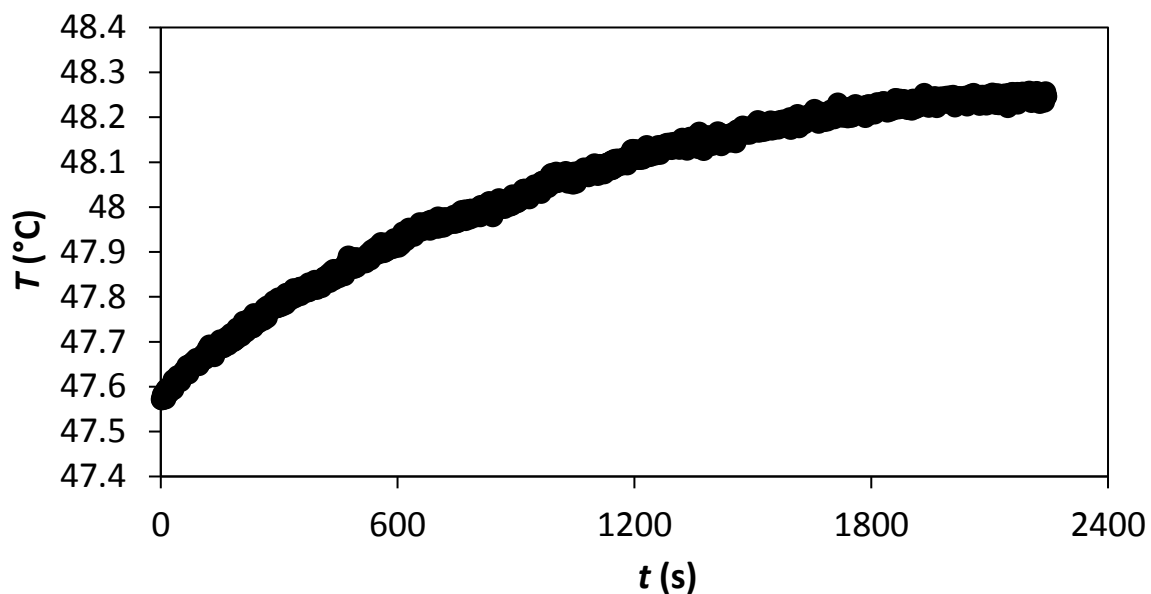


Figure 3.9: Temperature change with time at $x/H = 50$ and $Re = 920$.

The pressure transducers were calibrated before taking the measurements, see Appendix C. The pressure drop data was taken isothermally at ambient temperature conditions so there was no need to wait for steady-state after the frequency drive had been used to adjust to the desired flow rate. The scanning valve was used to switch between pressure taps, taking 1 200 readings at a frequency of 200 Hz at each of the 37 pressure taps. The measurements at each pressure tap were then averaged to find a single data point shown in Appendix G.

The pressure drops over the orifice plates were measured continuously at a frequency of 200 Hz for all tests and 12 000 readings were averaged to find the Reynolds number. Temperature and pressure data were found at each flow rate after which the flow rate was adjusted, starting at $Re = 640$ and increasing chronologically to $Re = 12\,500$. Three tests were then repeated at $Re = 9\,700$, $Re = 4\,000$, and $Re = 920$ to ensure that the friction factor and average Nusselt number remained within the calculated uncertainty. After these tests were done, the positions of the cylindrical arrays were moved 2.5mm relative to the wall in the x -direction to evaluate if the data remains consistent at the three repeated Reynolds numbers $Re = 920$, $Re = 4\,000$, and $Re = 9\,700$.

3.8. Experimental test matrix

The experimental tests were conducted at 15 different Reynolds numbers for the heat transfer and pressure drop tests for each of the eight different cylindrical cross-bar arrays. The tests were repeated

at three different Reynolds numbers to verify repeatability. The cylindrical arrays were then moved $x/H = 0.2$ downstream for tests to be repeated to see if the position of the pressure valves and thermocouples influenced the measurements. For cylindrical cross-bar configurations with larger pressure drops, the maximum centrifugal fan setting was used to determine the largest achievable Reynolds number. The geometry with the largest d/p ratio of 0.2 with an angle of $\theta = 90^\circ$ was able to be tested at a maximum Reynolds number of 9 700.

The number of tests done for each of the cylindrical cross-bar configurations is shown in Table 3.3. The number of repeats is included in the respective columns and is six for each test for each cross-bar configuration i.e. one test is defined as applying the fan setting for the certain Reynolds number, after which the pressure drops or surface temperatures were measured at each of the pressure taps or thermocouples, independent of the measuring frequency. The number of experimental tests done is 360 which does not include the experimental tests for CFD validation. The isothermal pressure drop tests and heat transfer tests could be combined to find the thermal performance coefficient because of the negligible air density changes at the tested temperatures.

Table 3.3: Experimental test matrix

d/p	θ	Reynolds number range	No. of heat transfer tests	No. of pressure drop tests
Plane channel	-	640 – 12 500	15	15
0.025	90°	640 – 12 500	21	21
0.025	45°	640 – 12 500	21	21
0.05	90°	640 – 12 500	21	21
0.05	45°	640 – 12 500	21	21
0.1	90°	640 – 12 500	21	21
0.1	45°	640 – 12 500	21	21
0.2	90°	640 – 9 700	18	18
0.2	45°	640 – 12 500	21	21

3.9. Uncertainty analysis

The method of Figliola and Beasley [50] and Dunn [51] was used for determining the uncertainty for the measured and calculated parameters including the geometric uncertainties, pressure drops over the orifice plates, mass flow-rates, mean flow velocities, Reynolds numbers, temperature measurements, heat flux uncertainties, average Nusselt numbers, pressure measurements, friction factors, and thermal performance coefficients. The uncertainty of independent parameters was found using the root sum square method of standard deviation and the dependent variables' uncertainties were calculated as functions of the independent parameters. Consult Appendix B for the calibration of the thermocouples, Appendix C for the calibration of the pressure transducers and Appendix D for uncertainty equations and calculation examples.

The uncertainty of the instruments used for measurement is shown in Table 3.4. The thermocouples were used to measure the ambient, wall, and insulation temperatures for the calculation of the Nusselt numbers. The pressure transducers were used to measure the pressure drop over the orifice plates for finding the mass flow rate and the wall pressures for finding the friction factors. The barometer was used for measuring the ambient pressure. The multimeter was used to find the voltage across the heaters more accurately than the power supply display and to reduce the error of the current measurement by creating a correlation line between the multimeter and the power supply display.

Table 3.4: Instrumentation.

Instrument	Range	Accuracy
Thermocouples	-200 – 200 °C	± 0.13 °C
Pressure transducer	0 – 62 Pa	± 1.62 Pa
	0 – 124 Pa	± 2.15 Pa
	0 – 245 Pa	± 2.55 Pa
	0 – 497 Pa	± 4.99 Pa
	0 – 1875 Pa	± 19.03 Pa
	0 – 3750 Pa	± 38.05 Pa
	0 – 7500 Pa	± 75.43 Pa
Barometer	70 – 110 kPa	± 0.3 hPa
Multimeter	0 – 10 A	± 1.5% of nominal value
	0 – 1000 V	± 0.3% of nominal value

The percentage uncertainty for the Reynolds number, mean flow velocity, and mass flow rate is shown in Figure 3.10. As the Reynolds number increases, the uncertainty generally reduces except from $Re = 1\ 800$ to $Re = 3\ 000$. This is because the larger orifice plate is being used in the 4" tube instead of the 2" tube with the smaller orifice plate, where the pressure drop is larger. The uncertainty in the pressure drop over the orifice plate increases when the larger orifice plate is being used, which increases the uncertainty in the mass flow rate measurement. Because the Reynolds number and average flow velocity are functions of the mass flow rate, the uncertainty was affected and changed with the uncertainty in the mass flow rate. Between a Reynolds number of 3 000 and 12 500, the uncertainty reduces as the pressure drop over the orifice plate increases with the fraction of the calibration uncertainty of the pressure transducer reducing.

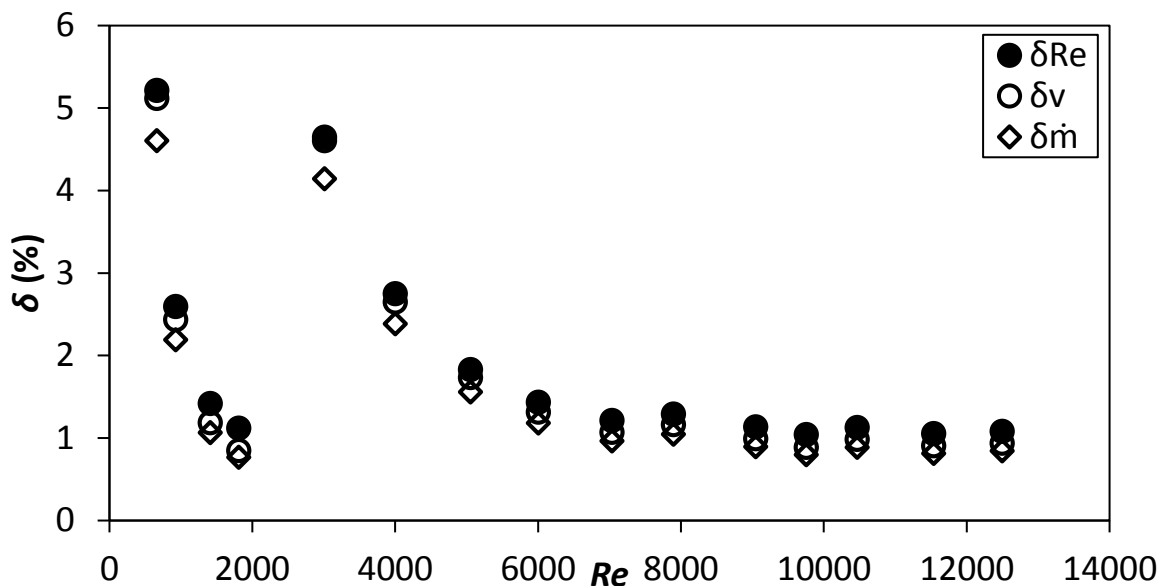


Figure 3.10: Flow rate uncertainty.

The uncertainty for the mean, fully developed Nusselt number is shown in Figure 3.11 and Figure 3.12 for the cylindrical cross-bar configurations with $\theta = 90^\circ$ and $\theta = 45^\circ$ respectively. With an increase in mass flow rate, there is a decrease in uncertainty. The local mean fluid temperature is a function of the inverse of the mass flow rate, therefore the uncertainty in the local mean fluid temperature reduces with an increase in mass flow rate. There is also an increase in the difference between the wall temperature and fluid temperature with an increase in the mass flow rate, because of a higher heat flux being used. The uncertainty of the local Nusselt number is a function of the inverse of the

difference between the wall temperature and the mean fluid temperature and reduces with an increase in the difference between these temperatures. The uncertainty of the mean Nusselt numbers is a function of the uncertainty of the local Nusselt numbers and is calculated using the integral average of the uncertainty of the local Nusselt numbers. The integral average is being used instead of a normal average, because of the difference between the distances between the wall thermocouples. The distances between the thermocouples are less towards the end of the test section than halfway in the test section.

The uncertainties in the Nusselt numbers are generally lower for $\theta = 45^\circ$ in comparison with $\theta = 90^\circ$. In the cases where $\theta = 45^\circ$, the temperature difference between the wall temperatures and fluid temperatures are larger than in the cases where $\theta = 90^\circ$, with the same induced heat flux, because of a decrease in convective heat transfer, causing the uncertainty to be lower for $\theta = 45^\circ$.

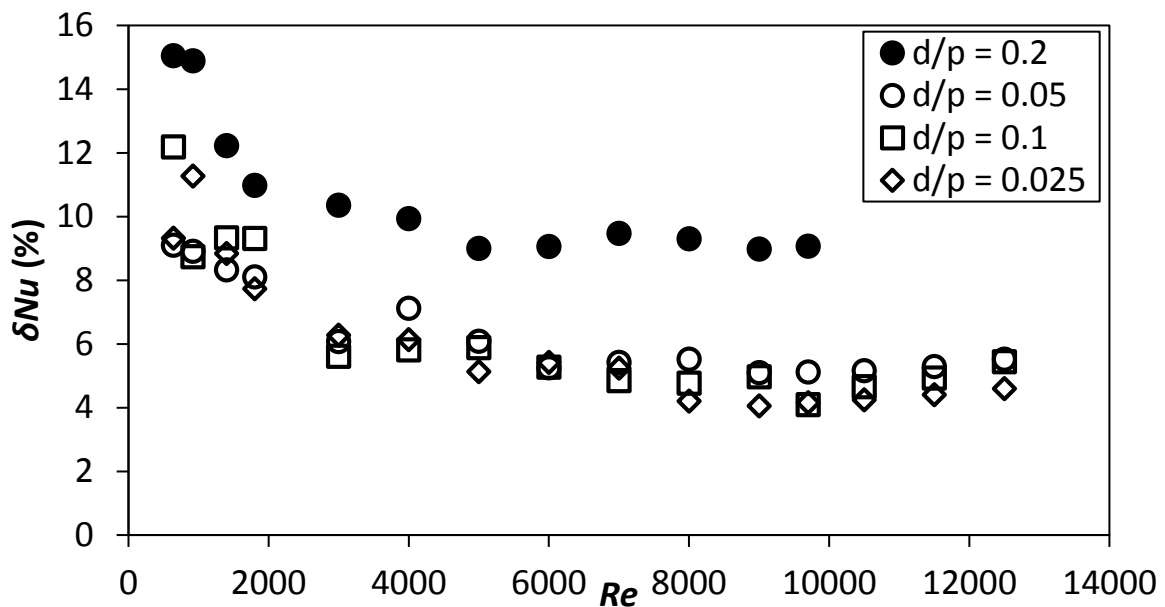


Figure 3.11: Nusselt number uncertainty, $\theta = 90^\circ$.

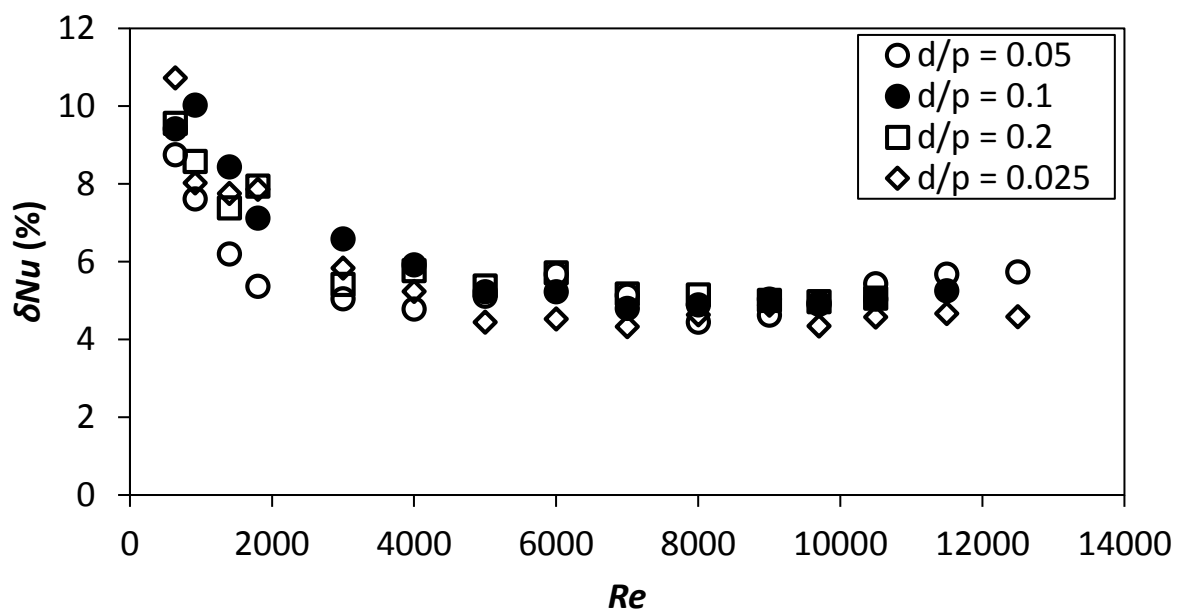


Figure 3.12: Nusselt number uncertainty, $\theta = 45^\circ$.

The uncertainty of the friction factors is shown in Figure 3.13 and Figure 3.14 for $\theta = 90^\circ$ and $\theta = 45^\circ$ respectively. The uncertainty generally decreases with an increase in Reynolds number because the friction factor uncertainty is a function of the inverse of the mean flow velocity squared, which increases quadratically with an increase in Reynolds number. Between a Reynolds number of 1 800 and 3 000, there is an increase in the uncertainty of the friction factor because of the increase in the uncertainty of the mean flow velocity explained in the paragraph above Figure 3.10.

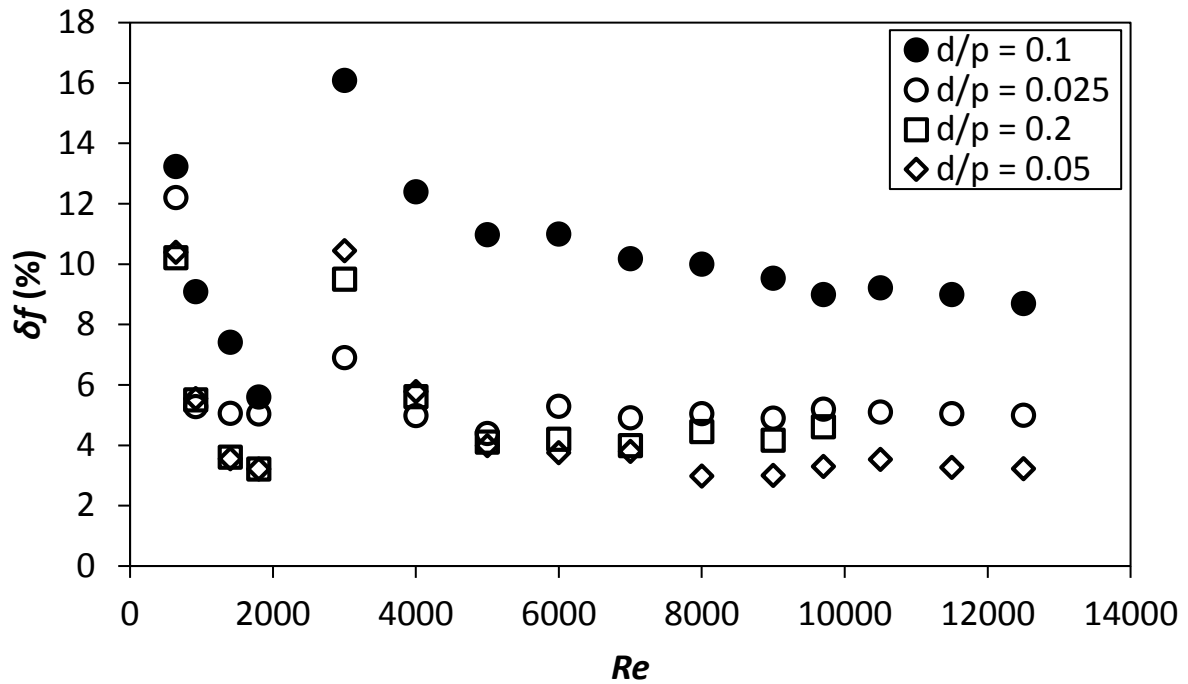


Figure 3.13: Friction factor uncertainty, $\theta = 90^\circ$.

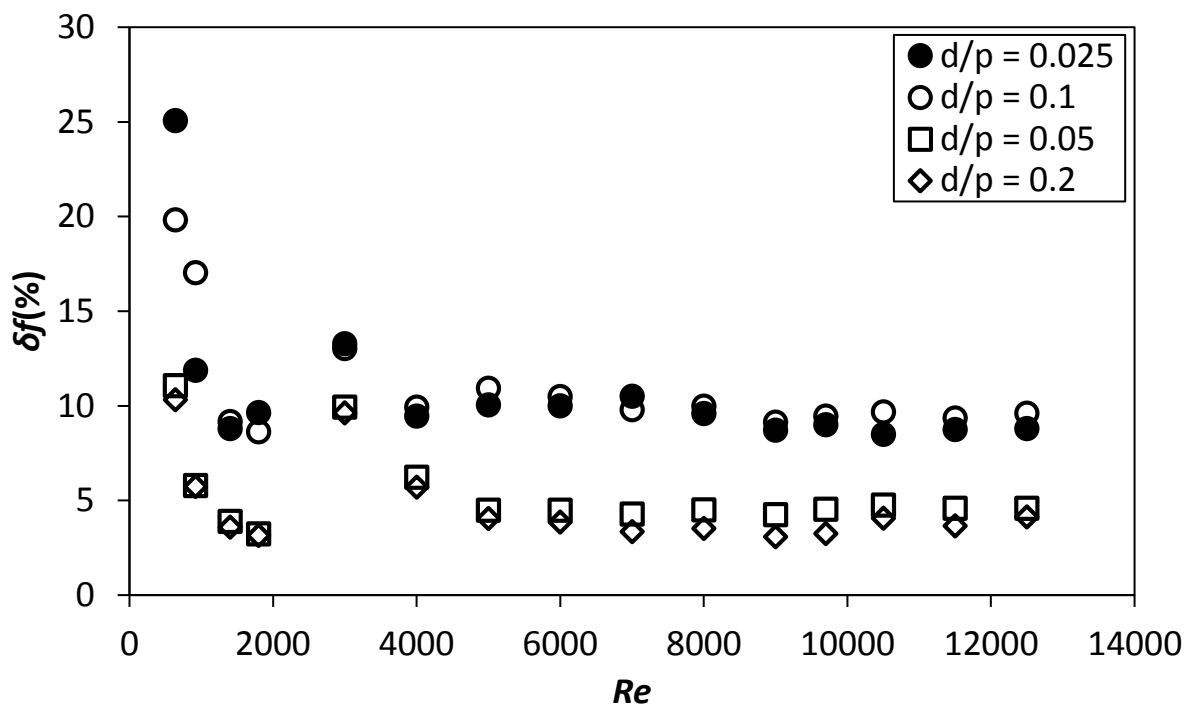


Figure 3.14: Friction factor uncertainty, $\theta = 45^\circ$.

The uncertainty of the thermal performance coefficients is shown in Figure 3.15 and Figure 3.16 as a function of Reynolds number for $\theta = 90^\circ$ and $\theta = 45^\circ$ respectively. The uncertainty generally decreases with an increase in Reynolds number from $Re = 640$ to $Re = 1\,800$ and then increases at $Re = 3\,000$ after which it decreases again with an increase in Reynolds number. One of the variables that it is a function of is the friction factor uncertainty, which shows the increase in uncertainty between $Re = 1\,800$ and $Re = 3\,000$.

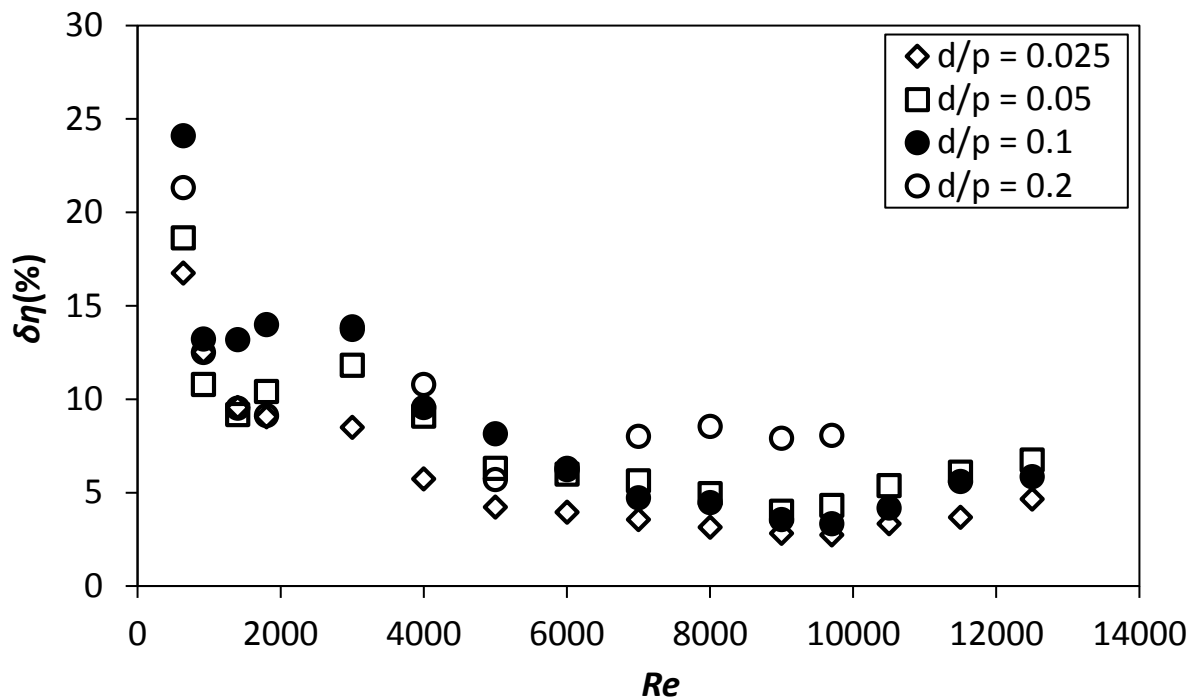


Figure 3.15: Thermal performance coefficient uncertainty, $\theta = 90^\circ$.

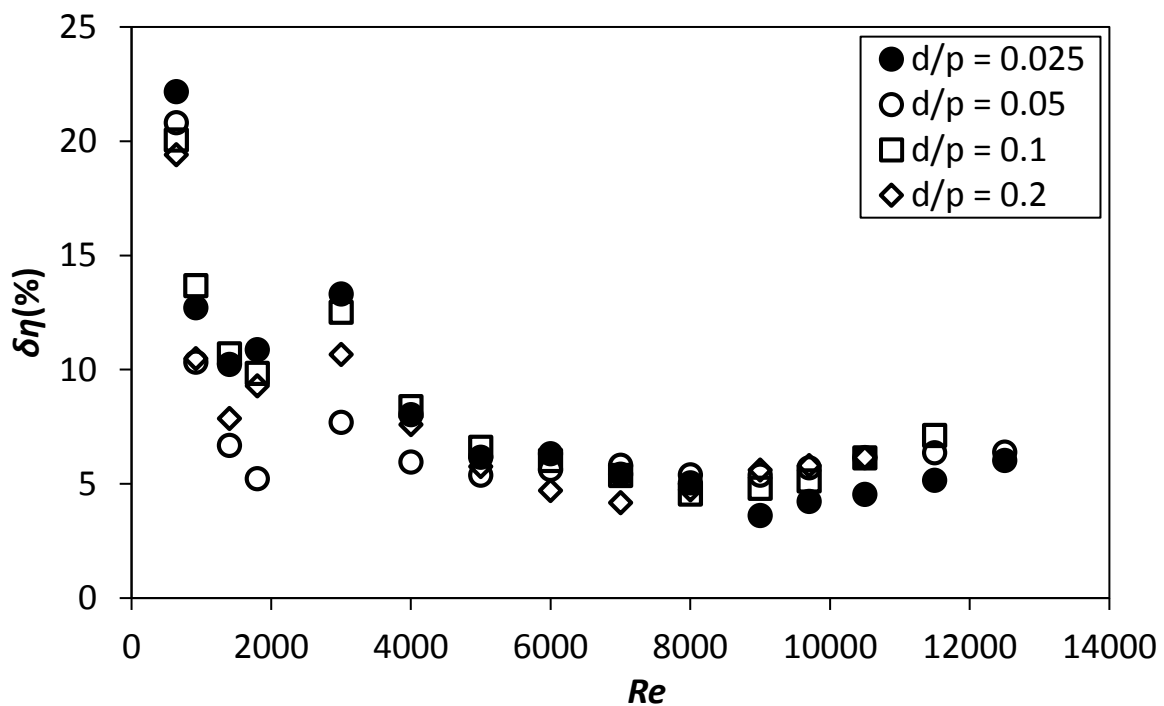


Figure 3.16: Thermal performance coefficient uncertainty, $\theta = 90^\circ$.

3.10. Repeatability

Experimental tests were repeated for every cylindrical cross-bar configuration at three Reynolds numbers: $Re = 920$, $Re = 4\,000$, and $Re = 9\,700$, for the heat transfer and pressure drop tests. The repeated tests were done twice, with the cylindrical array in the same position as with the first iteration and moved 1 d/H downstream, with respect to the inlet of the test section. The first repeat was done after all the first tests were done at every Reynolds number instead of directly after the first test at the respective Reynolds number. The absolute value of the percentage difference of the first and the repeated tests were used to quantify the repeatability of the tests.

The repeated heat transfer test results for the average Nusselt number are shown in Table 3.5. The percentage difference between the first iteration of the tests and the repeats generally decreases with an increase in Reynolds number. There is a direct correlation in the results with the cylindrical configurations in the first and the second position where the geometrical arrays were moved 1 d/H downstream and are therefore independent of the position of the cylindrical cross-bar arrays relative to the thermocouple positions on the test section wall. The difference between the repeated test results and the first test results is lower than the calculated uncertainty for all the repeated experimental average Nusselt number results.

Table 3.5: Nusselt number average repeatability.

d/p	θ	Re	Nu_{avg1}	Nu_{avg2} (%)	Nu_{avg3} (%)
0.025	90°	920	12.44	11.76 (5.44%)	11.43 (8.17%)
		4 000	24.16	25.03 (3.64%)	24.81 (2.71%)
		9 700	45.09	44.67 (0.92%)	44.53 (1.23%)
0.025	45°	920	10.99	11.37 (3.47%)	11.46 (4.30%)
		4 000	23.29	22.32 (4.14%)	22.05 (5.32%)
		9 700	41.06	41.03 (0.08%)	42.34 (3.10%)
0.05	90°	920	12.02	12.60 (4.82%)	12.04 (0.18%)
		4 000	33.22	32.32 (8.48%)	30.40 (2.71%)
		9 700	56.31	57.80 (2.63%)	56.31 (3.47%)
0.05	45°	920	11.67	11.51 (1.39%)	11.50 (1.48%)
		4 000	25.16	25.73 (2.21%)	26.41 (4.72%)
		9 700	44.59	44.59 (0.87%)	44.12 (1.07%)
0.1	90°	920	13.12	12.81 (2.38%)	11.95 (8.88%)
		4 000	29.61	28.93 (2.30%)	29.00 (2.07%)
		9 700	49.07	48.09 (1.99%)	50.73 (3.38%)
0.1	45°	920	12.73	13.13 (3.20%)	12.51 (1.73%)
		4 000	28.21	28.82 (2.16%)	27.74 (1.68%)
		9 700	49.55	50.33 (1.58%)	48.56 (2.00%)
0.2	90°	920	13.54	13.88 (2.50%)	13.71 (1.24%)
		4 000	36.35	35.69 (1.81%)	36.25 (0.27%)
		9 700	66.33	68.21 (2.83%)	65.66 (1.01%)
0.2	45°	920	12.88	12.45 (3.33%)	13.44 (4.35%)
		4 000	33.12	34.58 (4.40%)	32.52 (1.81%)
		9 700	55.66	53.45 (3.97%)	56.17 (0.92%)

The temperature data and the repeated data for $d/p = 0.025$, $\theta = 90^\circ$ at $Re = 9\,700$ is shown in Figure 3.17. The wall temperature for the first repetition where the cylindrical cross-bar array had the same position, has the same locations for the peaks and the troughs on the graph. For the third repetition

where the position of the array was moved $1 d/H$ downstream relative to the inlet of the test section, the peaks and troughs moved approximately $1 d/H$ downstream. The local Nusselt numbers and the repeated cases for $d/p = 0.025$, $\theta = 90^\circ$ at $Re = 9\,700$ are shown in Figure 3.18. The first repetition where the position of the array was not changed has the same location for the peaks and troughs on the graph and moved $1 d/H$ downstream for the third repetition where the array was moved $1 d/H$ downstream.

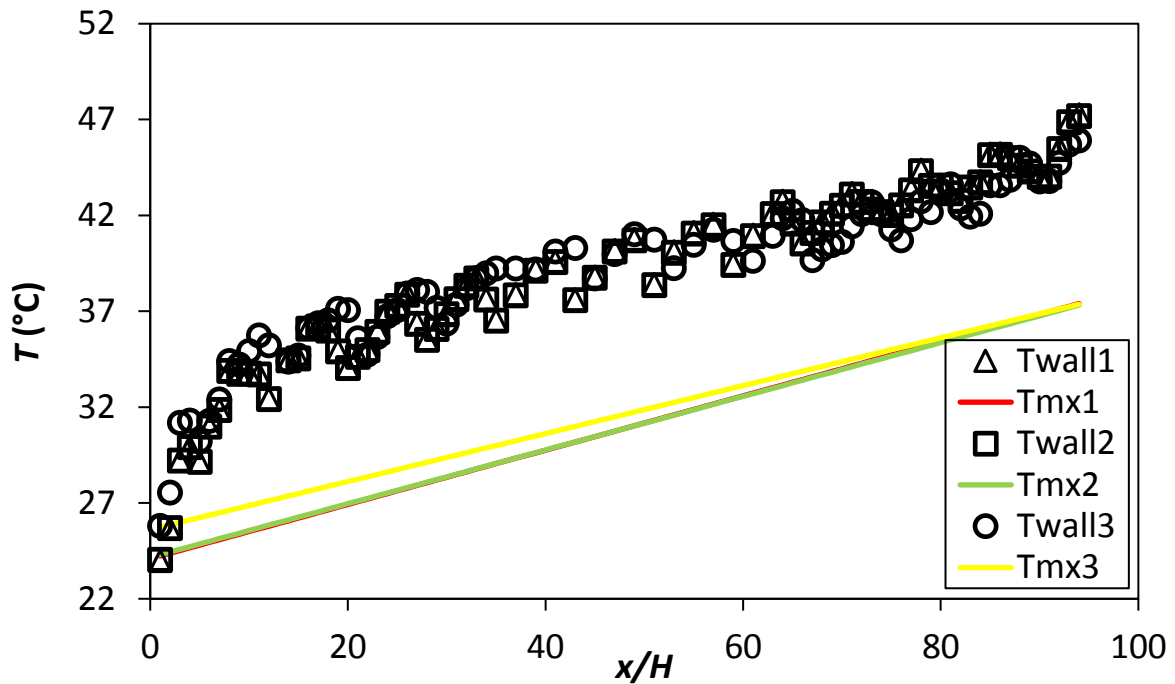


Figure 3.17: Wall and mean local air temperature data of $d/p = 0.025$, $\theta = 90^\circ$ at $Re = 9\,700$ plotted with repeated test data.

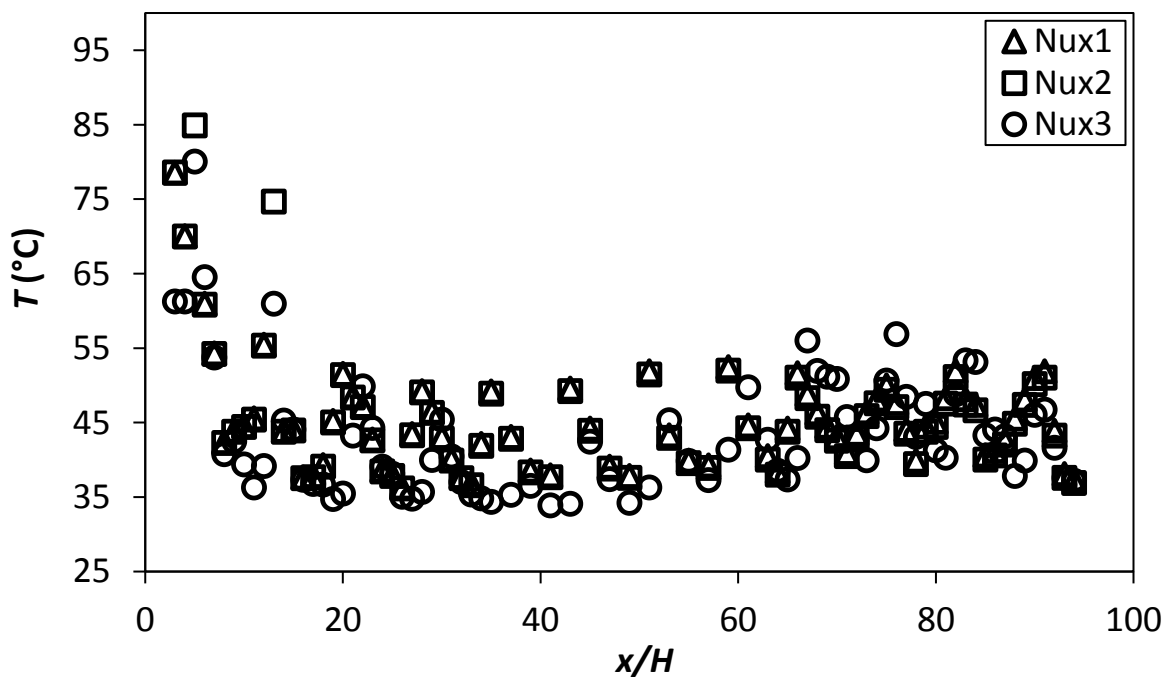


Figure 3.18: Local Nusselt number data of $d/p = 0.025$, $\theta = 90^\circ$ at $Re = 9\,700$ plotted with repeated test data.

The repeated pressure test results for the friction factor is shown in Table 3.6. The results generally correspond more closely as the Reynolds number increases. For the change in the position of the cylindrical cross-bar arrays with respect to the inlet of the test section, there is no direct correlation to the magnitude of the difference between the initial tests and repeated tests and is therefore independent of the position of the cylindrical cross-bar arrays relative to the pressure taps on the test section of the channel wall.

Table 3.6: Friction factor repeatability.

d/p	θ	Re	f_1	f_2 (%)	f_3 (%)
0.025	90°	920	0.0815	0.0855 (4.84%)	0.0750 (8.03%)
		4 000	0.0426	0.0430 (1.12%)	0.0391 (8.26%)
		9 700	0.0332	0.0338 (1.76%)	0.0329 (1.00%)
0.025	45°	920	0.0547	0.0592 (8.15%)	0.0572 (4.65%)
		4 000	0.0263	0.0270 (2.57%)	0.0271 (2.92%)
		9 700	0.0212	0.0218 (2.71%)	0.0216 (1.46%)
0.05	90°	920	0.135	0.140 (3.85%)	0.136 (0.59%)
		4 000	0.0687	0.0646 (6.20%)	0.656 (4.68%)
		9 700	0.0493	0.0479 (2.88%)	0.0476 (3.55%)
0.05	45°	920	0.0978	0.0979 (0.08%)	0.105 (7.35%)
		4 000	0.0410	0.0416 (1.48%)	0.0392 (4.35%)
		9 700	0.0395	0.0399 (0.98%)	0.0415 (5.01%)
0.1	90°	920	0.121	0.121 (0.19%)	0.125 (3.17%)
		4 000	0.0676	0.0672 (0.58%)	0.0674 (0.23%)
		9 700	0.0630	0.0622 (1.21%)	0.0635 (0.87%)
0.1	45°	920	0.101	0.102 (1.02%)	0.104 (3.07%)
		4 000	0.0480	0.0491 (2.20%)	0.0491 (2.13%)
		9 700	0.0454	0.0458 (1.03%)	0.0431 (4.89%)
0.2	90°	920	0.253	0.249 (1.62%)	0.274 (7.78%)
		4 000	0.142	0.141 (1.06%)	0.149 (4.20%)
		9 700	0.128	0.127 (0.74%)	0.126 (1.22%)
0.2	45°	920	0.180	0.176 (2.40%)	0.178 (1.03%)
		4 000	0.0870	0.0865 (0.60%)	0.0898 (3.17%)
		9 700	0.0779	0.0782 (0.33%)	0.0781 (0.23%)

The pressure data and the repeated data for $d/p = 0.025$, $\theta = 90^\circ$ at $Re = 9\,700$ is shown in Figure 3.19. Peaks and troughs in the data are not visible as in Figure 3.17 and Figure 3.18 because of the larger sensor spacing used for the pressure tests. The pressure taps on the channel wall were spaced in 15 mm steps and the thermocouples on the channel wall were spaced in 5 mm steps.

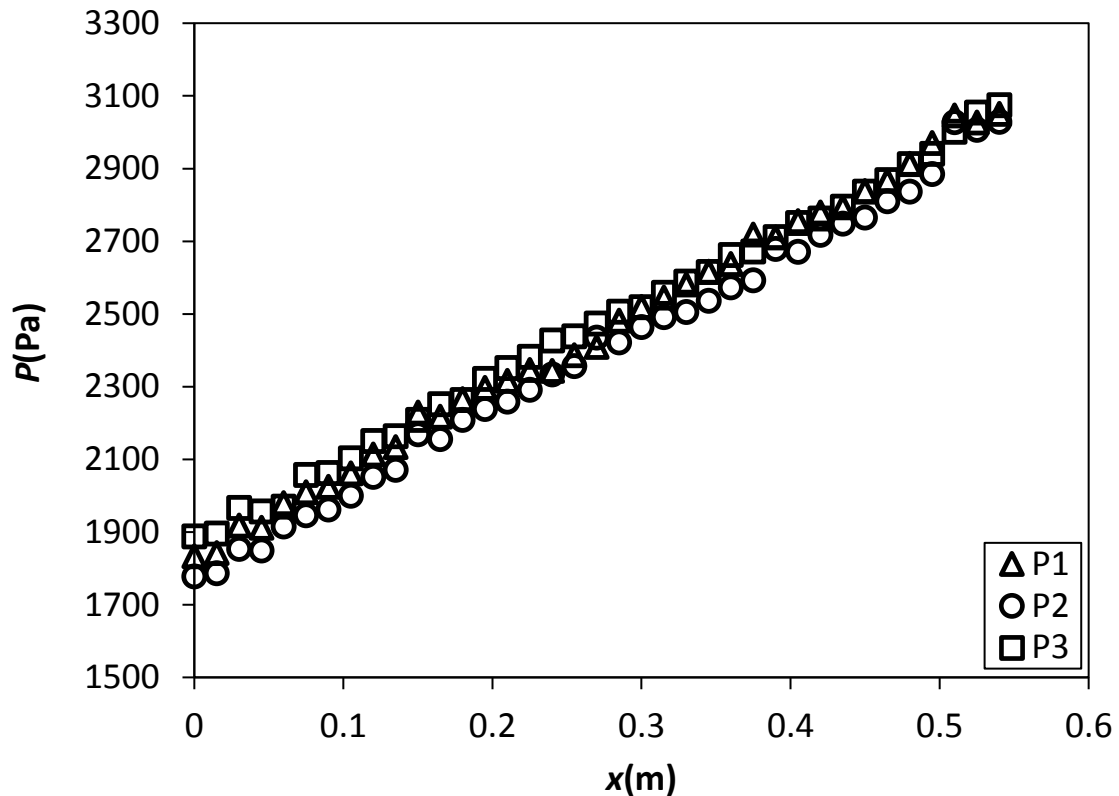


Figure 3.19: Pressure data of $d/p = 0.025$, $\theta = 90^\circ$ at $Re = 9\ 700$ plotted with repeated test data.

3.11. Summary

A total number of eight different cylindrical cross-bar configurations were tested. The cylinder diameter, pitch between cylinders, and the orientation to the flow direction was varied. The smaller diameter cylinders were in a staggered configuration while the larger cylinders were in-line to keep the blockage ratio constant.

Heat transfer and pressure drop tests were done to find the Nusselt number and friction factor at each of the 15 different Reynolds numbers and were repeated at three different flow rates to study repeatability. Steady-state was verified for the heat transfer tests by monitoring temperature vs time graphs at three different thermocouples in the test section.

The heat loss is found by measuring the temperature difference across the insulation and using thermal conduction at eight different local spots. The integral average of the local heat loss is then used to find the total heat loss.

The data reduction method was explained in this chapter. After the Nusselt number and friction factor were found, it was possible to find the thermal performance coefficient to compare the modified channel with the cylindrical cross-bars to a plane channel.

The uncertainty in the calculation of the Reynolds numbers, mean flow velocities, mass flow rates, average Nusselt numbers, and friction factors were analysed. For all the parameters, there is a decrease in uncertainty with an increase in the Reynolds number. A repeatability study was done in tandem with the uncertainty analysis to confirm that the repeated tests yielded results within the uncertainty range.

4. Baseline Measurements without Inserts

4.1. Introduction

This chapter focuses on the qualification of the experimental method. The heat transfer and pressure drop experimental data were compared to various correlations, and previously conducted studies. The local heat transfer data for the smooth channel is shown in Section 4.2, with the average Nusselt numbers in the fully thermally developed flow in Section 4.3. The experimental friction factors in the smooth channel were compared to different correlations in Section 4.4.

4.2. Local Nusselt numbers

The local heat transfer data in the laminar, smooth channel flow was compared to the correlation of Worsøe-Schmidt [6] and Shah [7]a and [7]b, summarized in Table 2.1. The thermally fully developed Nusselt number of Marco and Han [9] is also plotted in Figure 4.1 to show that the flow becomes fully developed at approximately $x/H = 17$.

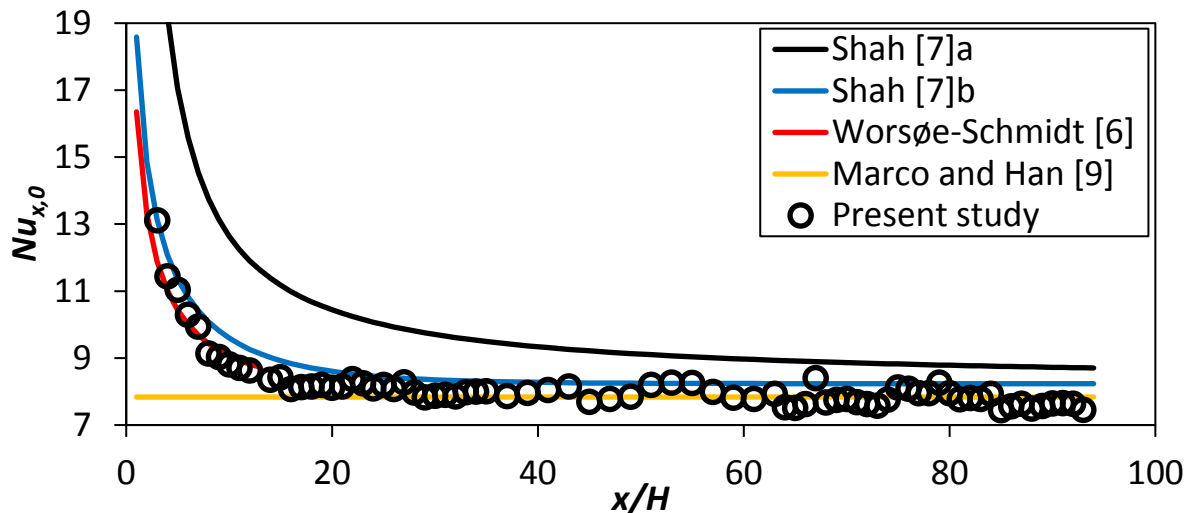


Figure 4.1: Local Nusselt number plotted against x/H at $Re = 920$ for the smooth channel.

The average difference between the experimental local Nusselt numbers and the correlations of the previously conducted research is shown in Table 4.1. The difference is within the uncertainty for the correlations of Worsøe-Schmidt [6] and Shah [7]a and [7]b.

Table 4.1: Comparison of experimental laminar local Nusselt number to correlations at $Re 920$.

Correlation	Equation number	Average difference: $\frac{\sum_i^n \text{abs} \left(\left(\frac{Nu_{x,0}}{Nu_{x,th,0}} - 1 \right) \times 100 \right)}{n}$
Worsøe-Schmidt [6]	(2.7)	4.25%
Shah [7]a	(2.11)	5.26%
Shah [7]b	(2.14)	17.21%

The correlation of Gnielinski [15]a, Equation (2.23) is used for comparison to the experimental data in the transitional flow regime in the smooth channel for the local Nusselt numbers at $Re = 4\,000$ and is shown in Figure 4.2. The fully thermally developed Nusselt number of Gnielinski [15]b, Equation (2.24),

is also plotted to show that the experimental data is fully developed after approximately $x/H = 15$. The average difference between the experimental results and Gnielinski [15]a, Equation (2.23) is 6.47% and is within the uncertainty.

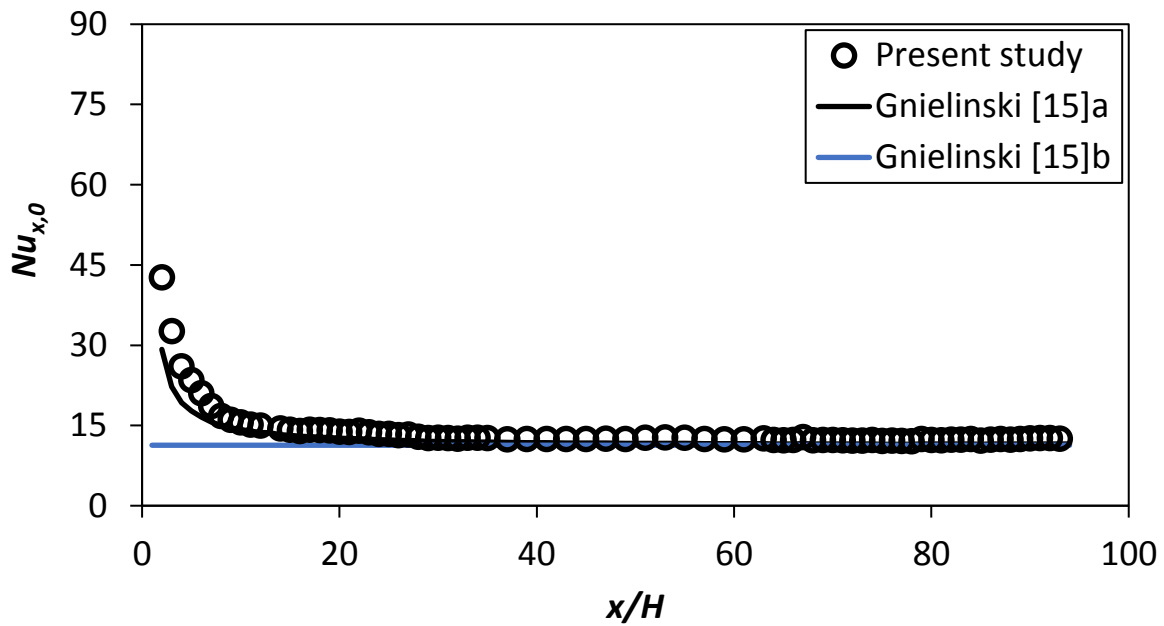


Figure 4.2: Local Nusselt number plotted against x/H at $Re = 4\,000$ for the smooth channel.

Figure 4.3 shows the comparison of the experimental local Nusselt number with Gnielinski [15]a, Equation (2.23). The average ratio of the experimental results and the Gnielinski [15]a correlation is 4.07%. The correlation of the second Petukhov [22], Nusselt number for fully thermally flow, Equation (2.31), is plotted to show that the experimental heat transfer data is fully developed after approximately $x/H = 11$.

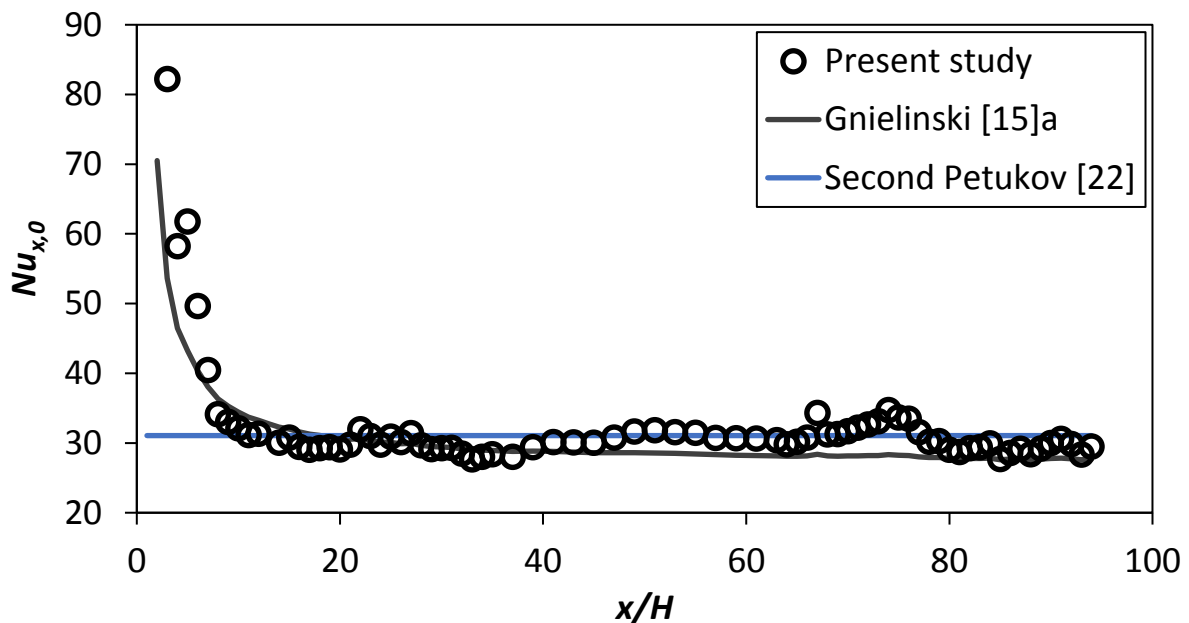


Figure 4.3: Local Nusselt number plotted against x/H at $Re = 10\,500$ for the smooth channel.

The experimental method was qualified with respect to the local Nusselt number because the difference between the data and the correlations are within the uncertainty.

4.3. Average Nusselt numbers

The thermally fully developed average Nusselt number was qualified with respect to the smooth channel. The smooth channel Nusselt numbers are calculated using the integral average of the local Nusselt numbers after the flow has been fully thermally developed, Equation (3.12).

The comparison of the experimental Nusselt number average with the laminar flow theoretical correlations of Schmidt [8] and Marco and Han [9] is shown in Figure 4.4. The largest difference between experimental results and the correlations was at $Re = 640$ where the difference is 4.98% to the Marco and Han [9] correlation, which was within the uncertainty, and 9.58% to the Schmidt [8] correlation. The Marco and Han [9] correlation equation is more accurate because it accounts for the aspect ratio of the channel.

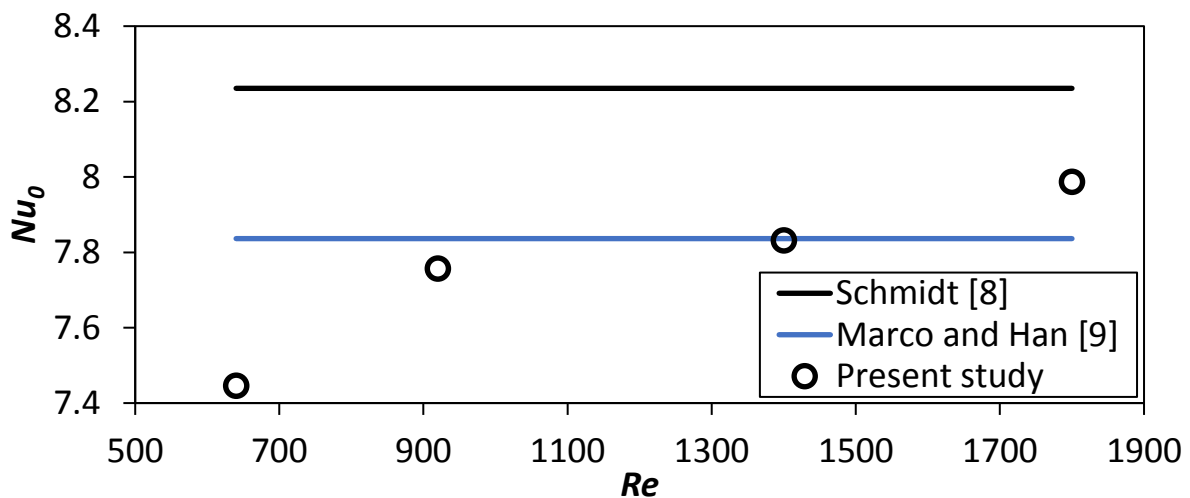


Figure 4.4: Average Nusselt numbers for the smooth channel with laminar flow.

The average Nusselt number is shown in Figure 4.5 for the transitional flow regime, where the experimental data is compared to Gnielinski [15]a, Equation (2.24) and Chilton-Colburn [19], Equation (2.28). The experimental data lies between the two correlations with the difference shown in Table 4.2.

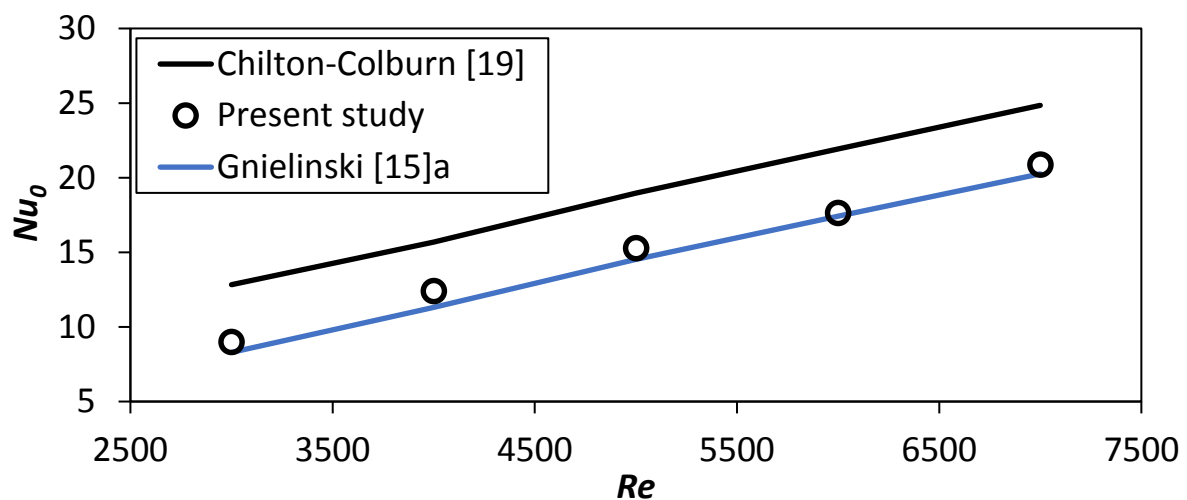


Figure 4.5: Average Nusselt numbers for the smooth channel with transitional flow.

Table 4.2: Qualification of experimental transitional average Nusselt number to correlations.

<i>Re</i>	Difference: $\left(\frac{Nu_0}{Nu_{th,0}} - 1\right) \times 100$	
	Gnielinski [15]a	Chilton-Colburn [19]
3 000	8.55 %	-29.82 %
4 000	9.85 %	-20.84 %
5 000	5.33 %	-19.32 %
6 000	1.32 %	-19.47 %
7 000	3.14 %	-15.92 %

The average Nusselt numbers for turbulent flow in a plane channel were qualified against Gnielinski [15]a, Colburn [20], Chilton-Colburn [19], second Petukhov [22], and Dittus-Boelter [21] with the equations summarized in Table 2.5 and Table 2.7.

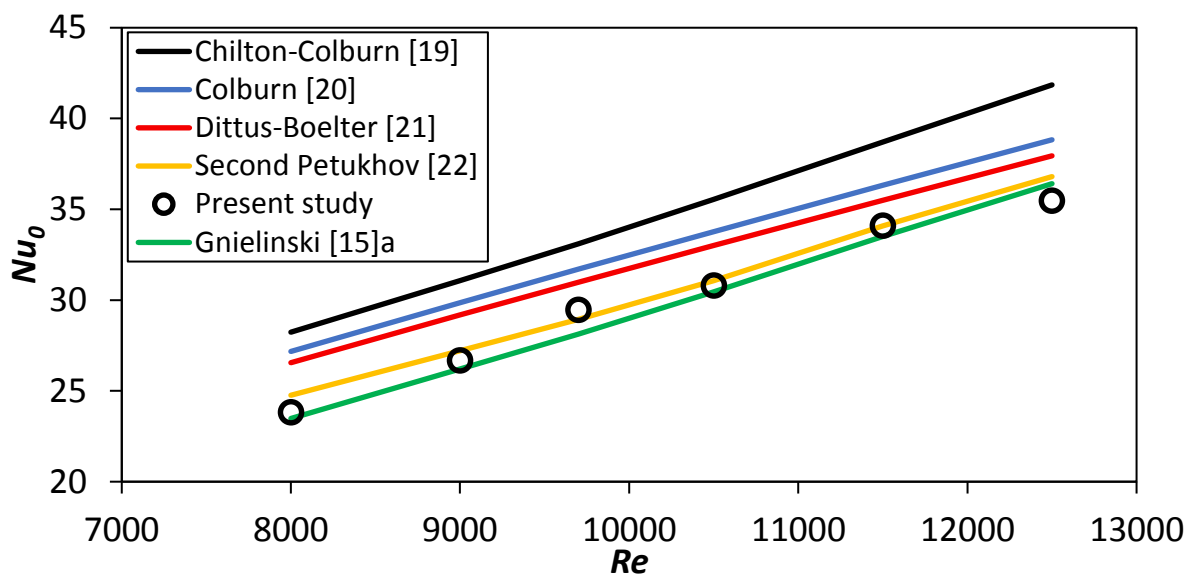


Figure 4.6: Average Nusselt numbers for the smooth channel with turbulent flow.

The difference between the experimental data and the correlations is shown in Table 4.3. The difference between the experimental results and the second Petukhov [22] correlation is within the uncertainty.

Table 4.3: Qualification of experimental turbulent average Nusselt number to correlations.

<i>Re</i>	Difference: $\left(\frac{Nu_0}{Nu_{th,0}} - 1\right) \times 100$				
	Gnielinski [15]a	Petukhov [22]	Dittus-Boelter [21]	Colburn [20]	Chilton-Colburn [19]
8 000	1.46 %	-3.79 %	-10.28 %	-12.32 %	-15.62 %
9 000	1.79 %	-1.96 %	-8.59 %	-10.68 %	-14.19 %
9 700	4.74 %	1.79 %	-4.89 %	-7.06 %	-11.00 %
10 500	1.14 %	-0.86 %	-6.68 %	-8.81 %	-13.37 %
11 500	1.10 %	0.02 %	-3.94 %	-6.13 %	-12.60 %
12 500	-2.59 %	-2.91 %	-6.52 %	-8.65 %	-15.25 %

The experimental method was qualified with respect to the average Nusselt number in the turbulent flow regime, where the flow is fully thermally developed because the difference between the data and the correlations are within the uncertainty for all the tested flow rates.

4.4. Friction Factors

The pressure data was qualified in the smooth channel for laminar flow in Figure 4.7 and Table 4.4 shows the percentage difference against the Shah and London [12], Rohsenow and Choi [10], Tirunarayanan and Ramachandran [13] and Rothfus *et al.* [14] equations, summarized in Table 2.3.

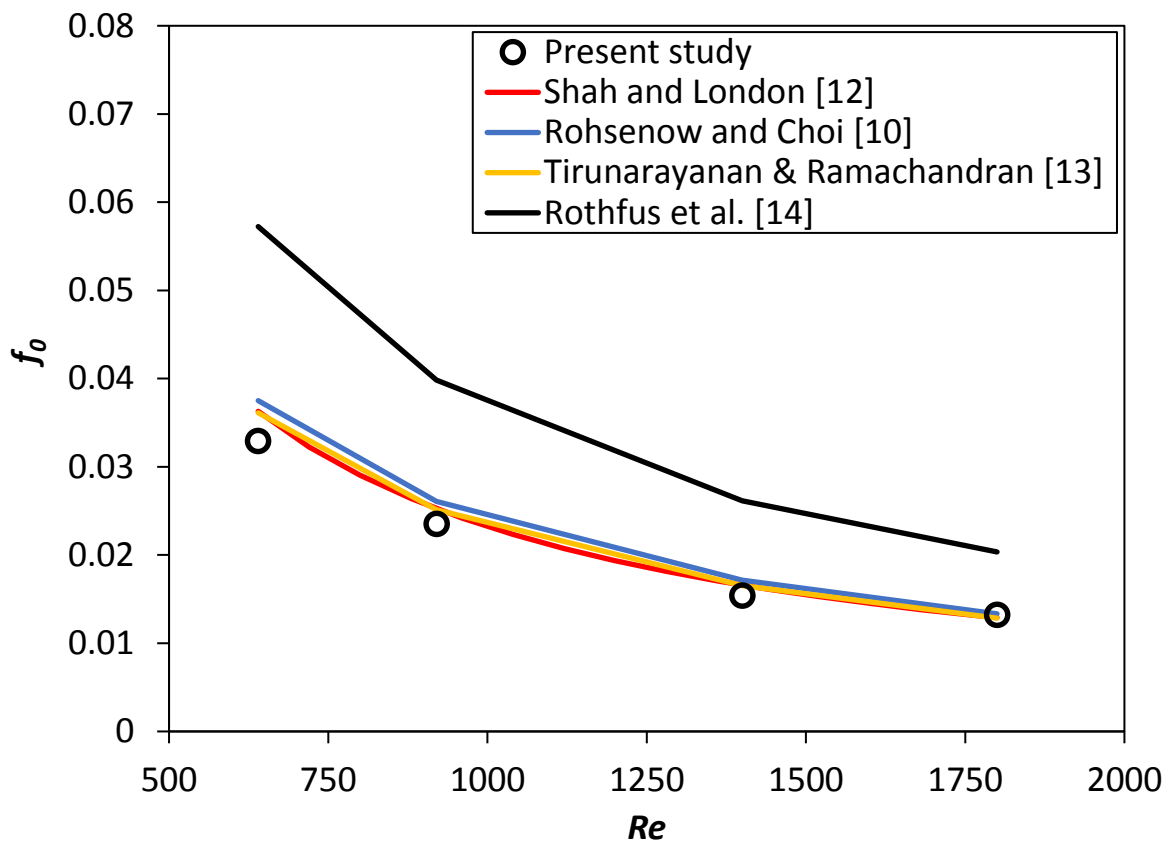


Figure 4.7: Laminar friction factor for the smooth channel plotted with correlations.

The difference between the experimental data and the correlation of Tirunarayanan and Ramachandran [13] lies within the calculated uncertainty of the experimental friction factor. The data of the present study has a large deviation with Rothfus *et al.* [14] because their equation fits data well for $a^* \geq 0.125$ and $a^* = 0.025$ in the present study.

Table 4.4: Difference between laminar experimental friction factor and correlations for smooth channel.

Re	Difference:			
	$\left(\frac{f_0}{f_{th,0}} - 1\right) \times 100$			
	Shah and London [12]	Rohsenow and Choi [10]	Tirunarayanan and Ramachandran [13]	Rothfus <i>et al.</i> [14]
640	-9.35 %	-12.27 %	-8.93 %	-42.51 %
920	-6.93 %	-9.92 %	-6.50 %	-40.98 %
1 400	-7.18 %	-10.17 %	-6.76 %	-41.14 %
1 800	2.30 %	-1.00 %	2.77 %	-35.13 %

The transitional friction factor data for the smooth channel was qualified against the correlations of Blasius [16], modified Blasius [17], and Taitel and Dukler [18], summarized in Table 2.6. The data and correlations are plotted in Figure 4.8 and the difference is shown in Table 4.5

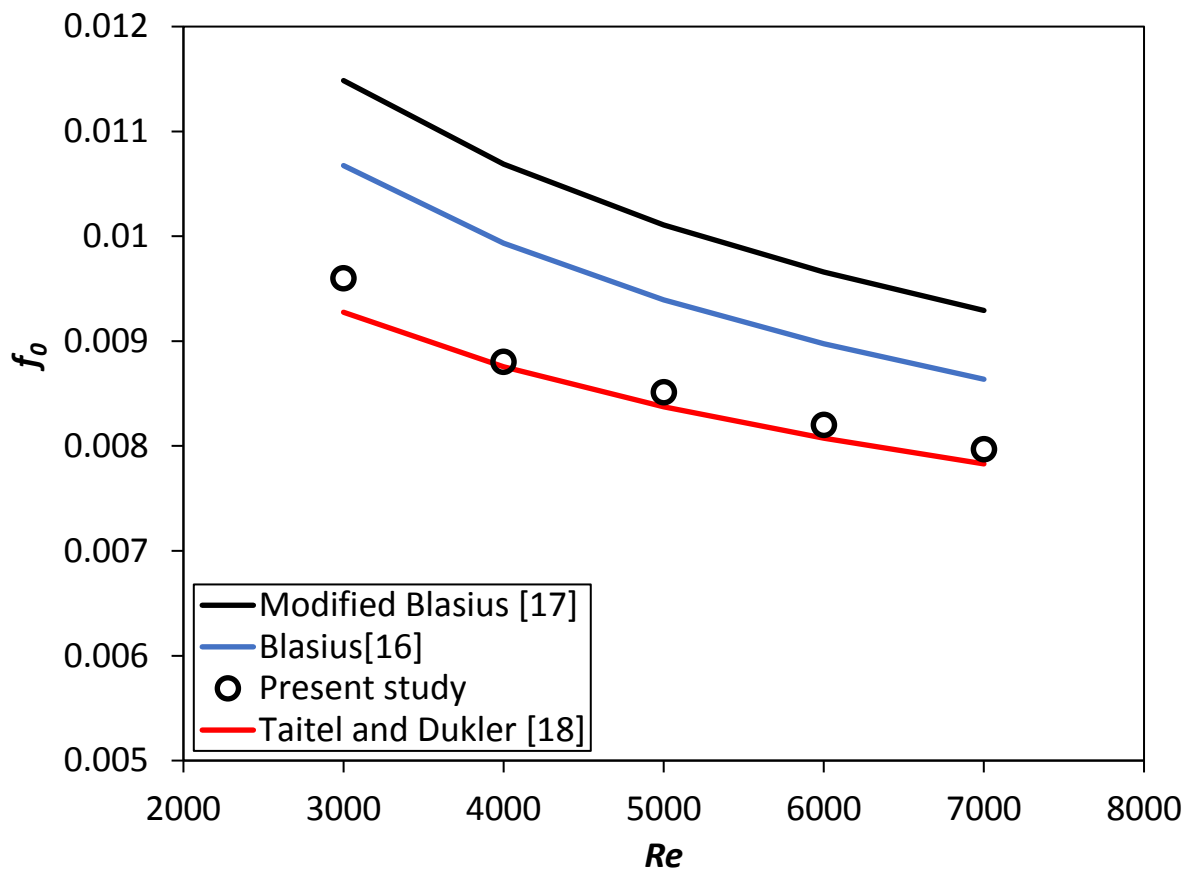


Figure 4.8: Transitional friction factor for smooth channel plotted with correlations.

The correlation of Taitel and Dukler [18] fits the experimental data very closely with a maximum difference of 3.5% at $Re = 3000$.

Table 4.5: Difference between transitional experimental friction factor and correlations for the smooth channel.

Re	Difference:		
	$\left(\frac{f_0}{f_{th,0}} - 1\right) \times 100$		
	Blasius [16]	Modified Blasius [17]	Taitel and Dukler [18]
3 000	-10.07 %	-16.41 %	3.50 %
4 000	-11.38 %	-17.64 %	0.53 %
5 000	-9.40 %	-15.79 %	1.64 %
6 000	-8.65 %	-15.09 %	1.55 %
7 000	-7.74 %	-14.26 %	1.77 %

The friction factor of the smooth channel for turbulent flow is shown in Figure 4.9. It was qualified against the correlations of Blasius [16], modified Blasius [17], Kármán-Nikuradse [23], and Petukhov [24] summarized in Table 2.6 and Table 2.8.

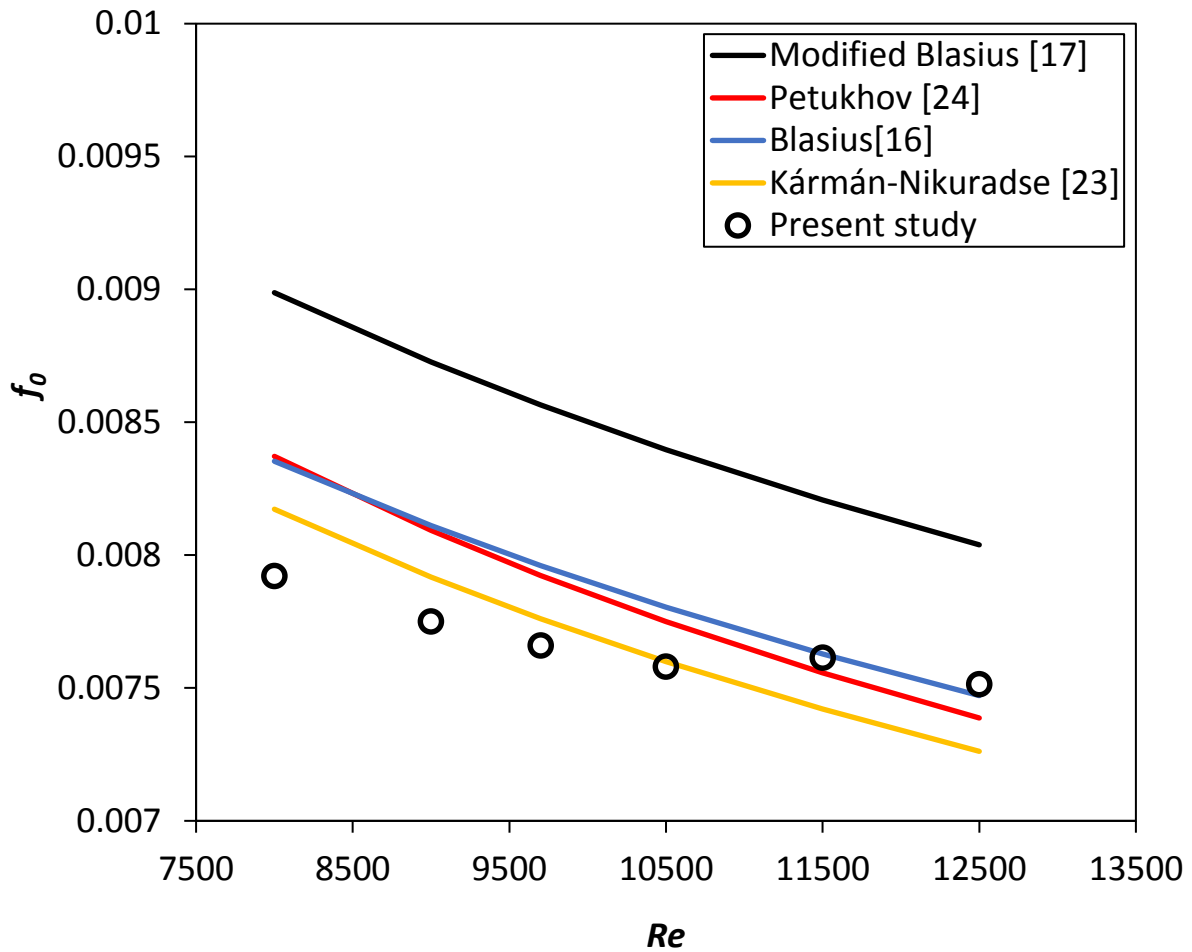


Figure 4.9: Turbulent friction factor for smooth channel plotted with correlations.

The percentage difference between the experimental friction factor and the correlations for turbulent flow in the smooth channel are shown in Table 4.6. The difference in the experimental results and the Kármán-Nikuradse [23] correlation is within 3.5% and is within the calculated uncertainty for all Reynolds numbers.

Table 4.6: Difference between turbulent experimental friction factor and correlations for the smooth channel.

Re	Difference:			
	$\left(\frac{f_0}{f_{th,0}} - 1\right) \times 100$			
	Kármán-Nikuradse [23]	Petukhov [24]	Blasius [16]	Modified Blasius [17]
8 000	-3.08 %	-5.38 %	-5.17 %	-11.87 %
9 000	-2.11 %	-4.25 %	-4.45 %	-11.19 %
9 700	-1.29 %	-3.33 %	-3.77 %	-10.57 %
10 500	-0.25 %	-2.19 %	-2.87 %	-9.72 %
11 500	2.61 %	0.75 %	-0.19 %	-7.24 %
12 500	3.49 %	1.73 %	0.58 %	-6.52 %

The experimental setup was qualified with respect to the pressure tests, where the flow was fully hydraulically developed because the difference between the experimentally found friction factor and the correlations were within the uncertainty for all the tested flow rates.

4.5. Summary and conclusions

The experimental setup and data reduction method were qualified in this chapter in the order of local Nusselt number, mean Nusselt number, and friction factor.

The local Nusselt number was within 4.3% from the theoretical correlation with a thermal entry length estimated as $x/H = 17$ for laminar flow, within 6.5% for transitional flow with a thermal entry length estimated as $x/H = 15$, and within 4.1% with a thermal entry length of $x/H = 11$ for fully turbulent flow.

The average fully developed Nusselt number for the laminar flow was within 5% of the theoretical correlation with the transitional flow within 10% and the turbulent flow within 4%.

The friction factor for the laminar flow in the smooth channel was within 9% of the correlation, 4% for the transitional flow, and 3.5% for the turbulent flow.

Because the difference between the qualified experimental results is within the uncertainty percentages, the experimental method used during this study is deemed to be working correctly.

5. Numerical Study

5.1. Introduction

The secondary flow field is primarily responsible for the heat transfer behavior and enhancement in the cylindrical insert channel, conduction from the cylinder is not dominant as of no direct contact between cylinder and heated walls, detailed secondary flow field measurements are difficult in the channel due to geometric constraints.

Numerical simulations were done to investigate the secondary flow fields for two different geometries, $d/p = 0.2$ and $d/p = 0.05$, for $\theta = 90^\circ$, at a Reynolds numbers of 920 and 9 700. Ansys Fluent version 17.1 was used for running the simulations. The simulations were done using the $k-\Omega$ SST (shear stress transport) turbulence model. Transient simulations were run to capture the secondary flow field in the wake of the cylinders. The same model was used by [46], [47], and [48] to capture the unsteady secondary flows and vortex shedding.

The domain and mesh structure are shown in Section 5.2, with an explanation of the tested cylindrical cross-bar geometries used in the CFD analysis. The dimensions were increased by a factor of five for validation purposes against the corresponding experimental cases which were done with a channel width, $W = 203$ mm, height, $H = 25$ mm, length, $L = 1300$ mm, and aspect ratio, $W/H = 8.12$. The boundary conditions are defined in Section 5.4 and the mathematical model in Section 5.3.

The mesh was validated for conversion in mesh size as well as temporal discretization so that the difference in the simulation data does not change by more than 1% between different meshes and time step sizes and is described in Section 5.5. The CFD results were compared to experimental results to validate the numerical as well as experimental results in Section 5.6. The results are shown and discussed in Section 5.7.

5.2. Domain and mesh structure

Simulations were done using a 2D domain for two experimentally tested cross-bar configurations: $d/p = 0.05$, $\theta = 90^\circ$, where $d = 5$ mm, and $p = 100$ mm, and $d/p = 0.2$, $\theta = 90^\circ$, where $d = 10$ mm and $p = 50$ mm. Using a 2D domain was possible because the large aspect ratio, $W/H = (203/25) = 8$, is high enough to be considered as a parallel channel. Only eight cylinders were used in the simulations because flow fully develops after only four or five cylinders in the streamwise direction as found from comparing velocity profiles behind cylinders plotted from the CFD data.

Inflation layers were used next to the cylinders and the channel wall to capture viscous flow velocity gradients. The y^+ value next to the channel wall and the cylinders was a maximum of 0.2. The inflation values were 0.1 for the cylinder boundaries and 0.2 for the channel walls with the number of cells in the inflation layers 15 for the channel walls and 25 for the cylinder boundaries. All the cells in the grid were quadrilateral, both inside and outside of the inflation layers.

The domain and mesh structure are shown in Figure 5.1. The boundaries are as follows: Γ_1 is the flow inlet with the flow in the x -direction, Γ_2 the boundary walls of the channel walls and cylinders, Γ_3 the flow exit. The non-dimensional dimensions relative to the channel height of 25 mm are shown: channel length, $L/H = 20$, and channel wall to cylinder distance, $s/H = 0.25$.

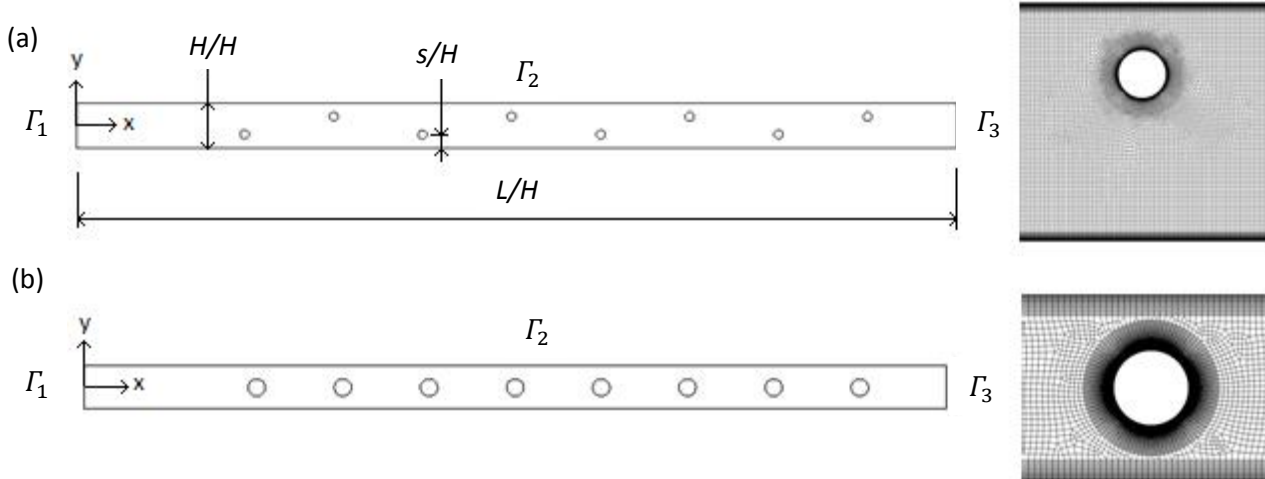


Figure 5.1: Geometry and mesh detail of (a) $d/p = 0.05$, $\theta = 90^\circ$. (b) $d/p = 0.2$, $\theta = 90^\circ$.

5.3. Mathematical model

The governing equations were the continuity equation, Equation (5.1), and the $k-\Omega$ SST model, derived in Equations (5.2) to (5.11), from the $k-\varepsilon$ and $k-\Omega$ equations by Menter [43], with the convergence criterion set to a residual of 10^{-6} for the parameters: continuity, x -velocity, y -velocity, k and Ω . The $k-\Omega$ SST model is a combination of the $k-\varepsilon$ and $k-\Omega$ turbulence models is frequently used where there are adverse pressure gradients and to accurately predict flow-separation. The $k-\varepsilon$ is more accurate in free-stream turbulence predictions and $k-\Omega$ for flow separation near walls. Depending on the distance of the cell to the channel walls, $k-\Omega$ SST blends between $k-\varepsilon$ and $k-\Omega$, increasing the percentage to $k-\Omega$ how closer the cell is to the channel wall.

Continuity:

$$\nabla \cdot (\rho \mathbf{v}) = 0 \quad (5.1)$$

$k-\varepsilon$ model:

$$\frac{\partial(\rho k)}{\partial t} + \nabla \cdot (\rho \mathbf{v} k) = \nabla \cdot \left(\left(\mu + \frac{\mu_t}{\sigma_k} \right) \nabla k \right) + P_k - \rho \varepsilon \quad (5.2)$$

And,

$$\frac{\partial(\rho \varepsilon)}{\partial t} + \nabla \cdot (\rho \mathbf{v} \varepsilon) = \nabla \cdot \left(\left(\mu + \frac{\mu_t}{\sigma_k} \right) \nabla \varepsilon \right) + C_{1,\varepsilon} P_k \frac{\varepsilon}{k} - C_{2,\varepsilon} \rho \frac{\varepsilon^2}{k} \quad (5.3)$$

$k-\Omega$ model:

$$\frac{\partial(\rho \Omega)}{\partial t} + \nabla \cdot (\rho \mathbf{v} \Omega) = \nabla \cdot \left(\left(\mu + \frac{\mu_t}{\sigma_k} \right) \nabla \Omega \right) + \frac{\gamma}{\nu_t} P_k - \beta \rho \Omega^2 \quad (5.4)$$

But,

$$\varepsilon = C_\mu k \Omega \quad (5.5)$$

If substituted it into the dissipation equation:

$$\frac{\partial(\rho \Omega)}{\partial t} + \nabla \cdot (\rho \mathbf{v} \Omega) = \nabla \cdot \left(\left(\mu + \frac{\mu_t}{\sigma_k} \right) \nabla \Omega \right) + \frac{\gamma}{\nu_t} P_k - \beta \rho \Omega^2 + 2 \frac{\rho \sigma_\Omega^2}{\Omega} \nabla k : \nabla \Omega \quad (5.6)$$

Then multiply the extra term, $2 \frac{\rho \sigma_{\Omega^2}}{\Omega} \nabla k : \nabla \Omega$, by $(1 - F_1)$, to blend between the $k-\varepsilon$ and $k-\Omega$ models by varying F_1 between 0 and 1 depending on the distance to the channel wall. Finally:

$$\frac{\partial(\rho\Omega)}{\partial t} + \nabla \cdot (\rho \mathbf{v} \Omega) = \nabla \cdot \left(\left(\mu + \frac{\mu_t}{\sigma_k} \right) \nabla \Omega \right) + \frac{\gamma}{\nu_t} P_k - \beta \rho \Omega^2 + 2(1 - F_1) \frac{\rho \sigma_{\Omega^2}}{\Omega} \nabla k : \nabla \Omega \quad (5.7)$$

A viscosity limiter is also used with another blending function for flow separation near the walls to reduce the viscous stress estimation for better validating to experimental results:

$$\mu_t = \frac{a_1 \rho k}{\max(a_1 \Omega, SF_2)} \quad (5.8)$$

Is used in the SST model, rather than:

$$\mu_t = \frac{\rho k}{\Omega} \quad (5.9)$$

Where,

$$F_2 = \tanh(\text{arg}_2^2) \quad (5.10)$$

And,

$$\text{arg}_2 = \max\left(\frac{2\sqrt{k}}{\beta \Omega d}, \frac{500\nu}{\Omega d^2}\right) \quad (5.11)$$

Where the second blending function again depends on the distance to the channel walls.

The following solution methods were used:

- Pressure-velocity coupling scheme
- Second-order pressure scheme
- Second-order upwind momentum scheme
- First-order upwind turbulent kinetic energy solver
- Second-order implicit transient formulation

5.4. Boundary conditions

An inlet velocity profile boundary condition was used where the velocity profile of a long plane channel simulation outlet velocity profile was exported:

For the plane channel simulation:

$$v_{0,x} = v_x \quad \text{on } \Gamma_3$$

And,

$$v_{0,y} = v_y \quad \text{on } \Gamma_3$$

Then the plane channel outlet velocity profile was used as an inlet velocity profile for turbulator simulations:

$$v_x = v_{0,x} \quad \text{on } \Gamma_1$$

And,

$$v_y = v_{0,y} \quad \text{on } \Gamma_1$$

No-slip condition on walls:

$$v_x = v_y = 0 \quad \text{on } \Gamma_2$$

Pressure outlet with zero-gauge pressure:

$$p_x = p_y = 0 \quad \text{on } \Gamma_3$$

Adiabatic walls:

$$\dot{q} = 0 \quad \text{on } \Gamma_2$$

5.5. Mesh validation

To estimate mesh-size dependence the local flow velocity, $v_{H/4}$ or $v_{H/2}$ was obtained at a location of two-cylinder diameters downstream of the fifth cylinder and normalized by the average as indicated in Figure 5.2. The average velocity, v_{avg} , is the mass-averaged velocity in the channel. Convergence was measured by increasing the number of mesh elements by 50% from the previous simulation as a new simulation is started using the same boundary conditions until the change in the dimensionless velocity was less than 0.01. The temporal discretization dependence was estimated using the time step averaged velocity at the same position as for the mesh size convergence study.

The simulations were also verified against the experimental setup that provided measurements of the pressure profile on the cylinder wall and the fine distributions of pressure along the channel wall. The setup for these measurements employed the same test stand as the heat transfer test facility. However, the channel height, H was increased to 25 mm, cylinder diameter, d , was increased to 5 mm and 10 mm, and cylinder pitch, p , in cylinder-array was 50 mm and 100 mm to maintain the same non-dimensional H/d and p/d as the friction factor and heat transfer test geometry. The larger channel dimensions facilitate the measurements of wall pressure distributions in finer resolutions for the CFD result validations.

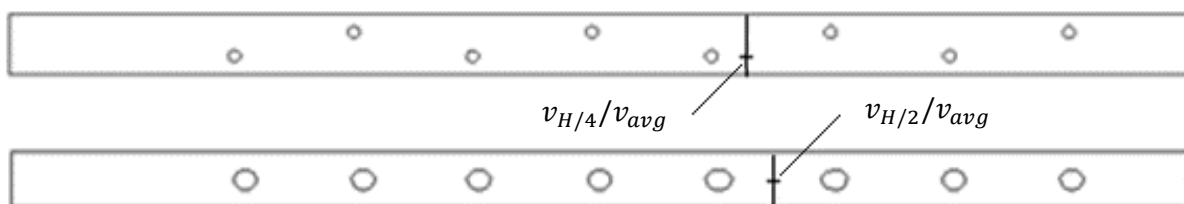


Figure 5.2: Parameter used to estimate grid convergence.

Figure 5.3 and Figure 5.4 show the results obtained from the CFD model as the number of mesh was increased. The normalized velocity converged at the grid size of 360×10^3 for both $Re = 920$ and $Re = 9\,700$ for domain $d/p = 0.05$, $\theta = 90^\circ$ in Figure 5.3, and at the grid size of 315×10^3 again at the same Reynolds numbers for $d/p = 0.2$, $\theta = 90^\circ$ in Figure 5.4.

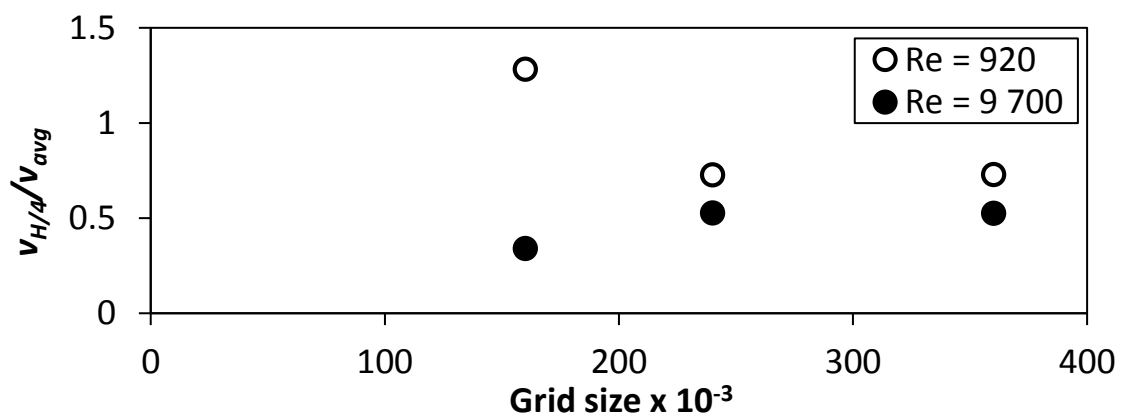


Figure 5.3: Grid convergence of $d/p = 0.05$, $\theta = 90^\circ$.

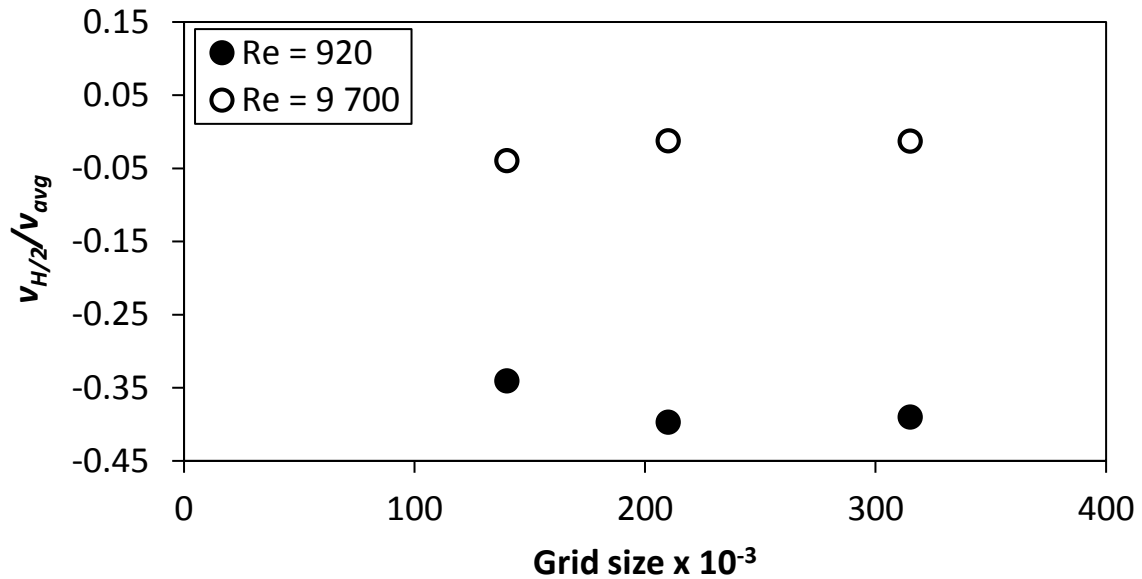


Figure 5.4: Grid convergence of $d/p = 0.2$, $\theta = 90^\circ$.

5.6. CFD to experimental validation

The CFD simulations were validated against the experimental data for $Re = 9700$ near the 6th cylinder. The non-dimensionalized test data was compared to the time-averaged CFD results. The experimental test section height, length, and rod diameters were enlarged five times to be able to take the data so that 5mm and 10mm diameter tubes could be used instead of 1mm and 2mm diameter rods.

5.6.1. Pressure profile on rods

The pressure profiles on the sixth cylinder were measured by sealing one end of the tube and extending the other end through a hole in the channel wall, sealing the perimeter with a grommet between the wall and the cylinder. A 0.3 mm hole was drilled in the cylinder to allow for the pressure measurement. The hole in the cylinder was located at the mid-width position between the channel sidewalls. A silicone tube connected the open end of the cylinder to a pressure transducer. The cylinder was rotated in 15° increments to measure the pressure around the cylinder. A schematic drawing of the test section used for measuring the pressure profiles is shown in Figure 5.5.

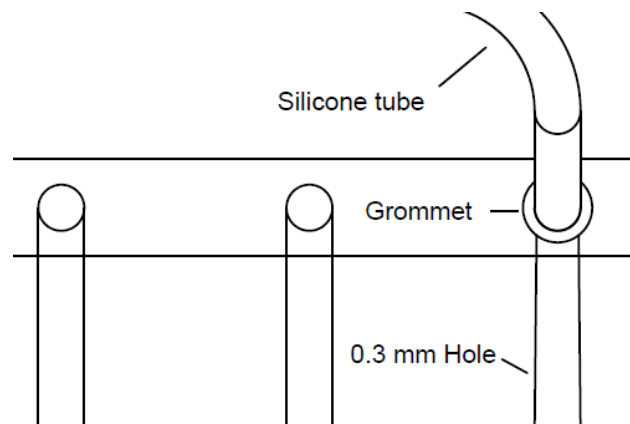


Figure 5.5: Schematic diagram of the pressure profile test setup.

The measured wall pressure on the cylinder, P_{loc} , was non-dimensionalized by using Equation (5.12). The stagnation pressure, P_{stag} , of Equation (5.12) was measured at the stagnation point, $\alpha = 0^\circ$, as shown in Figure 5.6, and divided by the dynamic pressure.

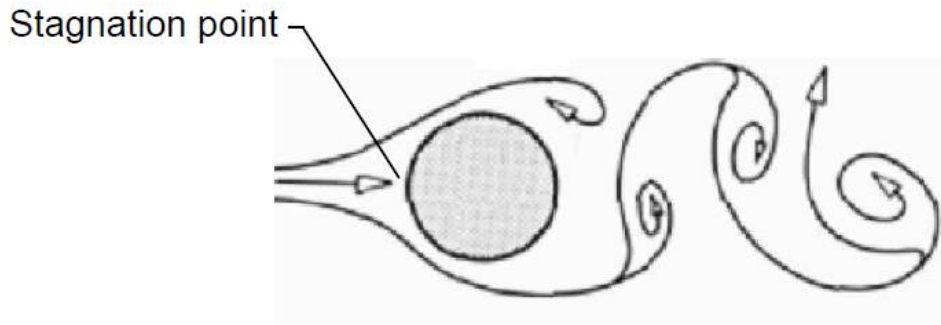


Figure 5.6: Stagnation point, Cengel and Ghajar [22].

$$\Delta P_{\alpha} = \frac{P_{stag} - P_{loc}}{\frac{1}{2} \rho v_{avg}^2} \quad (5.12)$$

The CFD and experimental pressure profiles are given by the plot of ΔP_{α} vs. α are compared in Figure 5.8 and Figure 5.9 for $d/p = 0.05$, $\theta = 90^{\circ}$ and $d/p = 0.2$, $\theta = 90^{\circ}$ with 0° referring to the stagnation point. The distributions of ΔP_{α} is zero at $\alpha = 0^{\circ}$ and then increase away from the stagnation location as the velocity increases and pressure decreases along the cylinder periphery. The largest values of ΔP_{α} either in Figure 5.8 or Figure 5.9 are seen at approximately $\alpha = 77^{\circ}$ and $\alpha = -77^{\circ}$. These are the starting locations of flow deceleration and pressure starts to increase further downstream along the cylinder periphery. The regions of $77^{\circ} < \alpha < 180^{\circ}$ and $-77^{\circ} < \alpha < 180^{\circ}$ are then the locations of adverse flow and pressure regions in Figure 5.8 and Figure 5.9 where the boundary layer separates from the cylinder wall. For the $d/p = 0.2$, $\theta = 90^{\circ}$, where the cylinders are in-line, the pressure profile is symmetric about the stagnation point, $\alpha = 0^{\circ}$. Contrarily the pressure profile in Figure 5.8 is not symmetric about the stagnation point for the $d/p = 0.05$, $\theta = 90^{\circ}$ geometry where the cylinders are staggered. At $\alpha = -77^{\circ}$ in Figure 5.8, where the flow is away from the channel wall and the velocity is high on the cylinder boundary layer flow, the non-dimensional pressure is 4.67. In comparison the $\Delta P_{\alpha} = 4.55$ in Figure 5.8 at $\alpha = 77^{\circ}$, where the flow is between the cylinder and the channel wall. The flow accelerates and pressure decreases between the cylinder and channel wall for the staggered cylinder array. However, because of the high flow restrictions between the cylinder and channel wall, the local mass flux is reduced and the local pressure on the cylinder is not reduced at $\alpha > 77^{\circ}$ as much as at $\alpha < -77^{\circ}$ in Figure 5.8. The average difference in the measured data and CFD data in Figure 5.8 and Figure 5.9 is 8.6% and 12.15%, respectively. The highest difference in the data between the measurements and CFD is 48% at $\alpha = 30^{\circ}$ in Figure 5.9. The differences between the CFD results and measurements are higher in the region of $-30^{\circ} < \alpha < -70^{\circ}$ and in the region of $30^{\circ} < \alpha < 70^{\circ}$ where the boundary layer transitions from laminar to turbulent flow.

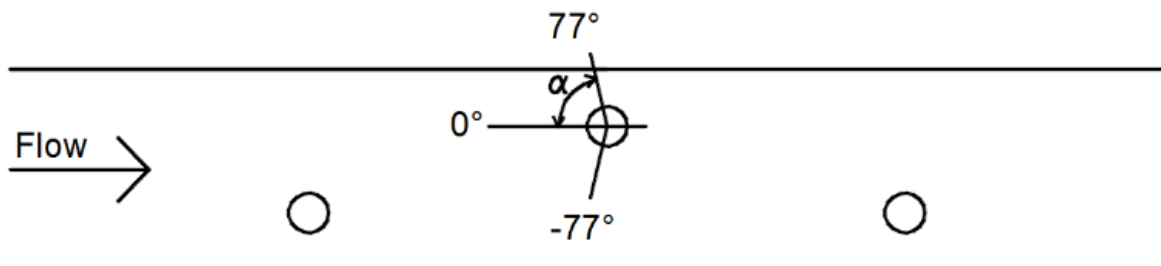


Figure 5.7: Flow separation points, $d/p = 0.05$, $\theta = 90^{\circ}$.

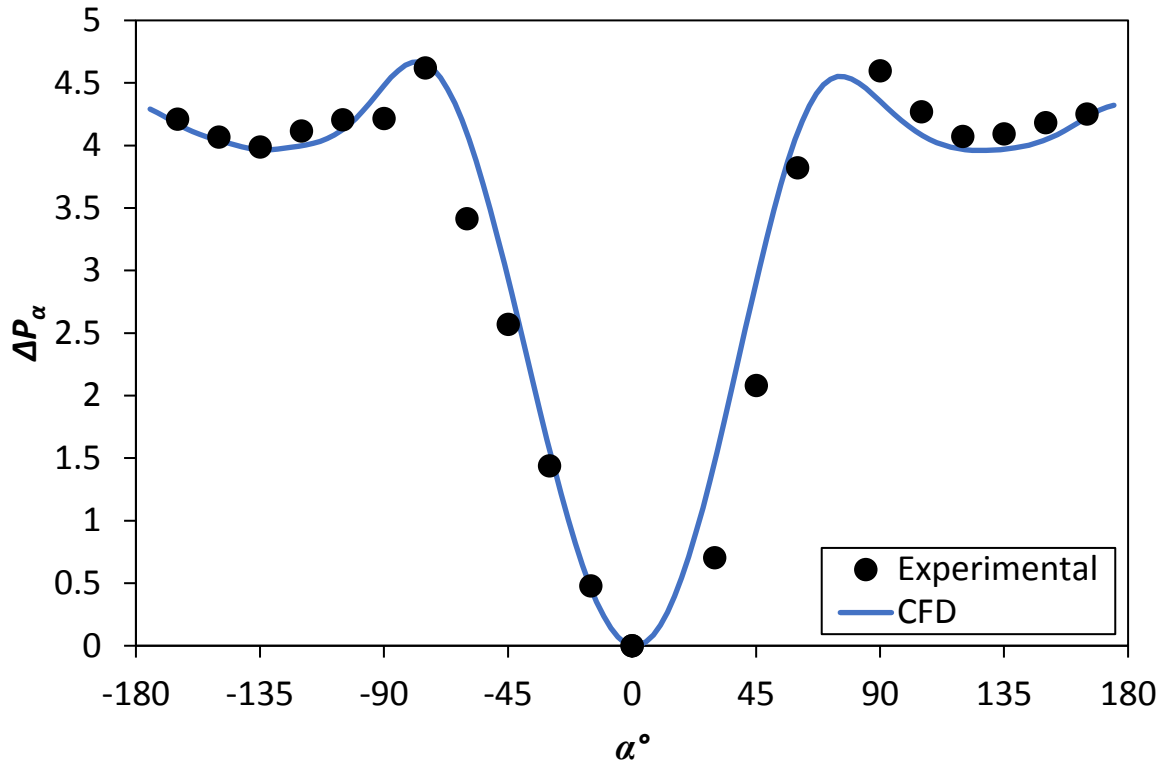


Figure 5.8: ΔP_α , $\theta = 90^\circ$, $d/p = 0.05$, $Re = 9700$.

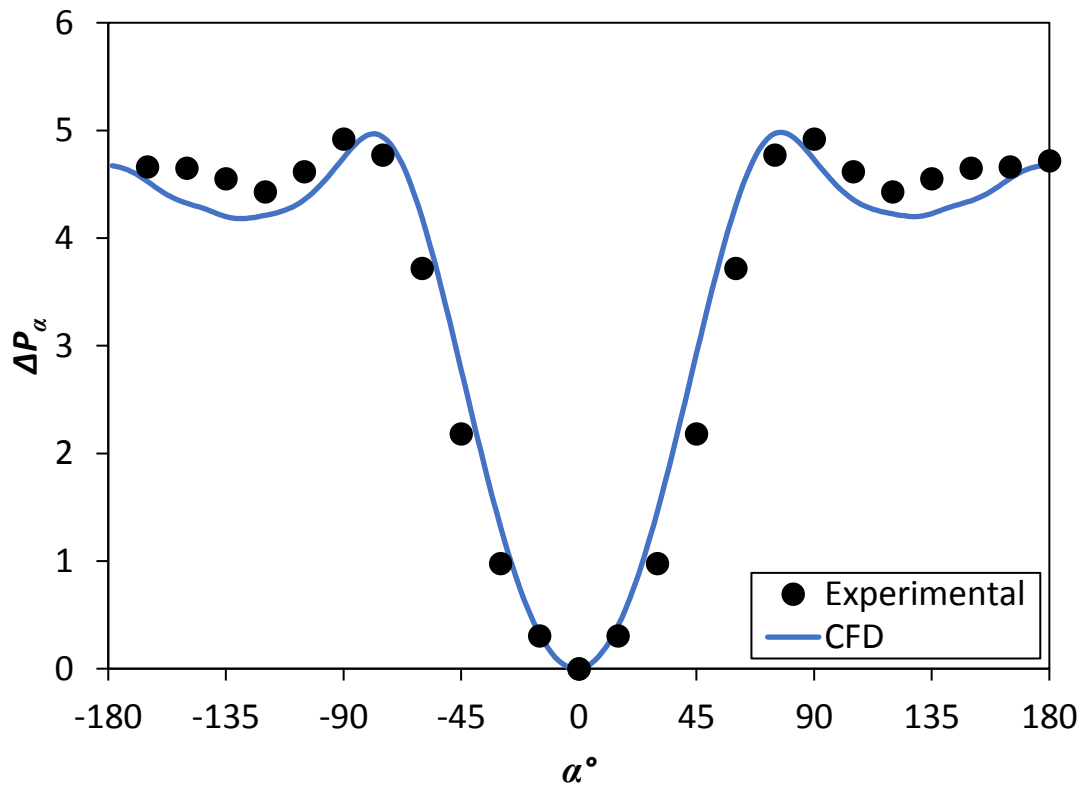


Figure 5.9: ΔP_α , $\theta = 90^\circ$, $d/p = 0.2$, $Re = 9700$.

5.6.2. High-resolution wall pressure

Pressure measurements with fine spacings of $x/H = 0.036$ between the measurement locations were taken experimentally on the channel wall. Three rows of pressure taps were used to facilitate the small gaps between the pressure taps and are indicated schematically in Figure 5.10. As shown in the figure, there are 10 pressure taps located in the vicinity of the 6th cylinder region in the channel wall. Each tap has a diameter of 0.3 mm. The non-dimensional pressure coefficient, ΔP , for the measured local wall pressure, P_{loc} , was found by subtracting the local pressures from the reference upstream pressure and dividing the pressure difference by the dynamic pressure as shown in Equation (5.13). The V_{avg} in the equation is the mass-averaged flow velocity of the channel.

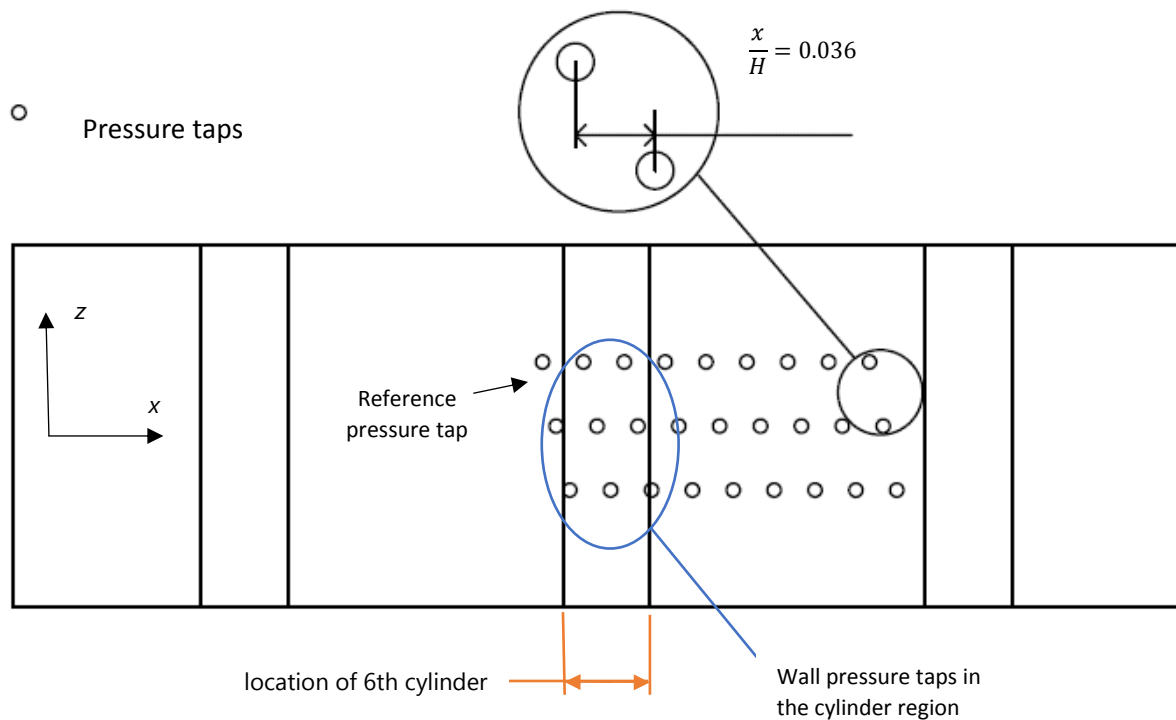


Figure 5.10: Fine spacing between pressure taps in the channel wall for measurements to validate CFD results.

Non-dimensional pressure:

$$\Delta P = \frac{P_{ref} - P_{loc}}{\frac{1}{2} \rho v_{avg}^2} \quad (5.13)$$

The non-dimensional pressure of the experimental data and CFD simulations are compared in Figure 5.11 and Figure 5.12 for $d/p = 0.05$, $\theta = 90^\circ$ and $d/p = 0.2$, $\theta = 90^\circ$ respectively. The non-dimensional ΔP increases along the wall in the cylinder region due to the flow acceleration and decrease in wall pressure. The graphs peak at the location right under the centre of the 6th cylinder where the velocity is the largest, after which there is a trough between the two cylinders and peaks again at the next cylinder in the array. For the staggered array, $d/p = 0.05$, $\theta = 90^\circ$ in Figure 5.11, the width of the second peak is different than the first peak width because the second cylinder is located near the other wall of the channel. With the in-line array, $d/p = 0.2$, $\theta = 90^\circ$ in Figure 5.12, the width of the peaks is similar. The average difference between the CFD results and measurements in Figure 5.11 and Figure 5.12 is 5% and 7% respectively. The maximum difference in ΔP between the CFD and measurements in the figures is 20% in Figure 5.12.

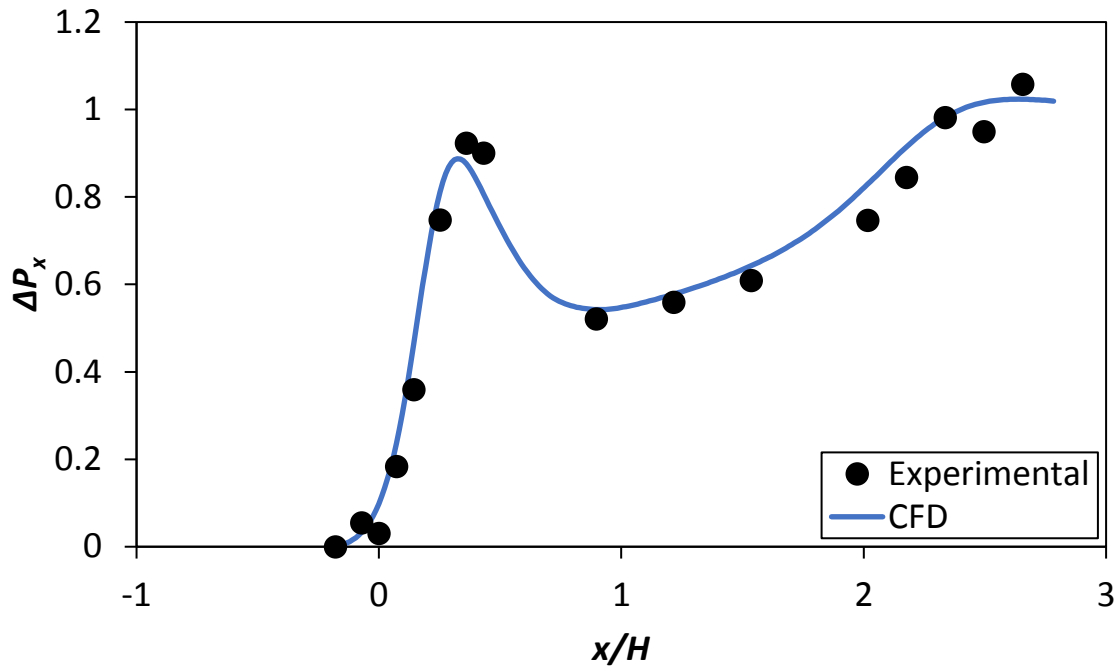


Figure 5.11: ΔP for $d/p = 0.05$, $\theta = 90^\circ$ at $Re = 9700$.

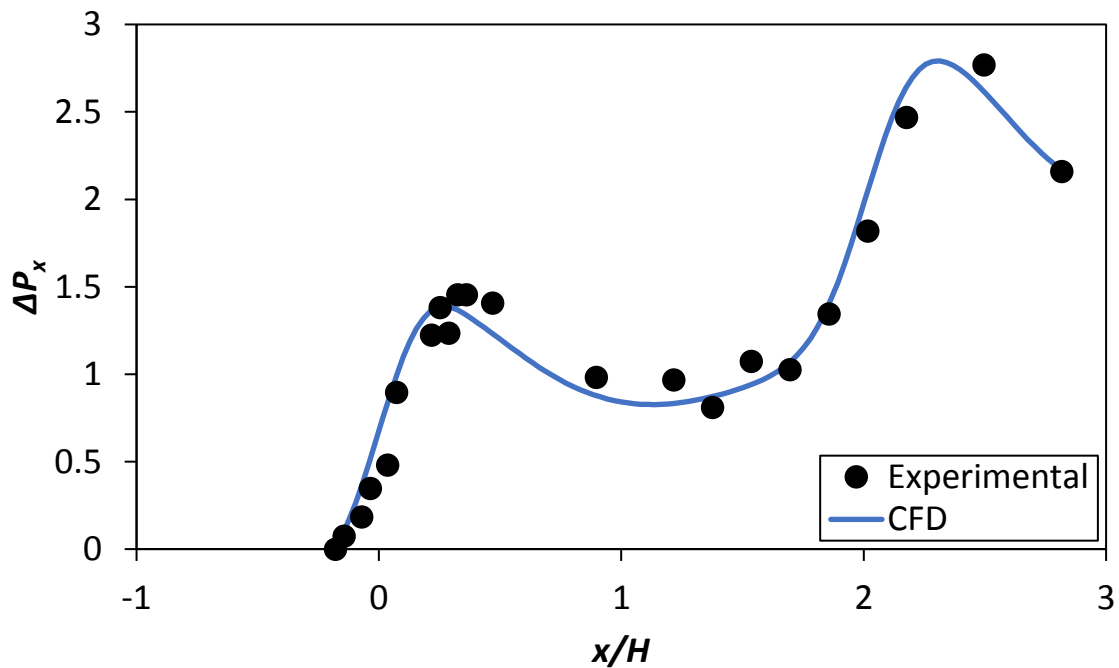


Figure 5.12: ΔP for $d/p = 0.2$, $\theta = 90^\circ$, at $Re = 9700$.

5.7. CFD results

Non-dimensional vorticity of Equation (5.15), the non-dimensional velocity of Equation (5.16) and Strouhal numbers of Equation (5.17) were used to analyse the CFD results and are plotted at non-dimensional time steps of Equation (5.18).

Non-dimensional vorticity:

$$\frac{d\boldsymbol{\omega}}{dt} = (\boldsymbol{\omega} \cdot \nabla)\mathbf{v} + \mathbf{v}\nabla^2\boldsymbol{\omega} \quad (5.14)$$

$$\omega_z^* = \frac{\omega_z H}{v_{avg}} \quad (5.15)$$

Non-dimensional x-velocity:

$$v_x^* = \frac{v_x}{v_{avg}} \quad (5.16)$$

Strouhal number:

$$St = \frac{Fd}{v_{avg}} = \frac{1}{\Delta t} \frac{d}{v_{avg}} \quad (5.17)$$

Non-dimensional time:

$$t^* = \frac{\Delta t}{H/v_{avg}} \quad (5.18)$$

The vortex shedding cycles are shown in Figure 5.13 (i) to (vi) for (a) $d/p = 0.05$, $\theta = 90^\circ$ and (b) $d/p = 0.2$, $\theta = 90^\circ$ at $Re = 920$. The total duration of time steps, $\Delta t^* = 0.94$ captures one complete period of shedding of the large eddy in the cylinder wake region. A single eddy is formed for (a), smaller in circumference, and closer to the cylinder in comparison with the two larger eddies forming and extending further behind the cylinders in (b). For (a) and (b) the eddies alternate between forming at the bottom side of the cylinder, frame (i), and detaching from frame (ii) to (ii) and then at the top side of the cylinder, frame(iv), and detaching at frame (v) to (vi). The magnitude of the vorticity is larger near the boundaries of the cylinders after the stagnation point where flow separation is taking place and next to the channel walls where the cylinders are placed. The stagnation points are changing with time, staying perpendicular to the largest point of the velocity from the upstream flow. The secondary flow patterns for (b) changes symmetrically with time because the cylinders are in-line and in the centre of the channel, and asymmetrically for (a) because the cylinders are staggered and closer to the channel walls.

The Strouhal number explains the magnitudes of unsteadiness in the shedding of large eddies in the cylinder wake. The unsteadiness in the large eddies is responsible for the flow mixing and local wall heat transfer enhancements under the cylinder wake region. The large eddy shedding also explains the friction factor difference between the two cylinder arrays which provide the same blockage ratio in the channel flow. By using $\Delta t^* = 0.94$ for one complete period of shedding a large eddy in the wake region of the cylinder for Figure 5.13 (a), the Strouhal number could be calculated:

$$\Delta t = \frac{t^* H}{v_{avg}} = \frac{(0.94)(0.025)}{0.38} = 0.0618$$

$$St = \frac{1}{v_{avg}} d = \frac{1}{0.0618} (0.025) = 0.213$$

The Strouhal number for Figure 5.13 (b) is 0.426 which is twice as large. This explains that the heat transfer enhancement for the case in Figure 5.13 (b) should be larger but also at a larger pressure penalty.

The non-dimensional velocity in the x-direction is shown in Figure 5.14 (i) to (vi) for (a) $d/p = 0.05$, $\theta = 90^\circ$ and (b) $d/p = 0.2$, $\theta = 90^\circ$ at $Re = 920$. Flow acceleration is taking place next to the cylinders where the flow is constricted to flow through smaller cross-sectional areas. The large fluid velocity sections next to the cylinders traverse periodically downstream with relation to time and can be seen by comparing the figures from (i) to (iv). There is flow in the reverse direction behind the cylinders, caused by the flow separation creating low pressure in the wake of the cylinders. The reverse flow is detached from the cylinder with the flow in the positive direction on the boundary of the cylinder. There is more disruption in the flow for (b) than for (a) with longer sections of accelerated and reverse flow because the cylinders are in-line and larger in diameter, increasing the local blockage ratio. Larger flow velocities are seen at the top of the cylinder in (a), further away from the wall than at the bottom where the flow resistance is larger.

The vortex cycles for $Re = 9\,700$ are shown in Figure 5.15 (i) to (vi) for (a) $d/p = 0.05$, $\theta = 90^\circ$ and (b) $d/p = 0.2$, $\theta = 90^\circ$. Eddies for (a) are forming closer to the cylinder in comparison with $Re = 920$ and for (b) there aren't forming complete eddies behind the cylinder because of the larger velocity of the flow.

The Strouhal number for the case in Figure 5.15 (a) is 0.213 and 0.426 in Figure 5.15 (b). The estimated Strouhal numbers are the same for the cases in Figure 5.13, where the Reynolds number was 920 compared to 9 700 as with Figure 5.15. This is because the full period time is estimated and does not fall exactly on the time steps chosen to run the simulations.

The non-dimensional velocity in the x-direction for $Re = 9\,700$ is shown in Figure 5.16 (i) to (vi) for (a) $d/p = 0.05$, $\theta = 90^\circ$ and (b) $d/p = 0.2$, $\theta = 90^\circ$. Flow detachment are closer to the cylinder for (a) and (b) than at $Re = 920$ with the pressure drag vacuum at a closer distance to the cylinder.

The reverse flow and formation of vortices, together with the flow acceleration and adverse pressure gradients are resulting in the pressure drop penalty but also the boundary layer disruption and increase in temperature difference between the fluid and the channel wall, causing the heat transfer rate to enhance in comparison with the smooth channel without turbulators.

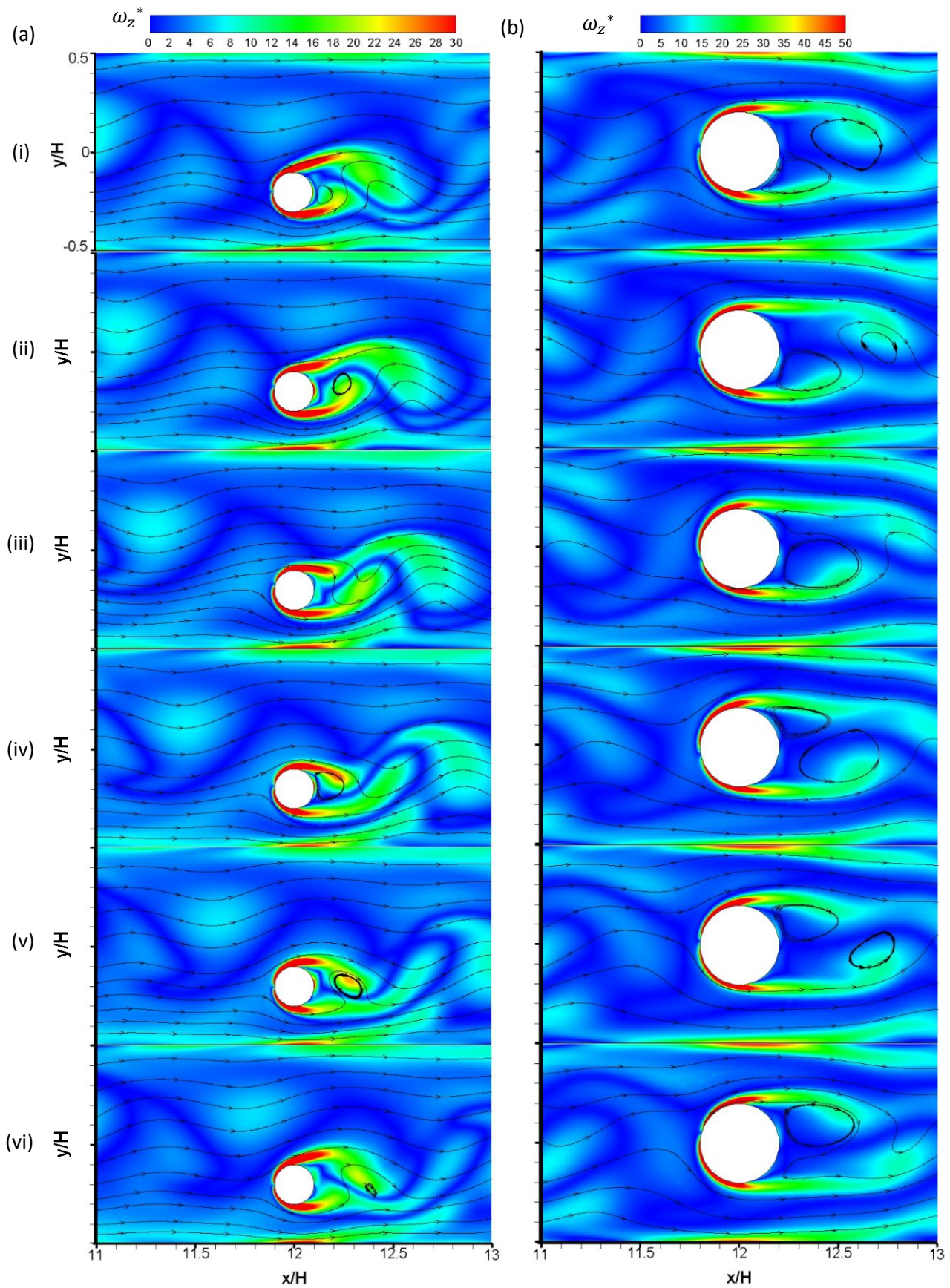


Figure 5.13: ω_z^* and streamlines for $Re = 920$, $\theta = 90^\circ$. (a) $d/p = 0.05$. (b) $d/p = 0.2$. (i) $t^* = 0.16$. (ii) $t^* = 0.32$. (iii) $t^* = 0.48$. (iv) $t^* = 0.64$. (v) $t^* = 0.8$. (vi) $t^* = 0.94$.

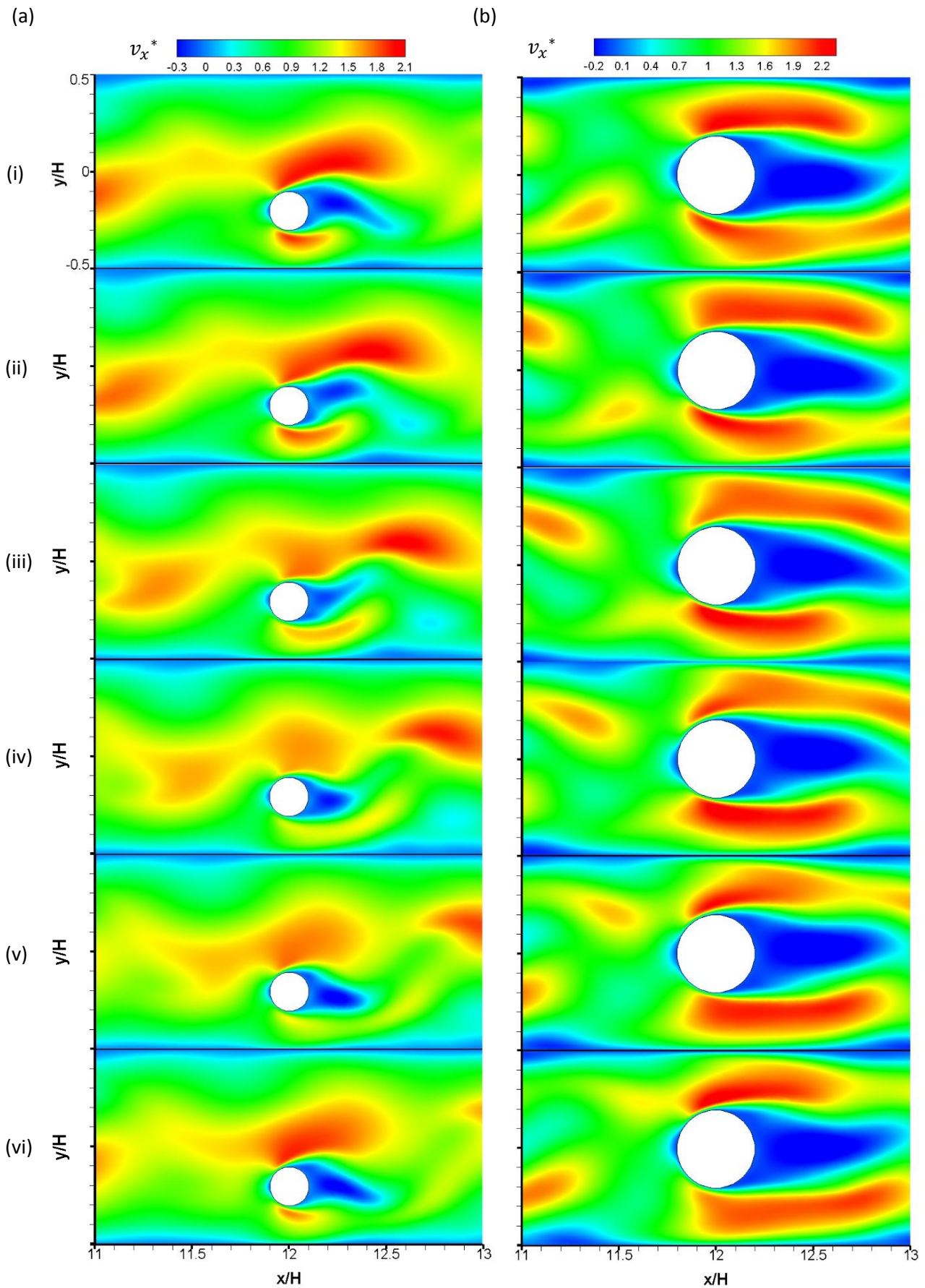


Figure 5.14: v_x^* for $Re = 920$, $\theta = 90^\circ$. (a) $d/p = 0.05$. (b) $d/p = 0.2$. (i) $t^* = 0.16$. (ii) $t^* = 0.32$. (iii) $t^* = 0.48$. (iv) $t^* = 0.64$. (v) $t^* = 0.8$. (vi) $t^* = 0.94$.

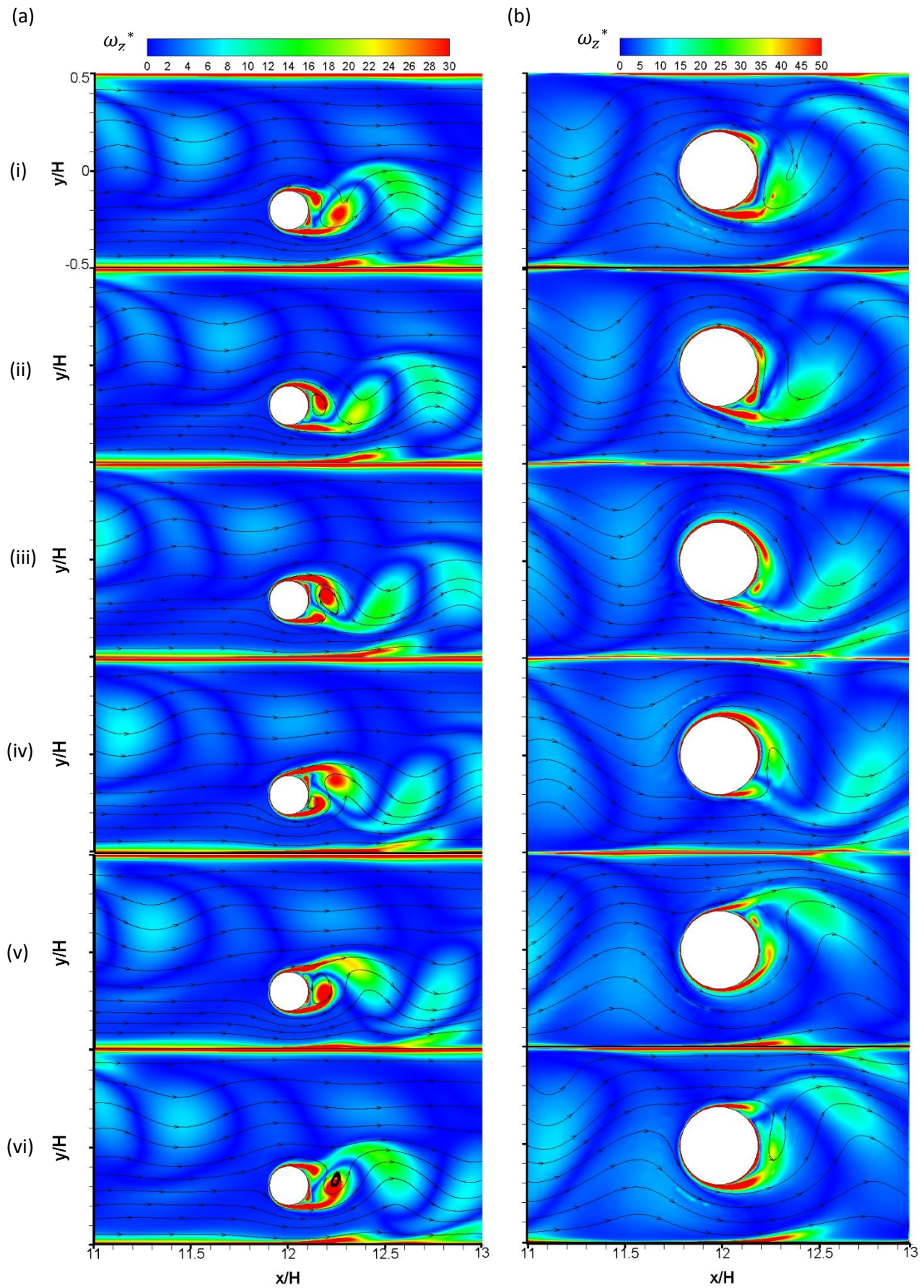


Figure 5.15: ω_z^* and streamlines for $Re = 9\,700$, $\theta = 90^\circ$. (a) $d/p = 0.05$. (b) $d/p = 0.2$. (i) $t^* = 0.16$. (ii) $t^* = 0.32$. (iii) $t^* = 0.48$. (iv) $t^* = 0.64$. (v) $t^* = 0.8$. (vi) $t^* = 0.94$.

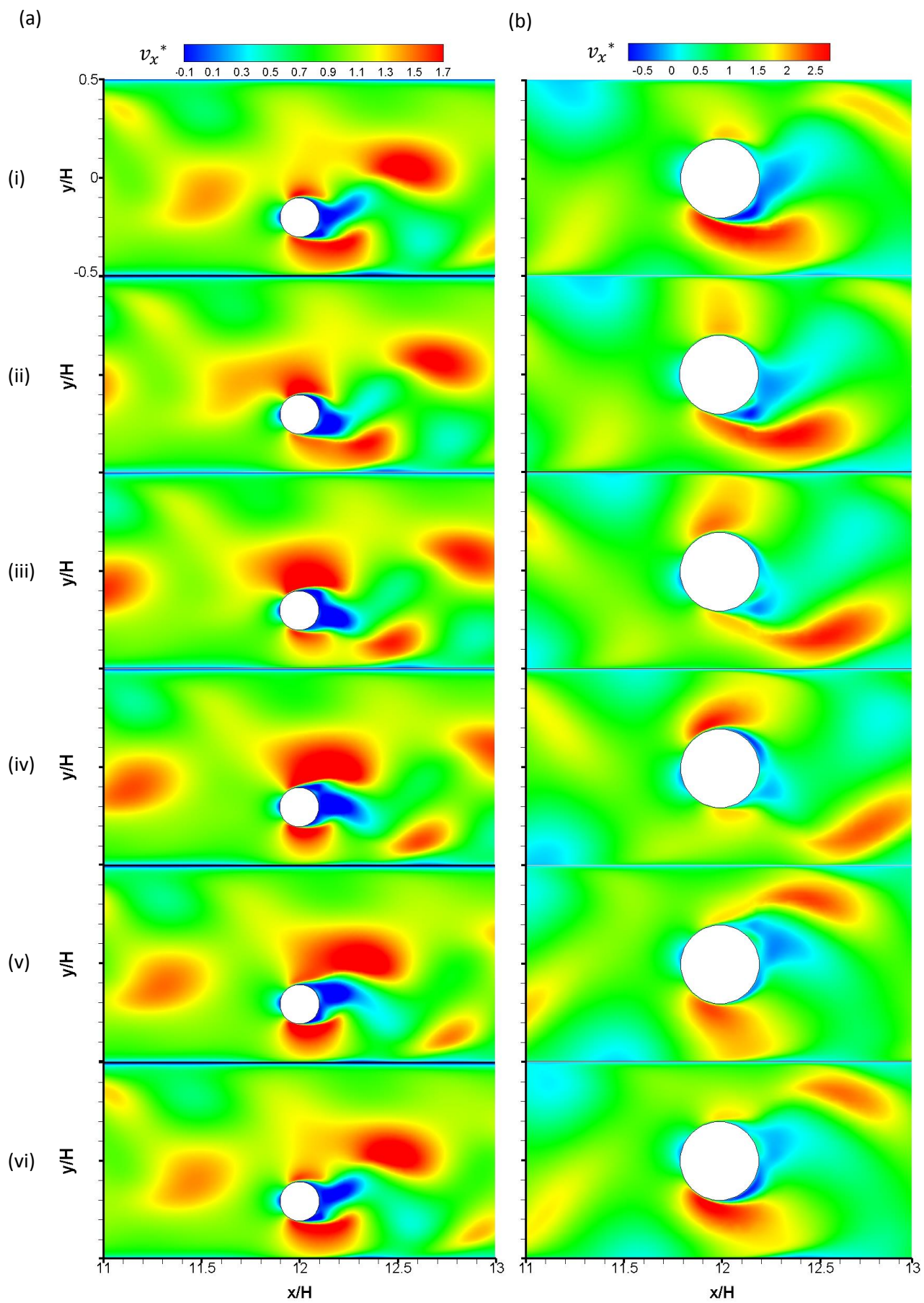


Figure 5.16: v_x^* for $Re = 9700$, $\theta = 90^\circ$. (a) $d/p = 0.05$. (b) $d/p = 0.2$. (i) $t^* = 0.16$. (ii) $t^* = 0.32$. (iii) $t^* = 0.48$. (iv) $t^* = 0.64$. (v) $t^* = 0.8$. (vi) $t^* = 0.94$.

5.8. Summary and conclusions

CFD simulations were done using the $k-\Omega$ SST turbulence model for $d/p = 0.05$, $\theta = 90^\circ$ and $d/p = 0.2$, $\theta = 90^\circ$, at $Re = 920$ and $Re = 9\,700$, to analyse the secondary flow field responsible for the increase in pressure drop penalty and heat transfer enhancement in comparison with smooth channels.

Two-dimensional simulations were valid because of the small aspect ratio of the channel, $AR = 0.025$. Mesh refinement was done near the channel walls and on the cylinder boundaries to better capture the velocity gradients. Inlet velocity profiles were used from long smooth channel simulation outlet profiles to accurately define fully developed flow, saving domain and mesh size for the turbulated channel simulations. The meshes were validated against the experimental setup by measuring the pressure profiles around the cylinders and high-resolution wall pressure for one period between two cylinders experimentally and comparing the non-dimensionalized values to the CFD time-averaged results.

For analysing the CFD results, non-dimensional vorticity with super-imposed streamlines and non-dimensional velocity were plotted on contour graphs. The Strouhal number of the eddy formation for the smaller diameter to pitch ratio configuration was half of the larger diameter to pitch ratio where the diameter of the cylinders is twice as large. The vorticity was the largest on the boundaries of the cylinders after the stagnation around the cylinders and next to the channel walls where the cylinders are situated. At $Re = 9\,700$ the vorticity magnitude was larger than for $Re = 920$ but complete eddies didn't form as in the case of $Re = 920$. The velocity contours showed an increase in velocity next to the cylinders and reverse flow behind the cylinders, as well as flow separation on the boundary of the cylinders after the stagnation point at the head of the cylinders. Larger flow accelerations were observed next to the cylinders for $d/p = 0.2$, $\theta = 90^\circ$ than for $d/p = 0.05$, $\theta = 90^\circ$ and at $Re = 9\,700$ in comparison with $Re = 920$. The flow separation, increase in vorticity, flow acceleration, and eddy formation were responsible for the increase in pressure penalty and the heat transfer augmentation.

6. Experimental Results

6.1. Introduction

The results found during the experimental tests are shown in this chapter. The local Nusselt number is shown in Section 6.2 for the channel with cylindrical turbulators at three different Reynolds numbers: in the laminar flow, transitional flow, and turbulent flow.

The fully developed mean Nusselt numbers are shown in Section 6.3 and the friction factors in Section 6.5. The Nusselt number ratio of the fully developed Nusselt number of the channel with cylindrical arrays to the smooth channel Nusselt number is shown in Section 6.4 and the friction factor ratio in Section 6.6. The thermohydraulic performance coefficients are shown in Section 6.7.

6.2. Local Nusselt number

The local Nusselt numbers were calculated at each of the 96 surface thermocouples in the test section by using the necessary variables described in Section 3.6. In this section, the distributions of local Nu along the channel are shown for each of the eight different cylindrical cross-bar arrays at $Re = 920$, $Re = 4\,000$, and $Re = 9\,700$. The distributions of local Nu for the other Re are presented in Appendix E.

The equation for finding the local Nusselt number explained in Section 3.6:

$$Nu_x = \frac{\dot{q}_{con} D_h}{k_{air}(T_{wall} - T_{mx})} \quad (3.6)$$

Figure 6.1 shows the local wall temperature and local mean fluid temperature used to calculate the wall-to-mean fluid temperature difference, $(T_{wall} - T_{mx})$, at a Reynolds number of 9 700 for cylindrical cross-bar geometry $d/p = 0.025$, $\theta = 90^\circ$. The data are necessary to calculate the local Nusselt numbers. The temperature data were captured after steady-state was reached by taking the average at each thermocouple with a sampling rate of 1 Hz for five minutes. The quasi-steady-state was considered when the temperature data at each thermocouple did not change more than $\pm 0.2^\circ\text{C}$ for ten minutes. The temperature data are shown in Appendix F for all the cross-bar arrays and the smooth channel tests at all the 15 Reynolds numbers.

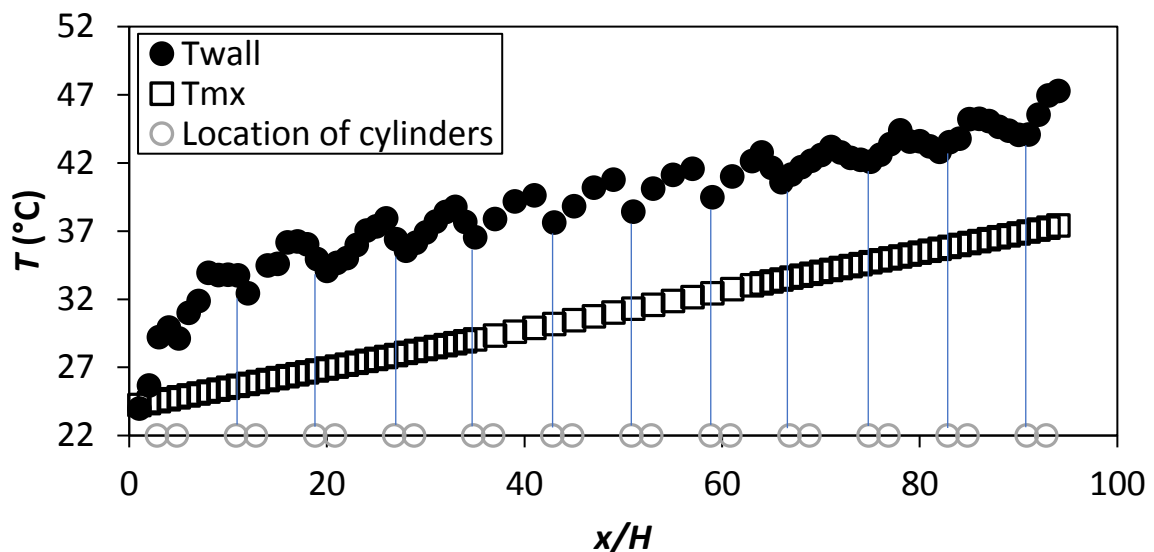


Figure 6.1. Temperature plotted against x/H at $Re = 9\,700$ for setup: $d/p = 0.025$, $\theta = 90^\circ$. Cylinders are arranged in staggered array.

The peaks and troughs in T_{wall} in Figure 6.1 are because of the staggered cylinder pairs positioned in the channel flow. At the first cylinder in each pair, positioned near the wall where the thermocouples were placed, the flow accelerates in the narrow area between the cylinder and the wall. Together with the flow acceleration, local unsteadiness in vortex shedding takes place causing high flow mixing between the cold mainstream flow and hot wall region, increasing the heat transfer coefficients and Nusselt numbers. At $x/H = 20$ the flow becomes fully thermally developed, i.e. a slope through the peaks of T_{wall} becomes constant.

The local Nusselt numbers for cylindrical configuration $d/p = 0.025$ and $\theta = 90^\circ$ are shown in Figure 6.2, plotted along the normalized length of the channel x/H . With an increase in Re , the local Nu_x increases. The thermal entry length for this insert is approximately $x/H = 20$. After the flow becomes fully thermally developed, a repetitive pattern can be seen where the peaks of the Nu_x are seen downstream of each cylinder, where the flow creates an eddy that mixes the fluid to create a larger temperature gradient between the heated wall and the fluid. The peaks are larger at higher Re , and the Nu increases with Re because of the higher mass flux in the wall boundary layer at higher Re . The thermal entry length with an increase in Re remains constant at $x/H = 20$. This shows that the inclusion cylinders make the flow turbulent, even at $Re = 640$, and is in accordance with literature where the thermal entry length is $10D_h/H = 19.5$ [22].

Section 5.7 shows the numerical study with the flow patterns with the eddies and vorticity to further explain the heat transfer increase. See Appendix E for the local Nusselt numbers at all the Reynolds numbers for the cylindrical inserts and the smooth channel.

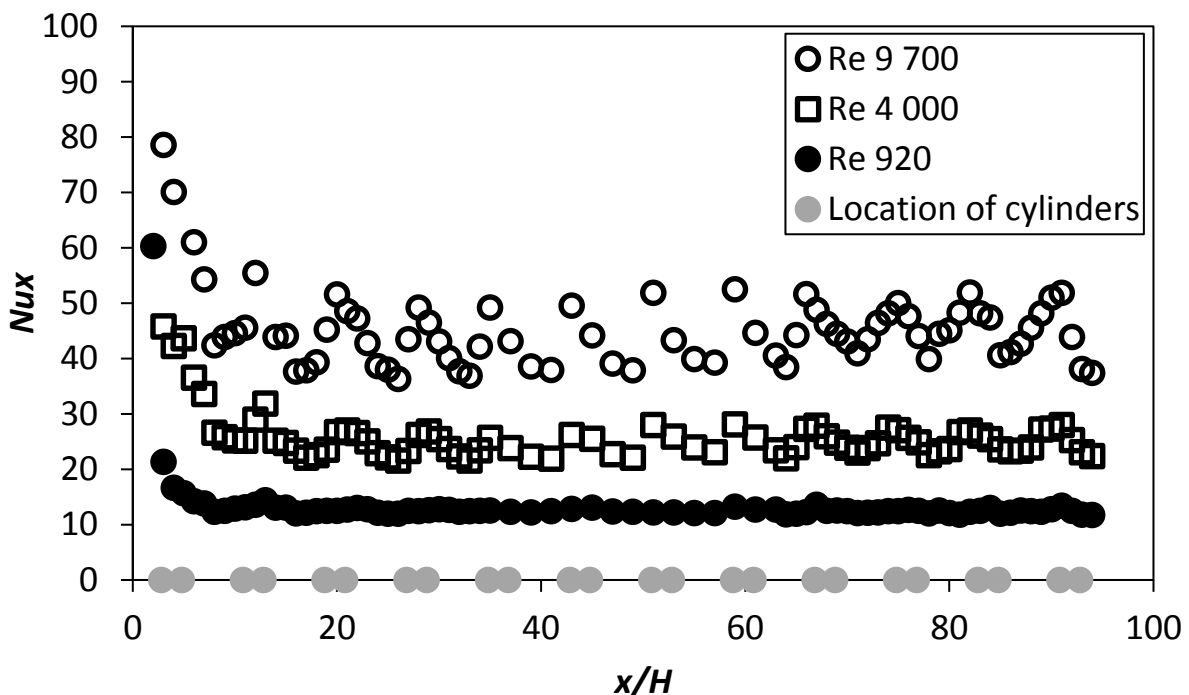


Figure 6.2: Local Nusselt number plotted against x/H coordinate for array: $d/p = 0.025$, $\theta = 90^\circ$ at $Re = 920$, $Re = 4000$ and $Re = 9700$. Cylinders are arranged in staggered array.

Figure 6.3 shows the local Nusselt numbers for $d/p = 0.025$, $\theta = 45^\circ$ plotted against x/H . The distributions of peaks and troughs in the Nu_x are less distinctive in Figure 6.3 than in Figure 6.2 as in and the Nu_x in Figure 6.3 is lower even though the d/p ratio is the same. The 45° orientated cylinder cross-bars create a smaller vortex structure in the wake of the cylinders with a smaller disturbance in

the boundary layer that limits the heat transfer coefficient. The Nu_x entry length in Figure 6.3 is harder to approximate from the graph as in Figure 6.2 but is still approximately $x/H = 20$.

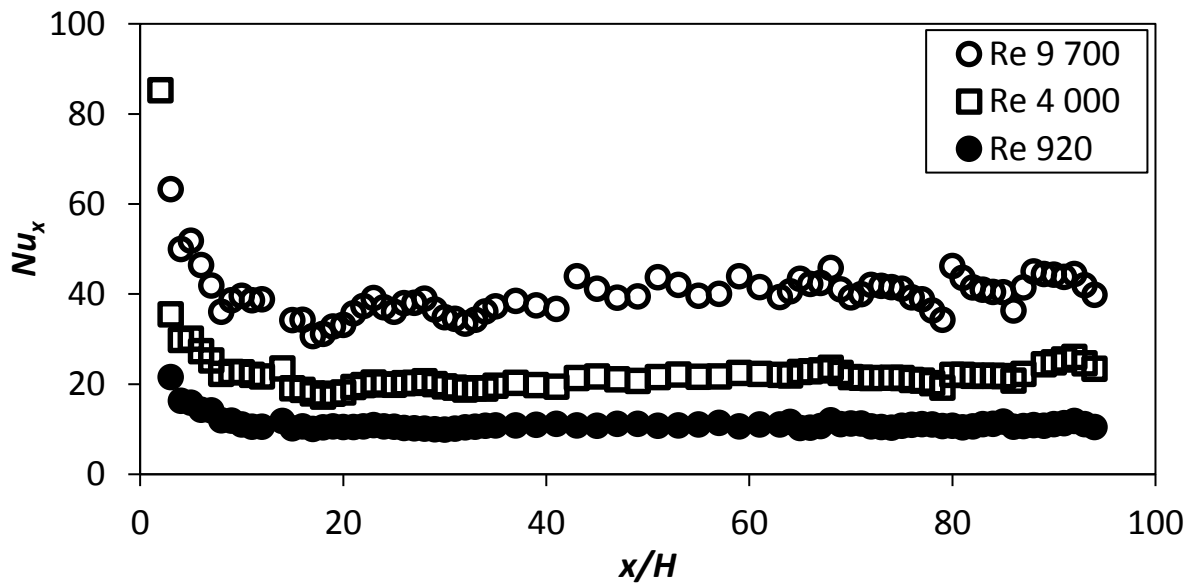


Figure 6.3: Local Nusselt number plotted against x/H coordinate for array: $d/p = 0.025$, $\theta = 45^\circ$ at $Re = 920$, $Re = 4\,000$ and $Re = 9\,700$. Cylinders are arranged in staggered array.

The local Nusselt number is plotted against x/H in Figure 6.4 for the cylindrical configuration where $d/p = 0.05$ and $\theta = 90^\circ$. The larger $d/p = 0.05$ ratio means that the pitch between the cylinders is shorter, but the cylinder diameter is the same as in the $d/p = 0.025$ cases. With the distance between the cylinders being closer to one another, Nu_x and heat transfer coefficients are higher when compared to the similar case with larger distances, i.e. $d/p = 0.025$, between the cylinders. The shorter pitch, i.e., $d/p = 0.05$ case causes the wake of one cylinder to interact with the downstream cylinder and its wake resulting in larger disturbances in the wall boundary layer and augmentation in the heat transfer. The thermal entry length in Figure 6.4 can be estimated as approximately $x/H = 16$ which is a bit smaller than in the previous cases with $d/p = 0.025$.

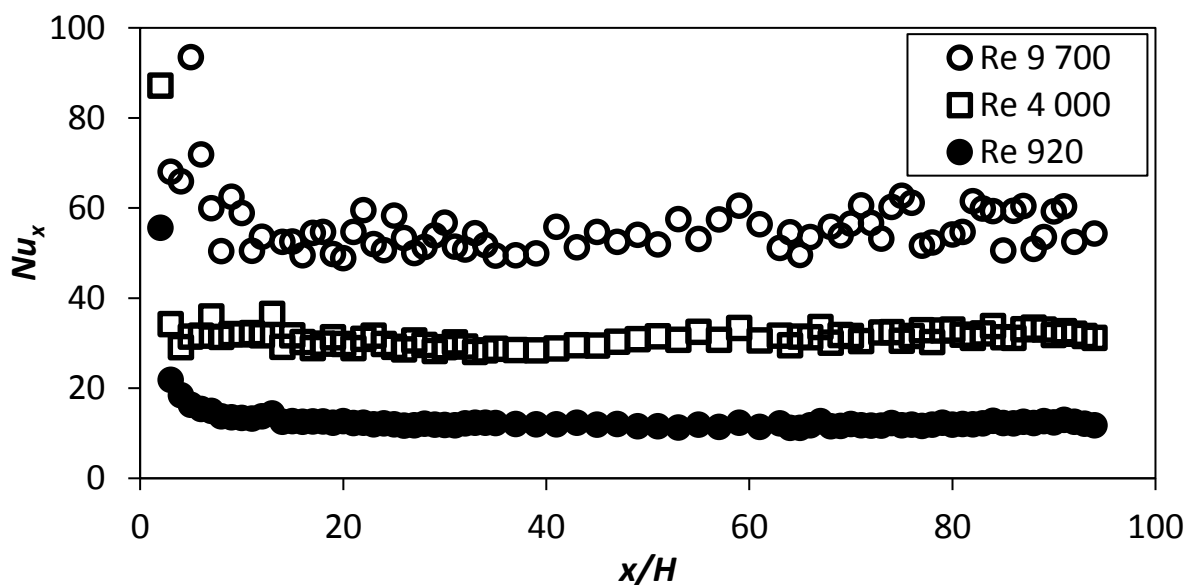


Figure 6.4: Local Nusselt number plotted against x/H coordinate for array: $d/p = 0.05$, $\theta = 90^\circ$ at $Re = 920$, $Re = 4\,000$ and $Re = 9\,700$. Cylinders are arranged in staggered array.

Figure 6.5 shows the local Nusselt numbers for configuration $d/p = 0.05$, $\theta = 45^\circ$. The heat transfer coefficient is less than in the $d/p = 0.05$, $\theta = 90^\circ$ case. From Figure 6.5, the Nu_x entry length can be estimated as $x/H = 20$.

Figure 6.2 to Figure 6.5 shows all the cases where the diameter of the cylinders are 1 mm and the cylinders is in a staggered layout.

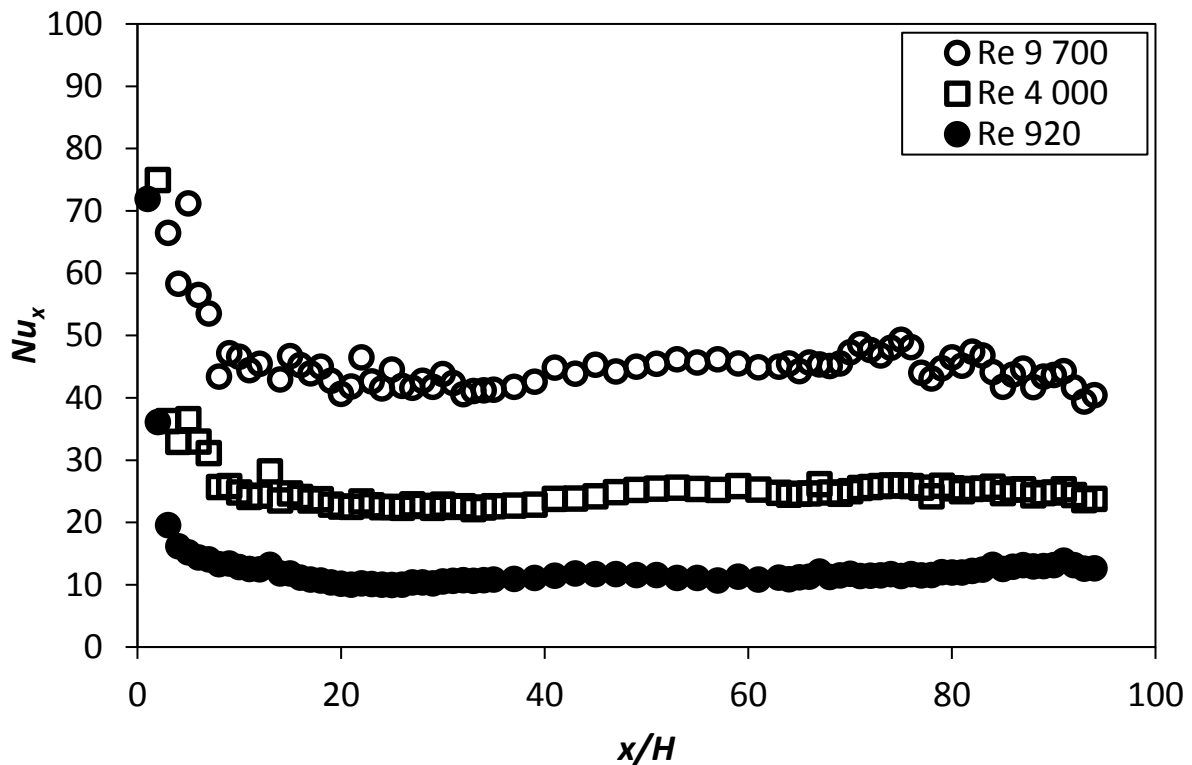


Figure 6.5: Local Nusselt number plotted against x/H coordinate for array: $d/p = 0.05$, $\theta = 45^\circ$ at $Re = 920$, $Re = 4\ 000$ and $Re = 9\ 700$. Cylinders are arranged in staggered array.

Figure 6.6 to Figure 6.9 shows the cases with the cylinders of diameter 2 mm that are the in-line array layout. The pitch of the cylinders in Figure 6.6 and Figure 6.7 are the same as in Figure 6.2 and Figure 6.3. The local Nu_x distributions in Figure 6.6 and Figure 6.7 do not have pronounced peaks and troughs at $x/H > 12$ when the flow becomes thermally fully developed. The 2 mm cylinder positions are further away from the heated wall. The flow acceleration in the space between the cylinder and heated walls and the wake from the cylinders do not affect the wall heat transfer locally as strongly as those in Figure 6.2 and Figure 6.3. However, the local Nu_x values are generally slightly higher in Figure 6.6 and Figure 6.7 at the corresponding Re than those in Figure 6.2 and Figure 6.3, respectively, because of higher mass flux in the wall boundary layer region. Also, the thermal entrance length for the Nu_x data in Figure 6.6 and Figure 6.7 seem to be in between $0 < x/H < 12$ compared to the entrance length between $0 < x/H < 20$ in Figure 6.2 and Figure 6.3. When the pitch distance between the cylinders is decreased for the cases in Figure 6.6 and Figure 6.7, the Nu_x distributions in the fully developed region at $x/H > 12$ increase as shown in Figure 6.8 and Figure 6.9. Compared to the data in Figure 6.4 and Figure 6.5 at the corresponding Re , the Nu_x values are also slightly higher in the fully developed region in Figure 6.8 and Figure 6.9 whereas the cylinder pitch remains the same in the figures. The $\theta = 90^\circ$ cases in Figure 6.6 and Figure 6.8 exhibit higher heat transfer coefficients at the corresponding Re in $x/H > 12$ than those in the $\theta = 45^\circ$ cases in Figure 6.7 and Figure 6.9 respectively.

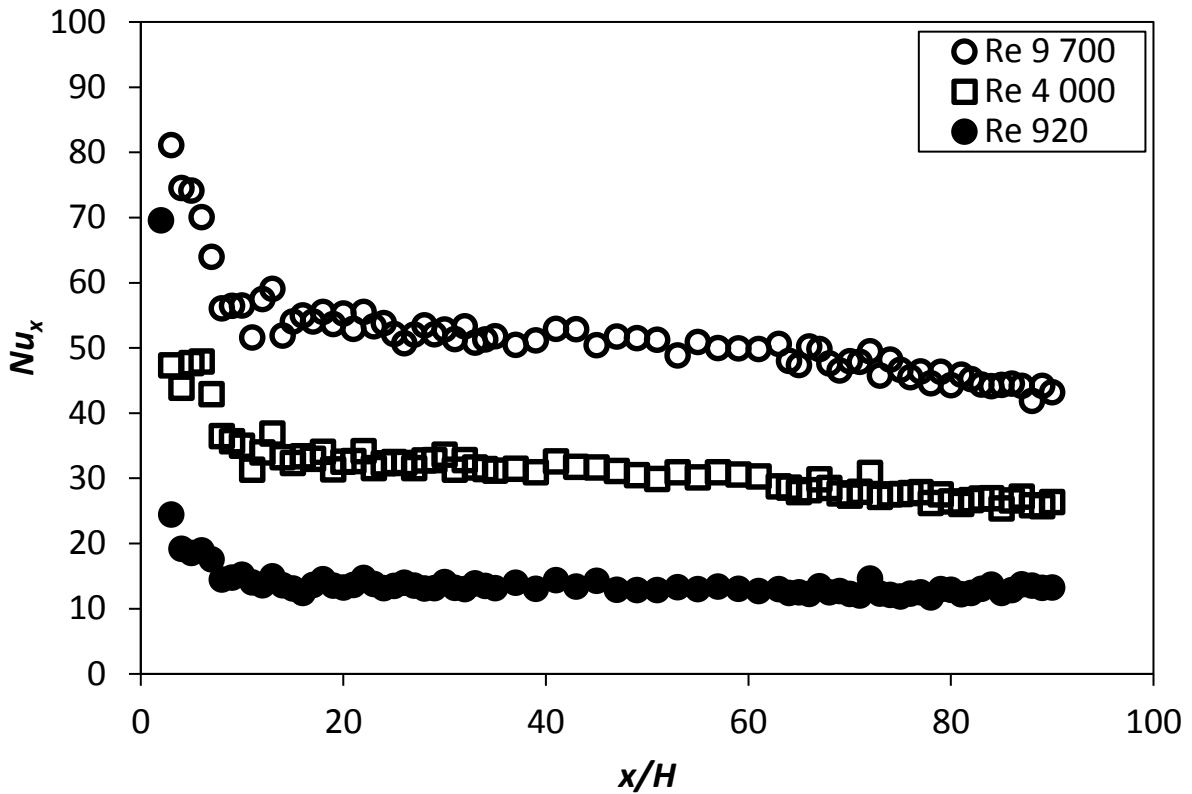


Figure 6.6: Local Nusselt number plotted against x/H coordinate for array: $d/p = 0.1$, $\theta = 90^\circ$ at $Re = 920$, $Re = 4\,000$ and $Re = 9\,700$. Cylinders are arranged in in-line array.

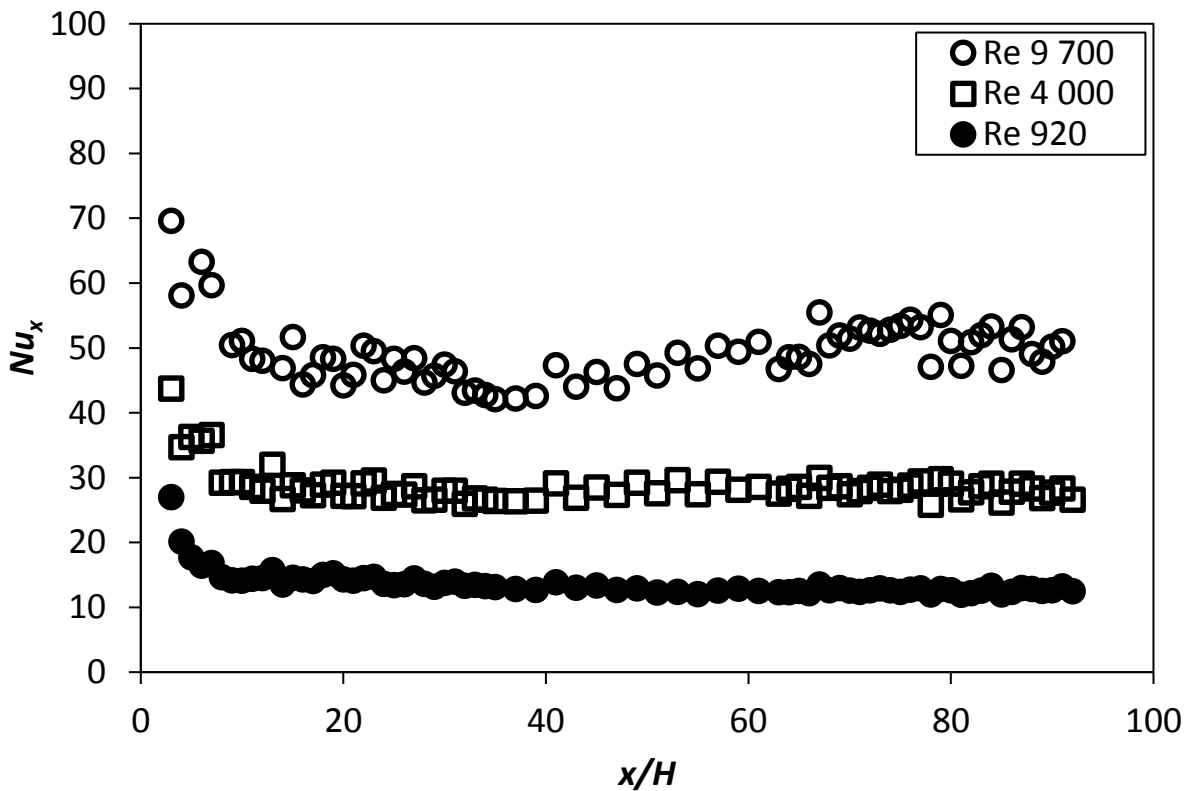


Figure 6.7: Local Nusselt number plotted against x/H coordinate for array: $d/p = 0.1$, $\theta = 45^\circ$ at $Re = 920$, $Re = 4\,000$ and $Re = 9\,700$. Cylinders are arranged in in-line array.

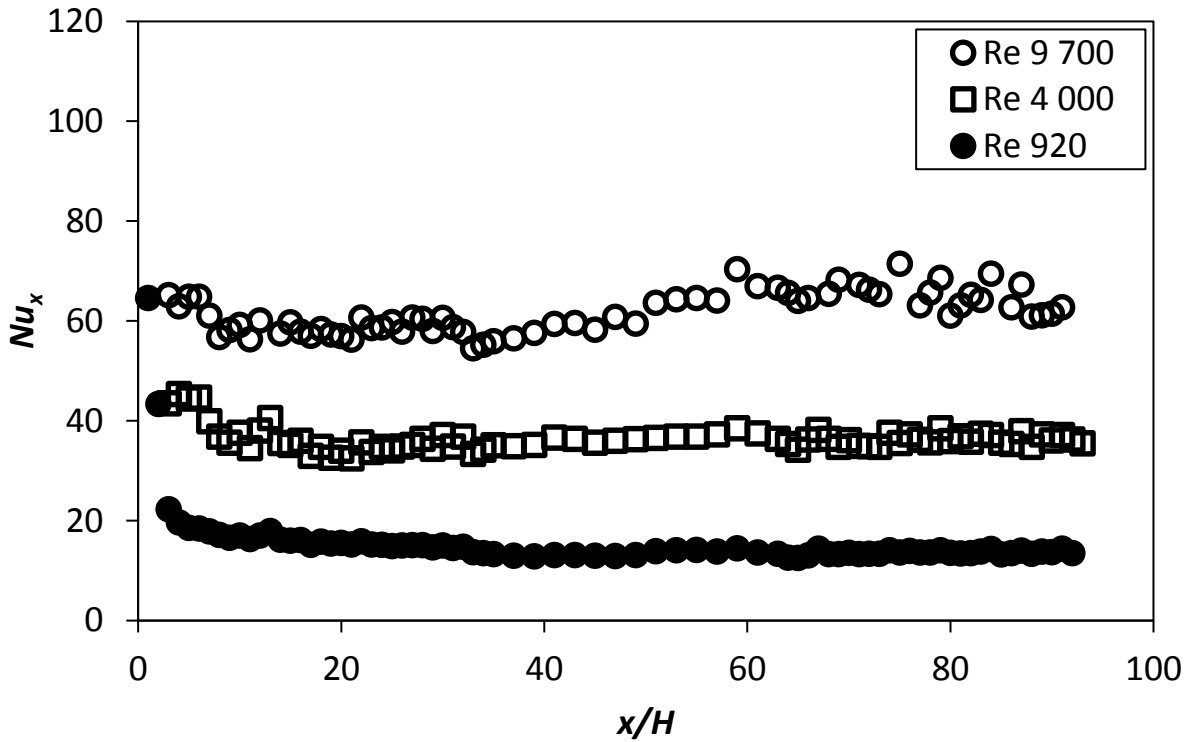


Figure 6.8: Local Nusselt number plotted against x/H coordinate for array: $d/p = 0.2$, $\theta = 90^\circ$ at $Re = 920$, $Re = 4\,000$ and $Re = 9\,700$. Cylinders are arranged in in-line array.

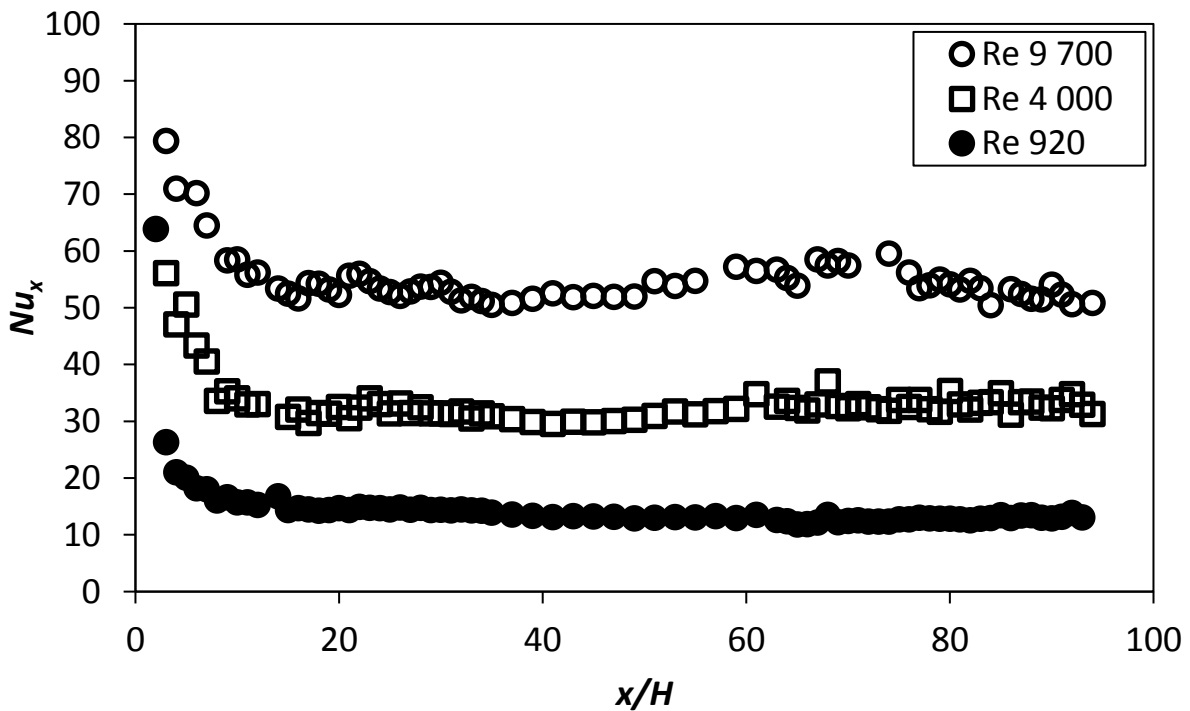


Figure 6.9: Local Nusselt number plotted against x/H coordinate for array: $d/p = 0.2$, $\theta = 45^\circ$ at $Re = 920$, $Re = 4\,000$ and $Re = 9\,700$. Cylinders are arranged in in-line array.

6.3. Average Nusselt number

The average Nusselt numbers were found with the integral average of the local Nusselt numbers from $x/H = 60$ to $x/H = 90$, where the flow is fully thermally developed:

$$Nu = \frac{1}{L-x} \int_x^L Nu_x dx \quad (3.12)$$

In Equation 3.12 $L = 450$, $x = 300$, that corresponds to $x/H = 90$ and $x/H = 60$.

The variations in average Nusselt numbers show an increase with an increase in the selected range of Reynolds number, irrespectively of the d/p ratio and the angle to the flow direction, θ , and is larger than the average Nusselt number for the plane channel in all the cases.

The average Nusselt number for $\theta = 90^\circ$ is plotted against Reynolds number in Figure 6.10 and for $\theta = 45^\circ$ in Figure 6.11. With both variations of θ , the average Nusselt number increases with an increase in the d/p ratio except for $d/p = 0.05$ at $\theta = 90^\circ$ which is larger than $d/p = 0.1$ because the cylinders are more densely arranged, causing an increase in turbulence *i.e.* larger boundary layer disturbance. The magnitude of the average Nusselt number corresponds with the friction factor shown in Section 6.5. The friction factor of $d/p = 0.05$, $\theta = 90^\circ$, is larger than the friction factor of $d/p = 0.1$, $\theta = 90^\circ$, in all the cases of tests done in the selected Reynolds number range.

Eiamsa-ard and Promvong [52] did a study of the thermal characteristics of flow in rib-grooved channel. The rib-groove combinations are 90° to the flow direction. The turbulators in their study with the highest thermal performance was triangular-rib and triangular-groove combination with a pitch ratio of 6.6. The Nu_{avg} , f , and η will be shown for this turbulator combination in the graphs of $\theta = 90^\circ$ for reference. The rib-groove combination had a Nu_{avg} of 18 to 52 at $Re = 3\,000$ to $Re = 10\,500$ and is comparable to $d/p = 0.025$, $\theta = 90^\circ$ with a Nu_{avg} of 21 to 48 at $Re = 3\,000$ to $Re = 10\,500$.

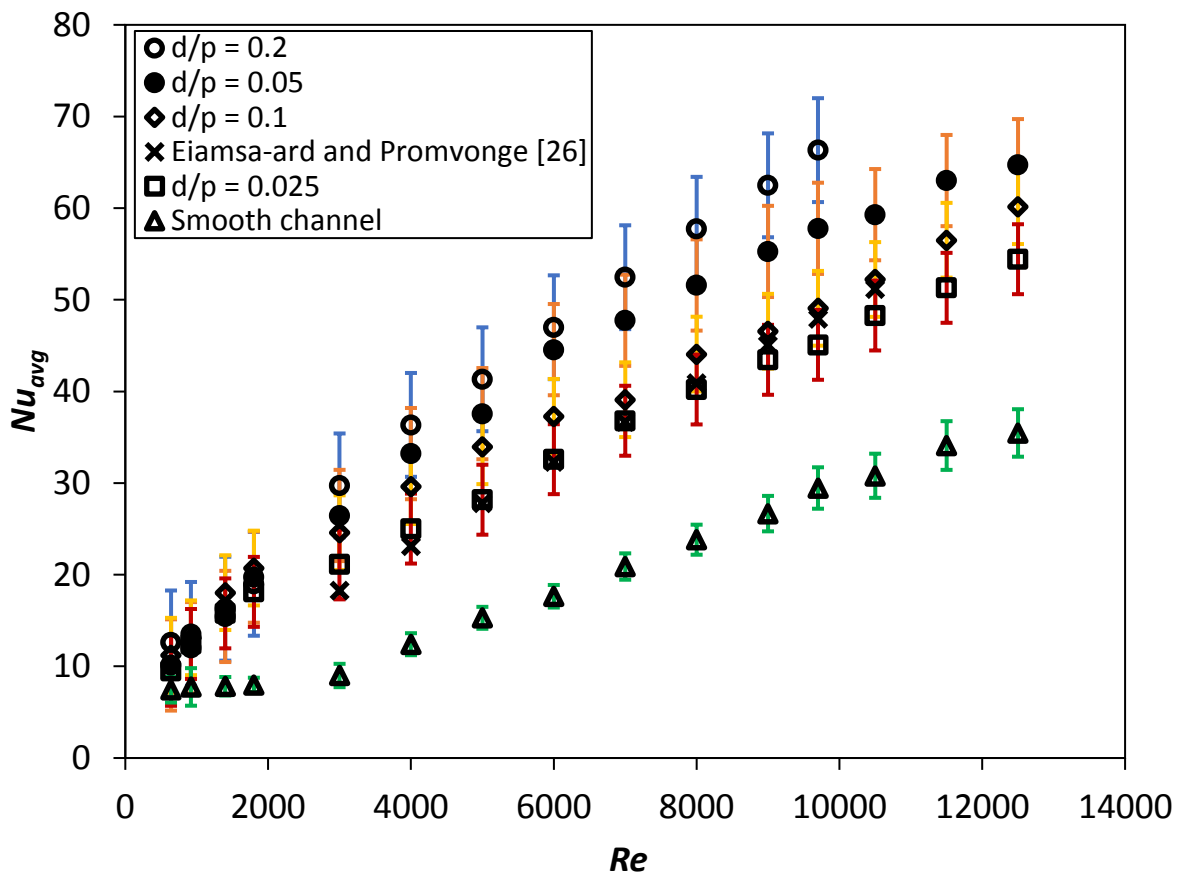


Figure 6.10: Average Nusselt number plotted against Reynolds number for cylindrical arrays with $\theta = 90^\circ$ and the Eiamsa-ard and Promvong [52] data for TR and TG, PR = 6.6.

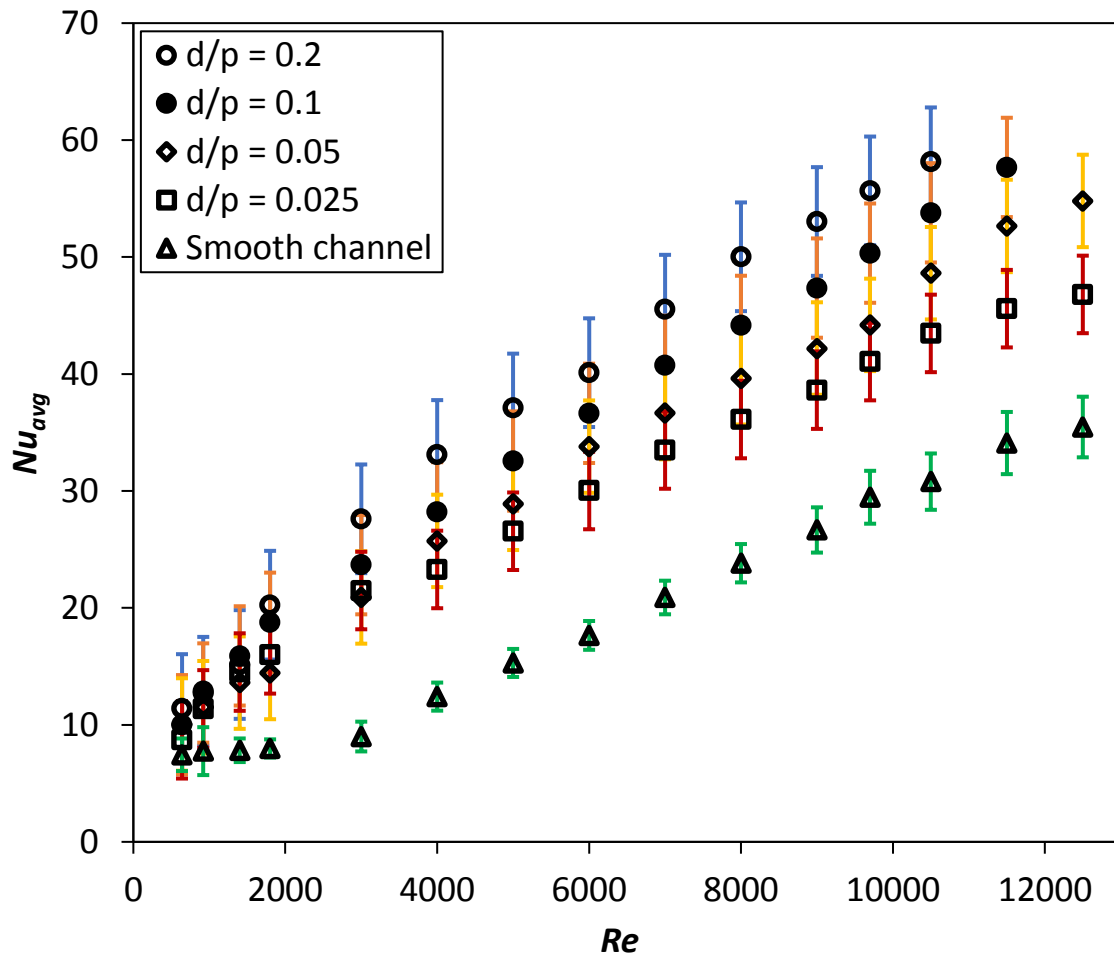


Figure 6.11: Average Nusselt number plotted against Reynolds number for cylindrical arrays with $\theta = 45^\circ$.

With a comparison between the $\theta = 90^\circ$ and $\theta = 45^\circ$ cases, the $\theta = 90^\circ$ has larger average Nusselt numbers for the same d/p ratio at all the selected Reynolds numbers. This is because there are larger fluid accelerations next to the cylinders and larger eddy formations in the wake of the cylinders in the $\theta = 90^\circ$ cases. The in-line configurations with the larger diameter cylinders have larger average Nusselt numbers than the staggered configurations. Because of the larger Strouhal numbers, the unsteadiness of the flow in the wake of the cylinders are larger, causing more boundary layer disturbance and mixing of the flow. See Section 5.7 for the numerical CFD results that show the secondary flow structures and vorticity.

The largest average Nusselt number for the $\theta = 90^\circ$ case is $Nu_{avg} = 66.3$ for the d/p ratio of 0.2 at a Reynolds number of 9 700 and the smallest was for d/p ratio of 0.025 at a Reynolds number of 640 with $Nu_{avg} = 9.5$. This was the largest Reynolds number the test setup was able to reach because of the large pressure drop for this cylindrical cross-bar configuration.

The largest average Nusselt number in the case of $\theta = 45^\circ$ is $Nu_{avg} = 58.1$ for the d/p ratio of 0.2 at a Reynolds number of 10 500, again the largest flow-rate the test setup could reach for this cylindrical cross-bar configuration. The lowest average Nusselt number for $\theta = 45^\circ$ was $Nu_{avg} = 8.7$ for d/p ratio of 0.025.

The power functions providing the correlation between the average Nusselt numbers and Re are shown in Table 6.1, as functions of the Reynolds number. Correlations were found by doing least square linear fit regression analyses on the data plots and converting them to power functions by

finding the natural logarithms on the left and right sides of the equations. Correlations are shown for Reynolds numbers smaller than or equal to 1 800 and for larger than 1 800 to best fit the average Nusselt number data.

Table 6.1: Correlation power function for average Nusselt numbers, Nu_{avg} .

$d/p = 0.2$ In-line	$\theta = 90^\circ$	$Nu_{avg} = \begin{cases} 0.938Re^{0.397}, & Re \leq 1800 \\ 0.129Re^{0.679}, & Re > 1800 \end{cases}$	(6.1)
$d/p = 0.2$ In-line	$\theta = 45^\circ$	$Nu_{avg} = \begin{cases} 0.377Re^{0.522}, & Re \leq 1800 \\ 0.232Re^{0.596}, & Re > 1800 \end{cases}$	(6.2)
$d/p = 0.1$ In-line	$\theta = 90^\circ$	$Nu_{avg} = \begin{cases} 0.206Re^{0.615}, & Re \leq 1800 \\ 0.192Re^{0.606}, & Re > 1800 \end{cases}$	(6.3)
$d/p = 0.1$ In-line	$\theta = 45^\circ$	$Nu_{avg} = \begin{cases} 0.213Re^{0.597}, & Re \leq 1800 \\ 0.122Re^{0.656}, & Re > 1800 \end{cases}$	(6.4)
$d/p = 0.05$ Staggered	$\theta = 90^\circ$	$Nu_{avg} = \begin{cases} 0.169Re^{0.630}, & Re \leq 1800 \\ 0.186Re^{0.624}, & Re > 1800 \end{cases}$	(6.5)
$d/p = 0.05$ Staggered	$\theta = 45^\circ$	$Nu_{avg} = \begin{cases} 0.984Re^{0.360}, & Re \leq 1800 \\ 0.101Re^{0.666}, & Re > 1800 \end{cases}$	(6.6)
$d/p = 0.025$ Staggered	$\theta = 90^\circ$	$Nu_{avg} = \begin{cases} 0.179Re^{0.618}, & Re \leq 1800 \\ 0.093Re^{0.674}, & Re > 1800 \end{cases}$	(6.7)
$d/p = 0.025$ Staggered	$\theta = 45^\circ$	$Nu_{avg} = \begin{cases} 0.198Re^{0.590}, & Re \leq 1800 \\ 0.182Re^{0.589}, & Re > 1800 \end{cases}$	(6.8)

The Nu_{avg} correlation equations are compared to the experimental values in Figure 6.12 and the error is between $\pm 10\%$.

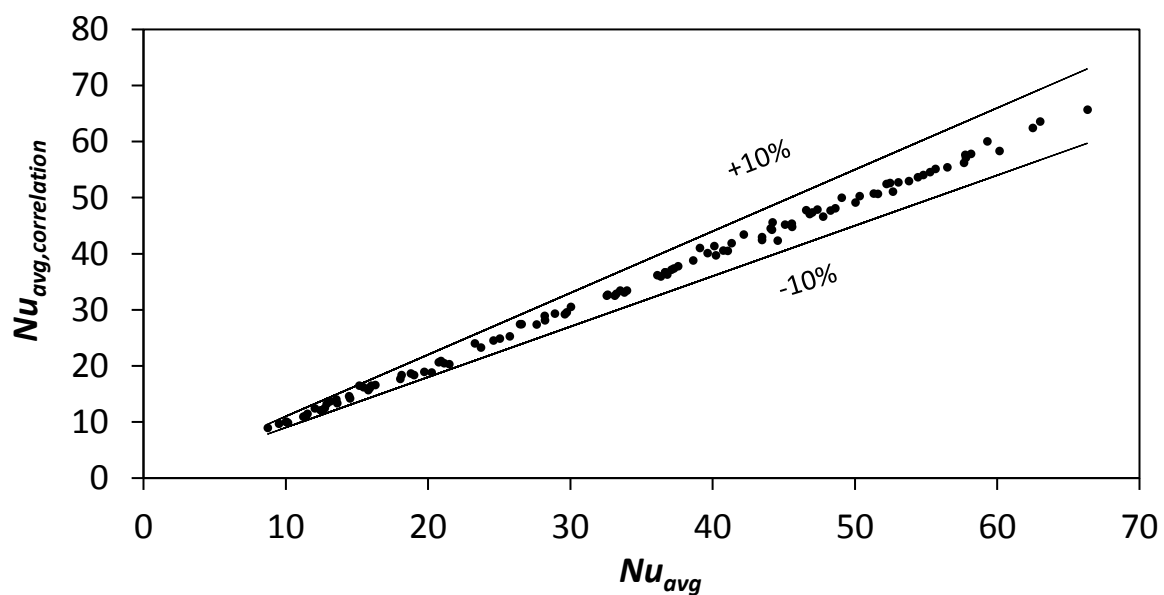


Figure 6.12: Comparison between Nusselt number average and correlations, including all the correlations from Equation (6.1) to (6.8).

6.4. Nusselt number ratio

The ratio of the Nusselt number average of the channel with the cylindrical cross-bar turbulators to the plane channel Nusselt numbers are plotted against the Reynolds number in Figure 6.13 for $\theta = 90^\circ$ and in Figure 6.14 for $\theta = 45^\circ$. The maximum Nusselt number ratio occurs at $Re = 3\ 000$ in all the cases in the tested Reynolds number range. For rectangular plane channel flow, this is in the transitional flow regime [3][4]. This peak in the Nusselt number ratio is caused by the turbulators transforming the flow from transitional to turbulent flow.

There is an increase in the Nusselt number ratio from a Reynolds number of 640 to 3 000. After the Nusselt number ratio reaches its peak, there is a steady decline in the Nusselt ratio as the Reynolds number is increased.

The Nusselt number ratio follows the same trend as the average Nusselt numbers, where the largest d/p ratios have the largest Nusselt number ratios. The largest Nusselt number ratio is for $d/p = 0.2$, $\theta = 90^\circ$ with $Nu_{avg}/Nu_{0,avg} = 3.3$ at $Re = 3\ 000$. The lowest Nusselt number ratio is for $d/p = 0.025$, $\theta = 45^\circ$ with a ratio of $Nu_{avg}/Nu_{0,avg} = 1.17$.

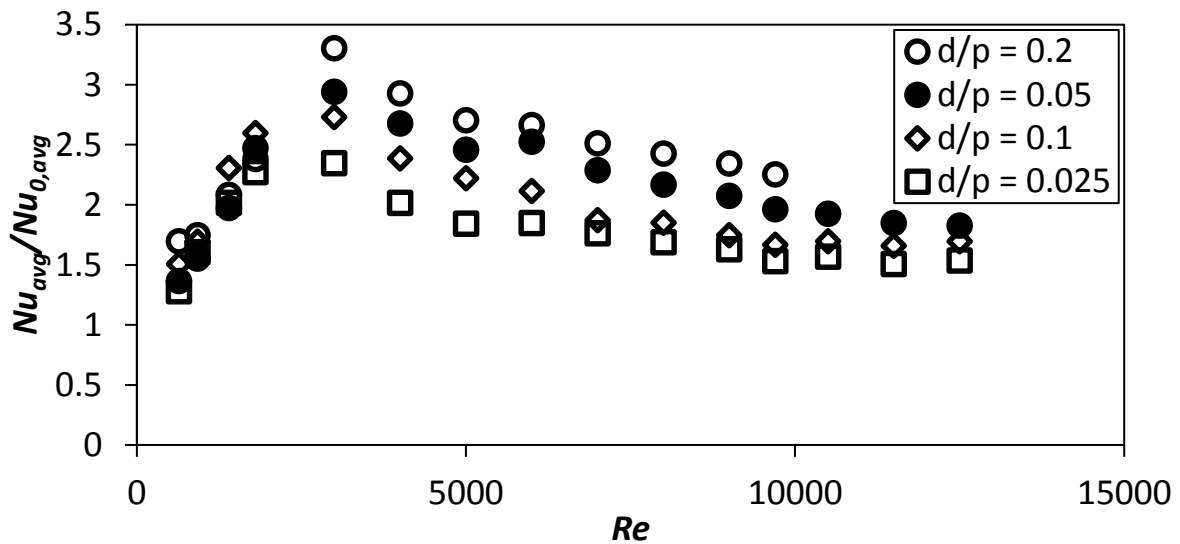


Figure 6.13: Nusselt number ratio plotted against Reynolds number for with cylindrical arrays with $\theta = 90^\circ$.

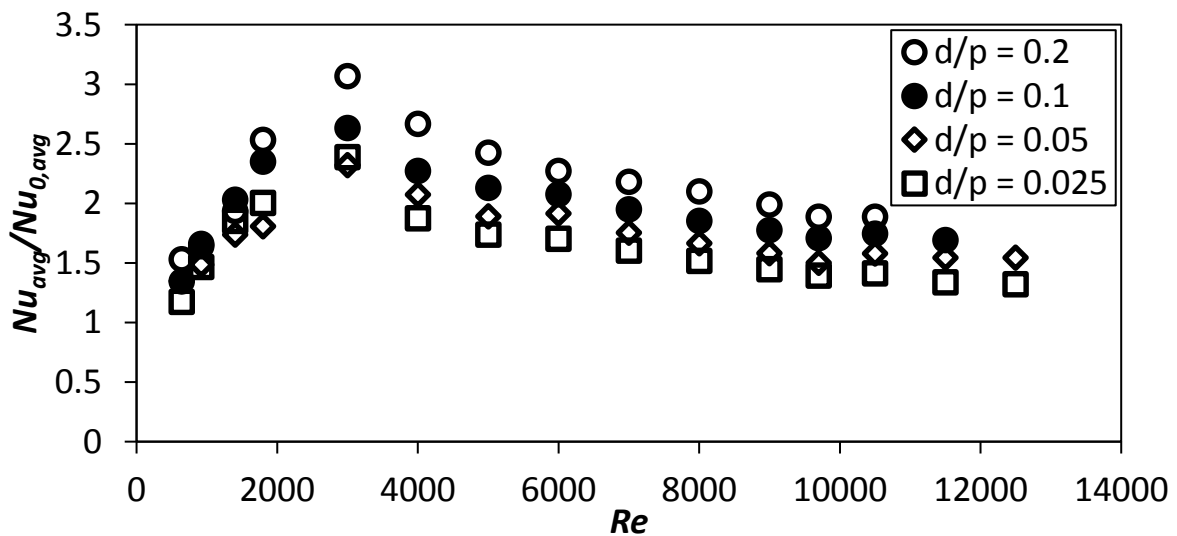


Figure 6.14: Nusselt number ratio plotted against Reynolds number for with cylindrical arrays with $\theta = 45^\circ$.

Table 6.2 shows the power function correlations for the Nusselt number ratios. The correlations are split into the data smaller than or equal to a Reynolds number of 1 800 and larger than 1 800 to best fit the data shown in Figure 6.13 and Figure 6.14, for the Nusselt number ratios of $\theta = 90^\circ$ and $\theta = 45^\circ$ respectively. The shape of the trend lines results in the data of a Reynolds number below and equal to 1 800 being positive power functions and negative power functions for Reynolds numbers larger than 1 800.

Table 6.2: Correlation power functions for Nusselt number ratios $Nu_{avg}/Nu_{0,avg}$.

$d/p = 0.2$	$\theta = 90^\circ$		
In-line		$Nu_{avg}/Nu_{0,avg} = \begin{cases} 0.189Re^{0.335}, & Re \leq 1800 \\ 36.881Re^{-0.304}, & Re > 1800 \end{cases}$	(6.9)
$d/p = 0.2$	$\theta = 45^\circ$		
In-line		$Nu_{avg}/Nu_{0,avg} = \begin{cases} 0.0752Re^{0.459}, & Re \leq 1800 \\ 63.607Re^{-0.381}, & Re > 1800 \end{cases}$	(6.10)
$d/p = 0.1$	$\theta = 90^\circ$		
In-line		$Nu_{avg}/Nu_{0,avg} = \begin{cases} 0.041Re^{0.553}, & Re \leq 1800 \\ 48.018Re^{-0.3651}, & Re > 1800 \end{cases}$	(6.11)
$d/p = 0.1$	$\theta = 45^\circ$		
In-line		$Nu_{avg}/Nu_{0,avg} = \begin{cases} 0.043Re^{0.535}, & Re \leq 1800 \\ 33.567Re^{-0.322}, & Re > 1800 \end{cases}$	(6.12)
$d/p = 0.05$	$\theta = 90^\circ$		
Staggered		$Nu_{avg}/Nu_{0,avg} = \begin{cases} 0.034Re^{0.568}, & Re \leq 1800 \\ 46.698Re^{-0.343}, & Re > 1800 \end{cases}$	(6.13)
$d/p = 0.05$	$\theta = 45^\circ$		
Staggered		$Nu_{avg}/Nu_{0,avg} = \begin{cases} 0.196Re^{0.298}, & Re \leq 1800 \\ 25.292Re^{-0.301}, & Re > 1800 \end{cases}$	(6.14)
$d/p = 0.025$	$\theta = 90^\circ$		
Staggered		$Nu_{avg}/Nu_{0,avg} = \begin{cases} 0.036Re^{0.556}, & Re \leq 1800 \\ 23.373Re^{-0.293}, & Re > 1800 \end{cases}$	(6.15)
$d/p = 0.025$	$\theta = 45^\circ$		
Staggered		$Nu_{avg}/Nu_{0,avg} = \begin{cases} 0.039Re^{0.528}, & Re \leq 1800 \\ 45.481Re^{-0.378}, & Re > 1800 \end{cases}$	(6.16)

The $Nu_{avg}/Nu_{0,avg}$ correlation equations are compared to the experimental values in Figure 6.15 and the error is between $\pm 10\%$.

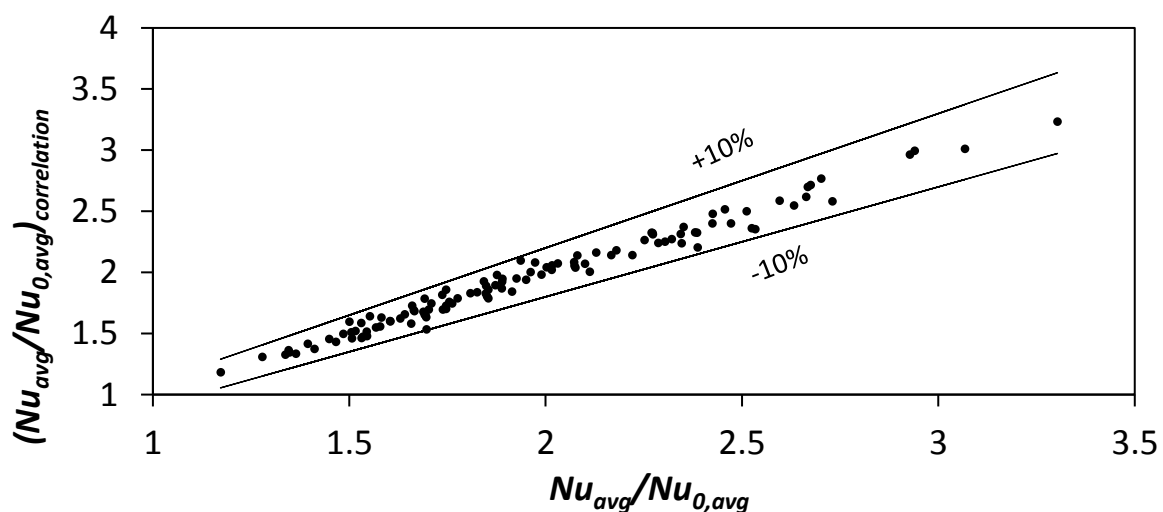


Figure 6.15: Comparison between Nusselt number ratio and correlations, including all the correlations from Equation (6.9) to (6.16).

6.5. Friction factor

The friction factor, Equation (3.13), is a function of the pressure drop gradient, $\Delta P/\Delta x$, and the square of the mean velocity of the flow, v^2 . The hydraulic diameter, D_h , is a constant, and the density of the fluid, ρ , was found by using the ideal gas law with ambient conditions measured daily.

$$f = \frac{(\Delta P/\Delta x)(D_h/4)}{\frac{1}{2}\rho v^2} = \frac{(\Delta P/\Delta x)(D_h)}{2\rho v^2} \quad (3.13)$$

To find the pressure drop gradient, the pressure, measured on the centre-line of the channel wall, is plotted against x . The gradient $\Delta P/\Delta x$ is then obtained from the slope of the least square fit line through the plotted data employing the linear regression analysis. The line fits the data points at the test section where the flow is fully developed as the slope remains about constant. The fully developed flow condition is found at the axial location $x/L \geq 0.5$ for all the test conditions. The wall pressure graph is shown for $d/p = 0.025$, $\theta = 90^\circ$ and $d/p = 0.025$, $\theta = 45^\circ$ at $Re = 9\,700$ in Figure 6.16. The pressure values along x in the figure are obtained as the pressure difference between the ambient pressure and the channel pressure inside the test section. The equation of the least square fit line along with its slope is shown in the legend box of Figure 6.16. The coefficient of determination, R^2 , is 0.985 of the line fit through the data points at $0.315\text{ m} < x < 0.54\text{ m}$ is at the least 0.98 for all the P vs. x plots. See Appendix G for all the pressure data for all the cylindrical cross-bar arrays taken at each Reynolds number in the selected range.

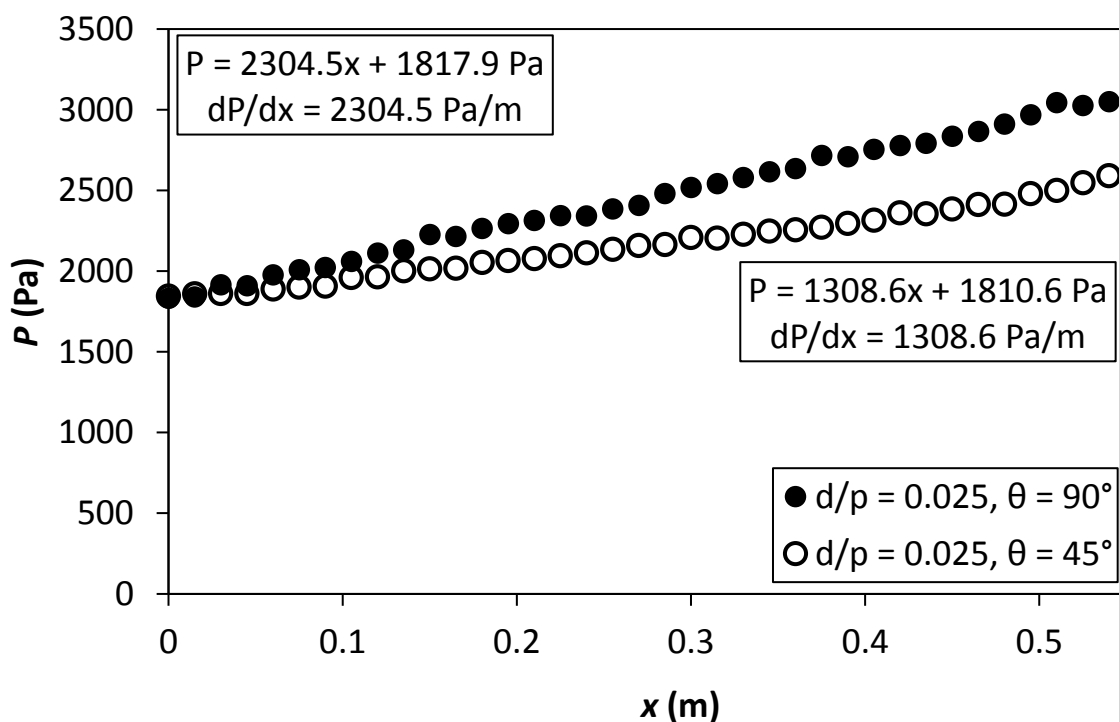


Figure 6.16: Static pressure plotted against the x coordinate at $Re = 9\,700$ for setup: $d/p = 0.025$, 90° and $d/p = 0.025$, 45° .

The friction factors of the cylindrical arrays plotted versus the Reynolds number with $\theta = 90^\circ$ is shown in Figure 6.17 and with $\theta = 45^\circ$ in Figure 6.18. Pressure loss characteristics of the tests done in the selected Reynolds number range follow the same trend as with the Nusselt numbers in the sense that the largest cylindrical cross-bar d/p ratio has the highest friction factors, except again for $d/p = 0.05$, $\theta = 90^\circ$ and $d/p = 0.1$, $\theta = 90^\circ$. The increase of the friction factor with an increase in d/p ratio occurs because the block of the flow is larger, resulting in a larger pressure drop. The friction factor for the

Eiamsa-ard and Promvonge [52] triangular-rib and triangular-groove combination with a pitch ratio of 6.6 is shown in Figure 6.17. It is larger than the friction factors for the turbulators tested in this study at the corresponding Re .

The friction factor magnitude reduces as the Reynolds number increases until it reaches an asymptote of a certain value. This means that the pressure drop gradient increases quadratically after a certain Reynolds number to stay in relation to the velocity squared in the denominator. When the f value at a given d/p is compared between Figure 6.17 and Figure 6.18 at the corresponding Re , the friction factor values are usually smaller for the $\theta = 45^\circ$ cylinders. This can be the result of reduced form drags and separation regions on the cylinders when they are oriented at an angle smaller than 90° with respect to the flow direction. The internal ribbed channel shows similar behaviour on the f distributions as the Re varies when the ribs are angled relative to the flow direction as in the study done by Aharwal *et al.* [53] where the friction factor increased with an increase in wedge angle at corresponding Reynolds numbers.

The largest friction factor occurs at $d/p = 0.2$, $\theta = 90^\circ$, $Re = 640$, where $f = 0.3$ and the lowest friction factor at $d/p = 0.025$, $\theta = 45^\circ$, $Re = 12\,500$, where $f = 0.02$. In all the tested cases the friction factor of the channels with cylindrical inserts is larger than with the smooth/plane channel because of the flow obstruction caused by the cylindrical cross-bars.

The friction factors for the cases where $\theta = 90^\circ$ is larger than where $\theta = 45^\circ$ with the same d/p ratio, at the same Reynolds number. This is because the $\theta = 45^\circ$ cylinders have lower pressure drag and are more streamlined than in the cases where $\theta = 90^\circ$. The in-line configurations with the larger diameter cylinders have larger friction factors than the staggered configurations. Because of the larger Strouhal numbers, the unsteadiness of the flow in the wake of the cylinders are larger, causing more boundary layer disturbance and mixing of the flow, causing larger pressure drops. See Section 5.7 for the numerical CFD results that show the secondary flow structures and vorticity.

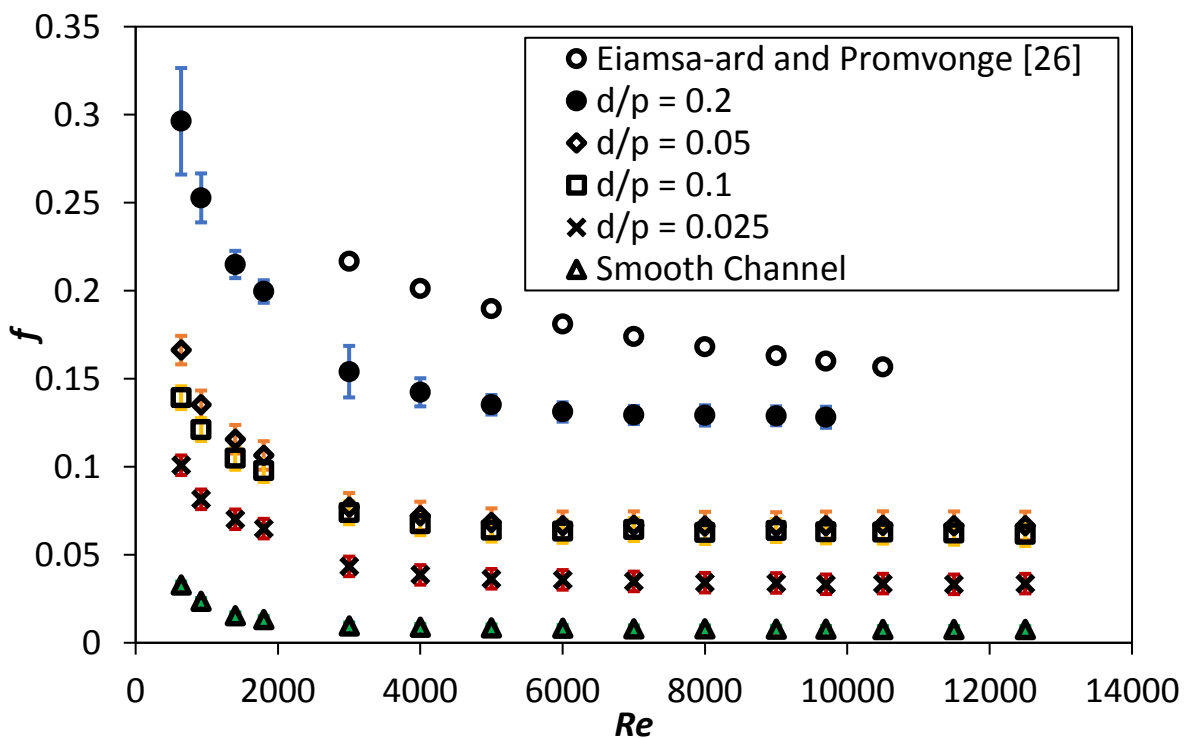


Figure 6.17 Friction factor plotted against Reynolds number for cylindrical arrays with $\theta = 90^\circ$ and the Eiamsa-ard and Promvonge [52] data for TR and TG, PR = 6.6.

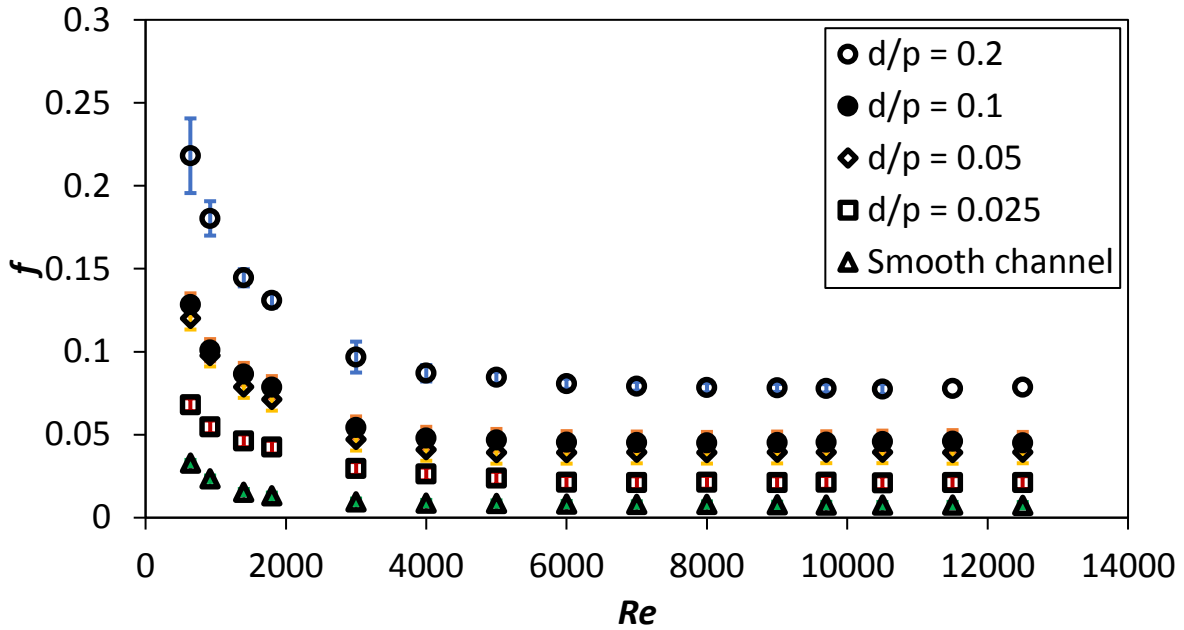


Figure 6.18. Friction factor plotted against Reynolds number for cylindrical arrays with $\theta = 45^\circ$.

The correlation functions for the friction factors are shown in Table 6.3. For Reynolds numbers smaller than or equal to 4 000, power functions correlations are shown and constant functions for Reynolds numbers larger than 4 000. The pressure-drop gradient and average velocity squared started to increase at the same rate with an increase in Reynolds number resulting in the friction factors becoming constant with an increase in Reynolds number.

Table 6.3: Correlation functions for friction factors, f .

$d/p = 0.2$	$\theta = 90^\circ$		
In-line		$f = \begin{cases} 4.045Re^{-0.405}, & Re \leq 4\,000 \\ 0.130, & Re > 4\,000 \end{cases}$	(6.17)
$d/p = 0.2$	$\theta = 45^\circ$		
In-line		$f = \begin{cases} 5.7794Re^{-0.508}, & Re \leq 4\,000 \\ 0.0792, & Re > 4\,000 \end{cases}$	(6.18)
$d/p = 0.1$	$\theta = 90^\circ$		
In-line		$f = \begin{cases} 1.8805Re^{-0.401}, & Re \leq 4\,000 \\ 0.0630, & Re > 4\,000 \end{cases}$	(6.19)
$d/p = 0.1$	$\theta = 45^\circ$		
In-line		$f = \begin{cases} 4.005Re^{-0.533}, & Re \leq 4\,000 \\ 0.0455, & Re > 4\,000 \end{cases}$	(6.20)
$d/p = 0.05$	$\theta = 90^\circ$		
Staggered		$f = \begin{cases} 3.258Re^{-0.462}, & Re \leq 4\,000 \\ 0.0666, & Re > 4\,000 \end{cases}$	(6.21)
$d/p = 0.05$	$\theta = 45^\circ$		
Staggered		$f = \begin{cases} 5.726Re^{-0.594}, & Re \leq 4\,000 \\ 0.0394, & Re > 4\,000 \end{cases}$	(6.22)
$d/p = 0.025$	$\theta = 90^\circ$		
Staggered		$f = \begin{cases} 3.069Re^{-0.526}, & Re \leq 4\,000 \\ 0.0343, & Re > 4\,000 \end{cases}$	(6.23)
$d/p = 0.025$	$\theta = 45^\circ$		
Staggered		$f = \begin{cases} 1.9265Re^{-0.517}, & Re \leq 4\,000 \\ 0.0215, & Re > 4\,000 \end{cases}$	(6.24)

The f correlation equations are compared to the experimental values in Figure 6.19 and the error is between $\pm 10\%$.

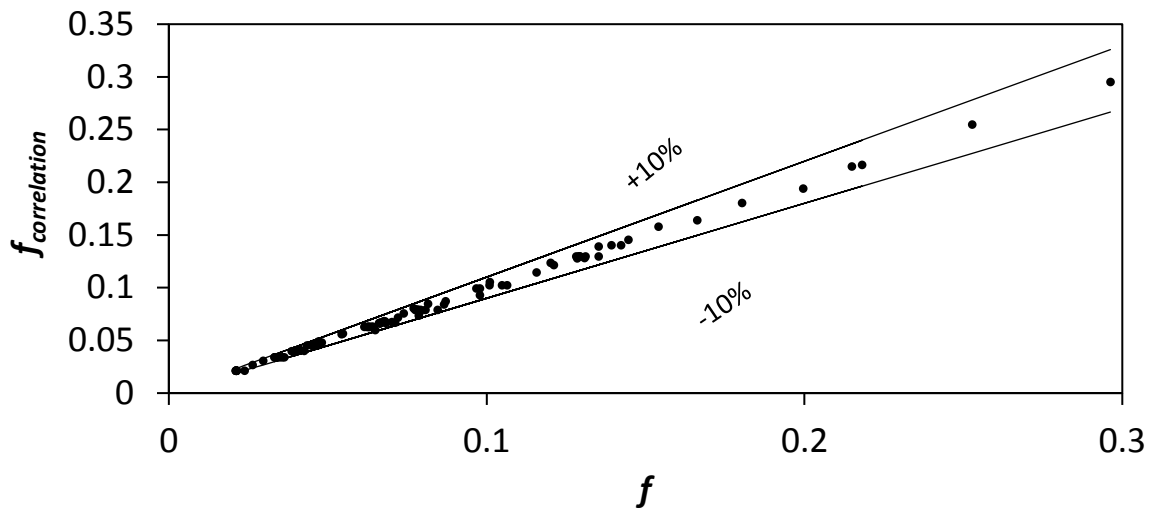


Figure 6.19: Comparison between friction factor and correlations, including all the correlations from Equation (6.17) to (6.24).

6.6. Friction factor ratio

The friction factor ratios of the channel with the turbulators to the smooth channel are shown in Figure 6.20 for $\theta = 90^\circ$ and Figure 6.21 for $\theta = 45^\circ$. The ratio is larger for all the cases with $\theta = 90^\circ$ compared to $\theta = 45^\circ$, for the same d/p ratio and the ratios decrease as the d/p ratio decreases except for the $\theta = 90^\circ$ case between $d/p = 0.05$ and $d/p = 0.1$. The ratios increase as the Reynolds number increases up until approximately $Re = 2\,000$, where it reaches a plateau.

The largest friction factor ratio is for $d/p = 0.2$, $\theta = 90^\circ$ at $Re = 9\,700$, where the friction factor for the channel with the turbulator array is 16.7 times larger than for the smooth channel, which is a very large pressure penalty. The smallest friction factor ratio is for $d/p = 0.025$, $\theta = 45^\circ$, at $Re = 640$ where the ratio is 2.1.

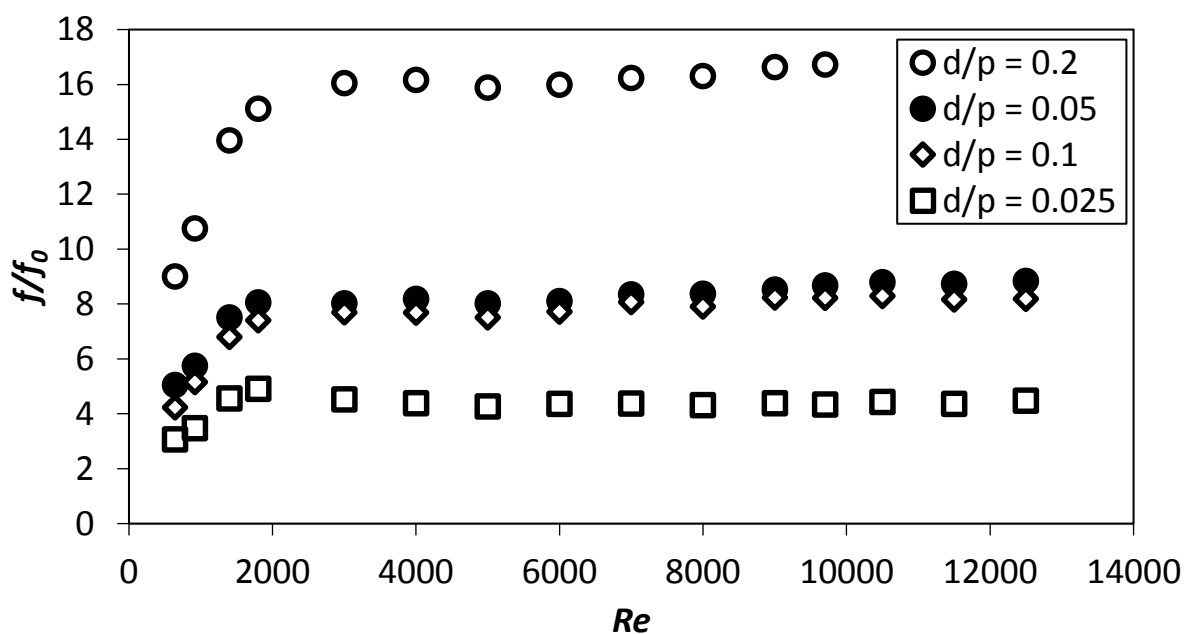


Figure 6.20: Friction factor ratio plotted against Reynolds number for with cylindrical arrays with $\theta = 90^\circ$.

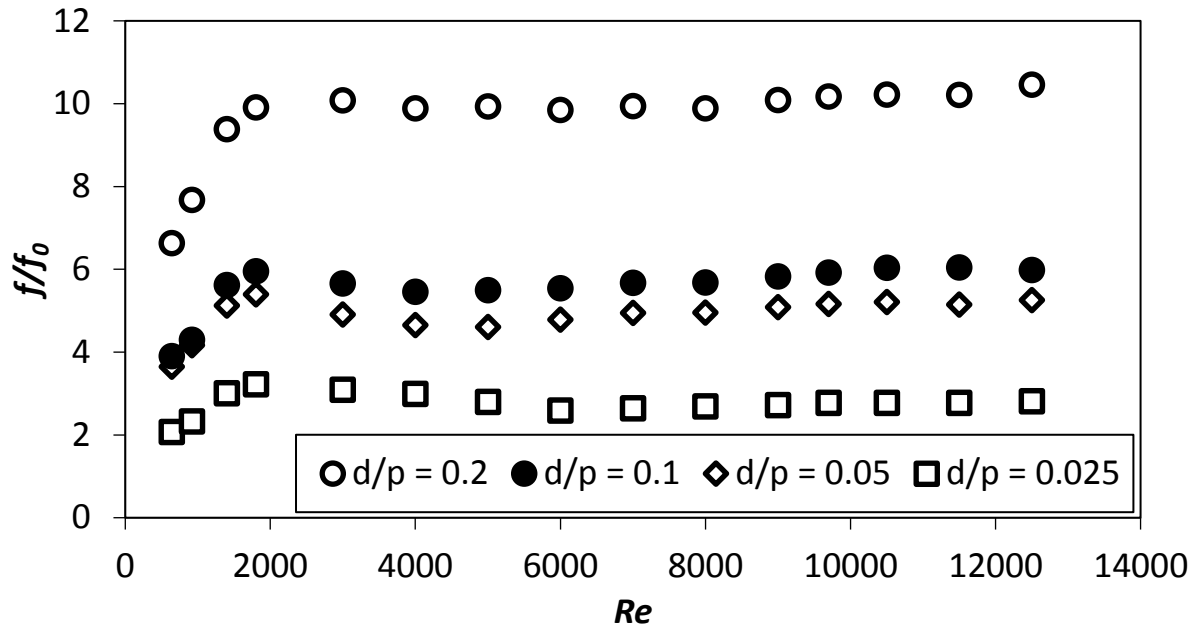


Figure 6.21: Friction factor ratio plotted against Reynolds number for with cylindrical arrays with $\theta = 45^\circ$.

Table 6.4 shows the correlation functions for the friction factor ratios as a function of the Reynolds number. Power functions were used to correlate the friction factor ratios for Reynolds numbers smaller than or equal to 1 800 and constants for Reynolds numbers larger than 1 800 where the friction function ratios started to become constant with an increase in Reynolds number. Using the friction factor ratio correlations for Reynolds numbers larger than 1 800 is a convenient way to determine the pressure penalty for the cylindrical cross-bar configurations.

Table 6.4: Correlation functions for the friction factor ratios, f/f_0 .

$d/p = 0.2$ In-line	$\theta = 90^\circ$	$f/f_0 = \begin{cases} 0.313Re^{0.520}, & Re \leq 1800 \\ 16.248, & Re > 1800 \end{cases}$	(6.25)
$d/p = 0.2$ In-line	$\theta = 45^\circ$	$f/f_0 = \begin{cases} 0.490Re^{0.404}, & Re \leq 1800 \\ 10.066, & Re > 1800 \end{cases}$	(6.26)
$d/p = 0.1$ In-line	$\theta = 90^\circ$	$f/f_0 = \begin{cases} 0.1131Re^{0.561}, & Re \leq 1800 \\ 8.266, & Re > 1800 \end{cases}$	(6.27)
$d/p = 0.1$ In-line	$\theta = 45^\circ$	$f/f_0 = \begin{cases} 0.222Re^{0.441}, & Re \leq 1800 \\ 5.968, & Re > 1800 \end{cases}$	(6.28)
$d/p = 0.05$ Staggered	$\theta = 90^\circ$	$f/f_0 = \begin{cases} 0.228Re^{0.478}, & Re \leq 1800 \\ 8.732, & Re > 1800 \end{cases}$	(6.29)
$d/p = 0.05$ Staggered	$\theta = 45^\circ$	$f/f_0 = \begin{cases} 0.283Re^{0.396}, & Re \leq 1800 \\ 5.159, & Re > 1800 \end{cases}$	(6.30)
$d/p = 0.025$ Staggered	$\theta = 90^\circ$	$f/f_0 = \begin{cases} 0.1327Re^{0.4835}, & Re \leq 1800 \\ 4.550, & Re > 1800 \end{cases}$	(6.31)
$d/p = 0.025$	$\theta = 45^\circ$		

Staggered

$$f/f_0 = \begin{cases} 0.109Re^{0.454}, & Re \leq 1800 \\ 2.896, & Re > 1800 \end{cases} \quad (6.32)$$

The f/f_0 correlation equations are compared to the experimental values in Figure 6.22 and the error is between $\pm 10\%$.

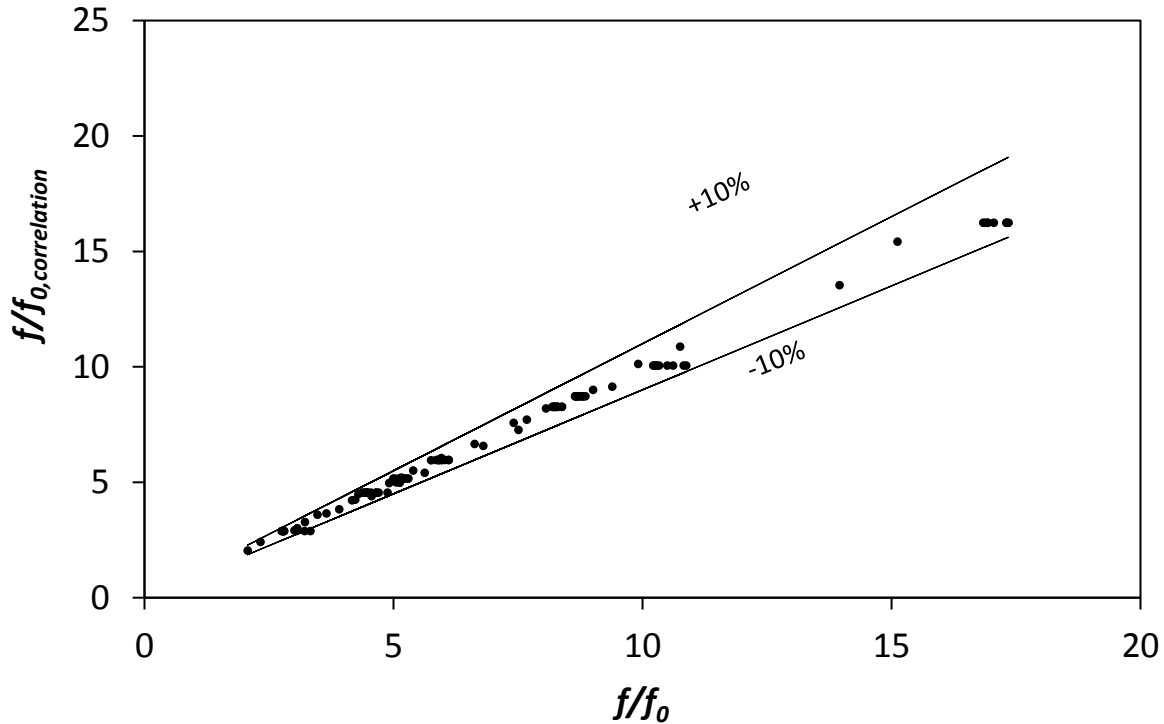


Figure 6.22: Comparison between friction factor ratio and correlations, including all the correlations from Equation (6.25) to (6.32).

6.7. Thermal performance

Equation (3.14) shows how the thermal performance coefficient is defined. It is the Nusselt number ratio of the cylindrical cross-bar channel to the smooth channel divided by the friction factor ratio to the power $1/3$. If the thermal performance coefficient is equal to one, there is no performance advantage between using a modified channel to a smooth channel with worse performance if $\eta < 1$ and increased performance if $\eta > 1$.

$$\eta = \frac{\frac{Nu}{Nu_0}}{\left(\frac{f}{f_0}\right)^{\frac{1}{3}}} \quad (3.14)$$

Figure 6.23 and Figure 6.24 shows the thermal performance coefficient at $\theta = 90^\circ$ and $\theta = 45^\circ$ respectively plotted versus Reynolds number for the tested flow-rate variations. There is a general increase in the thermal performance coefficient with an increase in flow rate, up to $Re = 3000$ for all the cases of d/p ratio and cylinder orientation θ . For flow-rates larger than $Re = 3000$, the thermal performance coefficients decrease steadily with an increase in the Reynolds number. The thermal performance coefficient for the Eiamsa-ard and Promvonge [52] triangular-rib and triangular-groove combination with a pitch ratio of 6.6 is shown in Figure 6.23. The peak of their data at $Re = 3000$ is smaller than for the turbulators tested in this study at the corresponding Re .

The smaller d/p ratios tend to have larger thermal performance coefficients for both $\theta = 90^\circ$ and $\theta = 45^\circ$ but do not show clear trends as with the other tested parameters such as average Nusselt numbers, friction factors, and Nusselt number and friction factor ratios.

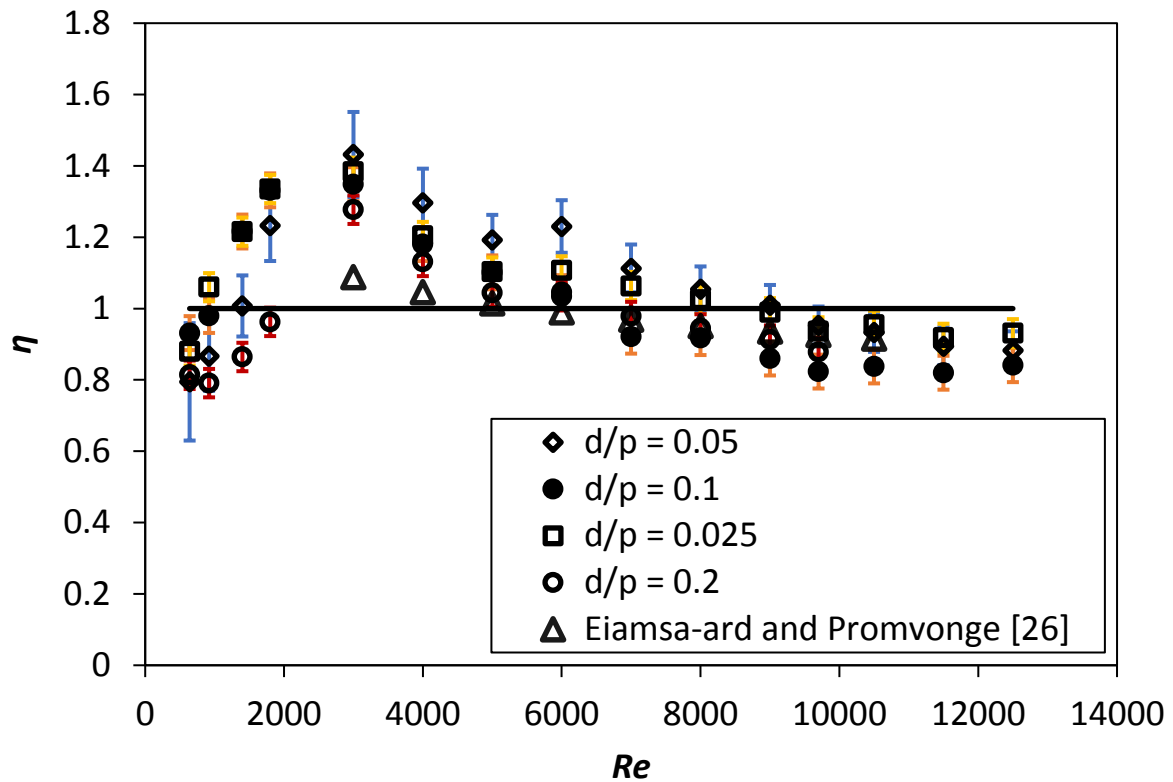


Figure 6.23: Thermal performance plotted against Reynolds number for with cylindrical arrays with $\theta = 90^\circ$ and the Eiamsa-ard and Promvong [52] data for TR and TG, PR = 6.6.

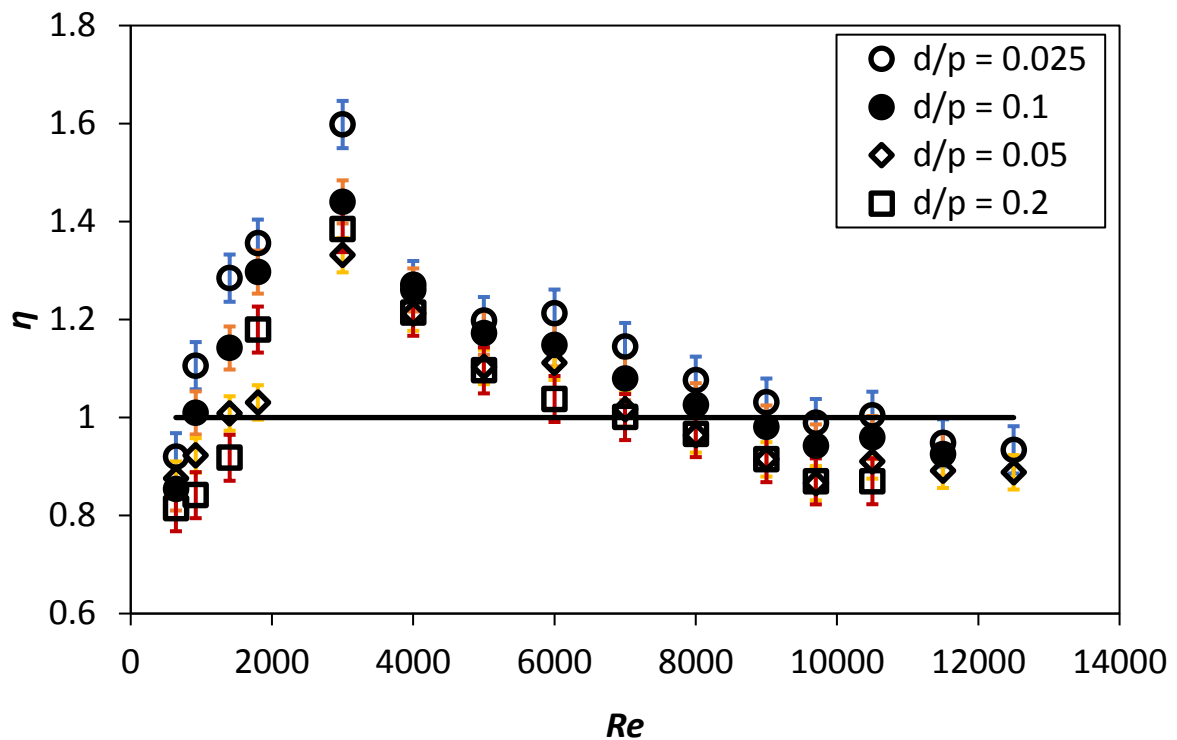


Figure 6.24: Thermal performance plotted against Reynolds number for with cylindrical arrays with $\theta = 45^\circ$.

The correlation power functions are shown in Table 6.5 as a function of the Reynolds number. For Reynolds numbers smaller than or equal to 1 800 the power function correlations are positive and negative for Reynolds numbers larger than 1 800. Power functions were used because it fits the shape of the data well shown in Figure 6.23 and Figure 6.24 for $\theta = 90^\circ$ and $\theta = 45^\circ$ respectively.

Table 6.5: Correlation power functions for thermal performance coefficients, η .

$d/p = 0.2$ In-line	$\theta = 90^\circ$	$\eta = \begin{cases} 0.275Re^{0.162}, & Re \leq 1800 \\ 13.222Re^{-0.294}, & Re > 1800 \end{cases}$	(6.33)
$d/p = 0.2$ In-line	$\theta = 45^\circ$	$\eta = \begin{cases} 0.0954Re^{0.325}, & Re \leq 1800 \\ 24.93Re^{-0.364}, & Re > 1800 \end{cases}$	(6.34)
$d/p = 0.1$ In-line	$\theta = 90^\circ$	$\eta = \begin{cases} 0.0848Re^{0.366}, & Re \leq 1800 \\ 23.753Re^{-0.361}, & Re > 1800 \end{cases}$	(6.35)
$d/p = 0.1$ In-line	$\theta = 45^\circ$	$\eta = \begin{cases} 0.070Re^{0.388}, & Re \leq 1800 \\ 18.656Re^{-0.323}, & Re > 1800 \end{cases}$	(6.36)
$d/p = 0.05$ Staggered	$\theta = 90^\circ$	$\eta = \begin{cases} 0.055Re^{0.4082}, & Re \leq 1800 \\ 23.306Re^{-0.346}, & Re > 1800 \end{cases}$	(6.37)
$d/p = 0.05$ Staggered	$\theta = 45^\circ$	$\eta = \begin{cases} 0.299Re^{0.166}, & Re \leq 1800 \\ 15.246Re^{-0.306}, & Re > 1800 \end{cases}$	(6.38)
$d/p = 0.025$ Staggered	$\theta = 90^\circ$	$\eta = \begin{cases} 0.070Re^{0.394}, & Re \leq 1800 \\ 11.518Re^{-0.270}, & Re > 1800 \end{cases}$	(6.39)
$d/p = 0.025$ Staggered	$\theta = 45^\circ$	$\eta = \begin{cases} 0.083Re^{0.376}, & Re \leq 1800 \\ 22.053Re^{-0.336}, & Re > 1800 \end{cases}$	(6.40)

The η correlation equations are compared to the experimental values in Figure 6.25 and the error is between $\pm 10\%$.

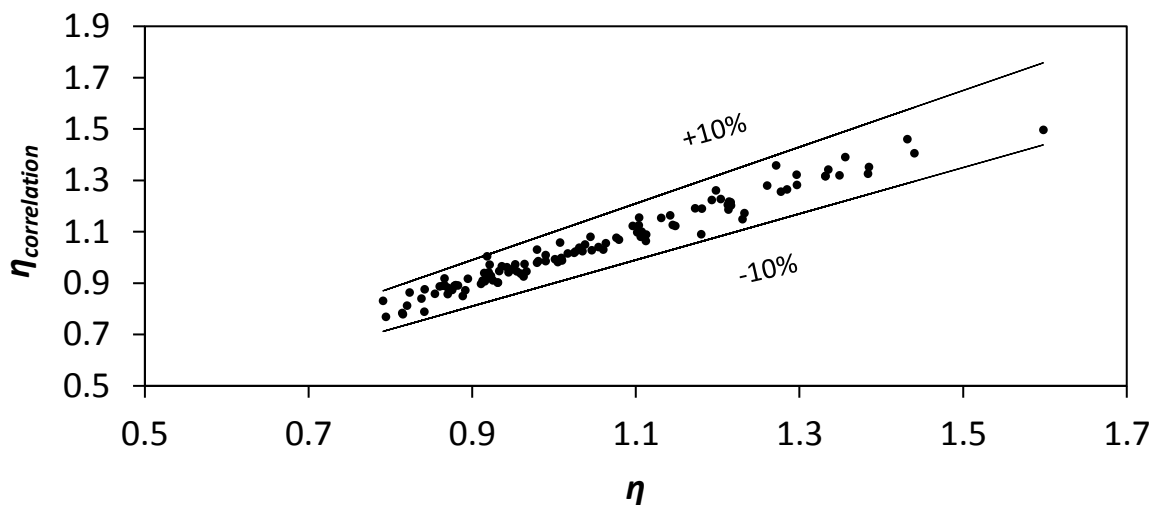


Figure 6.25: Comparison between friction factor ratio and correlations, including all the correlations from Equation (6.33) to (6.40).

6.8. Summary and conclusions

The local Nusselt number becomes fully developed after a certain entry length, after which the average Nusselt number is found by using the integral average over the length of the remainder of the test section. The average Nusselt numbers increase with an increase in Reynolds number for all the cylindrical cross-bar configurations. Average Nusselt numbers for $\theta = 90^\circ$ are larger than at $\theta = 45^\circ$ at the same d/p ratio and Reynolds number, where the largest average Nusselt number is 66.3, for the largest d/p ratio of 0.2 with $\theta = 90^\circ$ at the largest tested Reynolds number of 9 700, for this cylindrical cross-bar configuration. The smallest average Nusselt number was 8.7, for the smallest d/p ratio of 0.025 with $\theta = 45^\circ$, at the lowest tested Reynolds number of 640. The average Nusselt number ratios of the turbulated channels to that of the smooth channel are the largest at a Reynolds number of 3 000 for all the cylindrical cross-bar configurations. It follows the same trends as with the average Nusselt numbers, where the ratios are the larger for larger d/p ratios and for the cases where $\theta = 90^\circ$ compared to $\theta = 45^\circ$, where the largest ratio is 3.3, for $d/p = 0.2$, $\theta = 90^\circ$, at $Re = 3\ 000$. The smallest Nusselt number ratio was 1.1, found at $d/p = 0.025$, $\theta = 45^\circ$, $Re = 640$.

The friction factors decreased with an increase in Reynolds number until it reached an asymptote where it remained constant with an increase in Reynolds number. This means that the pressure-drop increased quadratically with an increase in velocity because of the way that friction factor is defined, with the slope of the pressure drop in the numerator and the square of the velocity in the denominator. The largest friction factor was 0.3, for the largest d/p ratio of 0.2, with $\theta = 90^\circ$ at $Re = 640$, and the smallest friction factor was 0.02 for $d/p = 0.025$, $\theta = 45^\circ$ at a Reynolds number of 12 500. The friction factor ratio of the turbulated channels to that of the smooth channel increases as the Reynolds number increases until the numerator and the denominator becomes constant with an increase in Reynolds number, where the friction factor ratio reaches an asymptote. The largest friction factor ratio is 16.7, for the cross-bar configuration $d/p = 0.2$, $\theta = 90^\circ$, at a Reynolds number of 9 700, with the smallest friction factor ratio equal to 2.1, for $d/p = 0.025$, $\theta = 45^\circ$, at a Reynolds number of 640.

The thermal performance coefficient increases with an increase in Reynolds number from 640 to 3 000, after which it decreases until approximately a Reynolds number of 10 500, where it seems to reach an asymptote, for all the cylindrical cross-bar configurations. The largest thermal performance coefficient is 1.6, for $d/p = 0.025$, $\theta = 45^\circ$, at $Re = 3\ 000$. The flow regime where the turbulator with the best performance $d/p = 0.025$, $\theta = 45^\circ$ could be used in a heat exchanger is between $Re = 920$ and $Re = 9\ 000$ where the thermal performance was larger than one. The largest thermal performance coefficients were for the staggered cylinders with the smaller, 1mm diameters, in both the $\theta = 45^\circ$ and $\theta = 90^\circ$ cases. For the smaller diameter cylinders in staggered arrays, the friction factors were much smaller with comparable Nusselt numbers to the in-line arrays with larger cylinders explaining their larger thermal performance coefficients. The lowest thermal performance coefficient is 0.79, for $d/p = 0.05$, $\theta = 90^\circ$, at $Re = 640$. There is a general increase in thermal performance coefficient with a decrease in d/p ratio when the in-line cylindrical cross-bar configurations, which has larger cylinder diameters, are considered and is larger for $\theta = 45^\circ$ than for $\theta = 90^\circ$. This shows that the pressure penalty has a larger influence on the thermal performance coefficient than the heat transfer augmentation caused by the addition of the bluff bodies in the channel flow. For the smaller cylinder diameter, staggered configurations, the $\theta = 45^\circ$ outperforms the $\theta = 90^\circ$ configurations with the same d/p ratio. The thermal performance data followed the same form of trends with an increase in Reynolds number as [26-30].

7. Summary, Conclusion and Recommendations

7.1. Summary

Heat exchangers are used in a wide variety of applications in different fields in the engineering industry, including HVAC, solar air heaters, fossil fuel power stations, nuclear power, oil refineries, vehicle cooling systems, and chemical plants. The optimization of heat exchangers is critical to realize a reduction in operating costs and sizing while increasing the effectiveness and efficiency of heat exchangers. By promoting turbulence in channel flow, heat transfer can be increased. This can be done by adding bluff bodies in the channel flow, adding steps or grooves on the channel walls, or using fin pins. Increasing the pressure drop penalty is a result of using these methods, causing the necessary pumping power to increase to maintain a similar flow rate in comparison to a smooth channel. The purpose of this study was to find the heat transfer and pressure drop characteristics of a rectangular channel with arrays of circular cylindrical cross-bars.

An experimental setup used in previous studies was modified, updated, and validated to accommodate for the current study. The test section was built from polycarbonate plates and had a length of 500 mm, channel thickness of 203 mm, and channel height of 5 mm. Orifice plates were used to determine the mass flow rates through the test section and were converted to Reynolds numbers. Heat transfer and pressure drop tests were done for eight different circular cylindrical cross-bar arrays at 15 different Reynolds numbers, in the range of 640 to 12 500. Eight different cross-bar configurations were tested: the cylinder diameter to pitch ratios were, $d/p = 0.025$, $d/p = 0.05$, $d/p = 0.1$ and $d/p = 0.2$, and the angle to the flow direction, was $\theta = 90^\circ$ and $\theta = 45^\circ$ for each of the four different diameter-to-pitch ratios. Thermocouples were spaced 5 mm apart on the centerline of the channel wall for the first third of the test section, 10 mm for the second third, and then 5 mm again for the last third of the test section for the heat transfer tests. Heat loss was estimated using the thermal conduction equation by measuring the temperature difference across the insulation at eight different locations on the top wall and taking the integral average. The pressure taps were spaced 15 mm apart on the centerline of the channel wall for the pressure drop tests.

Transient CFD simulations were done using Ansys fluent for $d/p = 0.05$ and $d/p = 0.2$, for $\theta = 90^\circ$, at Reynolds numbers of 920 and 9 700, to analyze the secondary flow structures in the wake of the cylinders, partly responsible for the heat transfer and pressure drop increase in the channel flow with regards to the smooth channel. The $k-\Omega$ shear stress transport (SST) model was used for the simulations. An inlet velocity profile boundary condition was used where the velocity profile of a long plane channel simulation outlet velocity profile was exported. To estimate mesh-size dependence, the channel velocity two-cylinder diameters downstream from the fifth cylinder in the center of the channel was used as a comparison between mesh sizes in steady-state simulations, increasing the number of mesh elements by half the number of elements used in the previous simulation until the change in the dimensionless velocity was less than 0.01. The temporal discretization dependence was estimated using the time step averaged velocity at the same position as for the mesh size convergence study. The simulations were also verified against the experimental setup by using pressure profiles around the cylinders, where 5 mm and 10 mm tubes were used instead of 1 mm and 2 mm, and high-resolution wall pressure tests.

An uncertainty analysis was done to estimate the uncertainty in the calculation of the average flow velocities, mass flow rates, Reynolds numbers, friction factors, and Nusselt numbers. The uncertainties generally decreased with an increase in Reynolds number. A repeatability study was also done to confirm that the repeated data falls between the uncertainty estimates, which was the case during this study

7.2. Conclusion

After qualifying the experimental method against literature for the smooth channel friction factors and Nusselt numbers, pressure tests were done. The hydraulic entry length was estimated, by using the data plots of the local pressures, as a quarter of the test section length for the $d/p = 0.1$ and $d/p = 0.2$ cross-bars and half of the length of the test section for $d/p = 0.05$ and $d/p = 0.025$. The pressure drop gradient was found from the test data for the hydraulically developed part of the test section to calculate the friction factors. With an increase in Reynolds number, the friction factors decreased until reaching an asymptotic value for all the cross-bar configurations. It is because the pressure gradient and average flow velocity squared start to increase at the same rate beyond a certain Reynolds number. For $\theta = 90^\circ$ the friction factors were larger than for $\theta = 45^\circ$ for the same d/p ratio and Reynolds number. With an increase in d/p , the friction factors increased. The largest measured friction factor was $f = 0.3$, for configuration $d/p = 0.2$, $\theta = 90^\circ$, at $Re = 640$ and the smallest measured friction factor $f = 0.02$, for $d/p = 0.025$, $\theta = 45^\circ$, at $Re = 12\,500$. The friction factor ratio was then used to quantify the pressure penalty for using cylindrical cross-bars in the channel flow to enhance heat transfer. The maximum friction factor ratio, $f/f_0 = 16.7$ occurred at $Re = 9\,700$, for $d/p = 0.2$, $\theta = 90^\circ$ and the minimum friction factor ratio, $f/f_0 = 2.1$, at $Re = 640$, for $d/p = 0.025$, $\theta = 45^\circ$.

For the heat transfer tests, the comparison between the local wall temperature and the local mean air temperature was used to determine the thermal entry length. After the thermal entry region, the local wall temperature and local mean air temperature increase with the same gradient. The average Nusselt numbers were then calculated using the spatial integral average of the local Nusselt numbers. With an increase in the Reynolds number, there was an increase in the average Nusselt number for all the cylindrical cross-bar configurations. For larger d/p ratios and $\theta = 90^\circ$ cases, the average Nusselt numbers were larger than for smaller d/p ratios and $\theta = 45^\circ$. The largest average Nusselt number was $Nu_{avg} = 66.3$, at $Re = 9\,700$ for $d/p = 0.2$, $\theta = 90^\circ$ and the smallest average Nusselt number, $Nu_{avg} = 8.7$, at $Re = 640$ for $d/p = 0.025$, $\theta = 45^\circ$. The Nusselt number ratio could then be used to quantify the heat transfer enhancement of the cylindrical cross-bar channel to that of the smooth channel, where the largest Nusselt number ratio was, $Nu_{avg}/Nu_{0,avg} = 3.3$, for $d/p = 0.2$, $\theta = 90^\circ$, at $Re = 3\,000$ and the smallest $Nu_{avg}/Nu_{0,avg} = 1.1$, for $d/p = 0.025$, $\theta = 45^\circ$, at $Re = 640$.

The CFD results concluded that the pressure drop increase and heat transfer enhancement were caused by the flow acceleration, flow separation, eddy formation, vorticity increase, and boundary layer deformation next to and behind the cylinders. The Strouhal number for the larger d/p ratios suggested that the unsteadiness in the flow is higher for the cylinder arrays with a larger diameter, increasing both the heat transfer enhancement and friction factor in comparison with the smaller diameter cylinder arrays

Finally, the thermal performance coefficients could be calculated by using the friction factor ratios and Nusselt number ratios. The thermal performance coefficient combines the effects of the heat transfer and pressure penalty increase. The thermal performance coefficients increased from $Re = 640$ until $Re = 3\,000$ after which it decreased with an increase in Reynolds number. This is because the pressure penalty starts to outweigh the heat transfer increase caused by the turbulators. The largest thermal

performance coefficient was $\eta = 1.6$, for $d/p = 0.025$, $\theta = 45^\circ$, at $Re = 3\ 000$, and the lowest, $\eta = 0.79$, for $d/p = 0.05$, $\theta = 90^\circ$, at $Re = 640$.

7.3. Recommendations

The following recommendations are suggested:

- Test circular cylindrical cross-bars with different angles to the flow direction.
- Use smaller d/p ratios, regarding that the smallest d/p ratio had the largest thermal performance coefficient.
- Do 3D simulations for arrays that are not 90° to the flow direction.
- Use a larger blower to be able to test large d/p ratios at larger Reynolds numbers, $Re = 9\ 700$ was the largest achievable Reynolds number for $d/p = 0.2$, $\theta = 90^\circ$.

References

- [1] R. Webb and E. Eckert, "Application of Rough Surfaces to Heat Exchanger Design," *Int. J. Heat Mass Transfer.*, vol. 15, pp. 1647-1658.
- [2] W. J.M. and W. Tao, "Numerical study on laminar convection heat transfer in a rectangular channel with longitudinal vortex generator. Part A: Verification of field synergy principle," *International Journal of Heat and Mass Transfer*, vol. 51, no. 5-6, pp. 1179-1191, 2008.
- [3] F. M. White, *Fluid Mechanics*, University of Rhode Island: McGraw-Hill, 2011.
- [4] W. Rohsenow, J. Hartnett and Y. Cho, *Handbook of heat transfer*, McGraw-Hill, 1998.
- [5] S. A. Orszag, "Accurate solution of the Orr–Sommerfeld stability equation," *Journal of Fluid Mechanics*, vol. 50, no. 4, pp. 689-703, 1971.
- [6] P. M. Worsøe-Schmidt, "Heat transfer in the thermal entrance region of circular tubes and annular passages with fully developed laminar flow," *Int. J. Heat Mass Transfer*, no. 10, pp. 541-551, 1967.
- [7] R. K. Shah, "Thermal entry length solutions for the circular tube and parallel plates," in *Process National Heat Mass Transfer Conf, 3rd, Indian Institute of Technology, Bombay*, 1975.
- [8] F. W. Schmidt, "Personal communication," Mechanical Engineering Department, Pennsylvania, 1971.
- [9] S. M. Marco and L. S. Han, "A note on limiting laminar Nusselt number in ducts with constant temperature gradient by analogy to thin-plate theory," *ASME*, no. 77, pp. 625-630, 1955.
- [10] W. M. Rohsenow and H. Y. Choi, *Heat, Mass and Momentum Transfer*, Prentice Hall, Englewood Cliffs, New Jersey, 1961.
- [11] P. A. McCuen, W. M. Kays and W. C. Reynolds, "Heat Transfer with Laminar and Turbulent Flow between Parallel Planes with Constant and Variable Wall Temperature and Heat Flux," Department of Mechanical Engineering, Stanford University, Stanford, California, 1962.
- [12] A. L. R.K. Shah, *Laminar flow forced convection in ducts*, New York, San Francisco, London: Academic press, 1978, p. 205.
- [13] M. A. Tirunarayanan and A. Ramachandran, "Correlation of isothermal pressure drop in rectangular ducts," in *Proc. Australas. Conference of Hydraulics Fluid Mechanics, 2nd, University of Auckland*, Auckland, 1965.
- [14] R. R. Rothfus, R. I. Kermode and J. H. Hackworth, "Pressure drop in rectangular ducts," *Chemical Engineering*, no. 71, pp. 175-176, 7 December 1964.
- [15] V. Gnielinski, "New equations for heat and mass transfer in turbulent pipe and channel flow," *International Chemical Engineering*, no. 16, pp. 359-368, 1976.

- [16] B. H. "Forschungsarbeiten auf dem Gebiete des Ingenieursens," p. 131, 1913.
- [17] B. S. Massey, "Mechanics of Fluids," 8th ed., Taylor & Francis, 2006.
- [18] Y. Taitel and A. E. Dukler, "A model for predicting flow regime transition in horizontal and near horizontal gas-liquid flow," *AIChE J*, vol. 22, pp. 47-55, 1976.
- [19] T. H. Chilton and A. P. Colburn, "Mass transfer coefficients prediction from data on heat transfer and fluid friction," *Industrial & engineering chemistry*, no. 26, pp. 1183-1187, 1934.
- [20] A. P. Colburn, "A method of correlating forced convection heat-transfer data and a comparison with fluid friction," *International Journal of Heat and Mass Transfer*, no. 7, pp. 1359-1384, 1964.
- [21] F. Dittus and L. Boelter, "Publications on Engineering," *University of California at Berkley*, no. 2, p. 443, 1930.
- [22] Y. A. Cengel and A. J. Ghajar, *Heat and Mass Transfer Fundamentals and Applications*, 4th ed.
- [23] J. Nikuradse, "Stromungsgesetze in rauhen rohren," *VDI-Forschungsheft*, no. 361, 1950.
- [24] B. S. Petukhov, "Advances in Heat Transfer," *Academic Press*, vol. 6, pp. 503-504, 1970.
- [25] W. M. Kays and M. E. Crawford, *Convective heat and mass transfer*, 3rd ed., McGraw-Hill, 1987, p. 250.
- [26] X. Li, G. Xie, J. Liu and B. Sunden, "Parametric study on flow characteristics and heat transfer in rectangular channels with strip slits in ribs on one wall," *International Journal of Heat and Mass Transfer*, vol. 149, 2020.
- [27] D. Zheng, X. Wang and Q. Yuan, "The flow and heat transfer characteristics in a rectangular channel with convergent and divergent slit ribs," *International Journal of Heat and Mass Transfer*, vol. 141, pp. 464-475, 2019.
- [28] M. Sahu, K. Pandey and S. Chatterjee, "Thermo-hydraulic performance of rectangular channel roughened with combined semi-circular and triangular ribs," *Heat and Mass Transfer*, vol. 55, 2019.
- [29] S. Skullong, P. Promvong, C. Thianpong, N. Jayranaiwachira and M. Pimsarn, "Heat transfer augmentation in a solar air heater channel with combined winglets and wavy grooves on absorber plate," *Applied Thermal Engineering*, vol. 122, pp. 268-284, 2017.
- [30] Z. Brodniaska, "Experimental investigation of convective heat transfer between corrugated heated surfaces of rectangular channel," *Heat and Mass Transfer*, vol. 55, p. 3151-3164, 2019.
- [31] W. Rena, Y. Chen, X. Muc, B. Khoo, F. Zhang and Y. Xu, "Heat transfer enhancement and drag reduction in transverse groove-bounded microchannels with offset," *International Journal of Thermal Sciences*, vol. 130, pp. 240-255, 2018.
- [32] N. Eren and S. Caliskan, "Effect of grooved pin-fins in a rectangular channel on heat transfer augmentation and friction factor using Taguchi method," *International Journal of Heat and Mass Transfer*, vol. 102, pp. 1108-1122, 2016.

- [33] Y.-C. H. Y.-C. H. C.-F. H.-S. H. Y.-C. H. Y.-C. H. C.-F. H. Shou-Shing Hsieh, "Hsieh, Shou-Shing; Hsieh, Yu-Cheng; Hsu, Ya-Chiao; Huang, Ching-Feng," *International Communications in Heat and Mass Transfer*, vol. 112, 2020.
- [34] H. Xie, B. Yang and S. S. M. Zhang, "Research on the mechanism of heat transfer enhancement in microchannel heat sinks with micropin fins," *International journal of energy research*, 2019.
- [35] K. Nanan, N. Piriyaungrod, C. Thianpong, K. Wongcharee and S. Eiamsa-ard, "Numerical and experimental investigations of heat transfer enhancement in circular tubes with transverse twisted-baffles," *Heat Mass Transfer*, vol. 52, pp. 2177-2192, 2016.
- [36] S. EIAMSA-ARD, K. NANAN, K. WONGCHAREE, K. YONGSIRI and C. THIANPONG, "Thermohydraulic Performance of Heat Exchanger Tube Equipped with Single-, Double-, and Triple-Helical Twisted Tapes," *Chemical Engineering Communications*, vol. 202, pp. 606-615, 2015.
- [37] M. G. Jehad, H. E. Ahmed, O. T. Fadhil and A. Kherbeet, "Optimal hydrothermal design of internal flow pipe with insertion of straight and helical metal foam fins," *Heat Transfer*, vol. 49, pp. 3134-3160, 2020.
- [38] A. S. R. Suri, A. Kumar and R. Maithani, "Experimental investigation of heat transfer and fluid flow behaviour in multiple square perforated twisted tape with square wing inserts heat exchanger tube," *Heat and Mass Transfer*, vol. 54, pp. 1813-1826, 2018.
- [39] A. Kumar and A. Layek, "Nusselt number-friction characteristic for a twisted rib roughened rectangular duct using liquid crystal thermography," *Experimental Thermal and Fluid Science*, vol. 97, pp. 205-217, 2018.
- [40] H. Ranjan, A. K. Bharti, M. S. Emani, J. P. Meyer and S. K. Saha, "New combined heat transfer enhancement techniques used in laminar flow through non-circular ducts," *Applied Thermal Engineering*, vol. 163, 2019.
- [41] S. Leonardi, P. Orlandi, L. Djenidi and R. Antonie, "Heat transfer in a turbulent channel flow with square bars or circular rods on one wall," *J. Fluid Mech.*, vol. 776, pp. 512-530, 2015.
- [42] L. B. Vujisic, "Heat transfer at transition to turbulence in channel flows with eddy promoters," Massachusetts Institute of Technology, Massachusetts, 1994.
- [43] F. Menter, "Two-Equation Eddy-Viscosity Turbulence Models for Engineering Applications," *AIAA Journal*, vol. 32, no. 8, pp. 1598-1605, 1994.
- [44] D. Apsley and M. Leschziner, "Advanced turbulence modelling of separated flow in a diffuser," *Flow, Turbulence and Combustions*, vol. 63, pp. 81-112, 2000.
- [45] C. Rumsey, "Turbulence modelling resource," NASA Langley Research Centre.
- [46] M. Fiebig, A. Valencia and N. Mitra, "Local heat transfer and flow losses in fin-and-tube heat exchangers with vortex generators: A comparison of round and flat tubes.," *Experimental Thermal Fluid Science*, vol. 8, pp. 35-45, 1994.

- [47] B. Lotfi, B. Sundén and Q. Wang, "An investigation of the thermo-hydraulic performance of the smooth wavy fin-and-elliptical tube heat exchangers utilizing new type vortex generators," *Appl Energ*, vol. 162, pp. 1282-1302, 2016.
- [48] A. Sinha, H. Chattopadhyay, A. Iyengar and G. Biswas, "Enhancement of heat transfer in a fin-tube heat exchanger using rectangular winglet type vortex generators," *International journal of heat and mass transfer*, vol. 101, pp. 667-681, 2016.
- [49] P. Pavlaseck, C. J. Elliott, J. Pearce, S. Duris, R. Palencar, M. Koval and G. Machin, "Hysteresis Effects and Strain-Induced Homogeneity Effects in Base Metal Thermocouples," *International Journal of Thermophysics*, no. 36, 2015.
- [50] R. S. Figliola and D. E. Beasley, *Theory and Design for Mechanical Measurements*, 5th ed., Clemson, South Carolina: John Wiley and Sons, Inc, 2011, pp. 161-182.
- [51] P. F. Dunn, *Measurement and Data Analysis for Engineering and Science*, 2nd ed., Boca Raton: CRC Press, 2010.
- [52] S. Eiamsa-ard and P. Promvong, "Thermal characteristics of turbulent rib-grooved channel flows," *International Communications in Heat and Mass Transfer*, vol. 36, pp. 705-711, 2009.
- [53] K. R. Aharwal, C. B. Pawar and A. Chaube, "Heat transfer and fluid flow analysis of artificially roughened ducts having rib and groove roughness," *Heat Mass Transfer*, vol. 50, pp. 835-847, 2014.
- [54] E. W. Lemmon and R. T. Jacobsen, "Viscosity and Thermal Conductivity Equations for Nitrogen, Oxygen, Argon, and Air," *International Journal of Thermophysics*, no. 25, p. 21–69, 2004.
- [55] F. E. Jones, "The Air Density Equation and the Transfer of the Mass Unit," *JOURNAL OF RESEARCH of the Notional Bureau of Standards*, vol. Vol. 83, no. No. 5, 29 June 1978.
- [56] A. C. Scott, A. I. Johns, J. T. R. Watson and A. A. Clifford, "Thermal conductivity of air in the range 312 to 373 K and 0.1 to 24 MPa," *International Journal of Thermophysics*, vol. 2, p. 103–114, 1981.
- [57] International Organization for Standardisation, "Measurement of fluid flow by means of pressure differential devices inserted in circular cross-section conduits running full - Part 1: General principles and requirements," March 2003. [Online]. Available: <https://www.iso.org/standard/28064.html>.
- [58] International Organization for Standardization, "Measurement of fluid flow by means of pressure differential devices inserted in circular cross-section conduits running full - Part 2: Orifice plates," March 2003. [Online]. Available: <https://www.iso.org/standard/30190.html>.
- [59] A. L. R.K. Shah, *Laminar flow forced convection in ducts*, New York, San Francisco, London: Academic press, 1978, p. 182.
- [60] R. K. Shah and A. L. London, "Laminar Flow Forced Convection Heat Transfer and Flow Friction in Straight and Curved Ducts - A Summary of Analytical Solutions," Department of Mechanical Engineering, Stanford University, Stanford, California, 1971.

- [61] S. Alfawari, S. Abdel-Moneim and A. Bodalal, "Experimental investigations of heat transfer enhancement from rectangular duct roughened by hybrid ribs," *International Journal of Thermal Sciences*, vol. 118, pp. 123-138, 2017.
- [62] Q. Wang, M. Zeng, T. Ma, X. Du and J. Yang, "Recent development and application of several high-efficiency surface heat exchangers for energy conversion and utilization," *Appl Energ*, vol. 135, pp. 748-777, 2014.

Appendix A: Finding the Reynolds Number

This chapter describes how the Reynolds numbers were found in the channel flow by using the orifice plates. Two PVC pipes were connected in parallel between the plenum space after the test section and the plenum space at the blower fan, refer to Figure 3.1. The pipe diameters were 2" and 4", fitted with butterfly valves to measure the pressure drop over the orifice plates and convert the pressure drop to a mass flow rate so that the Reynolds numbers could be calculated. Table A.1 shows the properties of the orifice plates used to find the Reynolds number in the test section.

Table A.1: Properties of Orifice Plates

	<i>Pipe inside diameter, D</i>	
	2"	4"
<i>D[mm]</i>	50.8	101.6
<i>d[mm]</i>	15.24	50.6
<i>β[-]</i>	0.3	0.5
<i>l₁[mm]</i>	51	101.6
<i>l₂[mm]</i>	25.5	50.8

The ambient air density was calculated using the ideal gas law, Equation (A. 1). The ambient air pressure and temperature were found using a Kestrel 5500 weather meter. Air was assumed to be incompressible because the maximum velocity in the test section was far from the Mach 1 velocity at the pressure in the test section. The dynamic viscosity of air is found using the ambient temperature and pressure as inputs to the CoolProp library's function in Python.

$$\rho = \frac{P_{amb}}{RT_{amb}} \quad (A. 1)$$

A_1 was the variable used to define the convergence criteria where d is the inside diameter of the orifice plate and β the ratio of d to the tube inside diameter D :

$$A_1 = \frac{\varepsilon d^2 \sqrt{2\Delta P \rho}}{\mu D \sqrt{1 - \beta^4}} \quad (A. 2)$$

With the expansibility factor being one because the flow was estimated to be incompressible:

$$\varepsilon = 1 \quad (A. 3)$$

The convergence criteria were then defined as:

$$\left| \frac{A_1 - \frac{Re_D}{C}}{A_1} \right| < 1 \times 10^{-n} \quad (A. 4)$$

The coefficient of discharge was calculated iteratively until the convergence criteria were met:

$$\begin{aligned}
C = & 0.5961 + 0.0261 \times \beta^2 - 0.216\beta^8 + 0.000521 \left(\frac{10^6 \beta}{Re_D} \right)^{0.7} & (A. 5) \\
& + (0.0188 + 0.0063A)\beta^{3.5} \left(\frac{10^6}{Re_D} \right)^{0.3} \\
& + (0.043 + 0.08e^{-10L_1} - 0.123e^{-7L_1})(1 - 0.11A) \left(\frac{\beta^4}{1 - \beta^4} \right) \\
& - 0.031 * (M'_2 - 0.8M'_2{}^{1.1})\beta^4
\end{aligned}$$

Where the parameters were defined as:

$$A = \left(\frac{19000\beta}{Re_D} \right)^{0.8} \quad (A. 6)$$

$$Re_D = A_1 C \quad (A. 7)$$

$$L1 = l1/D \quad (A. 8)$$

$$L2 = l2/D \quad (A. 9)$$

$$M'_2 = \frac{2L2}{1 - \beta} \quad (A. 10)$$

After the iterative calculation had converged, the mean velocity in the tube could then be calculated to find the mass flow rate in the tube:

$$v_d = \frac{Re_D \mu}{\rho D} \quad (A. 11)$$

$$A_d = \frac{\pi}{4} D^2 \quad (A. 12)$$

$$A_c = WH \quad (A. 13)$$

$$p = 2W + 2H \quad (A. 14)$$

$$D_h = \frac{4A_c}{p} \quad (A. 15)$$

The mass flow rate in the channel is equal to the mass flow rate in the tube:

$$\dot{m}_c = \dot{m}_d \quad (A. 16)$$

Appendix B: Calibration of Thermocouples

B.1. Introduction

The calibration process of the thermocouples is shown in this chapter. The calibration process will be shown in Section B.2 and the uncertainty in Section D.3.

B.2. Calibration process

T-type thermocouples were used with a 32-gauge diameter of constantan and copper wire. The length of the wire was kept to 1 m to eliminate the bulk of the noise. The ends were soldered together using a thermocouple soldering iron. Thermocouples were calibrated using a thermal bath.

A total number of 99 thermocouples were calibrated, 16 thermocouples were used to estimate the heat loss from the test section and 83 were used to find the wall temperature. Data were captured at a rate of 1 Hz at each thermocouple, with 20 data points at each thermal bath temperature in a range of 20-65 °C. The temperature of the thermal bath was raised in smaller increments between 30°C and 40°C because it was anticipated that most of the captured data will lie in this domain with 2°C temperature steps and 5°C temperature steps in the rest of the calibration range.

By plotting the thermal bath temperature against the thermocouple temperature, a linear least-squares regression line could be found to estimate thermocouple temperatures. One of the thermocouple calibration trend lines is shown in Figure B.1.

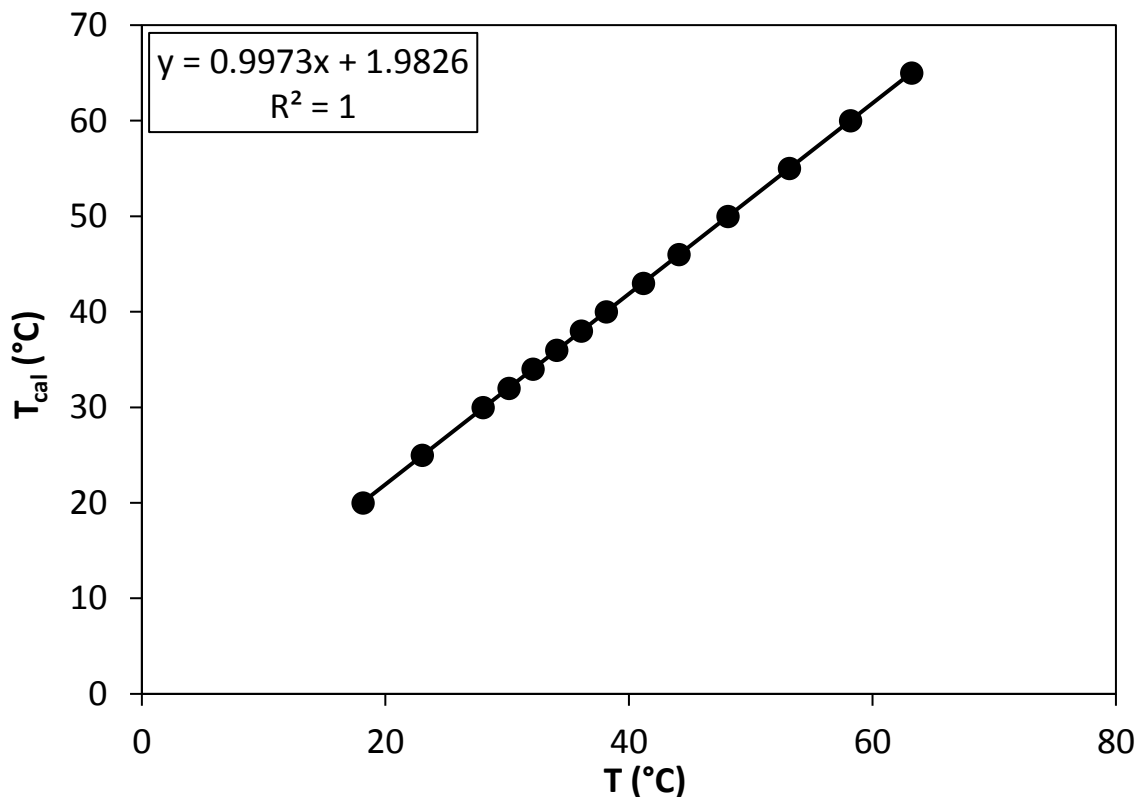


Figure B.1: Thermocouple calibration curve.

Appendix C: Calibration of Pressure Transducers

C.1. Introduction

The calibration of the orifice plate and test section pressure transducers are shown in this chapter. Differential pressure transducers were used for all tests. Transducers with different capacities were used as necessary during tests. Where the pressure drop through the test section was larger, transducers with larger capacities were used. For pressure drop over the orifice plate, larger pressure transducers were used in the 2" tube than the 4" tube because of the larger blockage of the orifice plate used in the 2" tube.

C.2. Calibration procedure

The pressure transducers related to the high- and low-pressure sides to the low-pressure transducer calibration machine with tubes. After the machine was tared, voltage readings were taken at 200 Hz, in increments from 0 Pa to 90% full-scale of the pressure transducer being calibrated. Pressure steps were used inclining from zero to full-scale pressure and three steps declining to test for hysteresis. The pressure-transducer charts could then be plotted with the voltage output on the x-axis and the pressure on the y axis. A linear least-squares regression line was then used to determine the current pressure induced on the instrument. Some of the pressure transducers that were used are 0-5V and the other 0-10V.

C.3. Calibration figures of pressure transducers

Figure C.1 shows the calibration curves of the pressure transducers used to find the pressure drop over the orifice plates. Certain transducers were used for particular Reynolds number ranges.

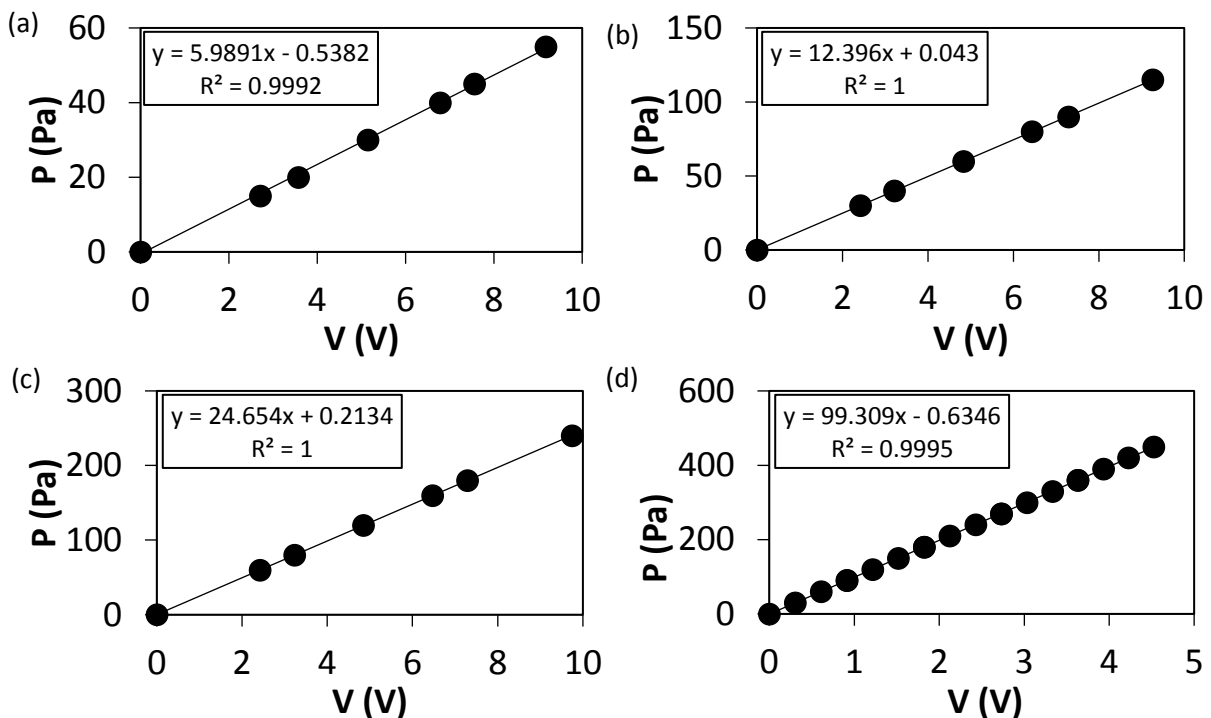


Figure C.1: Orifice pressure transducer calibration curves. (a) $3\,000 \leq Re \leq 7\,000$. (b) $7\,000 < Re \leq 10\,500$. (c) $12\,500 \geq Re$. (d) $Re < 2\,000$.

Figure C.2 shows the calibration graphs used to find the pressure drop in the test section. For larger pressure drops, transducers with a higher-pressure range were used. The pressure drop increases as the Reynolds number increases and is larger for certain turbulator geometries at the same Reynolds number. Therefore, the same transducer couldn't always be used for the same Reynolds number range between the different cylindrical cross-bar arrays. The pressure calibration machine has a maximum applied pressure of 3 750 Pa, so for the largest transducer, only up until half maximum pressure was used for calibration and at larger values, extrapolation had to be used. This is not an issue because the calibration lines are almost exactly linear.

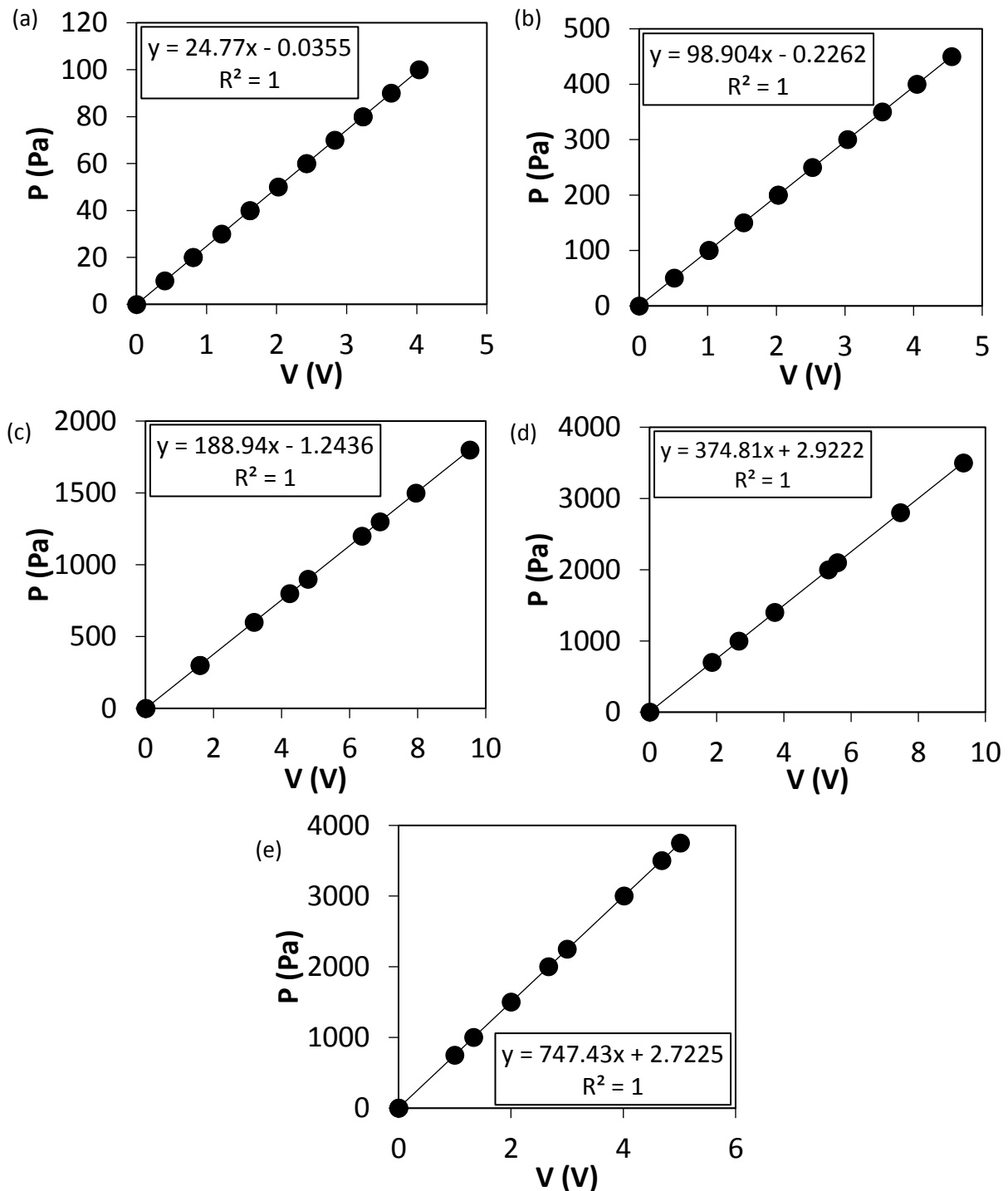


Figure C.2: Channel pressure transducer calibration curves. (a) $0 \leq P \leq 125$. (b) $250 < P \leq 450$. (c) $450 < P < 1\ 875$. (d) $1\ 875 \leq P \leq 3\ 750$. (e) $3\ 750 \leq P \leq 7\ 500$.

Appendix D: Uncertainty Analysis

D.1. Introduction

The method and examples for calculating the uncertainty of Reynolds number, Nusselt number and friction factor will be described in this chapter. The uncertainty of the fluid properties will be shown in Section D.4, with the uncertainty of the test setup geometry in Section D.5 and the bias error of the measuring equipment in Section D.3, after which the uncertainty calculation methods will be shown. Examples for calculated parameter uncertainties will then follow.

D.2. Formulation

The uncertainty error is classified into two types: the bias error and precision error. The bias error is primarily caused by sensor calibration, sensor resolution and erroneous measurement techniques and has a constant value between the measurement mean and true value. The precision error is random relative to the mean with no fixed value and is primarily caused by equipment sensitivity.

$$\delta x = \sqrt{(\delta b)^2 + (\delta p)^2} \quad (D.1)$$

The bias error can directly be estimated through the calibration of a measurement sensor and the precision error through a statistical analysis of the data output from the sensor.

$$x_i = \bar{x} \pm \delta p = \bar{x} \pm t_{v,p} S_x \quad (D.2)$$

Equation (D.2) shows that there is a p% probability that the measured x_i will lie between $\pm t_{v,p} S_x$ of the mean value of the measured variable known as the confidence interval, where S_x and $t_{v,p}$ is the standard deviation and the Student-t distribution variable respectively. The Student-t variable is a function of the number of readings taken $v = N-1$ (degrees of freedom) and the confidence interval p. A 95% confidence interval was used for the uncertainty calculations in this study.

The statistical analysis and precision errors can only be found from directly measured parameters. For the uncertainty of a calculated parameter, δR , it is necessary to allow for the propagation of a measured variable:

$$R = R(x_1, x_2, x_3, \dots, x_n) \quad (D.3)$$

$$\delta R = \left[\left(\frac{\partial R}{\partial x_1} \delta x_1 \right)^2 + \left(\frac{\partial R}{\partial x_2} \delta x_2 \right)^2 + \dots + \left(\frac{\partial R}{\partial x_n} \delta x_n \right)^2 \right]^{1/2} \quad (D.4)$$

Where δx_i are the individual uncertainties of the measured parameters which include the bias and precision error.

D.3. Sensor calibration uncertainty

The bias errors of the thermocouples and pressure transducers are found in this chapter. To estimate the uncertainty of the calibration equations, the following steps were taken:

$$S_{yx} = \left[\frac{\sum_{i=1}^N (y_i - y_{ci})^2}{v} \right]^{1/2} \quad (D.5)$$

Where y_i is the calibration value at sensor output value x_i and y_{ci} is the value taken from the line of best fit shown in Section B.2 and Section C.3 for the thermocouples and the pressure transducers respectively.

$$\delta_x = \left[(t_{v,95} S_x)^2 + (A_{tran})^2 \right]^{1/2} \quad (D.6)$$

With A_{tran} is the transducer accuracy in volts.

$$S_{xi} = \left[\frac{1}{(n-1)} \sum_{i=1}^n (x_i - \bar{x})^2 \right]^{1/2} \quad (D.7)$$

Where n is the number of sample readings taken during the calibration at the sample sensor output value x_i . The standard deviation can then be taken of the standard deviations at each of the individual calibrator operating points used during the calibration process:

$$S_x = \left[\frac{1}{(N-1)} \sum_{i=1}^N S_{xi}^2 \right]^{1/2} \quad (D.8)$$

The precision uncertainty of the pressure transducers' calibration equations with a 95% confidence could then be calculated:

$$\delta_{cal} = \left[(t_{v,95} S_{yx})^2 + (A_{cal})^2 + (a_1 \delta_x)^2 \right]^{1/2} \quad (D.9)$$

Where A_{cal} is the uncertainty of the calibration machine and a_1 is the slope of the calibration equation.

D.4. Fluid properties uncertainty

The uncertainty of the fluid density was calculated as follows:

$$\rho = \frac{P_{amb}}{RT_{amb}} \quad (D.10)$$

$$\delta\rho = \left[\left(\frac{\partial\rho}{\partial P_{amb}} \delta P_{amb} \right)^2 + \left(\frac{\partial\rho}{\partial R} \delta R \right)^2 + \left(\frac{\partial\rho}{\partial T_{amb}} \delta T_{amb} \right)^2 \right]^{1/2}$$

$$\delta\rho = \left[\left(\frac{1}{RT_{amb}} \delta P_{amb} \right)^2 + \left(-\frac{P_{amb}}{R^2 T_{amb}} \delta R \right)^2 + \left(-\frac{P_{amb}}{RT_{amb}^2} \delta T_{amb} \right)^2 \right]^{1/2} \quad (D.11)$$

The uncertainty of the dynamic viscosity is within 5% of the value given by Lemmon and Jacobsen [54] as a function of temperature and pressure and the uncertainty of the ambient pressure was found in the datasheet of the measuring instrument. Jones [55] concluded that the uncertainty in the gas constant of air, R , is ± 0.01 J/kgK and Scott *et al.* [56], that the uncertainty in the thermal conductivity of air is 0.5%. The uncertainty in the values of the fluid properties is shown in Table D.1.

Table D.1: Fluid properties' uncertainty.

Property uncertainty	Error
δP_{amb}	± 0.3 hPa
δR	± 0.01 J/kgK
δT_{amb}	± 0.13 °C
$\delta\rho$	± 0.024 kg/m ³
$\delta\mu$	± 0.05 μ
δk	± 0.005 k
δC_p	± 0.01 C _p

D.5. Test section geometry uncertainty

The uncertainty in the hydraulic diameter was estimated as follows:

$$D_h = \frac{2WH}{(H+W)} \quad (D.12)$$

$$\delta D_h = \left[\left(\frac{\partial D_h}{\partial H} \delta H \right)^2 + \left(\frac{\partial D_h}{\partial W} \delta W \right)^2 \right]^{1/2}$$

$$\delta D_h = \left[\left(\frac{2W(H+W) - 2HW^2}{(H+W)^2} \delta H \right)^2 + \left(\frac{2H(H+W) - 2WH^2}{(H+W)^2} \delta W \right)^2 \right]^{1/2} \quad (D.13)$$

The uncertainty in the cross-sectional area of the test section was approximated as follows:

$$A_c = WH \quad (D.14)$$

$$\delta A_c = \left[\left(\frac{\partial A_c}{\partial H} \delta H \right)^2 + \left(\frac{\partial A_c}{\partial W} \delta W \right)^2 \right]^{1/2}$$

$$\delta A_c = [(W\delta H)^2 + (H\delta W)^2]^{1/2} \quad (D.15)$$

With,

$$\delta H = \delta W = \pm 0.00025 \text{ m} \quad (D.16)$$

D.6. Reynolds number uncertainty

By using the mass flow rate through the orifice plates, the uncertainty in the Reynolds number could be calculated as follows:

$$\dot{m} = \frac{\pi D_2^2 C \sqrt{2\rho \Delta P}}{4\sqrt{1-\beta^4}} \quad (D.17)$$

$$\delta \dot{m} = \left[\left(\frac{\partial \dot{m}}{\partial \rho} \delta \rho \right)^2 + \left(\frac{\partial \dot{m}}{\partial \Delta P} \delta \Delta P \right)^2 + \left(\frac{\partial \dot{m}}{\partial D_2} \delta D_2 \right)^2 \right]^{1/2}$$

$$\delta \dot{m} = \left[\left(\frac{\pi D_2^2 C \sqrt{2\Delta P}}{8\sqrt{\rho(1-\beta^4)}} \delta \rho \right)^2 + \left(\frac{\pi D_2^2 C \sqrt{2\rho}}{8\sqrt{\Delta P(1-\beta^4)}} \delta \Delta P \right)^2 + \left(\frac{\pi D_2 C \sqrt{2\rho}}{2\sqrt{(1-\beta^4)}} \delta D_2 \right)^2 \right]^{1/2} \quad (D.18)$$

Where,

$$\delta\Delta P = [(\delta_{cal})^2 + (a_1\delta_{xi})^2]^{1/2} \quad (D.19)$$

$$v_{ave} = \frac{\dot{m}}{\rho A_c} \quad (D.20)$$

$$\delta v_{ave} = \left[\left(\frac{\partial v_{ave}}{\partial \dot{m}} \delta \dot{m} \right)^2 + \left(\frac{\partial v_{ave}}{\partial \rho} \delta \rho \right)^2 + \left(\frac{\partial v_{ave}}{\partial A_c} \delta A_c \right)^2 \right]^{1/2}$$

$$\delta v_{ave} = \left[\left(\frac{1}{\rho A_c} \delta \dot{m} \right)^2 + \left(-\frac{\dot{m}}{\rho^2 A_c} \delta \rho \right)^2 + \left(-\frac{\dot{m}}{\rho A_c^2} \delta A_c \right)^2 \right]^{1/2} \quad (D.21)$$

With,

$$\delta D_2 = \pm 0.0001 \text{ m} \quad (D.22)$$

$$Re = \frac{\rho v_{ave} D_h}{\mu} \quad (D.23)$$

$$\delta Re = \left[\left(\frac{\partial Re}{\partial \rho} \delta \rho \right)^2 + \left(\frac{\partial Re}{\partial v_{ave}} \delta v_{ave} \right)^2 + \left(\frac{\partial Re}{\partial D_h} \delta D_h \right)^2 + \left(\frac{\partial Re}{\partial \mu} \delta \mu \right)^2 \right]^{1/2}$$

$$\delta Re = \left[\left(\frac{v_{ave} D_h}{\mu} \delta \rho \right)^2 + \left(\frac{\rho D_h}{\mu} \delta v_{ave} \right)^2 + \left(\frac{\rho v_{ave}}{\mu} \delta D_h \right)^2 + \left(-\frac{\rho v_{ave} D_h}{\mu^2} \delta \mu \right)^2 \right]^{1/2} \quad (D.24)$$

D.7. Nusselt number uncertainty

$$Nu = \frac{\dot{q}_{con} D_h}{k(T_{wall} - T_{mx})} \quad (D.25)$$

And,

$$\delta T_{mx} = T_{amb} + \frac{\dot{q}_{con} A(x)}{\dot{m} C_p} \quad (D.26)$$

$$\delta Nu = \left[\left(\frac{\partial Nu}{\partial \dot{q}_{con}} \delta \dot{q}_{con} \right)^2 + \left(\frac{\partial Nu}{\partial D_h} \delta D_h \right)^2 + \left(\frac{\partial Nu}{\partial k} \delta k \right)^2 + \left(\frac{\partial Nu}{\partial T_{wall}} \delta T_{wall} \right)^2 + \left(\frac{\partial Nu}{\partial T_{mx}} \delta T_{mx} \right)^2 \right]^{1/2}$$

$$\delta Nu_x = \left[\left(\frac{D_h}{k(T_{wall} - T_{mx})} \delta \dot{q}_{con} \right)^2 + \left(\frac{\dot{q}_{con}}{k(T_{wall} - T_{mx})} \delta D_h \right)^2 + \left(-\frac{\dot{q}_{con} D_h}{k^2(T_{wall} - T_{mx})} \delta k \right)^2 + \left(-\frac{\dot{q}_{con} D_h}{k(T_{wall} - T_{mx})^2} \delta T_{wall} \right)^2 + \left(\frac{\dot{q}_{con} D_h}{k(T_{wall} - T_{mx})^2} \delta T_{mx} \right)^2 \right]^{1/2} \quad (D.27)$$

$$\delta Nu_x = \frac{1}{x_2 - x_1} \int_{x_1}^{x_2} \delta Nu(x) dx \quad (D.28)$$

Where,

$$\delta T_{mx} = \left[\left(\frac{\partial T_{mx}}{\partial T_{amb}} \delta T_{amb} \right)^2 + \left(\frac{\partial T_{mx}}{\partial \dot{q}_{con}} \delta \dot{q}_{con} \right)^2 + \left(\frac{\partial T_{mx}}{\partial A(x)} \delta A(x) \right)^2 + \left(\frac{\partial T_{mx}}{\partial \dot{m}} \delta \dot{m} \right)^2 + \left(\frac{\partial T_{mx}}{\partial C_p} \delta C_p \right)^2 \right]^{1/2}$$

$$\delta T_{mx} = \left[(\delta T_{amb})^2 + \left(\frac{A(x)}{\dot{m} C_p} \delta \dot{q}_{con} \right)^2 + \left(\frac{\dot{q}_{con}}{\dot{m} C_p} \delta A(x) \right)^2 + \left(-\frac{\dot{q}_{con} A(x)}{\dot{m}^2 C_p} \delta \dot{m} \right)^2 + \left(-\frac{\dot{q}_{con} A(x)}{\dot{m} C_p^2} \delta C_p \right)^2 \right]^{1/2} \quad (D.29)$$

And,

$$\delta \dot{q}_{con} = \left[\left(\frac{\partial \dot{q}_{con}}{\partial \dot{Q}} \delta \dot{Q} \right)^2 + \left(\frac{\partial \dot{q}_{con}}{\partial A} \delta A \right)^2 \right]^{1/2}$$

$$\delta \dot{q}_{con} = \left[\left(\frac{\delta \dot{Q}}{A} \right)^2 + \left(-\frac{\dot{Q}}{A^2} \delta A \right)^2 \right]^{1/2} \quad (D.30)$$

$$\delta \dot{Q} = \left[\left(\frac{\partial \dot{Q}}{\partial V} \delta V \right)^2 + \left(\frac{\partial \dot{Q}}{\partial I} \delta I \right)^2 \right]^{1/2}$$

$$\delta \dot{Q} = [(I \delta V)^2 + (V \delta I)^2]^{1/2} \quad (D.31)$$

$$\delta A = \left[\left(\frac{\partial A}{\partial L} \delta L \right)^2 + \left(\frac{\partial A}{\partial W} \delta W \right)^2 \right]^{1/2}$$

$$\delta A = [(2W \delta L)^2 + (2L \delta W)^2]^{1/2} \quad (D.32)$$

D.8. Friction factor uncertainty

$$f = \frac{D_h \Delta P}{\frac{1}{2} \rho v_{ave}^2} \quad (D.33)$$

$$\delta f = \left[\left(\frac{\partial f}{\partial D_h} \delta D_h \right)^2 + \left(\frac{\partial f}{\partial \Delta P / \Delta x} \delta \Delta P / \Delta x \right)^2 + \left(\frac{\partial f}{\partial \rho} \delta \rho \right)^2 + \left(\frac{\partial f}{\partial v_{ave}} \delta v_{ave} \right)^2 \right]^{1/2}$$

$$\delta f = \left[\left(\frac{\Delta P / \Delta x}{2 \rho v_{ave}^2} \delta D_h \right)^2 + \left(\frac{D_h}{2 \rho v_{ave}^2} \delta \Delta P / \Delta x \right)^2 + \left(-\frac{D_h \Delta P}{2 \rho^2 v_{ave}^2} \delta \rho \right)^2 + \left(-\frac{D_h \Delta P}{\rho v_{ave}^3} \delta v_{ave} \right)^2 \right]^{1/2} \quad (D.34)$$

Where,

$$\delta \Delta P / \Delta x = t_{v,95} S_{\Delta P / \Delta x} \quad (D.35)$$

And,

$$S_{\Delta P / \Delta x} = S_{yx} \left[\frac{N}{N \sum_{i=1}^N x_i^2 - (\sum_{i=1}^N x_i)^2} \right] \quad (D.36)$$

D.9. Thermal performance coefficient uncertainty

$$\eta = \frac{Nu}{\left(\frac{f}{f_0} \right)^{1/3}} \quad (D.37)$$

$$\delta \eta = \left[\left(\frac{\partial \eta}{\partial Nu} \delta Nu \right)^2 + \left(\frac{\partial \eta}{\partial Nu_0} \delta Nu_0 \right)^2 + \left(\frac{\partial \eta}{\partial f} \delta f \right)^2 + \left(\frac{\partial \eta}{\partial f_0} \delta f_0 \right)^2 \right]^{1/2}$$

$$\delta \eta = \left[\left(\frac{1}{\left(\frac{f}{f_0} \right)^{1/3}} \delta Nu \right)^2 + \left(\frac{-Nu}{\left(\frac{f}{f_0} \right)^{1/3}} \delta Nu_0 \right)^2 + \left(\left(-\frac{1}{3} \right) \frac{Nu}{f^{4/3}} \delta f \right)^2 + \left(\left(\frac{1}{3} \right) \frac{Nu}{f^{1/3} f_0^{2/3}} \delta f_0 \right)^2 \right]^{1/2} \quad (D.38)$$

D.10. Sample uncertainty calculation

The calculation of the uncertainty will be shown for Reynolds number, mean Nusselt number and friction factor for cylindrical cross-bar geometry $d/p = 0.05$, $\theta = 90^\circ$ at $Re = 4\ 000$. All the necessary steps are shown, including the calibration and fluid property uncertainties.

D.10.1 Thermocouples

$$S_{yx} = \left[\frac{\sum_{i=1}^N (y_i - y_{ci})^2}{\nu} \right]^{1/2}$$

$$\begin{aligned} \sum_{i=1}^N (y_i - y_{ci})^2 &= (20 - 20.101)^2 + (25 - 24.946)^2 + (30 - 29.932)^2 + (32 - 32.037)^2 \\ &+ (34 - 34.009)^2 + (36 - 35.961)^2 + (38 - 37.976)^2 + (40 - 40.024)^2 \\ &+ (43 - 43.05)^2 + (46 - 45.958)^2 + (50 - 49.969)^2 + (55 - 55.01)^2 \\ &+ (60 - 60.027)^2 + (65 - 65.019)^2 \end{aligned}$$

$$\sum_{i=1}^N (y_i - y_{ci})^2 = 0.0281$$

$$S_{yx} = \left[\frac{0.0281}{12} \right]^{1/2}$$

$$S_{yx} = 0.04836$$

$$S_{xi} = \left[\frac{1}{(n-1)} \sum_{i=1}^n (x_i - \bar{x})^2 \right]^{1/2}$$

$$\begin{aligned} S_{x1} &= \left[\left(\frac{1}{9} \right) \left((18.256 - 18.216)^2 + (18.175 - 18.216)^2 + (18.152 - 18.216)^2 \right. \right. \\ &+ (18.123 - 18.216)^2 + (18.195 - 18.216)^2 + (18.189 - 18.216)^2 \\ &+ (18.251 - 18.216)^2 + (18.279 - 18.216)^2 + (18.270 - 18.216)^2 \\ &\left. \left. + (18.265 - 18.216)^2 \right) \right]^{1/2} \end{aligned}$$

$$S_{x1} = 0.0555$$

$$S_x = \left[\frac{1}{(N-1)} \sum_{i=1}^N S_{xi}^2 \right]^{1/2}$$

$$\begin{aligned} S_x &= \left[\frac{1}{(13)} \left((0.0555)^2 + (0.00695)^2 + (0.00861)^2 + (0.00781)^2 + (0.01270)^2 + (0.0150)^2 \right. \right. \\ &+ (0.01764)^2 + (0.00526)^2 + (0.011109)^2 + (0.01266)^2 + (0.01562)^2 \\ &\left. \left. + (0.006967)^2 + (0.007747)^2 + (0.01543)^2 \right) \right]^{1/2} \end{aligned}$$

$$S_x = 0.01935$$

$$\delta_x = \left[(t_{v,95} S_x)^2 + (A_{tran})^2 \right]^{1/2}$$

$$\delta_x = [((2.16)(0.01935))^2 + (0.02)^2]^{1/2}$$

$$\delta_x = 0.0463$$

$$\delta_{cal} = [(t_{12,95}S_{yx})^2 + (A_{cal})^2 + (a_1\delta_x)^2]^{1/2}$$

$$\delta_{cal} = [(2.179 \times 0.0484)^2 + (0.05)^2 + (0.997 \times 0.0463)^2]^{1/2}$$

$$\delta_{cal} = 0.125 \text{ } ^\circ\text{C}$$

D.10.2 Pressure transducers

$$S_{yx} = \left[\frac{\sum_{i=1}^N (y_i - y_{ci})^2}{v} \right]^{1/2}$$

$$\begin{aligned} \sum_{i=1}^N (y_i - y_{ci})^2 &= (0 - -0.5382)^2 + (5 - 4.71366)^2 + (10 - 10.2677)^2 + (15 - 14.7347)^2 \\ &+ (20 - 20.4360)^2 + (25 - 25.1068)^2 + (30 - 29.8790)^2 + (35 - 34.9513)^2 \\ &+ \dots + (60 - 60.2851)^2 \end{aligned}$$

$$S_{yx} = \left[\frac{0.6852}{12} \right]^{1/2}$$

$$S_{yx} = 0.23896$$

$$S_{xi} = \left[\frac{1}{(n-1)} \sum_{i=1}^n (x_i - \bar{x})^2 \right]^{1/2}$$

$$S_{x1} = \left[\frac{1}{2} [(0.03528 - 0.035637)^2 + (0.03622 - 0.035637)^2 + (0.03541 - 0.035637)^2] \right]^{1/2}$$

$$S_{x1} = 0.000509346$$

$$S_x = \left[\frac{1}{(N-1)} \sum_{i=1}^N S_{xi}^2 \right]^{1/2}$$

$$\begin{aligned} S_x &= \left[\frac{1}{(12)} ((0.000509346)^2 + (0.0136427)^2 + (0.008256284)^2 + (0.000914112)^2 \right. \\ &+ (0.003083137)^2 + (0.005186678)^2 + (0.002437013)^2 + \dots \\ &\left. + (0.00579396)^2 \right]^{1/2} \end{aligned}$$

$$S_x = 0.006525415$$

$$\delta_x = [(t_{v,95}S_x)^2 + (A_{tran})^2]^{1/2}$$

$$\delta_x = [((4.303)(0.006525415))^2 + (0.1)^2]^{1/2}$$

$$\delta_x = 0.10387$$

$$\delta_{cal} = [(t_{12,95}S_{yx})^2 + (A_{cal})^2 + (a_1\delta_x)^2]^{1/2}$$

$$\delta_{cal} = [((2.179)(0.23896))^2 + (0.022)^2 + ((5.9891)(0.10387))^2]$$

$$\delta_{cal} = 0.8115$$

For the maximum transducer capability of 62.5 Pa, the calibration uncertainty is 1.3%.

D.10.3 Fluid density

$$\delta\rho = \left[\left(\frac{1}{RT_{amb}} \delta P_{amb} \right)^2 + \left(-\frac{P_{amb}}{R^2 T_{amb}} \delta R \right)^2 + \left(-\frac{P_{amb}}{RT_{amb}^2} \delta T_{amb} \right)^2 \right]^{1/2}$$

$$\delta\rho = \left[\left(\frac{1}{(287.05)(298.15)} (30) \right)^2 + \left(-\frac{87\,000}{(287.05)^2 (298.15)} (0.01) \right)^2 + \left(-\frac{87\,000}{(287.05)(298.15)^2} (0.13) \right)^2 \right]^{1/2}$$

$$\delta\rho = 0.0005662 \text{ kg/m}^3$$

For air density of 1.0165 kg/m³, the uncertainty is 0.055%.

D.10.4 Hydraulic diameter

$$\delta D_h = \left[\left(\frac{2W(H+W) - 2HW^2}{(H+W)^2} \delta H \right)^2 + \left(\frac{2H(H+W) - 2WH^2}{(H+W)^2} \delta W \right)^2 \right]^{1/2}$$

$$\begin{aligned} \delta D_h &= \left[\left(\frac{2(0.2032)(0.005 + 2032) - 2(0.005)(0.2032)^2}{(H+W)^2} (0.000025) \right)^2 \right. \\ &\quad \left. + \left(\frac{2(0.005)(0.005 + 0.2032) - 2(0.2032)(0.005)^2}{(0.005 + 0.2032)^2} (0.000025) \right)^2 \right]^{1/2} \end{aligned}$$

$$\delta D_h = 0.000048576 \text{ m}$$

For the hydraulic diameter of 0.0097598 m the uncertainty is 0.5%.

D.10.5 Cross-sectional channel area

$$\delta A_c = [(W\delta H)^2 + (H\delta W)^2]^{1/2}$$

$$\delta A_c = [((0.2032)(0.000025))^2 + ((0.005)(0.000025))^2]^{1/2}$$

$$\delta A_c = 0.0000050815 \text{ m}$$

For the channel cross-sectional area of 0.001016 m² the uncertainty is 0.5%.

D.10.6 Mass flow rate

$$\delta \dot{m} = \left[\left(\frac{\pi D_2^2 C \sqrt{2 \Delta P}}{8 \sqrt{\rho(1-\beta^4)}} \delta \rho \right)^2 + \left(\frac{\pi D_2^2 C \sqrt{2 \rho}}{8 \sqrt{\Delta P(1-\beta^4)}} \delta \Delta P \right)^2 + \left(\frac{\pi D_2 C \sqrt{2 \rho \Delta P}}{2 \sqrt{(1-\beta^4)}} \delta D_2 \right)^2 \right]^{1/2}$$

$$\delta \dot{m} = \left[\left(\frac{\pi(0.0508)^2(0.62541)\sqrt{2(17.165)}}{8\sqrt{(1.0165)(1-0.5^4)}}(0.0005662) \right)^2 + \left(\frac{\pi(0.0508)^2(0.62541)\sqrt{2(1.0165)}}{8\sqrt{(17.165)(1-\beta^4)}}\delta(0.89209) \right)^2 + \left(\frac{\pi(0.0508)(0.62541)\sqrt{2(1.0165)(17.165)}}{2\sqrt{(1-\beta^4)}}(0.0001) \right)^2 \right]^{1/2}$$

$$\delta \dot{m} = 0.00020111 \text{ kg/s}$$

For a mass flow rate of 0.0077339 kg/s, the uncertainty is 2.6%.

D.10.7 Flow mean velocity

$$\delta v_{ave} = \left[\left(\frac{1}{\rho A_c} \delta \dot{m} \right)^2 + \left(-\frac{\dot{m}}{\rho^2 A_c} \delta \rho \right)^2 + \left(-\frac{\dot{m}}{\rho A_c^2} \delta A_c \right)^2 \right]^{1/2}$$

$$\delta v_{ave} = \left[\left(\frac{1}{(1.0165)(1.00106)}(0.00020111) \right)^2 + \left(-\frac{0.0077339}{(1.0165)^2(0.001016)}(0.0005662) \right)^2 + \left(-\frac{0.0077339}{(1.0165)(0.001016)^2}(0.0000050815) \right)^2 \right]^{1/2}$$

$$\delta v_{ave} = 0.19834$$

D.10.8 Reynolds number

$$\delta Re = \left[\left(\frac{v_{ave} D_h}{\mu} \delta \rho \right)^2 + \left(\frac{\rho D_h}{\mu} \delta v_{ave} \right)^2 + \left(\frac{\rho v_{ave}}{\mu} \delta D_h \right)^2 + \left(-\frac{\rho v_{ave} D_h}{\mu^2} \delta \mu \right)^2 \right]^{1/2}$$

$$\delta Re = \left[\left(\frac{(7.4882)(0.00976)}{1.856 \times 10^{-5}}(0.0005662) \right)^2 + \left(\frac{(1.0165)(0.00976)}{1.856 \times 10^{-5}}(0.19834) \right)^2 + \left(\frac{(1.0165)(7.4882)}{1.856 \times 10^{-5}}(4.86 \times 10^{-4}) \right)^2 + \left(-\frac{(1.0165)(7.4882)(0.00976)}{(1.856 \times 10^{-5})^2} 9.281 \times 10^{-7} \right)^2 \right]^{1/2}$$

$$\delta Re = 109.97$$

With the Reynolds number of 4 000 that was used, the uncertainty is 2.65%.

D.10.9 Wall heat input

$$\delta \dot{Q} = [(I\delta V)^2 + (V\delta I)^2]^{1/2}$$

$$\delta \dot{Q} = [((4.57)(0.10170))^2 + ((33.9)(0.01))^2]^{1/2}$$

$$\delta \dot{Q} = 0.5749 \text{ W}$$

For the wall heat input of 154.77 W it has a 0.37 % uncertainty.

D.10.10 Heat flux

$$\delta A = [(2W\delta L)^2 + (2L\delta W)^2]^{1/2}$$

$$\delta A = [(2(0.2032)(0.001))^2 + (2(1.2)(0.000025))^2]^{1/2}$$

$$\delta A = 0.00041081 \text{ m}^2$$

$$\delta \dot{q}_{con} = \left[\left(\frac{\delta \dot{Q}}{A} \right)^2 + \left(-\frac{\dot{Q}}{A^2} \delta A \right)^2 \right]^{1/2}$$

$$\delta \dot{q}_{con} = \left[\left(\frac{0.5749}{0.001015} \right)^2 + \left(-\frac{154.77}{0.00041081^2} (0.00041081) \right)^2 \right]^{1/2}$$

$$\delta \dot{q}_{con} = 2.5393 \text{ W/m}^2$$

With a heat flux of 624.32 W/m², the uncertainty is 0.41 %.

D.10.11 Local mean temperature

The sample calculation indicates the uncertainty of the local mean temperature of the air 470 mm downstream from the start of the test section:

$$\delta T_{mx} = \left[(\delta T_{amb})^2 + \left(\frac{A(x)}{\dot{m}C_p} \delta \dot{q}_{con} \right)^2 + \left(\frac{\dot{q}_{con}}{\dot{m}C_p} \delta A(x) \right)^2 + \left(-\frac{\dot{q}_{con}A(x)}{\dot{m}^2C_p} \delta \dot{m} \right)^2 + \left(-\frac{\dot{q}_{con}A(x)}{\dot{m}C_p^2} \delta C_p \right)^2 \right]^{1/2}$$

$$\delta T_{mx} = \left[(0.13)^2 + \left(\frac{0.19082}{(0.0076)(1006.4)} (2.5393) \right)^2 + \left(\frac{624.32}{(0.0076)(1006.4)} (0.00041081) \right)^2 + \left(-\frac{(624.32)(0.19082)}{(0.0076)^2(1006.4)} (0.00020111) \right)^2 + \left(-\frac{(624.32)(0.19082)}{(0.0076)(1006.4)^2} (10.064) \right)^2 \right]^{1/2}$$

$$\delta T_{mx} = 0.45255 \text{ } ^\circ\text{C}$$

D.10.12 Nusselt number

The uncertainty calculation for a downstream distance of 475 mm from the inlet is shown:

$$\delta Nu_x = \left[\left(\frac{D_h}{k(T_{wall} - T_{mx})} \delta \dot{q}_{con} \right)^2 + \left(\frac{\dot{q}_{con}}{k(T_{wall} - T_{mx})} \delta D_h \right)^2 + \left(-\frac{\dot{q}_{con} D_h}{k^2(T_{wall} - T_{mx})} \delta k \right)^2 + \left(-\frac{\dot{q}_{con} D_h}{k(T_{wall} - T_{mx})^2} \delta T_{wall} \right)^2 + \left(\frac{\dot{q}_{con} D_h}{k(T_{wall} - T_{mx})^2} \delta T_{mx} \right)^2 \right]^{1/2}$$

$$\delta Nu_{0.47} = \left[\left(\frac{(0.0097596)}{(0.026783)(53.6 - 46.803)} (2.5393) \right)^2 + \left(\frac{(624.32)}{(0.026783)(53.6 - 46.803)} (0.000048576) \right)^2 + \left(-\frac{(624.32)(0.0097596)}{(0.026783)^2(53.6 - 46.803)} (0.00013392) \right)^2 + \left(-\frac{(624.32)(0.0097596)}{(0.026783)(53.6 - 46.803)^2} (0.1298) \right)^2 + \left(\frac{(624.32)(0.0097596)}{(0.026783)(53.6 - 46.803)^2} (0.45255) \right)^2 \right]^{1/2}$$

$$\delta Nu_{0.47} = 2.3345$$

The integral average is then used to find the mean Nusselt number uncertainty. For the mean Nusselt number, the uncertainty is 7.03 %.

D.10.13 Friction factor

$$\delta f = \left[\left(\frac{\Delta P / \Delta x}{2\rho v_{ave}^2} \delta D_h \right)^2 + \left(\frac{D_h}{2\rho v_{ave}^2} \delta \Delta P / \Delta x \right)^2 + \left(-\frac{D_h \Delta P}{2\rho^2 v_{ave}^2} \delta \rho \right)^2 + \left(-\frac{D_h \Delta P}{\rho v_{ave}^3} \delta v_{ave} \right)^2 \right]^{1/2}$$

$$\delta f = \left[\left(\frac{795.1}{2(1.0165)(7.487)^2} (0.000048576) \right)^2 + \left(\frac{0.0097598}{2(1.0165)(7.487)^2} (23.179) \right)^2 + \left(-\frac{(0.0097598)(795.1)}{2(1.0165)^2(7.487)^2} (0.0005663) \right)^2 + \left(-\frac{(0.0097598)(795.1)}{(1.0165)(7.487)^3} (0.19834) \right)^2 \right]^{1/2}$$

$$\delta f = 0.004132$$

The uncertainty is 5.7 % for the friction factor of 0.0721.

D.10.14 Thermal performance coefficient

The thermal performance coefficient sample calculation for $d/p = 0.05$, $\theta = 45^\circ$ at $Re = 640$ will be shown:

$$\delta\eta = \left[\left(\frac{1}{\left(\frac{f}{f_0}\right)^{1/3}} \delta Nu \right)^2 + \left(\frac{-Nu}{\left(\frac{f}{f_0}\right)^{1/3} Nu_0^2} \delta Nu_0 \right)^2 + \left(\left(-\frac{1}{3}\right) \frac{Nu}{\frac{f^{4/3}}{f_0^{1/3}}} \delta f \right)^2 + \left(\frac{1}{3} \frac{Nu}{f^{1/3} f_0^{2/3}} \delta f_0 \right)^2 \right]^{1/2}$$

$$\delta\eta = [(0.087 \times 0.766)^2 + (-0.118 \times 1.393)^2 + (-2.431 \times 0.0133)^2 + (8.87 \times 0.00331)^2]^{1/2}$$

$$\delta\eta = 0.182$$

The uncertainty is 20.81% for the thermal performance coefficient of 0.875.

Appendix E: Local Nusselt Numbers

The local Nusselt numbers for all the cylindrical cross-bar configurations are shown in this chapter at each Reynolds number. It is sorted from the smallest d/p ratio to the largest d/p ratio alternating between $\theta = 45^\circ$ and $\theta = 90^\circ$ so that the average Nusselt numbers increases from Figure E.1 to Figure E.8. Figure E.1 shows the cylindrical cross bar configuration $d/p = 0.025$, $\theta = 45^\circ$, $d/p = 0.025$, $\theta = 90^\circ$ on Figure E.2, $d/p = 0.05$, $\theta = 45^\circ$ on Figure E.3, $d/p = 0.05$, $\theta = 90^\circ$ on Figure E.4, $d/p = 0.1$, $\theta = 45^\circ$ on Figure E.5, $d/p = 0.1$, $\theta = 90^\circ$ on Figure E.6, $d/p = 0.2$, $\theta = 45^\circ$ on Figure E.7 and $d/p = 0.2$, $\theta = 90^\circ$ on Figure E.8. The local Nusselt numbers are large in the first part of the test section because the difference between the wall temperature and mean fluid temperature is small after which it reaches an asymptotic value in the middle section and end section of the test section.

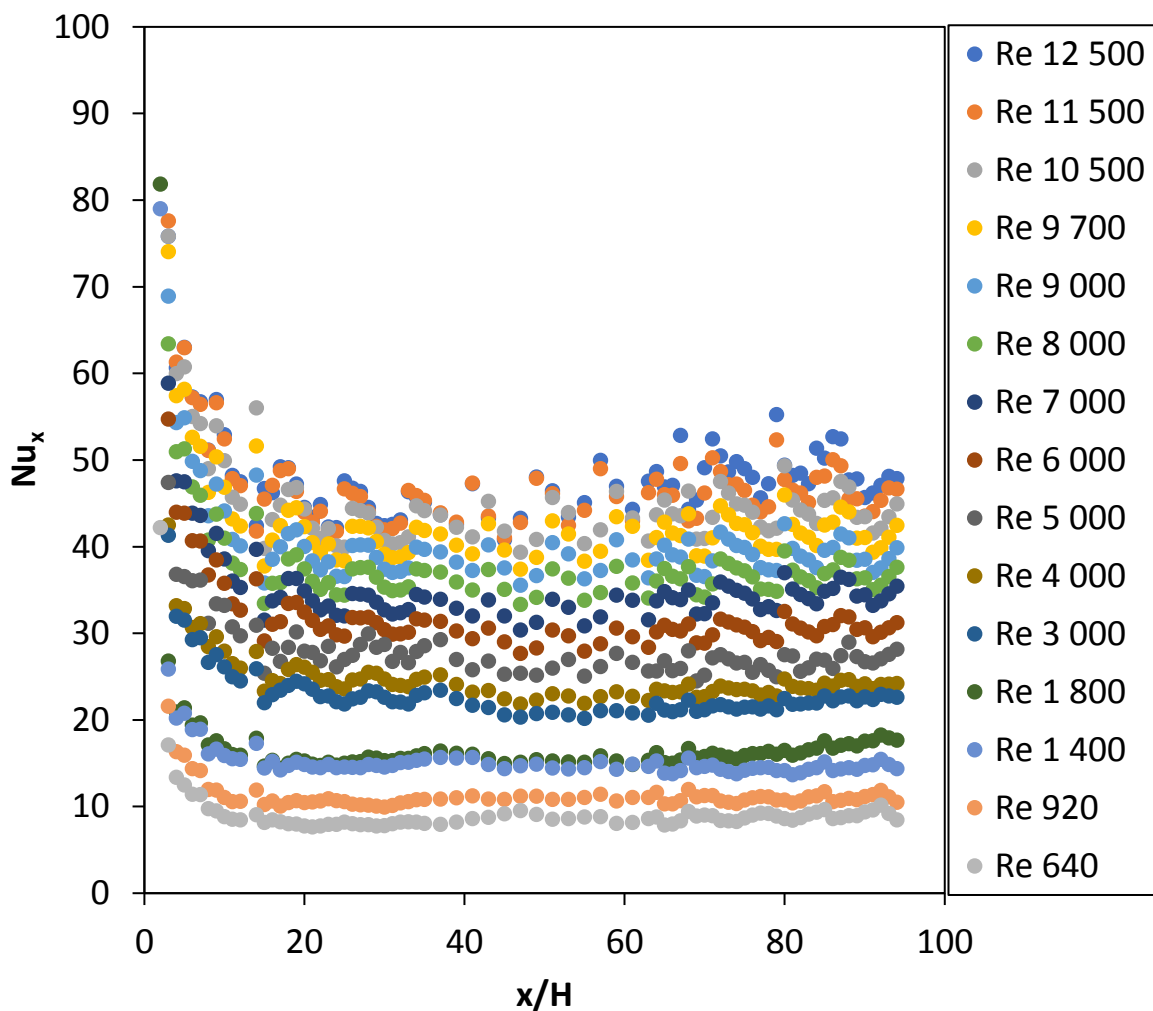


Figure E.1: Local Nusselt numbers, Nu_x , for $d/p = 0.025$, $\theta = 45^\circ$.

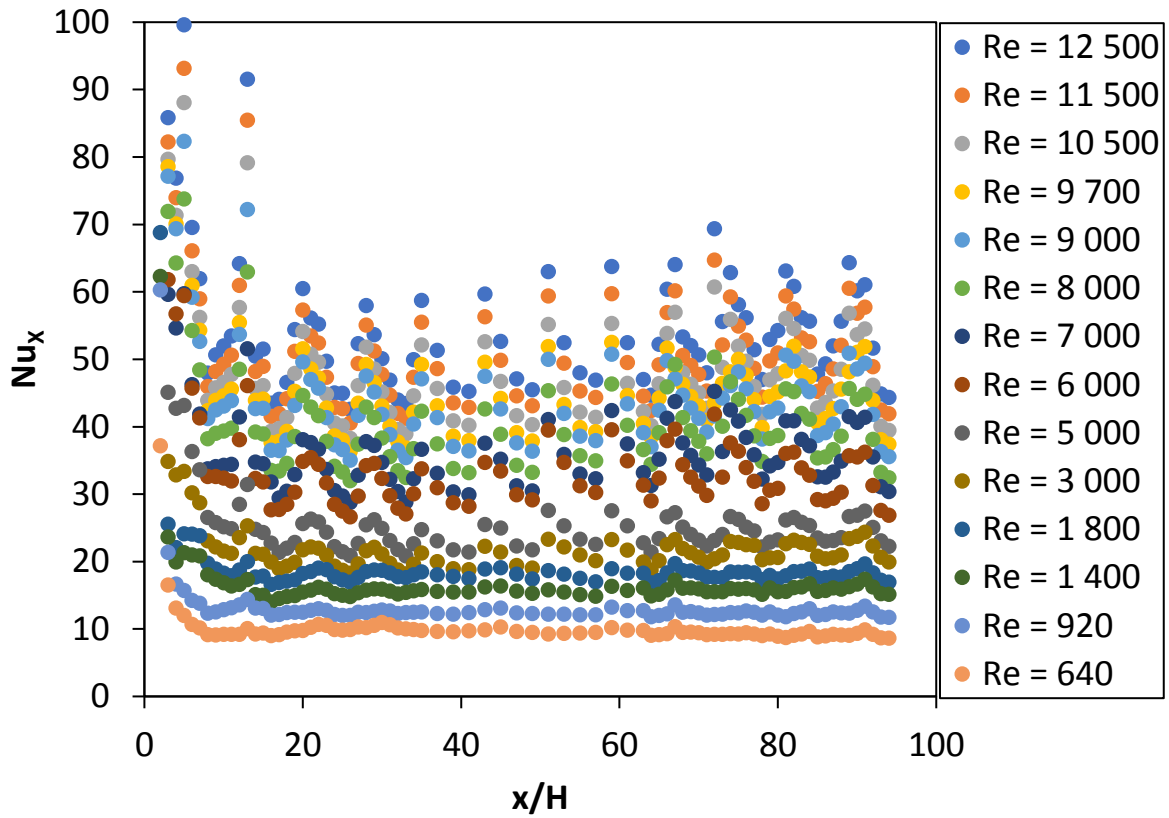


Figure E.2: Local Nusselt numbers, Nu_x , for $d/p = 0.025$, $\theta = 90^\circ$.

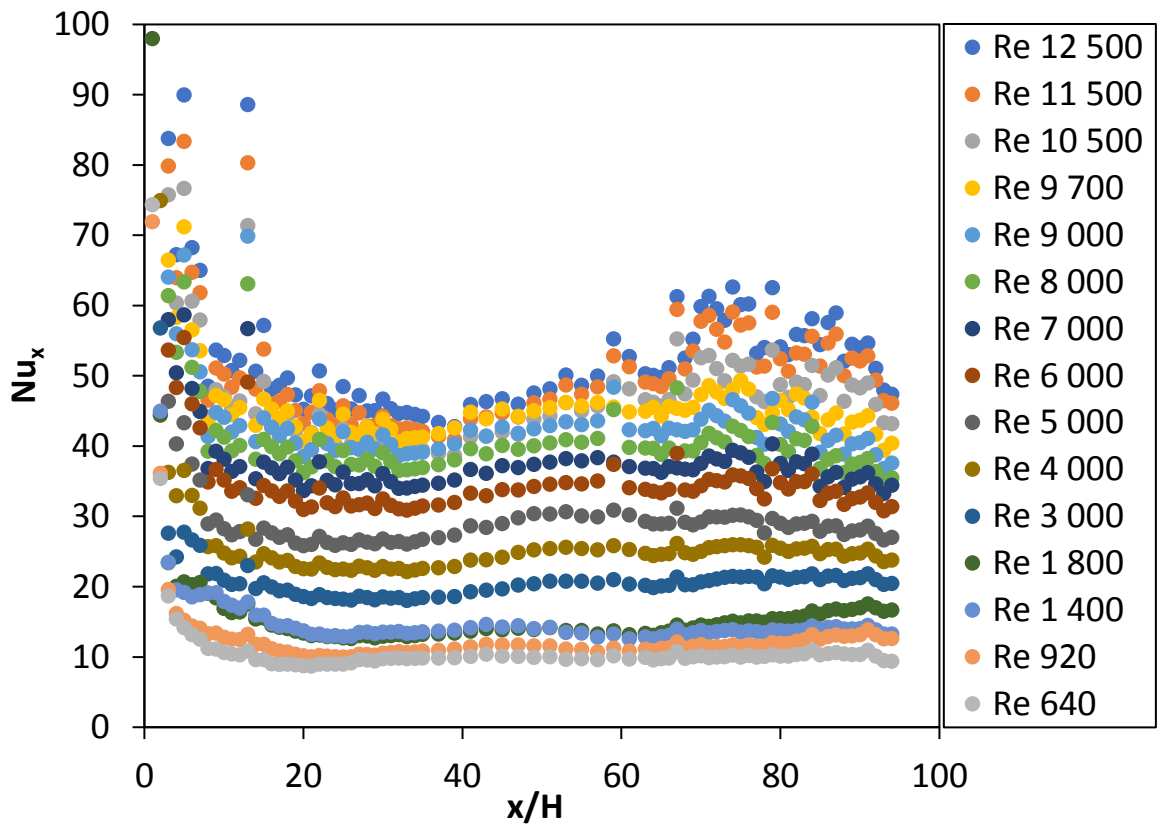


Figure E.3: Local Nusselt numbers, Nu_x , for $d/p = 0.05$, $\theta = 45^\circ$.

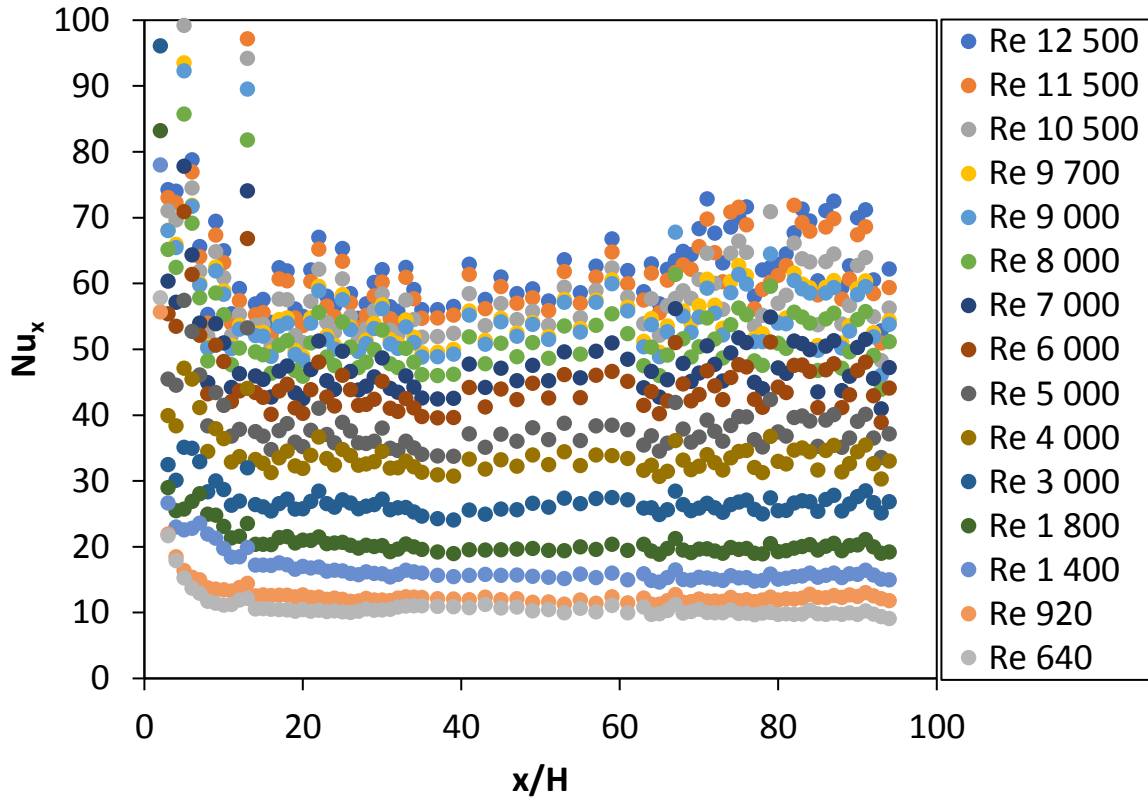


Figure E.4: Local Nusselt numbers, Nu_x , for $d/p = 0.05$, $\theta = 90^\circ$.

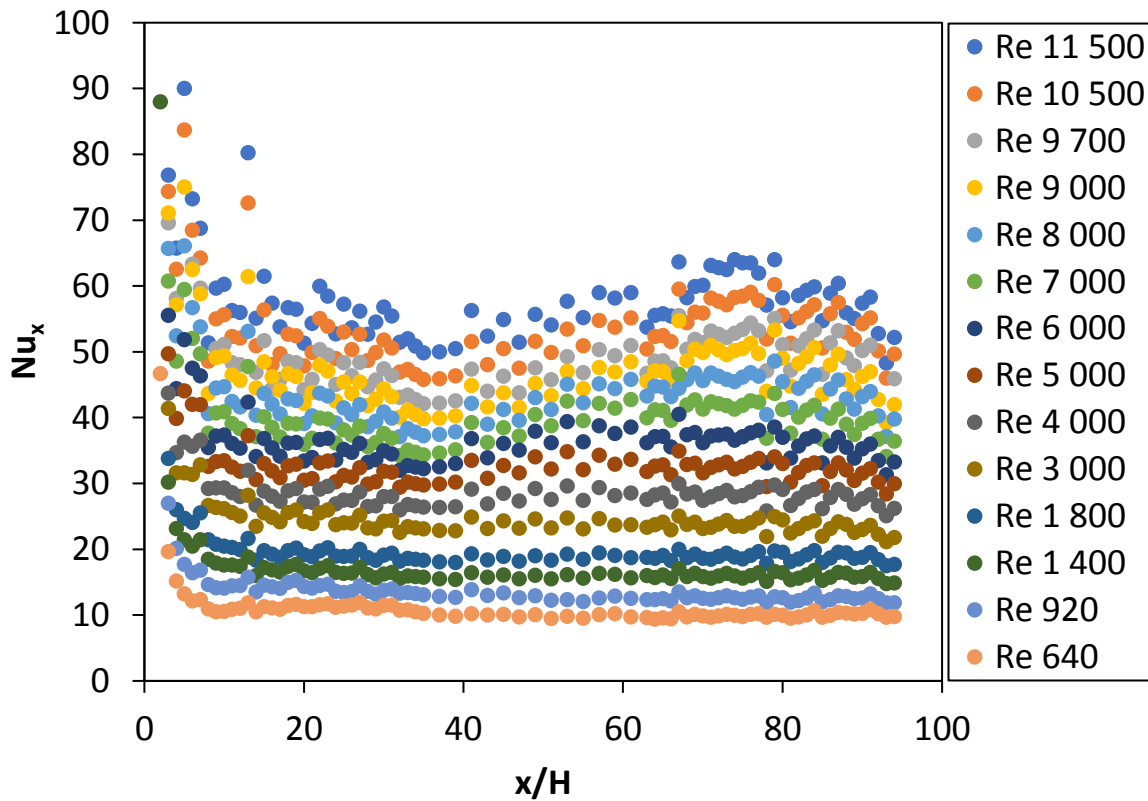


Figure E.5: Local Nusselt numbers, Nu_x , for $d/p = 0.1$, $\theta = 45^\circ$.

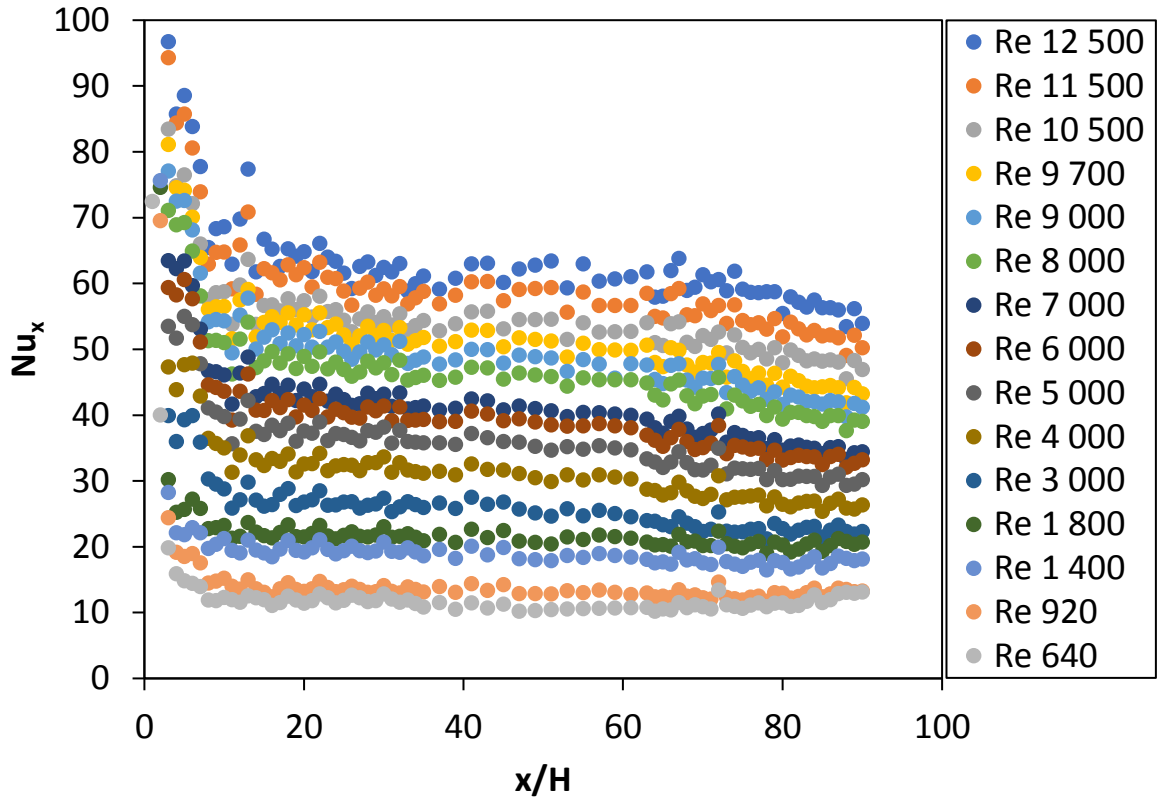


Figure E.6: Local Nusselt numbers, Nu_x , for $d/p = 0.1$, $\theta = 90^\circ$.

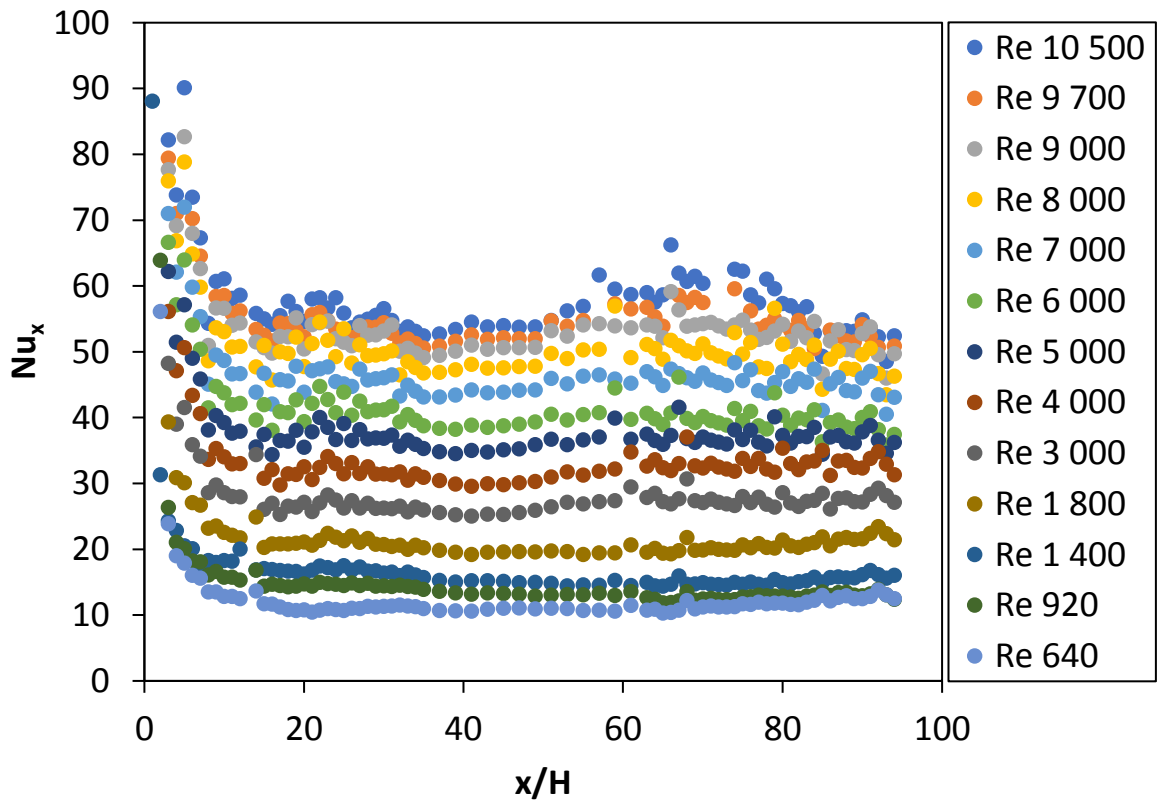


Figure E.7: Local Nusselt numbers, Nu_x , for $d/p = 0.2$, $\theta = 45^\circ$.

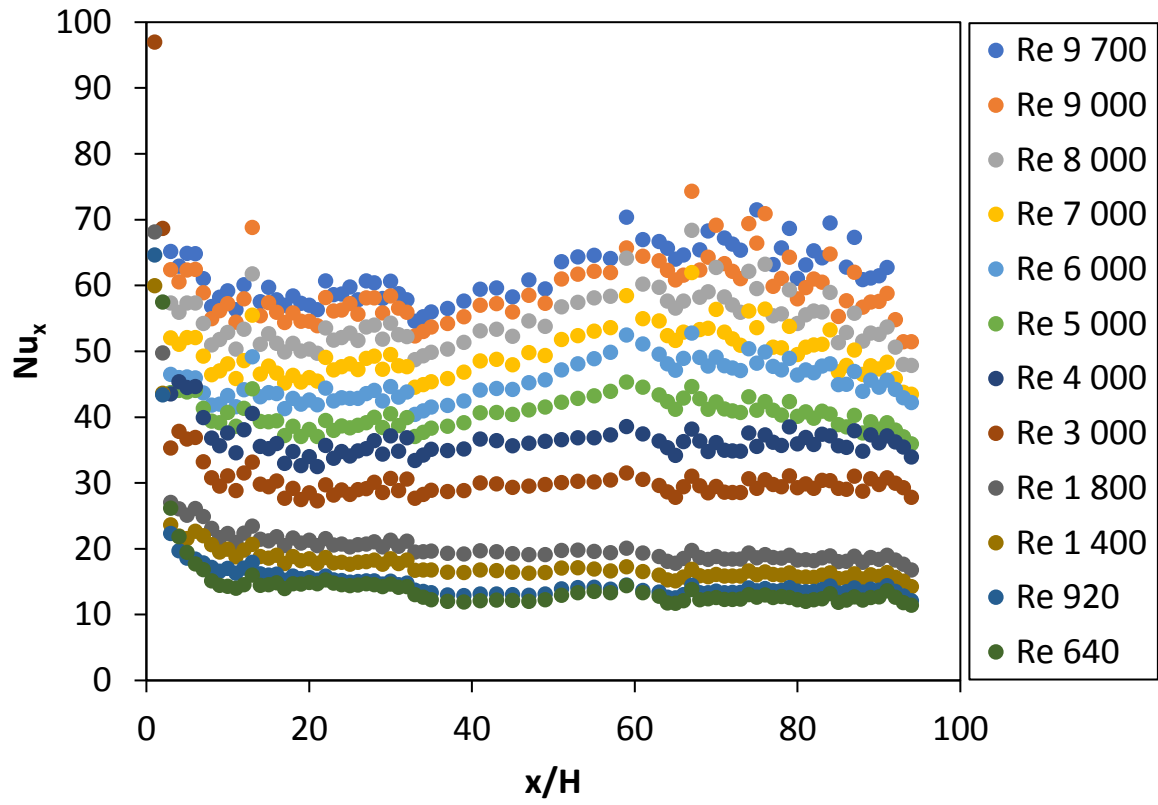


Figure E.8: Local Nusselt numbers, Nu_x , for $d/p = 0.2$, $\theta = 90^\circ$.

Appendix F: Temperature Data

Appendix F presents the temperature data taken in the heat transfer experimental tests done in the present study. The local wall temperature is shown as well as the local mean air temperature, after steady state has been reached.

F.1. Temperature data: smooth channel

The temperature data for the smooth channel is shown in Figure F.1 to Figure F.15.

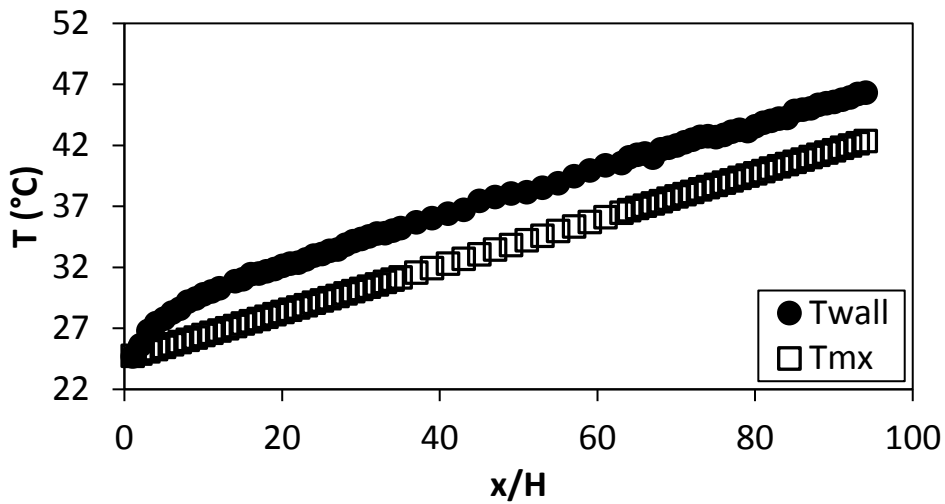


Figure F.1. Temperature plotted against x/H at $Re = 640$ for smooth channel.

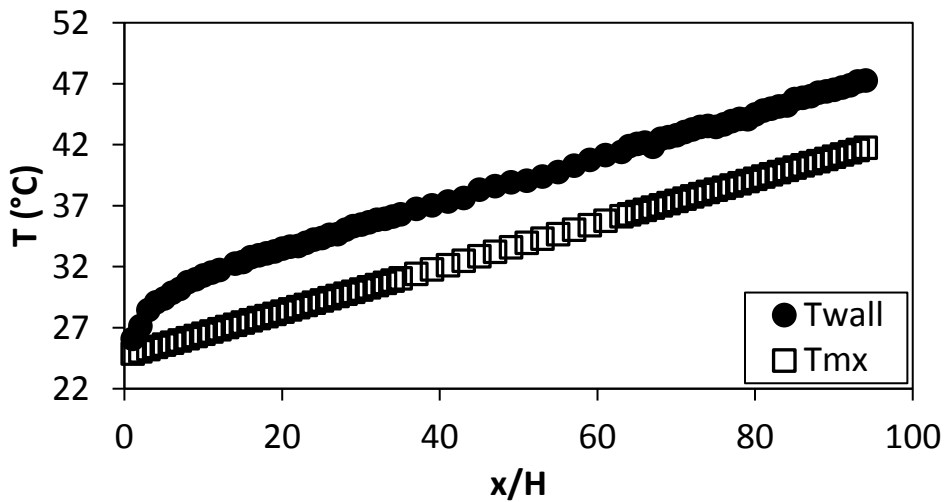


Figure F.2. Temperature plotted against x/H at $Re = 920$ for smooth channel.

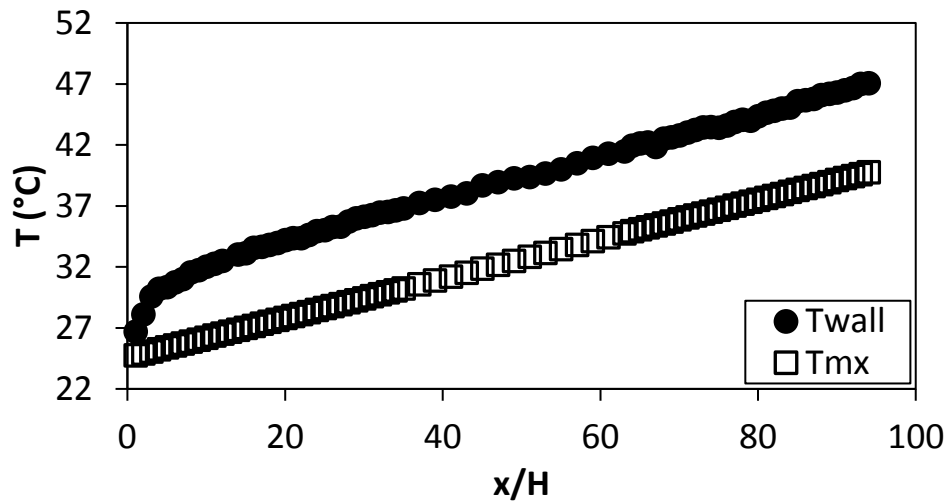


Figure F.3. Temperature plotted against x/H at $Re = 1\,400$ for smooth channel.

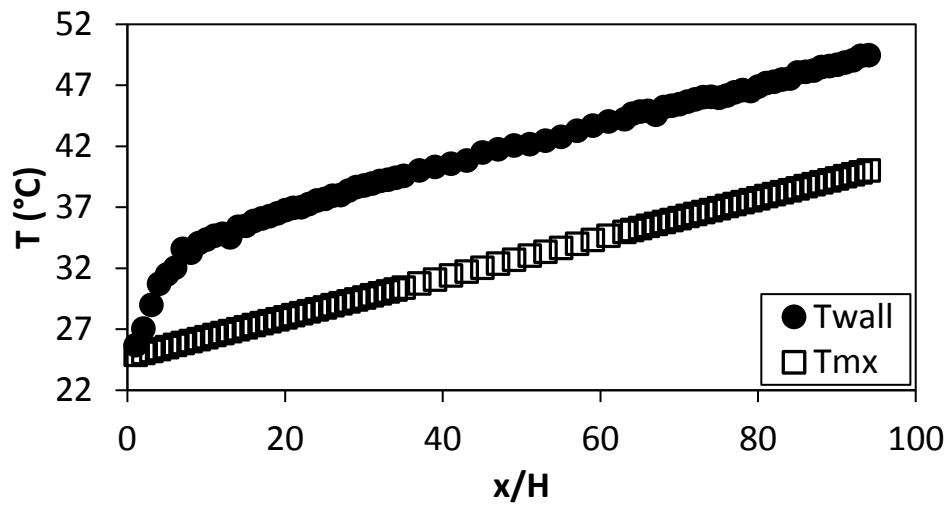


Figure F.4. Temperature plotted against x/H at $Re = 1\,800$ for smooth channel.

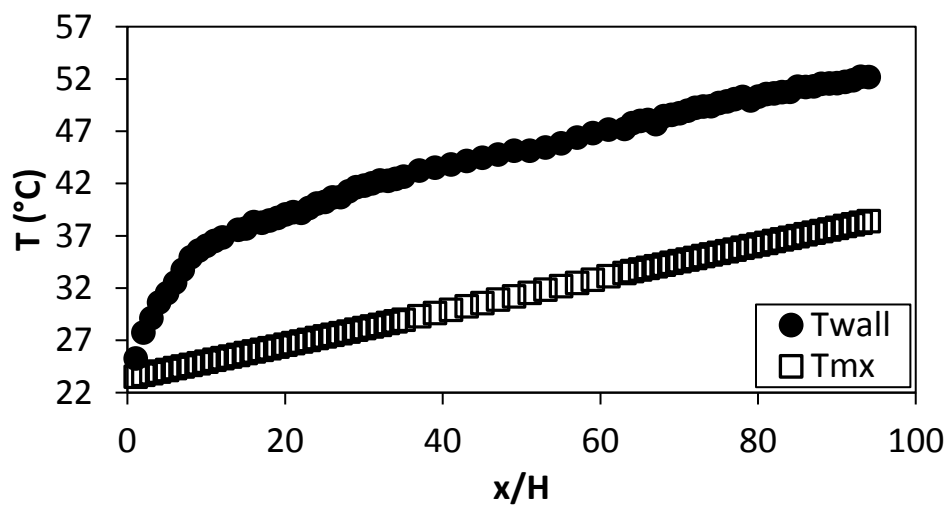


Figure F.5. Temperature plotted against x/H at $Re = 3\,000$ for smooth channel.

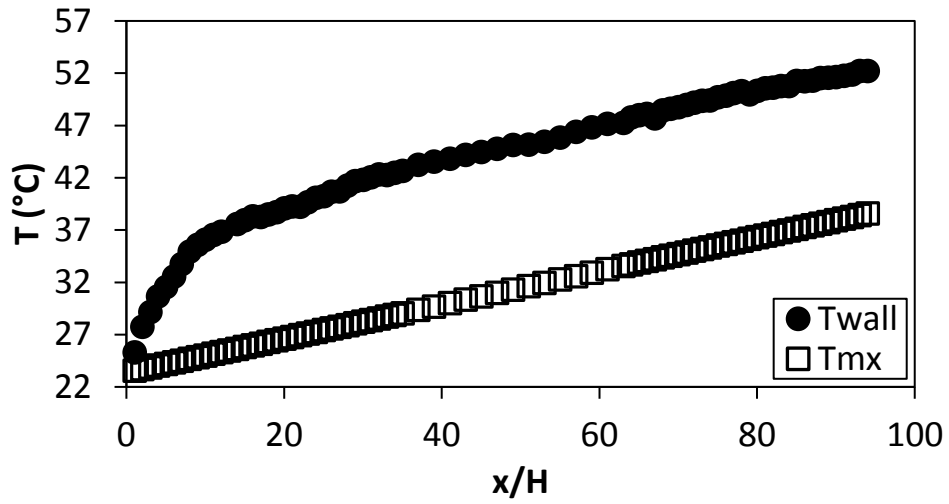


Figure F.6. Temperature plotted against x/H at $Re = 4\,000$ for smooth channel.

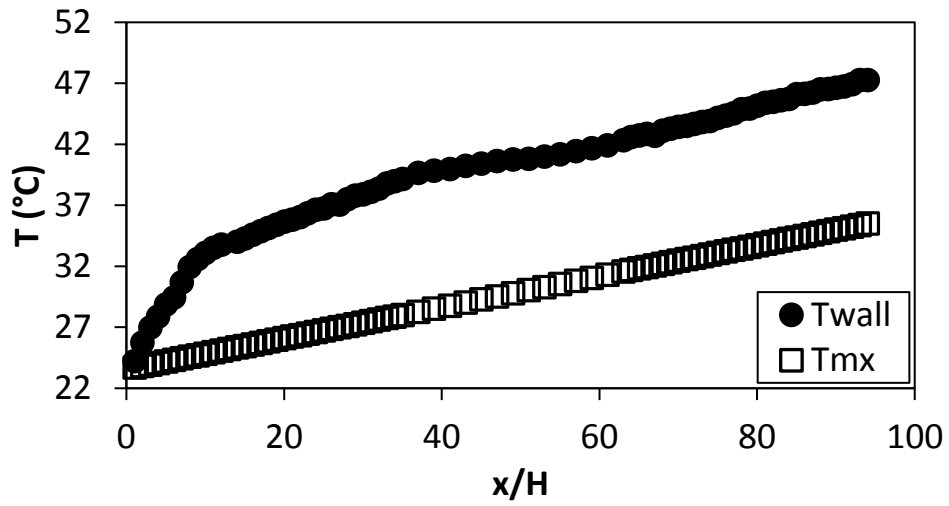


Figure F.7. Temperature plotted against x/H at $Re = 5\,000$ for smooth channel.

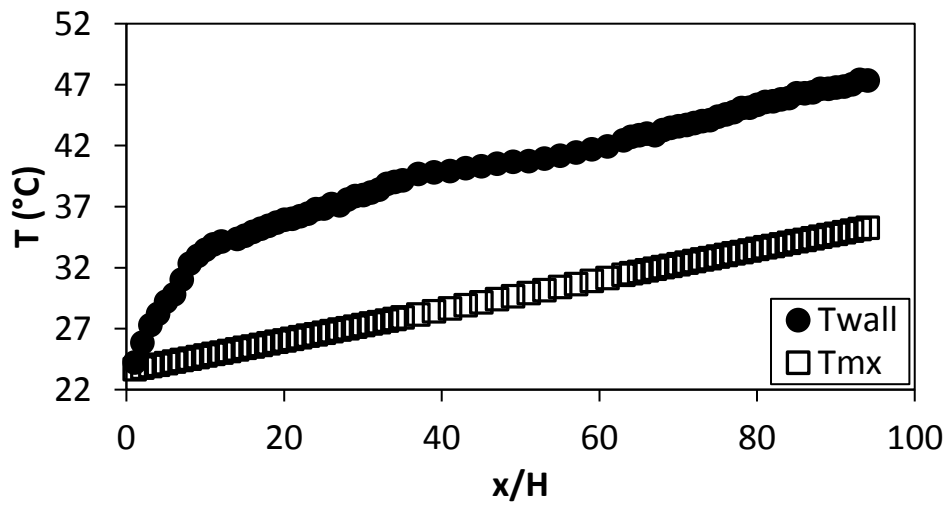


Figure F.8. Temperature plotted against x/H at $Re = 6\,000$ for smooth channel.

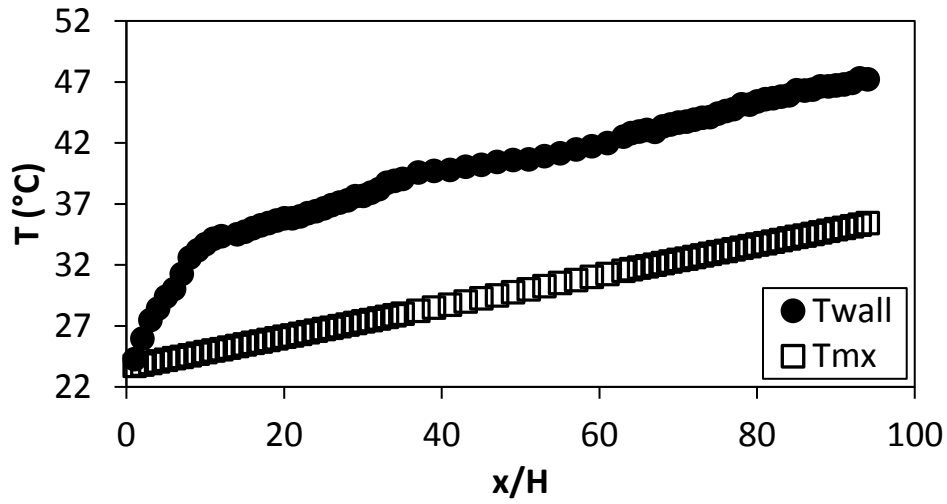


Figure F.9. Temperature plotted against x/H at $Re = 7000$ for smooth channel.

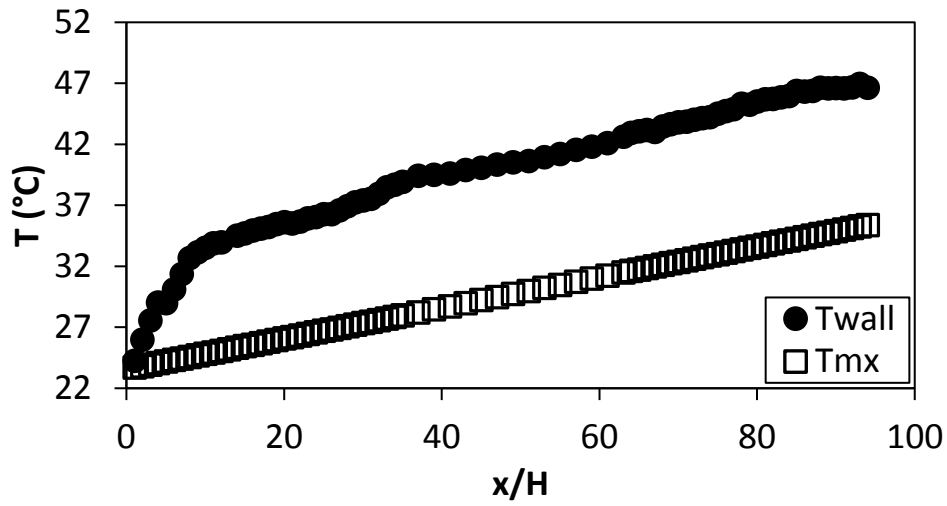


Figure F.10. Temperature plotted against x/H at $Re = 8000$ for smooth channel.

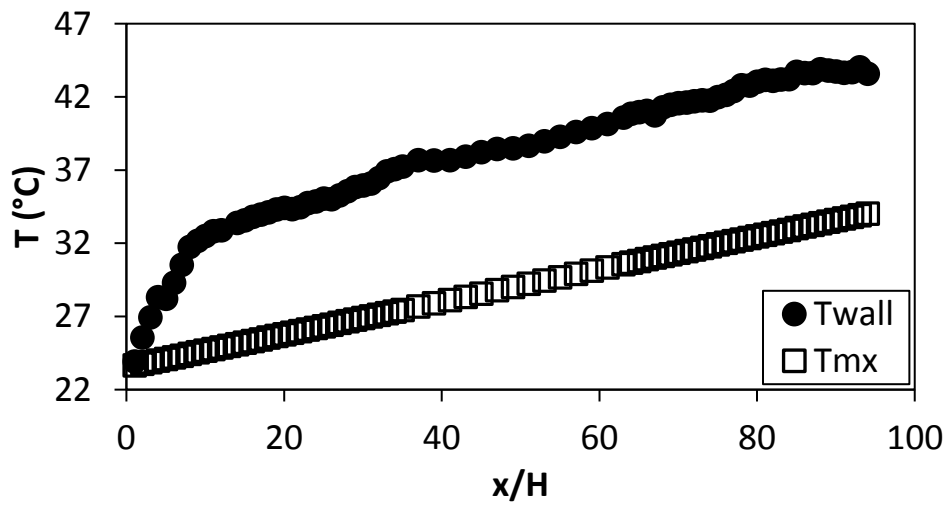


Figure F.11. Temperature plotted against x/H at $Re = 9000$ for smooth channel.

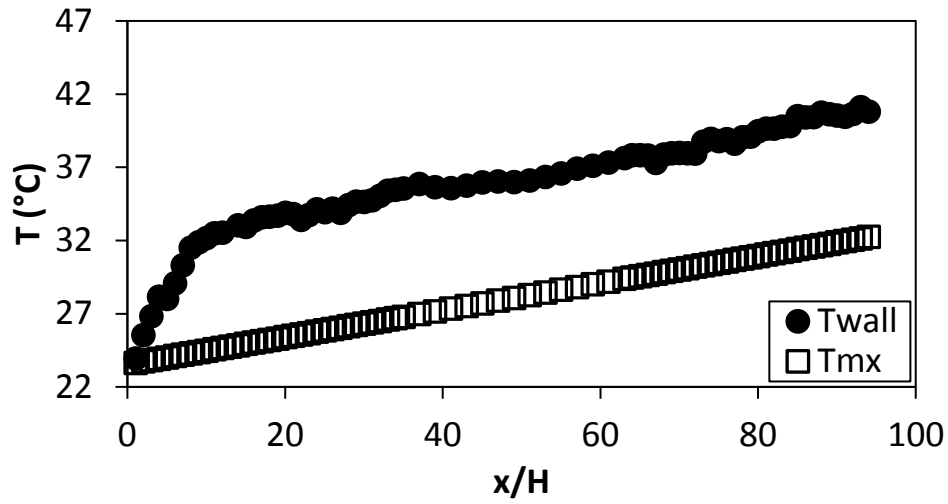


Figure F.12. Temperature plotted against x/H at $Re = 9\,700$ for smooth channel.

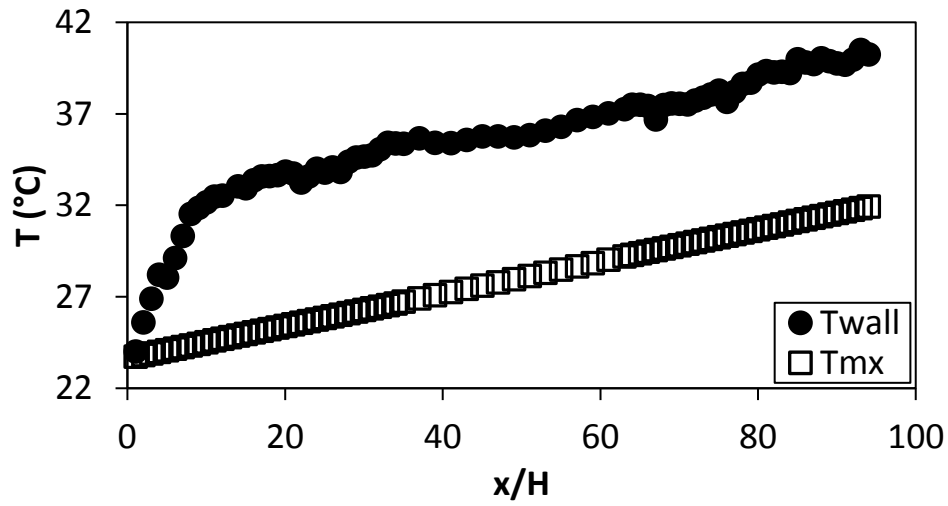


Figure F.13. Temperature plotted against x/H at $Re = 10\,500$ for smooth channel.

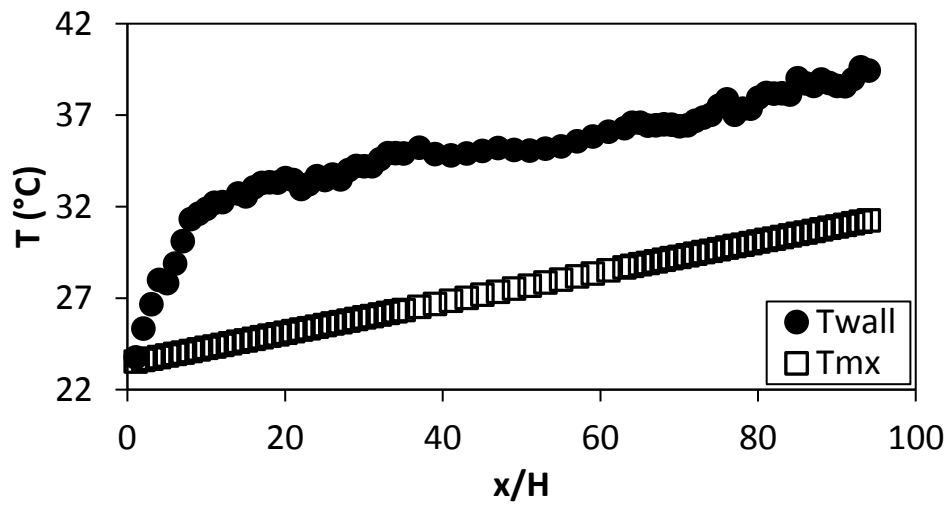


Figure F.14. Temperature plotted against x/H at $Re = 11\,500$ for smooth channel.

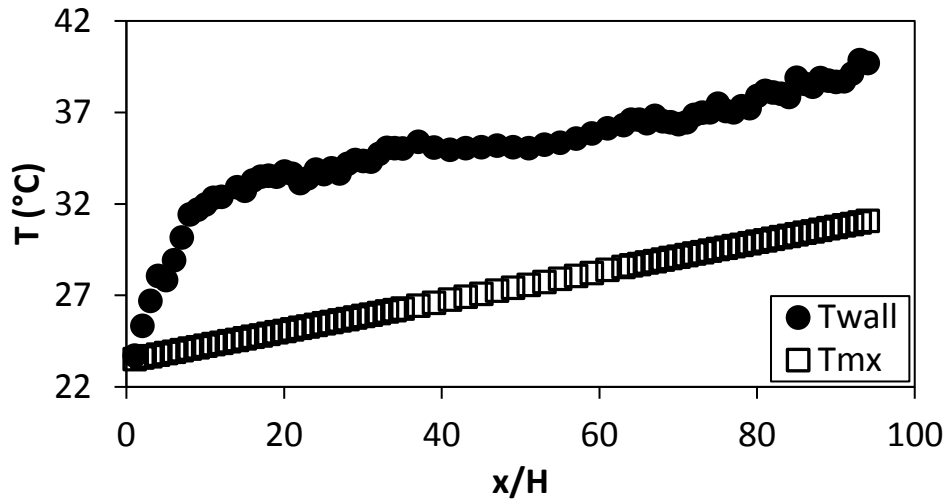


Figure F.15. Temperature plotted against x/H at $Re = 12\,500$ for smooth channel.

F.2. Temperature data: $d/p = 0.05$, 90° orientation to the flow direction
 The temperature data for the cylindrical insert with, $d/p = 0.05$, and flow direction 90° to the cylinders is shown in Figure F.16 to Figure F.30.

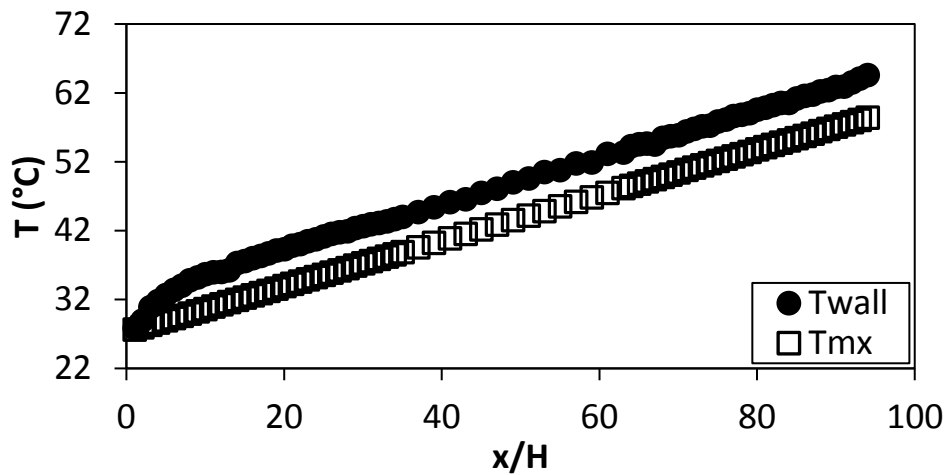


Figure F.16. Temperature plotted against x/H at $Re = 640$ for setup: $d/p = 0.05$, $\theta = 90^\circ$.

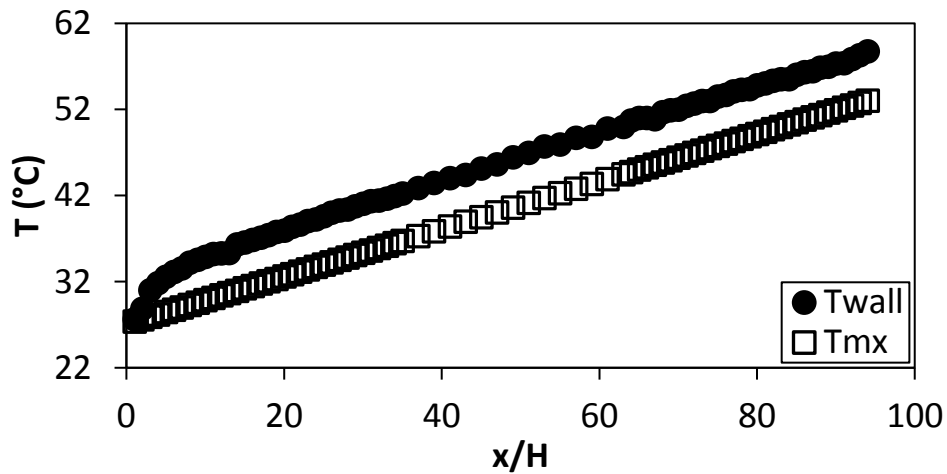


Figure F.17. Temperature plotted against x/H at $Re = 920$ for setup: $d/p = 0.05$, $\theta = 90^\circ$.

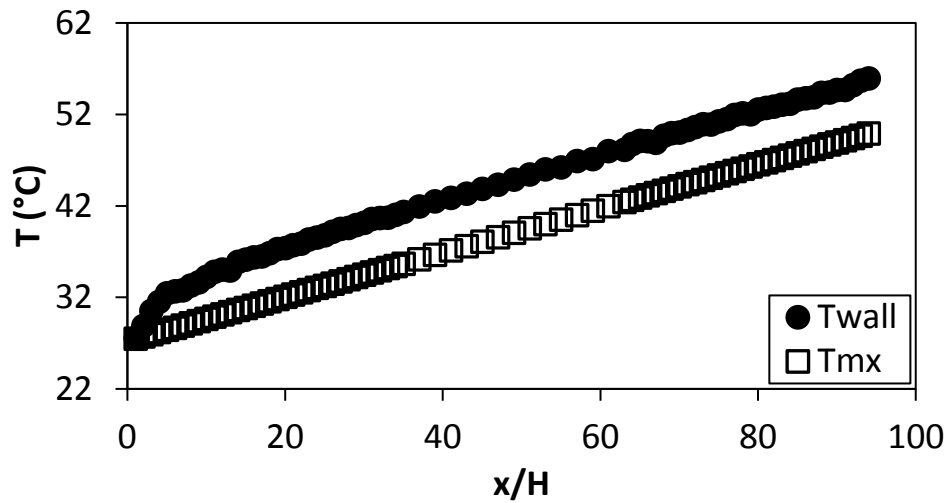


Figure F.18. Temperature plotted against x/H at $Re = 1\ 400$ for setup: $d/p = 0.05$, $\theta = 90^\circ$.

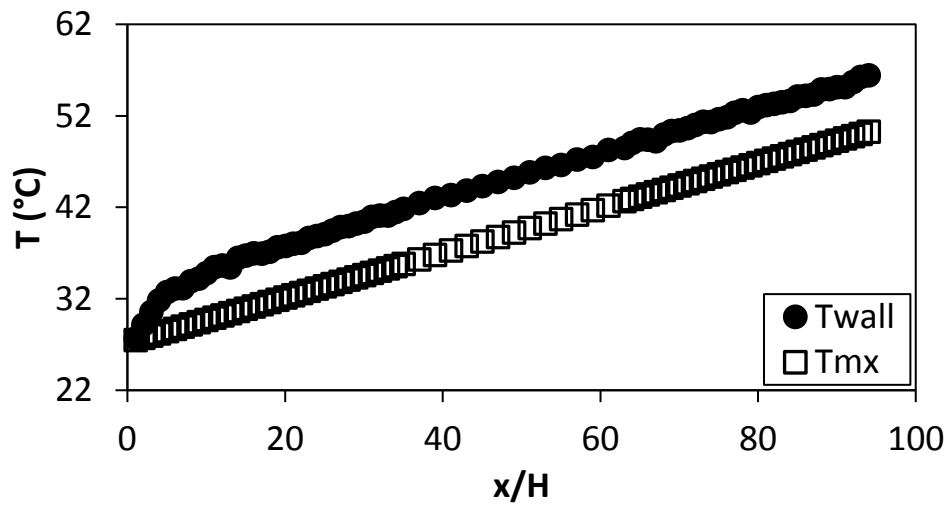


Figure F.19. Temperature plotted against x/H at $Re = 1\ 800$ for setup: $d/p = 0.05$, $\theta = 90^\circ$.

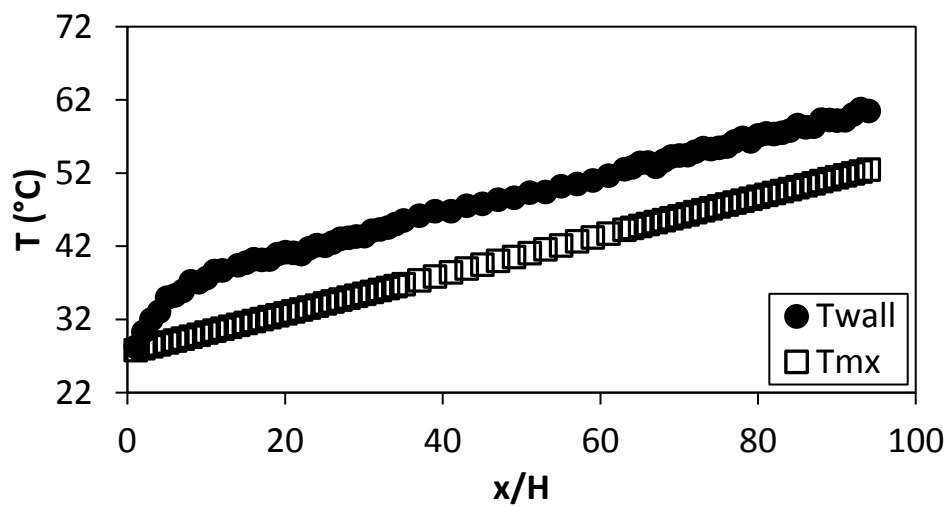


Figure F.20. Temperature plotted against x/H at $Re = 3\ 000$ for setup: $d/p = 0.05$, $\theta = 90^\circ$.

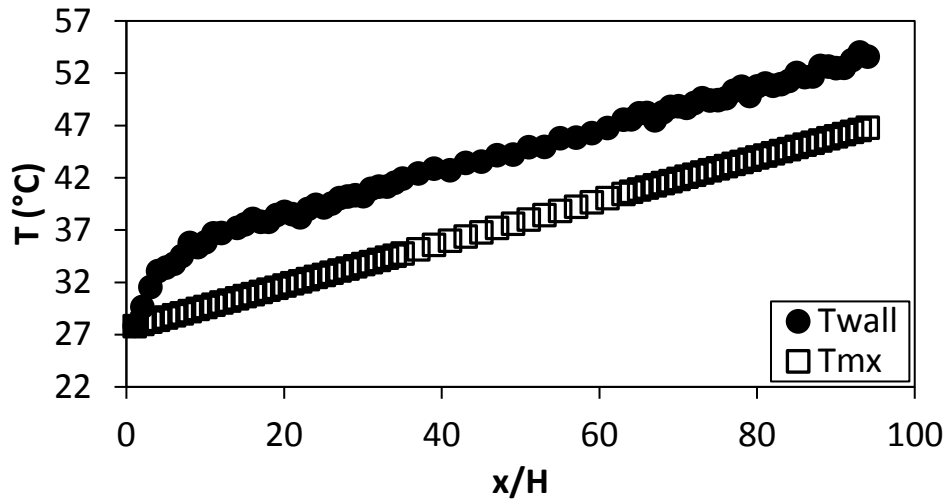


Figure F.21. Temperature plotted against x/H at $Re = 4\,000$ for setup: $d/p = 0.05$, $\theta = 90^\circ$.

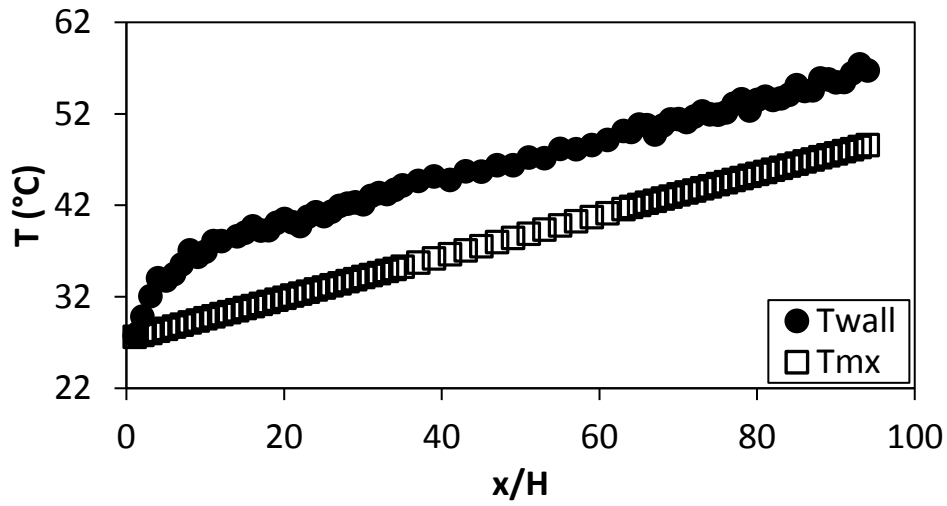


Figure F.22. Temperature plotted against x/H at $Re = 5\,000$ for setup: $d/p = 0.05$, $\theta = 90^\circ$.

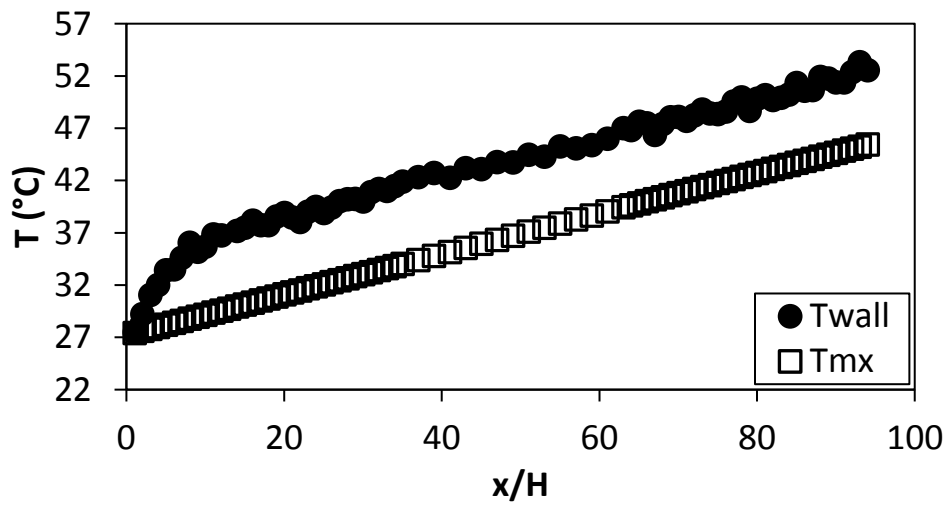


Figure F.23. Temperature plotted against x/H at $Re = 6\,000$ for setup: $d/p = 0.05$, $\theta = 90^\circ$.

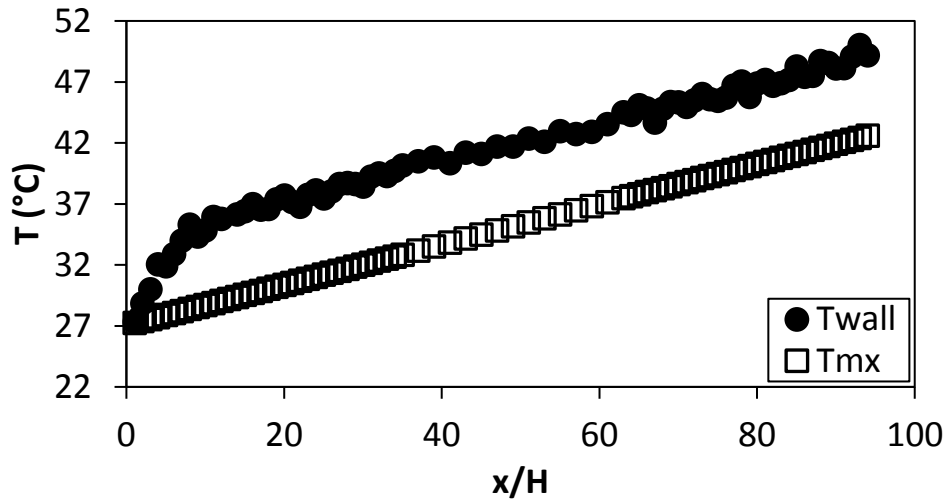


Figure F.24. Temperature plotted against x/H at $Re = 7\,000$ for setup: $d/p = 0.05$, $\theta = 90^\circ$.

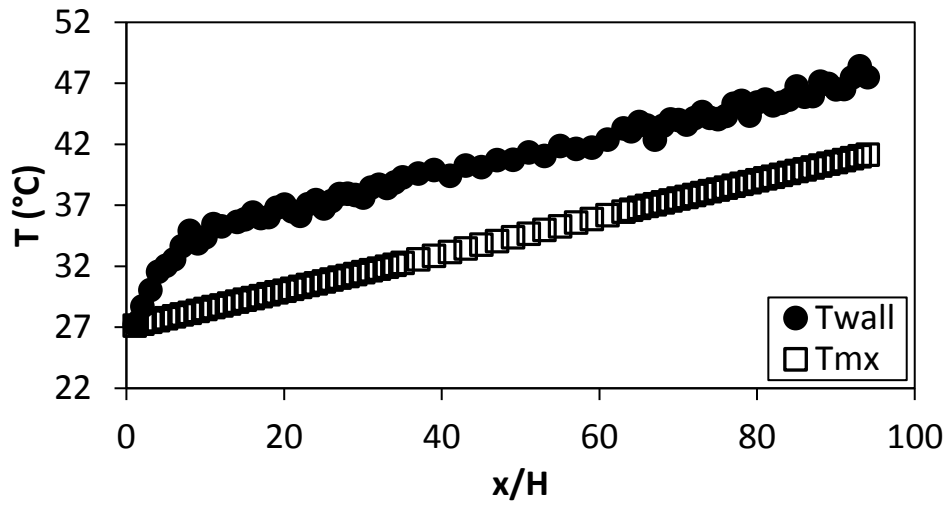


Figure F.25. Temperature plotted against x/H at $Re = 8\,000$ for setup: $d/p = 0.05$, $\theta = 90^\circ$.

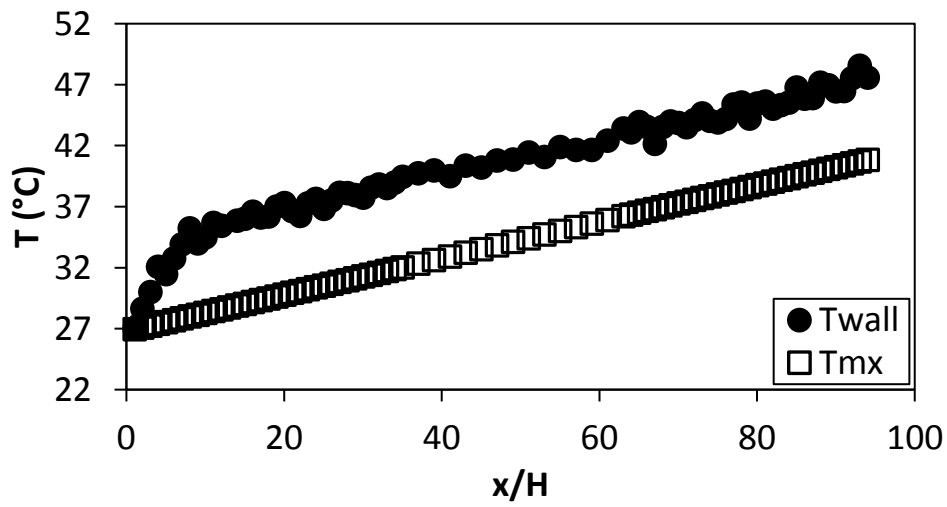


Figure F.26. Temperature plotted against x/H at $Re = 9\,000$ for setup: $d/p = 0.05$, $\theta = 90^\circ$.

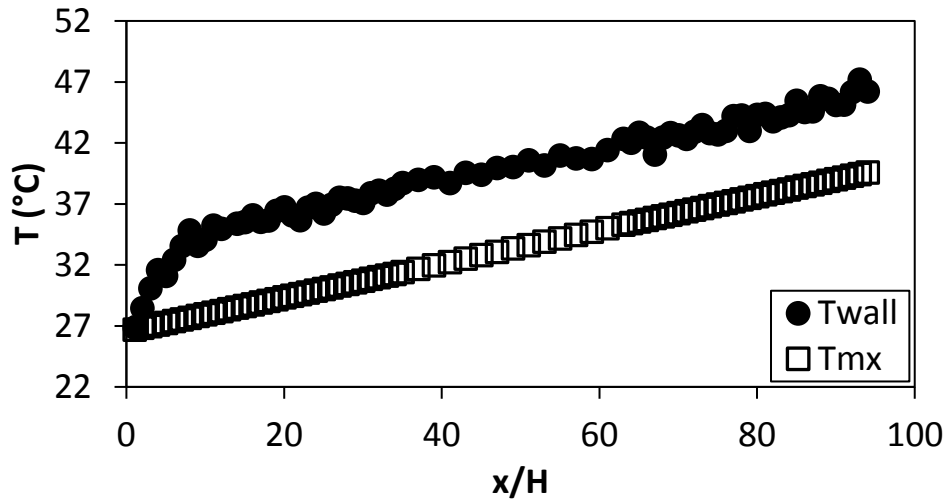


Figure F.27. Temperature plotted against x/H at $Re = 9\,700$ for setup: $d/p = 0.05$, $\theta = 90^\circ$.

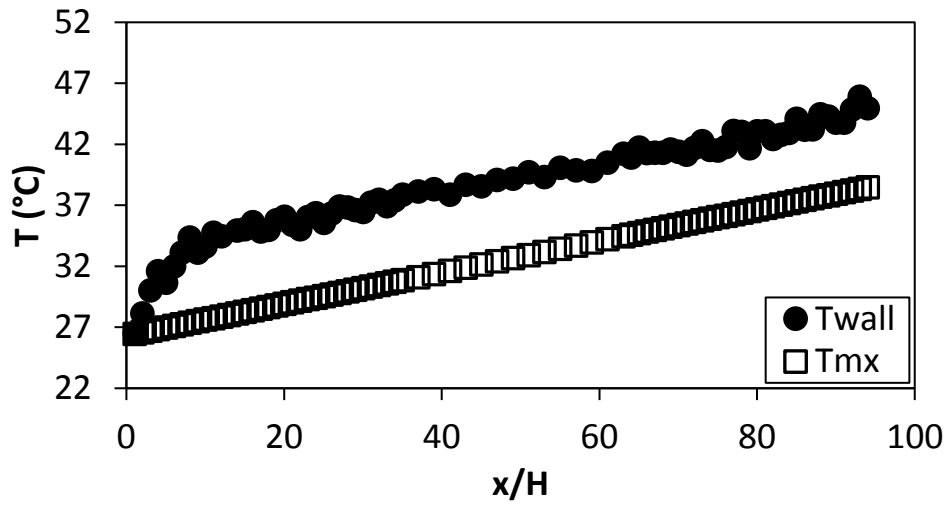


Figure F.28. Temperature plotted against x/H at $Re = 10\,500$ for setup: $d/p = 0.05$, $\theta = 90^\circ$.

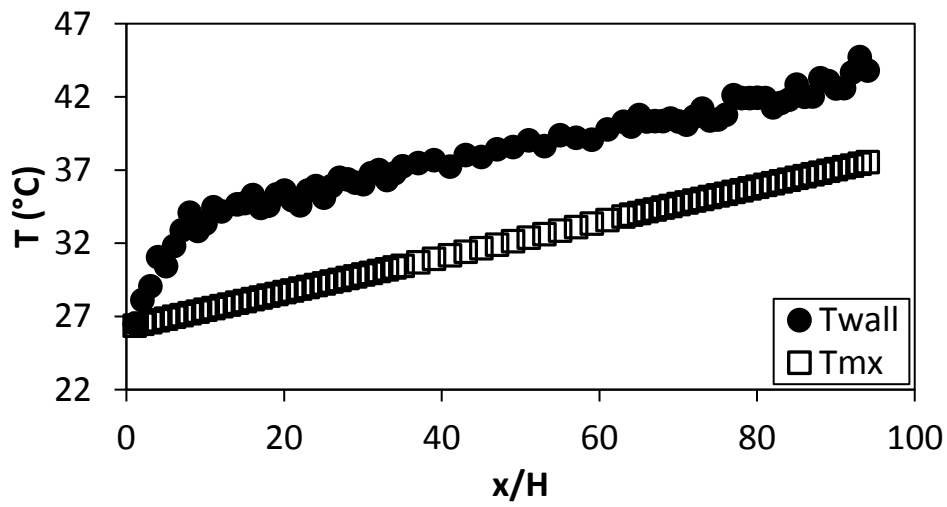


Figure F.29. Temperature plotted against x/H at $Re = 11\,500$ for setup: $d/p = 0.05$, $\theta = 90^\circ$.

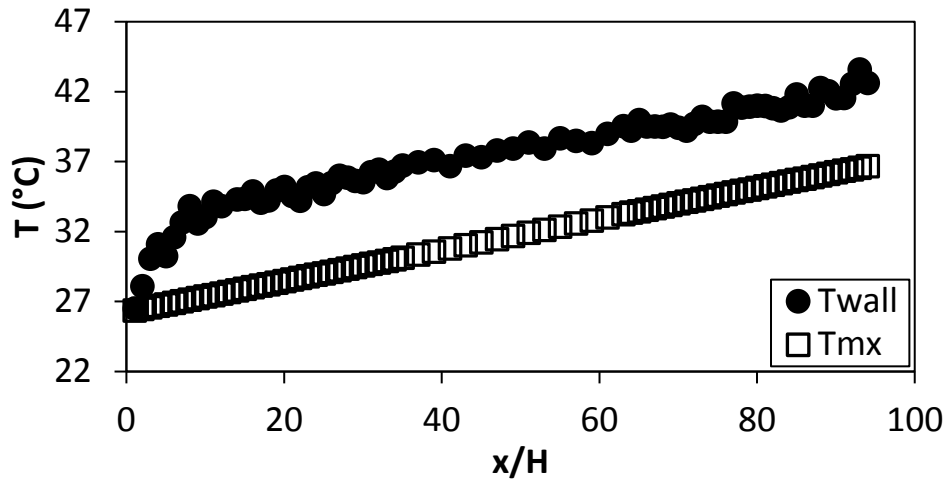


Figure F.30. Temperature plotted against x/H at $Re = 12\,500$ for setup: $d/p = 0.05$, $\theta = 90^\circ$.

F.3. Temperature data: $d/p = 0.05$, 45° orientation to the flow direction

The temperature data for the cylindrical insert with, $d/p = 0.05$, and flow direction 45° to the cylinders is shown in Figure F.31 to Figure F.45.

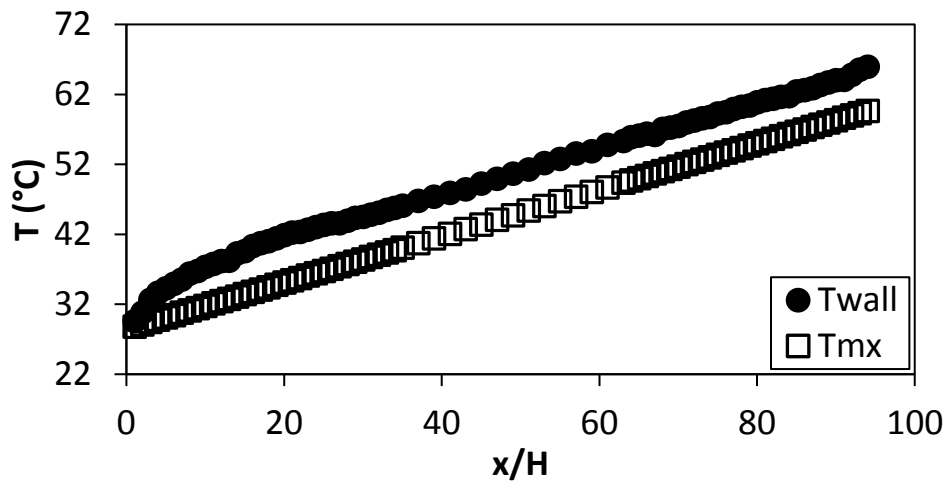


Figure F.31. Temperature plotted against x/H at $Re = 640$ for setup: $d/p = 0.05$, $\theta = 45^\circ$.

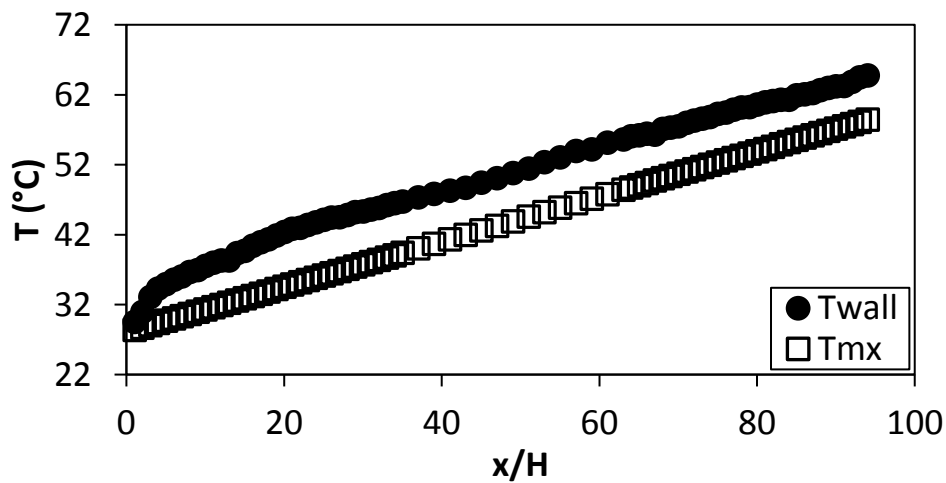


Figure F.32. Temperature plotted against x/H at $Re = 920$ for setup: $d/p = 0.05$, $\theta = 45^\circ$.

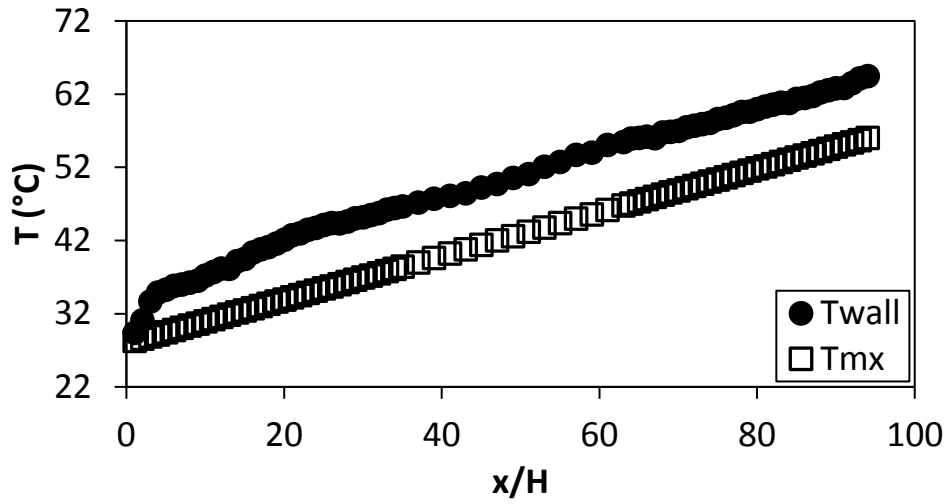


Figure F.33. Temperature plotted against x/H at $Re = 1\,400$ for setup: $d/p = 0.05$, $\theta = 45^\circ$.

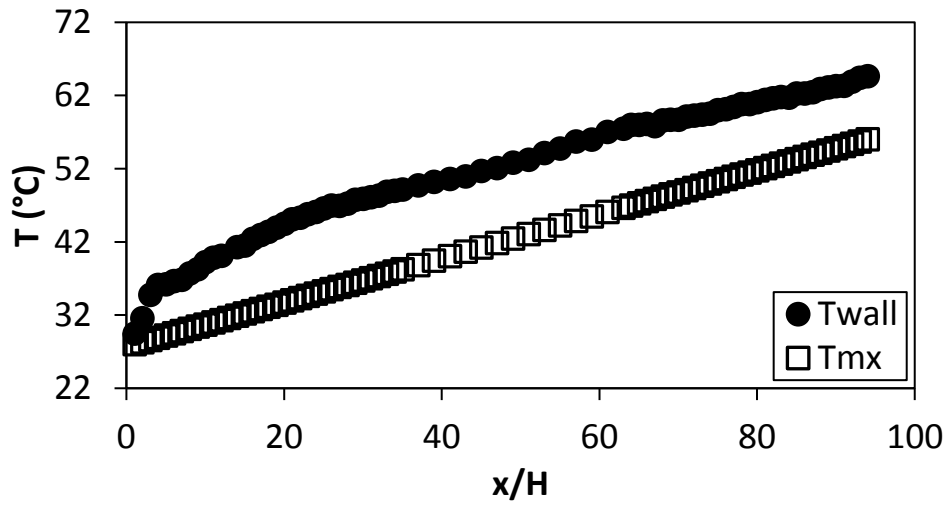


Figure F.34. Temperature plotted against x/H at $Re = 1\,800$ for setup: $d/p = 0.05$, $\theta = 45^\circ$.

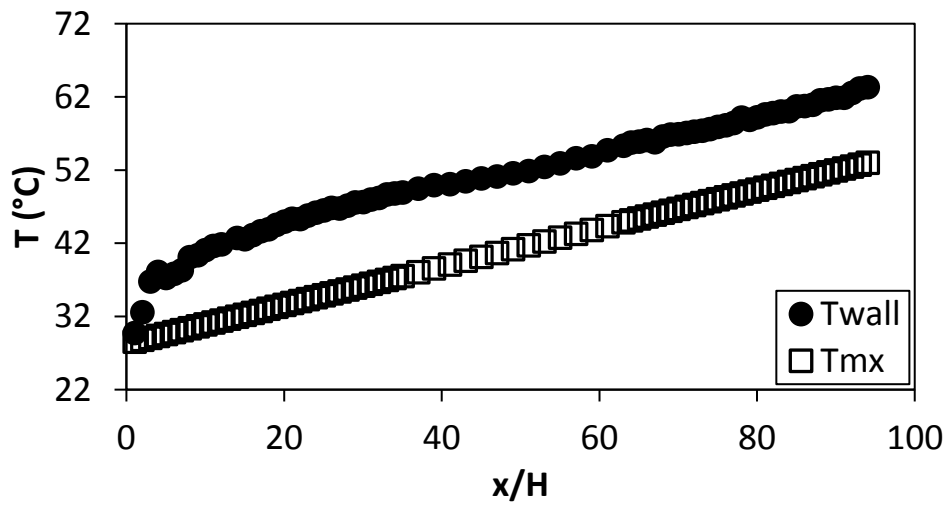


Figure F.35. Temperature plotted against x/H at $Re = 3\,000$ for setup: $d/p = 0.05$, $\theta = 45^\circ$.

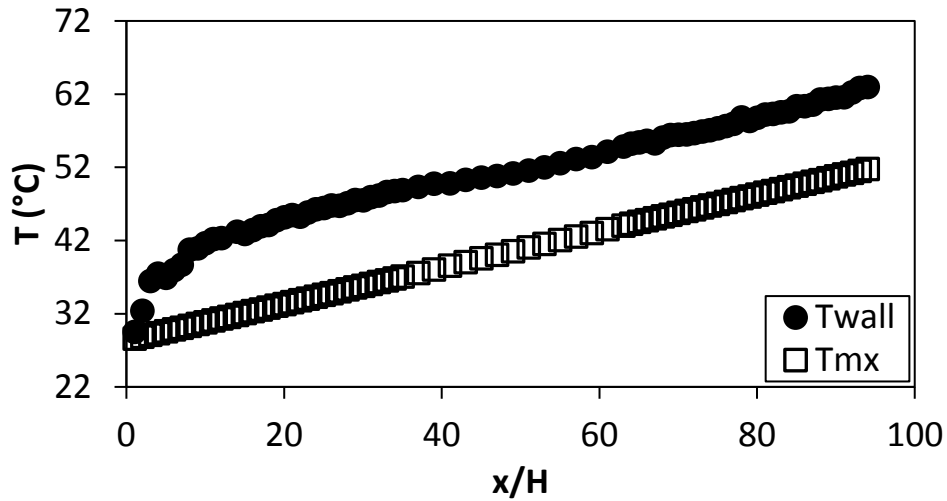


Figure F.36. Temperature plotted against x/H at $Re = 4\,000$ for setup: $d/p = 0.05$, $\theta = 45^\circ$.

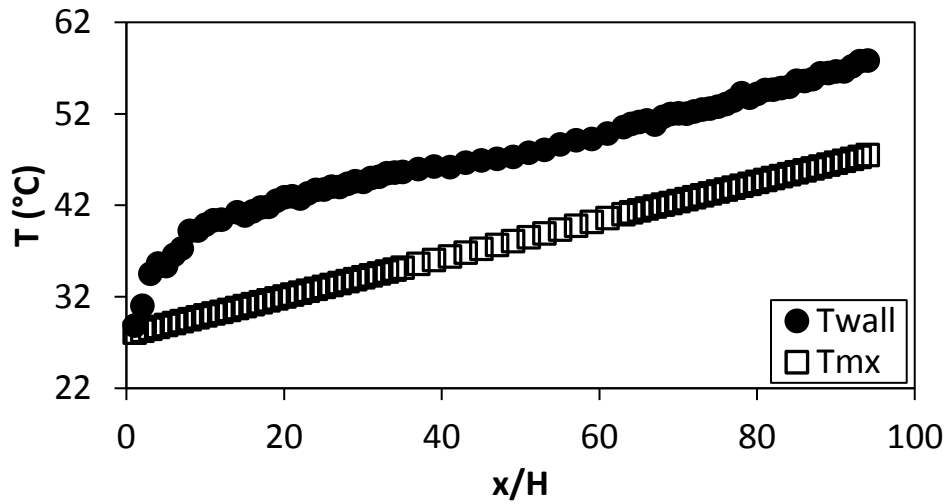


Figure F.37. Temperature plotted against x/H at $Re = 5\,000$ for setup: $d/p = 0.05$, $\theta = 45^\circ$.

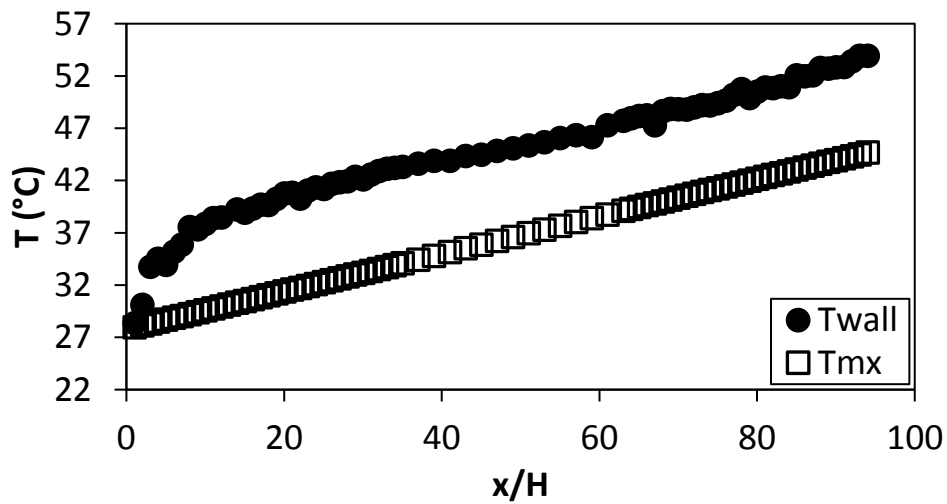


Figure F.38. Temperature plotted against x/H at $Re = 6\,000$ for setup: $d/p = 0.05$, $\theta = 45^\circ$.

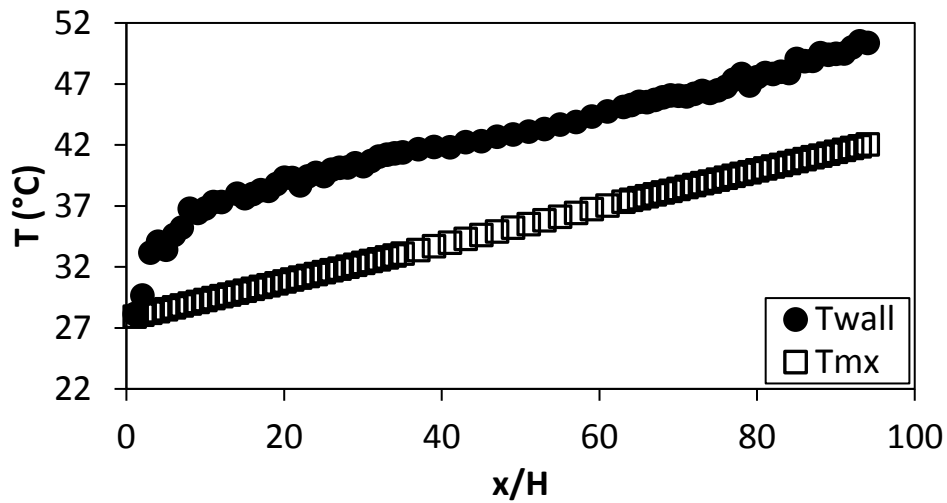


Figure F.39. Temperature plotted against x/H at $Re = 7\,000$ for setup: $d/p = 0.05$, $\theta = 45^\circ$.

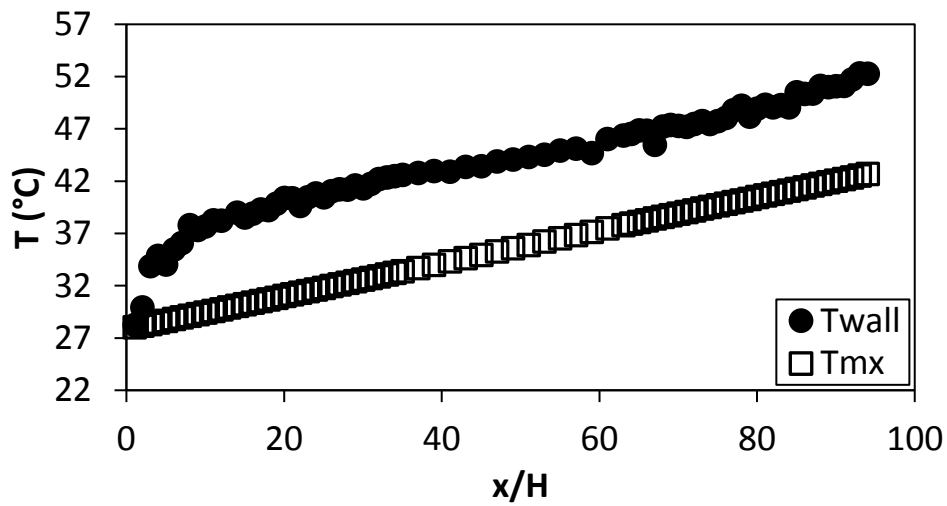


Figure F.40. Temperature plotted against x/H at $Re = 8\,000$ for setup: $d/p = 0.05$, $\theta = 45^\circ$.

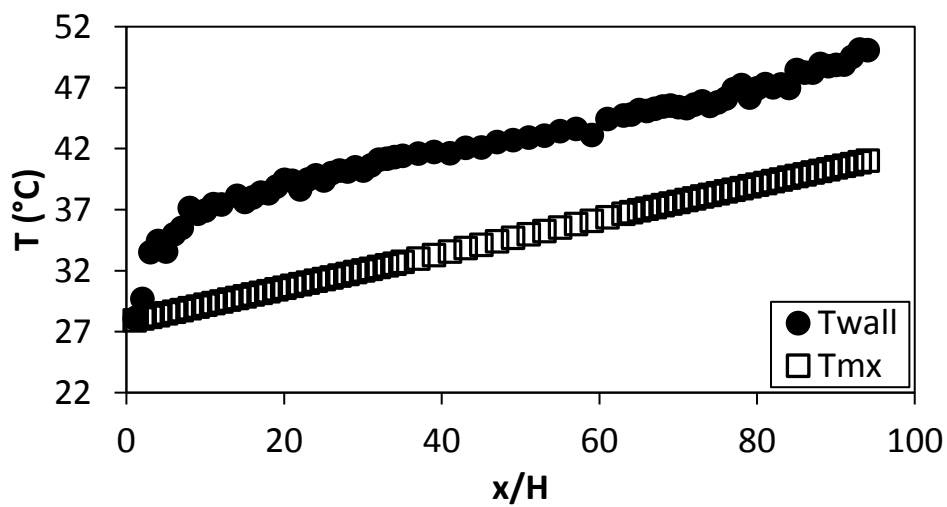


Figure F.41. Temperature plotted against x/H at $Re = 9\,000$ for setup: $d/p = 0.05$, $\theta = 45^\circ$.

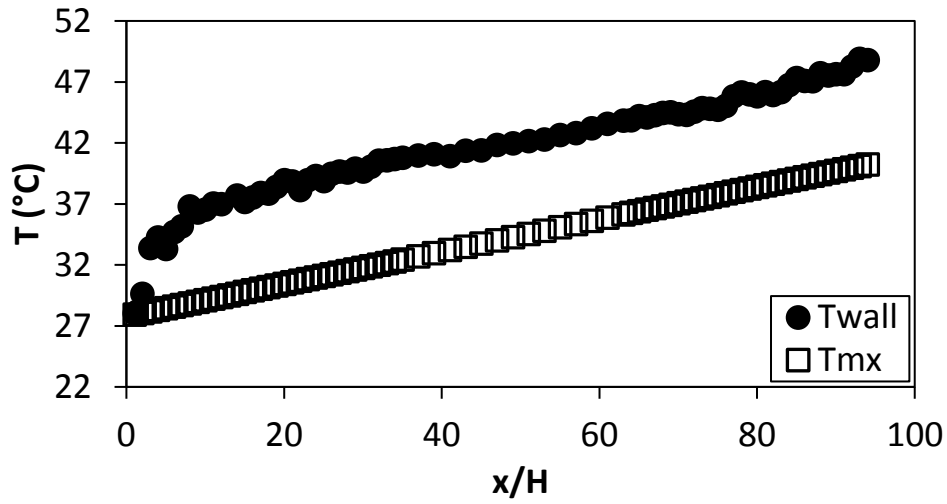


Figure F.42. Temperature plotted against x/H at $Re = 9700$ for setup: $d/p = 0.05$, $\theta = 45^\circ$.

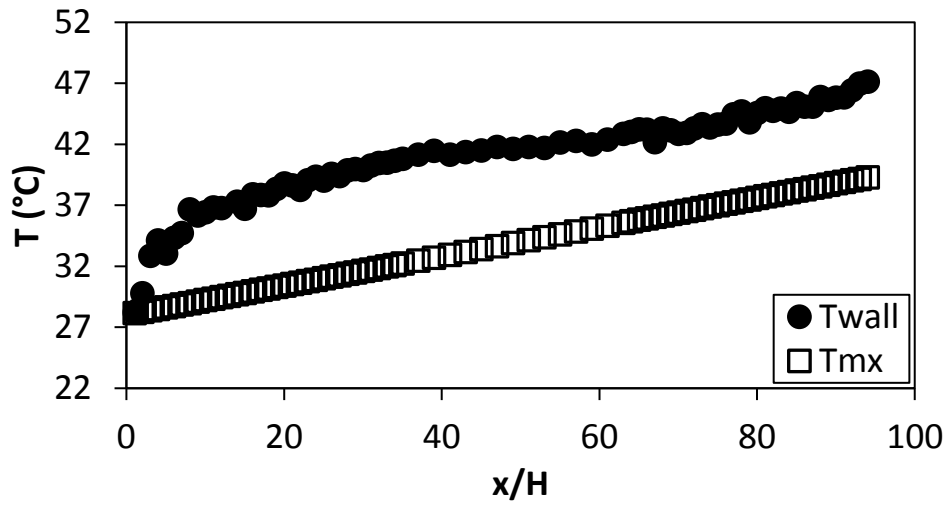


Figure F.43. Temperature plotted against x/H at $Re = 10500$ for setup: $d/p = 0.05$, $\theta = 45^\circ$.

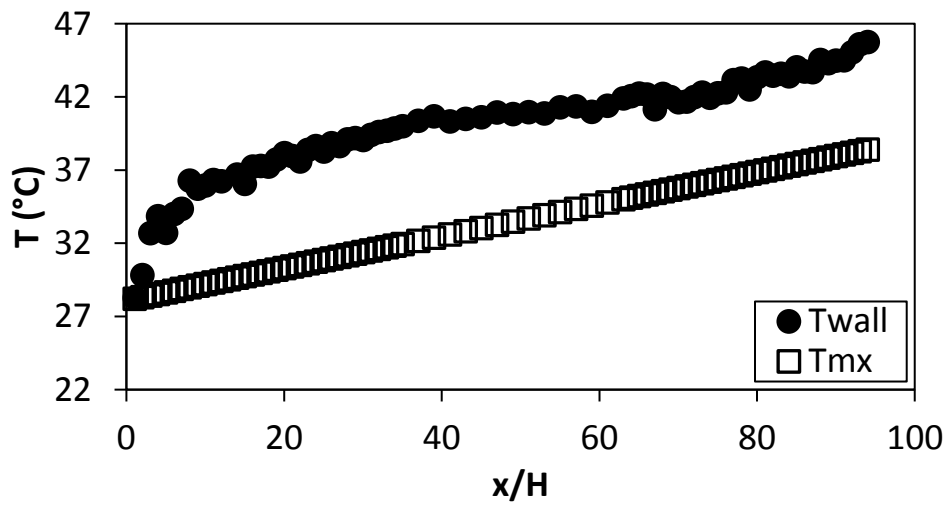


Figure F.44. Temperature plotted against x/H at $Re = 11500$ for setup: $d/p = 0.05$, $\theta = 45^\circ$.

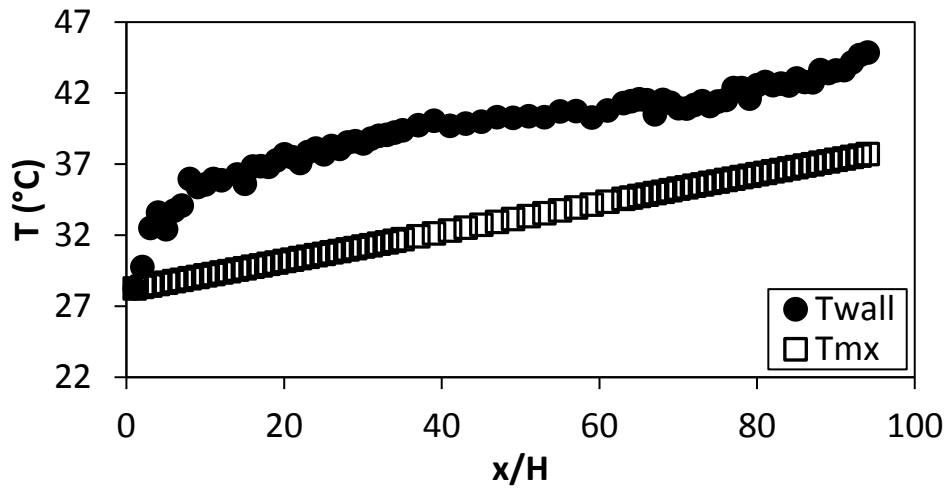


Figure F.45. Temperature plotted against x/H at $Re = 12\,500$ for setup: $d/p = 0.05$, $\theta = 45^\circ$.

F.4. Temperature data: $d/p = 0.025$, 90° orientation to the flow direction
 The temperature data for the cylindrical insert with, $d/p = 0.025$, and flow direction 90° to the cylinders is shown in Figure F.46 to Figure F.60.

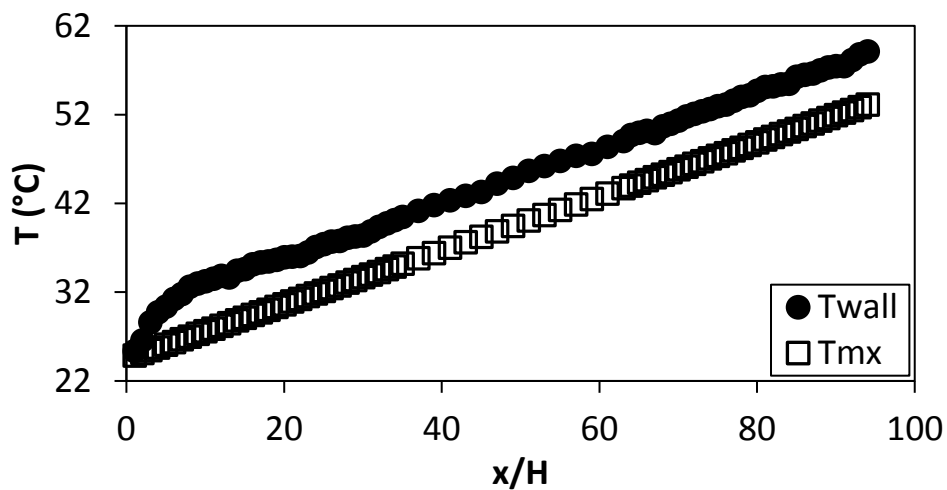


Figure F.46. Temperature plotted against x/H at $Re = 640$ for setup: $d/p = 0.025$, $\theta = 90^\circ$.

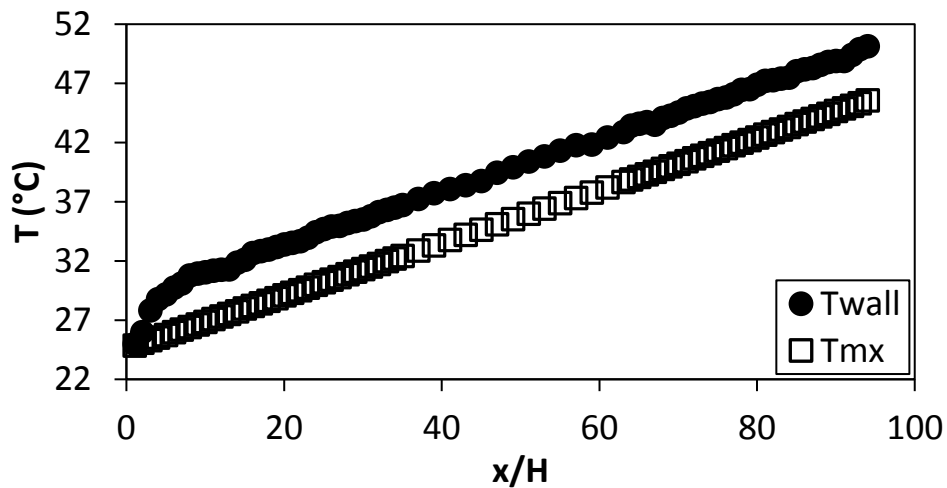


Figure F.47. Temperature plotted against x/H at $Re = 920$ for setup: $d/p = 0.025$, $\theta = 90^\circ$.

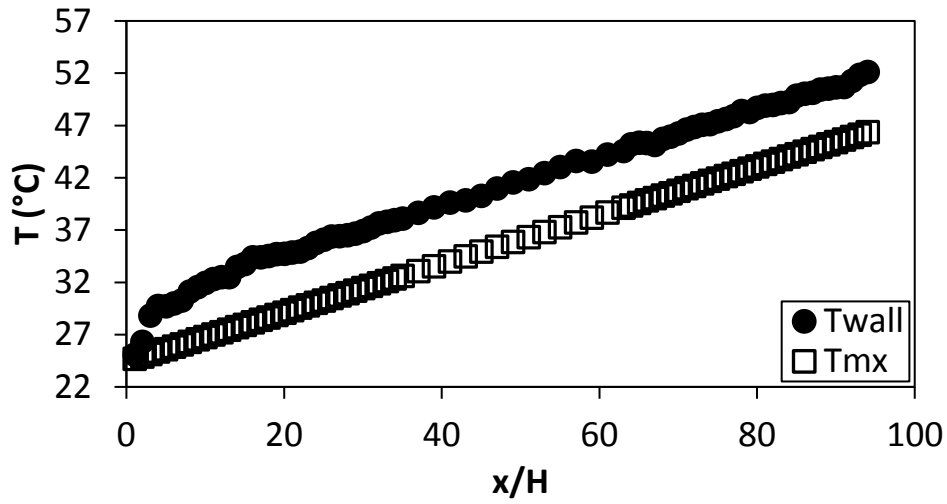


Figure F.48. Temperature plotted against x/H at $Re = 1\,400$ for setup: $d/p = 0.025$, $\theta = 90^\circ$.

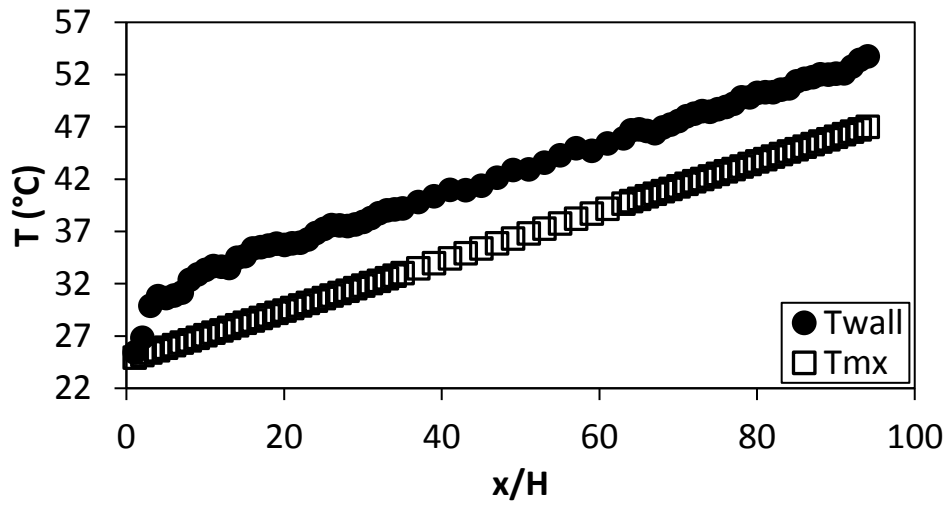


Figure F.49. Temperature plotted against x/H at $Re = 1\,800$ for setup: $d/p = 0.025$, $\theta = 90^\circ$.

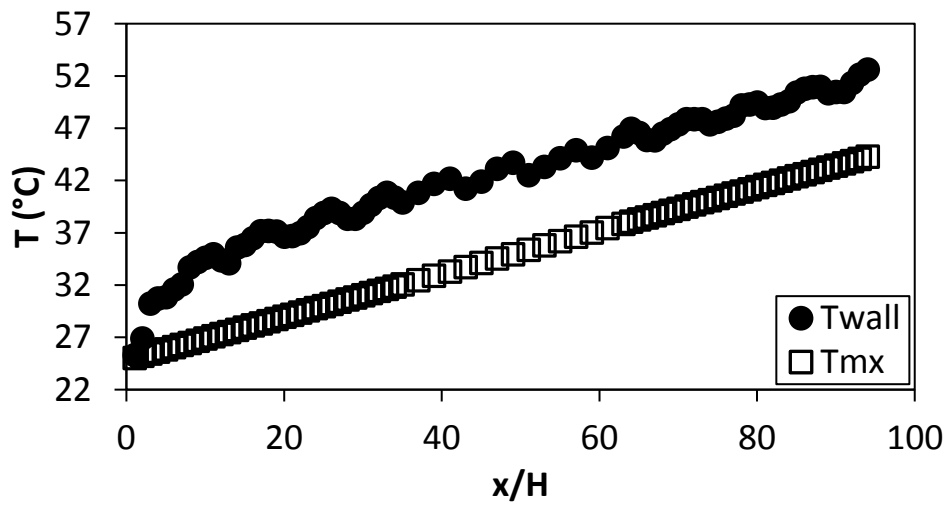


Figure F.50. Temperature plotted against x/H at $Re = 3\,000$ for setup: $d/p = 0.025$, $\theta = 90^\circ$.

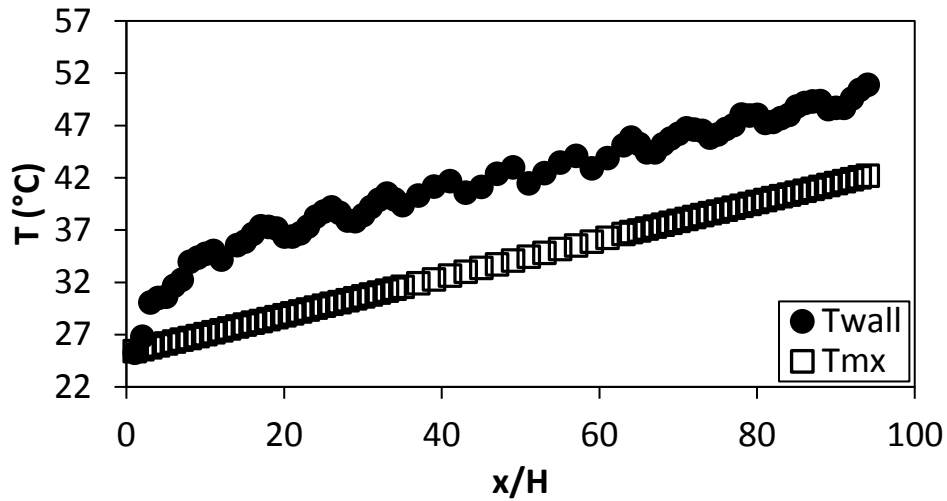


Figure F.51. Temperature plotted against x/H at $Re = 4\,000$ for setup: $d/p = 0.025$, $\theta = 90^\circ$.

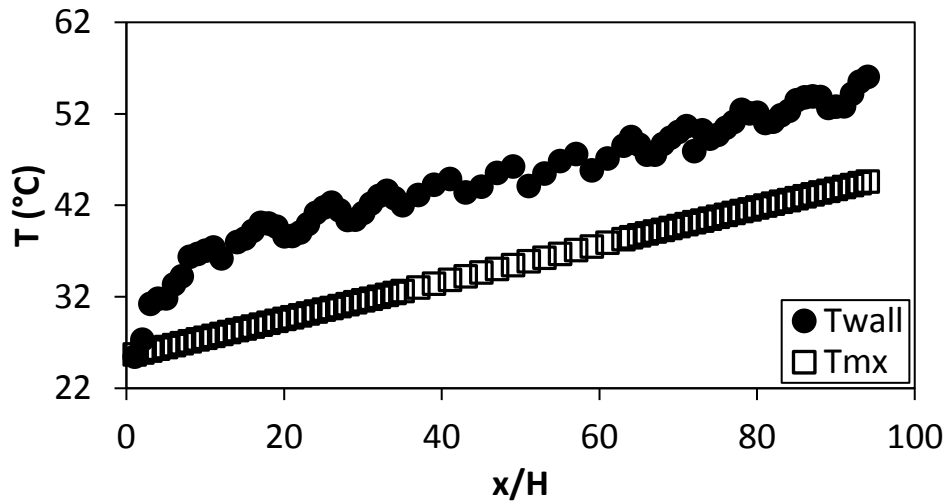


Figure F.52. Temperature plotted against x/H at $Re = 5\,000$ for setup: $d/p = 0.025$, $\theta = 90^\circ$.

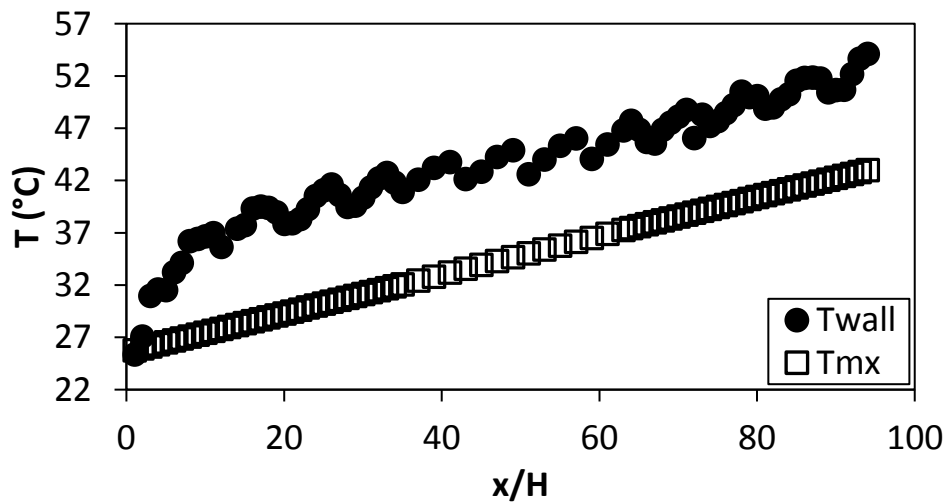


Figure F.53. Temperature plotted against x/H at $Re = 6\,000$ for setup: $d/p = 0.025$, $\theta = 90^\circ$.

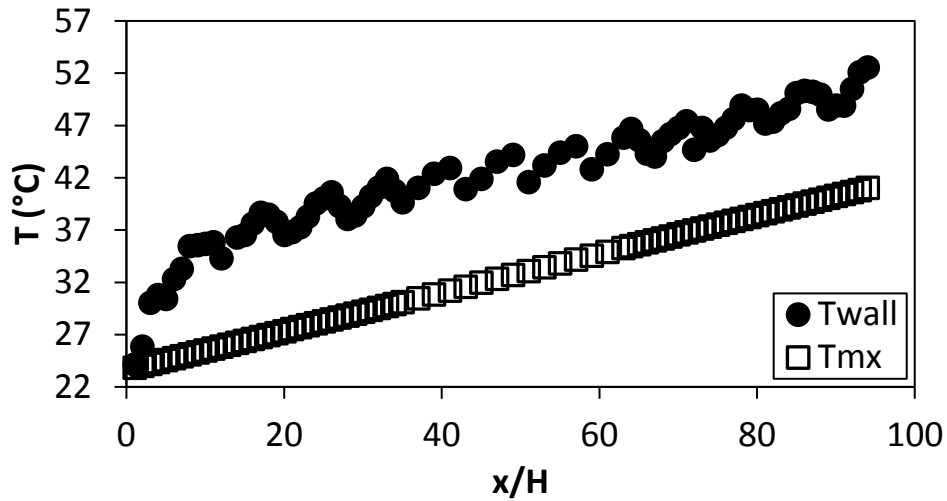


Figure F.54. Temperature plotted against x/H at $Re = 7\,000$ for setup: $d/p = 0.025$, $\theta = 90^\circ$.

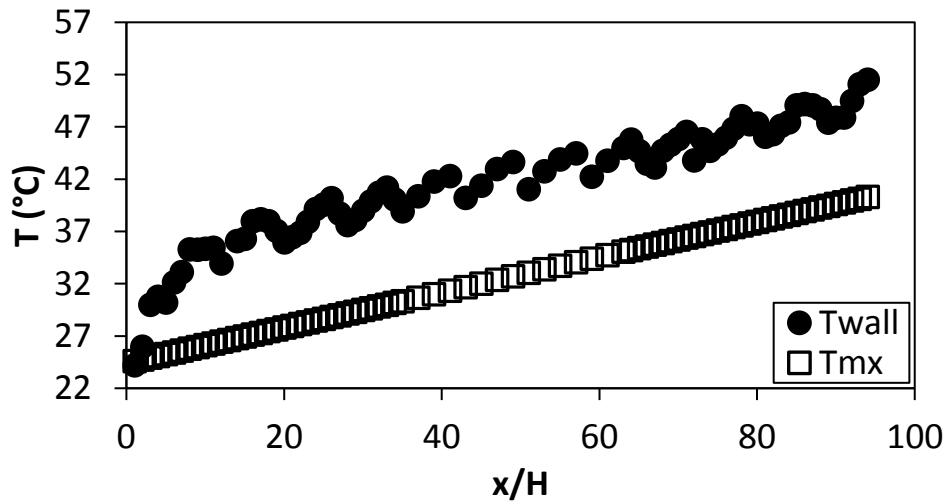


Figure F.55. Temperature plotted x/H at $Re = 8\,000$ for setup: $d/p = 0.025$, $\theta = 90^\circ$.

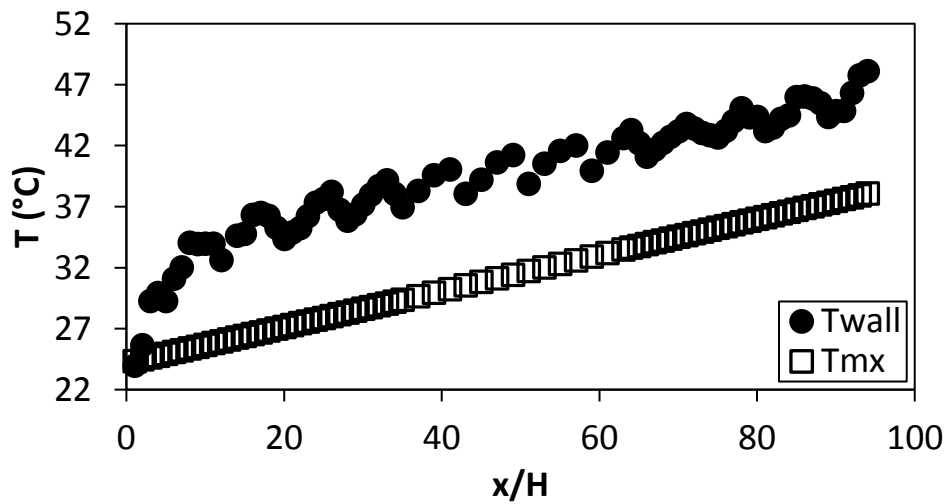


Figure F.56. Temperature plotted against x/H at $Re = 9\,000$ for setup: $d/p = 0.025$, $\theta = 90^\circ$.

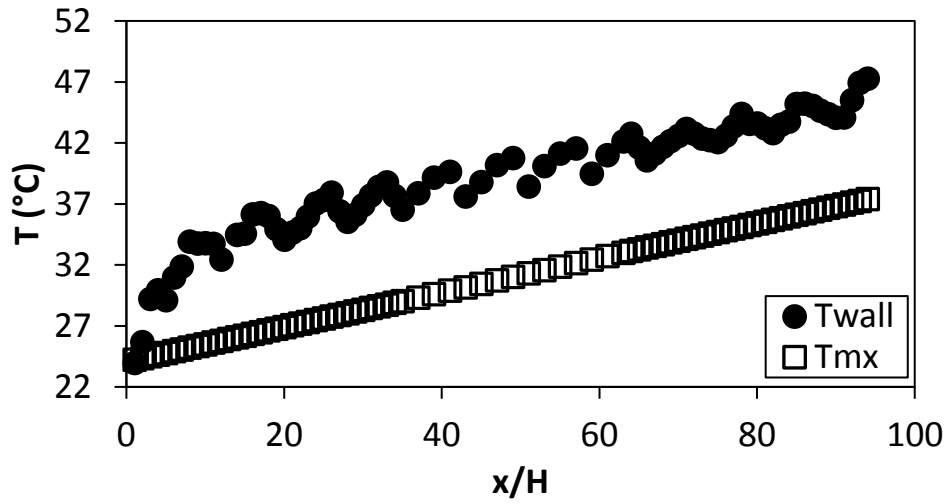


Figure F.57. Temperature plotted against x/H at $Re = 9\,700$ for setup: $d/p = 0.025$, $\theta = 90^\circ$.

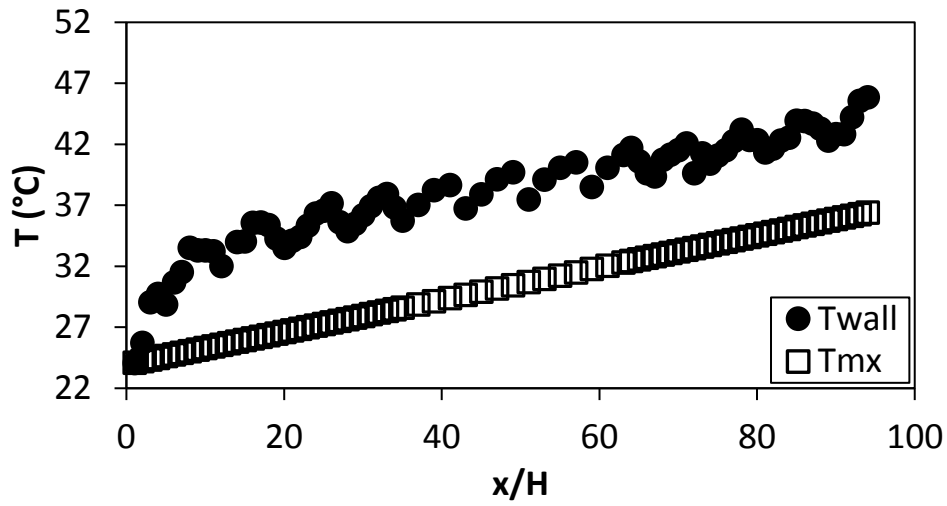


Figure F.58. Temperature plotted against x/H at $Re = 10\,500$ for setup: $d/p = 0.025$, $\theta = 90^\circ$.

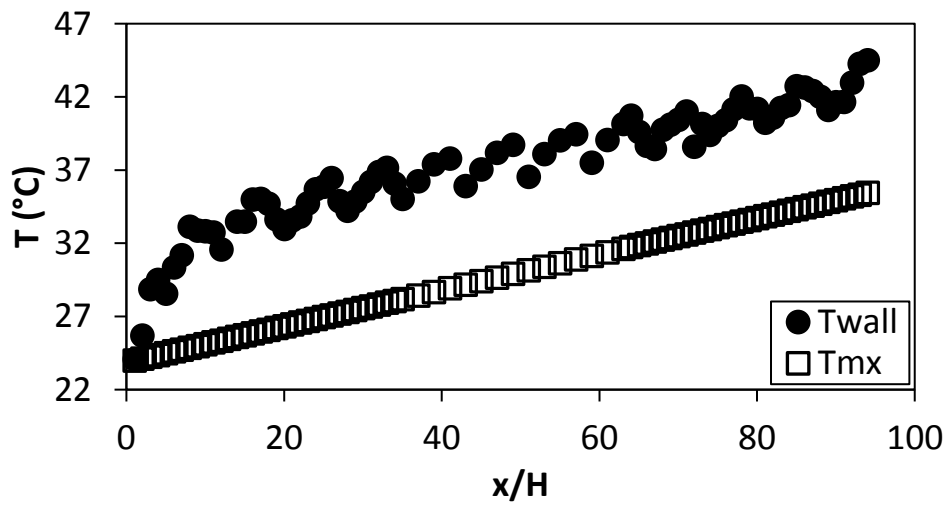


Figure F.59. Temperature plotted against the x/H at $Re = 11\,500$ for setup: $d/p = 0.025$, $\theta = 90^\circ$.

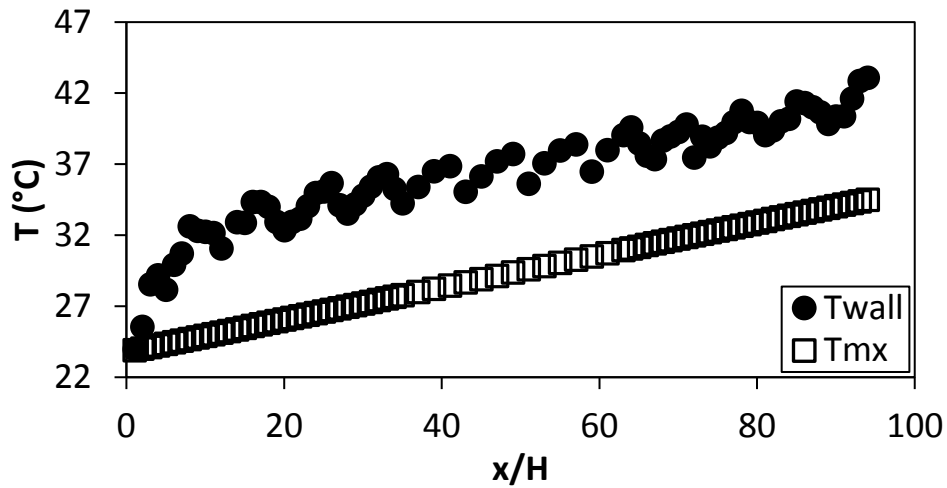


Figure F.60. Temperature plotted against the x/H at $Re = 12\,500$ for setup: $d/p = 0.025$, $\theta = 90^\circ$.

F.5. Temperature data: $d/p = 0.025$, 45° orientation to the flow direction
 The temperature data for the cylindrical insert with, $d/p = 0.025$, and flow direction 45° to the cylinders is shown in Figure F.61 to Figure F.75.

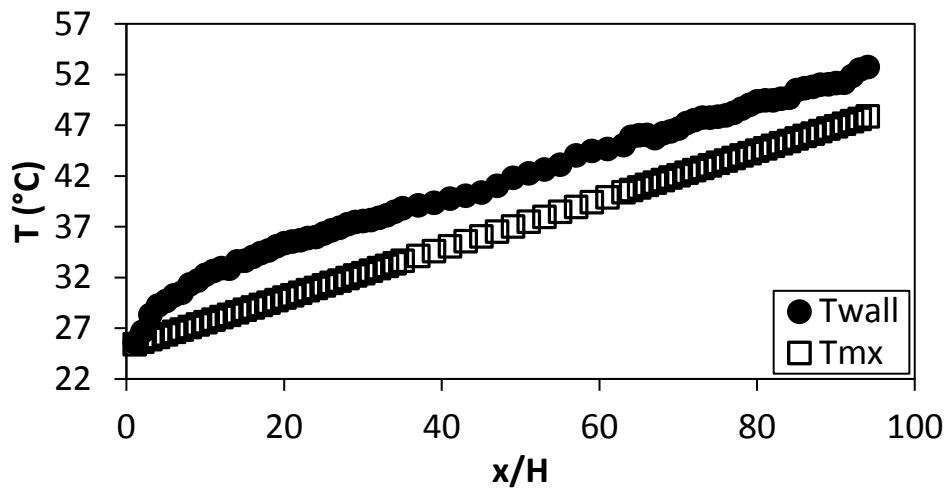


Figure F.61. Temperature plotted against x/H at $Re = 640$ for setup: $d/p = 0.025$, $\theta = 45^\circ$.

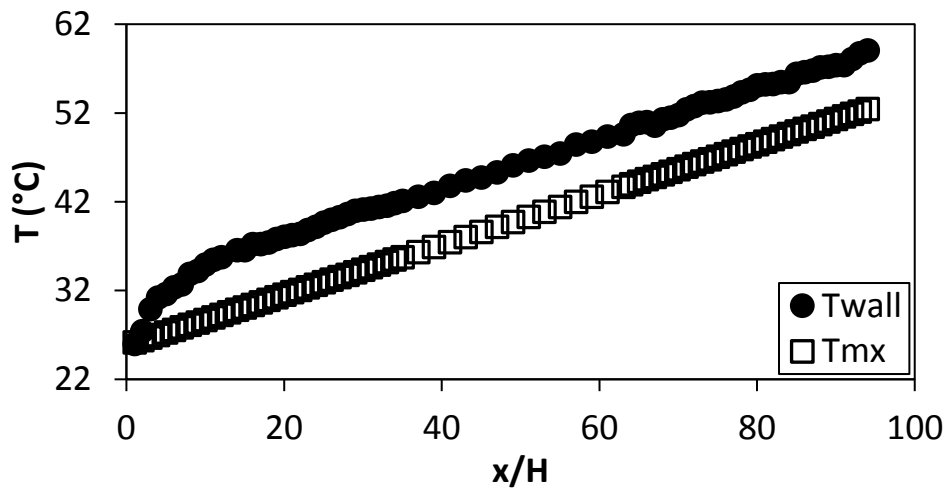


Figure F.62. Temperature plotted against x/H at $Re = 920$ for setup: $d/p = 0.025$, $\theta = 45^\circ$.

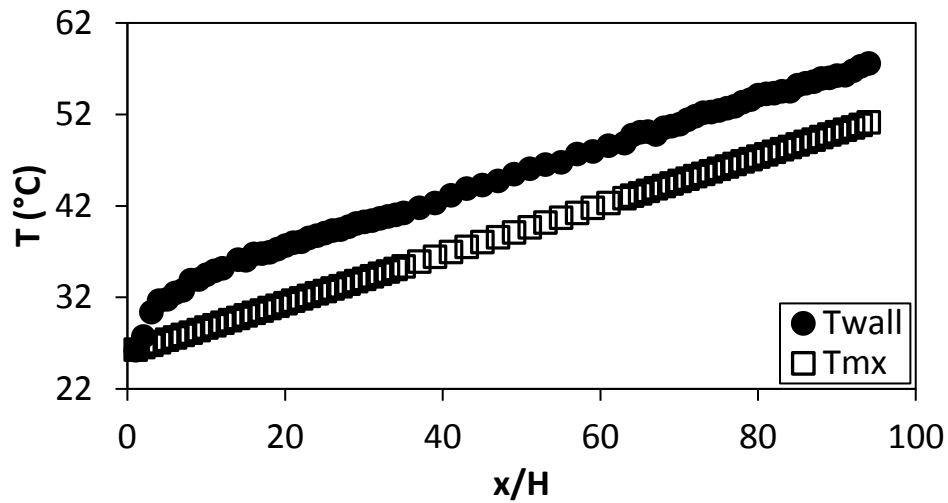


Figure F.63. Temperature plotted against x/H at $Re = 1\,400$ for setup: $d/p = 0.025$, $\theta = 45^\circ$.

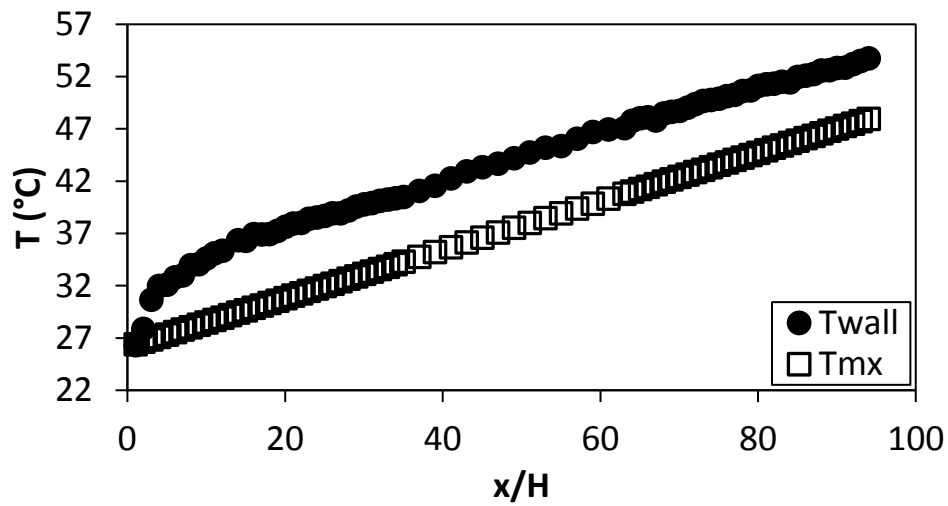


Figure F.64. Temperature plotted against x/H at $Re = 1\,800$ for setup: $d/p = 0.025$, $\theta = 45^\circ$.

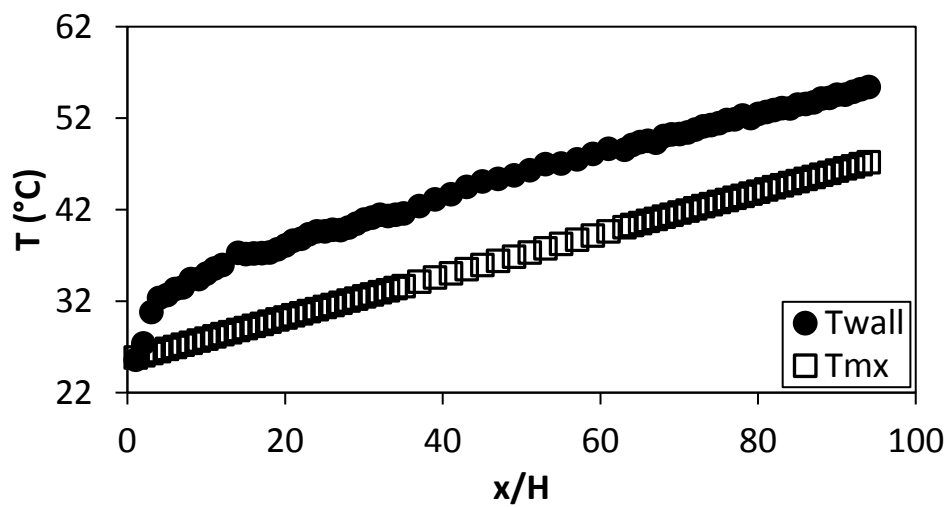


Figure F.65. Temperature plotted against x/H at $Re = 3\,000$ for setup: $d/p = 0.025$, $\theta = 45^\circ$.

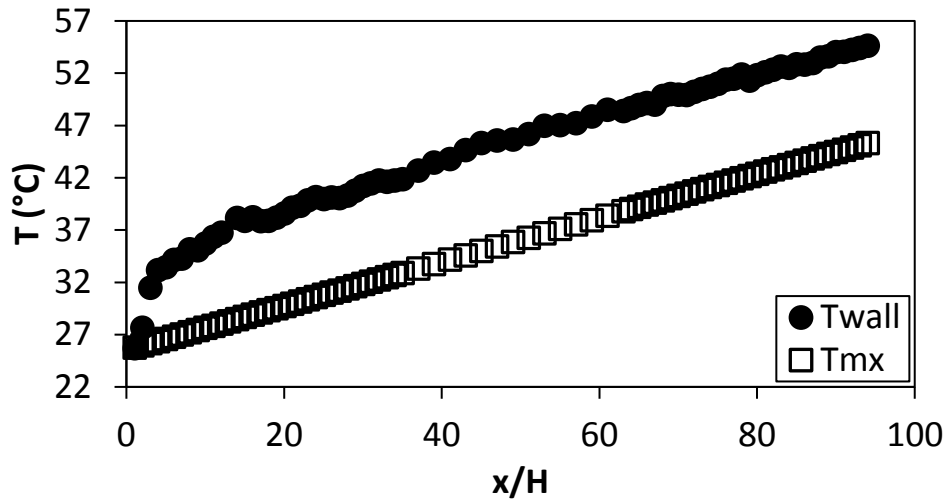


Figure F.66. Temperature plotted against x/H at $Re = 4\,000$ for setup: $d/p = 0.025$, $\theta = 45^\circ$.

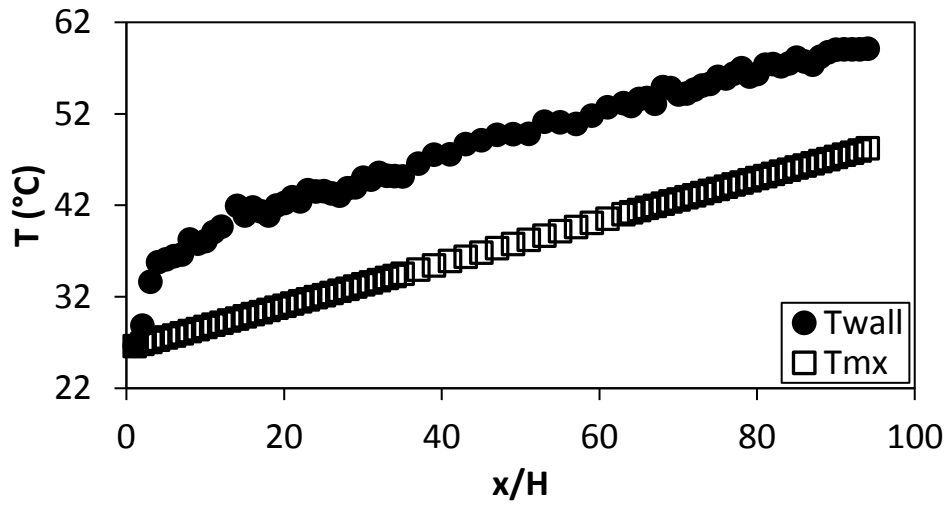


Figure F.67. Temperature plotted against x/H at $Re = 5\,000$ for setup: $d/p = 0.025$, $\theta = 45^\circ$.

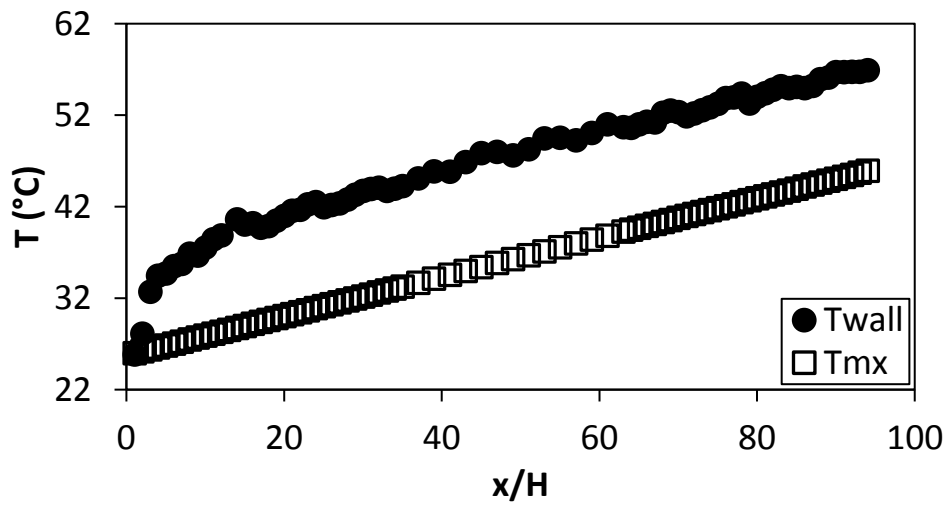


Figure F.68. Temperature plotted against x/H at $Re = 6\,000$ for setup: $d/p = 0.025$, $\theta = 45^\circ$.

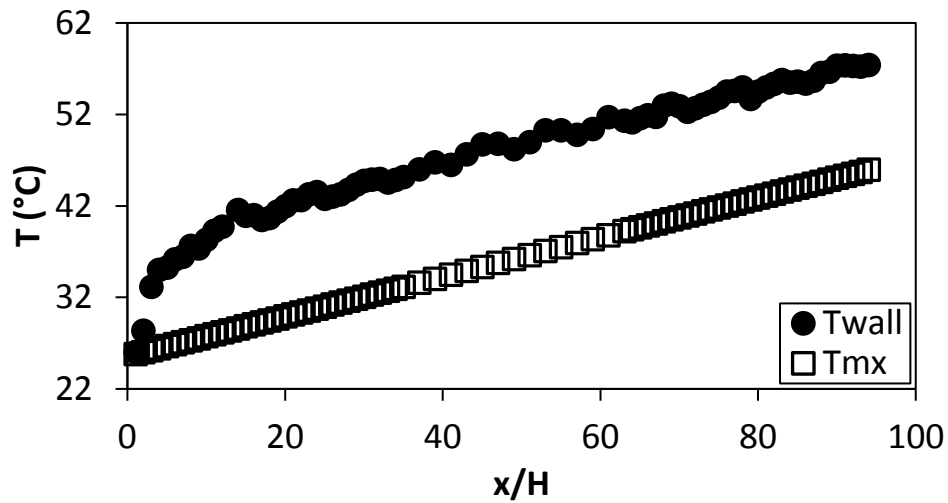


Figure F.69. Temperature plotted against x/H at $Re = 7\,000$ for setup: $d/p = 0.025$, $\theta = 45^\circ$.

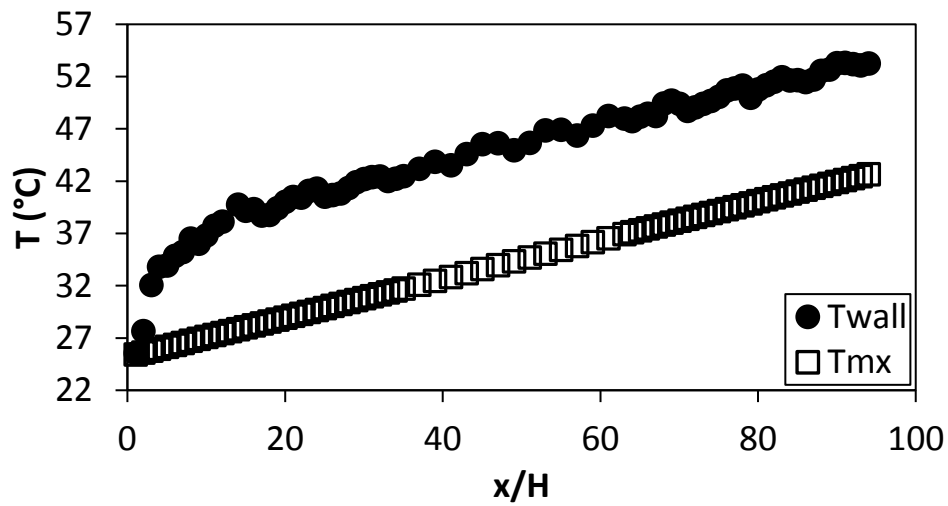


Figure F.70. Temperature plotted against x/H at $Re = 8\,000$ for setup: $d/p = 0.025$, $\theta = 45^\circ$.

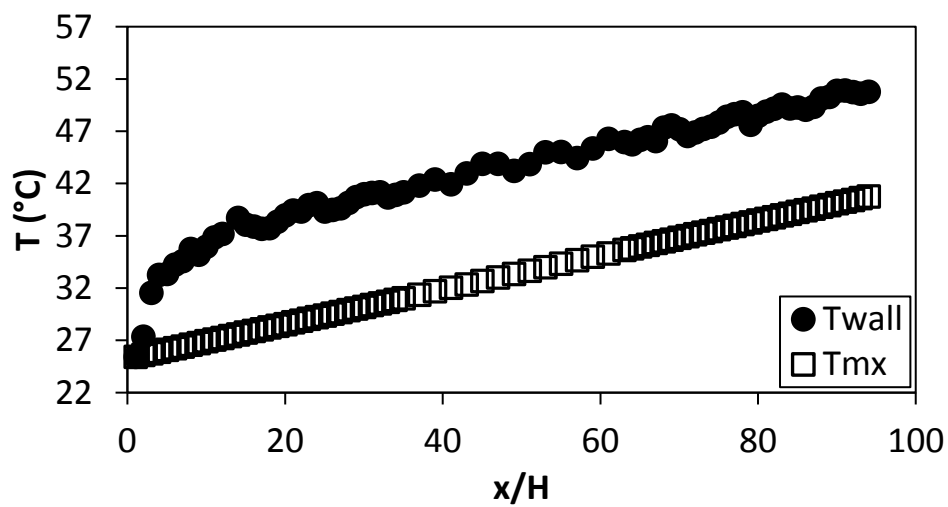


Figure F.71. Temperature plotted against x/H at $Re = 9\,000$ for setup: $d/p = 0.025$, $\theta = 45^\circ$.

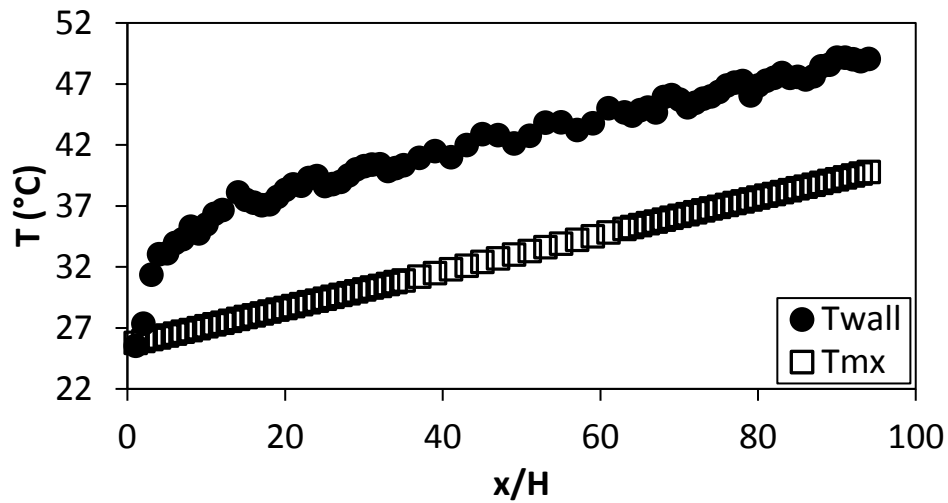


Figure F.72. Temperature plotted against x/H at $Re = 9\,700$ for setup: $d/p = 0.025$, $\theta = 45^\circ$.

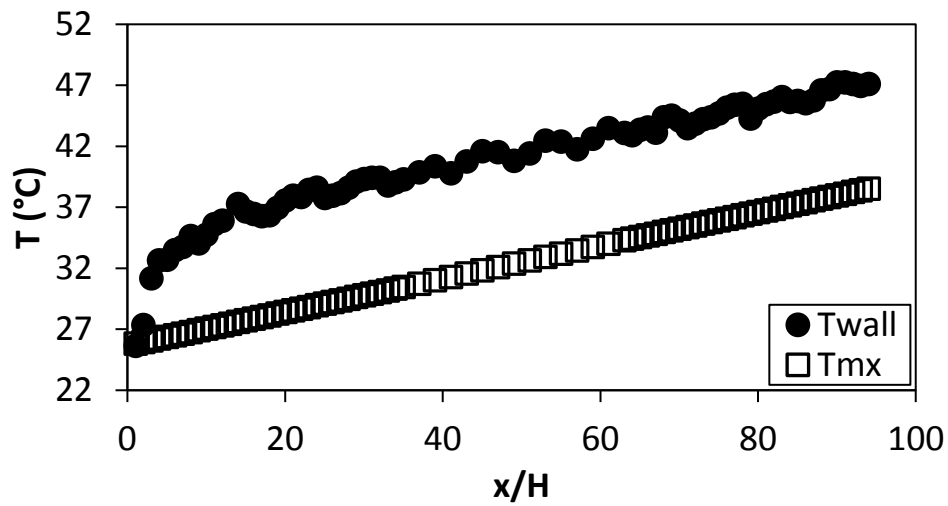


Figure F.73. Temperature plotted against x/H at $Re = 10\,500$ for setup: $d/p = 0.025$, $\theta = 45^\circ$.

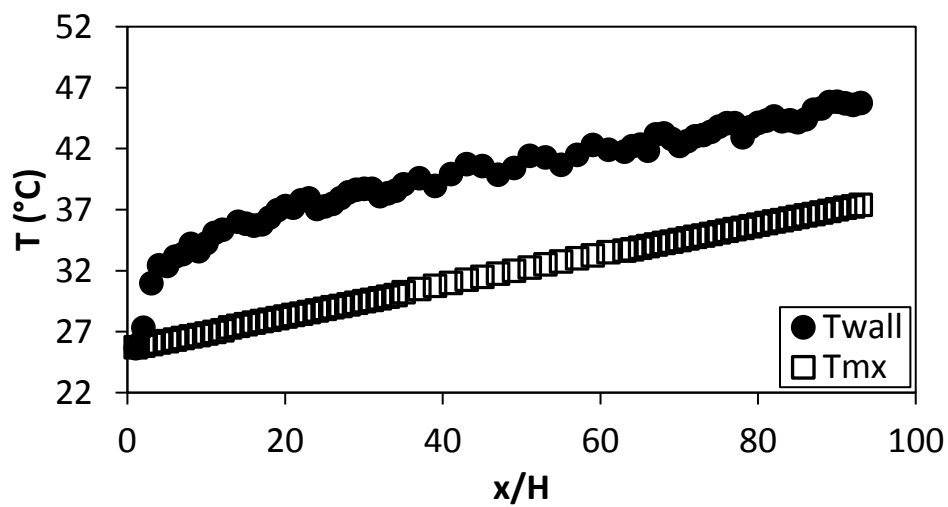


Figure F.74. Temperature plotted against x/H at $Re = 11\,500$ for setup: $d/p = 0.025$, $\theta = 45^\circ$.

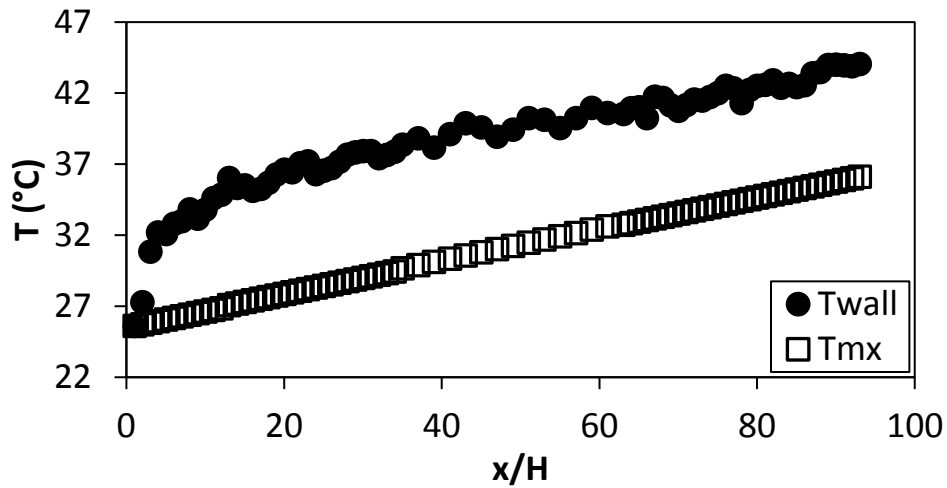


Figure F.75. Temperature plotted against x/H at $Re = 12\,500$ for setup: $d/p = 0.025$, $\theta = 45^\circ$.

F.6. Temperature data: $d/p = 0.2$, 90° orientation to the flow direction
 The temperature data for the cylindrical insert with, $d/p = 0.2$, and flow direction 90° to the cylinders is shown in Figure F.76 to Figure F.87.

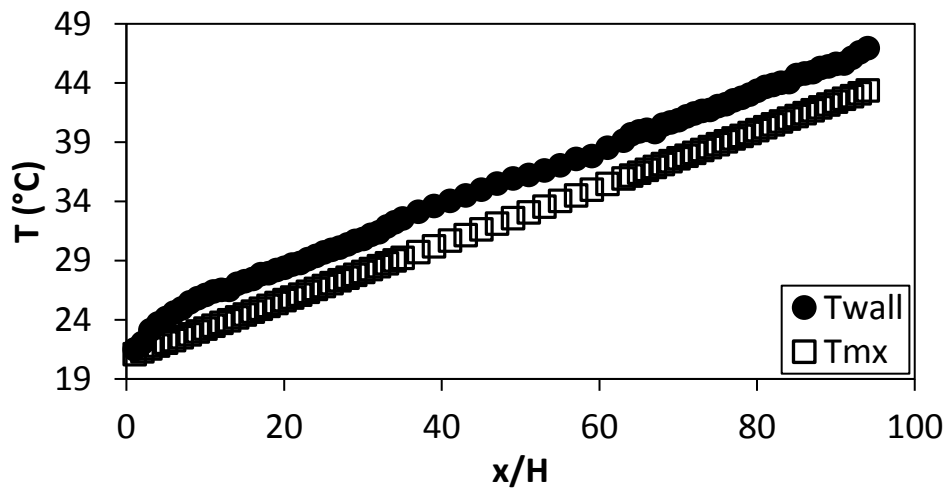


Figure F.76. Temperature plotted against x/H at $Re = 640$ for setup: $d/p = 0.2$, $\theta = 90^\circ$.

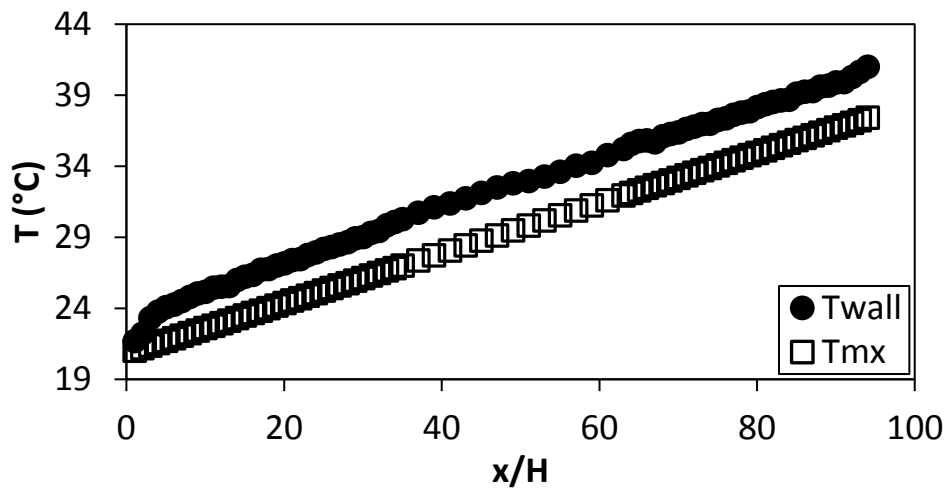


Figure F.77. Temperature plotted against x/H at $Re = 920$ for setup: $d/p = 0.2$, $\theta = 90^\circ$.

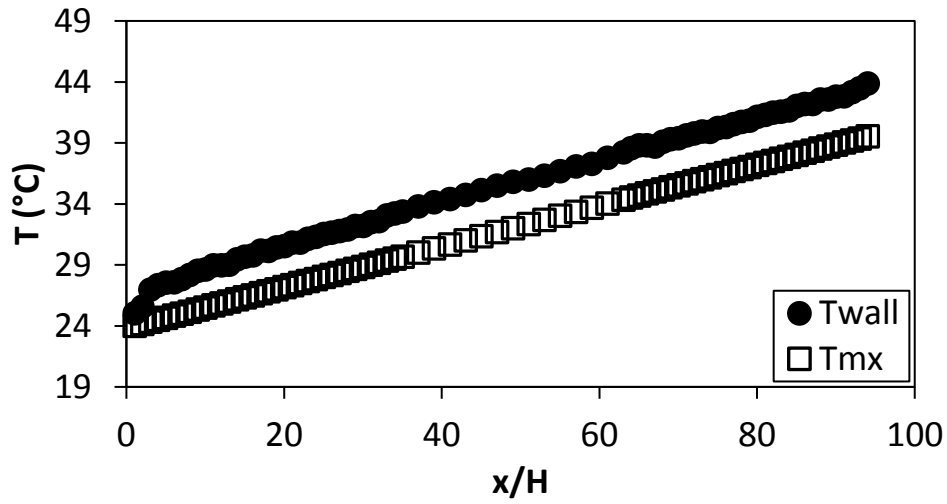


Figure F.78. Temperature plotted against x/H at $Re = 1\ 400$ for setup: $d/p = 0.2$, $\theta = 90^\circ$.

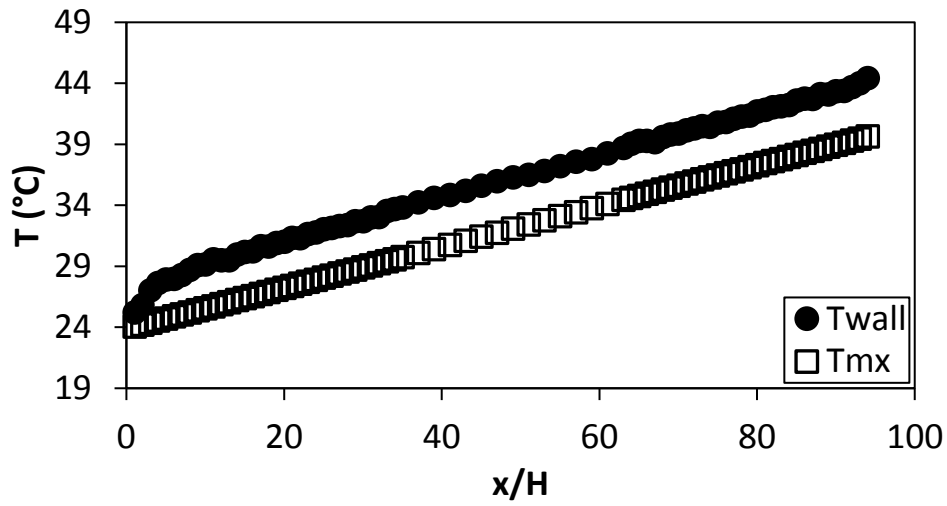


Figure F.79. Temperature plotted against x/H at $Re = 1\ 800$ for setup: $d/p = 0.2$, $\theta = 90^\circ$.

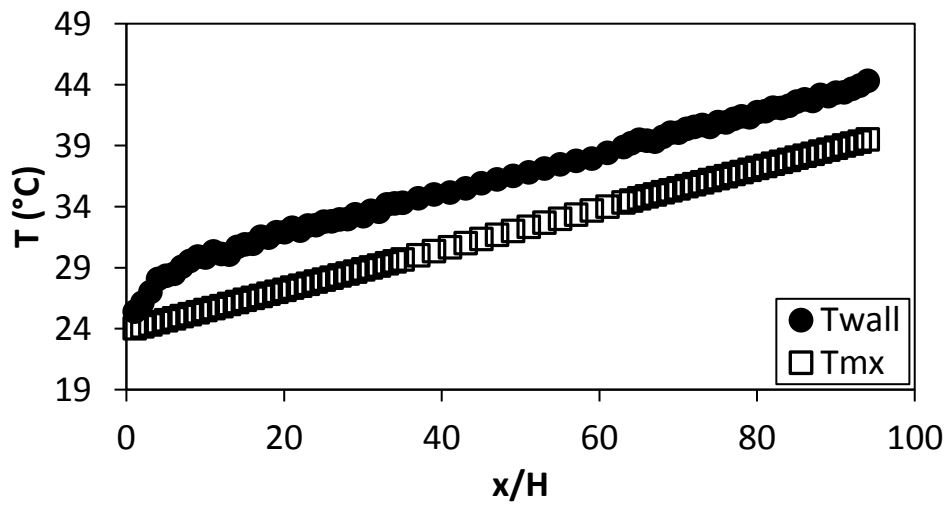


Figure F.80. Temperature plotted against x/H at $Re = 3\ 000$ for setup: $d/p = 0.2$, $\theta = 90^\circ$.

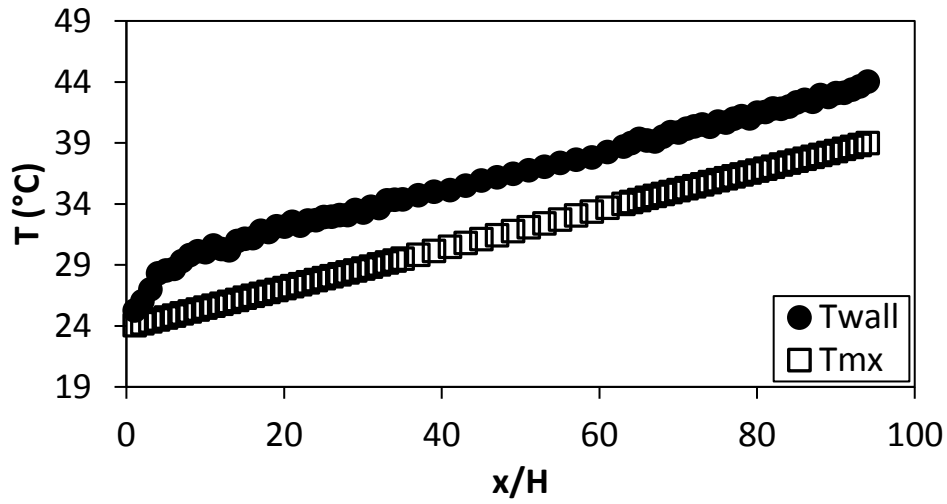


Figure F.81. Temperature plotted against x/H at $Re = 4\,000$ for setup: $d/p = 0.2$, $\theta = 90^\circ$.

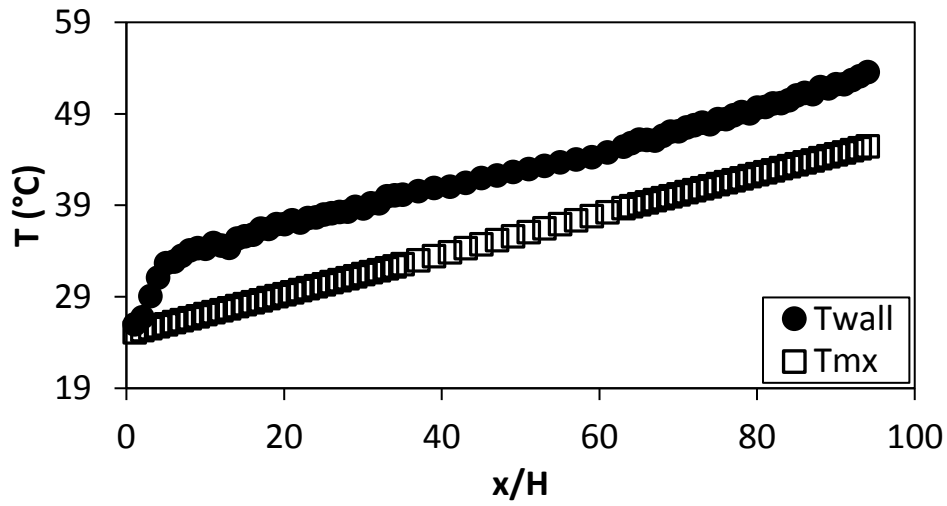


Figure F.82. Temperature plotted against x/H at $Re = 5\,000$ for setup: $d/p = 0.2$, $\theta = 90^\circ$.

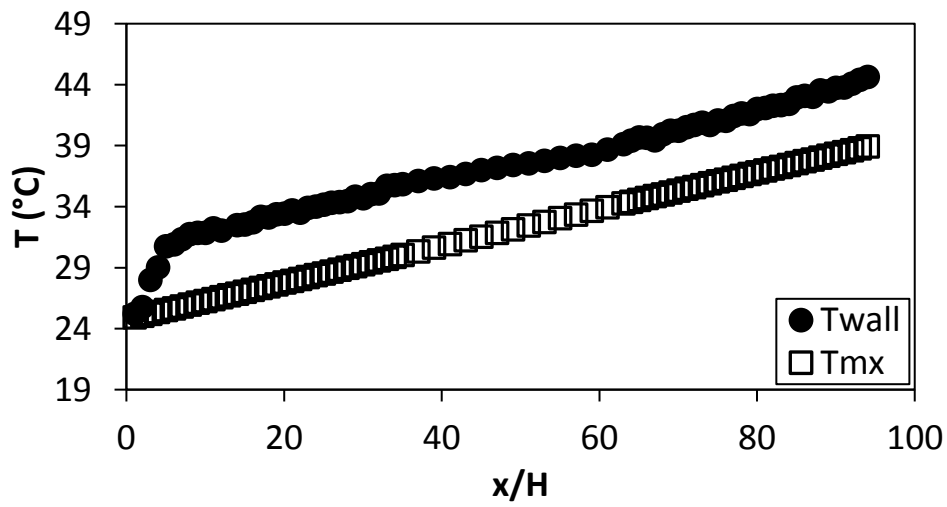


Figure F.83. Temperature plotted against x/H at $Re = 6\,000$ for setup: $d/p = 0.2$, $\theta = 90^\circ$.

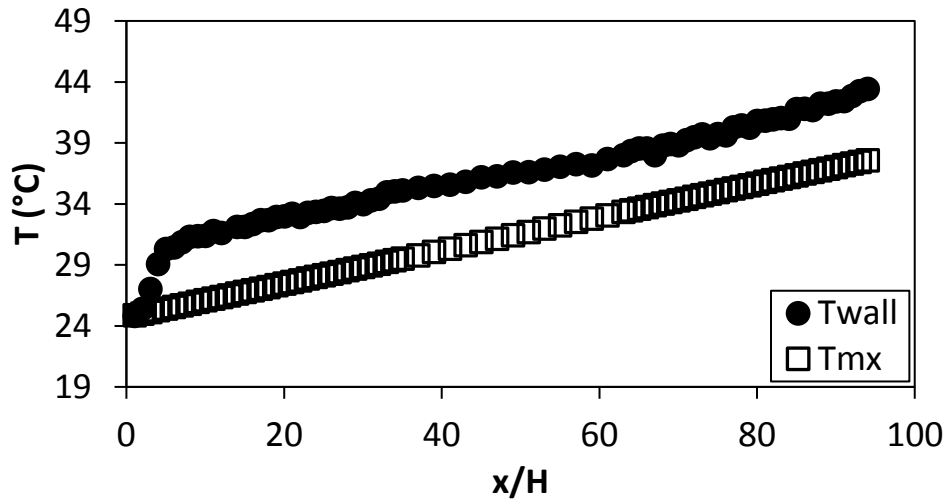


Figure F.84. Temperature plotted against x/H at $Re = 7\,000$ for setup: $d/p = 0.2$, $\theta = 90^\circ$.

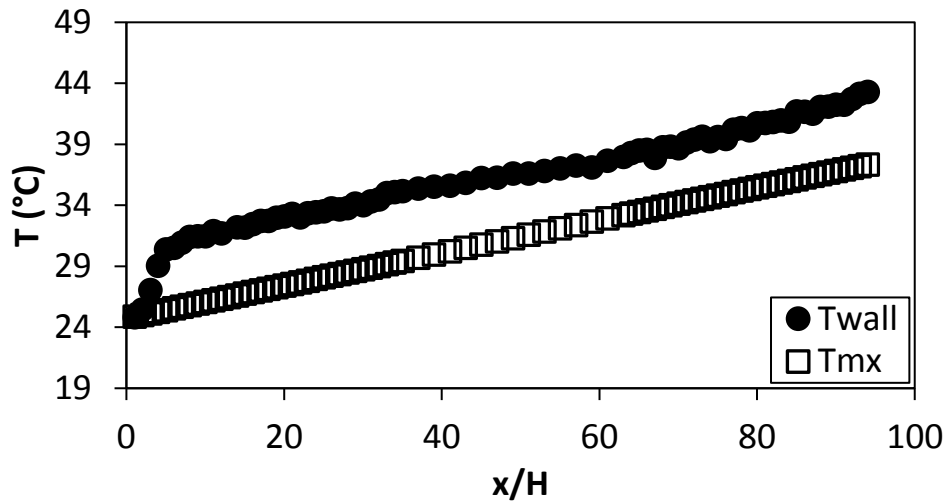


Figure F.85. Temperature plotted against x/H at $Re = 8\,000$ for setup: $d/p = 0.2$, $\theta = 90^\circ$.

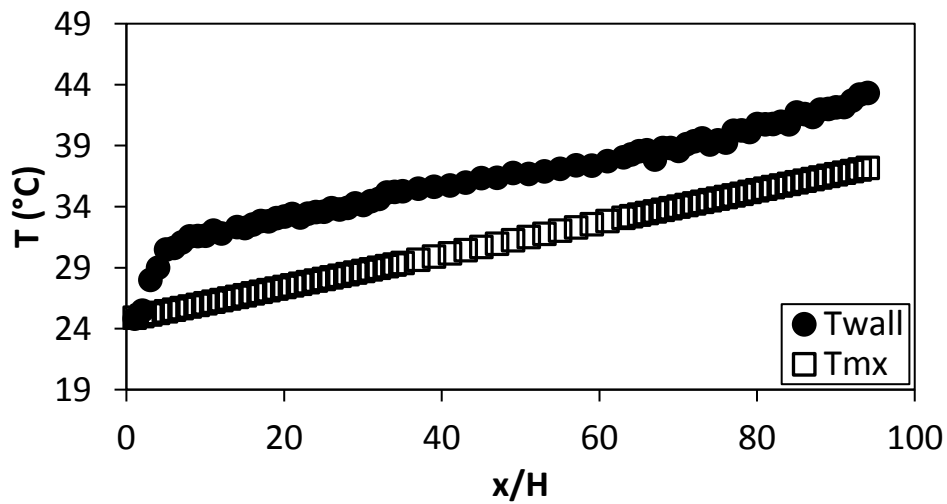


Figure F.86. Temperature plotted against x/H at $Re = 9\,000$ for setup: $d/p = 0.2$, $\theta = 90^\circ$.

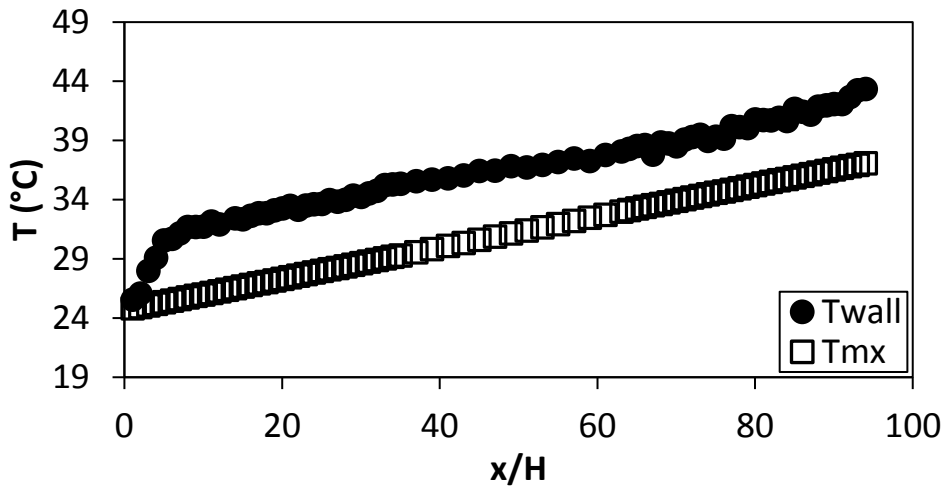


Figure F.87. Temperature plotted against x/H at $Re = 9\,700$ for setup: $d/p = 0.2$, $\theta = 90^\circ$.

F.7. Temperature data: $d/p = 0.2$, 45° orientation to the flow direction

The temperature data for the cylindrical insert with, $d/p = 0.2$, and flow direction 90° to the cylinders is shown in Figure F.88 to Figure F.100.

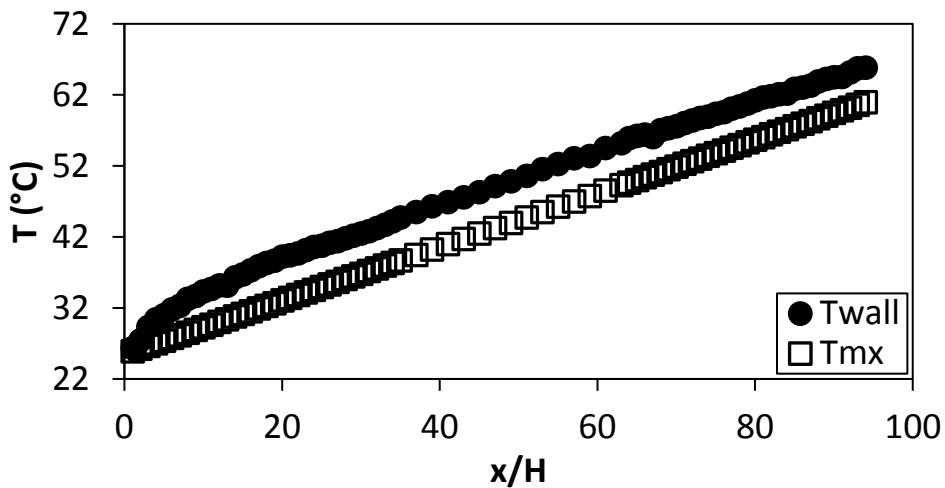


Figure F.88. Temperature plotted against x/H at $Re = 640$ for setup: $d/p = 0.2$, $\theta = 45^\circ$.

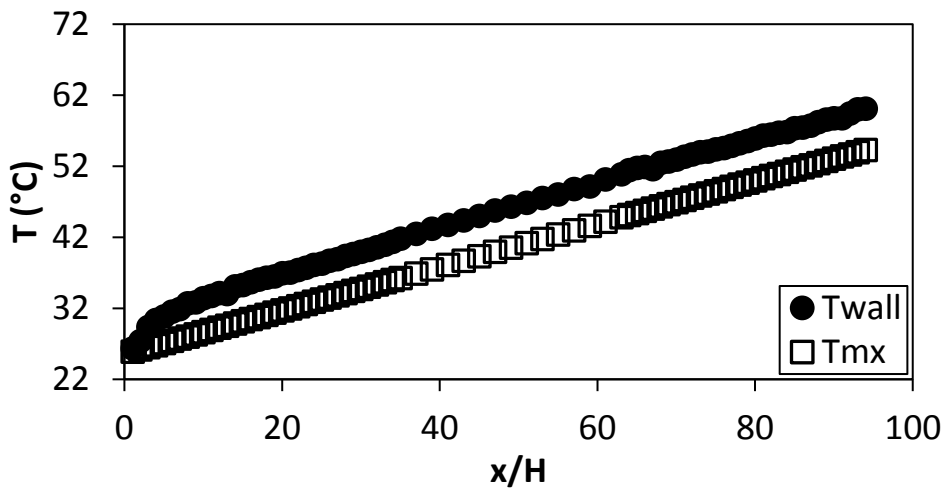


Figure F.89. Temperature plotted against x/H at $Re = 920$ for setup: $d/p = 0.2$, $\theta = 45^\circ$.

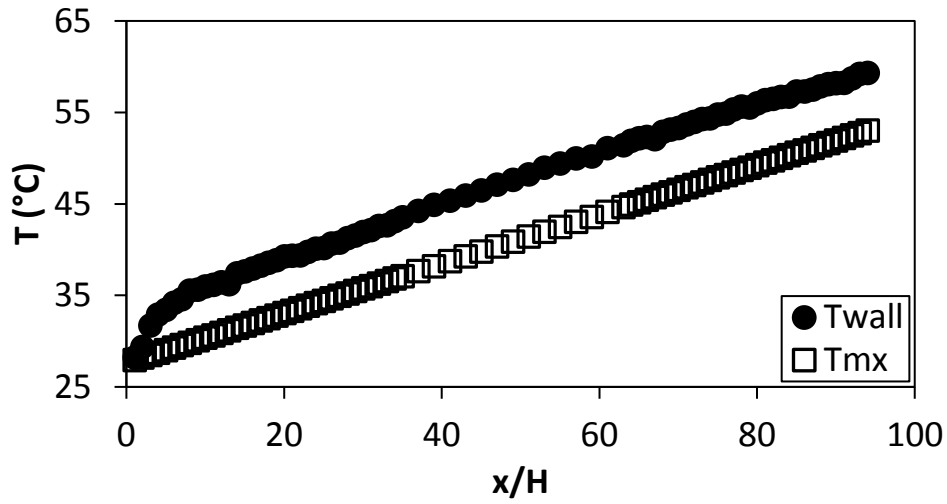


Figure F.90. Temperature plotted against x/H at $Re = 1\,400$ for setup: $d/p = 0.2$, $\theta = 45^\circ$.

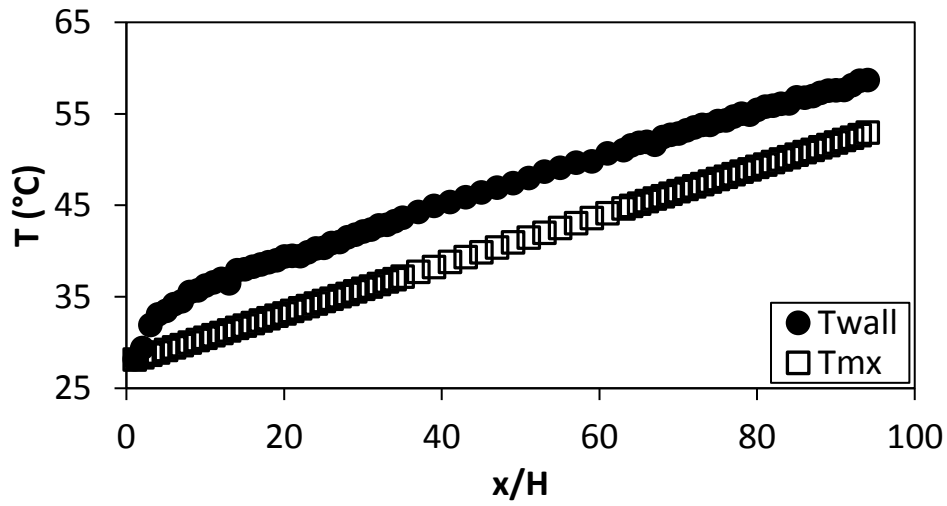


Figure F.91. Temperature plotted against x/H at $Re = 1\,800$ for setup: $d/p = 0.2$, $\theta = 45^\circ$.

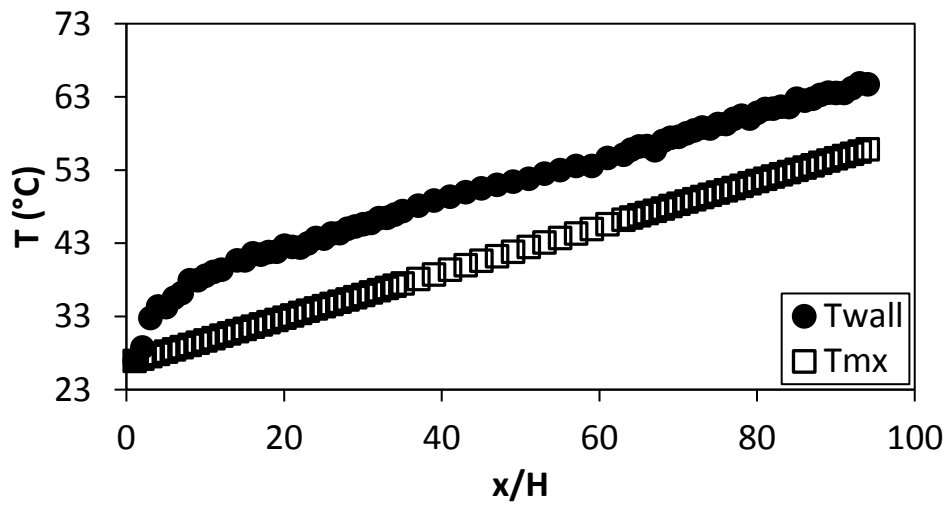


Figure F.92. Temperature plotted against x/H at $Re = 3\,000$ for setup: $d/p = 0.2$, $\theta = 45^\circ$.

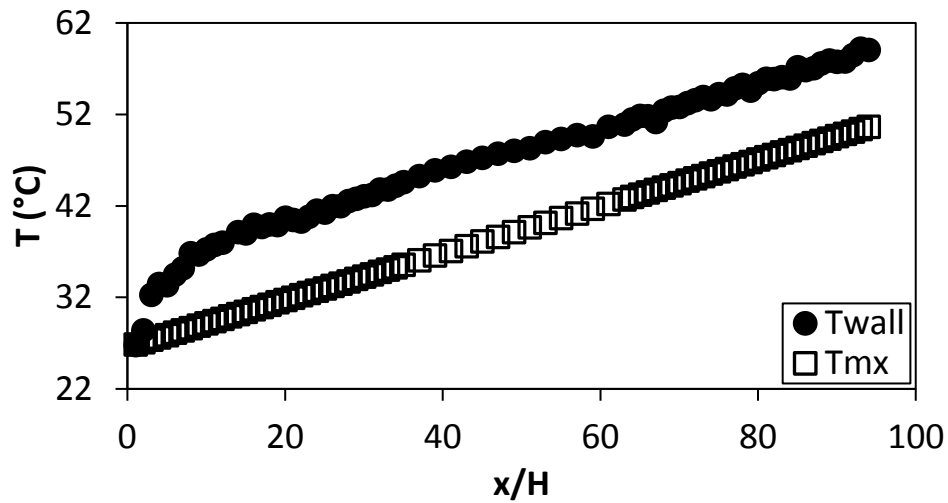


Figure F.93. Temperature plotted against x/H at $Re = 4\,000$ for setup: $d/p = 0.2$, $\theta = 45^\circ$.

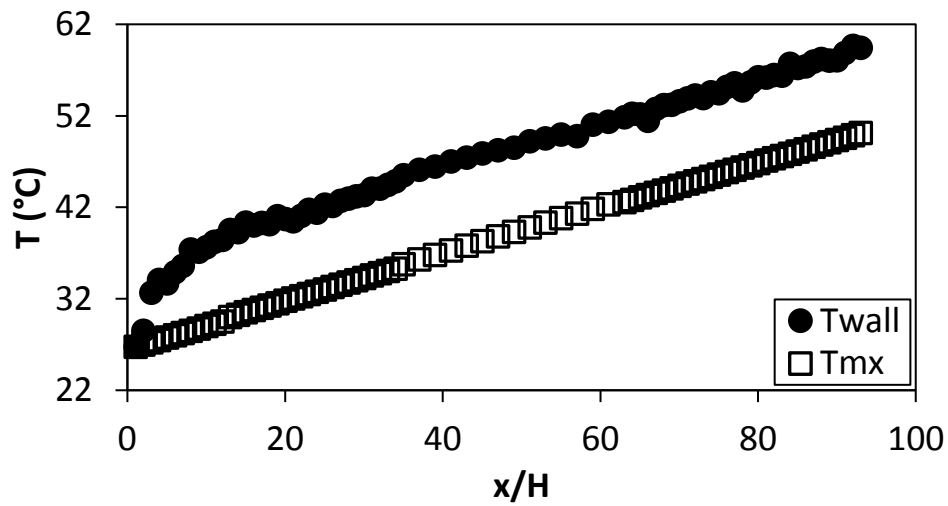


Figure F.94. Temperature plotted against x/H at $Re = 5\,000$ for setup: $d/p = 0.2$, $\theta = 45^\circ$.

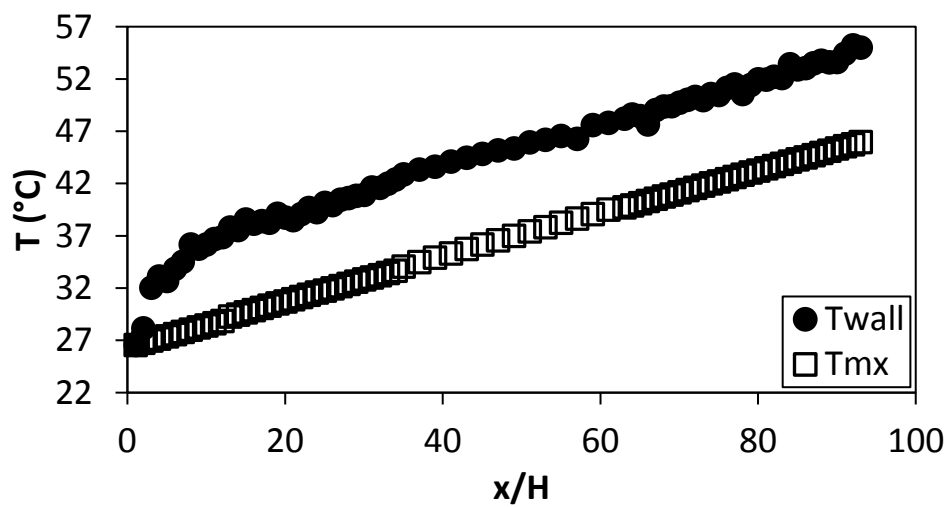


Figure F.95. Temperature plotted against x/H at $Re = 6\,000$ for setup: $d/p = 0.2$, $\theta = 45^\circ$.

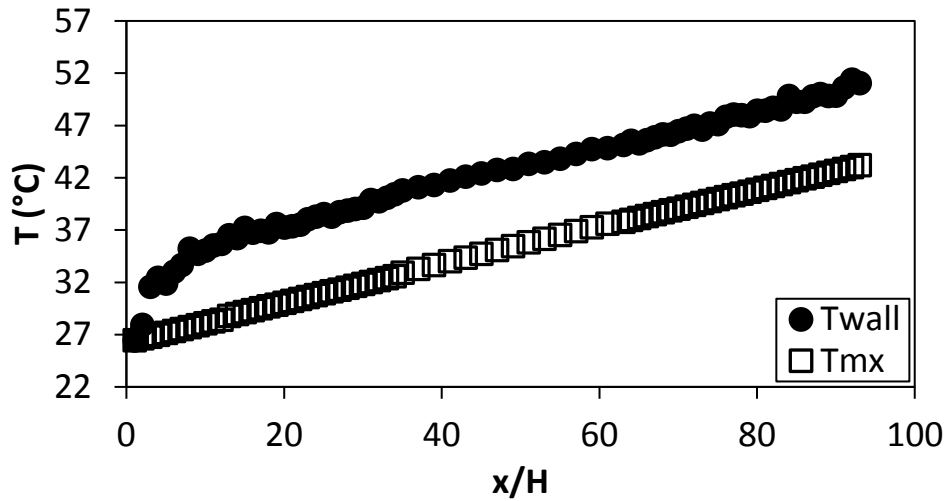


Figure F.96. Temperature plotted against x/H at $Re = 7\,000$ for setup: $d/p = 0.2$, $\theta = 45^\circ$.

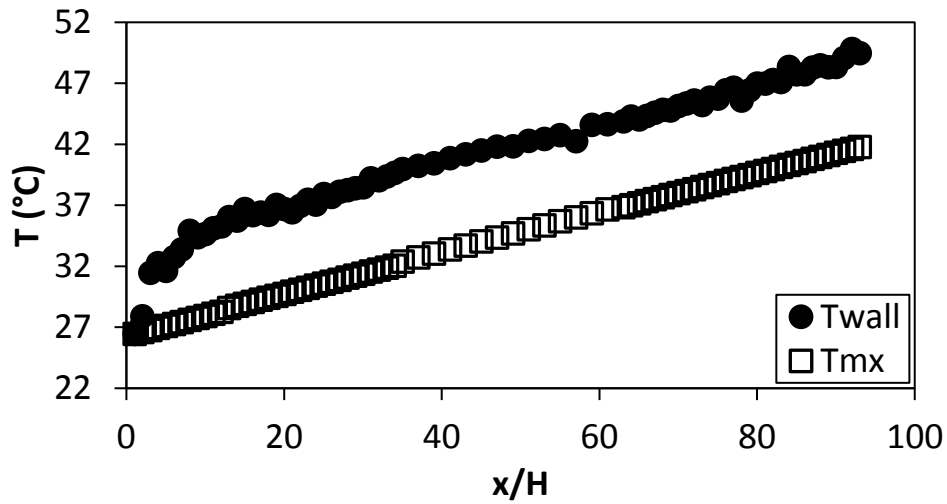


Figure F.97. Temperature plotted against x/H at $Re = 8\,000$ for setup: $d/p = 0.2$, $\theta = 45^\circ$.

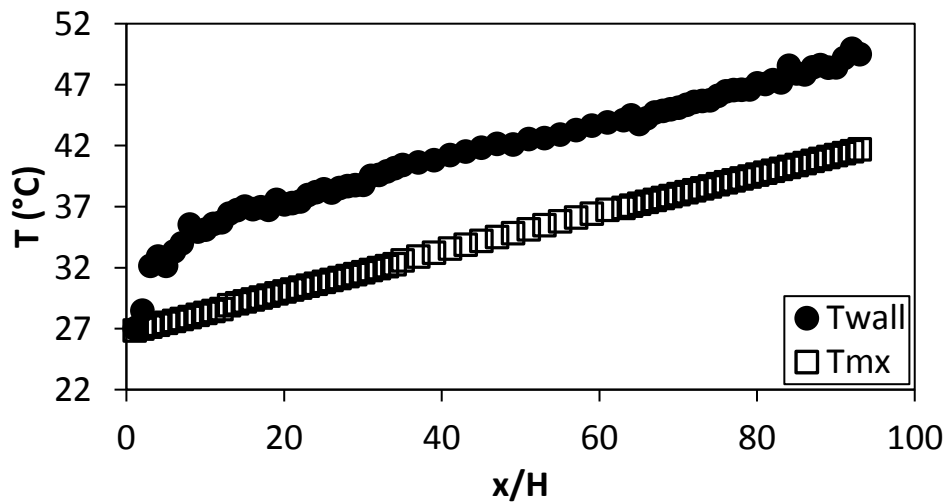


Figure F.98. Temperature plotted against x/H at $Re = 9\,000$ for setup: $d/p = 0.2$, $\theta = 45^\circ$.

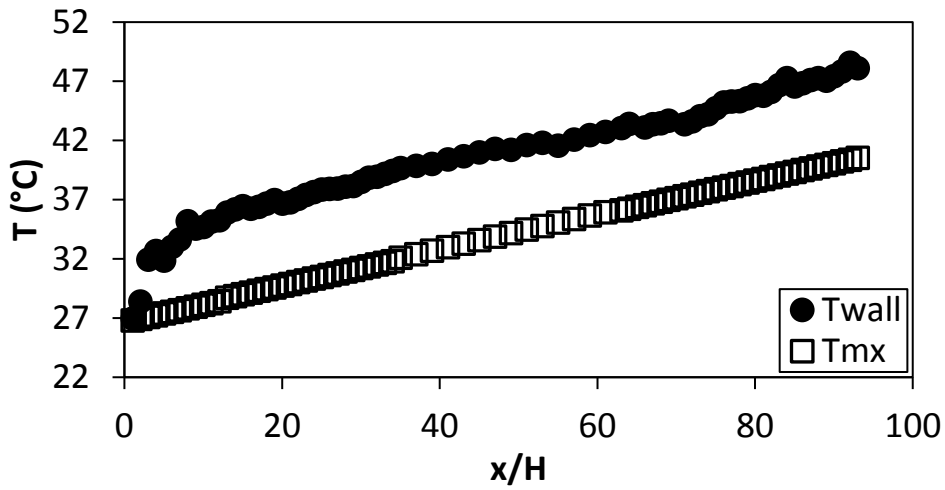


Figure F.99. Temperature plotted against x/H at $Re = 9\,700$ for setup: $d/p = 0.2$, $\theta = 45^\circ$.

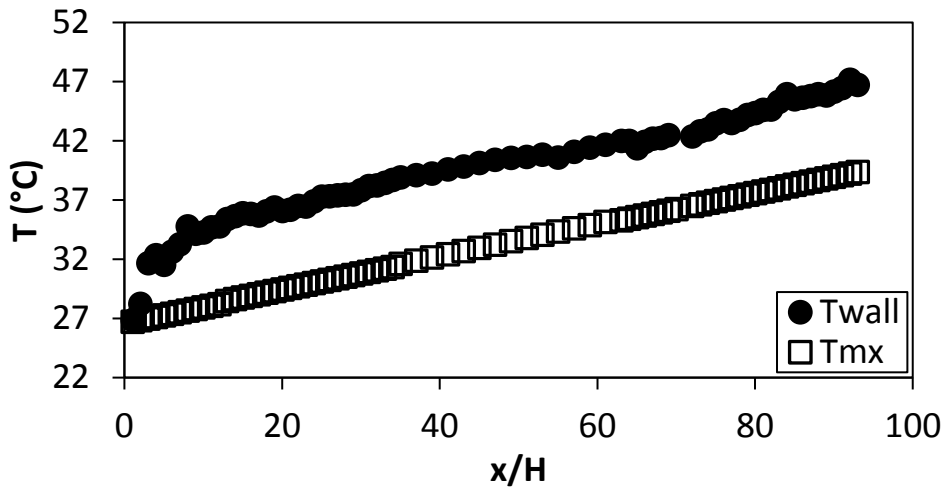


Figure F.100. Temperature plotted against x/H at $Re = 10\,500$ for setup: $d/p = 0.2$, $\theta = 45^\circ$.

F.8. Temperature data: $d/p = 0.1$, 90° orientation to the flow direction

The temperature data for the cylindrical insert with, $d/p = 0.1$, and flow direction 90° to the cylinders is shown in Figure F.101 to Figure F.115.

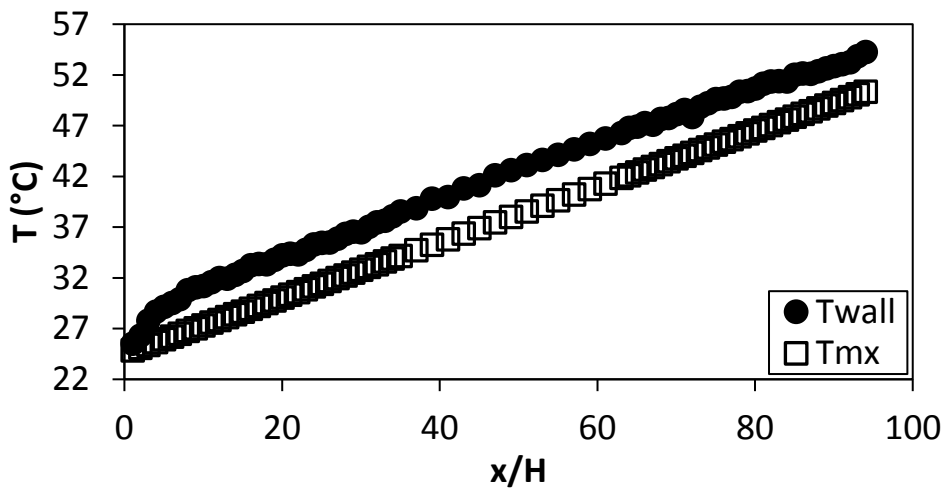


Figure F.101. Temperature plotted against x/H at $Re = 640$ for setup: $d/p = 0.1$, $\theta = 90^\circ$.

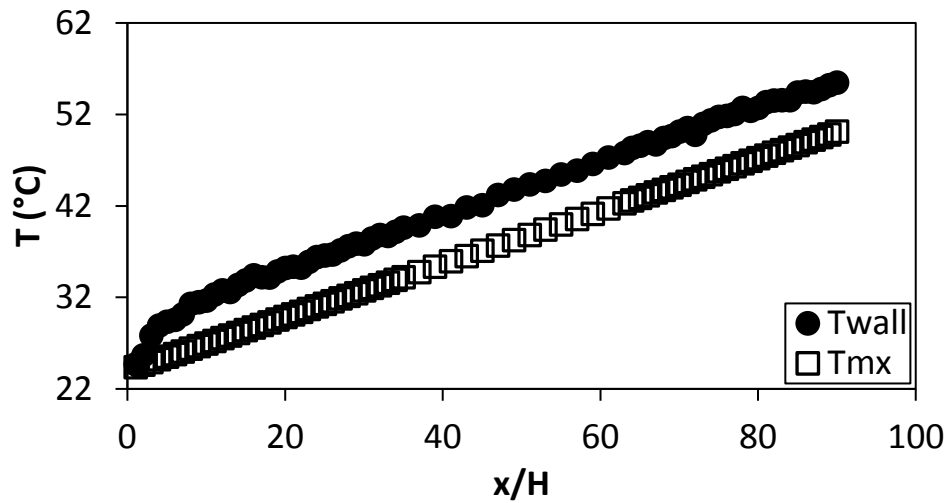


Figure F.102. Temperature plotted against x/H at $Re = 920$ for setup: $d/p = 0.1$, $\theta = 90^\circ$.

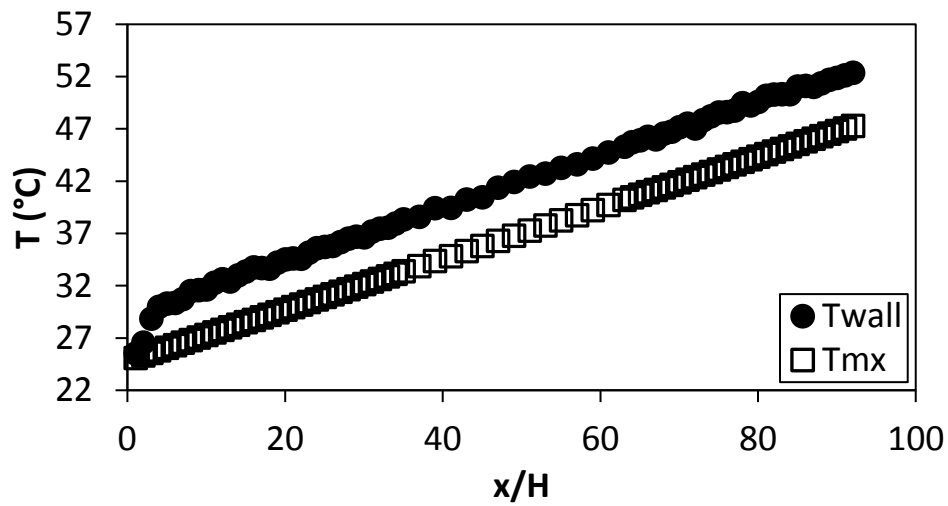


Figure F.103. Temperature plotted against x/H at $Re = 1\ 400$ for setup: $d/p = 0.1$, $\theta = 90^\circ$.

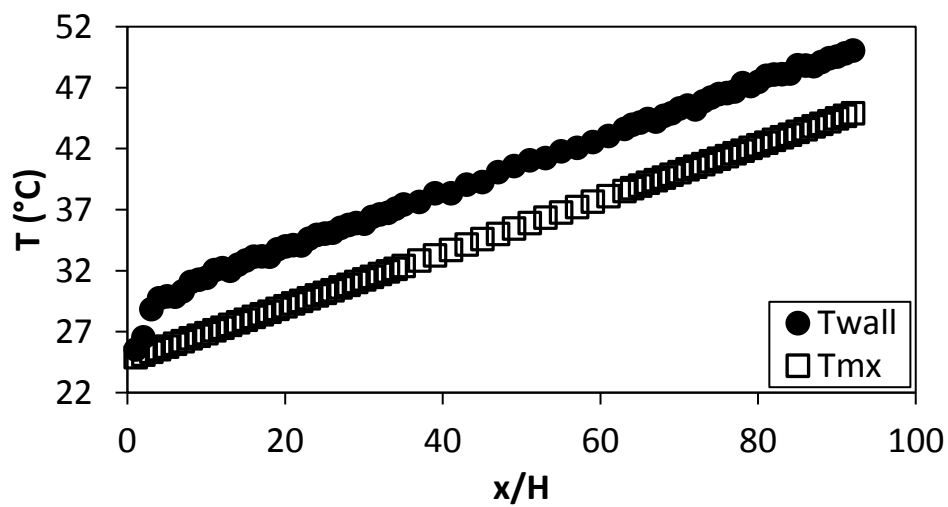


Figure F.104. Temperature plotted against x/H at $Re = 1\ 800$ for setup: $d/p = 0.1$, $\theta = 90^\circ$.

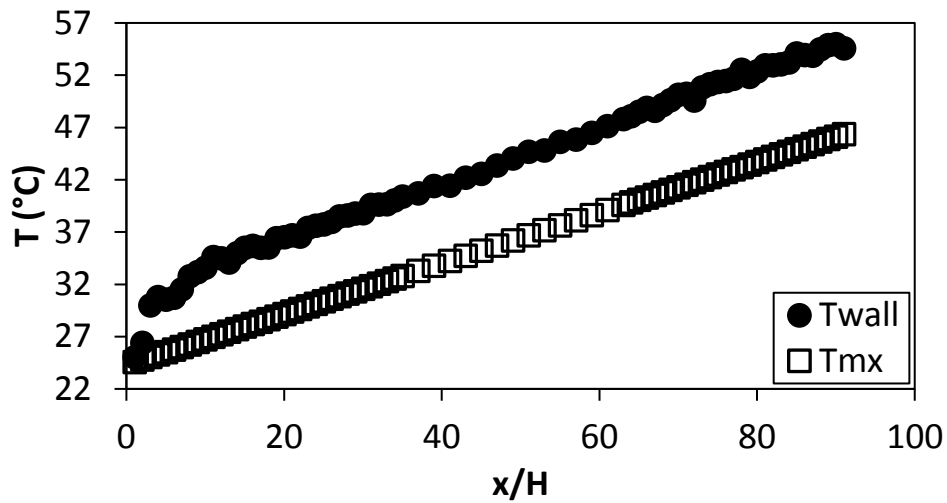


Figure F.105. Temperature plotted against x/H at $Re = 3\,000$ for setup: $d/p = 0.1$, $\theta = 90^\circ$.

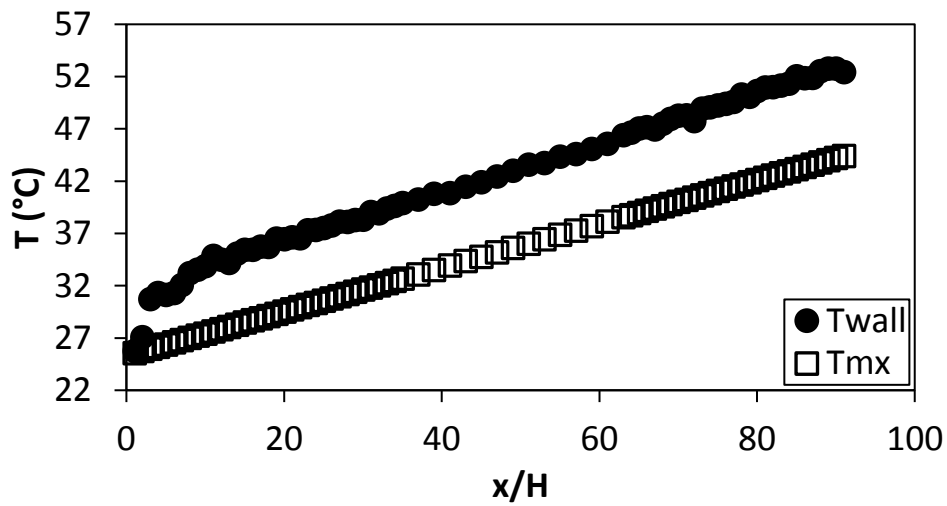


Figure F.106. Temperature plotted against x/H at $Re = 4\,000$ for setup: $d/p = 0.1$, $\theta = 90^\circ$.

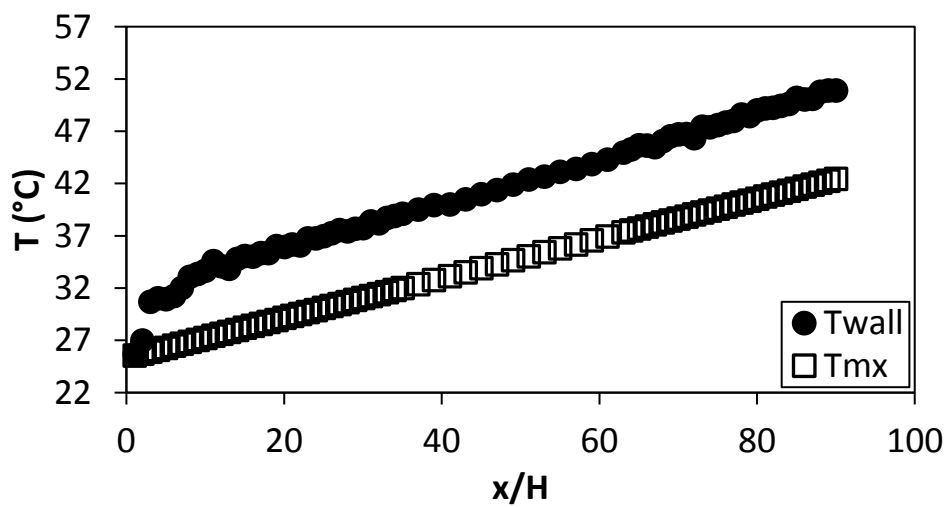


Figure F.107. Temperature plotted against x/H at $Re = 5\,000$ for setup: $d/p = 0.1$, $\theta = 90^\circ$.

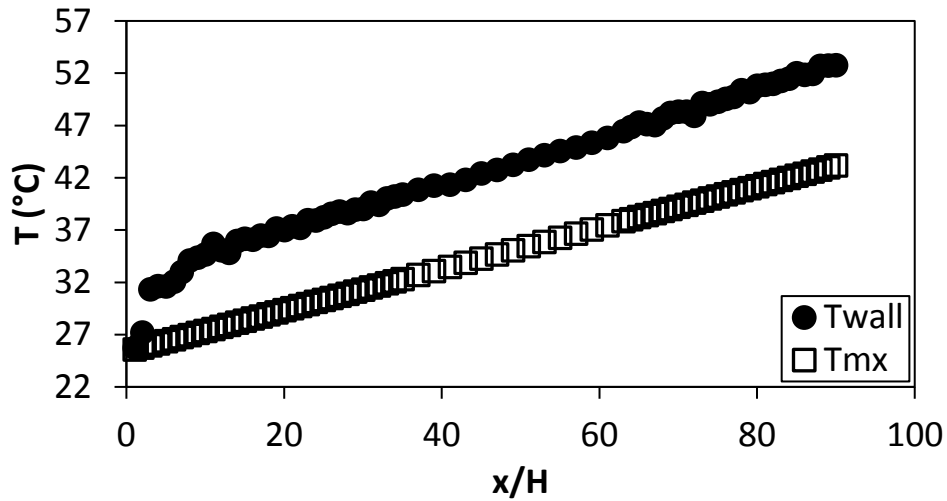


Figure F.108. Temperature plotted against x/H at $Re = 6\,000$ for setup: $d/p = 0.1$, $\theta = 90^\circ$.

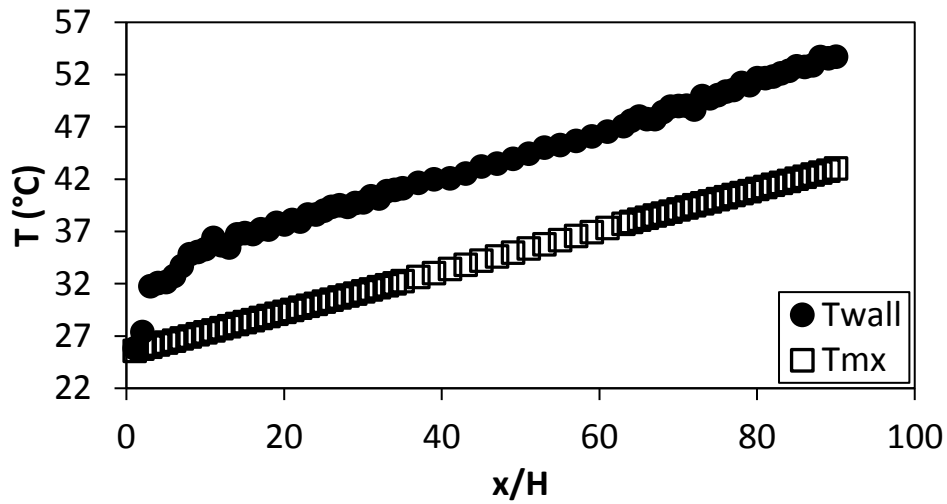


Figure F.109. Temperature plotted against x/H at $Re = 7\,000$ for setup: $d/p = 0.1$, $\theta = 90^\circ$.

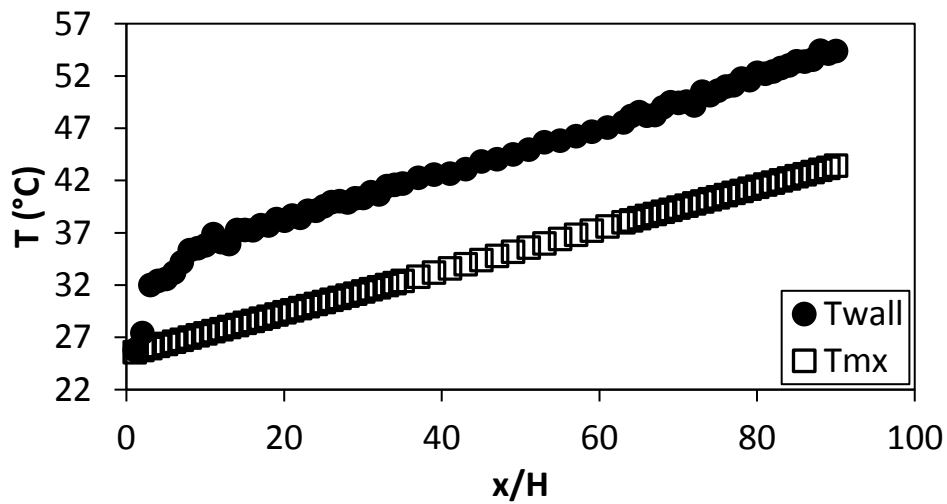


Figure F.110. Temperature plotted against x/H at $Re = 8\,000$ for setup: $d/p = 0.1$, $\theta = 90^\circ$.

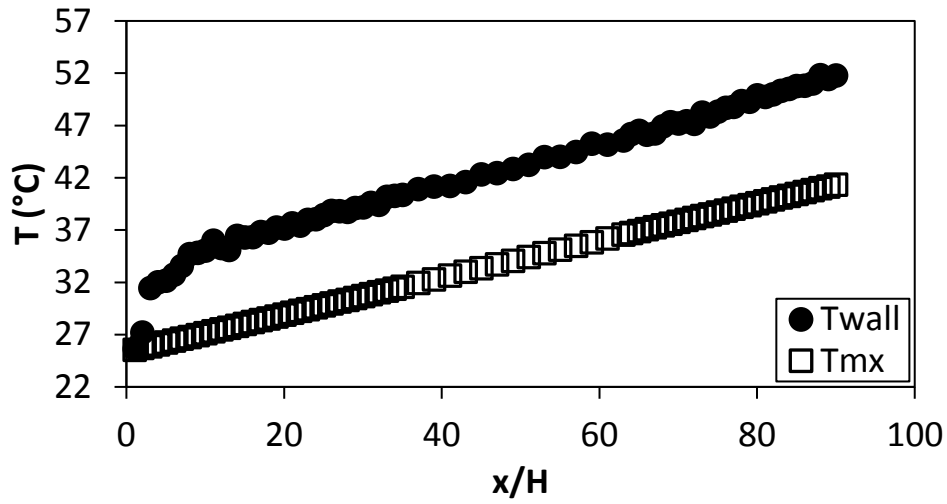


Figure F.111. Temperature plotted against x/H at $Re = 9\,000$ for setup: $d/p = 0.1$, $\theta = 90^\circ$.

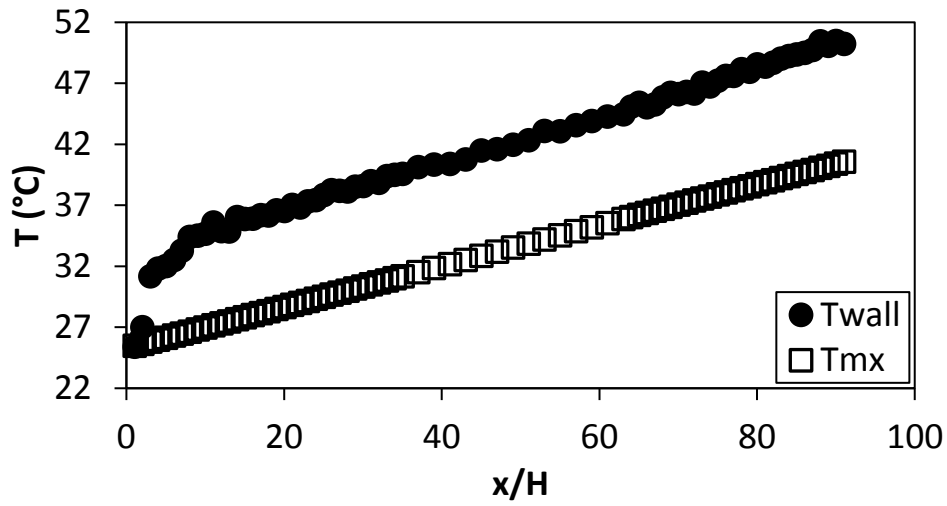


Figure F.112. Temperature plotted against x/H at $Re = 9\,700$ for setup: $d/p = 0.1$, $\theta = 90^\circ$.

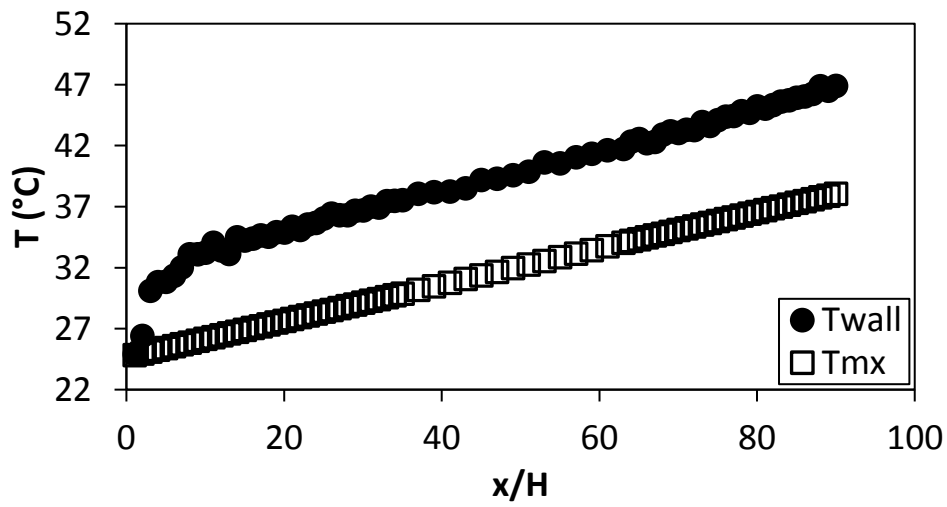


Figure F.113. Temperature plotted against x/H at $Re = 10\,500$ for setup: $d/p = 0.1$, $\theta = 90^\circ$.

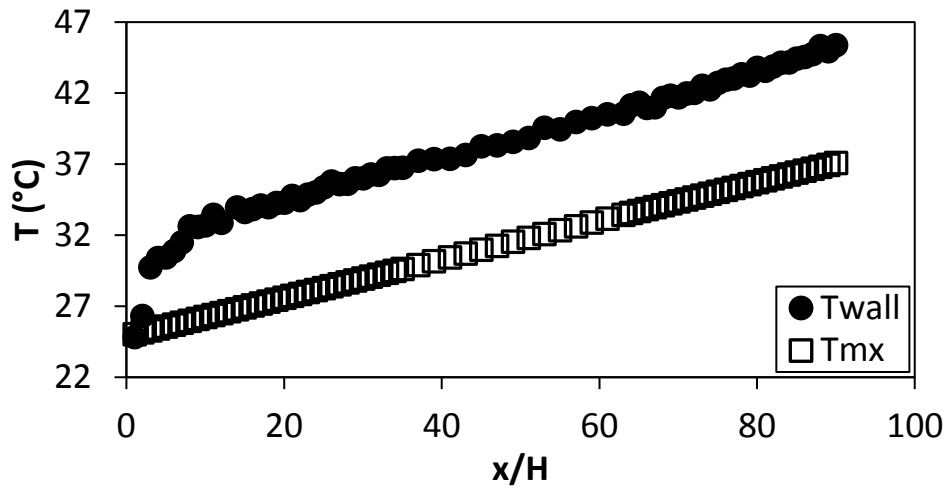


Figure F.114. Temperature plotted against x/H at $Re = 11\,500$ for setup: $d/p = 0.1$, $\theta = 90^\circ$.

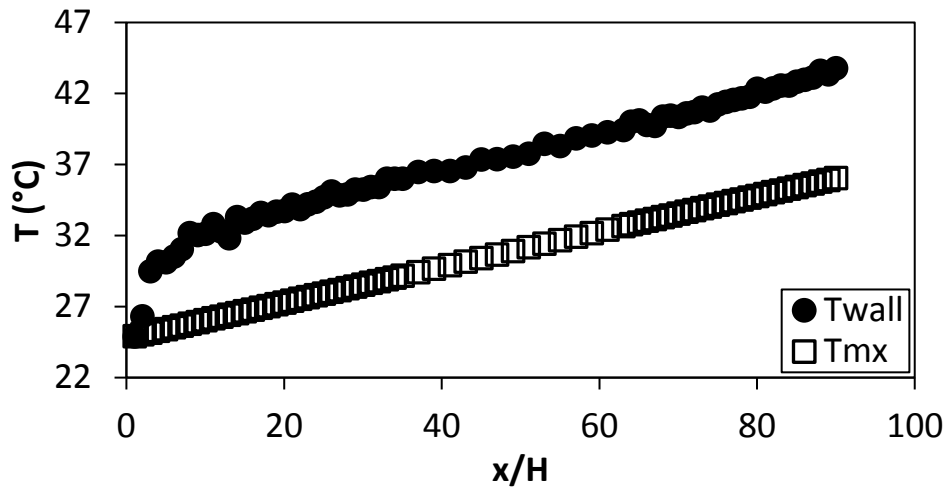


Figure F.115. Temperature plotted against x/H at $Re = 12\,500$ for setup: $d/p = 0.1$, $\theta = 90^\circ$.

F.9. Temperature data: $d/p = 0.1$, 45° orientation to the flow direction

The temperature data for the cylindrical insert with, $d/p = 0.1$, and flow direction 45° to the cylinders is shown in **Figure F.116** to **Figure F.129**.

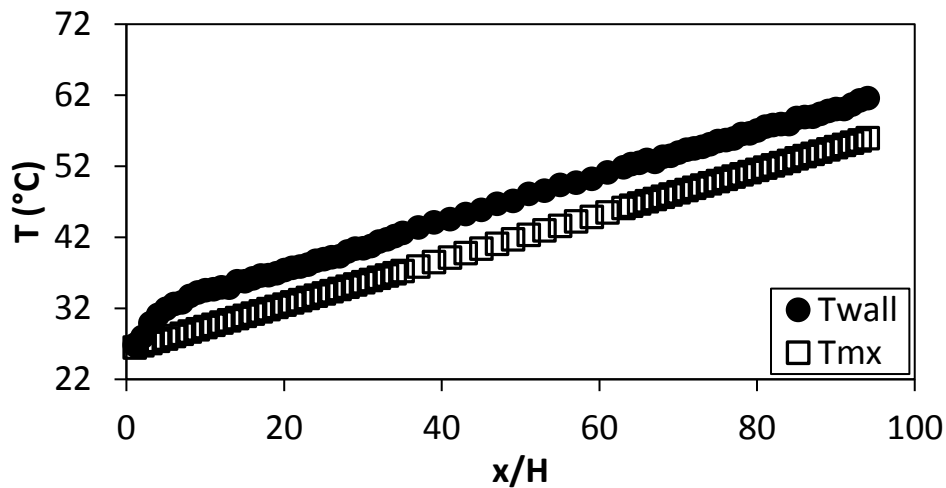


Figure F.116: Temperature plotted against x/H at $Re = 640$ for setup: $d/p = 0.1$, $\theta = 45^\circ$.

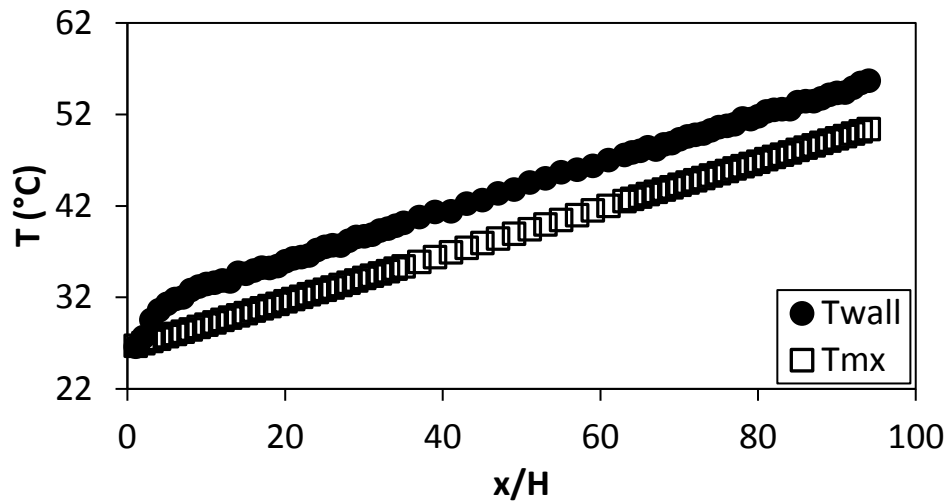


Figure F.117: Temperature plotted against x/H at $Re = 920$ for setup: $d/p = 0.1$, $\theta = 45^\circ$.

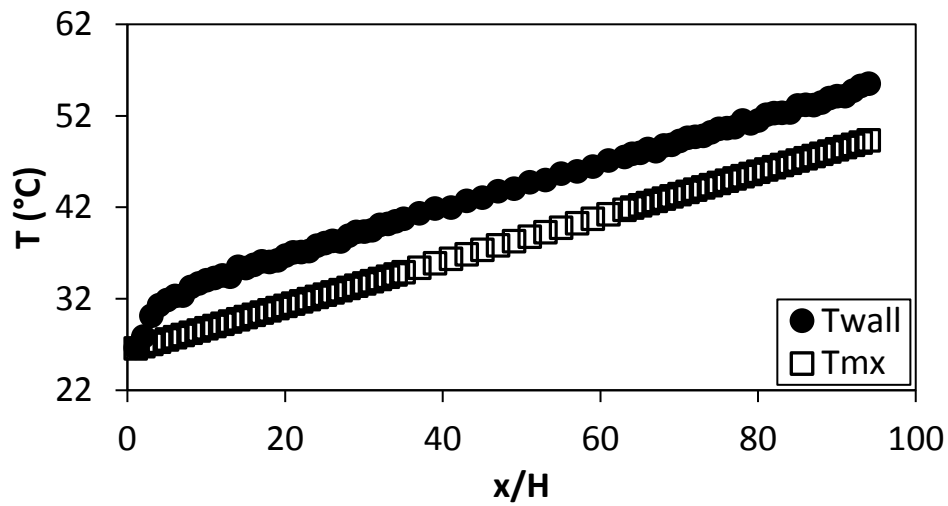


Figure F.118: Temperature plotted against x/H at $Re = 1\,400$ for setup: $d/p = 0.1$, $\theta = 45^\circ$.

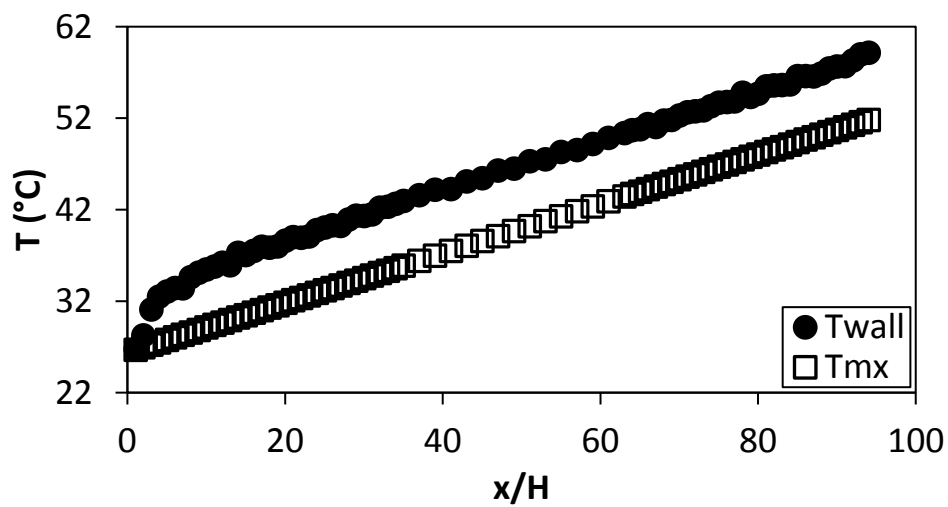


Figure F.119: Temperature plotted against x/H at $Re = 1\,800$ for setup: $d/p = 0.1$, $\theta = 45^\circ$.

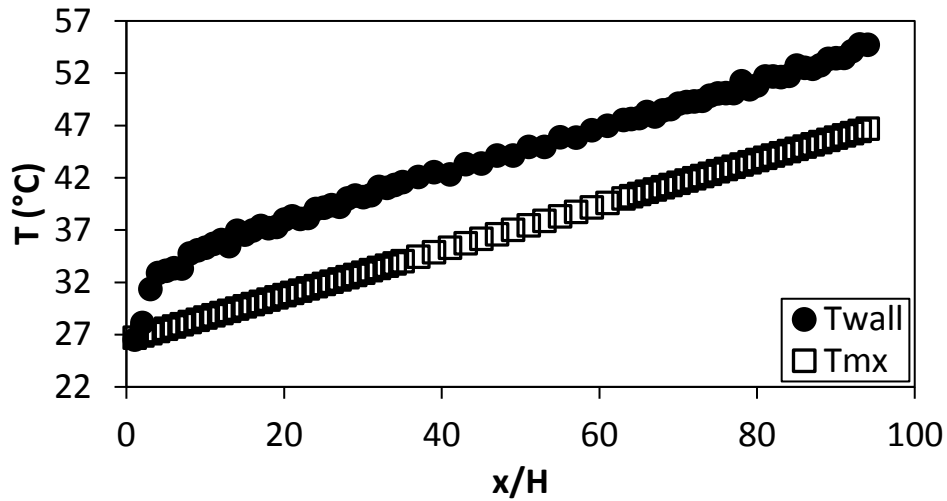


Figure F.120: Temperature plotted against x/H at $Re = 3\ 000$ for setup: $d/p = 0.1$, $\theta = 45^\circ$.

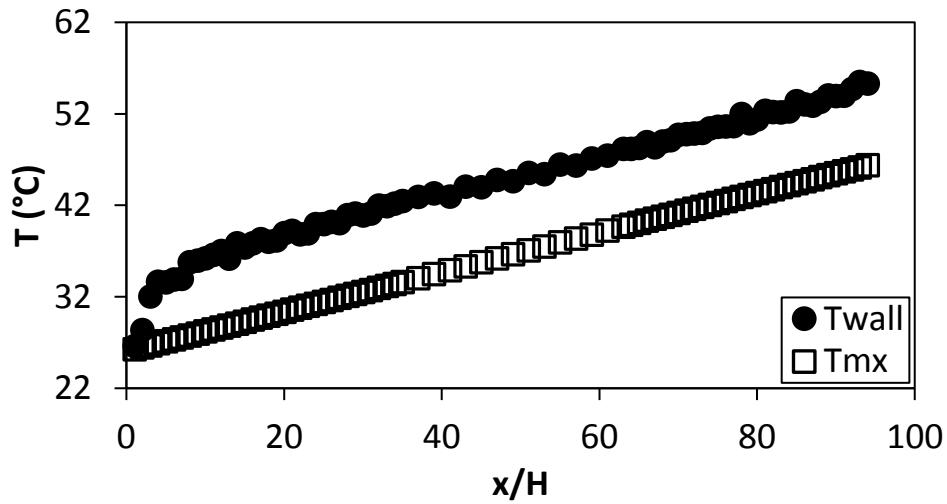


Figure F.121: Temperature plotted against x/H at $Re = 4\ 000$ for setup: $d/p = 0.1$, $\theta = 45^\circ$.

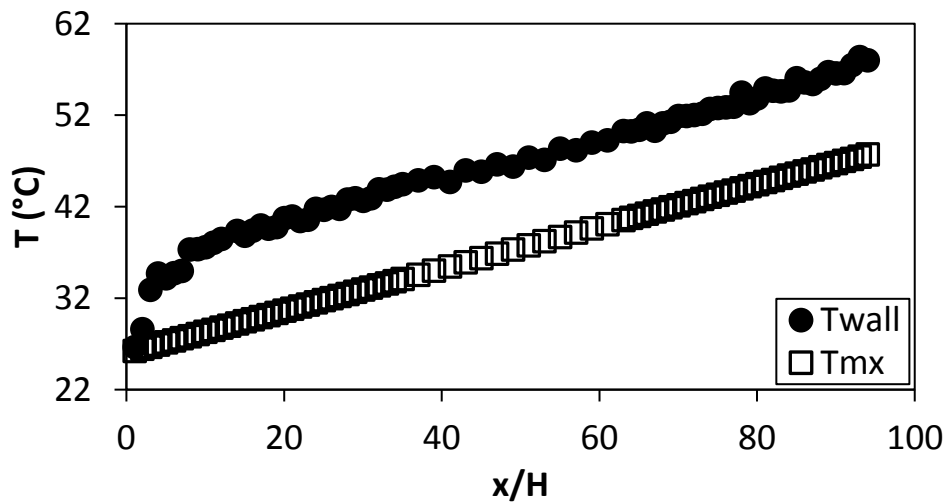


Figure F.122: Temperature plotted against x/H at $Re = 5\ 000$ for setup: $d/p = 0.1$, $\theta = 45^\circ$.

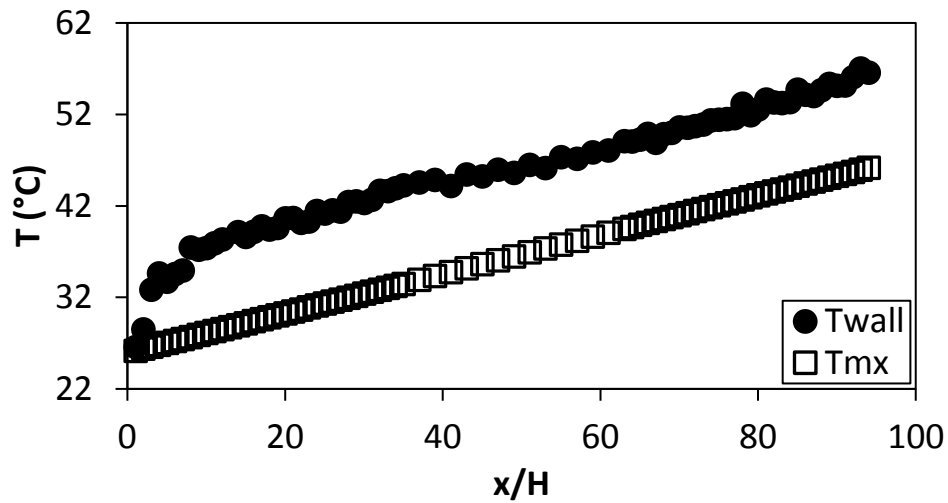


Figure F.123: Temperature plotted against x/H at $Re = 6\ 000$ for setup: $d/p = 0.1$, $\theta = 45^\circ$.

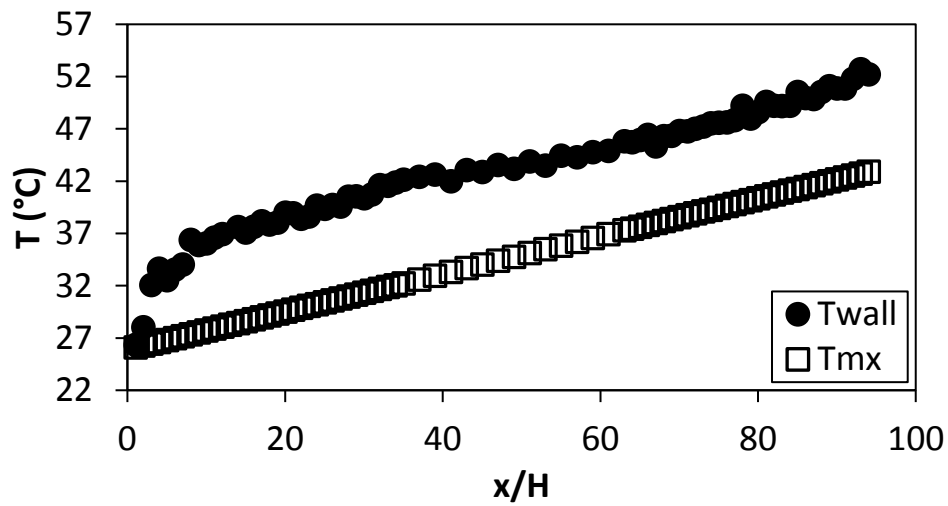


Figure F.124: Temperature plotted against x/H at $Re = 7\ 000$ for setup: $d/p = 0.1$, $\theta = 45^\circ$.

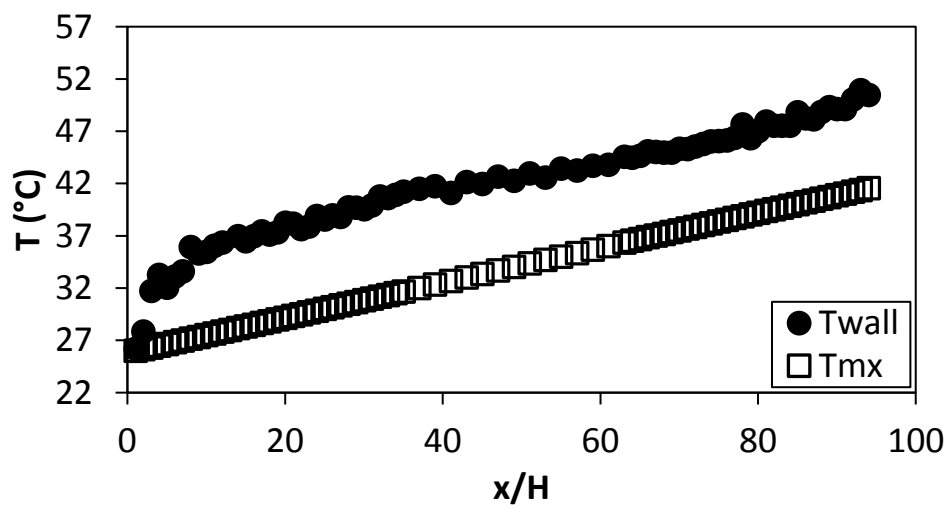


Figure F.125: Temperature plotted against x/H at $Re = 8\ 000$ for setup: $d/p = 0.1$, $\theta = 45^\circ$.

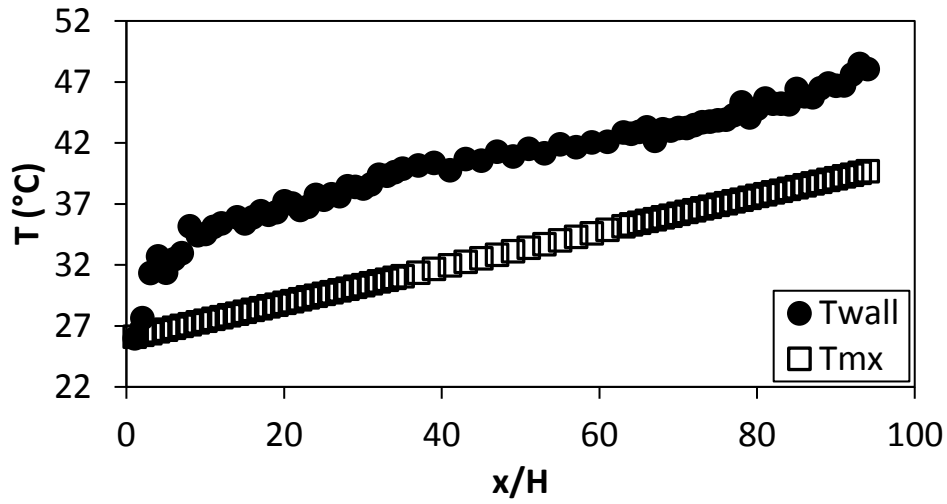


Figure F.126: Temperature plotted against x/H at $Re = 9\ 000$ for setup: $d/p = 0.1$, $\theta = 45^\circ$.

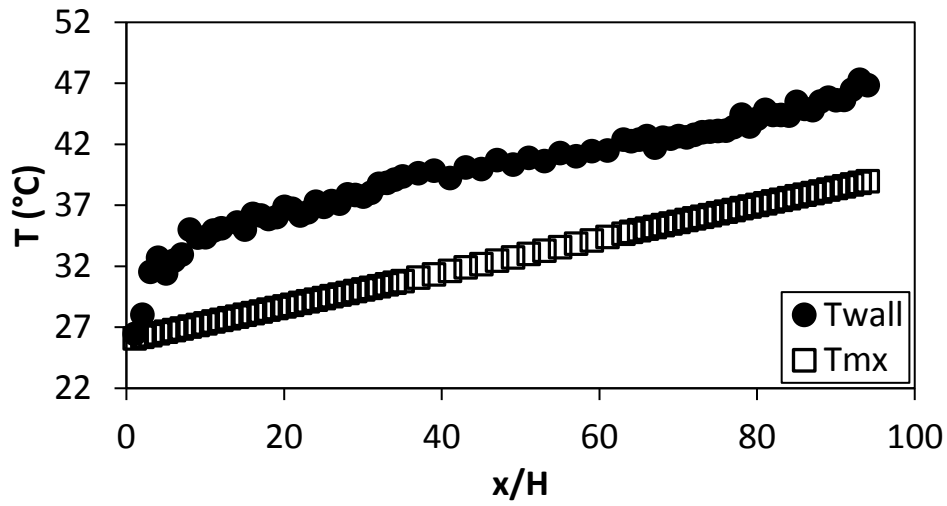


Figure F.127: Temperature plotted against x/H at $Re = 9\ 700$ for setup: $d/p = 0.1$, $\theta = 45^\circ$.

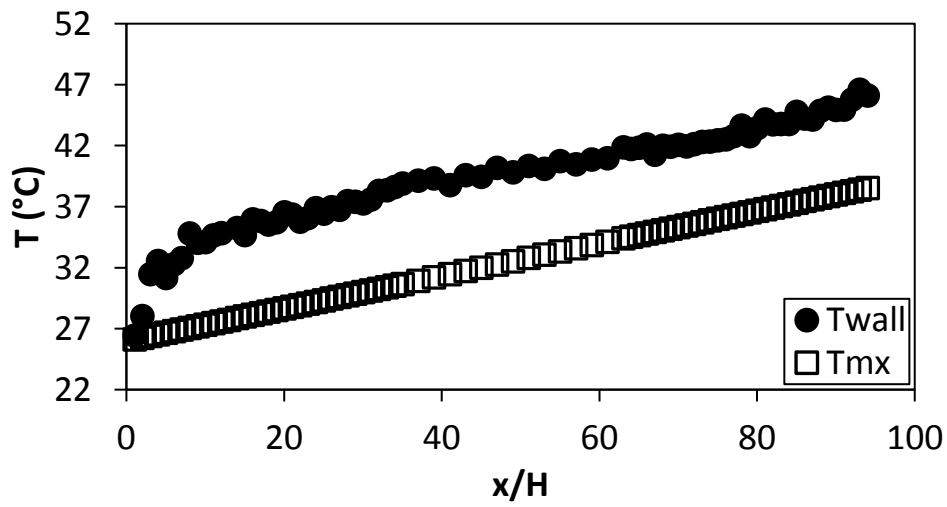


Figure F.128: Temperature plotted against x/H at $Re = 10\ 500$ for setup: $d/p = 0.1$, $\theta = 45^\circ$.

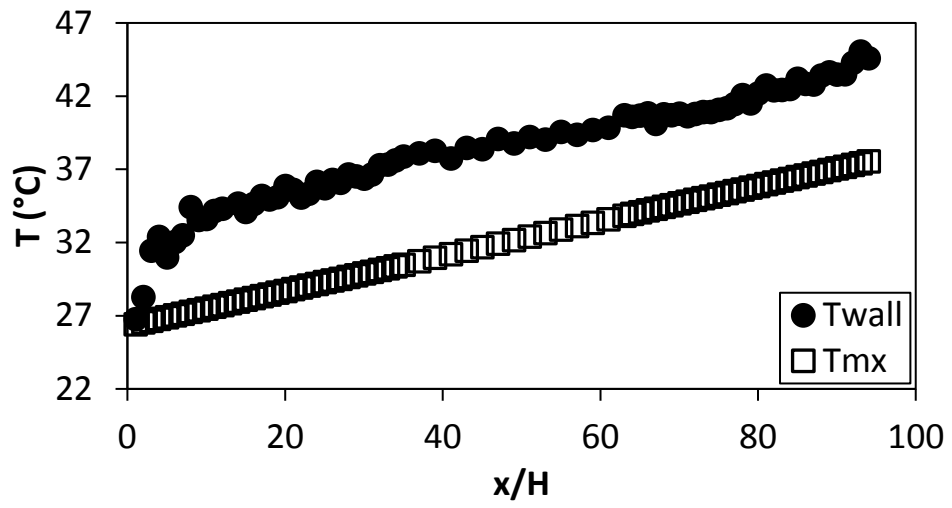


Figure F.129: Temperature plotted against x/H at $Re = 11\,500$ for setup: $d/p = 0.1$, $\theta = 45^\circ$.

Appendix G: Pressure Data

The negative of the wall pressure in the channel is plotted against the x-distance to find the gradient of the pressure drop, in the test section, dP/dx , by using a linear least squares regression line. The test section starts after a 2m inlet section where the flow is hydrodynamically fully developed for the smooth channel. When the pitch is smaller, the slope of the line becomes constant after approximately a quarter of the test section length where the flow is fully developed for the insert. With larger pitches the flow becomes fully developed after approximately the half of the test section length. The friction factor is found for the fully developed region of the test section. Four pressure values upstream from the test section is also plotted. Pressure taps on the wall are spaced in 15 mm intervals on the centre line of the wall.

G.1. Pressure data for smooth channel

Figure G.1 to Figure G.15 shows the smooth channel wall pressure.

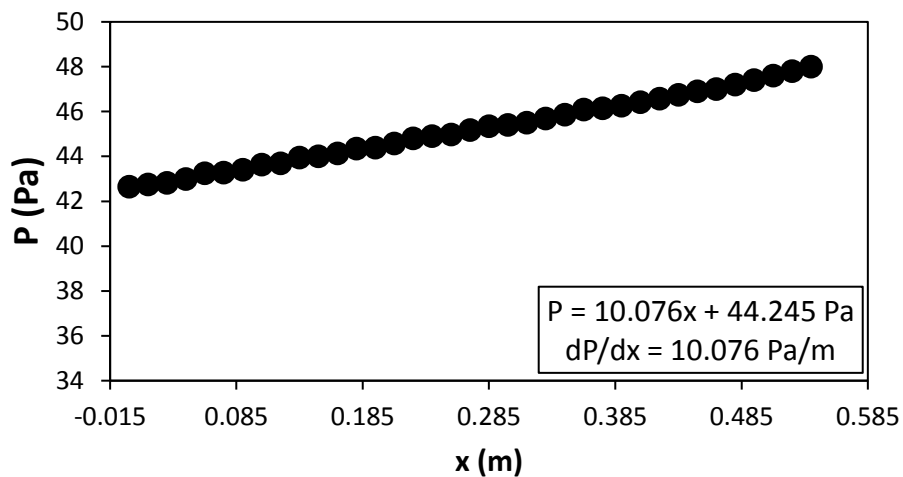


Figure G.1: Static pressure plotted against the x coordinate at $Re = 640$ for smooth channel.

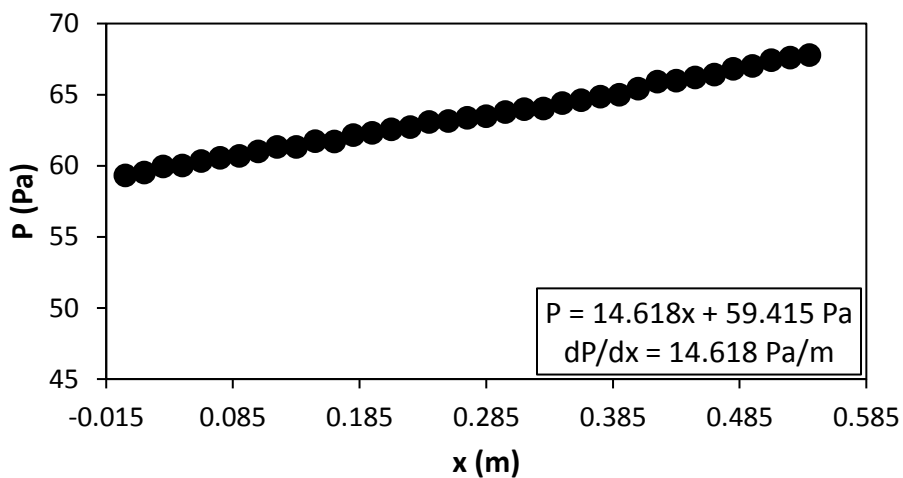


Figure G.2: Static pressure plotted against the x coordinate at $Re = 920$ for smooth channel.

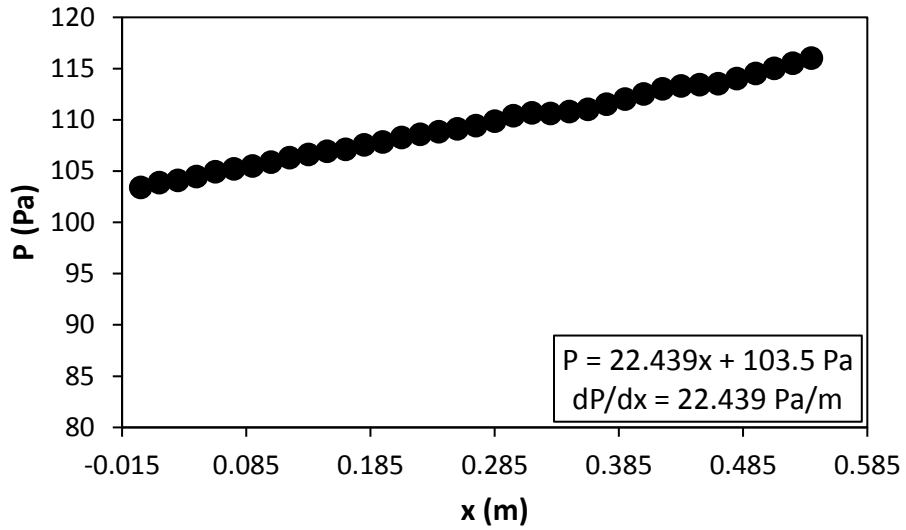


Figure G.3: Static pressure plotted against the x coordinate at $Re = 1400$ for smooth channel.

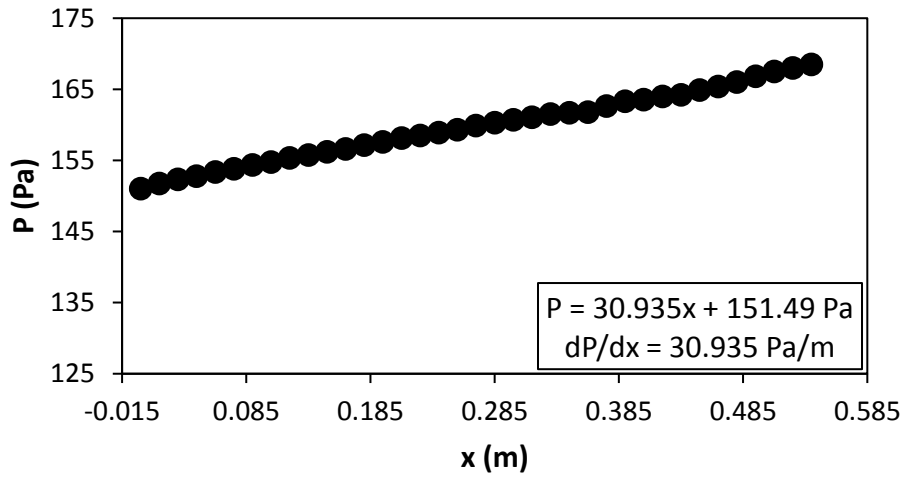


Figure G.4: Static pressure plotted against the x coordinate at $Re = 1800$ for smooth channel.

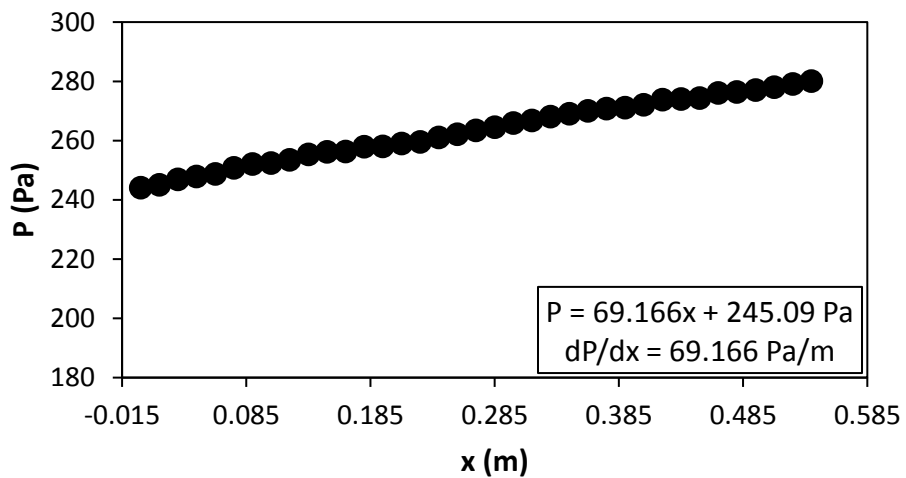


Figure G.5: Static pressure plotted against the x coordinate at $Re = 3000$ for smooth channel.

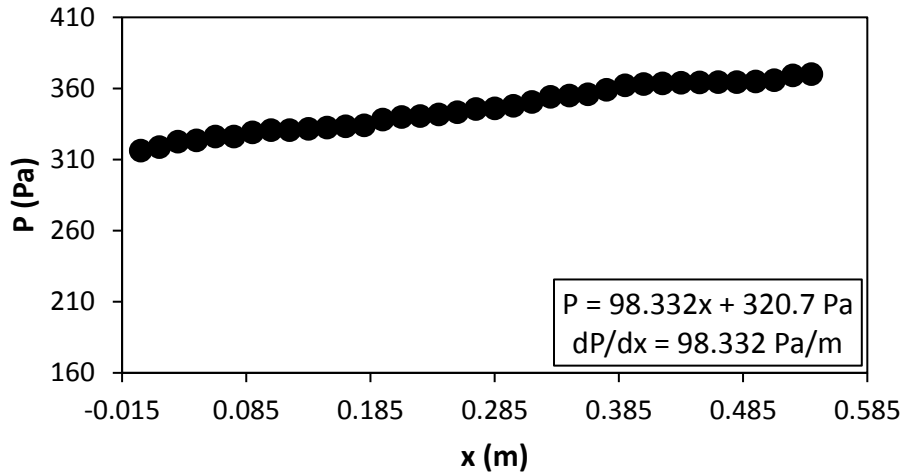


Figure G.6: Static pressure plotted against the x coordinate at $Re = 4000$ for smooth channel.

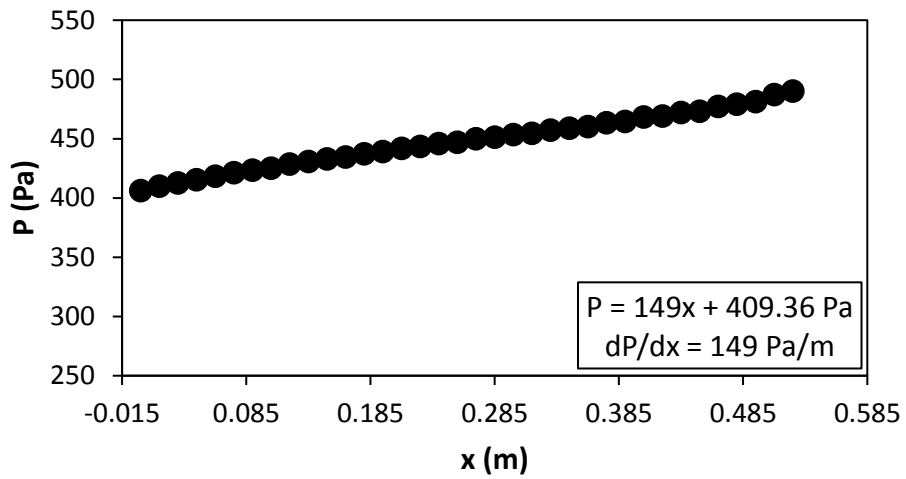


Figure G.7: Static pressure plotted against the x coordinate at $Re = 5000$ for smooth channel.

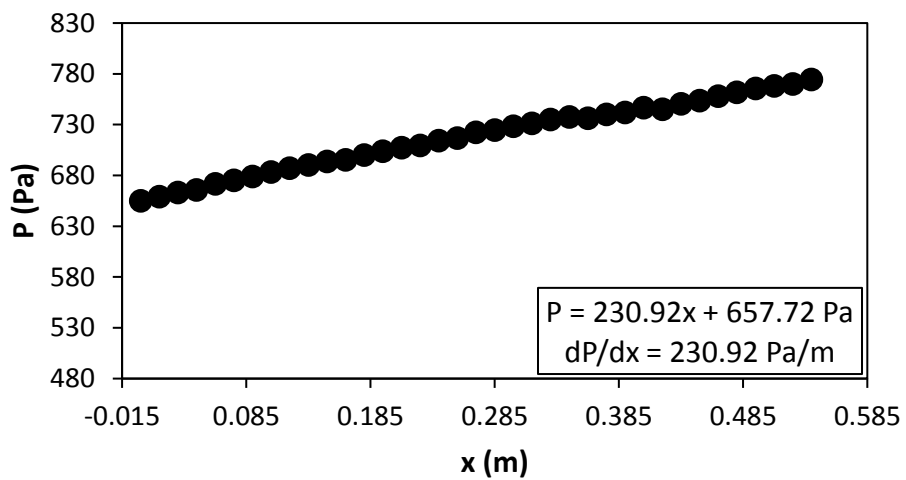


Figure G.8: Static pressure plotted against the x coordinate at $Re = 6000$ for smooth channel.

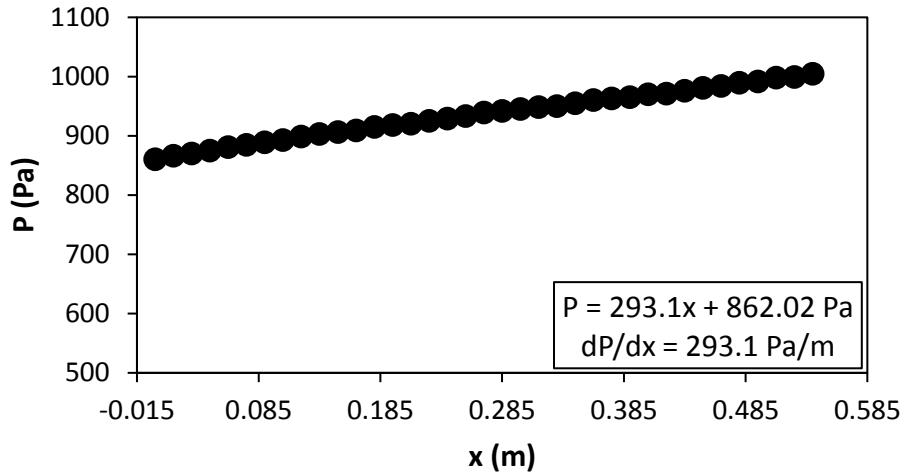


Figure G.9: Static pressure plotted against the x coordinate at $Re = 7000$ for smooth channel.

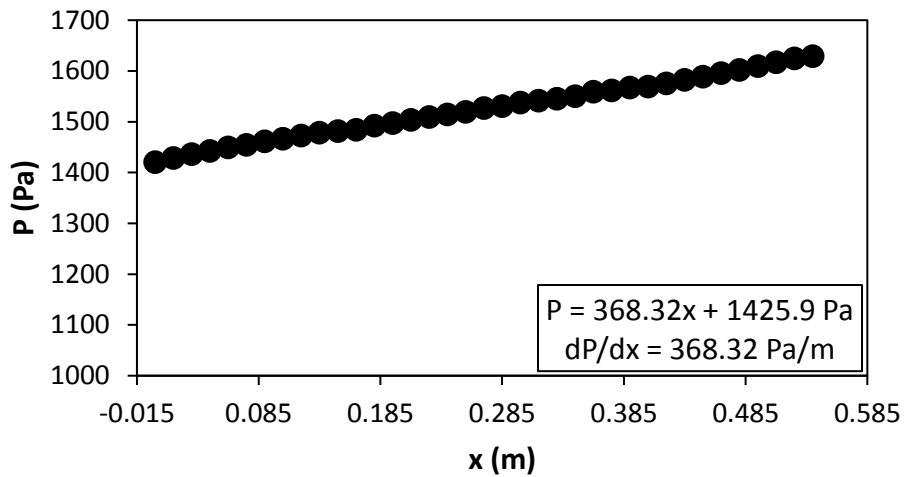


Figure G.10: Static pressure plotted against the x coordinate at $Re = 8000$ for smooth channel.

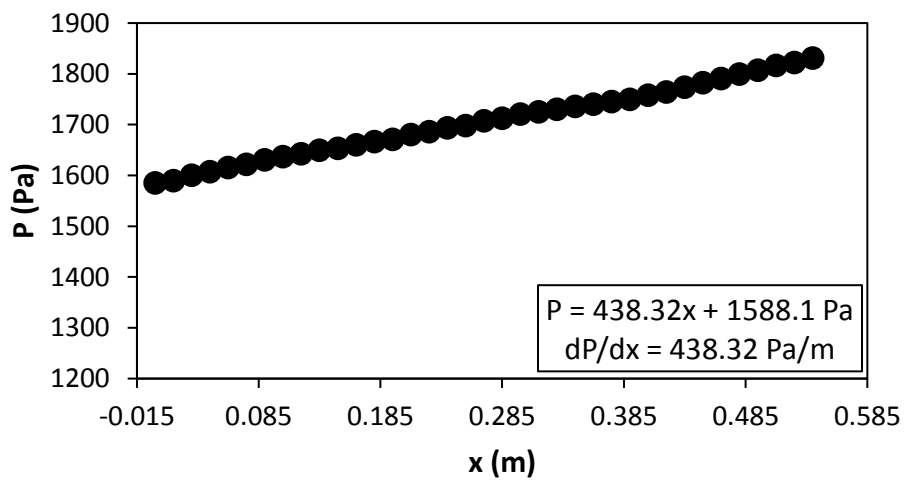


Figure G.11: Static pressure plotted against the x coordinate at $Re = 9000$ for smooth channel.

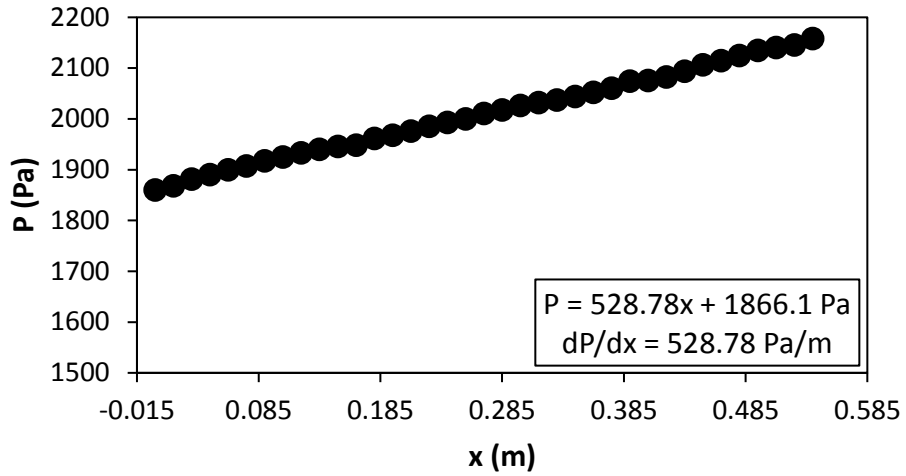


Figure G.12: Static pressure plotted against the x coordinate at Re = 9 700 for smooth channel.

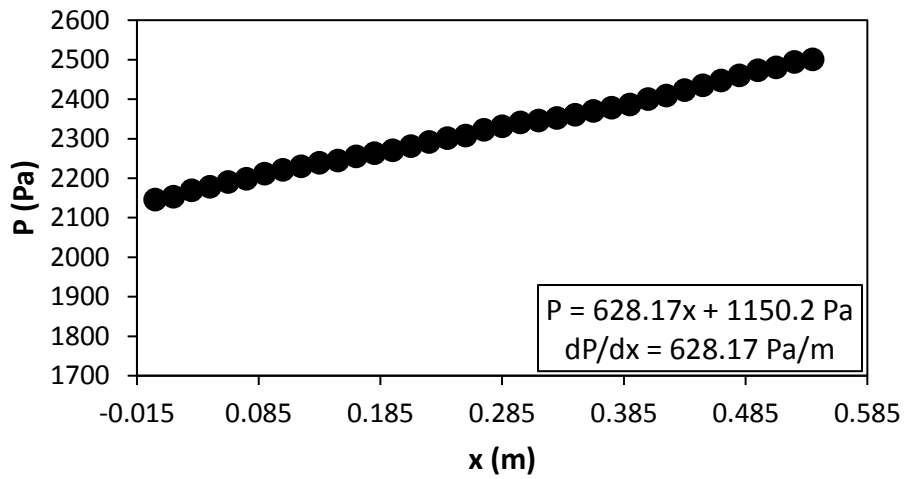


Figure G.13: Static pressure plotted against the x coordinate at Re = 10 500 for smooth channel.

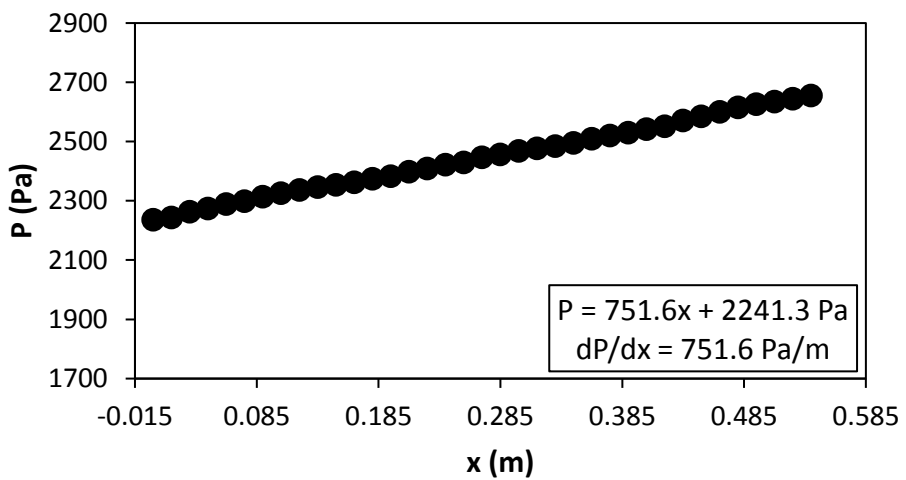


Figure G.14: Static pressure plotted against the x coordinate at Re = 11 500 for smooth channel.

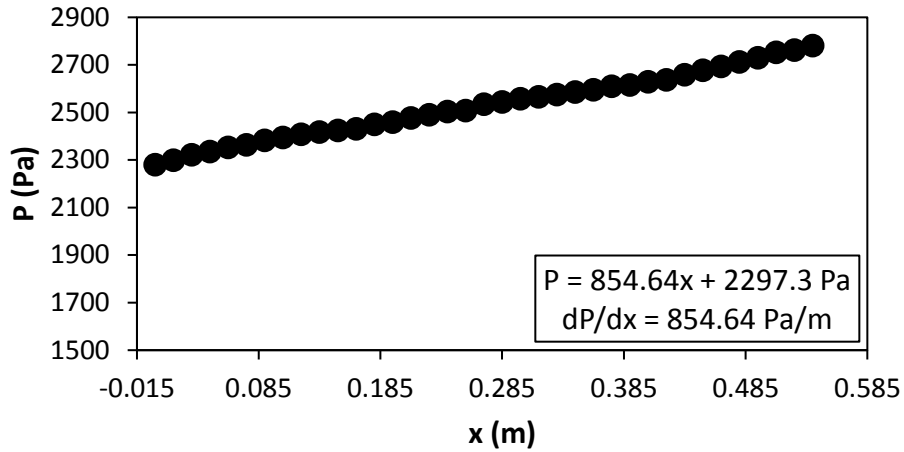


Figure G.15: Static pressure plotted against the x coordinate at $Re = 12\ 500$ for smooth channel.

G.2. Pressure data: $d/p = 0.05$, 90° orientation to the flow direction

Figure G.16 to Figure G.30 shows the channel wall pressure for the $d/p = 0.05$ cylinders, orientated 90° to the flow direction.

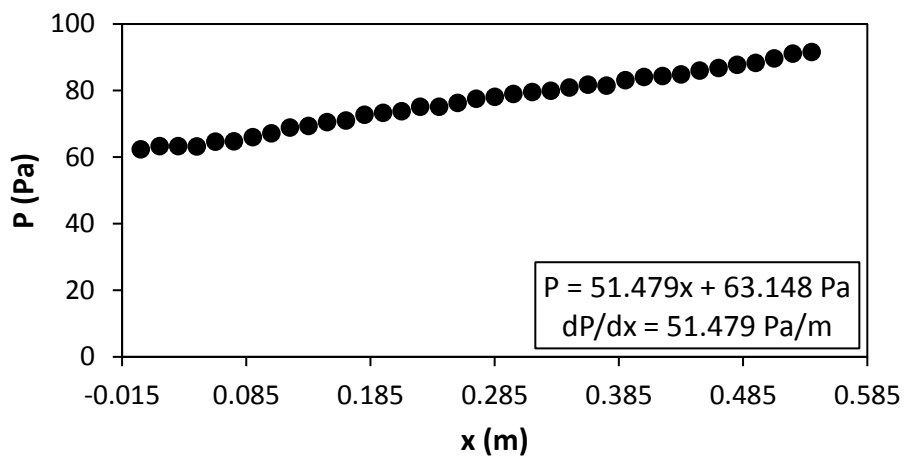


Figure G.16: Static pressure plotted against the x coordinate at $Re = 640$ for setup: $d/p = 0.05$, 90° to the flow direction.

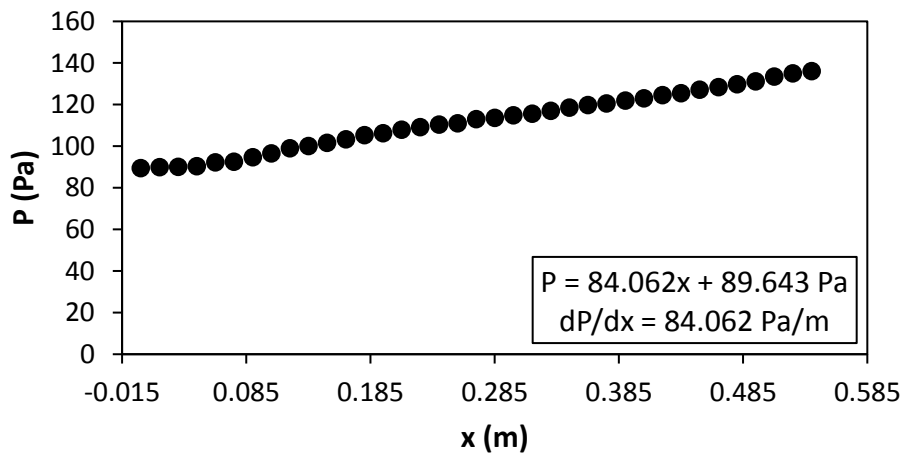


Figure G.17: Static pressure plotted against the x coordinate at $Re = 920$ for setup: $d/p = 0.05$, 90° to the flow direction.

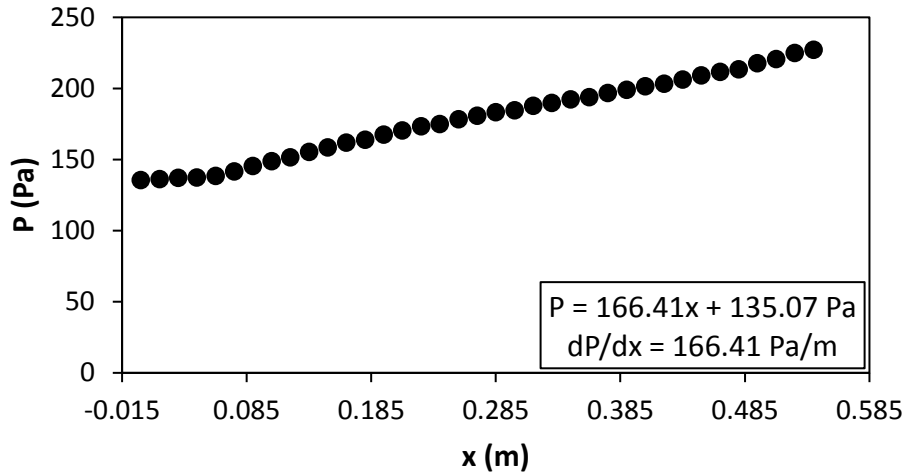


Figure G.18: Static pressure plotted against the x coordinate at $Re = 1\,400$ for setup: $d/p = 0.05$, 90° to the flow direction.

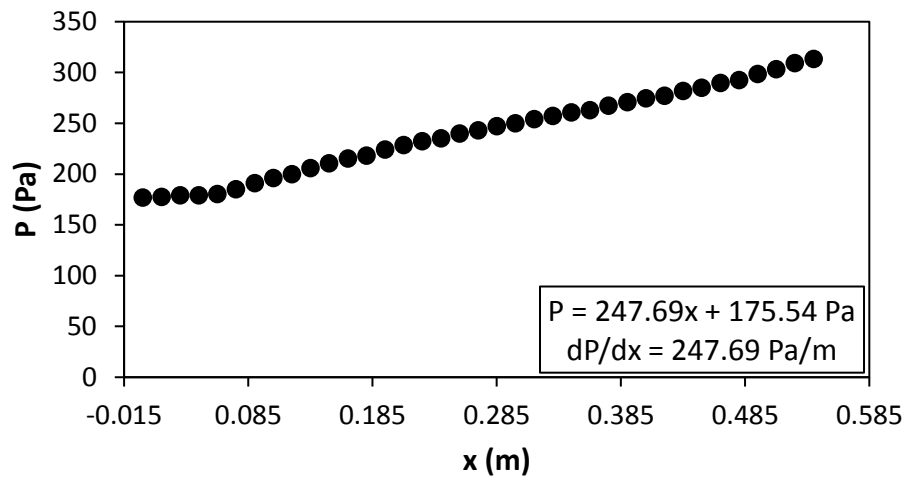


Figure G.19: Static pressure plotted against the x coordinate at $Re = 1\,800$ for setup: $d/p = 0.05$, 90° to the flow direction.

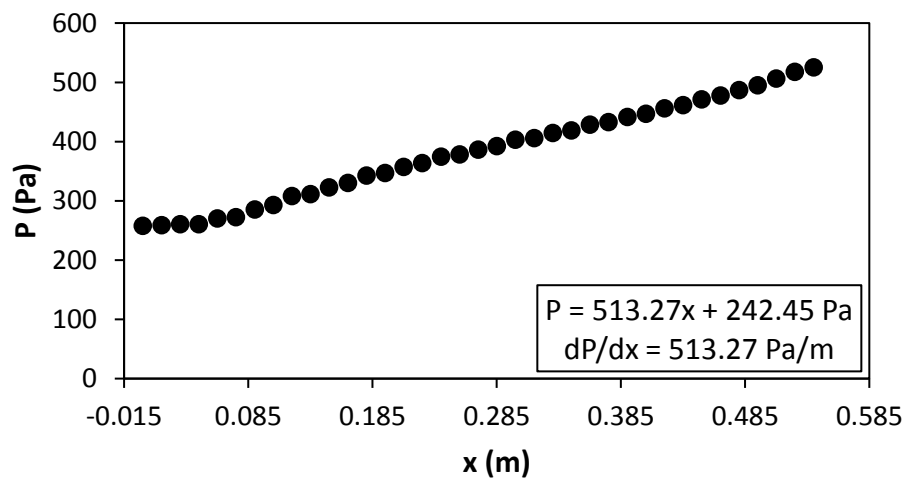


Figure G.20: Static pressure plotted against the x coordinate at $Re = 3\,000$ for setup: $d/p = 0.05$, 90° to the flow direction.

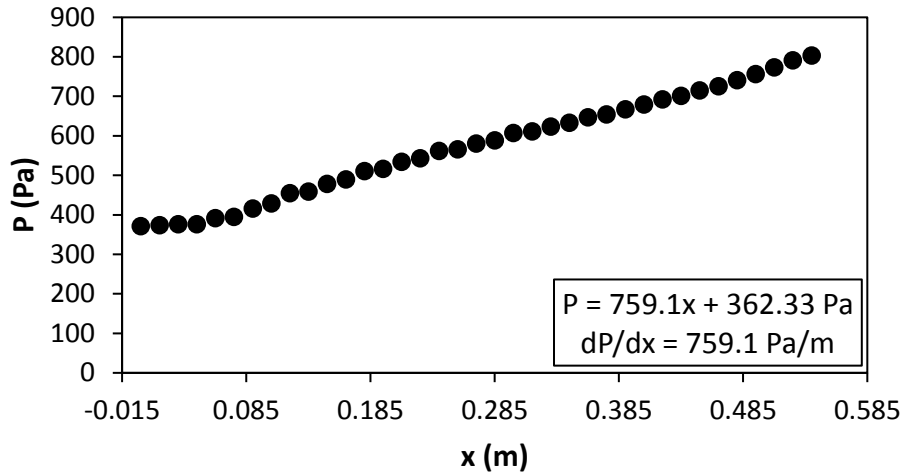


Figure G.21: Static pressure plotted against the x coordinate at $Re = 4000$ for setup: $d/p = 0.05$, 90° to the flow direction.

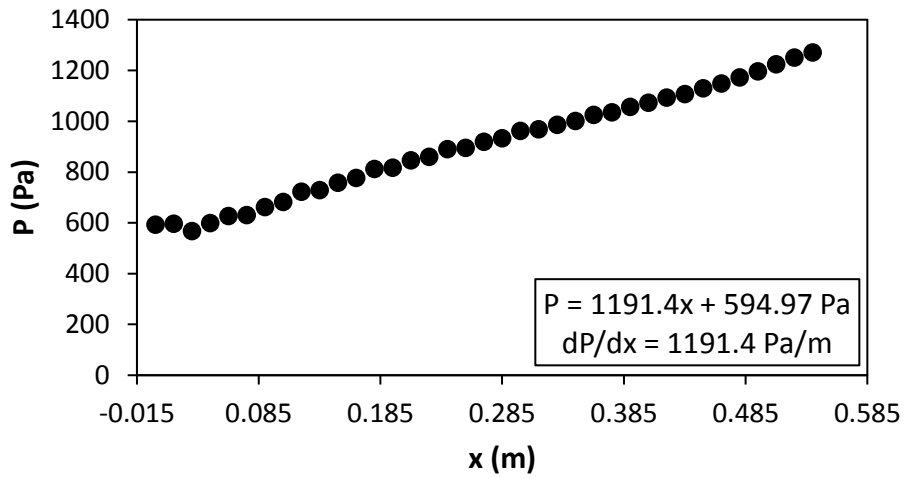


Figure G.22: Static pressure plotted against the x coordinate at $Re = 5000$ for setup: $d/p = 0.05$, 90° to the flow direction.

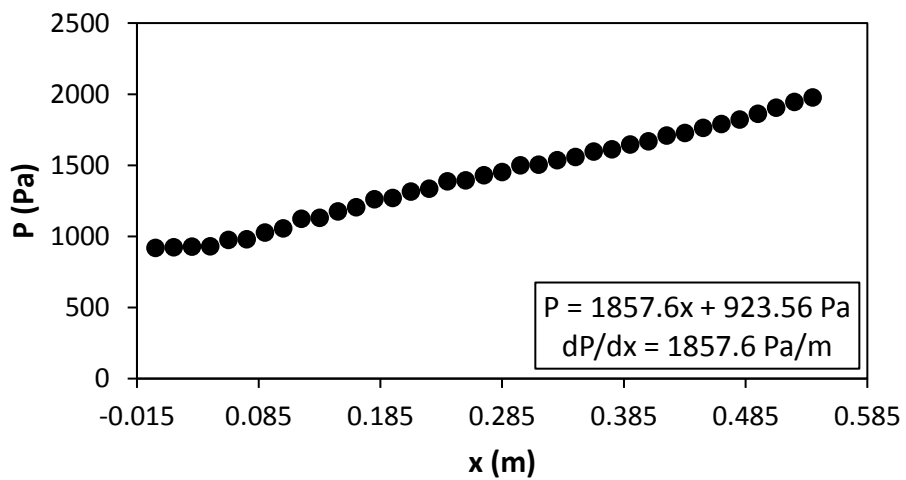


Figure G.23: Static pressure plotted against the x coordinate at $Re = 6000$ for setup: $d/p = 0.05$, 90° to the flow direction.

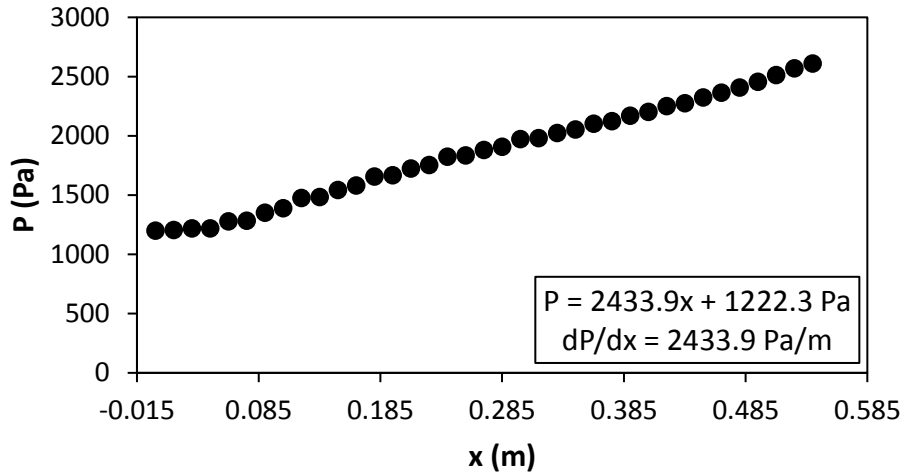


Figure G.24: Static pressure plotted against the x coordinate at $Re = 7000$ for setup: $d/p = 0.05$, 90° to the flow direction.

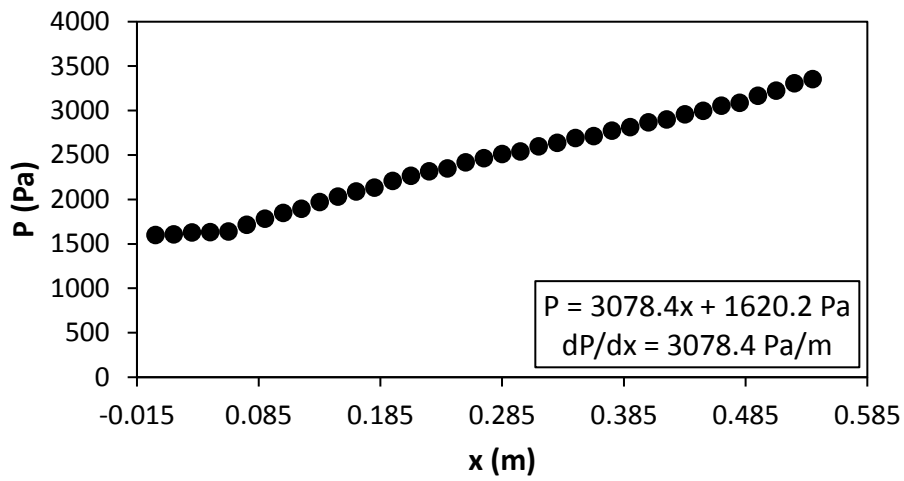


Figure G.25: Static pressure plotted against the x coordinate at $Re = 8000$ for setup: $d/p = 0.05$, 90° to the flow direction.

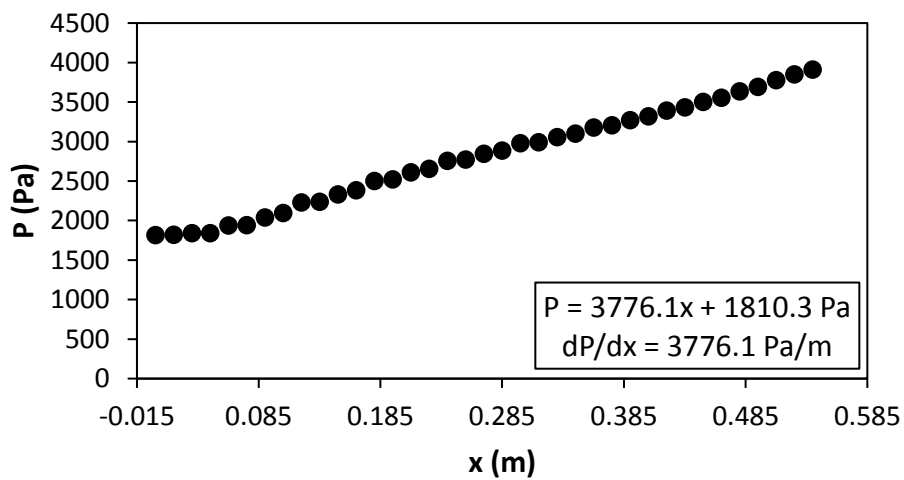


Figure G.26: Static pressure plotted against the x coordinate at $Re = 9000$ for setup: $d/p = 0.05$, 90° to the flow direction.

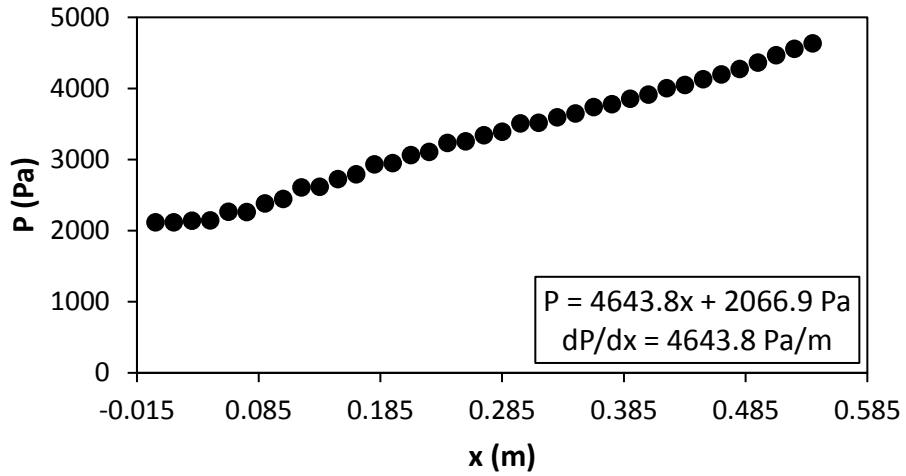


Figure G.27: Static pressure plotted against the x coordinate at $Re = 9700$ for setup: $d/p = 0.05$, 90° to the flow direction.

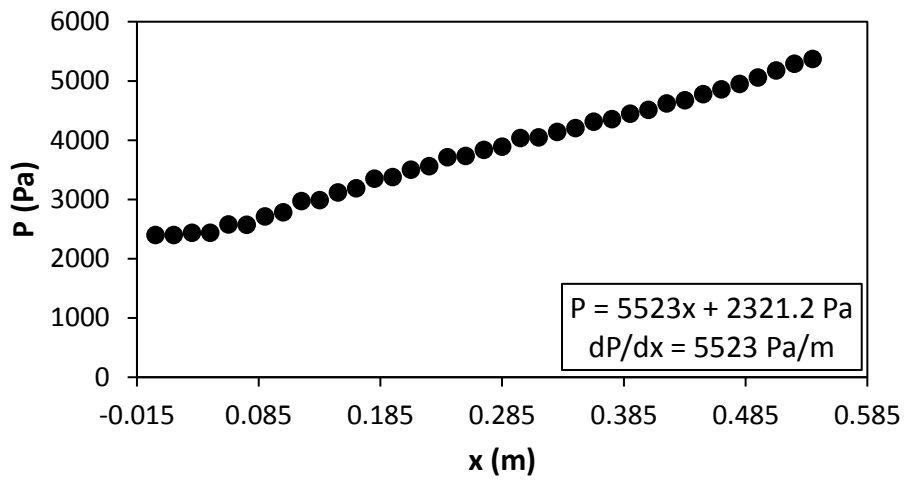


Figure G.28: Static pressure plotted against the x coordinate at $Re = 10500$ for setup: $d/p = 0.05$, 90° to the flow direction.

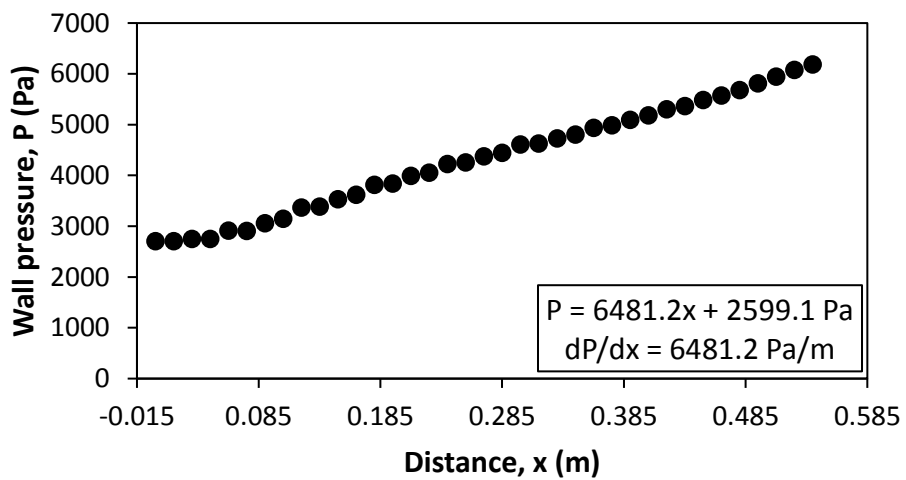


Figure G.29: Static pressure plotted against the x coordinate at $Re = 11500$ for setup: $d/p = 0.05$, 90° to the flow direction.

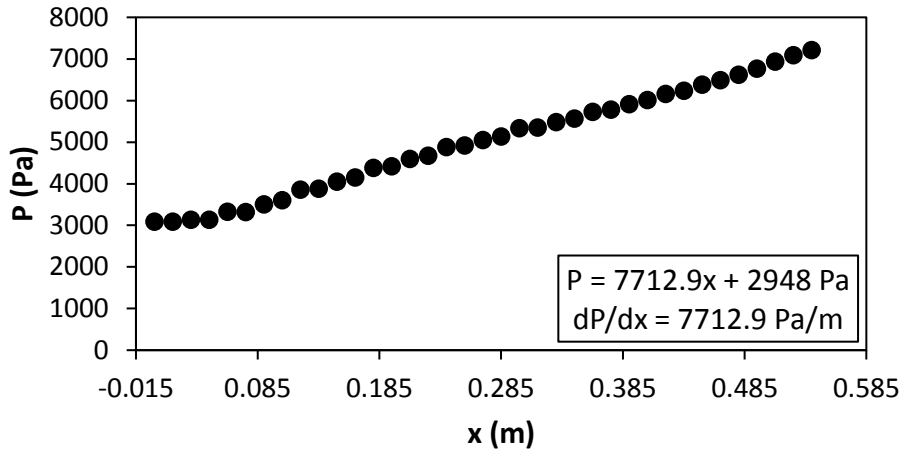


Figure G.30: Static pressure plotted against the x coordinate at $Re = 12\,500$ for setup: $d/p = 0.05$, 90° to the flow direction.

G.3. Pressure data: $d/p = 0.05$, 45° orientation to the flow direction

Figure G.31 to Figure G.45 shows the channel wall pressure for the $d/p = 0.05$ cylinders, orientated 45° to the flow direction.

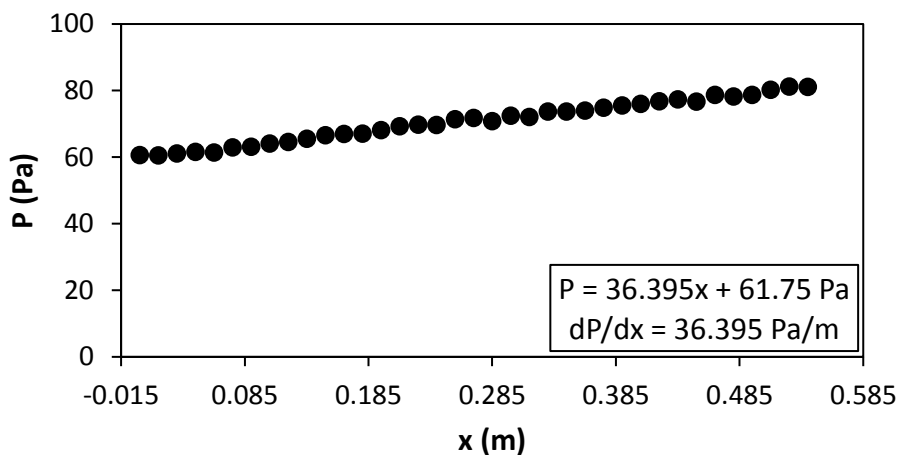


Figure G.31: Static pressure plotted against the x coordinate at $Re = 640$ for setup: $d/p = 0.05$, 45° to the flow direction.

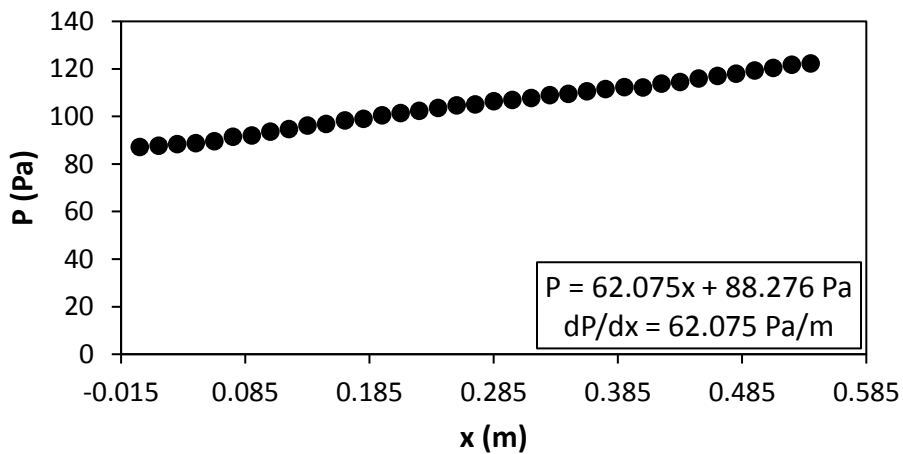


Figure G.32: Static pressure plotted against the x coordinate at $Re = 920$ for setup: $d/p = 0.05$, 45° to the flow direction.

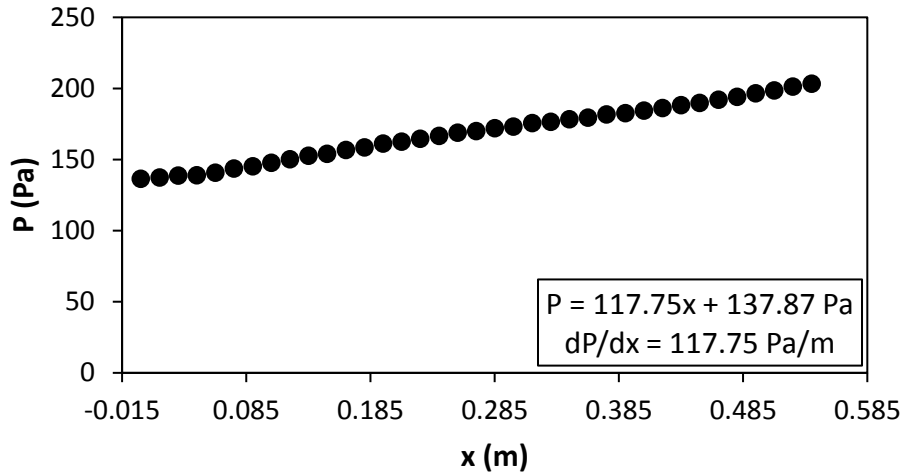


Figure G.33: Static pressure plotted against the x coordinate at $Re = 1\,400$ for setup: $d/p = 0.05$, 45° to the flow direction.

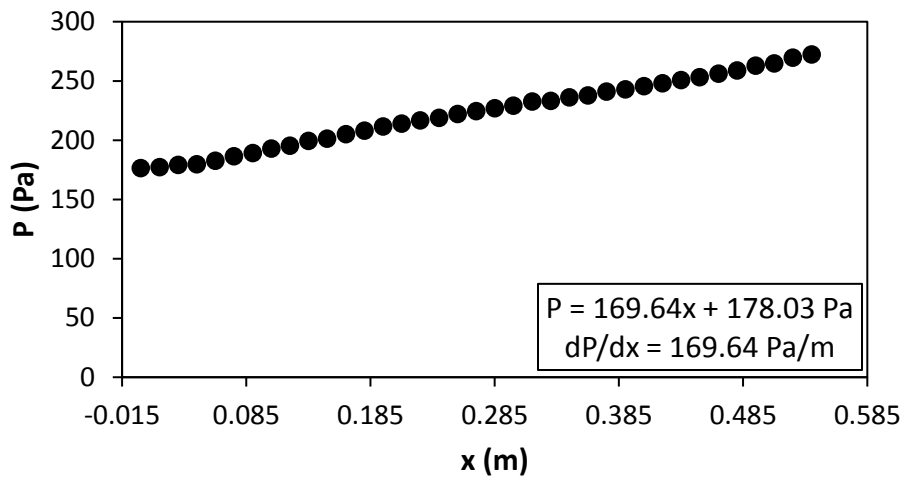


Figure G.34: Static pressure plotted against the x coordinate at $Re = 1\,800$ for setup: $d/p = 0.05$, 45° to the flow direction.

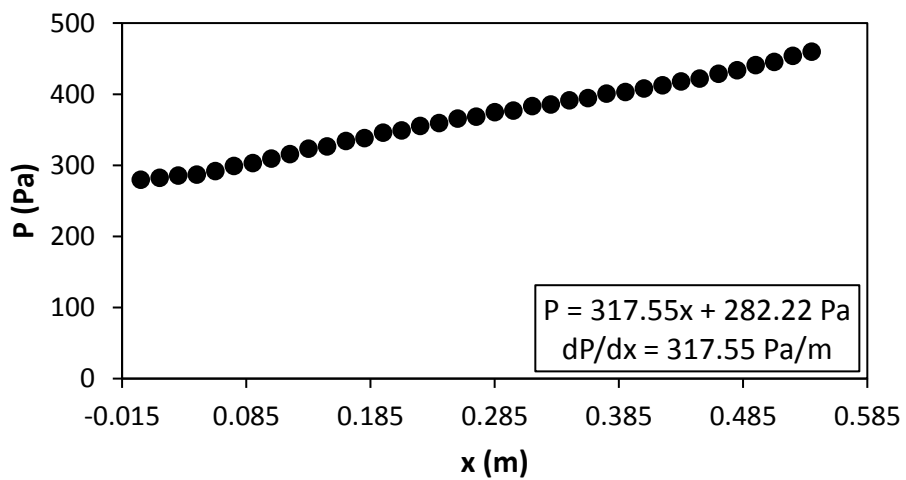


Figure G.35: Static pressure plotted against the x coordinate at $Re = 3\,000$ for setup: $d/p = 0.05$, 45° to the flow direction.

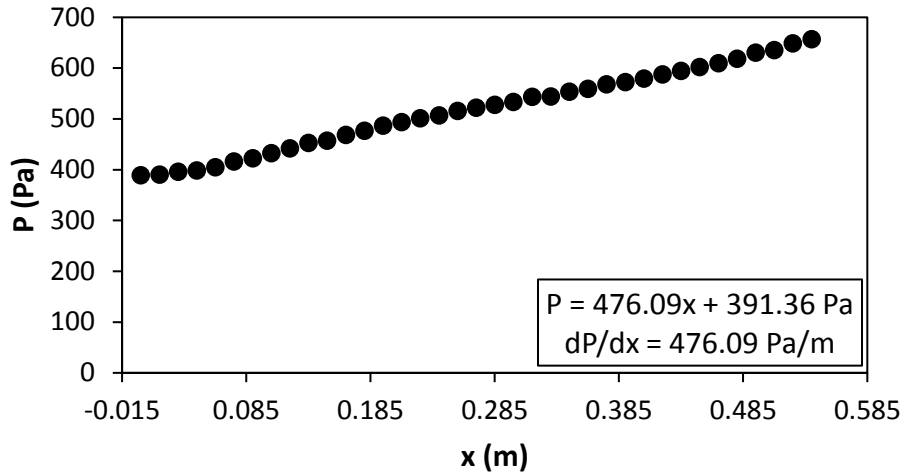


Figure G.36: Static pressure plotted against the x coordinate at $Re = 4000$ for setup: $d/p = 0.05$, 45° to the flow direction.

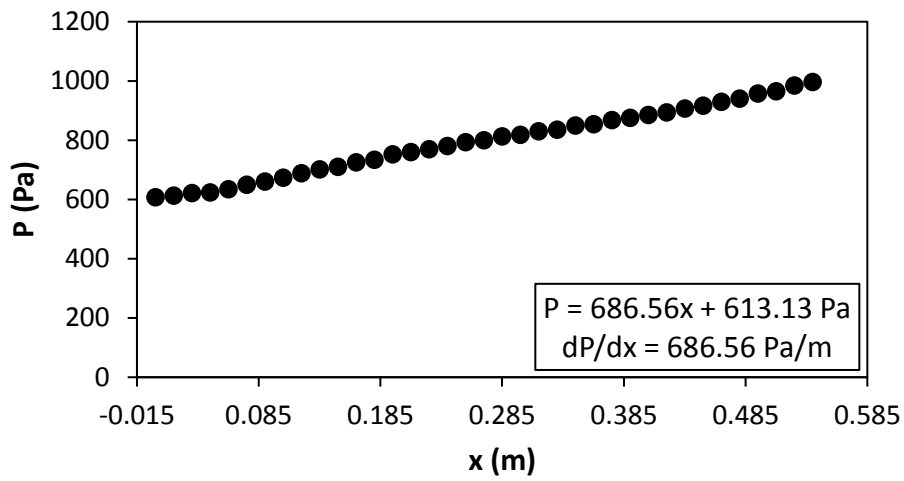


Figure G.37: Static pressure plotted against the x coordinate at $Re = 5000$ for setup: $d/p = 0.05$, 45° to the flow direction.

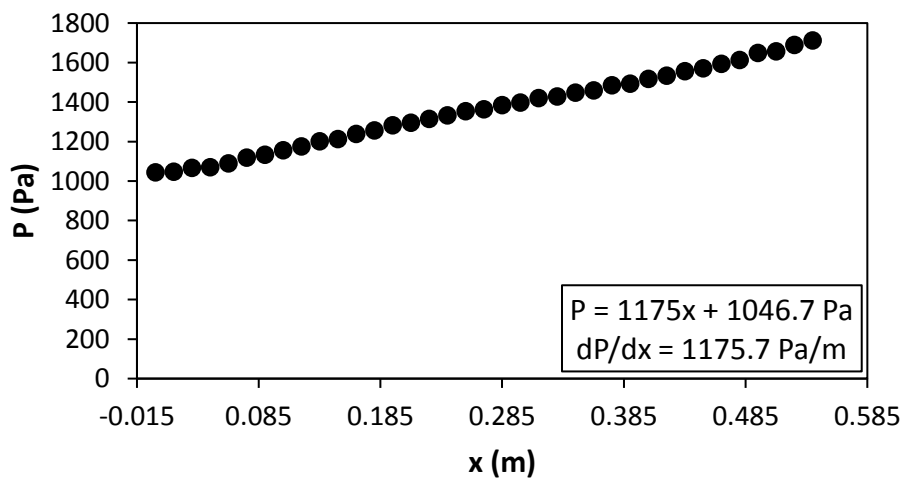


Figure G.38: Static pressure plotted against the x coordinate at $Re = 6000$ for setup: $d/p = 0.05$, 45° to the flow direction.

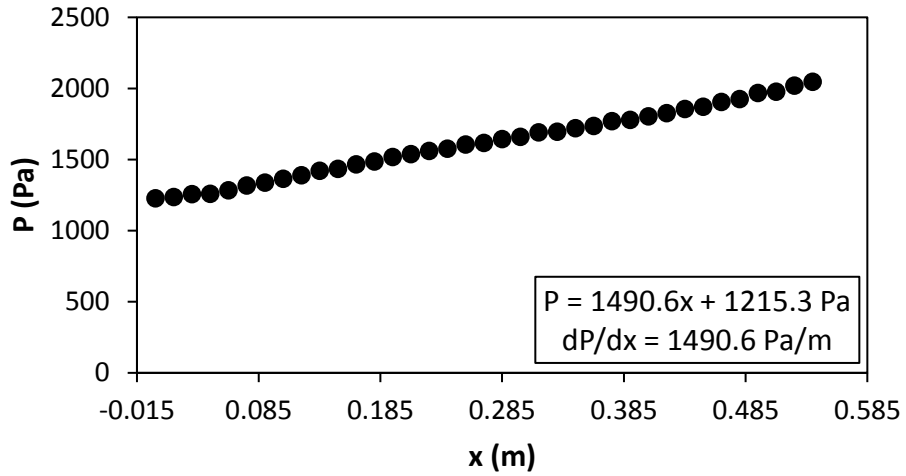


Figure G.39: Static pressure plotted against the x coordinate at $Re = 7000$ for setup: $d/p = 0.05$, 45° to the flow direction.

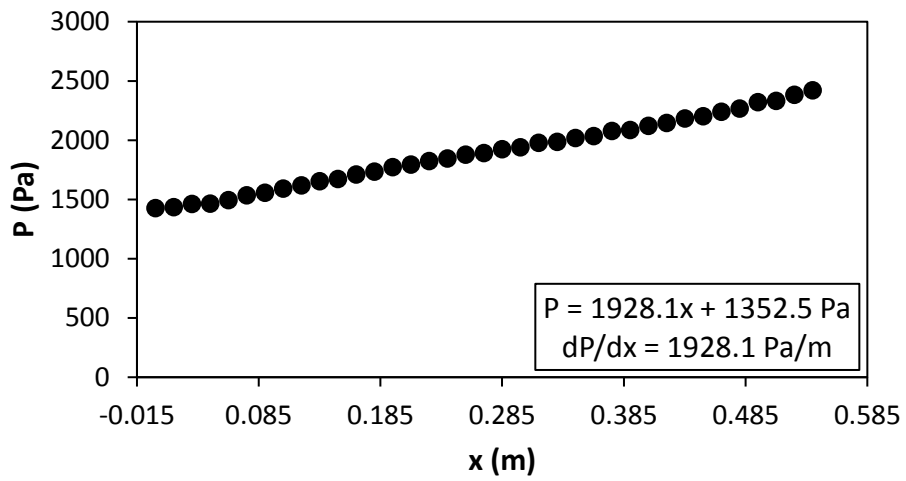


Figure G.40: Static pressure plotted against the x coordinate at $Re = 8000$ for setup: $d/p = 0.05$, 45° to the flow direction.

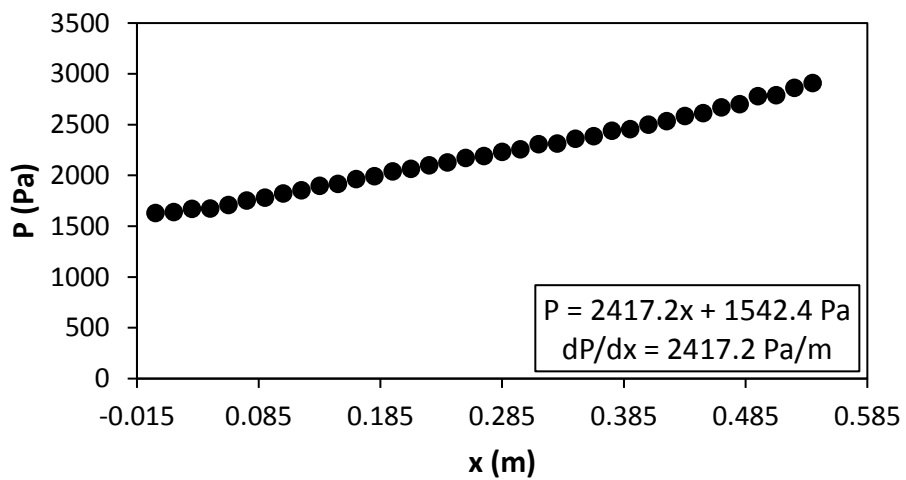


Figure G.41: Static pressure plotted against the x coordinate at $Re = 9000$ for setup: $d/p = 0.05$, 45° to the flow direction.

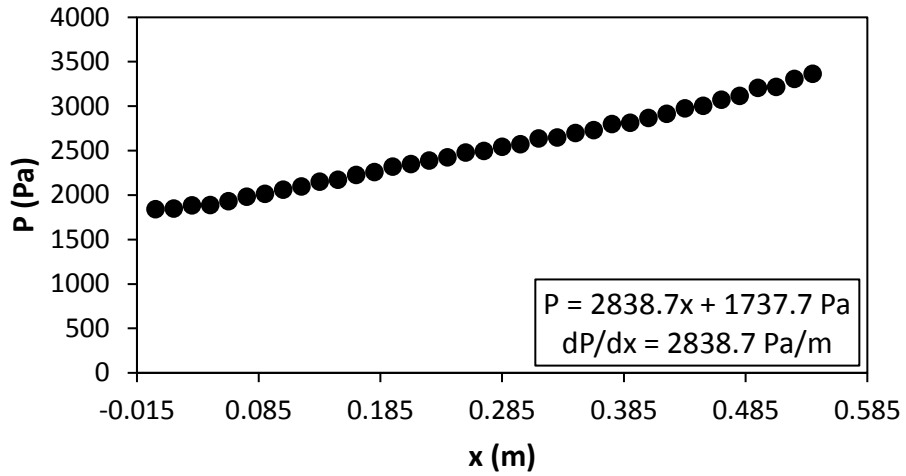


Figure G.42: Static pressure plotted against the x coordinate at $Re = 9700$ for setup: $d/p = 0.05$, 45° to the flow direction.

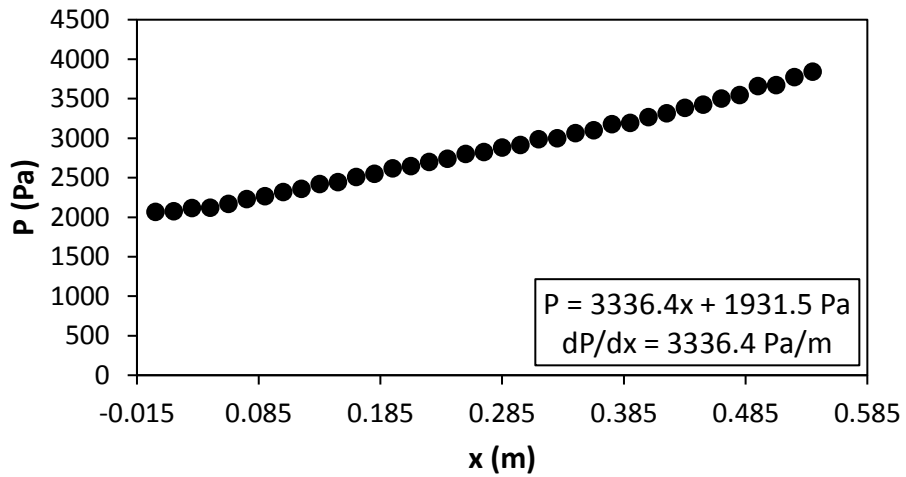


Figure G.43: Static pressure plotted against the x coordinate at $Re = 10500$ for setup: $d/p = 0.05$, 45° to the flow direction.

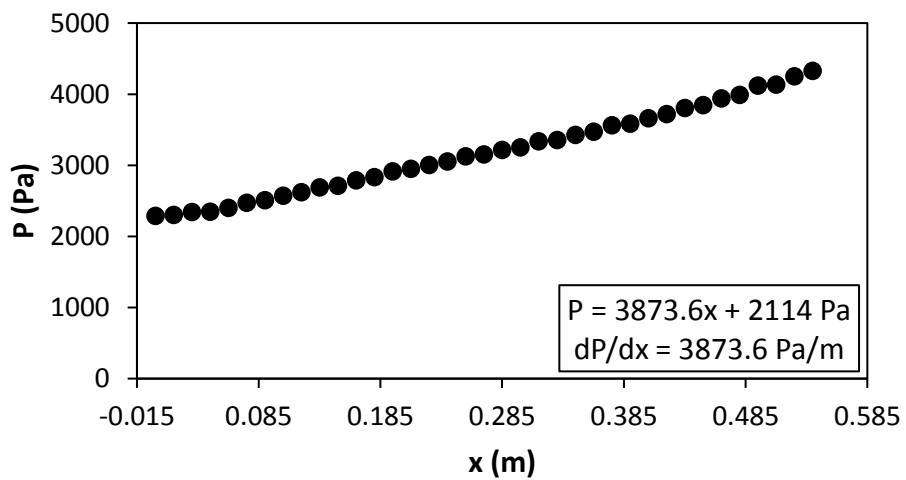


Figure G.44: Static pressure plotted against the x coordinate at $Re = 11500$ for setup: $d/p = 0.05$, 45° to the flow direction.

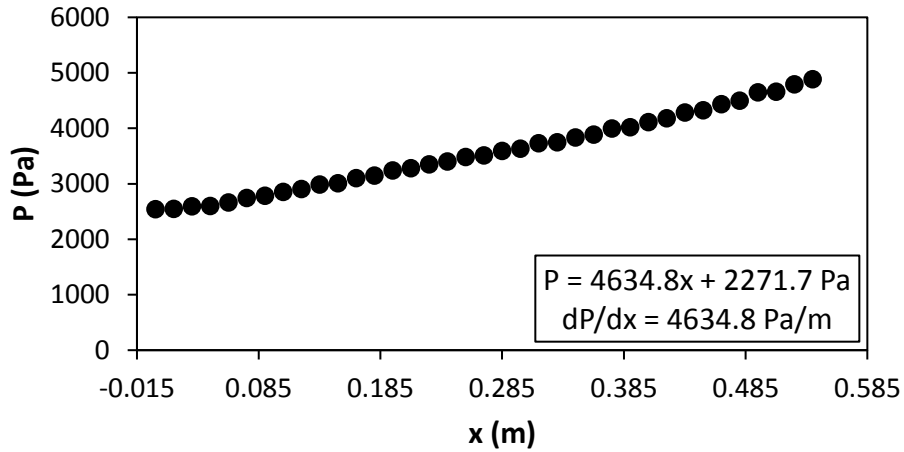


Figure G.45: Static pressure plotted against the x coordinate at Re = 12 500 for setup: d/p = 0.05, 45° to the flow direction.

G.4. Pressure data: d/p = 0.025, 90° orientation to the flow direction

Figure G.46 to Figure G.60 shows the channel wall pressure for the d/p = 0.025 cylinders, orientated 90° to the flow direction.

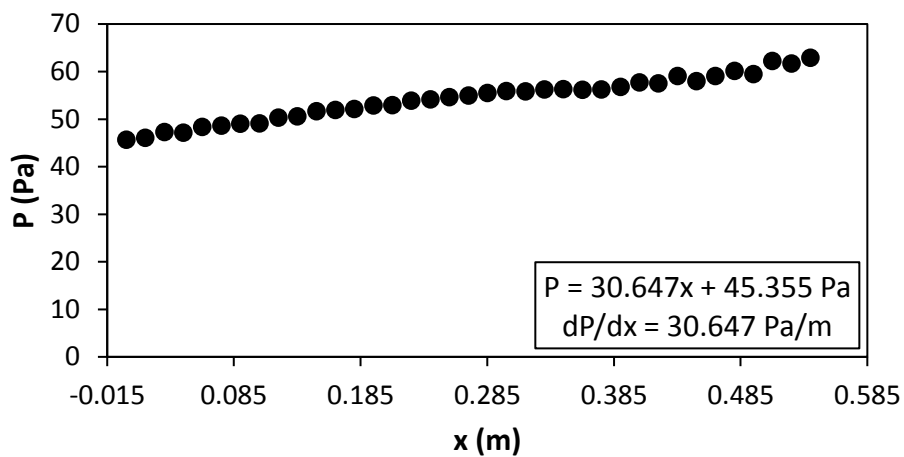


Figure G.46: Static pressure plotted against the x coordinate at Re = 640 for setup: d/p = 0.025, 90° to the flow direction.

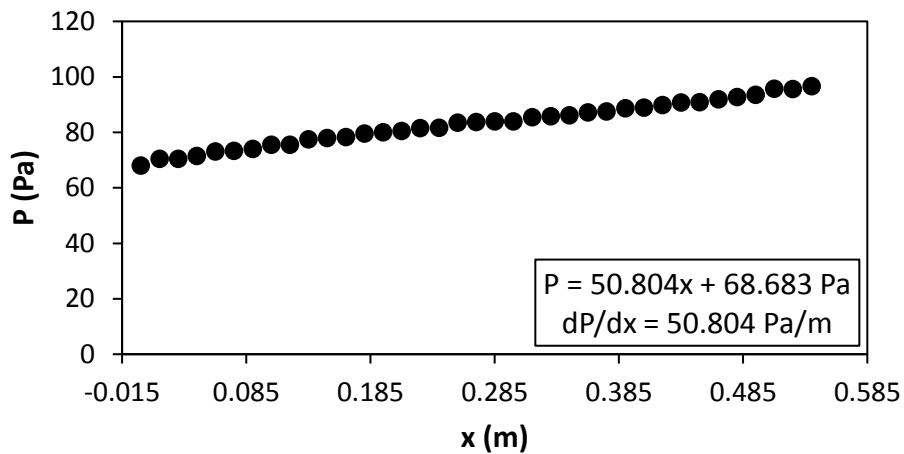


Figure G.47: Static pressure plotted against the x coordinate at Re = 920 for setup: d/p = 0.025, 90° to the flow direction.

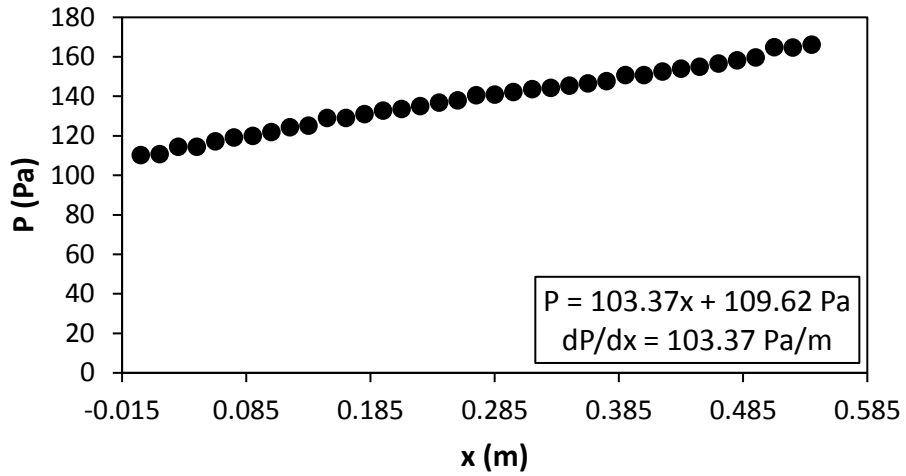


Figure G.48: Static pressure plotted against the x coordinate at $Re = 1400$ for setup: $d/p = 0.025$, 90° to the flow direction.

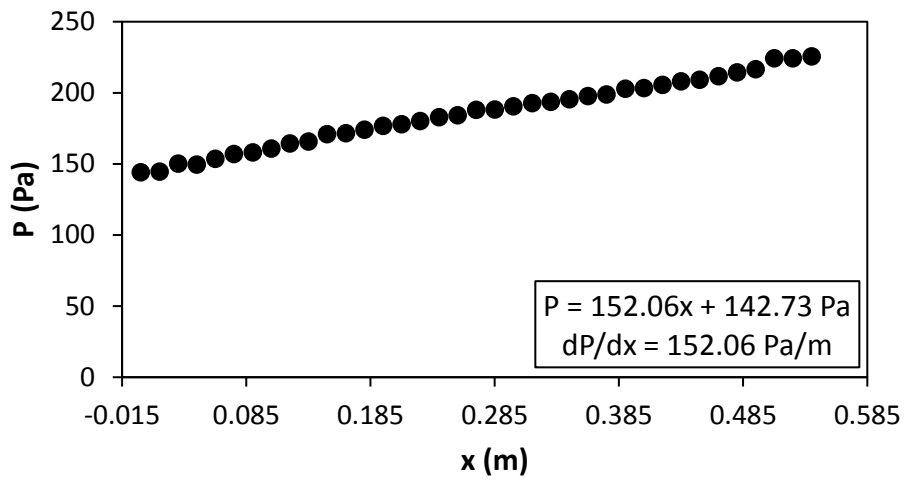


Figure G.49: Static pressure plotted against the x coordinate at $Re = 1800$ for setup: $d/p = 0.025$, 90° to the flow direction.

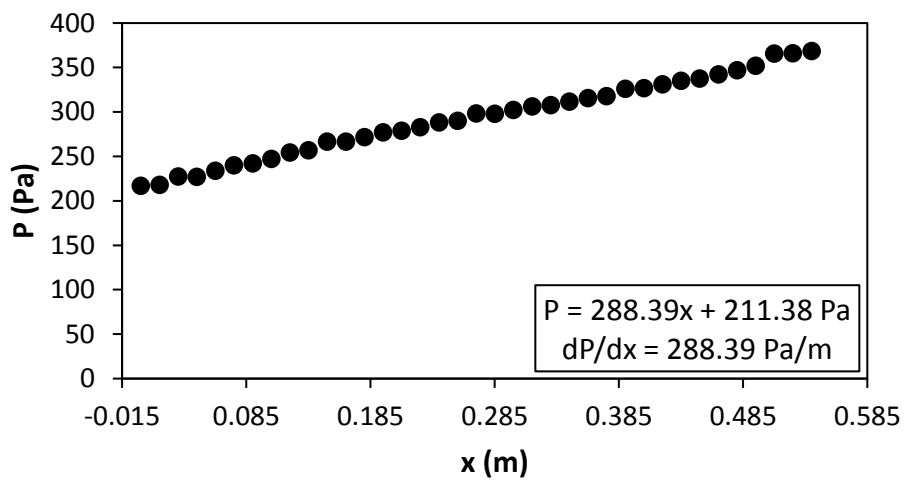


Figure G.50: Static pressure plotted against the x coordinate at $Re = 3000$ for setup: $d/p = 0.025$, 90° to the flow direction.

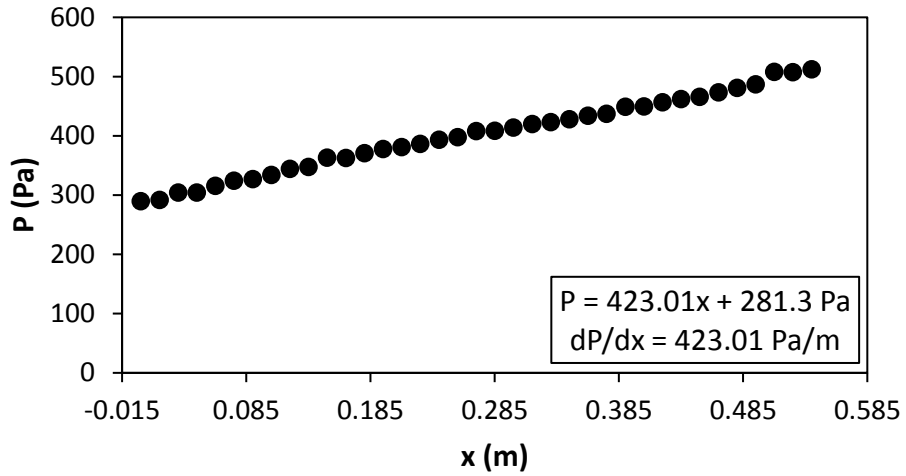


Figure G.51: Static pressure plotted against the x coordinate at $Re = 4000$ for setup: $d/p = 0.025$, 90° to the flow direction.

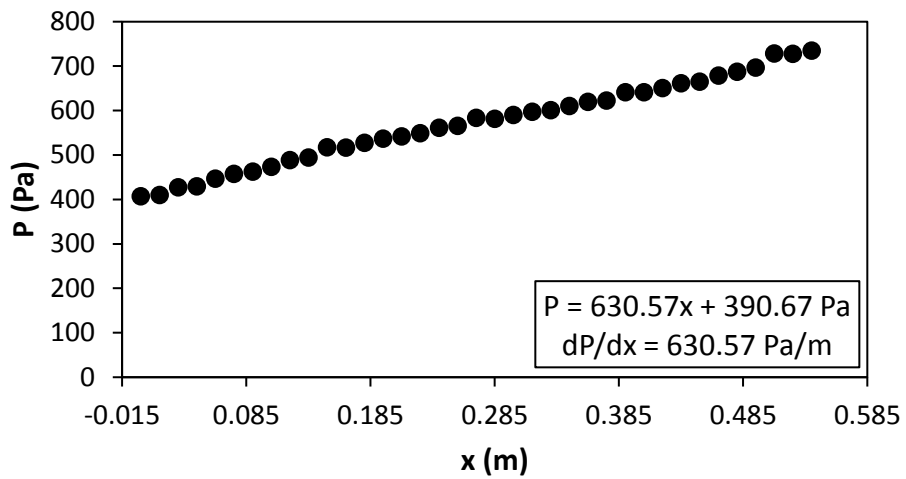


Figure G.52: Static pressure plotted against the x coordinate at $Re = 5000$ for setup: $d/p = 0.025$, 90° to the flow direction.

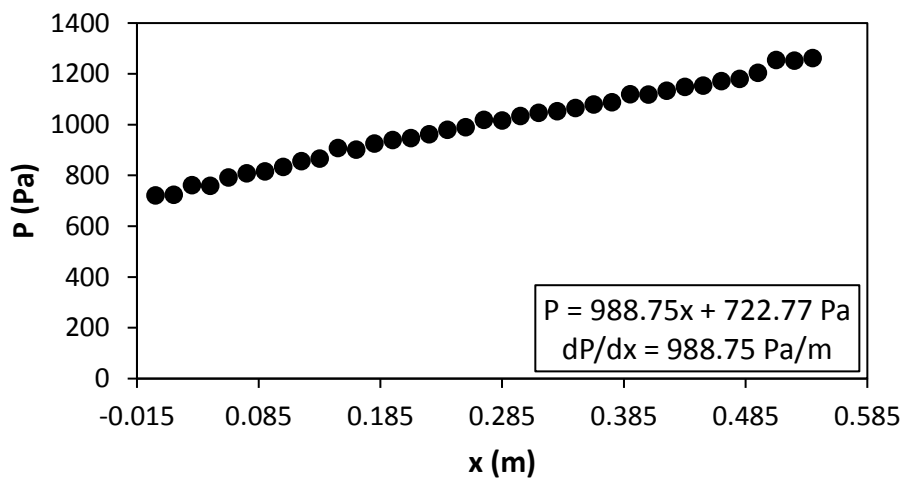


Figure G.53: Static pressure plotted against the x coordinate at $Re = 6000$ for setup: $d/p = 0.025$, 90° to the flow direction.

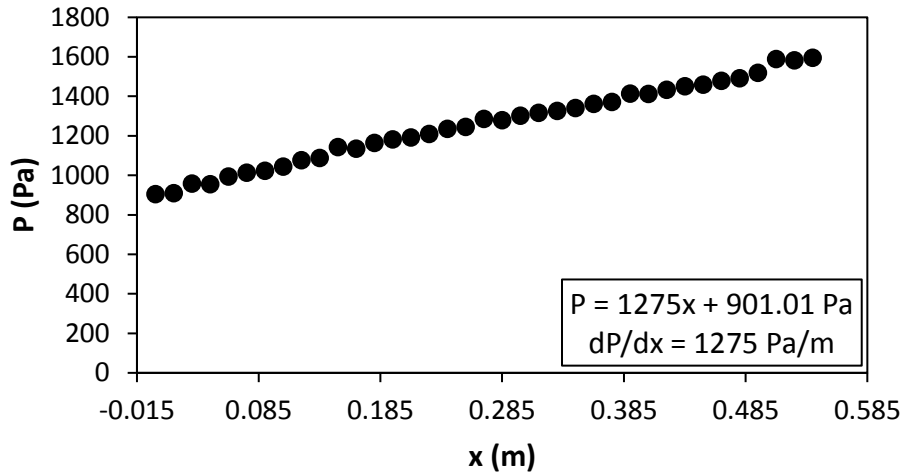


Figure G.54: Static pressure plotted against the x coordinate at $Re = 7000$ for setup: $d/p = 0.025$, 90° to the flow direction.

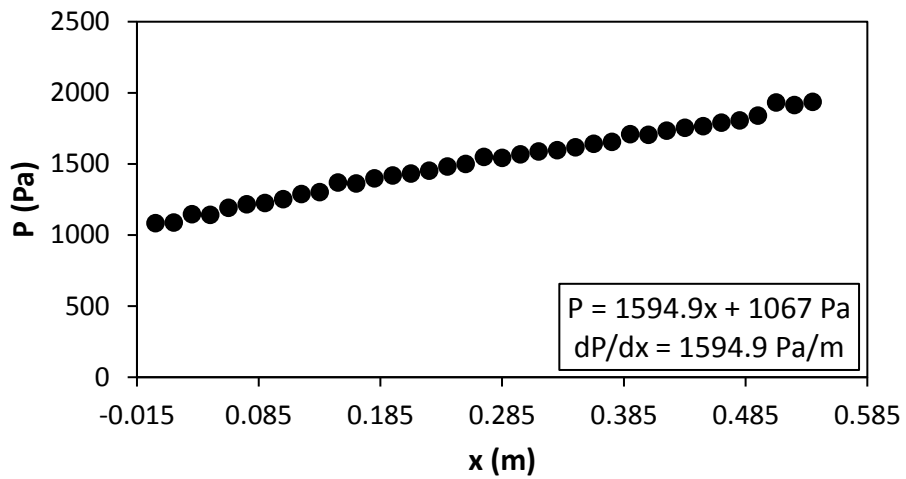


Figure G.55: Static pressure plotted against the x coordinate at $Re = 8000$ for setup: $d/p = 0.025$, 90° to the flow direction.

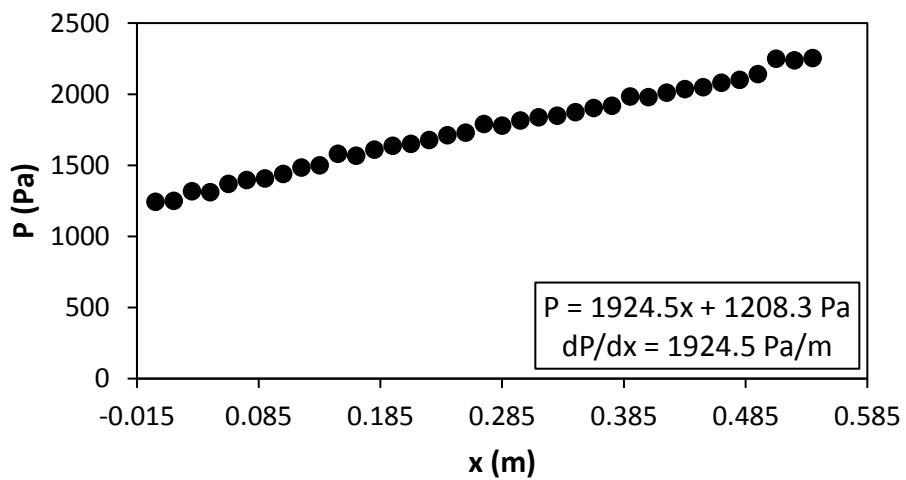


Figure G.56: Static pressure plotted against the x coordinate at $Re = 9000$ for setup: $d/p = 0.025$, 90° to the flow direction.

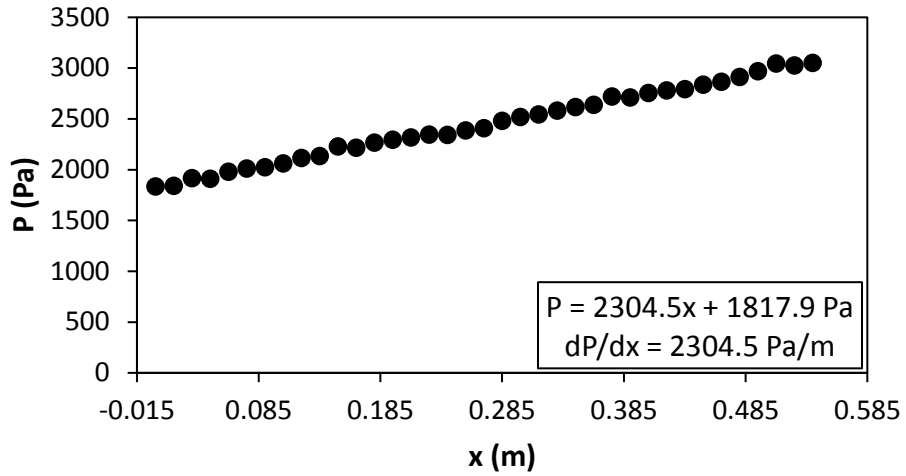


Figure G.57: Static pressure plotted against the x coordinate at Re = 9 700 for setup: $d/p = 0.025$, 90° to the flow direction.

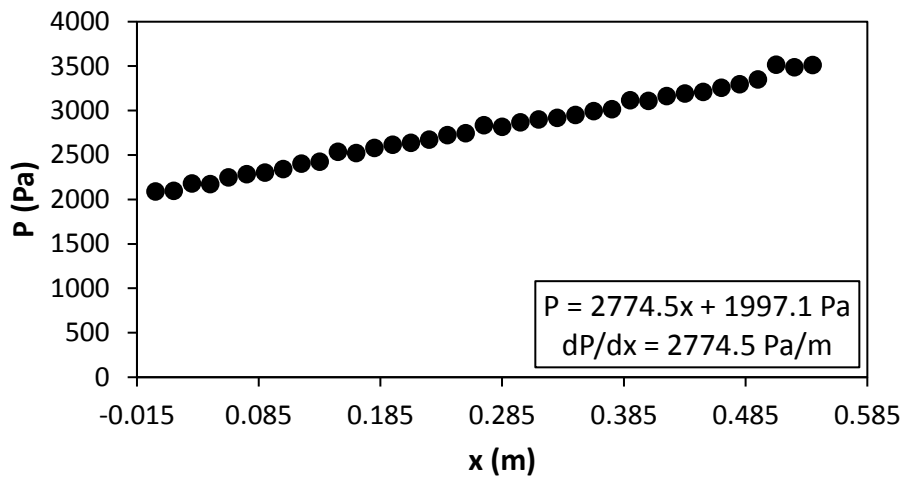


Figure G.58: Static pressure plotted against the x coordinate at Re = 10 500 for setup: $d/p = 0.025$, 90° to the flow direction.

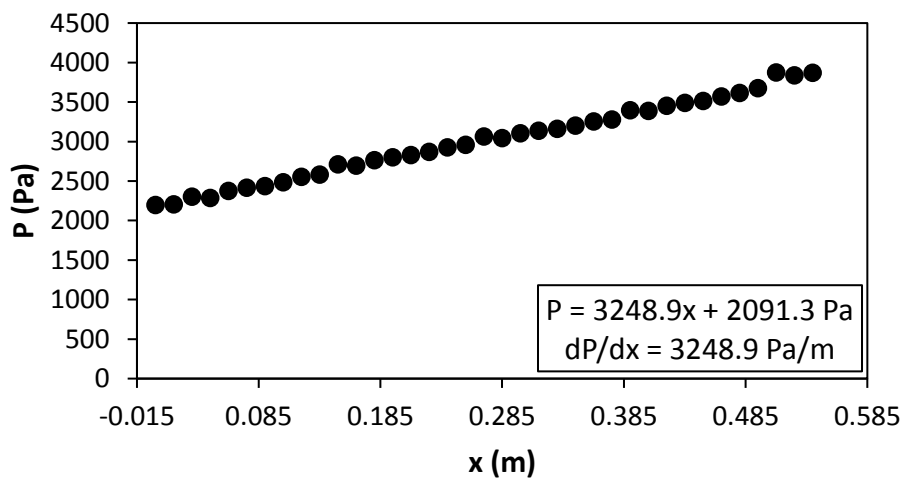


Figure G.59: Static pressure plotted against the x coordinate at Re = 11 500 for setup: $d/p = 0.025$, 90° to the flow direction.

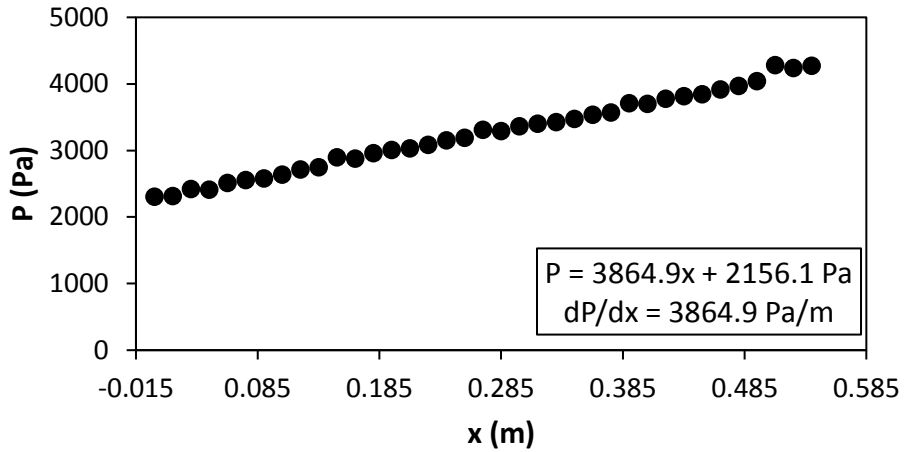


Figure G.60: Static pressure plotted against the x coordinate at Re = 12 500 for setup: $d/p = 0.025$, 90° to the flow direction.

G.5. Pressure data: $d/p = 0.025$, 45° orientation to the flow direction

Figure G.61 to Figure G.75 shows the channel wall pressure for the $d/p = 0.025$ cylinders, orientated 45° to the flow direction.

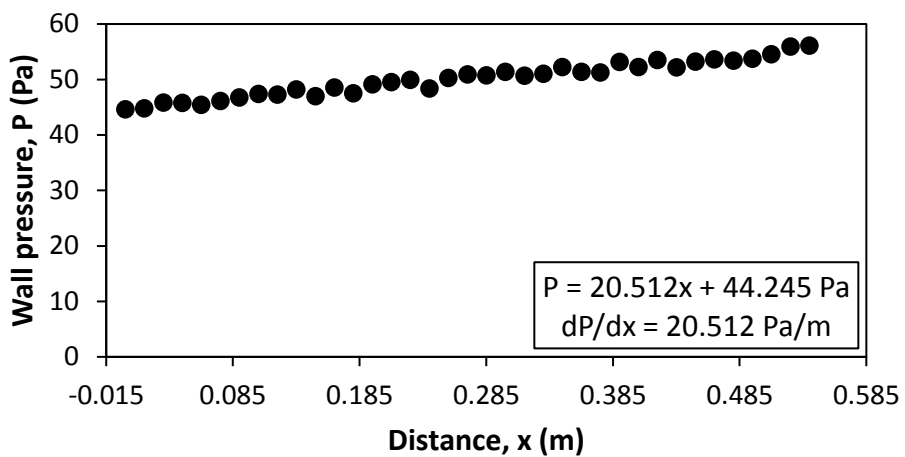


Figure G.61: Static pressure plotted against the x coordinate at Re = 640 for setup: $d/p = 0.025$, 45° to the flow direction.

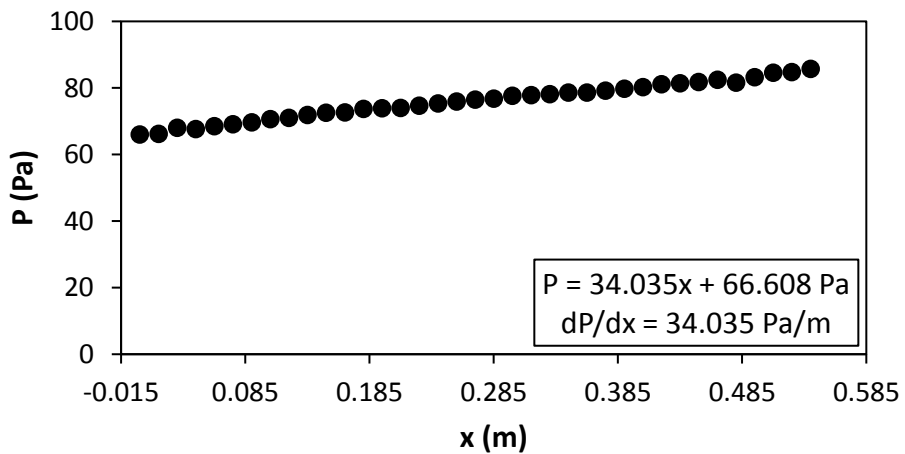


Figure G.62: Static pressure plotted against the x coordinate at Re = 920 for setup: $d/p = 0.025$, 45° to the flow direction.

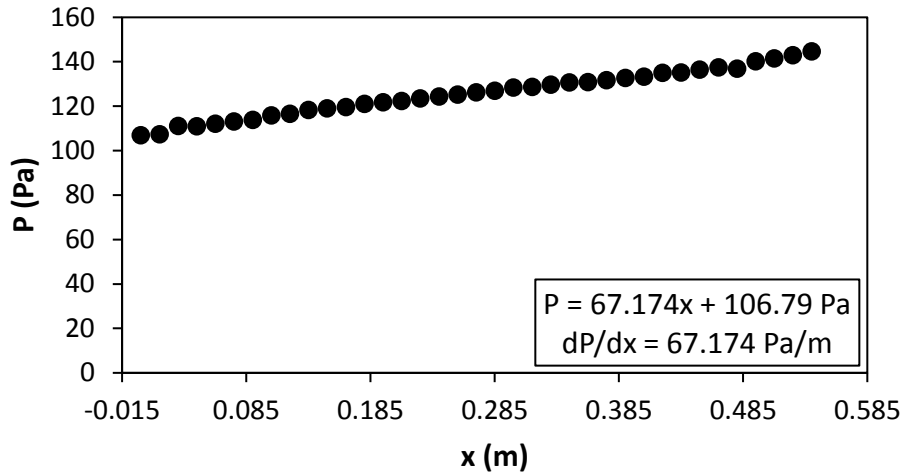


Figure G.63: Static pressure plotted against the x coordinate at $Re = 1\,400$ for setup: $d/p = 0.025$, 45° to the flow direction.

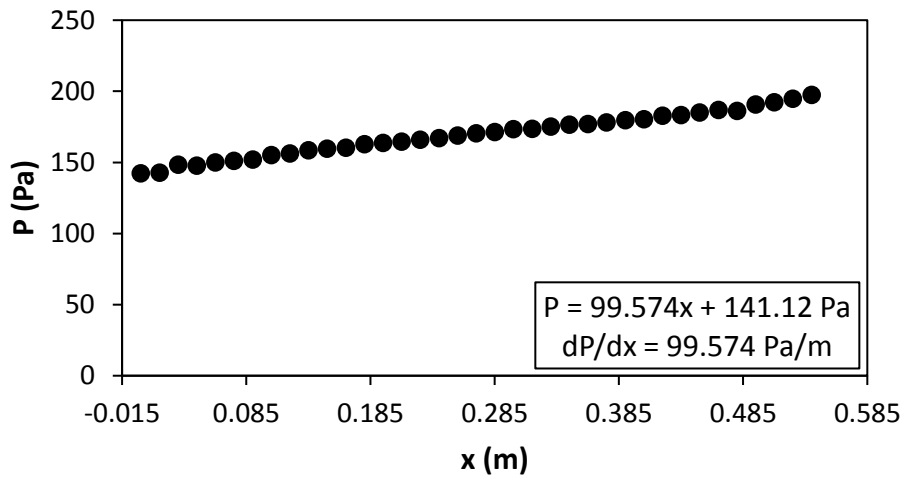


Figure G.64: Static pressure plotted against the x coordinate at $Re = 1\,800$ for setup: $d/p = 0.025$, 45° to the flow direction.

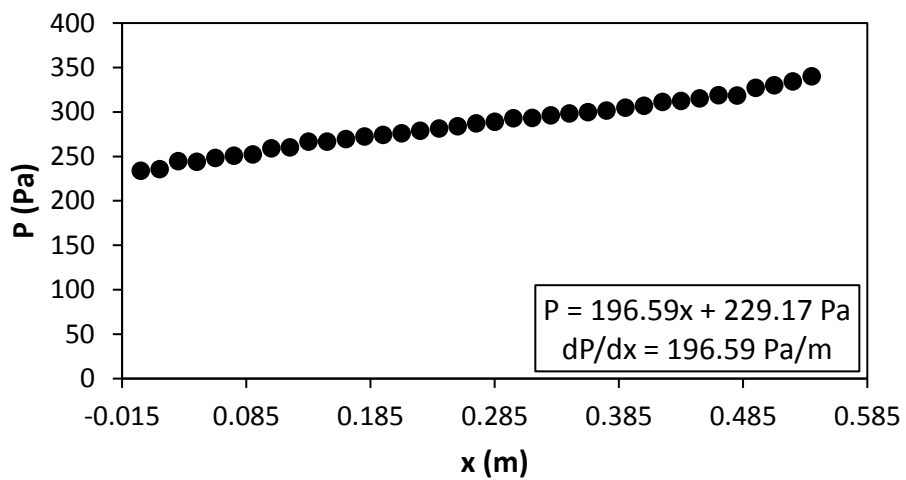


Figure G.65: Static pressure plotted against the x coordinate at $Re = 3\,000$ for setup: $d/p = 0.025$, 45° to the flow direction.

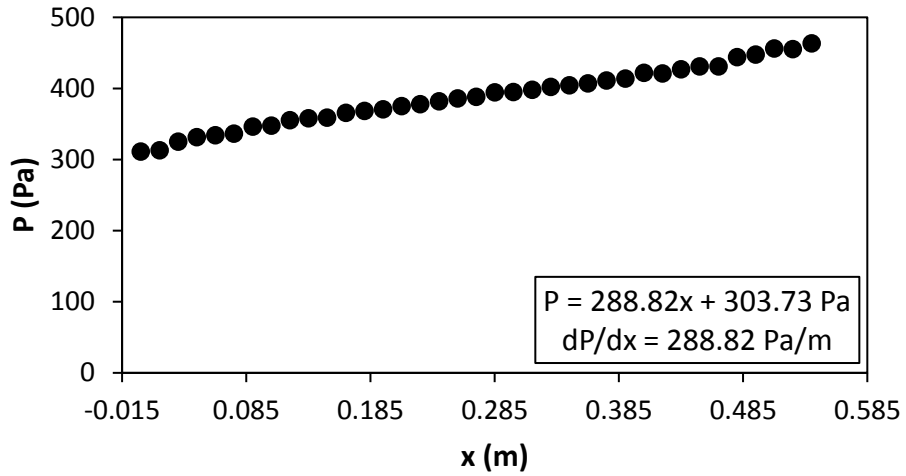


Figure G.66: Static pressure plotted against the x coordinate at $Re = 4\,000$ for setup: $d/p = 0.025$, 45° to the flow direction.

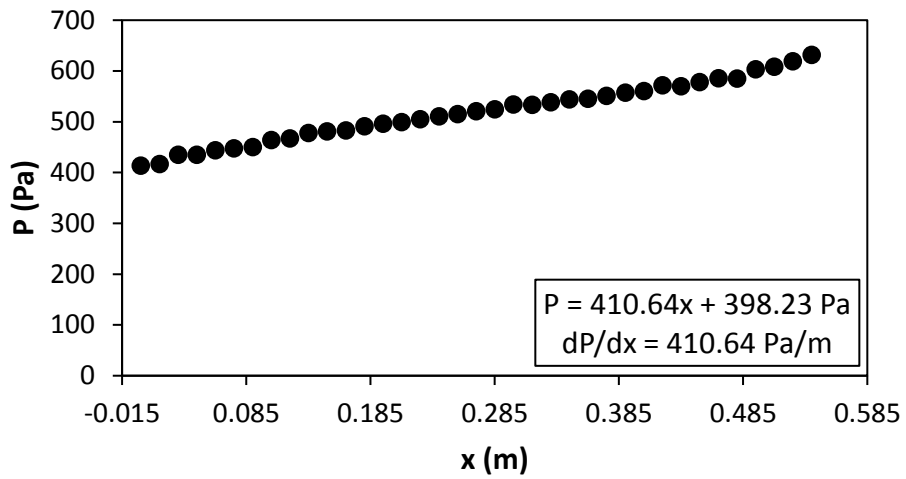


Figure G.67: Static pressure plotted against the x coordinate at $Re = 5\,000$ for setup: $d/p = 0.025$, 45° to the flow direction.

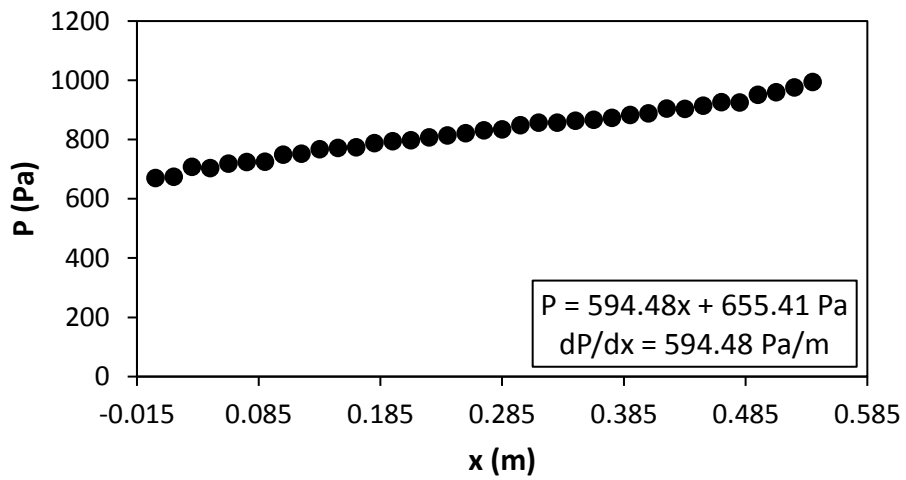


Figure G.68: Static pressure plotted against the x coordinate at $Re = 6\,000$ for setup: $d/p = 0.025$, 45° to the flow direction.

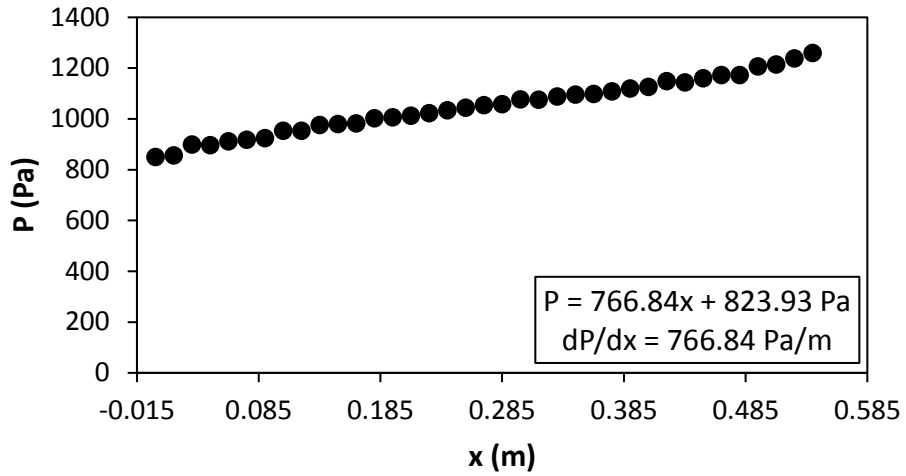


Figure G.69: Static pressure plotted against the x coordinate at $Re = 7000$ for setup: $d/p = 0.025$, 45° to the flow direction.

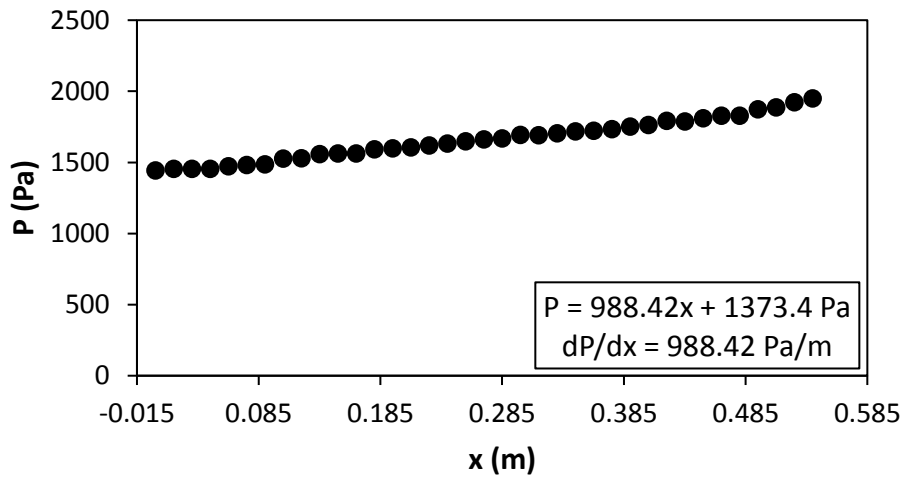


Figure G.70: Static pressure plotted against the x coordinate at $Re = 8000$ for setup: $d/p = 0.025$, 45° to the flow direction.

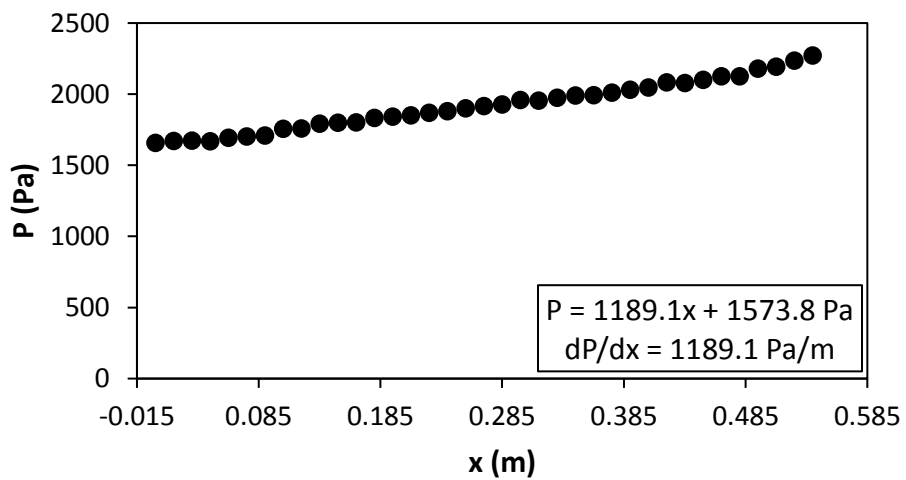


Figure G.71: Static pressure plotted against the x coordinate at $Re = 9000$ for setup: $d/p = 0.025$, 45° to the flow direction.

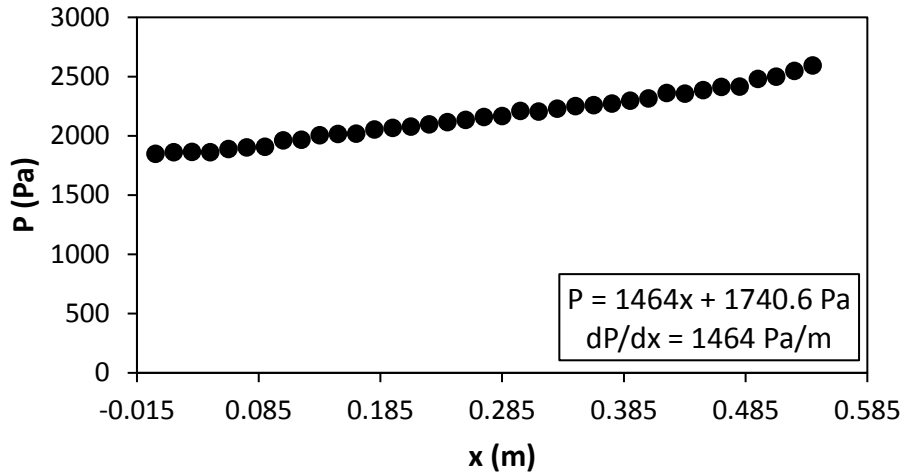


Figure G.72: Static pressure plotted against the x coordinate at $Re = 9\,700$ for setup: $d/p = 0.025$, 45° to the flow direction.

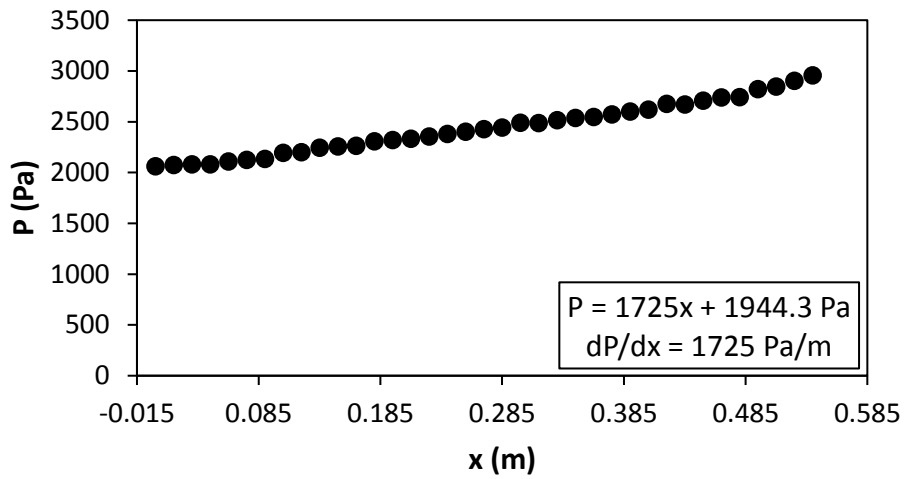


Figure G.73: Static pressure plotted against the x coordinate at $Re = 10\,500$ for setup: $d/p = 0.025$, 45° to the flow direction.

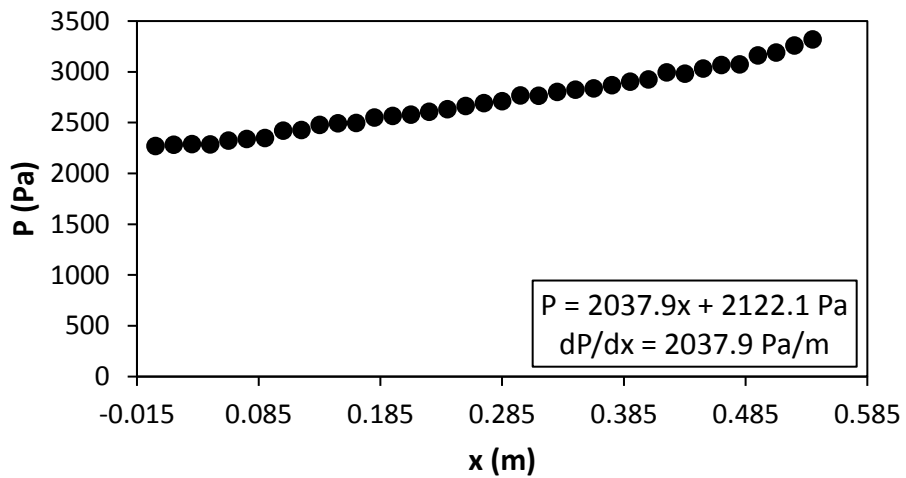


Figure G.74: Static pressure plotted against the x coordinate at $Re = 11\,500$ for setup: $d/p = 0.025$, 45° to the flow direction.

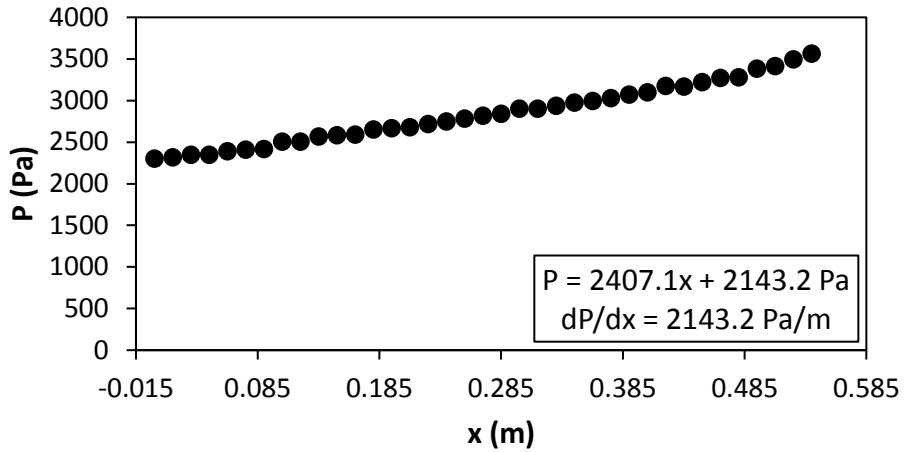


Figure G.75: Static pressure plotted against the x coordinate at $Re = 12\,500$ for setup: $d/p = 0.025$, 45° to the flow direction.

G.6. Pressure data: $d/p = 0.2$, 90° orientation to the flow direction

Figure G.76 to Figure G.87 shows the channel wall pressure for the $d/p = 0.2$ cylinders, orientated 90° to the flow direction.

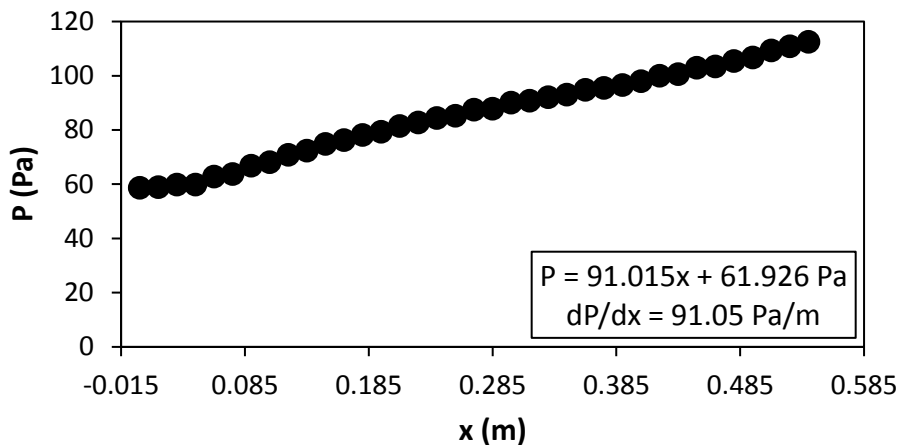


Figure G.76: Static pressure plotted against the x coordinate at $Re = 640$ for setup: $d/p = 0.2$, 90° to the flow direction.

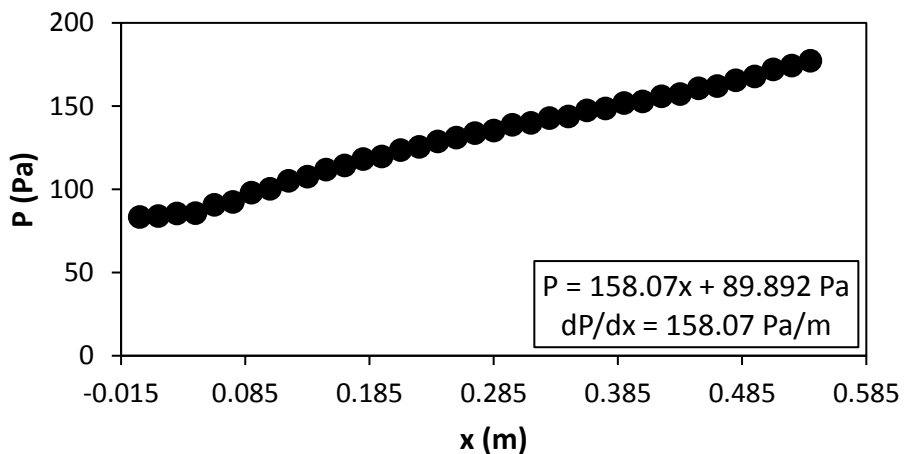


Figure G.77: Static pressure plotted against the x coordinate at $Re = 920$ for setup: $d/p = 0.2$, 90° to the flow direction.

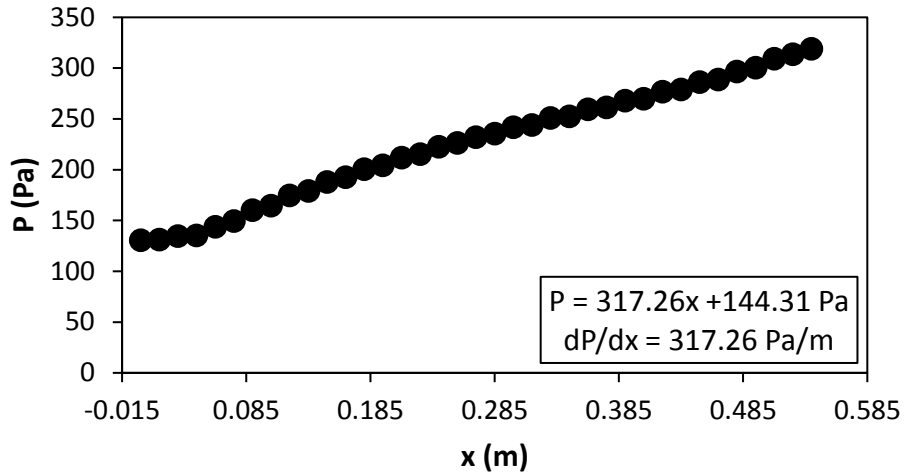


Figure G.78: Static pressure plotted against the x coordinate at $Re = 1400$ for setup: $d/p = 0.2$, 90° to the flow direction.

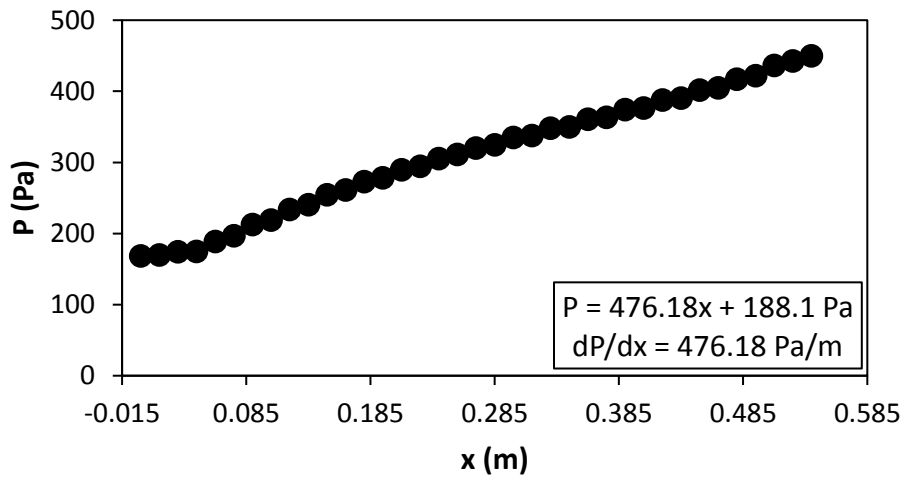


Figure G.79: Static pressure plotted against the x coordinate at $Re = 1800$ for setup: $d/p = 0.2$, 90° to the flow direction.

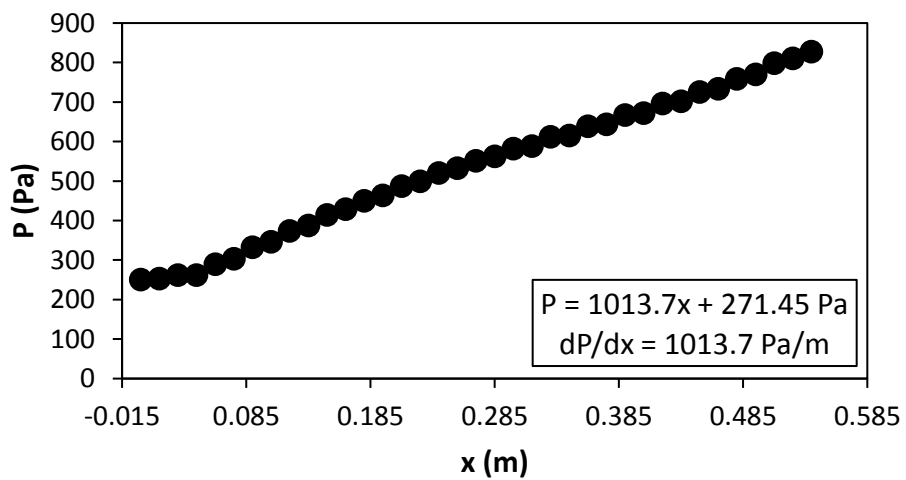


Figure G.80: Static pressure plotted against the x coordinate at $Re = 3000$ for setup: $d/p = 0.2$, 90° to the flow direction.

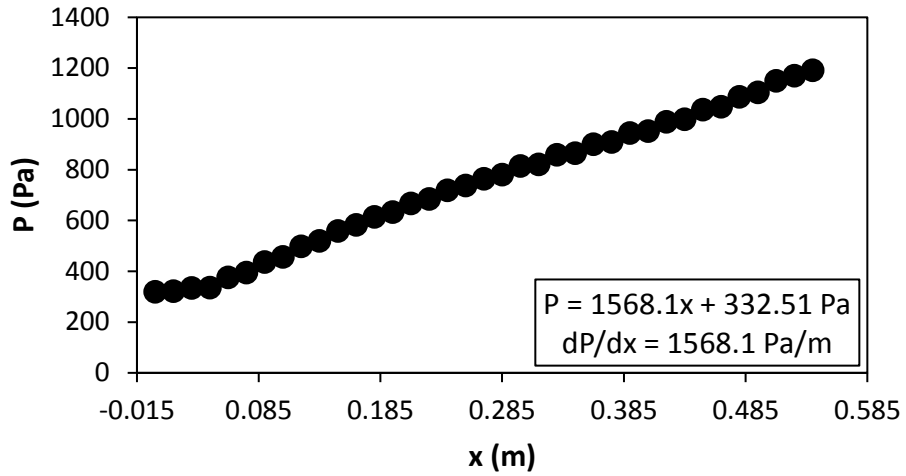


Figure G.81: Static pressure plotted against the x coordinate at Re = 4 000 for setup: $d/p = 0.2$, 90° to the flow direction.

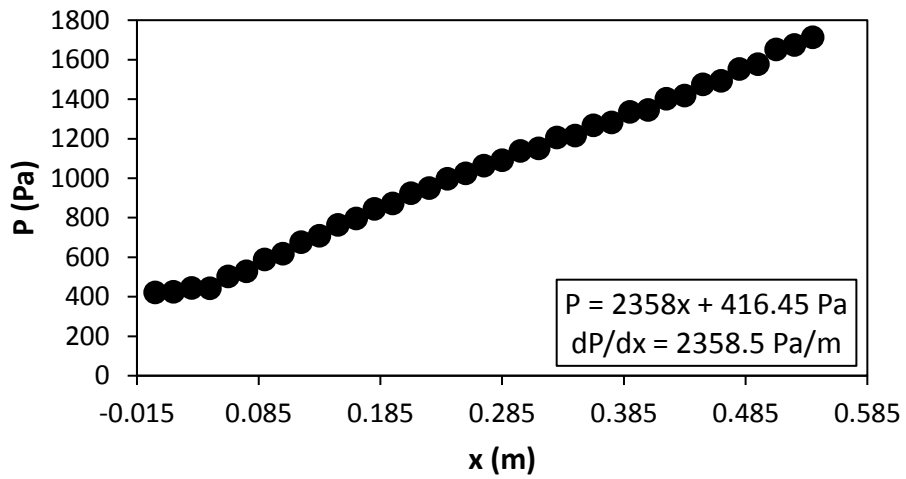


Figure G.82: Static pressure plotted against the x coordinate at Re = 5 000 for setup: $d/p = 0.2$, 90° to the flow direction.

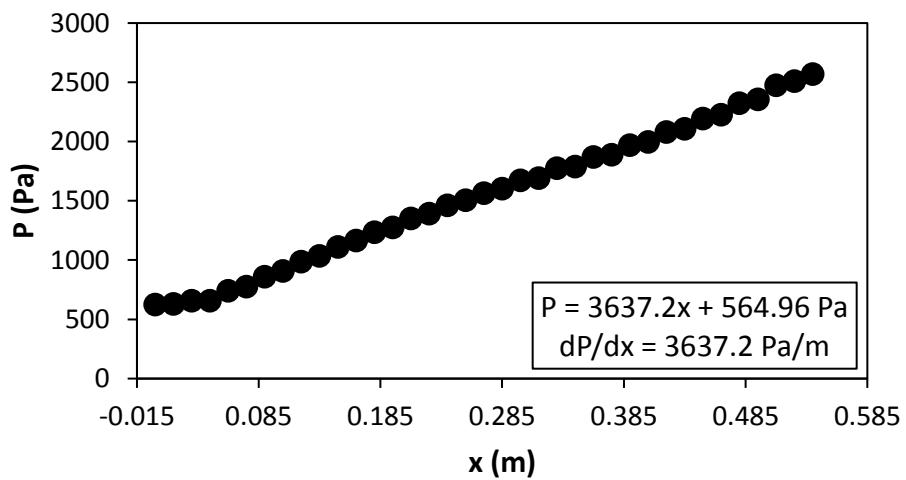


Figure G.83: Static pressure plotted against the x coordinate at Re = 6 000 for setup: $d/p = 0.2$, 90° to the flow direction.

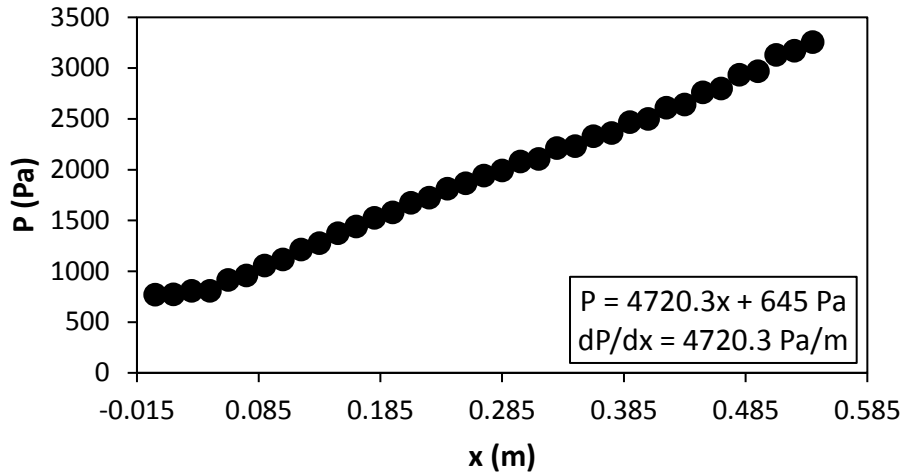


Figure G.84: Static pressure plotted against the x coordinate at Re = 7 000 for setup: $d/p = 0.2$, 90° to the flow direction.

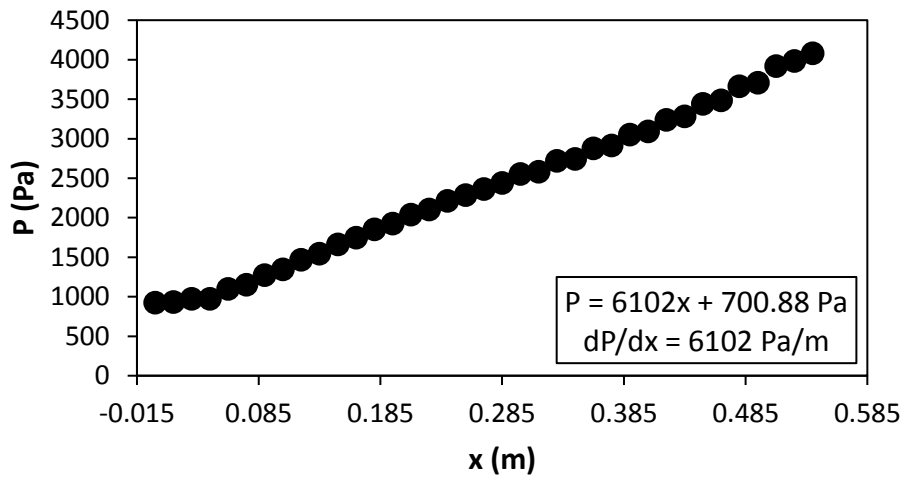


Figure G.85: Static pressure plotted against the x coordinate at Re = 8 000 for setup: $d/p = 0.2$, 90° to the flow direction.

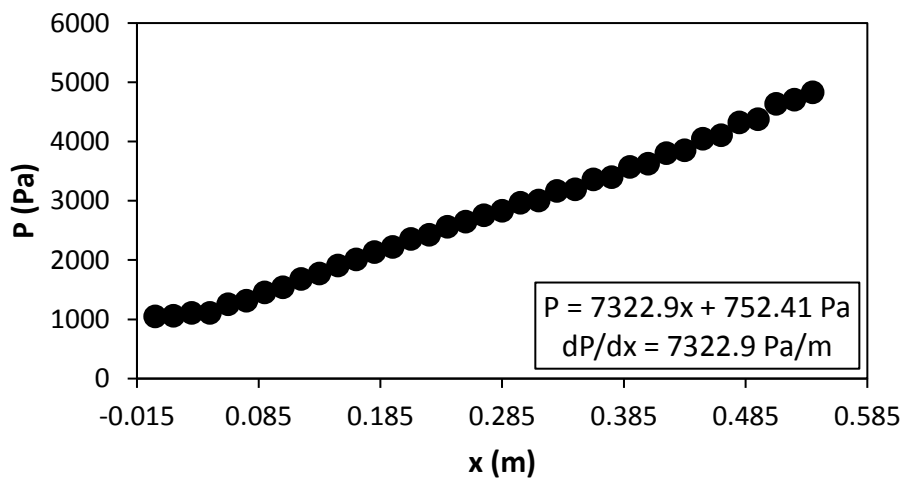


Figure G.86: Static pressure plotted against the x coordinate at Re = 9 000 for setup: $d/p = 0.2$, 90° to the flow direction.

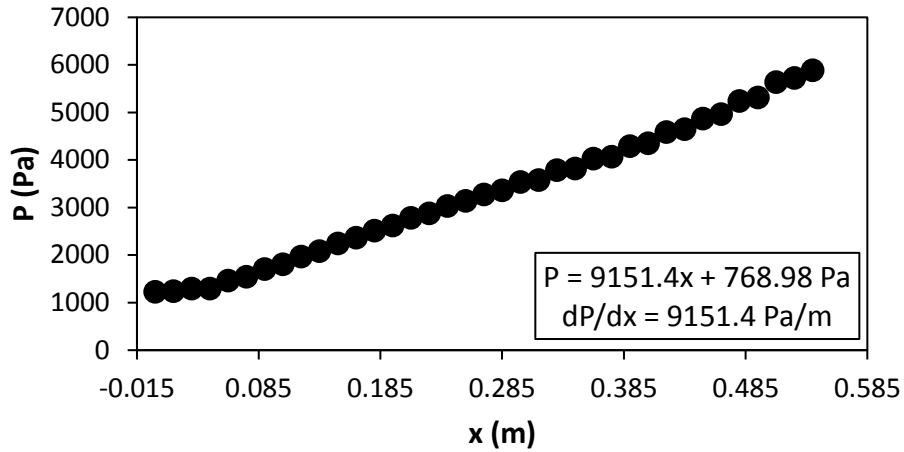


Figure G.87: Static pressure plotted against the x coordinate at Re = 9 700 for setup: $d/p = 0.2$, 90° to the flow direction.

G.7. Pressure data: $d/p = 0.2$, 45° orientation to the flow direction

Figure G.88 to Figure G.102 shows the channel wall pressure for the $d/p = 0.2$ cylinders, orientated 45° to the flow direction.

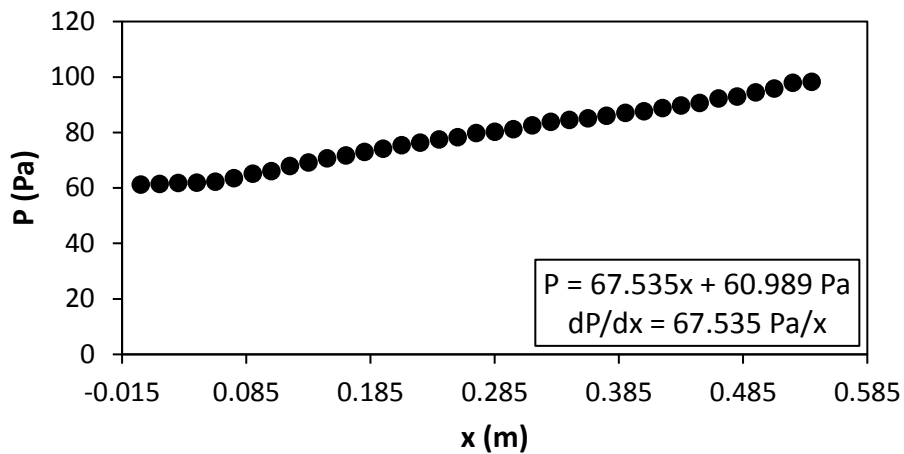


Figure G.88: Static pressure plotted against the x coordinate at Re = 640 for setup: $d/p = 0.2$, 45° to the flow direction.

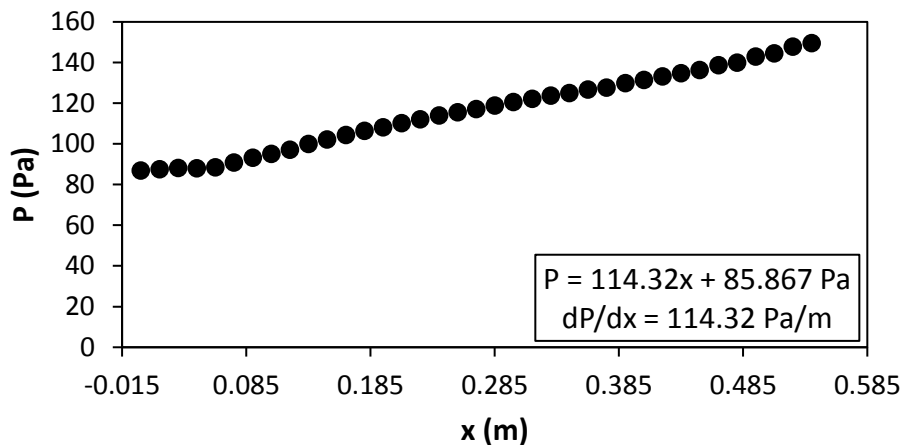


Figure G.89: Static pressure plotted against the x coordinate at Re = 920 for setup: $d/p = 0.2$, 45° to the flow direction.

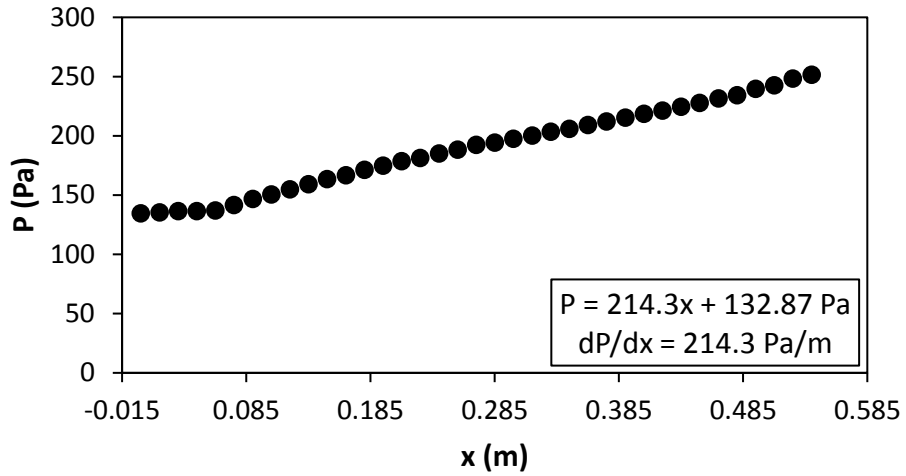


Figure G.90: Static pressure plotted against the x coordinate at $Re = 1\,400$ for setup: $d/p = 0.2$, 45° to the flow direction.

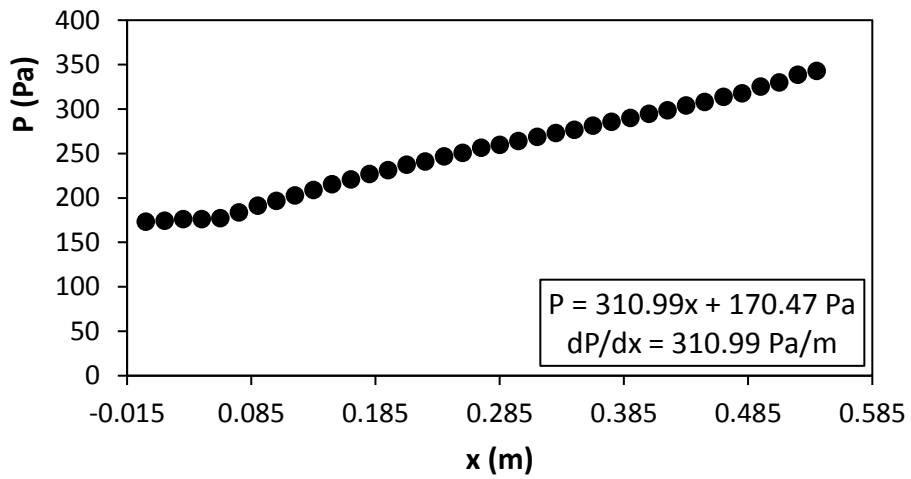


Figure G.91: Static pressure plotted against the x coordinate at $Re = 1\,800$ for setup: $d/p = 0.2$, 45° to the flow direction.

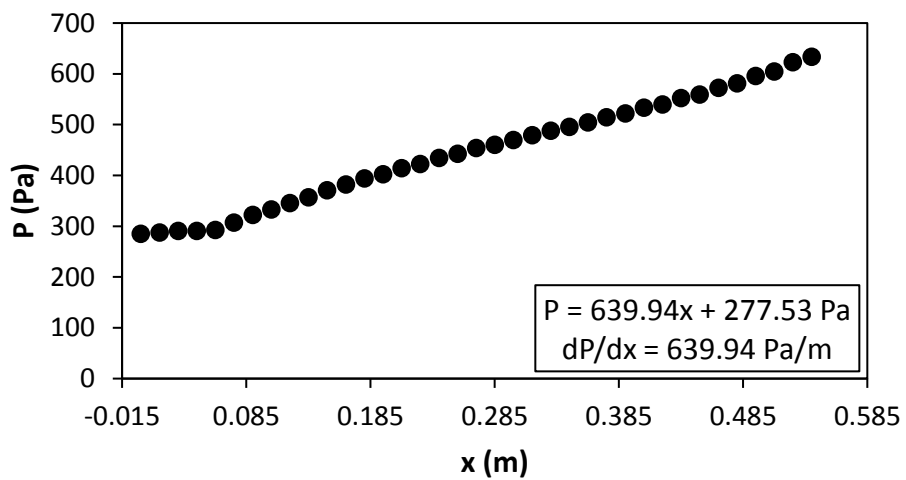


Figure G.92: Static pressure plotted against the x coordinate at $Re = 3\,000$ for setup: $d/p = 0.2$, 45° to the flow direction.

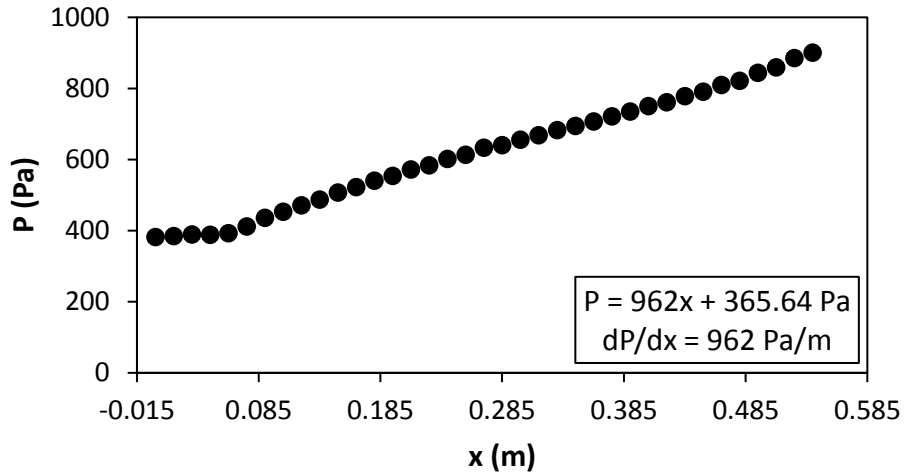


Figure G.93: Static pressure plotted against the x coordinate at Re = 4 000 for setup: $d/p = 0.2$, 45° to the flow direction.

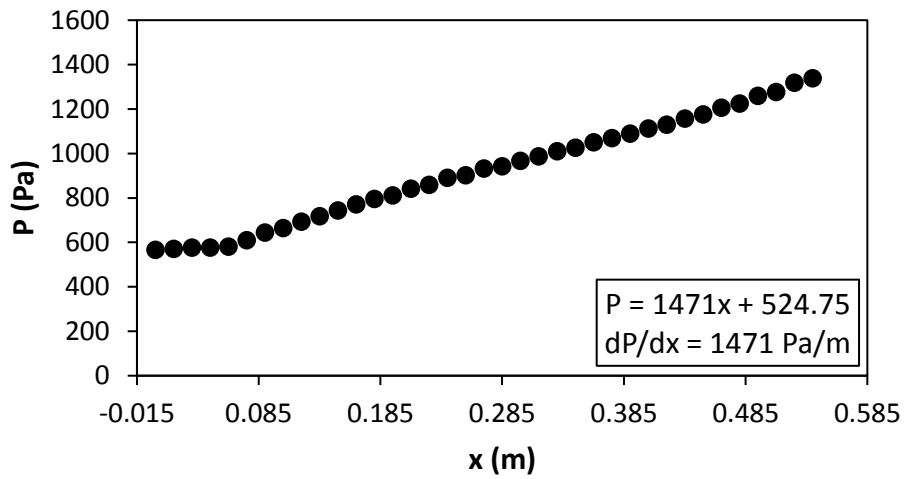


Figure G.94: Static pressure plotted against the x coordinate at Re = 5 000 for setup: $d/p = 0.2$, 45° to the flow direction.

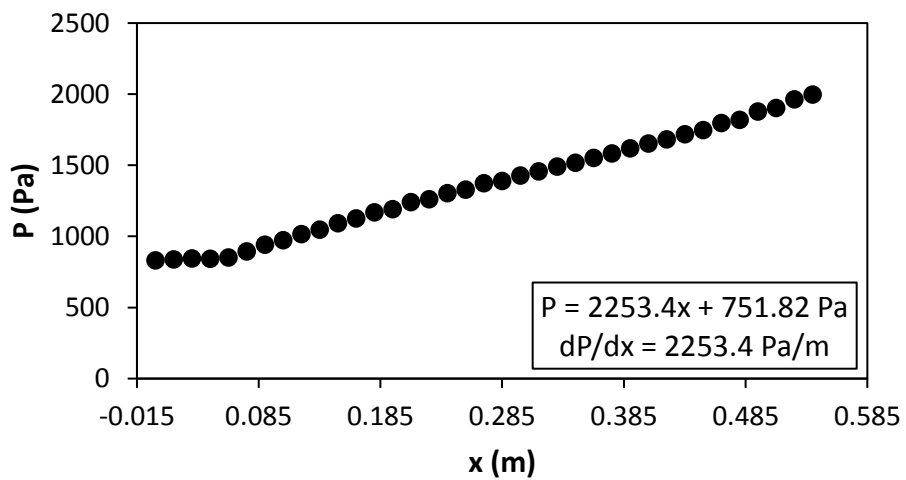


Figure G.95: Static pressure plotted against the x coordinate at Re = 6 000 for setup: $d/p = 0.2$, 45° to the flow direction.

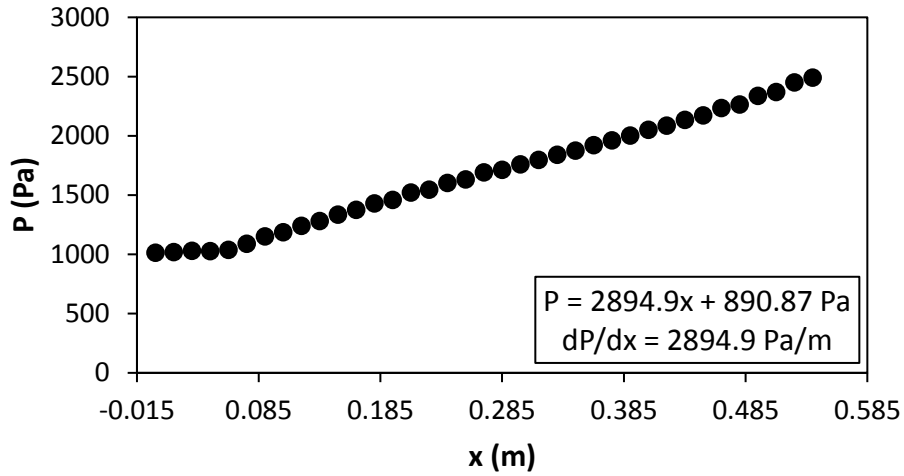


Figure G.96: Static pressure plotted against the x coordinate at $Re = 7000$ for setup: $d/p = 0.2$, 45° to the flow direction.

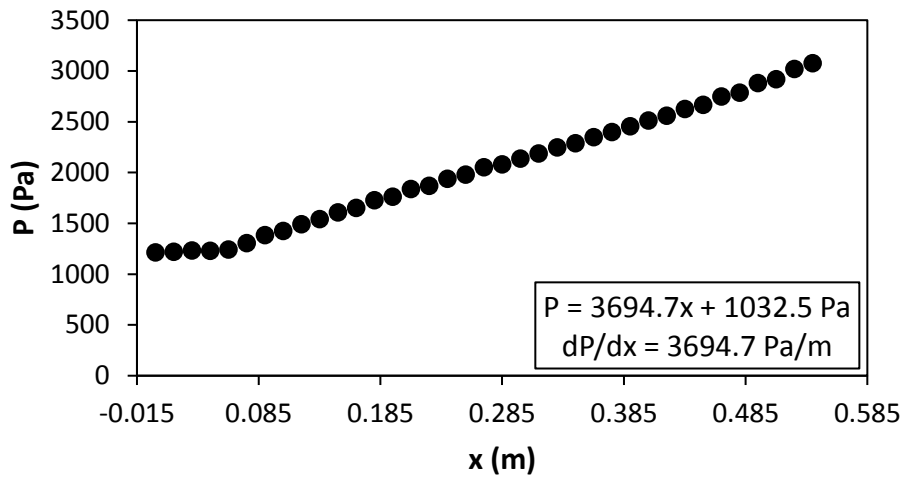


Figure G.97: Static pressure plotted against the x coordinate at $Re = 8000$ for setup: $d/p = 0.2$, 45° to the flow direction.

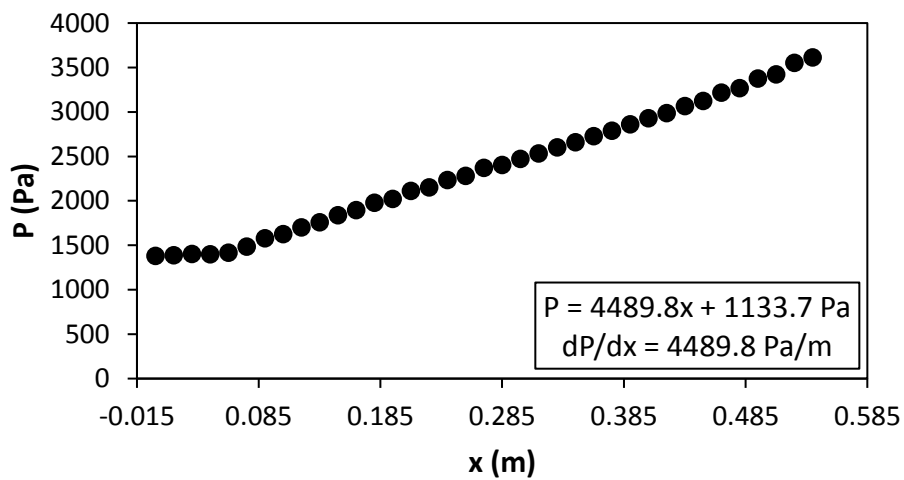


Figure G.98: Static pressure plotted against the x coordinate at $Re = 9000$ for setup: $d/p = 0.2$, 45° to the flow direction.

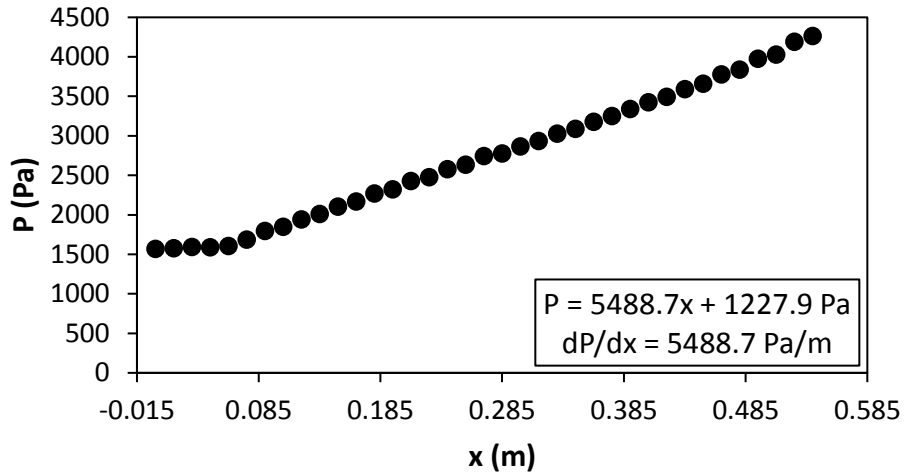


Figure G.99. Static pressure plotted against the x coordinate at $Re = 9\,700$ for setup: $d/p = 0.2$, 45° to the flow direction.

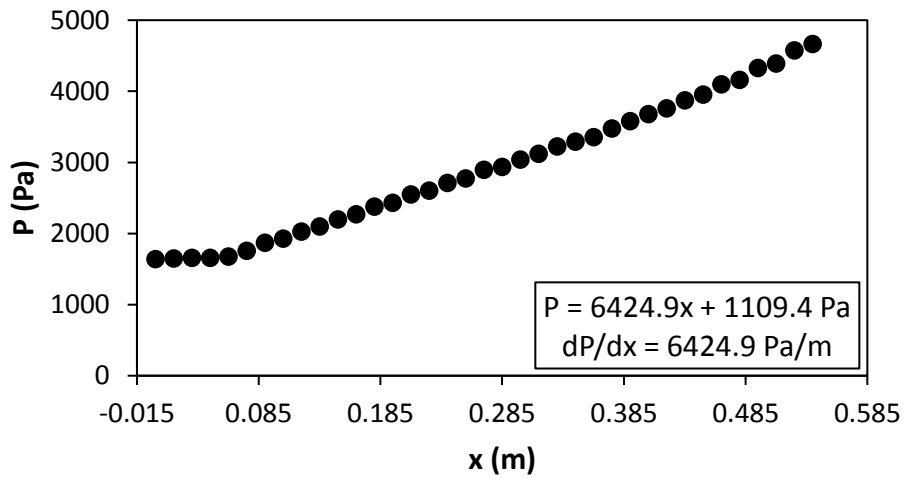


Figure G.100: Static pressure plotted against the x coordinate at $Re = 10\,500$ for setup: $d/p = 0.2$, 45° to the flow direction.

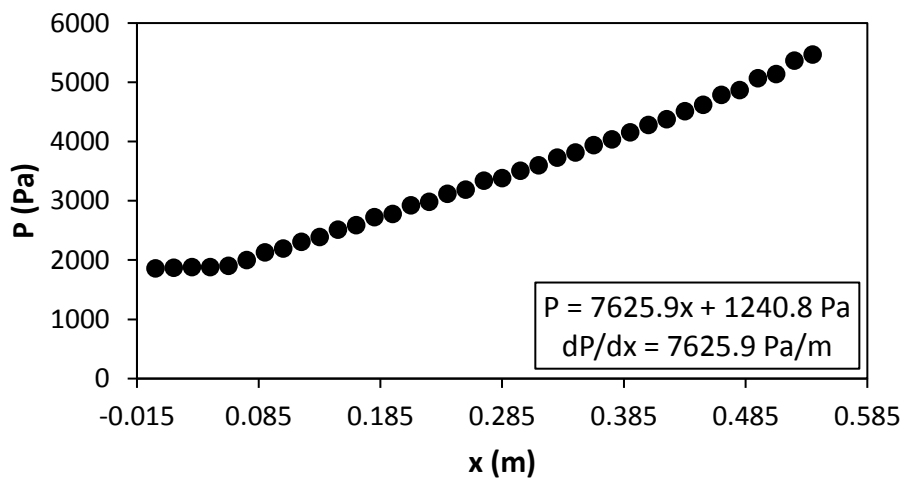


Figure G.101: Static pressure plotted against the x coordinate at $Re = 11\,500$ for setup: $d/p = 0.2$, 45° to the flow direction.

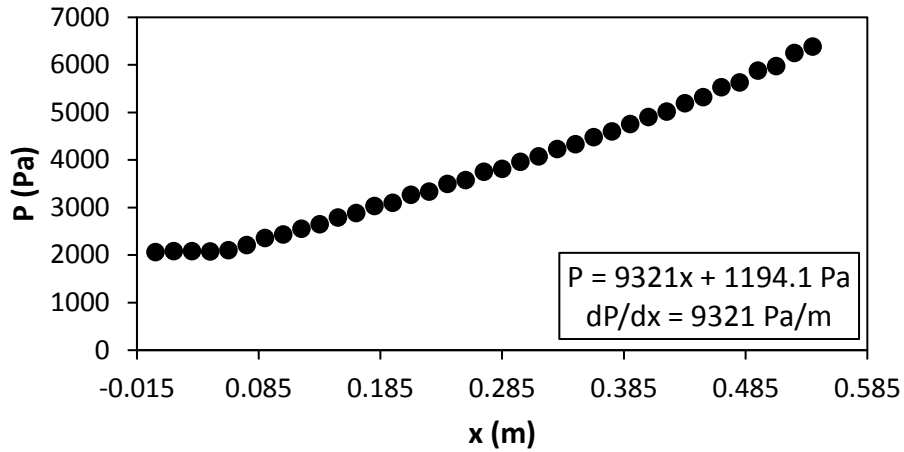


Figure G.102: Static pressure plotted against the x coordinate at $Re = 12\,500$ for setup: $d/p = 0.2$, 45° to the flow direction.

G.8. Pressure data: $d/p = 0.1$, 90° orientation to the flow direction

Figure G.103 to Figure G.117 shows the channel wall pressure for the $d/p = 0.1$ cylinders, orientated 90° to the flow direction.

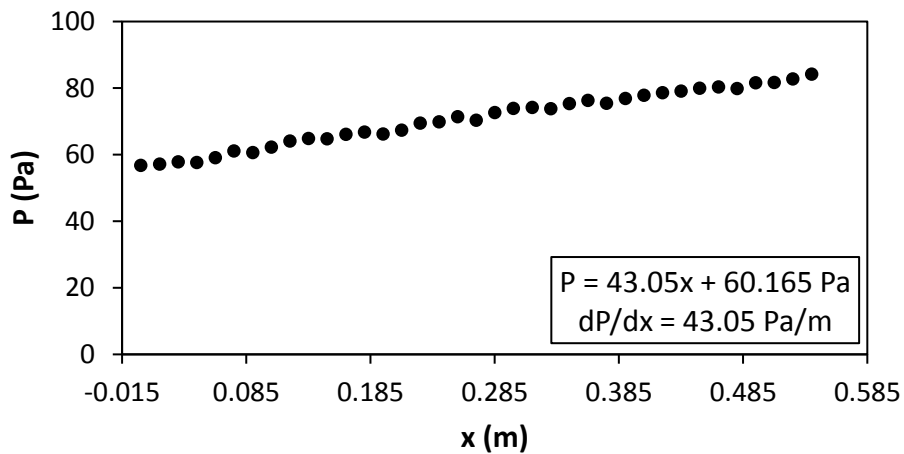


Figure G.103: Static pressure plotted against the x coordinate at $Re = 640$ for setup: $d/p = 0.1$, 90° to the flow direction.

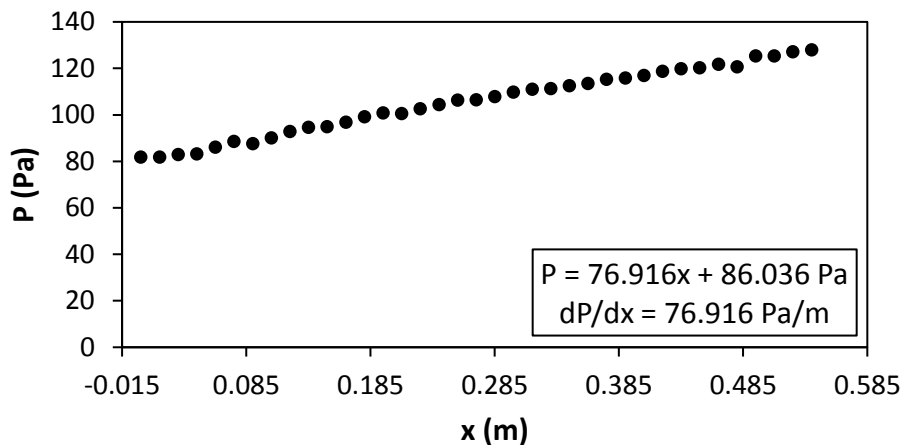


Figure G.104: Static pressure plotted against the x coordinate at $Re = 920$ for setup: $d/p = 0.1$, 90° to the flow direction.

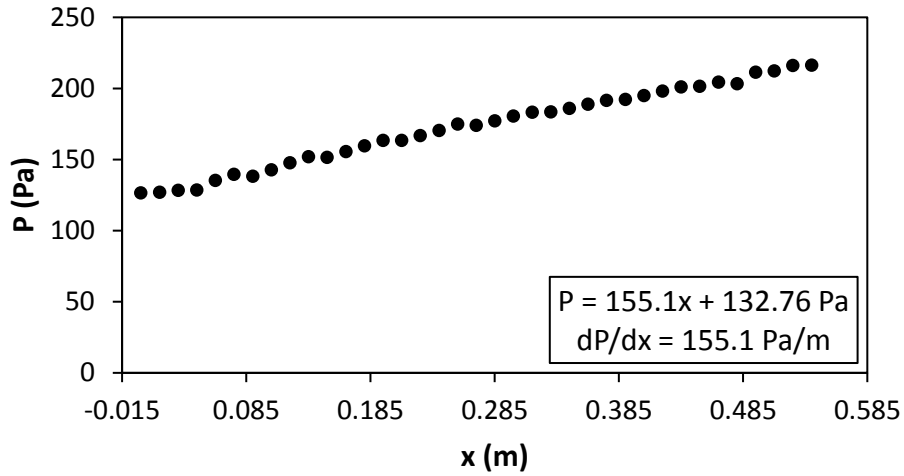


Figure G.105: Static pressure plotted against the x coordinate at $Re = 1\,400$ for setup: $d/p = 0.1$, 90° to the flow direction.

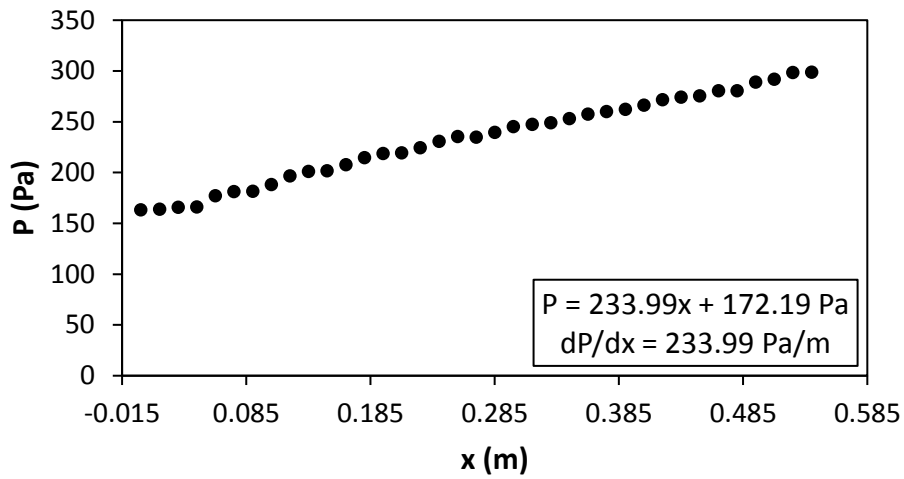


Figure G.106: Static pressure plotted against the x coordinate at $Re = 1\,800$ for setup: $d/p = 0.1$, 90° to the flow direction.

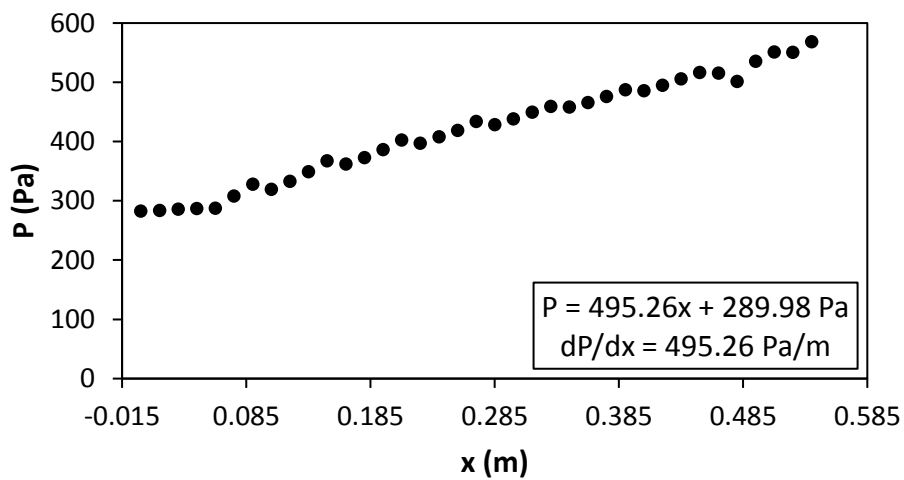


Figure G.107: Static pressure plotted against the x coordinate at $Re = 3\,000$ for setup: $d/p = 0.1$, 90° to the flow direction.

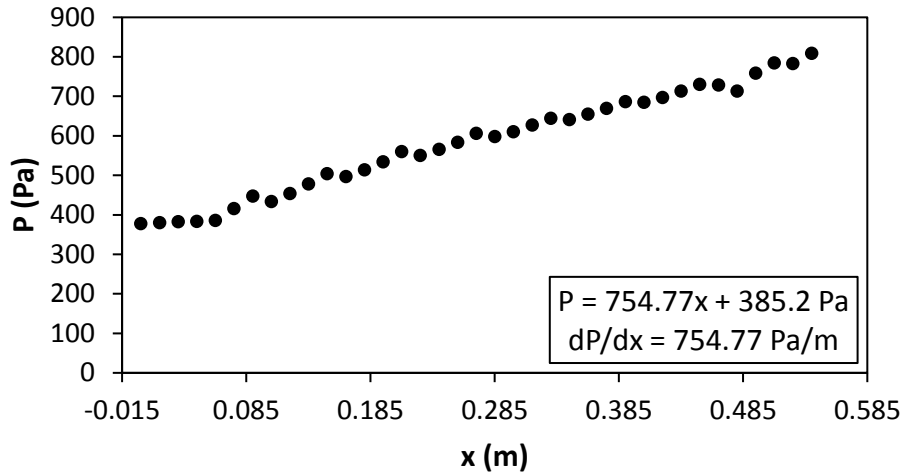


Figure G.108: Static pressure plotted against the x coordinate at $Re = 4\ 000$ for setup: $d/p = 0.1$, 90° to the flow direction.

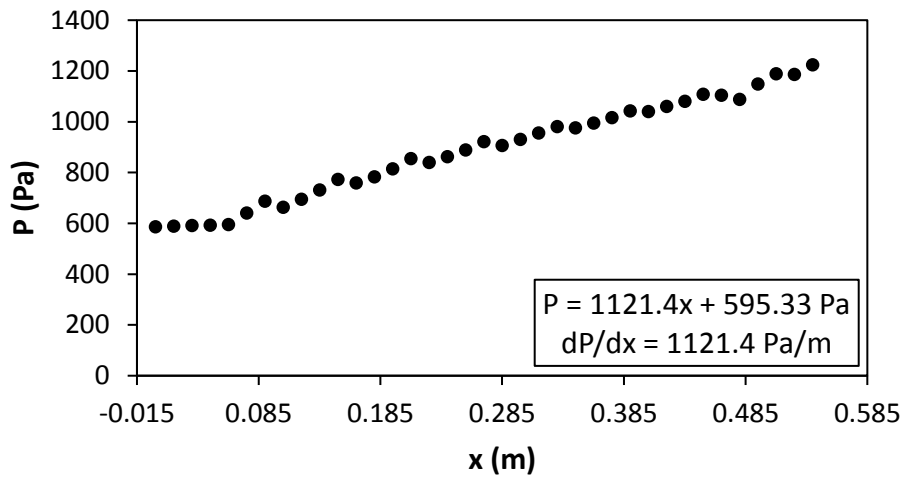


Figure G.109: Static pressure plotted against the x coordinate at $Re = 5\ 000$ for setup: $d/p = 0.1$, 90° to the flow direction.

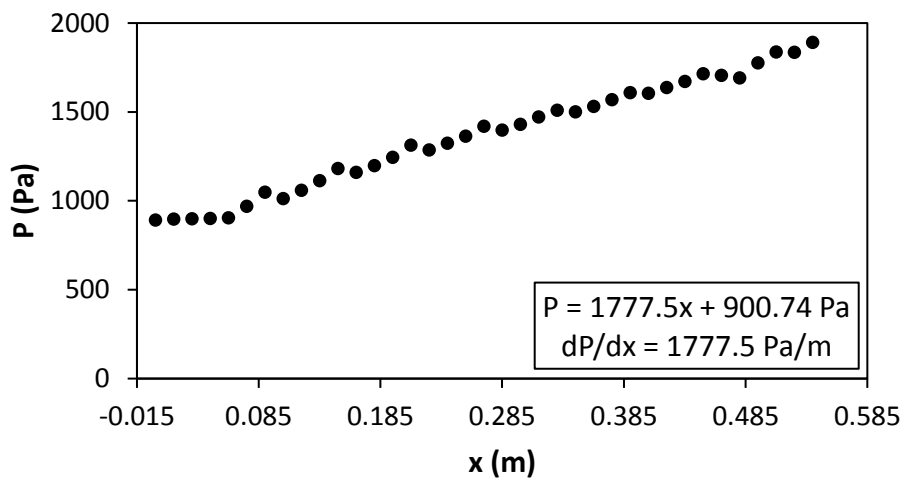


Figure G.110: Static pressure plotted against the x coordinate at $Re = 6\ 000$ for setup: $d/p = 0.1$, 90° to the flow direction.

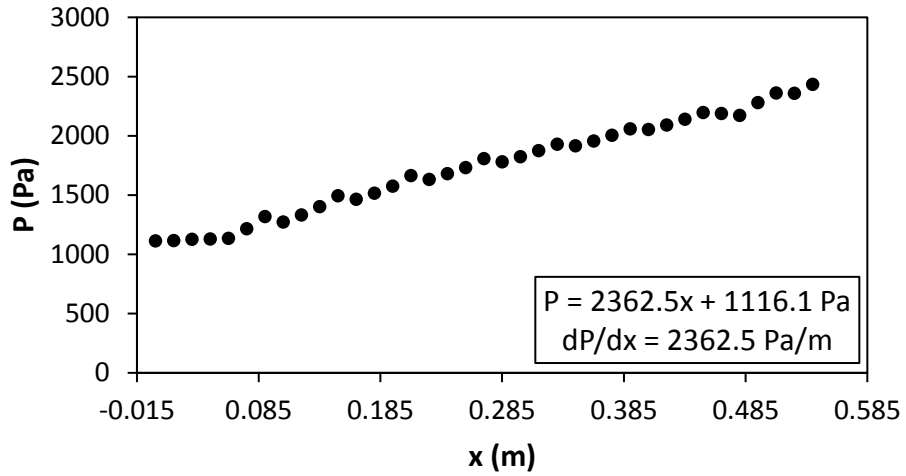


Figure G.111: Static pressure plotted against the x coordinate at $Re = 7\ 000$ for setup: $d/p = 0.1$, 90° to the flow direction.

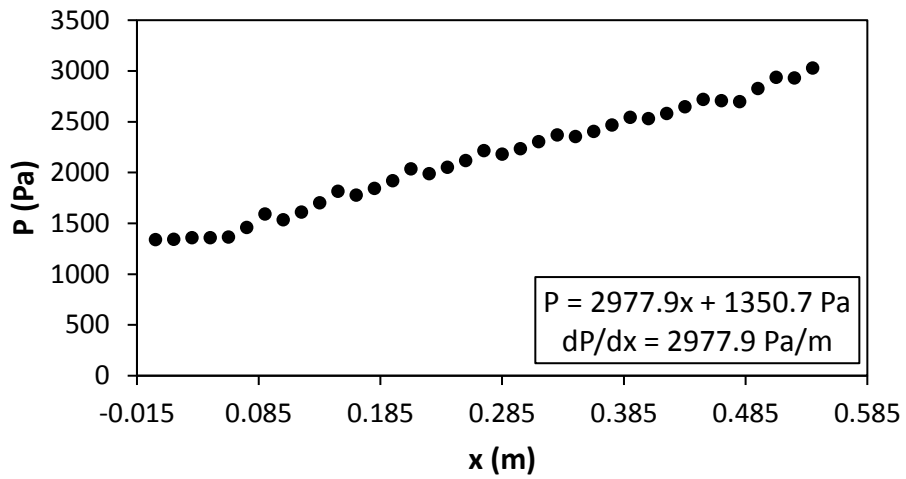


Figure G.112: Static pressure plotted against the x coordinate at $Re = 8\ 000$ for setup: $d/p = 0.1$, 90° to the flow direction.

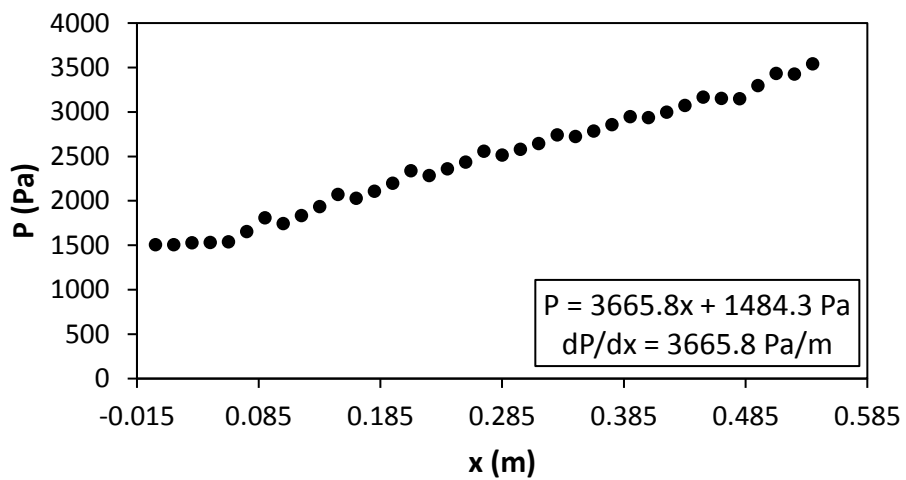


Figure G.113: Static pressure plotted against the x coordinate at $Re = 9\ 000$ for setup: $d/p = 0.1$, 90° to the flow direction.

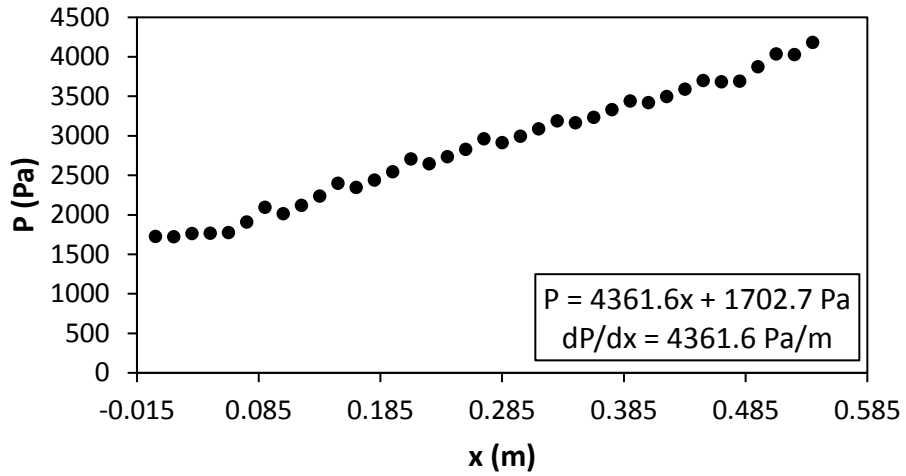


Figure G.114: Static pressure plotted against the x coordinate at $Re = 9700$ for setup: $d/p = 0.1$, 90° to the flow direction.

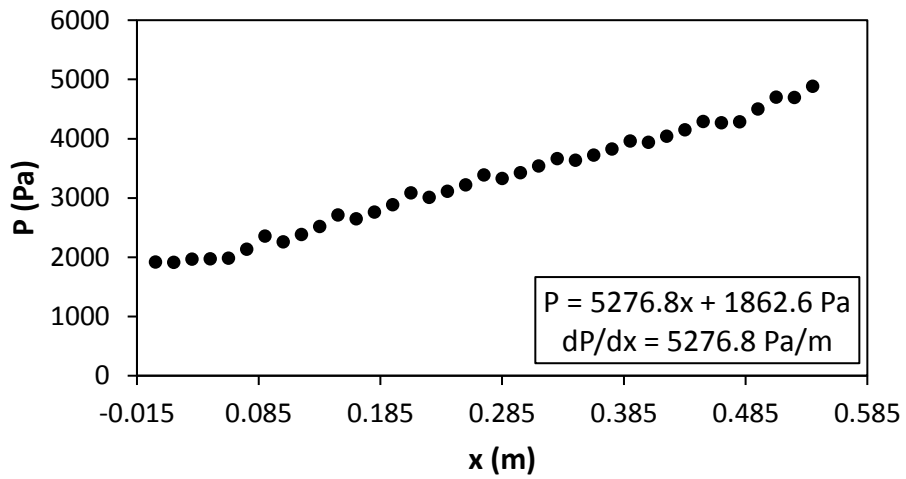


Figure G.115: Static pressure plotted against the x coordinate at $Re = 10500$ for setup: $d/p = 0.1$, 90° to the flow direction.

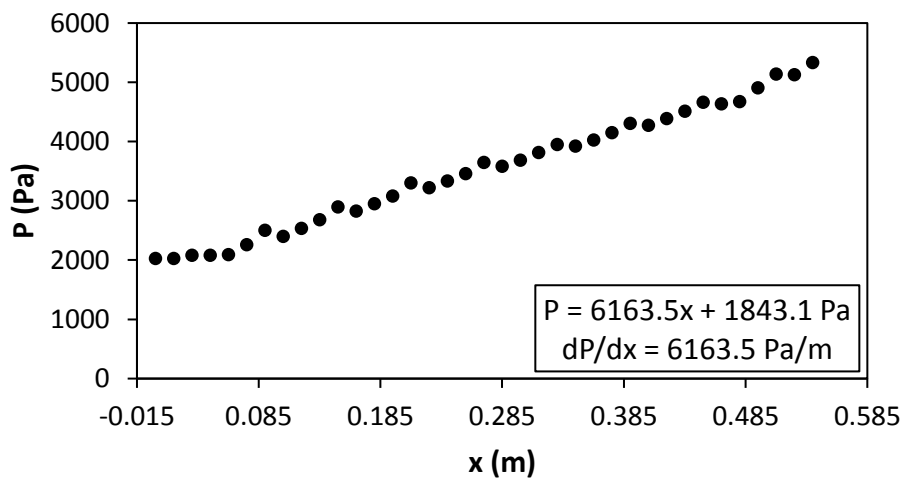


Figure G.116: Static pressure plotted against the x coordinate at $Re = 11500$ for setup: $d/p = 0.1$, 90° to the flow direction.

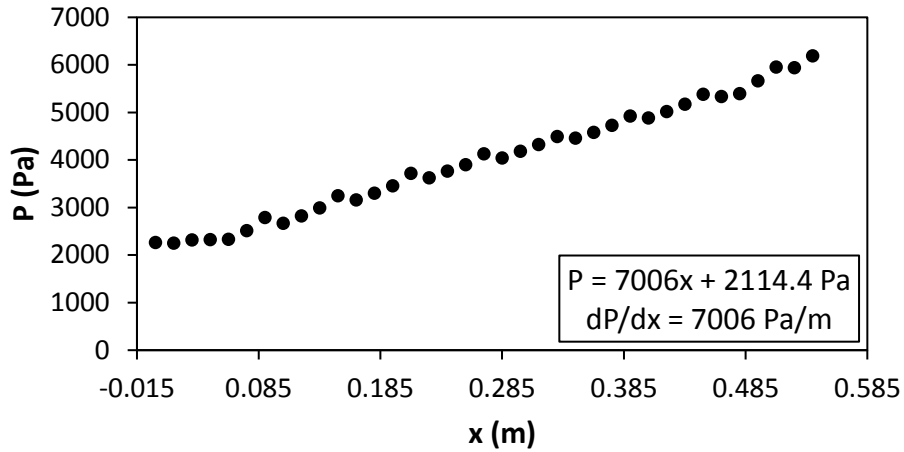


Figure G.117: Static pressure plotted against the x coordinate at $Re = 12\,500$ for setup: $d/p = 0.1$, 90° to the flow direction.

G.9. Pressure data: $d/p = 0.1$, 45° orientation to the flow direction

Figure G.118 to Figure G.132 shows the channel wall pressure for the $d/p = 0.1$ cylinders, orientated 45° to the flow direction.

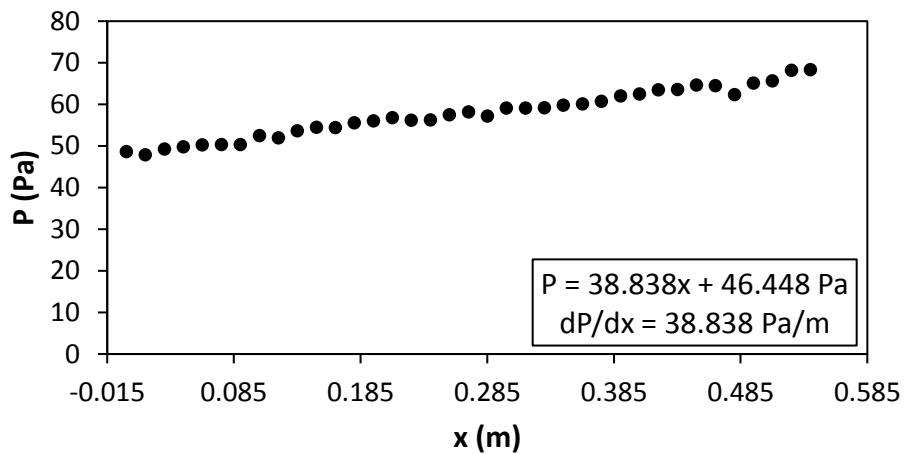


Figure G.118: Static pressure plotted against the x coordinate at $Re = 640$ for setup: $d/p = 0.1$, 45° to the flow direction.

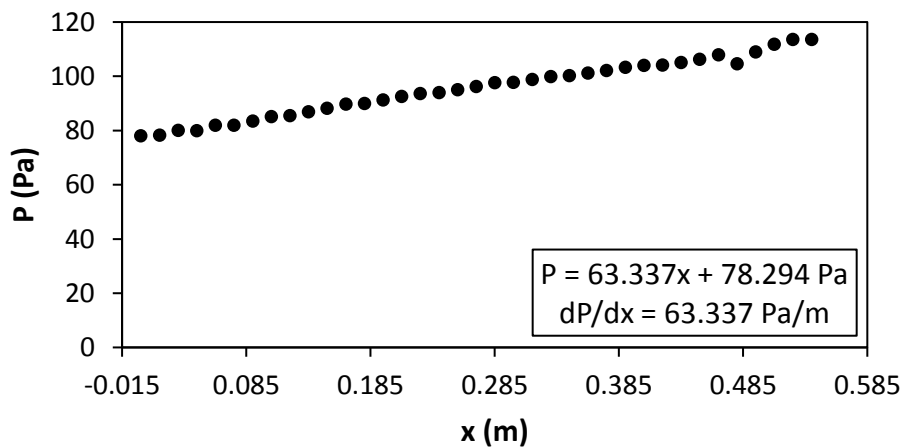


Figure G.119: Static pressure plotted against the x coordinate at $Re = 920$ for setup: $d/p = 0.1$, 45° to the flow direction.

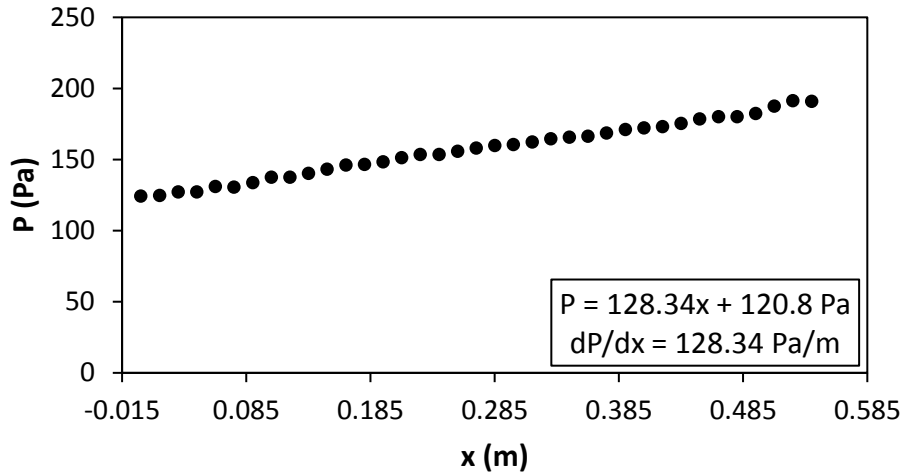


Figure G.120: Static pressure plotted against the x coordinate at $Re = 1\,400$ for setup: $d/p = 0.1$, 45° to the flow direction.

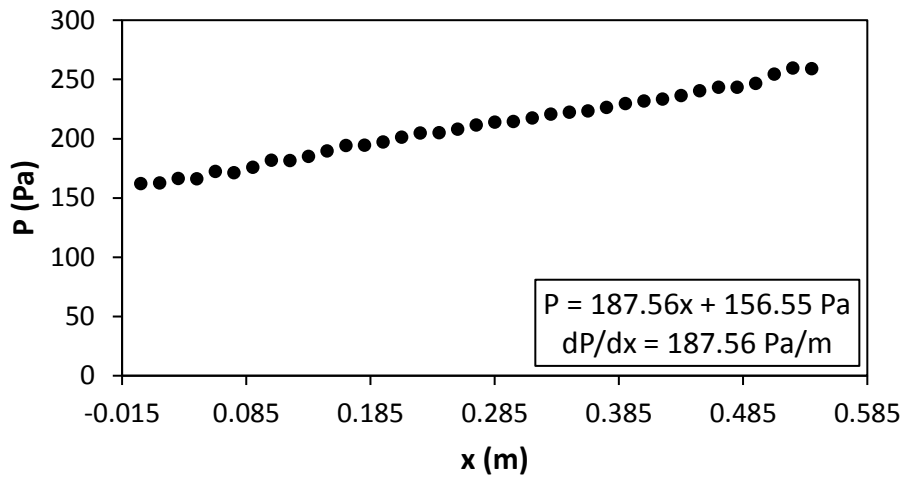


Figure G.121: Static pressure plotted against the x coordinate at $Re = 1\,800$ for setup: $d/p = 0.1$, 45° to the flow direction.

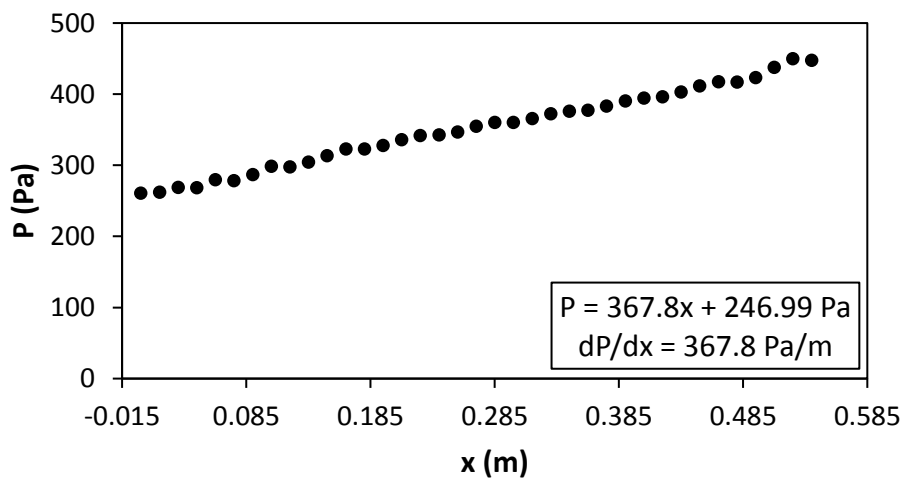


Figure G.122: Static pressure plotted against the x coordinate at $Re = 3\,000$ for setup: $d/p = 0.1$, 45° to the flow direction.

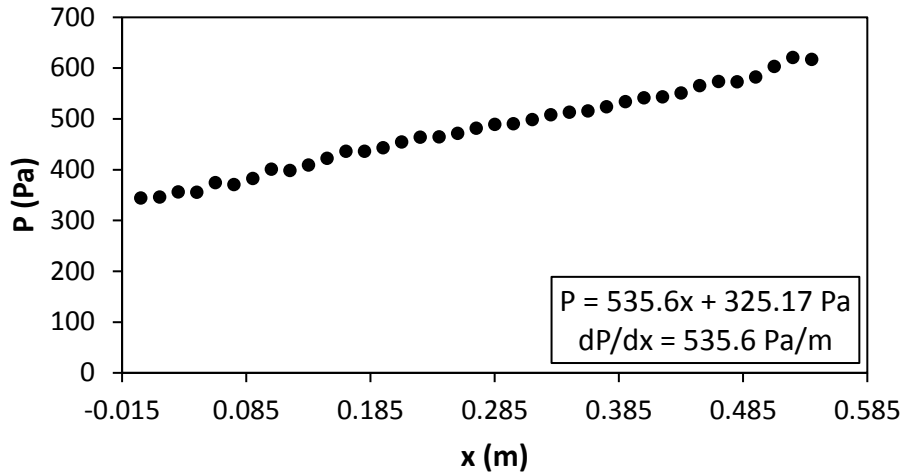


Figure G.123: Static pressure plotted against the x coordinate at $Re = 4\,000$ for setup: $d/p = 0.1$, 45° to the flow direction.

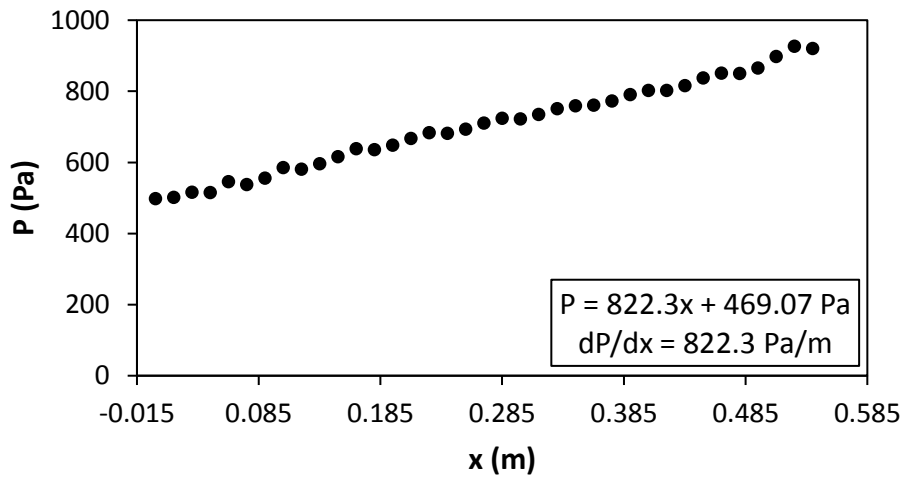


Figure G.124: Static pressure plotted against the x coordinate at $Re = 5\,000$ for setup: $d/p = 0.1$, 45° to the flow direction.

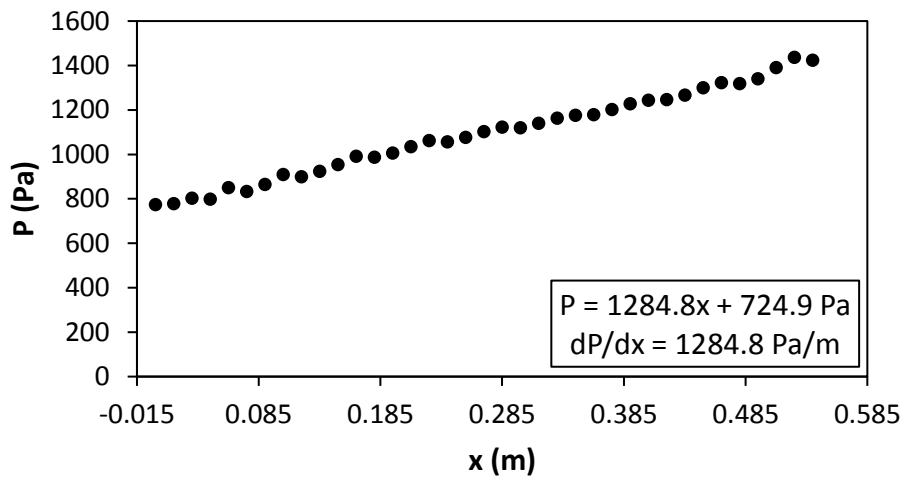


Figure G.125: Static pressure plotted against the x coordinate at $Re = 6\,000$ for setup: $d/p = 0.1$, 45° to the flow direction.

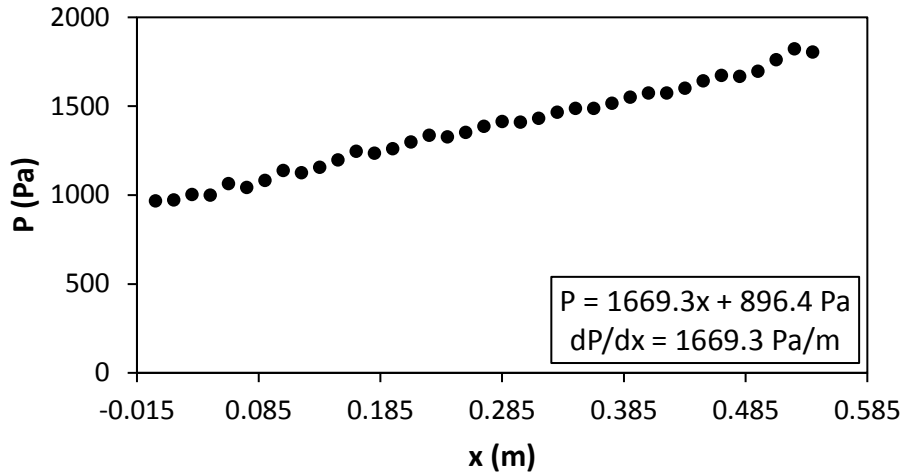


Figure G.126: Static pressure plotted against the x coordinate at $Re = 7\,000$ for setup: $d/p = 0.1$, 45° to the flow direction.

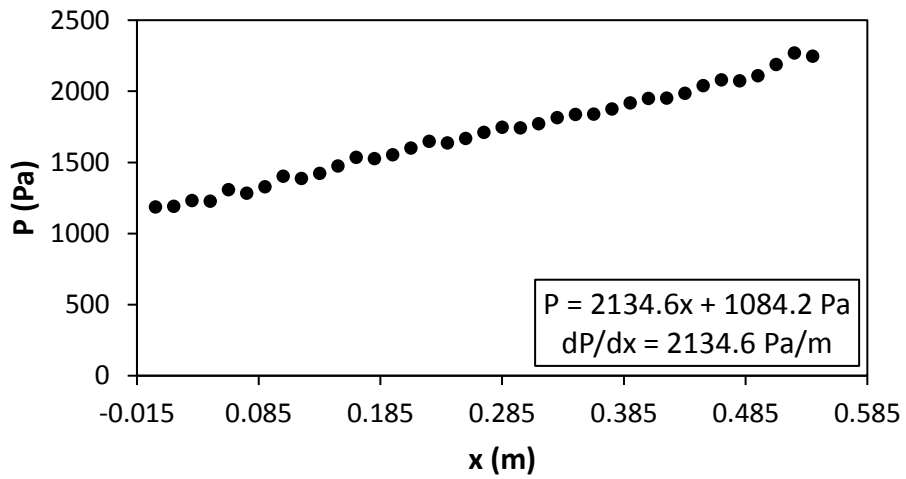


Figure G.127: Static pressure plotted against the x coordinate at $Re = 8\,000$ for setup: $d/p = 0.1$, 45° to the flow direction.

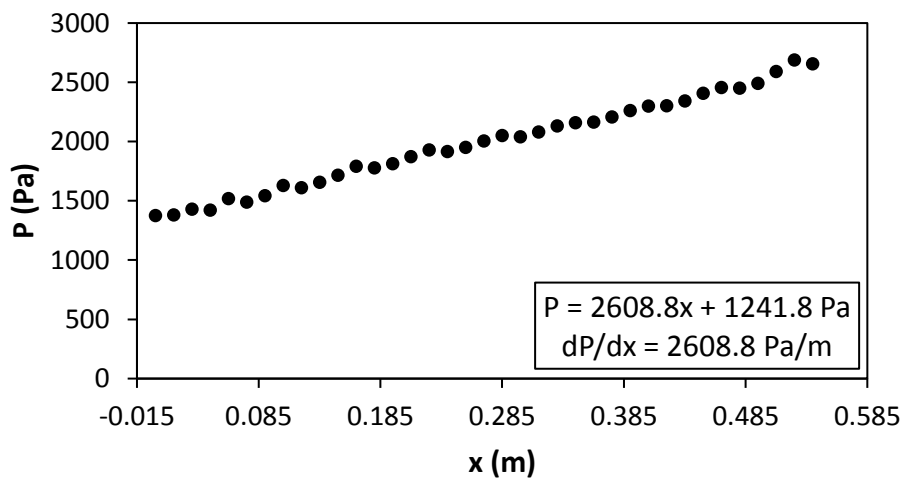


Figure G.128: Static pressure plotted against the x coordinate at $Re = 9\,000$ for setup: $d/p = 0.1$, 45° to the flow direction.

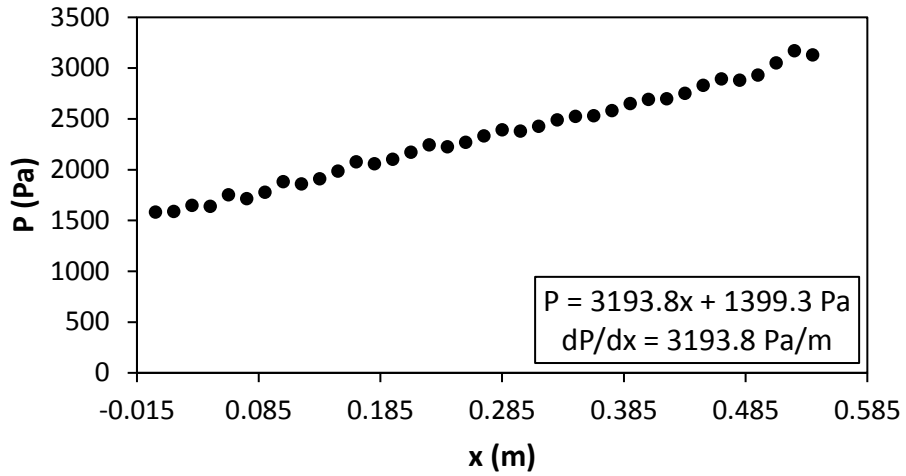


Figure G.129: Static pressure plotted against the x coordinate at $Re = 9\,700$ for setup: $d/p = 0.1$, 45° to the flow direction.

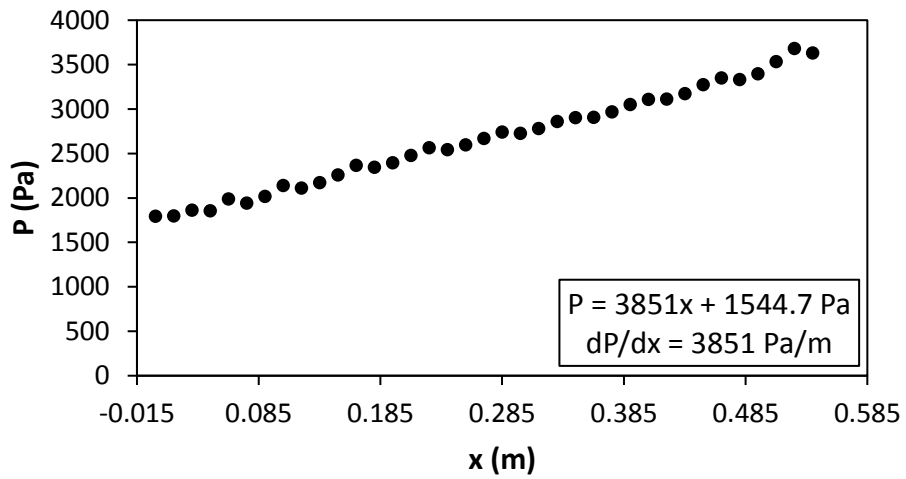


Figure G.130: Static pressure plotted against the x coordinate at $Re = 10\,500$ for setup: $d/p = 0.1$, 45° to the flow direction.

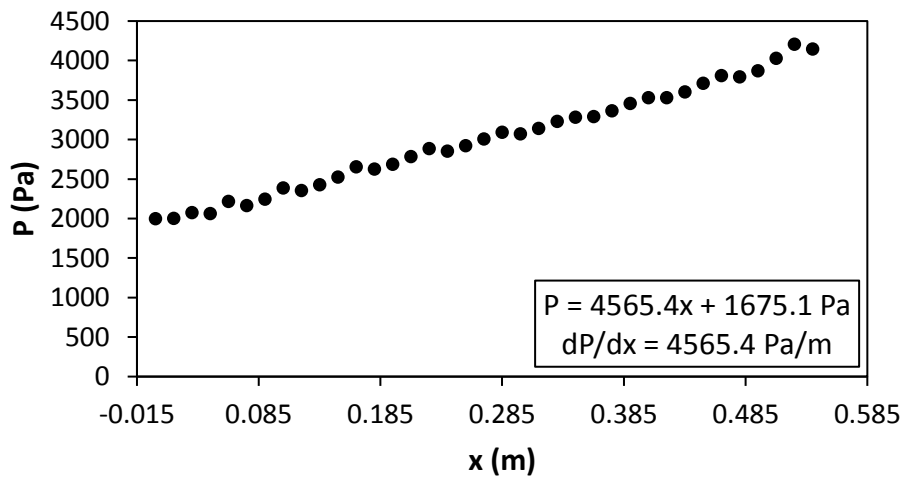


Figure G.131: Static pressure plotted against the x coordinate at $Re = 11\,500$ for setup: $d/p = 0.1$, 45° to the flow direction.

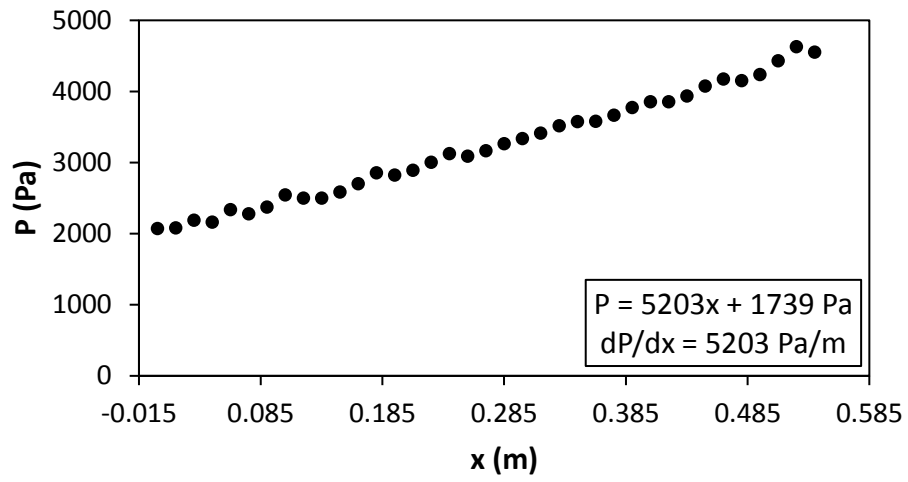


Figure G.132: Static pressure plotted against the x coordinate at $Re = 12\,500$ for setup: $d/p = 0.1$, 45° to the flow direction.